Vol. 63 ▪ No. 6 ▪ June 2022

IMPACT FACTOR
10.057

#1 NUCLEAR MEDICINE, MOLECULAR IMAGING AND MOLECULAR RADIOTHERAPY JOURNAL

JNM

The Journal of Nuclear Medicine

FEATURED ARTICLE

Head-to-Head Comparison of ^{68}Ga-PSMA-11 PET/CT and mpMRI with a Histopathology Gold Standard in the Detection, Intraprostatic Localization, and Determination of Local Extension of Primary Prostate Cancer: Results from a Prospective Single-Center Imaging Trial. Ida Sonni et al. See page 847.

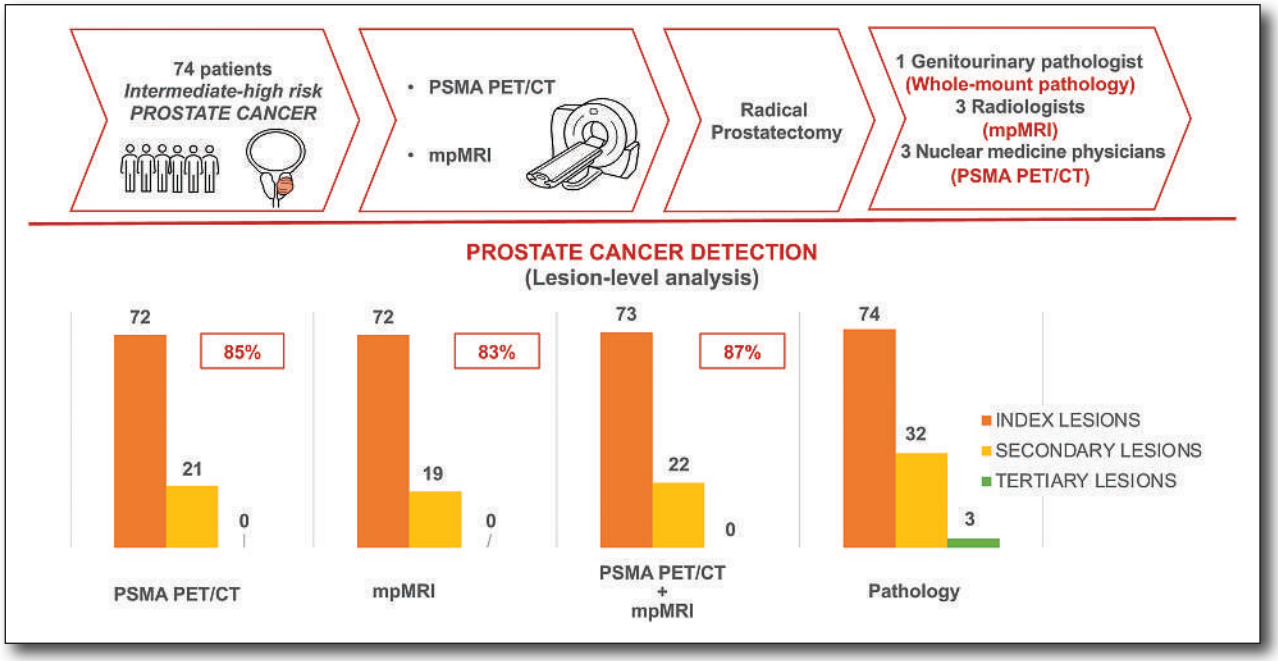

FAPI ligands: the promising pharmacokinetics of albumin binder–conjugated fibroblast activation protein inhibitors for cancer therapy. Mengxin Xu et al. See page 952.

SNMMI Value Initiative
SOCIETY OF NUCLEAR MEDICINE & MOLECULAR IMAGING


ALZHEIMER'S® ASSOCIATION | AAIC 22
WHERE DEMENTIA SCIENCE AND CAREERS ADVANCE.
Register today for the world's premier dementia research conference.
Join us in San Diego or online for the Alzheimer's Association International Conference® (AAIC®), the largest and most influential international forum dedicated to advancing dementia science. Meet with colleagues from around the world to share discoveries that will lead to methods of prevention and treatment and improvements in diagnosis for Alzheimer's disease.
AAIC 2022: July 31-Aug. 4, San Diego, USA, and Online
Educational Workshops and Preconferences: July 28-30
Exhibits: July 31-Aug. 3
Register at alz.org/AAIC-22.

SPECTRUM
DYNAMICS MEDICAL

VERITON-CT®

DIGITAL SPECT/CT

Optimization of Every Step

Spectrum Dynamics has integrated its ground-breaking BroadView Technology design into the VERITON-CT system, providing a digital platform enabling routine 3D imaging in Nuclear Medicine. The result is optimization of every step, from image acquisition to interpretation.

VERITON-CT digital SPECT/CT combines the best-in-class CZT detectors, novel system design, high resolution CT, and advanced software technology to elevate the performance of 360° digital SPECT/CT.

BroadView Technology
Proprietary swiveling detector design provides increased sensitivity for faster scans

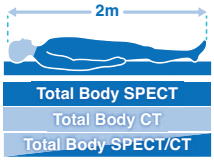

Total Body 3D Imaging
200cm continuous coverage vertex to feet
SPECT | CT | SPECT/CT

80cm NM and CT bore
Wide Bore SPECT/CT
80cm NM and CT bore

Choice of 16/64 slice
Choice of high-resolution CT for diagnostic applications and low dose total body CTAC

TruView Console
One platform, one location for clinical care decision-making:
1. Acquisition
2. Advanced quantitative reconstruction
3. Both 3D and 4D data analysis and review

VERITON-CT Feature Application: 3D Dynamic Imaging

TruFlow for VERITON-CT offers real-time 3D in-vivo fast dynamic imaging to capture the radiopharmaceutical distribution, uptake, or clearance over time in 3D SPECT/CT parametric imaging.

TruFlow

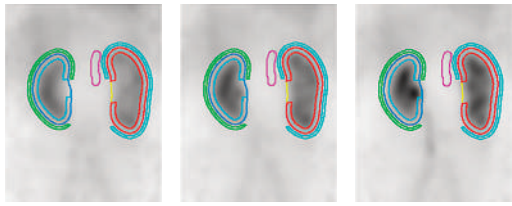

spectrum-dynamics.com

HERMIA

The All-in-One Vendor-Neutral Molecular Imaging Software

Powerful and vendor-neutral software enables clinicians to simplify their workflow, increase consistency and quality and keep pace with the fast development of scanners, tracers and procedures in nuclear medicine.

Introducing HERMIA – your smart choice in the multifaceted world of MI. Our state-of-the-art software suite provides many new ground-breaking functionalities for all PET/SPECT/CT/MR reporting.

Discover more at our booth #339 at SNMMI.

hermesmedical.com

HERMES MEDICAL SOLUTIONS

JNM

Volume 63 • Number 6 • June 2022

SNMMI NEWSLINE

EDITOR'S PAGE

COMMENTARY

DISCUSSIONS WITH LEADERS

ISSUES AND CONTROVERSIES

EDITORIAL

THE STATE OF THE ART

CONTINUING EDUCATION

HOT TOPICS

THERANOSTICS

Clinical

Translational

ONCOLOGY

Clinical

JNM The Journal of NUCLEAR MEDICINE

The Official Publication of SNMMI

MISSION STATEMENT: *The Journal of Nuclear Medicine* advances the knowledge and practice of molecular imaging and therapy and nuclear medicine to improve patient care through publication of original basic science and clinical research.

JNM (ISSN 0161-5505 [print]; ISSN 2159-662X [online]) is published monthly by SNMMI, 1850 Samuel Morse Drive, Reston, VA 20190-5316. Periodicals postage is paid at Herndon, VA, and additional mailing offices. Postmaster, send address changes to *The Journal of Nuclear Medicine,* 1850 Samuel Morse Drive, Reston, VA 20190-5316. The costs of publication of all nonsolicited articles in *JNM* were defrayed in part by the payment of page charges. Therefore, and solely to indicate this fact, these articles are hereby designated "advertisements" in accordance with 18 USC section 1734.

DISCLOSURE OF COMMERCIAL INTEREST: Johannes Czernin, MD, editor-in-chief of *The Journal of Nuclear Medicine,* has indicated that he is a founder of Sofie Biosciences and holds equity in the company and in intellectual property invented by him, patented by the University of California, and licensed to Sofie Biosciences. He is also a founder and board member of Trethera Therapeutics and holds equity in the company and in intellectual property invented by him, patented by the University of California, and licensed to Triangle. He also serves on the medical advisory board of Actinium Pharmaceuticals and on the scientific advisory boards of POINT Biopharma, RayzeBio, and Jubilant Pharma and is a consultant for Amgen. No other potential conflicts of interest were reported. Manuscripts submitted to *JNM* with potential conflicts are handled by a guest editor.

EDITORIAL COMMUNICATIONS should be sent to: Editor-in-Chief, Johannes Czernin, MD, *JNM* Office, SNMMI, 1850 Samuel Morse Drive, Reston, VA 20190-5316. Phone: (703) 326-1185; Fax: (703) 708-9018. To submit a manuscript, go to https://submit-jnm.snmjournals.org.

BUSINESS COMMUNICATIONS concerning permission requests should be sent to the publisher, SNMMI, 1850 Samuel Morse Drive, Reston, VA 20190-5316; (703) 708-9000; home page address: jnm.snmjournals.org. Subscription requests and address changes should be sent to Membership Department, SNMMI at the address above. Notify the Society of change of address and telephone number at least 30 days before date of issue by sending both the old and new addresses. Claims for copies lost in the mail are allowed within 90 days of the date of issue. Claims are not allowed for issues lost as a result of insufficient notice of change of address. For information on advertising, contact Team SNMMI (Kevin Dunn, Rich Devanna, and Charlie Meitner; (201) 767-4170; fax: (201) 767-8065; TeamSNMMI@cunnasso.com). Advertisements are subject to editorial approval and are restricted to products or services pertinent to nuclear medicine. Closing date is the first of the month preceding the date of issue.

INDIVIDUAL SUBSCRIPTION RATES for the 2022 calendar year are $603 within the United States and Canada; $648 elsewhere. Make checks payable to the SNMMI. CPC IPM Sales Agreement No. 1415158. Sales of individual back copies from 1999 through the current issue are available for $60 at http://www.snmmi.org/subscribe (subscriptions@snmmi.org; fax: (703) 667-5134). Individual articles are available for sale online at http://jnm.snmjournals.org.

JNM The Journal of NUCLEAR MEDICINE

Lantheus Xenon Xe-133 Gas

PROVEN | RELIABLE | TRUSTED

- Optimized vial size and delivery system[1]
- Calidose® Dispenser System is specifically designed and FDA approved for use with Lantheus Medical Imaging Xenon-133[1]
- Lantheus Medical Imaging is a leading U.S. manufacturer of Xenon-133[2]
- We are the longest continuous supplier of Xenon-133 since its launch in 1971[3]

Calidose® Dispenser

Specify *Lantheus Xenon Xe-133*
when ordering from your local Radiopharmacy

To order from Lantheus, contact your Lantheus Sales Representative or call Customer Service: 1-800-299-3431
www.lantheus.com

Lantheus

FIND > FIGHT > FOLLOW™

Please see full Prescribing Information on following page.

INDICATIONS AND USAGE:
Inhalation of Xenon Xe 133 Gas has proved valuable for the evaluation of pulmonary function and for imaging the lungs. It may also be applied to assessment of cerebral flow.

CONTRAINDICATIONS:
None known.

Important Safety Information:
Adverse reactions related to the use of this agent have not been reported to date.

WARNINGS:
Xenon Xe 133 Gas delivery systems, i.e., respirators or spirometers, and associated tubing assemblies must be leakproof to avoid loss of radioactivity into environs not specifically protected by exhaust systems.

Xenon Xe 133 adheres to some plastics and rubber and should not be allowed in tubing or respirator containers.

The unrecognized loss of radioactivity from the dose for administration may render the study non-diagnostic.

The vial stopper contains dry natural rubber latex and may cause allergic reactions in providers or patients who are sensitive to latex.

PRECAUTIONS:
General:
Xenon Xe 133, as well as other radioactive drugs, must be handled with care and appropriate safety measures should be used to minimize radiation exposure to patients and to clinical personnel.

Radiopharmaceuticals should be used only by physicians who are qualified by training and experience in the safe use and handling of radionuclides and whose experience and training have been approved by the appropriate government agency authorized to license the use of radionuclides.

References: 1. Xenon Xe-133 Gas [package insert], N. Billerica, MA: Lantheus Medical Imaging, Inc. 2. ©2022 Millennium Research Group, Inc. All rights reserved. Reproduction, distribution, transmission or publication is prohibited. Reprinted with permission. 3. Quality data on file, Lantheus Medical Imaging, Inc.

XENON Xe 133 GAS

FOR DIAGNOSTIC USE

DESCRIPTION: Xenon Xe 133 Gas is supplied in a mixture of xenon gas (5%) in carbon dioxide (95%). It is contained within septum sealed glass vials and is suitable for inhalation in the diagnostic evaluation of pulmonary function and imaging, as well as assessment of cerebral blood flow. Xenon Xe 133 Gas is reactor-produced as a by-product of Uranium U235 fission. Each vial contains the labeled amount of Xenon Xe 133 radioactivity at the time of calibration. The contents of the vial are in gaseous form, contain no preservatives, and are ready for use.

Xenon Xe 133 is chemically and physiologically related to elemental Xenon, a non-radioactive monoatomic gas which is physiologically inert except for anesthetic properties at high doses.

PHYSICAL CHARACTERISTICS

Xenon Xe 133 decays by beta and gamma emissions with a half-life of 5.245 days.[1] Significant radiations which are emitted by the nuclide are listed in Table 1.

Table 1. Principal Radiation Emission Data from Xenon-133

Radiation	Mean Energy (KeV)	Mean % per Disintegration
Beta-2	100.6	99.3
Ce-K-2	45.0	53.3
Ce-L-2	75.3	8.1
Ce-M-2	79.8	1.7
Gamma-2	81.0	36.5
$K_{\alpha 2}$X-ray	30.6	13.6
$K_{\alpha 1}$X-ray	31.0	25.3
K_{β}X-ray	35.0	9.1

[1]Kocher, David C., "Radioactive Decay Data Tables," DOE/TIC-11026, p. 138,1981.

EXTERNAL RADIATION

The specific gamma ray constant for Xenon Xe 133 is 3.6 microcoulombs/Kg-MBq-hr (0.51R/hr-mCi) at 1 cm. The first half value thickness of lead is 0.0035 cm. A range of values for the relative attenuation of the radiation emitted by this radionuclide that results from the interposition of various thicknesses of Pb is shown in Table 2. For example, the use of 0.20 cm of Pb will decrease the external radiation exposure by a factor of 1,000.

Table 2. Radiation Attenuation by Lead Shielding

cm of Pb	Radiation Attenuation Factor
0.0035	0.5
0.037	10^{-1}
0.12	10^{-2}
0.20	10^{-3}
0.29	10^{-4}

To correct for physical decay of this radionuclide, the fractions that remain at selected time intervals after the time of calibration are shown in Table 3.

Table 3. Xenon Xe 133 Physical Decay Chart (Half Life 5.245 days)

Day	Fraction Remaining	Day	Fraction Remaining
0*	1.000	8	.349
1	.877	9	.302
2	.768	10	.268
3	.674	11	.235
4	.591	12	.206
5	.518	13	.181
6	.452	14	.157
7	.398		

* Calibration day

CLINICAL PHARMACOLOGY: Xenon Xe 133 is a readily diffusible gas which is neither utilized nor produced by the body. It passes through cell membranes and freely exchanges between blood and tissue. It tends to concentrate more in body fat than in blood, plasma, water or protein solutions. In the concentrations used for diagnostic purposes it is physiologically inactive. Inhaled Xenon Xe 133 Gas will enter the alveolar wall and enter the pulmonary venous circulation via the capillaries. Most of the Xenon Xe 133 that enters the circulation from a single breath is returned to the lungs and exhaled after a single pass through the peripheral circulation.

INDICATIONS AND USAGE: Inhalation of Xenon Xe 133 Gas has proved valuable for the evaluation of pulmonary function and for imaging the lungs. It may also be applied to assessment of cerebral flow.

CONTRAINDICATIONS: None known.

WARNINGS:

Xenon Xe 133 Gas delivery systems, i.e., respirators or spirometers, and associated tubing assemblies must be leakproof to avoid loss of radioactivity into the environs not specifically protected by exhaust systems.

Xenon Xe 133 adheres to some plastics and rubber and should not be allowed to stand in tubing or respirator containers. The unrecognized loss of radioactivity from the dose for administration may render the study non-diagnostic.

The vial stopper contains dry natural rubber latex and may cause allergic reactions in providers or patients who are sensitive to latex.

PRECAUTIONS:

General

Xenon Xe 133, as well as other radioactive drugs, must be handled with care and appropriate safety measures should be used to minimize radiation exposure to clinical personnel. Also, care should be taken to minimize radiation exposure to patients consistent with proper patient management.

Exhaled Xenon Xe 133 Gas should be controlled in a manner that is in compliance with the appropriate regulations of the government agency authorized to license the use of radionuclides.

Radiopharmaceuticals should be used only by physicians who are qualified by training and experience in the safe use and handling of radionuclides and whose experience and training have been approved by the appropriate government agency authorized to license the use of radionuclides.

Carcinogenesis, Mutagenesis, Impairment of Fertility

No long term animal studies have been performed to evaluate carcinogenic potential or whether Xenon Xe 133 affects fertility in males or females.

Pregnancy

Animal reproductive studies have not been conducted with Xenon Xe 133 Gas. It is also not known whether Xenon Xe 133 Gas can cause fetal harm when administered to a pregnant woman or can affect reproduction capacity. Xenon Xe 133 Gas should be given to a pregnant woman only if clearly needed.

Ideally, examination using radiopharmaceuticals, especially those elective in nature in a woman of childbearing capability, should be performed during the first few (approximately 10) days following the onset of menses.

Nursing Mothers

It is not known whether Xenon Xe 133 is excreted in human milk. Many drugs are excreted in human milk, therefore formula feedings should be substituted for breast feeding, because of the potential for adverse reactions in nursing infants.

Pediatric Use

Safety and effectiveness in the pediatric population has not been established.

Geriatric Use

Clinical studies of Xenon Xe 133 Gas did not include sufficient numbers of subjects aged 65 and over to determine whether they respond differently from younger subjects. Other reported clinical experience has not identified differences in responses between the elderly and younger patients. In general, dose selection for an elderly patient should be cautious, usually starting at the low end of the dosage range, reflecting the greater frequency of decreased hepatic, renal, or cardiac function, and of concomitant disease or other drug therapy.

ADVERSE REACTIONS: Adverse reactions related to the use of this agent have not been reported to date.

DOSAGE AND ADMINISTRATION: Xenon Xe 133 Gas is administered by inhalation from closed respirator systems or spirometers.

The suggested activity range employed for inhalation by the average adult patient (70 kg) is:

Pulmonary function including imaging: 74-1110 MBq (2-30 mCi) in 3 liters of air.

Cerebral blood flow: 370-1110 MBq (10-30 mCi) in 3 liters of air.

The patient dose should be measured by a suitable radioactivity calibration system immediately prior to administration.

RADIATION DOSIMETRY

The estimated absorbed radiation doses[2] to an average patient (70 kg) for pulmonary perfusion and cerebral blood flow studies from a maximum dose of 1110 MBq (30 mCi) of Xenon Xe 133 in 3 liters of air are shown in Table 4.

Table 4. Radiation Doses

	Effective Half-Time	Lungs*	Brain	Whole Body
			mGy/1110 MBq	(rads/30 mCi)
Pulmonary Perfusion	2 min.	2.5 (0.25)	0.014 (0.0014)	0.027 (0.0027)
Cerebral Blood Flow	5 min.	6.3 (0.63)	0.035 (0.0035)	0.068 (0.0068)

* 99% of activity is in lungs.

[2]Method of Calculation: A Schema for Absorbed-Dose Calculation for Biologically Distributed Radionuclides, Supplement No. 1, MIRD pamphlet No. 1, *J. Nucl. Med.*, p.7 (1968).

HOW SUPPLIED: The Xenon Xe 133 Gas is supplied as part of the Calidose™ system, consisting of 3 mL unit dose vials and the Calidose™ dispenser for shielded dispensing.

Normally vials containing either 370 or 740 MBq (10 or 20 mCi)/vial, packed 1 vial or 5 vials per shield tube, are supplied.

The NDC number for: 10 mCi vial is 11994-127; 20 mCi vial is 11994-128.

Store at room temperature.

This radiopharmaceutical is approved for distribution to persons licensed pursuant to the Code of Massachusetts Regulations 105 CMR 120.100 for the uses listed in 105 CMR 120.547 or 120.552 or under equivalent regulations of the U.S. Nuclear Regulatory Commission, an Agreement State, or a Licensing State.

The contents of the vial are radioactive. Adequate shielding and handling precautions must be maintained.

Lantheus Medical Imaging, Inc.

331 Treble Cove Rd., N. Billerica, MA 01862 USA
For Ordering Tel. Toll Free 800-299-3431
(For Massachusetts & International, Call 978-667-9531)
All Other Business 800-362-2668

Patent: http://www.lantheus.com/patents/index.html

Printed in U.S.A.
515083-0719

Letter from Ukraine: Kmetyuk Yaroslav, a Kyiv physician whose hospital departments perform both nuclear medicine imaging and radiation therapy, reports on the challenges of providing continuity of care in an environment of wartime shortages and uncertainties. . . . . ***Page 807***

Discussions with leaders: Lale Kostakoglu talks with Peter J. O'Dwyer, Group Cochair of the Eastern Cooperative Oncology Group–American College of Radiology Imaging Network Cancer Research Group, about the role of precision medicine in cooperative trials. . . . . ***Page 808***

PSMA−/^{18}F-FDG+ mCRPC: Jadvar focuses on the utility of adding ^{18}F-FDG imaging in the clinical setting of prostate-specific membrane antigen radioligand therapy in metastatic castration-resistant prostate cancer. . . . . ***Page 812***

VISION trial and PET criteria: Kuo and colleagues review the origins of the VISION trial and the development of novel PET/CT criteria for patient selection. . . . . ***Page 816***

Guidelines for theranostics: Lee and colleagues from Australia summarize suggested theranostic guidelines for nuclear medicine, addressing specialist qualifications, patient care, radiopharmaceutical production, radiation safety, and dosimetry. . . . . ***Page 819***

^{177}Lu-PSMA and prostate cancer: Sartor and Herrmann provide an educational overview of the critical elements of the VISION phase III trial and the ways in which these elements are likely to shape regulatory decision making and clinic practice. . . . . ***Page 823***

Tau, amyloid, and atrophy: Malpetti and colleagues review the evolution of PET radiotracers that bind selectively to amyloid-β plaques and tau neurofibrillary tangles, highlighting the promise of tau PET in precision medicine approaches to Alzheimer disease. . . . . ***Page 830***

Comparative PSMA ligand dosimetry: Feuerecker and colleagues compare pretherapeutic clinical dosimetry data for ^{177}Lu-rhPSMA-7.3 and ^{177}Lu-PSMA I&T in patients with metastatic castration-resistant prostate cancer. . . . . ***Page 833***

^{225}Ac-PSMA RLT in mCRPC: Lee and Kim detail the results of a metaanalysis of reports on the therapeutic effects of ^{225}Ac-PSMA radioligand therapy in patients with metastatic castration-resistant prostate cancer. . . . . ***Page 840***

PET and DLBCL response: Sonni and colleagues contrast the diagnostic performances of ^{68}Ga-PSMA-11 PET/CT, multiparametric MRI, and the 2 techniques combined with that of histopathology in detection, intraprostatic localization, and determination of local extension of primary prostate cancer. . . . . ***Page 847***

Clinical ^{18}F-DCFPyL PET: Song and colleagues review key data that justify clinical use of ^{18}F-DCFPyL, as well as aspects of protocol implementation and image interpretation important to physicians who will interpret ^{18}F-DCFPyL PET/CT and PET/MR imaging. . . . . ***Page 855***

PET and FAPI dimers: Younis and colleagues provide perspective on the promise and challenges of fibroblast activation protein inhibitors in targeted radionuclide theranostics and preview a related article in this issue of *JNM*. . . . . ***Page 860***

^{68}Ga-labeled FAPI dimer: Zhao and colleagues detail the design of and initial studies with ^{68}Ga-DOTA-2P(fibroblast activation protein inhibitor)$_2$ to optimize pharmacokinetics and evaluate its effectiveness compared with monomeric analogs. . . . . ***Page 862***

^{124}I-MIBG PET/CT in pheochromocytoma: Weber and colleagues analyze the sensitivity, specificity, and positive- and negative-predictive values of ^{124}I-MIBG PET in suspected recurrence of pheochromocytoma and compare detection rates with those of contrast-enhanced CT. . . . . ***Page 869***

FAPI PET/CT in HNCUP: Gu and colleagues evaluate the performance of ^{68}Ga-FAPI PET/CT for detecting primary tumors in patients with head and neck cancer of unknown primary and negative ^{18}F-FDG findings. . . . . ***Page 875***

Predictors of toxicity after ^{90}Y RE: Cousins and colleagues report on pretreatment blood cytokine levels as predictors of toxicity after ^{90}Y radioembolization in intrahepatic malignancies, with potential as a biomarker-driven personalized approach to treatment. . . . . ***Page 882***

^{68}Ga-FAPI PET pitfalls: Kessler and colleagues summarize common findings and pitfalls in interpretation and assessment of fibroblast-activation protein inhibitor PET/CT imaging as part of the diagnostic workup of patients with cancer. . . . . ***Page 890***

PD-L1 and melanoma brain mets: Nimmagadda looks at the potential for noninvasive quantification of programmed cell death ligand 1 in immunotherapeutic approaches in melanoma brain metastases and previews a related article in this issue of *JNM*. . . . . ***Page 897***

PET and PD-L1 in melanoma: Nienhuis and colleagues use ^{18}F-BMS986192 PET to assess programmed cell death ligand 1 expression and variability in metastatic tracer uptake in relation to tumor response, with a focus on melanoma brain metastases. . . . . ***Page 899***

Surveillance PET/CT in MCC: Mahajan and colleagues investigate the diagnostic and prognostic value of ^{18}F-FDG PET/CT for surveillance imaging in patients treated for stage III Merkel cell carcinoma. . . . . ***Page 906***

PARPi-FL in BCC diagnosis: Sahu and colleagues describe the use of this exogenous nuclear poly(adenosine diphosphate ribose) polymerase–targeted fluorescent contrast agent in combined fluorescence and reflectance confocal microscopy to improve basal cell carcinoma diagnosis. . . . . ***Page 912***

NSCLC PET radiomics: Kolinger and colleagues explore how radiomic features associated with intratumoral heterogeneity in non–small cell lung cancer are affected by changes in ^{18}F-FDG uptake time, image reconstruction, lesion delineation, and radiomic binning settings. . . . . ***Page 919***

Covariance analysis of ictal SPECT: Taherpour and colleagues analyze covariance patterns on ictal perfusion SPECT using a scaled subprofile model for unbiased identification of patterns predictive of outcomes in temporal lobe epilepsy surgery. . . . . ***Page 925***

Flortaucipir and 4R tau lesions: Josephs and colleagues explore whether ^{18}F-flortaucipir uptake on PET is associated with differential affinities for histologic lesion type in 4-repeat tauopathies such as progressive supranuclear palsy and corticobasal degeneration. . . . . ***Page 931***

GluN2B subunit imaging in humans: Rischka and colleagues report on the performance characteristics of (*R*)-^{11}C-Me-NB1 in a first-in-humans study using PET to map GluN2B-enriched *N*-methyl-D-aspartate receptors in the brain. . . . . ***Page 936***

Preclinical SV2A PET in HD: Bertoglio and colleagues delineate changes in synaptic vesicle glycoprotein 2A density by means of ^{11}C-UCB-J small-animal PET imaging in the central nervous system of mice with Huntington disease. . . . . ***Page 942***

In vivo arterial FAPI imaging: Wu and colleagues explore the potential of a ^{68}Ga-labeled fibroblast-activating protein inhibitor for PET/CT imaging of fibroblast activation in the arterial wall. . . . . ***Page 948***

Radiotherapy ligands for FAP: Xu and colleagues describe development and initial studies in mice of 2 albumin binder–conjugated fibroblast activation protein inhibitor radiotracers for cancer therapy. . . . . ***Page 952***

Ultra-low ^{18}F-FDG activity: Hu and colleagues evaluate the feasibility of ultra-low ^{18}F-FDG activity in total-body PET/CT oncologic studies. . . . . ***Page 959***

LILLY IN ALZHEIMER'S DISEASE:

ADVANCING THE SCIENCE, CARING FOR PEOPLE

At Lilly, patients and loved ones are at the center of everything we do. For over 30 years, we have been committed to the development of both diagnostics and therapeutics in the AD space. Through our innovation, we have advanced the field by helping to shape the standards for Alzheimer's Disease research.

VISIT LILLY.COM TO LEARN MORE

Lilly


Meet ITM, an established **global player in the radioisotope & radiopharmaceutical field**, at the SNMMI 2022 Annual Meeting.
June 11-14, Vancouver
Visit us at booth #227
www.itm-radiopharma.com
Follow us:
itm
PASSION FOR PRECISION

JNM Editors' Choice Awards for 2021

Johannes Czernin, MD, editor-in-chief of *The Journal of Nuclear Medicine* (*JNM*), and his associate editors and editorial board announced in April the articles chosen as the most outstanding contributions to the journal appearing in 2021. The *JNM* Editors' Choice Awards are presented in June as part of the SNMMI Annual Meeting. Awarded articles are selected by the associate editors by anonymous vote. "Along with my colleagues on the editorial board, I am pleased to recognize these contributions as outstanding clinical and preclinical research," said Czernin. "Submissions to *JNM* remained strong and of extraordinarily high quality in 2021. Our awardees represent the cutting-edge clinical research activities that are advancing nuclear medicine, molecular imaging, and theranostics to the benefit of patients."

In the category of Best Clinical Article, the award went to Manuel Röhrich, from University Hospital Heidelberg (Germany), and coauthors Patrick Naumann, Frederik L. Giesel, Peter L. Choyke, Fabian Staudinger, Annika Wefers, Dawn P. Liew, Clemens Kratochwil, Hendrik Rathke, Jakob Liermann, Klaus Herfarth, Dirk Jäger, Jürgen Debus, Uwe Haberkorn, Matthias Lang, and Stefan A. Koerber for "Impact of ^{68}Ga-FAPI PET/CT imaging on the therapeutic management of primary and recurrent pancreatic ductal adenocarcinomas" (*J Nucl Med*. 2021;62:779–786). This contribution was also named the best overall article in *JNM* for 2021.

Mark G. MacAskill, from the University/BHF Centre for Cardiovascular Science at the University of Edinburgh (UK), and coauthors Agne Stadulyte, Lewis Williams, Timaeus E.F. Morgan, Nikki L. Sloan, Carlos J. Alcaide-Corral, Tashfeen Walton, Catriona Wimberley, Chis-Anne McKenzie, Nick Spath, William Mungall, Ralph BouHaidar, Marc R. Dweck, Gillian A. Gray, David E. Newby, Christophe Lucatelli, Andrew Sutherland, Sally L. Pimlott, and Adriana A.S. Tavares were the recipients of the award for Best Basic Science Article for "Quantification of macrophage-driven inflammation during myocardial infarction with ^{18}F-LW223, a novel TSPO radiotracer with binding independent of the rs6971 human polymorphism" (*J Nucl Med.* 2021;62:536–544).

"The associate editors and I are grateful for these remarkable contributions," said Czernin. "These and similar efforts ensure that *JNM* remains the journal of choice for publishing clinical, basic, and translational research in nuclear medicine, molecular imaging, radiopharmaceutical therapy, and theranostics."

Outstanding *JNMT* Articles for 2021

Kathy S. Thomas, MHA, CNMT, PET, editor-in-chief of the *Journal of Nuclear Medicine Technology* (*JNMT*), and members of the journal's board of editors announced in April the winners of annual awards for outstanding articles. These awards are presented each year to the authors of articles that have contributed significantly to practice, education, and scientific understanding in the field. The first-place Editors' Choice Award for 2021 went to Shannon N. Youngblood from the University of Arkansas for Medical Sciences (Little Rock) and Ochsner Medical Center (Baton Rouge, LA) for "Bullying in the nuclear medicine department and during clinical nuclear medicine education" (*J Nucl Med Technol* 2021;49:156–163). The second-place award was presented to Kyohei Okuda from Tottori University Hospital (Yonago, Japan) and coauthors Daisuke Hasegawa, Takashi Kamiya, Hajime Ichikawa, Takuro Umeda, Takushi Ohkubo, and Kenta Miwa for "Multicenter study of quantitative SPECT: Reproducibility of ^{99m}Tc quantitation using a conjugated-gradient minimization reconstruction algorithm" (*J Nucl Med Technol.* 2021;49:138–142).

Pietro Paolo de Barros, from the Federal Institute of Education, Science, and Technology of Santa Catarina–IFSC (Florianópolis, Brazil), and coauthors Tatiane Sabriela Cagol Camozzato, Tiago Jahn, Flávio Augusto Penna Soares, Letícia Machado da Silva, Jacqueline de Aguiar Soares, and Marco Antonio Neiva Koslosky received the third-place award for "Analysis of radiometry on patients undergoing radioactive iodine therapy" (*J Nucl Med Technol*. 2021;49:75–81).

Julie Bolin from the Nuclear Medicine Technology Program at GateWay Community College (Phoenix, AZ) was the recipient of the award for best continuing education article for "Thyroid follicular epithelial cell–derived cancer: New approaches and treatment strategies" (*J Nucl Med Techol.* 2021;49:199–208). The award for best educators' forum article went George Patchoros and Grace Wenzler from Bronx Community College (NY) for "Satisfying program-level outcomes by integrating primary literature into the online classroom" (*J Nucl Med Technol.* 2021;49:170–174).

"These outstanding articles show not only the diversity and complexity of research and education in our field, they represent extraordinary achievements by frontline care specialists during a very challenging time," said Thomas. "I am especially proud that these award-winning authors address not only technical and practice issues but ethical questions to which we all should be more sensitive. We congratulate this year's awardees and all those whose contributions continue to make *JNMT* a vital resource for our community."

Putting Patients First: A Year in Review

Richard L. Wahl, MD, SNMMI President

Over the past year, SNMMI has implemented many new initiatives focused on putting the patient first. As SNMMI president, I have worked with our dedicated leadership, volunteers, and staff to develop programs to improve access to care, advocate for appropriate reimbursement, encourage scientific advances, and ensure quality and safety. The resulting achievements will help propel the growth of the field, ultimately benefiting our patients.

Among the goals most important to me in this past year has been to ensure that historically underserved populations, rural and urban, receive equitable imaging and treatment. Appropriate reimbursement is critical to ensuring that patients have access to cutting-edge nuclear medicine and molecular imaging innovations. If a radiopharmaceutical is not adequately reimbursed, providers may not offer procedures that utilize it—which in turn limits patient access.

SNMMI has partnered with the Council on Radionuclides and Radiopharmaceuticals and the Medical Imaging and Technology Alliance to develop and advance major bipartisan legislation, the Facilitating Innovative Nuclear Diagnostics (FIND) Act, which would require Medicare to appropriately reimburse for radiopharmaceuticals. Widespread efforts have been made to promote the legislation, including briefings with key congressional staff and continuing conversations with government agencies, insurance providers, and patient groups to advocate for proper reimbursement. More than 80 groups now support the legislation. To find out more, visit www.snmmi.org/FindAct.

In addition to the FIND Act, long-term efforts by the society with the Centers for Medicare and Medicaid Services (CMS) resulted this year in 2 critical wins: coverage of ^{18}F-FDG PET for infection and inflammation and expansion of CMS coverage for nononcologic PET. Both advances will expand access to critical care for patients.

To further promote access to care, in March SNMMI hosted a successful summit on "Patient Access to and Health Disparities in Nuclear Medicine Procedures." The meeting gathered representatives from major stakeholders in the nuclear medicine and health equity spaces who identified and addressed barriers that prevent patients from accessing high-quality nuclear medicine scans and therapies.

In the past year, we have seen notable scientific advances in nuclear medicine and molecular imaging that will significantly accelerate growth in the field. The society is raising awareness about new radiopharmaceutical therapies (^{177}Lu-PSMA-617 and ^{177}Lu-DOTATATE, for example) with medical professionals, providing education materials, developing appropriate use criteria, and hosting an annual Therapeutics Conference. The society launched a new Radiopharmaceutical Therapy portal that contains detailed information for nuclear medicine professionals, referring physicians, and patients. SNMMI also launched a consumer media campaign in the fall of 2021 to raise public awareness of what nuclear medicine is and what it can accomplish, reaching nearly a billion consumers in its first 6 months.

Richard L. Wahl, MD

To encourage further advances in research, SNMMI approved the creation of 6 Cancer Cooperative Group Junior Faculty Mentorship Awards last year. These fellows will join the National Cancer Institute's National Clinical Trials Network cooperative groups in helping to influence, design, and lead trials. In addition, a ^{177}Lu Dosimetry Challenge was launched in early 2021, followed by a special *JNM* supplement published in December, with the ultimate goal of advancing the practice of personalized dosimetry.

SNMMI recognizes that quality and safety are major concerns of patients and is constantly striving to ensure that patients receive the best care. Earlier in 2022 SNMMI created the Radiopharmaceutical Therapy Center of Excellence program to certify sites that meet strict regulatory, training, qualification, experience, and performance criteria for radiopharmaceutical therapy. The response from clinical sites throughout the country has been strong, with more than 30 applicants and 9 designated sites as of this writing. With this prestigious designation, institutions can assure patients, their families, referring physicians, and payers that rigorous procedures are in place and followed, supporting appropriate patient selection and optimal outcomes from radiopharmaceutical therapy. To gather research on targeted radiopharmaceutical therapies, the SNMMI Board of Directors approved development of the Radiopharmaceutical Therapy Registry in 2021. This registry monitors anonymized data from patients who received radiopharmaceutical therapies.

Growing and sustaining the nuclear medicine and molecular imaging workforce are essential for nuclear medicine and molecular imaging. As part of its Value Initiative, SNMMI created a Workforce Pipeline task force this year to bring young talent into the field. SNMMI is also taking an active role in refining multidisciplinary care pathways and is leading the way in defining the new role of the nuclear oncologist.

Looking toward the future, SNMMI initiated its Mars Shot fund this year to radically transform the nature of disease treatment, prevention, diagnosis, and prognosis using visionary nuclear medicine procedures, radiopharmaceutical therapies, and research projects. By supporting training pathways and fellowships, our hope is to allow nuclear medicine physicians to integrate into patient management teams as key members, rather than remaining as outlying suppliers of imaging and treatment.

We must always remember to put patients first. I remain committed to advancing the field of nuclear medicine and molecular imaging and look forward to the continued growth and fruition of the society's efforts under the leadership of our incoming SNMMI president, Munir Ghesani, MD.

SNMMI Procedure Standard/EANM Practice Guideline for Nuclear Medicine Evaluation and Therapy of Differentiated Thyroid Cancer: Abbreviated Version

Anca M. Avram (cochair)[1], Luca Giovanella (cochair)[2], Bennett Greenspan[3], Susan A. Lawson[4], Markus Luster[5], Douglas Van Nostrand[6], Justin G. Peacock[7], Petra Petranović Ovčariček[8], Edward Silberstein[9], Mark Tulchinsky[10], Frederik A. Verburg[11], Alexis Vrachimis[12]

[1]Departments of Radiology and Medicine, MetroHealth Hospital, Case Western Reserve University, Cleveland, OH; [2]Clinic for Nuclear Medicine and Competence Center for Thyroid Diseases, Imaging Institute of Southern Switzerland, Bellinzona, Switzerland; [3]SNMMI, Reston, VA; [4]Department of Radiology, Division of Nuclear Medicine, University of Michigan; [5]Department of Nuclear Medicine, University Hospital Marburg, Germany; [6]MedStar Health Research Institute and Washington Hospital Center, Georgetown University School of Medicine, Washington, DC; [7]Department of Diagnostic Radiology, Brooke Army Medical Center, JBSA Fort Sam Houston, TX; [8]Department of Oncology and Nuclear Medicine, University Hospital Center "Sestre Milosrdnice", Zagreb, Croatia; [9]University of Cincinnati Medical Center, Cincinnati, OH; [10]Milton S. Hershey Medical Center, Penn State University, Hershey, PA; [11]Department of Radiology & Nuclear Medicine, Erasmus MC, Rotterdam, The Netherlands; and [12]Department of Nuclear Medicine, German Oncology Center, University Hospital of the European University, Limassol, Cyprus

Editor's note: *SNMMI and the European Association of Nuclear Medicine periodically define new standards/guidelines for nuclear medicine practice to help advance the science of nuclear medicine and to improve the quality of service to patients. Newsline is pleased to publish this somewhat abbreviated version of this most recent guideline with wide relevance to many practitioners and patients. The complete version is available at: https://www.snmmi.org/ClinicalPractice/content.aspx?ItemNumber=6414 and includes relevant background and important liability statements and acknowledgments.*

I. INTRODUCTION

Differentiated thyroid cancers (DTC) are slow-growing tumors with very low disease-specific mortality rates for local−regional disease (5-y survival: 99.9% for localized disease, 98.3% for regional metastatic disease). However, distant metastatic disease is associated with significantly worse prognosis (5-y survival: 54.9%) (*1*). Standard-of-care management for DTC includes risk-adapted surgery, postoperative ^{131}I therapy, and thyroid hormone therapy. In uncommon cases of radioiodine-refractory tumors, additional therapy may include reoperative surgical intervention, external radiotherapy, and interventional radiology for treatment of locoregional metastases and multikinase or tyrosine kinase inhibitors for treatment of distant metastatic disease.

II. EPIDEMIOLOGY AND CLASSIFICATION

Thyroid neoplasms are the most common endocrine tumors, with an annual incidence of 8−9 cases/100,000 people, with substantial variability between and within populations. DTC accounts for >90% of cases, is more frequent in women, and has excellent specific mortality and prognosis in most cases. The rising incidence of thyroid cancer observed in the last 30 y is mainly due to detection of small (≤ 2 cm) tumors as a result of increased and improved imaging (*2*). However, larger tumors (>2 and >5 cm) have also increased in incidence; therefore, a concomitant true rise in thyroid cancer incidence is possible (*3*). DTC is biologically and functionally heterogeneous, with different molecular pathways impacting cancer cell biology. The BRAF V600E mutation is particularly associated with reduced expression of all thyroid-specific genes involved in iodine metabolism, resulting in variably decreased responsiveness to ^{131}I therapy (*4*). For the main clinical and pathologic characteristics of DTC, see Table 1 (*5*).

III. DIAGNOSIS

Neck ultrasound (US), serum thyroid-stimulating hormone (TSH), and thyroid scintigraphy are used to select high-risk nodules for fine-needle aspiration (FNA) and filter out low-risk nodules from inappropriate additional procedures. Findings on US that are suspicious for thyroid cancer include hypoechogenicity, solid consistency, microcalcifications, irregular margins, extrathyroidal extension (ETE), and a taller-than-wide shape (*6*). Sonomorphologic nodule features have been used by several groups to produce a standardized risk assessment for thyroid malignancy, named the Thyroid Imaging Reporting and Data System (TIRADS) (*7,8*). In the absence of suspicious cervical lymph nodes, FNA is discouraged for nodules <1 cm, and the decision to aspirate larger nodules is guided by the TIRADS score in the context of nodule size. Cytologic findings are classified according to risk of malignancy using the Bethesda System for Reporting Thyroid Cytopathology (*9*). Certain cytologies are indeterminate, such as follicular neoplasm (or suspicious for follicular neoplasm), and the newly defined noninvasive

TABLE 1
Differentiated Thyroid Cancer: Clinical and Pathologic Characteristics (*5*)

Histological subtypes	Morphology	Molecular markers	Pattern of spread	RAI avidity
Papillary thyroid cancer (PTC)	Classical papillae Clear nuclei	BRAF V600E, RET/PTC fus	Lymph nodes	++++
PTC–follicular variant	Follicular structures Clear nuclei	BRAF K601E, RAS, PAX8/PPARγ	Lymph nodes	+++++
PTC–aggressive variants*	Specific cell features and structural changes	BRAF V600E, 1q amp, TERT promoter	Lymph nodes Lung	+++
Follicular thyroid cancer	Capsular invasion (MI) Vascular invasion (WI) Extrathyroidal invasion (WI)	RAS, PAX8/PPARγ, PTEN, TSHR, TERT promoter	Lung Bone	+++++
Hürthle cell thyroid carcinoma	Hürthle cells	RAS, PAX8/PPARγ, PTEN, TSHR, chromosomal loss, mitochondrial DNA mutations, TERT promoter	Lung Bone	++
Poorly differentiated thyroid cancer	Invasion Mitoses >3 Necrosis Convoluted nuclei	RAS, TERT promoter, TP53, PIK3CA, PTEN, CTNNB1, AKT1, EIF1AX, ALK fus	Lymph nodes Lung Bone	+/–
Anaplastic thyroid cancer	Undifferentiated cells with immunohistochemical or ultrastructural features of epithelial origin but of morphological and immunophenotypic markers of thyroid origin	TP53, TERT promoter, PI3K/AKT/mTOR, SWI/SNF subunts, RAS, EIF1AX, BRAF	Local invasion Lung Bone Lymph nodes	–

*Tall, columnar, solid, and hobnail variants.
RAI = radioiodine; MI = minimally invasive; WI = widely invasive; fus = fusion.

follicular thyroid neoplasm with papillary-like nuclear features. In such cases, FNA can be complemented by assessment of specific molecular alterations (e.g., BRAF or TERT mutations, RET fusions), as well as molecular imaging with ^{99m}Tc-MIBI or ^{18}F-FDG (*10*).

IV. THERAPY STRATEGIES

The current strategy for DTC management is a risk-stratified approach based on information from surgical histopathology, molecular markers, postoperative thyroglobulin (Tg) levels, and anatomic/functional imaging studies (*6*).

A. Surgical Treatment for DTC

(Near-) total thyroidectomy was traditionally performed in most DTC patients, with lobectomy reserved for cytologically indeterminate nodules or patients with unifocal micropapillary thyroid cancer (PTC) <1 cm. Current American Thyroid Association (ATA) guidelines recommend lobectomy for patients with unifocal intrathyroidal low-risk DTC in the absence of additional risk factors (i.e., no clinical evidence of nodal metastases, cN0), although high-level evidence is lacking (*6*). Management of low-risk DTC between 2 and 4 cm is a topic of debate; although a lobectomy may be proposed, total thyroidectomy is still largely advised, especially in Europe (*11*). Active surveillance has been recommended as an alternative to lobectomy for unifocal micro-PTC with no extracapsular extension or lymph node metastases (*12*). The decision for active surveillance is based primarily on age-related risk of progression, individual surgical risk factors, and patient preference (*13*). In all other cases, total thyroidectomy remains the preferred surgical approach.

Cervical lymph nodal metastases occur in 20%–60% of patients with DTC, and this nodal involvement varies from clinically relevant macrometastasis to seemingly clinically irrelevant micrometastases (*14,15*). When lymph nodal metastases are diagnosed preoperatively, central and/or lateral neck compartment dissection reduces the risk of locoregional recurrence. Prophylactic central neck dissection may improve regional control for invasive tumors (T3–T4), but it is discouraged for low-risk DTC, because potentially associated morbidities (i.e., hypoparathyroidism and recurrent laryngeal nerve damage) are not justified by a significant clinical benefit (*16*). Preoperative neck US generally suffices to plan surgery; however, additional cross-sectional imaging (e.g, contrast-enhanced CT, MRI) is used in locally advanced disease to inform the surgical approach. When iodinated contrast media are administered for preoperative CT, sufficient time (i.e., 4–6 wk) for elimination of iodine load is required before performing radioiodine imaging and therapy.

PET/CT with ^{18}F-FDG could be perfomed preoperatively in more aggressive DTC histotypes (i.e., poorly differentiated

thyroid cancer or Hürthle cell carcinoma) and anaplastic thyroid cancer (*17*). After surgery, the risk of structural disease recurrence and/or persistence is assessed using the 3-tier (low, intermediate, high) stratification recommended by the ATA in 2009 and modified in 2015 (*6*), whereas the risk of mortality from thyroid cancer is estimated using the American Joint Commission on Cancer/TNM staging system (*18*).

B. Postoperative ^{131}I Therapy

The goal of therapeutic ^{131}I administration after total thyroidectomy is outlined based on standardized definitions as follows: remnant ablation, adjuvant treatment, or treatment of known disease *(19,20)*. Upon integration of various parameters, including clinical/pathologic data and laboratory and imaging information, ^{131}I therapy is administered for the following reasons: (1) to eliminate normal thyroid tissue remnant in low-risk patients, thereby ensuring undetectable or minimal serum Tg levels (in the absence of neoplastic tissue), which facilitates follow-up (remnant ablation); (2) to irradiate suspected but unproven sites of neoplastic cells in low-intermediate– and intermediate-risk patients as determined by histopathologic features, thereby reducing the risk of disease recurrence (adjuvant treatment); and (3) to treat persistent or recurrent disease in patients with demonstrated metastatic disease (treatment of known disease).

The impact of ^{131}I therapy on clinical outcomes of thyroid cancer has been demonstrated in several large data series. An analysis of 2,936 DTC patients in the National Thyroid Cancer Therapy Cooperative Study Group (NTCTCS) reported improved overall survival (OS) and disease-specific survival in patients with advanced tumors and regional and/or distant metastatic disease who received postoperative ^{131}I therapy (*21*). An updated analysis of 4,941 patients in the NTCTCS study with a median follow-up of 6 y (longest follow-up, 25 y) confirmed improved OS in stage III and IV patients and also demonstrated improved disease-free survival for stage II patients receiving ^{131}I therapy (*22*). A meta-analysis of 31 patient-cohort studies regarding the effectiveness of ^{131}I therapeutic administration demonstrated a statistically significant effect on improving clinical outcomes at 10 y, with decreased risk for locoregional recurrence (RR, 0.31; CI, 0.2–0.49) and an absolute risk reduction of 3% for distant metastatic disease (*23*). An analysis of the National Cancer Database comprising 21,870 intermediate-risk patients (mean follow-up, 6 y; longest follow-up, 14 y) demonstrated that adjuvant ^{131}I treatment improved OS, both for younger (<45 y) and older (≥65 y) subsets of patients. Adjuvant ^{131}I therapy was associated with a 29% reduction in risk of death for all patients (*24*). The beneficial effects of postoperative ^{131}I therapy are most evident in patients with locoregionally advanced and distant metastatic disease (stages IVA, IVB, and IVC). An analysis of the National Cancer Database comprising 11,832 patients demonstrated that administration of ^{131}I therapy was associated with significantly improved 5- and 10-y survival for both PTC and follicular thyroid cancer (FTC) patients, regardless of pathologic substage (stages IVA, IVB, or IVC), as follows: mortality rates in the PTC cohort (n = 10,796) at 5 and 10 y were 11% and 14%, respectively, in patients who received ^{131}I therapy, compared to 22.7% and 25.5%, respectively, in patients who received none; mortality rates in the FTC cohort (n = 1,036) at 5 and 10 y were 29.2% and 36.8%, respectively, in patients who received ^{131}I therapy, compared to 45.5% and 51%, respectively, in patients who received none *(25)*. For patients with distant metastases, a delay of >6 mo in administration of ^{131}I therapy is associated with decreased survival, demonstrated after a follow-up period of only 5–6 y (*26*).

C. Preparation for ^{131}I Therapy

Evaluation with radioiodine scintigraphy and therapy is scheduled at a minimum of 4 wk after surgery, which allows time for patient preparation and for reaching postoperative Tg plateau levels, used as a marker for residual thyroid tissue and/or metastatic thyroid cancer after total thyroidectomy. Tg is synthesized exclusively in the thyroid follicular cells as a precursor of thyroid hormones, and manipulation of the thyroid gland during surgical resection releases significant Tg amounts in the systemic circulation. Tg is subsequently metabolized in the liver with a mean elimination half-life (Tg $t_{1/2}$) of 65.2 h (*27*). Correct timing of serum sampling for Tg measurement in regard to surgery is important, and measurements should not be performed sooner than 25 d after total thyroidectomy to allow for clearance of the postsurgical Tg peak (10 × Tg $t_{1/2}$) (*27*). Tg levels must always be interpreted in the context of concomitant TSH level (unstimulated vs. stimulated Tg) and type of TSH stimulation (endogenous vs. exogenous) (*28*). Tg antithyroglobulin antibodies (TgAb) need to be measured in conjunction with Tg in each serum sample provided for Tg testing. Every specimen needs TgAb testing to authenticate that the Tg measurement is not compromised by TgAb interference. When present, TgAb concentrations can be monitored as a surrogate tumor marker *(29)*.

Patient preparation for optimal ^{131}I uptake by residual thyroid tissue and metastatic disease includes 1–2 wk of low-iodine diet (LID) and adequate TSH stimulation (TSH ≥30 mIU/L measured 1–3 d prior to ^{131}I administration) by either thyroid hormone withdrawal (THW) or recombinant human TSH (rhTSH) stimulation (*30,31*). However, a recent article showed that lower TSH levels may be sufficient for remnant ablation without influencing remnant ablation success rates (*32*). For childbearing females (12–50 y old) a negative pregnancy test is required within 72 h of ^{131}I administration or prior to the first rhTSH injection (if used), unless the patient is status posthysterectomy or postmenopausal.

Dietary deprivation of stable iodine (^{127}I) restricts consumption of iodine to <50 μg/d and is important for minimizing interference with ^{131}I uptake. In a study of 120 patients (LID group, n = 59; control group, n = 61) LID preparation decreased 24-h urinary iodine excretion by 83% and increased radioiodine uptake in thyroid remnants by

65% ($P < 0.001$) as compared with controls. The efficacy of ^{131}I treatment (assessed at 6 mo and defined by absent neck activity and Tg < 2 ng/mL) was also improved by LID: successful ablation was achieved in 65% of LID patients compared with 48% of patients in the control group ($P < 0.001$) (*33*).

Dietary iodine consumption varies widely, depending on ethnic culinary behavior, with reported average iodine intake of 195 μg/d for U.S., 469 μg/d for Korean, and 544 μg/d for Japanese individuals (*34–36*).

Patient compliance with LID can be confirmed by measurement of spot urinary iodine (U.S. reference range, 26–705 μg/L) or urinary iodine/creatinine ratio (I/Cr) (U.S. reference range, <584 μg/g); The World Health Organization defines iodine status based on urinary iodine concentrations as insufficient iodine intake, <99 μg/L; adequate iodine intake, 100–199 μg/L; iodine intake above requirements, 200–299 μg/L; and excessive iodine intake, ≥300 μg/L (*37*).

In preparation for ^{131}I therapy the state of iodine deprivation induced by LID is considered adequate when spot urinary iodine is <100 μg/L and optimal when urinary iodine is <50 μg/L (or I/Cr is <50 μg/g) (*38,39*). A study of 101 patients comparing 2- and 4-wk LIDs showed no significant difference in urinary iodine levels, both periods resulting in optimal I/Cr for ^{131}I therapeutic administration (i.e., <50 μg/g) (*40*). Moreover, depending on patients' perceived difficulty with dietary iodine deprivation, compliance with LID may decrease as the duration of the diet is extended. Patients should be informed to avoid dietary supplements with high iodine content (e.g., iodine tablets [Iodoral], spirulina tablets, red dye food colorants). In addition, radiologic contrast agents and iodine-based antiseptics should be avoided for at least 4–6 wk prior to ^{131}I therapy administration. A medication review should always be performed, and amiodarone usage should be replaced with a different antiarrhythmic drug followed by serial serum/urinary iodine measurements over 3–6 mo after amiodarone discontinuation to ascertain clearance of excessive iodine load before ^{131}I treatment. Even when urinary iodine levels do not reach optimal values, the use of ^{131}I therapy should be discussed in cases of advanced thyroid cancer. Table 2 contains dietary information regarding LID preparation (*41*).

TSH is used for increasing sodium-iodide symporter (NIS) expression and function in metastatic lesions (and residual thyroid tissue), with the goal of increasing the diagnostic (Dx) sensitivity of ^{131}I scintigraphy and radiation absorbed dose to target lesions. The 2 major approaches for TSH stimulation are:

(1) Endogenous TSH stimulation, obtained through thyroid hormone deprivation following total thyroidectomy, thus inducing a hypothyroid state that must be carefully explained to patients in order to avoid major adverse consequences. For example, patients must be informed about precautions regarding driving and/or restrictions on operating

TABLE 2
Specific Dietary Instructions for Preparatory Low-Iodine Diet (Recommended Low-Iodine Diet Prior to Radioiodine Scintigraphy and Therapy [*41*])*

Dietary items	Allowed	Restricted
Baked goods, pasta	Flour, oatmeal, wheat, macaroni, noodles, pancakes, spaghetti, homemade bread prepared with noniodized salt	Cereals, rice, granola, popcorn; industrialized biscuits, breads, crackers
Meat, poultry, eggs	Beef, lamb, chicken, turkey, pork, veal; eggs- (max 2 eggs/wk)	All seafood (fish, shrimp, oysters, clams, etc.); processed, cured, smoked, or breaded meats
Condiments	Salt-free margarine, vegetable oil, mayonnaise, sugar, jelly, honey	Iodized salt, pickles, white sauce, meat sauces, creamy sauces, soy sauces, agar-agar, unsalted nuts, vinegar or alginate additives, red colorants
Fruits, juices	All raw fruits and homemade natural juices	Fruit cocktails, canned fruits, dried fruits
Beverages	Water, tea, coffee, wine, alcoholic drinks	Milk and all derivatives (yogurt, ice cream, cheese), soy beverages
Desserts	Homemade cookies, homemade fruit pies, homemade cakes (prepared with noniodized salt)	Chocolate, pudding, gelatin, ice cream, candies, industrialized desserts, foods with red colorants, molasses
Vegetables	Asparagus, beets, broccoli, cabbage, celery, carrots, cauliflower, corn, cucumber, lettuce, mushrooms, onions, peas, potatoes without peel, spinach, sweet potatoes (baked), tomatoes (fresh), zucchini	All canned vegetables, potatoes with peel, french fries, candied sweet potatoes, onion rings, beans
Combination dishes	Homemade dishes prepared with allowed ingredients	Pizza, lasagna, macaroni and cheese, industrialized foods, and foods with conservants

*All dishes must be prepared with noniodized salt. Avoid eating in restaurants.

heavy machinery, because severe but reversible impairments in attention and reaction time have been observed (*42*).

The hypothyroid stimulation protocol (THW) has 2 variants employed worldwide in practice (although insufficient evidence is available to prefer one over the other): *Levothyroxine (T4) withdrawal* for 4 wk. This interval is determined by the T4 elimination half-life (T4 $t_{1/2}$) of 7 d and the physiologic pituitary response to declining T4 concentrations. An acceptable variation involves repeated measurements of TSH during the second, third, and/or fourth wk of THW to expedite Dx radioiodine whole-body scanning (DxWBS) and/or ^{131}I therapy whenever possible, timing it to TSH measurement of >30 mU/L in cases of metastatic disease (*43*). A level of unpredictability for scheduling imaging and/or therapeutic ^{131}I administration is associated with this latter approach. Lower TSH levels may be sufficient for thyroid remnant ablation in low-risk patients, according to a single study that found no influence of TSH levels on postoperative ^{131}I remnant ablation success (defined as stimulated Tg <1 ng/mL). The study involved 1,873 patients without distant metastases and a majority (~80%) with stage I–II disease (of whom 15% had TSH <30 mU/L and demonstrated higher median Tg levels, suggestive of larger volumes of thyroid remnant tissue). Because NIS activity and, consequently, ^{131}I uptake are TSH mediated in a dose- and time-dependent manner, the area under the curve obtained by the TSH level plotted against time may achieve sufficient stimulation to result in uptake of therapeutically effective ^{131}I activities for ablation of thyroid tissue remnants that have high-constitutive NIS expression and function (*32*). However, the Guidelines Committee advises that this study's findings cannot be extrapolated to high-risk patients and/or patients undergoing further ^{131}I therapy for recurrent, persistent, or metastasized disease.

The second THW variant is *levothyroxine/liothyronine (T4/T3) substitution* for the first 2 wk, followed by discontinuation of T3 for 2 wk. This interval is based on T3 $t_{1/2}$ of 0.75 d. In practice, T4 is stopped and replaced by T3 in a typical dose of 25 μg once or twice daily (depending on age and body weight). This regimen is well tolerated and has the advantage of minimizing hypothyroid symptoms (*44*).

TSH levels occasionally remain suboptimal for ^{131}I therapy in patients with large thyroid remnants after surgery, in patients with limited pituitary functional reserve (e.g., history of head trauma, brain external-beam radiation, pituitary surgery, obesity, other comorbidities), or in patients with functional metastatic disease. Correlation of laboratory results with findings on postoperative Dx radioiodine scintigraphy is helpful for determining the etiology of suboptimal TSH elevation. This helps guide further steps in management, such as surgical resection for large thyroid remnants or bulky residual cervical metastatic disease, or dosimetry-guided ^{131}I therapy for secretory distant metastases. For patients with limited pituitary functional reserve, it is advisable to proceed with administration of exogenous TSH stimulation (rhTSH injections) to avoid further delay in ^{131}I therapy administration and limit hypothyroid symptoms (rhTSH augmentation protocol).

(2) For *exogenous TSH stimulation:* The patient continues T4 treatment and undergoes preparation with an LID. TSH elevation is obtained through administration of rhTSH (Thyrogen® stimulation protocol): a 0.9-mg rhTSH injection is administered intramuscularly on 2 consecutive d, followed by ^{131}I therapy administration at 48–72 h (*45*). When Dx ^{131}I scanning is performed as an integral part of ^{131}I therapeutic protocols (theranostics), the tracer ^{131}I activity is administered after the second rhTSH injection and the WBS scan is obtained 24 h later, followed by subsequent ^{131}I therapy administration.

The choice of preparation method (THW vs. rhTSH) must be individualized for each patient. The balance of published data show that for normal thyroid tissue (i.e., thyroid remnant ablation), rhTSH and THW stimulation are equivalent, because normal thyroid tissue has constitutive high expression of highly functional NIS and does not require prolonged TSH stimulation for adequate ^{131}I uptake and retention. However, metastatic thyroid cancer has lower density and poorer functionality of NIS; therefore, TSH elevation over time (area under the curve of TSH stimulation) is important to promote increased ^{131}I uptake and retention in tumors (*46,47*). In the setting of metastatic disease, it is possible to use rhTSH stimulation on an off-label basis. However, the combination of THW preparation and dosimetry-guided ^{131}I therapy is favored when clinically safe and the necessary expertise for dosimetry is available (*45,48,49*). Tumor vs. critical organ (e.g., bone marrow, lung) radiation absorbed dose (Gy) after rhTSH vs. THW-stimulation protocols needs further evaluation. Furthermore, no studies have yet reported relevant outcome measures (i.e., survival) with rhTSH and THW in patients with distant metastases.

The use of rhTSH is a more complex issue in the setting of adjuvant treatment, because this concept has been introduced only after studies employing rhTSH for remnant ablation were completed. As a result, there are no clear data in the literature allowing us to assess which of the 2 alternatives is better in the setting of adjuvant therapy separately from the setting of remnant ablation, especially with modern criteria for excellent response. However, rhTSH is registered for use for initial postoperative ^{131}I therapy in patients up to and including N1 M0 disease. Therefore, in the case of adjuvant treatment, rhTSH and THW should both be considered in accordance with the individual medical characteristics of the case, economic feasibility, quality of life, and expected efficacy (*20*).

D. Postoperative Thyroglobulin Measurement

Although postoperative serum Tg measurement can provide valuable information with regard to the likelihood of achieving remission or having persistent or recurrent disease in response to an initial therapy, its predictive value regarding residual disease is significantly influenced by a wide

variety of factors, as follows: the amount of residual thyroid cancer and/or thyroid remnants, TSH level at the time of Tg measurement, functional sensitivity of the Tg assay, time elapsed since total thyroidectomy, Tg cutoff used for analysis, and individual risk of having radioiodine-avid locoregional or distant metastasis (*50*). The fundamental role of Tg measurement in monitoring of DTC implies the need for high-quality Tg assays. A major problem that hampers accurate Tg measurement is the interference in the Tg assay by Tg antibodies (TgAb) and heterophile antibodies (HAb), resulting in under- or overestimation of the serum Tg concentration (*51*). Immunometric Tg assays are subject to a high-dose hook effect, leading to inappropriately normal or low Tg values in sera with very high Tg concentrations, which require dilution for accurate measurement (*52*). Absolute threshold values for Tg, whether the patient is prepared with THW or rhTSH, remain controversial. Several authors proposed that postoperative Tg values of about 10 ng/mL after THW and of 1 ng/mL after rhTSH stimulation achieve the best balance of sensitivity and specificity for predicting recurrent or persistent disease over time and poorer survival (*45,53*). Notably, because such results were obtained in patients treated with ^{131}I following thyroidectomy, they cannot be translated to those patients treated by surgery alone and used to decide for/against postsurgical ^{131}I administration. Indeed, some studies not only excluded patients with TgAb from analysis but also excluded patients showing evidence of extracervical metastases, introducing additional selection bias. Iodine-avid tissue with a corresponding undetectable stimulated serum Tg is detected in up to 20% of DTC patients by posttreatment WBS (PT-WBS). Moreover, up to 6% of such patients had confirmed locoregional or distant metastases in addition to thyroid tissue remnants (*54,55*). In a retrospective study, Matrone et al. (*56*) reported on a group of 505 low- to intermediate-risk DTC patients who had undergone total thyroidectomy and rhTSH-aided ablation with 1.1 GBq ^{131}I. Just before ablation, a neck US was performed and Tg levels on thyroxine were measured using a high sensitive assay (i.e., functional sensitivity of 0.1 ng/mL). A planar PT-WBS was performed and compared with preablation basal Tg and US assessments. Among the main findings, 150 patients had Tg levels $<$0.1 ng/mL and 1 of 150 showed cervical persistence of disease; 287 patients had Tg levels between 0.1 and 1.0 ng/mL, 15 of whom had nodal or distant metastases; and 68 patients had Tg levels exceeding 1.0 ng/mL, 11 of whom had neck metastases. Notably, in the 3 patients with lung metastases, basal Tg levels were 0.11, 0.12, and 0.94 ng/mL. A basal Tg level of 0.75 ng/mL was measured in 1 additional case of bone metastasis. This article submitted further evidence that basal Tg $<$ 1 ng/mL cannot be used to rule out the presence of distant metastases; 2 of the 4 patients with distant metastases had Tg levels of 0.11 and 0.12 ng/mL (*56*).

Recently, Schlumberger et al. (*57*) reported 5-y outcomes of ESTIMABL1, a randomized trial comparing 4 strategies of ^{131}I administration following thyroidectomy in low-risk thyroid cancer. In this study, the rate of patients with persistent structural disease after ^{131}I ablation was similar in 3 subgroups of stimulated Tg ranges (i.e., $\leq$1, $>$1–$\leq$5, and $>$ 5–$<$10 ng/mL) (*58*). In summary, with regard to decision-making on the need for postoperative ^{131}I administration, it appears that the serum Tg value is more helpful in identifying patients for whom the administered ^{131}I activity should be higher, rather than in identifying patients who do not require ^{131}I therapy.

E. Radioiodine Therapy Planning

An important goal of ^{131}I therapy is individualized treatment that maximizes benefit and reduces risk for each patient who belongs to a risk category associated with improved outcomes after ^{131}I therapy. There are 2 approaches to ^{131}I therapy delivery: the approach integrating functional imaging information obtained with postoperative preablation Dx radioiodine (^{123}I, ^{131}I, or ^{124}I) scans in the management algorithm (i.e., functional imaging-guided approach; theranostics) and the approach based on clinical–pathologic factors and institutional protocols (i.e., risk-adapted approach). The approach chosen depends on local factors, including quality of surgery, availability of and expertise with various imaging modalities, and physician as well as patient preferences.

F. Management and Integration of Functional Diagnostic Radioiodine Imaging

This theranostic approach to ^{131}I administration involves acquisition of a postoperative Dx radioiodine (^{123}I, ^{131}I, or ^{124}I) scan for planning ^{131}I therapy. DxWBS is performed with the intent of identifying and localizing regional and distant metastatic disease and for evaluating the capacity of metastatic deposits to concentrate ^{131}I. Depending on institutional protocols, findings on DxWBS may alter management, such as providing guidance for additional surgery or altering the prescribed ^{131}I therapy, either by adjusting empiric ^{131}I activity or by performing dosimetry calculations for determining the maximum tolerated therapeutic ^{131}I activity (MTA) for treatment of distant metastatic disease. Also, unnecessary ^{131}I therapy may be avoided if DxWBS finds no evidence of residual thyroid tissue or metastatic disease and the stimulated Tg is $<$1 ng/mL in the absence of interfering TgAb (*59*). Information acquired from DxWBS may also lead to additional functional metabolic imaging with ^{18}F-FDG PET/CT when non-iodine–avid metastatic disease is suspected (based on Tg elevation out of proportion to findings on DxWBS). Wherever available, it is preferable for postoperative DxWBS to be performed using integrated multimodality imaging (i.e., SPECT/CT).

DxWBS with or without SPECT/CT may detect metastases in normal-size cervical lymph nodes (not appreciated on postoperative neck US), may identify pulmonary micrometastases (which are too small to be detected on routine chest x-ray and may remain undetected on CT), and may diagnose bone metastases at an early stage before cortical disruption is visible on bone x-rays or CT. Because ^{131}I therapy is most

effective for smaller metastatic deposits, early identification of regional and distant metastases is most important for successful therapy (*60,61*).

Clinical experience with Dx ^{123}I scans demonstrated their usefulness in thyroid cancer management: preablation ^{123}I WBS provided additional critical information in 25% of 122 patients, by revealing unsuspected regional or distant metastases and thus guiding administration of higher ^{131}I therapeutic activities or revealing unexpected large thyroid remnants (*62*). In a cohort of 152 consecutive patients referred for postoperative ^{131}I ablative therapy, the information provided by Dx ^{123}I WBS led to a change in prescribed therapeutic ^{131}I activity in 49% of cases compared to the recommended ^{131}I activities based on surgical pathology alone (*63*). In a study based on review of 355 Dx radioiodine scans (after administration of 37–148 MBq [1–4 mCi] of either ^{123}I or ^{131}I) the imaging findings altered management in 29% of cases (*64*). Similar conclusions have been reached by other investigators who demonstrated that the information obtained from Dx ^{131}I WBS changed the prescribed therapeutic ^{131}I activity in 58% of cases (*65*).

A study comparing sensitivity for disease detection for Dx 74–185 MBq (2–5 mCi) ^{123}I WBS versus 111–185 MBq (3–5 mCi) ^{131}I WBS (both performed after THW protocol) demonstrated that, although ^{123}I is adequate for imaging residual thyroid tissue, it appears to be less sensitive than ^{131}I for imaging thyroid cancer metastases: ^{123}I missed metastases shown by ^{131}I in the neck, mediastinum, lungs, and bone. No lesion was better seen with ^{123}I than with ^{131}I (*66*). Other authors also found Dx ^{123}I WBS to be insensitive for metastatic disease detection and attributed this finding to the short half-life of ^{123}I (13 h), limiting imaging to no later than 24 h postinjection, which is too short for optimizing tracer tumor uptake (*67*). In addition to the radioiodine isotope used, the preparation protocol (THW vs. rhTSH stimulation) also has an impact on the Dx sensitivity of DxWBS for disease detection: across 2 phase 3 clinical trials enrolling 358 patients, rhTSH-stimulated DxWBS failed to detect remnant and/or cancer localized to the thyroid bed in 16% of patients in whom it was detected by a DxWBS obtained after THW. In addition, the rhTSH-stimulated DxWBS failed to detect metastatic disease in 24% of patients in whom it was detected by a THW DxWBS (*68–70*).

In a group of 320 thyroid cancer patients referred for postoperative ^{131}I therapy, Dx ^{131}I WBS with SPECT/CT imaging obtained after THW protocol detected regional metastases in 35% of patients and distant metastases in 8% of patients. This information changed staging in 4% of younger and 25% of older patients (*71*). Both imaging data and stimulated Tg levels acquired at the time of Dx ^{131}I WBS were consequential for ^{131}I therapy planning, providing information that changed clinical management in 29% of patients compared to a management strategy based on clinical and surgical pathology information alone (*72*).

The benefits of integrating Dx ^{131}I WBS in the management algorithm of intermediate- and high-risk thyroid cancer for guiding ^{131}I therapeutic administration have been demonstrated in a group of 350 patients evaluated to assess therapy response with a median follow-up of 3 y after primary treatment strategy (surgery and postoperative ^{131}I therapy): complete response (CR) to therapy was achieved in 88% patients with locoregional disease and in 42% patients with distant metastases after a single ^{131}I therapeutic administration (*73*). Further studies for evaluating long-term outcomes need to be performed.

Depending on the type of patient preparation, Dx radioiodine (^{123}I or ^{131}I) activities such as 37–74 MBq (1–2 mCi) for THW protocols and 110–148 MBq (3–4 mCi) for rhTSH-stimulation protocols are frequently used (*39*). The higher tracer activity (3–4 mCi) employed for rhTSH-stimulation protocols is to compensate for the competitive inhibition exerted by the iodine content of T4 (levothyroxine) on the uptake of radioiodine (^{131}I or ^{123}I) in thyroid tissue or metastatic lesions (*74*). T4 contains 63.5% iodine by molecular weight. The interference of T4 stable iodine content on radioiodine uptake is not surprising if we consider that the amount of iodine in 1.1 GBq (30 mCi) is only 5 μg, as compared to 50 μg stable iodine content in a daily dose of T4 (*75*). The dilution of radioiodine with nonradioactive iodine from any source may degrade WBS image quality and reduce the effectiveness of ^{131}I therapy. Replacement of levothyroxine with liothyronine (T3) during the preparation period for rhTSH-stimulation protocols has been proposed for decreasing the dilution effect of nonradioactive iodine on the uptake of radioiodine (*74*). T3 has lower iodine content per molecule (only 56.6% of T4 iodine content) and exerts an equivalent biologic effect by administration of ¼ of the necessary T4 dose (*76*). In addition to an LID, this therapeutic interchange from T4 to T3 during the preparatory period for rhTSH-stimulation protocol resulted in a further decrease in 24-h urinary iodine excretion by 56% as compared to T4 treatment (*74*).

Optimization of imaging acquisition parameters and current SPECT/CT gamma camera technology permit good quality visualization of distant metastatic disease using 37 MBq (1 mCi) ^{131}I Dx activity (*71,72,77,78*).

In all cases, ^{131}I therapy should be followed by acquisition of PT-WBS to determine therapeutic ^{131}I localization, which is routinely used to complete postoperative staging. However, the day to perform the PT-WBS after therapeutic ^{131}I administration remains controversial, ranging from 2–10 d (*79*). PT-WBS acquisition on 2 separate days may be valuable, as demonstrated by Salvatori et al. (*80*) in a group of 134 patients who underwent both early (at 3 d) and delayed (at 7 d) scans: 80.5% of detected lesions were concordant on both early and delayed scans; however, 7.5% of lesions were detected only on the early scans, whereas 12% of lesions were detected only on the delayed scans. By performing both early (at 3–6 d) and delayed (at 10–11 d) PT-WBS, Hung et al. (*81*) reported that 28% of nodal metastases, 17% of lung metastases, and 16% of bone metastases were visible only on the early scans. This is consistent with

the observation that ^{131}I therapeutic activities produce destructive cellular effects with resultant increased rates of ^{131}I loss from the tissue; this accelerated tissue ^{131}I loss after treatment may account for discrepancies reported between DxWBS and delayed PT-WBS in earlier studies, which has been interpreted as "stunning," as well as differences observed between early and delayed PT-WBS (*82*). However, delayed PT-WBS acquisition provides the advantage of increased contrast resolution due to time-dependent ^{131}I clearance from normal tissues. Chong et al. (*83*) reported in a group of 52 patients that 22% of lung metastases and 33% of bone metastases were visible only on the delayed PT-WBS (obtained at 7 d). Similarly, Kodani et al. (*84*) reported in a group of 24 patients that 29% of lung metastases and 20% of bone metastases were visible only on the delayed PT-WBS (obtained at 7–9 d).

Hybrid imaging with SPECT/CT improves the accuracy of PT-WBS and should be done whenever possible. A systematic review of 14 original research articles describing the incremental value of ^{131}I SPECT/CT demonstrated significant clinical benefit in terms of staging, risk stratification, alteration of management, and/or follow-up of DTC (*85*). This is especially important when DxWBS is not performed or when PT-WBS shows additional foci of activity as compared to DxWBS (*86*). A high level of concordance between DxWBS and PT-WBS findings has been demonstrated in 2 large single-institution data series from Stanford University (98% concordance in a group of 280 patients) and the University of Michigan (92% concordance in a group of 303 patients) (*71,87*). In summary, DxWBS is valuable for ^{131}I therapy planning in the paradigm of thyroid cancer theranostics (*88*).

DxWBS scintigraphy performed in follow-up evaluation after initial postoperative ^{131}I administration is important to (1) establish a new baseline after postoperative ^{131}I therapy (*89*); (2) determine interval response to ^{131}I treatment; and (3) assess the patient's thyroid cancer status. Along with basal and stimulated-Tg testing and cross-sectional anatomic imaging, the results of follow-up DxWBS contribute to dynamic risk restratification, which is usually performed at 6–12 mo after initial treatment strategy (surgery and postoperative ^{131}I therapy). For patients with rising Tg levels, DxWBS and PET/CT evaluation can be scheduled sequentially to assess for recurrent and/or metastatic disease and evaluate tumor biologic behavior for determining whether the patient would benefit from additional ^{131}I therapy (*73*). Of importance, a recent report examining the results of a large Surveillance, Epidemiology, and End Results Program database (28,220 patients diagnosed with DTC between 1998 and 2011) showed that follow-up DxWBS performed after primary treatment of DTC are the only imaging studies associated with improved disease-specific survival, demonstrating the clinical benefit of ^{131}I theranostics for DTC management (*90*). Figures 1 and 2 provide sample protocols for integration of DxWBS evaluation, ^{131}I therapy delivery, and PT-WBS imaging after THW and after rhTSH stimulation, respectively. Figures 3 and 4 present sample protocols for dosimetry-guided radioiodine theranostics after THW and after rhTSH stimulation, respectively.

G. Risk-Based Management Followed by Posttherapy ^{131}I Scans with Diagnostic Intent

The risk-based approach is generally used for thyroid remnant ablation and for adjuvant ^{131}I treatment. Empiric activity selection is the most commonly used approach in advanced DTC, in which the nuclear medicine physician chooses an activity based on convention, availability, experience with various imaging modalities, and patient-related parameters. With this therapeutic approach patients are most commonly given activities of 1.1 GBq (30 mCi), 1.85 GBq (50 mCi), 3.7GBq (100 mCi), 5.6 GBq (150 mCi), or 7.4 GBq (200 mCi) (*91*). Although there are theoretical disadvantages of this approach compared to dosimetric strategy in the treat-

Preparation*	Day 1	Day 2–3	Day 3–4	Day 5	Day 6–11 (2–7 d post-Rx)
Thyroid hormone management: • Replace T4 with T3 for first 2 wk • Then stop T3 for next 2 wk	Baseline blood tests: • Pregnancy • TSH, Tg, TgAb, F-T4 • CMP • CBC w. Diff	DxWBS: • Review/report scan • Review pathology • Review blood test results • ^{131}I therapy planning	^{131}I therapy administration		PT-WBS scan
Diet management: • Start LID for 2 wk (when T3 is stopped)	Dx RAI adm. (1–2 mCi)	Patient consult: • Explain findings, prognosis • Discuss indications for ^{131}I Rx • Discuss logistics of ^{131}I Rx • Discuss radiation precautions • Discuss management of post-operative hypothyroidism			
			• Patient education for radiation precautions • Patient signs informed consent and radiation precautions form documenting understanding and adherence to recommendations	Patient: • Starts normal diet • Starts T4 for reversal of hypothyroidism • Continues hydration and lemon candies for salivary protection	

FIGURE 1. Sample protocol for ^{131}I theranostics after thyroid hormone withdrawal (THW). *Initial consultation is recommended to discuss preparation protocol with patient and family and explain logistics and expectations of ^{131}I therapy and radiation precautions. RAI = radioiodine; T4 = levothyroxine; T3 = liothyronine; Dx RAI adm. = diagnostic radioiodine activity administration; DxWBS = diagnostic radioiodine whole-body scan; CMP = comprehensive metabolic panel; CBC = complete blood count; RAI Rx = ^{131}I therapy; PT-WBS = posttherapy ^{131}I whole-body scan; rhTSH = recombinant human TSH, Thyrogen®; LID = 2 wk of low-iodine diet; TSH = thyroid-stimulating hormone; F-T4 = free thyroxine; Tg = thyroglobulin.

Preparation*	Day 1	Day 2	Day 3–4	Day 4	Day 5	Days 6–11 (2–7 d post-Rx)
Thyroid hormone management: • Continue T4	Baseline blood tests: • Pregnancy • TSH, Tg, TgAb, F-T4 • CMP • CBC w. Diff	Late afternoon: Dx RAI adm. (3–4 mCi)	rhTSH stim. DxWBS: • Review/report scan • Review pathology • Review blood test results • ^{131}I therapy planning	^{131}I therapy administration		PT-WBS
Diet management: • Start LID for 2 wk	Morning rhTSH injection (0.9 mg IM adm.)	Morning rhTSH injection (0.9 mg IM adm.)	New patient consult: • Explain findings, prognosis • Discuss indications for ^{131}I Rx • Discuss logistics of ^{131}I Rx • Discuss radiation precautions • Discuss management of postoperative hypothyroidism	Prior to ^{131}I therapy administration, obtain blood sample for stimulated Tg.		
				• Patient education for radiation precautions • Patient signs informed consent and radiation precautions form documenting understanding and adherence to recommendations	Patient: • Starts normal diet • Continues hydration and lemon candies for salivary protection	

FIGURE 2. Sample protocol for ^{131}I theranostics after rhTSH-stimulation. *Initial consultation is recommended to discuss preparation protocol with patient and family and explain logistics and expectations of ^{131}I therapy and radiation precautions. RAI = radioiodine; T4 = levothyroxine; CMP = comprehensive metabolic panel; CBC = complete blood count; Dx RAI adm. = diagnostic radioiodine activity administration; Dx WBS = diagnostic radioiodine whole-body scan; RAI Rx = ^{131}I therapy; PT-WBS = posttherapy ^{131}I whole-body scan; THW = stimulation protocol by thyroid hormone withdrawal; rhTSH = recombinant human TSH; LID = 2 wk of low-iodine diet; TSH = thyroid stimulating hormone; F-T4 = free thyroxine; Tg = thyroglobulin.

Preparation*	Day 1	Day 2	Day 3	Days 4–5	Days 5–6	Days 6–11 (2–7 d post-Rx)
Thyroid hormone management: • Replace T4 withT3 for first 2 wk • Then stop T3 for next 2 wks	Baseline blood tests: • Pregnancy • TSH, Tg, TgAb, F-T4 • CMP • CBC w. Diff	DxWBS (24 h): • Review/report scan • Review pathology • Review blood test results Dosimetry: • 24-h WB counts • 24-h blood counts	DxWBS (48 h) Dosimetry: • 48-h WB counts • 48-h blood counts	Dosimetry: • 72- ± 96-h WB counts • 72- ± 96-h blood counts • Finalize dosimetry calculations		PT-WBS
Diet management: • Start LID for 2 wk (when T3 is stopped)	RAI Dx adm. (1–2 mCi)	New patient consult: • Explain findings, prognosis • Discuss indications for ^{131}I Rx • Discuss logistics of ^{131}I Rx • Discuss radiation precautions • Discuss management of postoperative hypothyroidism		^{131}I therapy administration		
	At 1 h post-RAI Dx: • Baseline WB counts • Baseline blood counts			• Patient education for radiation precautions • Patient signs informed consent and radiation precautions form documenting understanding and adherence to recommendations	Patient: • Starts normal diet • Starts T4 for reversal of hypothyroidism • Continues hydration and lemon candies for salivary protection	

FIGURE 3. Sample protocol for ^{131}I theranostics with dosimetry after thyroid hormone withdrawal (THW). *Initial consultation is recommended to discuss preparation protocol with patient and family and explain logistics and expectations of ^{131}I therapy and radiation precautions. RAI = radioiodine; T4 = levothyroxine; T3 = liothyronine; CMP = comprehensive metabolic panel; CBC = complete blood count; Dx RAI adm. = diagnostic radioiodine (^{123}I, ^{131}I) activity administration; DxWBS = diagnostic radioiodine whole-body scan; ^{131}I Rx = ^{131}I therapy; PT-WBS = posttherapy ^{131}I whole-body scan; THW = stimulation protocol by thyroid hormone withdrawal; LID = 2 wk of low-iodine diet; TSH = thyroid stimulating hormone; F-T4 = free thyroxine; Tg = thyroglobulin.

ment of locoregional and metastatic disease, no recommendation can be made for the superiority of 1 method of ^{131}I application over another. However, it is essential to emphasize that the MTA can be exceeded in patients undergoing empiric ^{131}I therapy escalation for treatment of advanced DTC, which may cause acute dose-related toxicities. Likewise, patients may be undertreated with this conventional therapeutic approach (*92*). (The full discussion on the limitations of the empiric approach as compared to the dosimetric strategy for treatment of metastatic DTC is available online in the full version of the guideline.)

Administration of empiric ^{131}I activities of ≤3.7 GBq (≤100 mCi) is generally not recommended for treatment of locoregionally advanced and/or distant metastatic DTC, as these patients require escalation of ^{131}I therapeutic activity and an individualized treatment approach. Particularly in the setting of diffuse iodine-avid distant metastatic disease, the attending physician or managing medical team should consider either performing dosimetry or referring the patient to a site that performs dosimetry-guided ^{131}I therapy, for 2 reasons: (1) to identify those patients who would have a higher likelihood of side effects if ≥5.6–7.4 GBq (150–200 mCi) ^{131}I therapeutic activity is administered; and/or (2) to administer the highest safe ^{131}I therapeutic activity (MTA) for maximizing tumor radiation absorbed dose. Current evidence suggests that dosimetry-based high-activity ^{131}I therapy in patients with advanced DTC may be more effective in improving outcomes and survival (*93,94*).

Each ^{131}I therapy should be followed by ^{131}I PT-WBS. Distinct advantages are offered by postsurgery ^{131}I activity administration for all risk stratification categories and irrespective of postoperative Tg levels, confirming the role of PT-WBS for early detection and treatment of locoregional and distant metastatic disease. Park et al. (*55*) demonstrated in a large cohort of 824 DTC patients who underwent ^{131}I therapy after T4 withdrawal protocol that 52 (6.3%) had functioning metastases identified on PT-WBS scans despite stimulated

Preparation* First week	Day 1	Day 2	Day 3	Day 4	Days 5–6
Thyroid hormone management: • Continue T4	Baseline blood tests: • Pregnancy • TSH, Tg, TgAb, F-T4 • CMP • CBC w. Diff	Late afternoon: Dx RAI adm. (2 mCi)	rhTSH stim. DxWBS (24 h): • Review/report scan • Review pathology • Review blood test results Dosimetry: • 24-h WB counts • 24-h blood counts	DxWBS (48 h) Dosimetry: • 48-h WB counts • 48-h blood counts	Dosimetry: • 72- ± 96-h WB counts • 72- ± 96-h blood counts • Finalize dosimetry calculations
Diet management: • Start LID for 2 wk	Morning: • rhTSH injection (0.9 mg IM adm.)	Morning: • rhTSH injection (0.9 mg IM adm.)	New patient consult: • Explain scan findings, prognosis • Discuss indications for ^{131}I Rx • Discuss logistics of ^{131}I Rx • Discuss radiation precautions • Discuss management of postoperative hypothyroidism		Obtain blood sample for stimulated Tg
		At 1 h post-RAI Dx: • Baseline WB counts • Baseline blood counts			
Second week	**Day 1**	**Day 2**	**Day 3**	**Day 4**	**Day 5–10**
Thyroid hormone management: • Continue T4	Morning: rhTSH injection (0.9 mg IM adm.)	Morning: rhTSH injection (0.9 mg IM adm.)	rhTSH stim. ^{131}I therapy (based on dosimetry calculations performed in prior week)		Obtain PT-WBS
Diet management: • Continue LID			Patient visit: • Discuss dosimetry results and prescribed ^{131}I activity • Discuss possible side effects and management strategies • Discuss management of postoperative hypothyroidism • Patient education for radiation precautions • Patient signs informed consent and radiation precautions form documenting understanding and adherence to recommendations	Patient: • Starts normal diet • Continues hydration and lemon candies for salivary protection	

FIGURE 4. Sample protocol for ^{131}I theranostics with dosimetry after rhTSH-stimulation. *Initial consultation is recommended to discuss preparation protocol with patient and family and explain logistics and expectations of ^{131}I therapy and radiation precautions. RAI = radioiodine; T4 = levothyroxine; CMP = comprehensive metabolic panel; CBC = complete blood count; Dx RAI adm. = diagnostic radioiodine activity administration; DxWBS = diagnostic radioiodine whole-body scan; RAI Rx = ^{131}I therapy; PT-WBS = posttherapy ^{131}I whole-body scan; THW = stimulation protocol by thyroid hormone withdrawal; rhTSH = recombinant human TSH; LID = 2 wk of low-iodine diet; TSH = thyroid stimulating hormone; F-T4 = free thyroxine; Tg = thyroglobulin.

Tg ≤ 2 ng/mL in the absence of interfering anti-Tg antibodies (TgAbs). A low stimulated Tg ≤ 2 ng/mL did not exclude the presence of distant metastases, because in this group 7 patients (13.5%) had pulmonary and osseous metastases, whereas the remaining 45 (86.5%) had cervical/mediastinal lymph nodal metastases. In a recent study by Campenni et al. (*95*) in 570 low- and low-intermediate–risk DTC patients (pT1–pT3) PT-WBS scans with SPECT/CT demonstrated metastases in 82 patients (14.4%), of whom 73 (90.2%) had postsurgical nonstimulated Tg ≤ 1 ng/mL; furthermore, in 44 patients (54%) stimulated Tg remained ≤ 1 ng/mL, despite the presence of metastases on PT-WBS scans. Therefore, postsurgical nonstimulated Tg levels cannot be used independently in deciding whether to pursue therapeutic ^{131}I administration, mainly in patients assigned as low-risk based solely on surgical pathology information. The body of published evidence regarding the outcome of postoperative ^{131}I ablation in low-risk patients (which in current terminology would encompass both remnant ablation and adjuvant treatment) demonstrates that these patients can be fully reassured by a complete treatment response and would not require Tg stimulation testing or periodic neck US examinations during long-term follow-up (*96*). In fact, cohorts in which all patients, including those at low risk with nonmetastasized, nonmicrocarcinoma disease, received ^{131}I therapy after surgery demonstrated that life expectancy is normal for >85% of patients; only patients with stage IV disease at diagnosis have a reduction in life expectancy (*97,98*). We are not aware of similar data available for individualized or more restrictive ^{131}I prescription strategies.

In conclusion, postoperative Tg levels are helpful in identifying high-risk patients who require higher ^{131}I activity but cannot be used for ruling out ^{131}I therapy. Omission of the procedure exposes the patients to the risk of late diagnosis of residual disease (*99,100*). Finally, early reassurance and more reliable follow-up are only possible when patients had received total thyroidectomy followed by postoperative ^{131}I therapy.

H. Determining the Prescribed Therapeutic ^{131}I Activity

Current practice guidelines recommend routine ^{131}I adjuvant therapy for patients with intermediate to high risk of recurrence (although there are some differences concerning intermediate-risk disease) and avoiding routine ^{131}I therapy for patients with a small (≤1 cm) intrathyroidal DTC and no evidence of locoregional or distant metastatic spread (*6,91*). However, ^{131}I therapy for other low-risk DTC patients (i.e., pT1b–T2) remains controversial. The various iterations of the ATA guidelines advised against the systematic use of ^{131}I in these patients (*6*), whereas in 2008 the European Association of Nuclear Medicine (EANM) suggested that ^{131}I therapy is helpful, citing the lack of prospective data showing that surveillance without ablation is noninferior to ^{131}I administration (*101*). Indeed, ATA, EANM, SNMMI, and the European Thyroid Association recently published a joint statement acknowledging the absence of high-quality evidence either for or against the postoperative use of ^{131}I in low-risk patients (*20*).

The decision for ^{131}I therapy and the prescribed ^{131}I activity depend on the goal of ^{131}I therapy as determined by estimated risk for persistent/recurrent disease. Table 3 lists

TABLE 3
Suggested Framework for ^{131}I Therapy

Strategy	Prescribed ^{131}I activity	Clinical/pathologic context
Risk-adapted ^{131}I therapy	1.11–1.85 GBq (30–50 mCi) ^{131}I*	Remnant ablation
Risk-adapted ^{131}I therapy	1.85–3.7 GBq (50–100 mCi) ^{131}I**	Adjuvant treatment
Risk-adapted ^{131}I therapy	3.7–5.6 GBq (100–150 mCi) ^{131}I	Treatment of small volume locoregional disease
Risk-adapted ^{131}I therapy	5.6–7.4 GBq (150–200 mCi) ^{131}I	Treatment of advanced locoregional disease and/or small volume distant metastatic disease
Whole-body/-blood dosimetry	≥7.4 GBq (≥200 mCi) ^{131}I, maximum tolerable safe ^{131}I activity	Treatment of diffuse distant metastatic disease

*FDA approved the use of rhTSH in combination with 100 mCi ^{131}I for remnant ablation in December 2007 (*139,140*).

**Some committee members recommend up to 5.6 GBq (150 mCi) without extant data regarding the effectiveness and toxicity profiles of 1.85 GBq (100 mCi) vs. 5.6 GBq (150 mCi) for adjuvant treatment. Current guidelines advise that frequency and severity of side effects are activity dependent, specifically, increased xerostomia risk for >3.7GBq (100 mCi) and sialadenitis risk for >5.6 GBq (150 mCi) (*141*).

suggested ^{131}I treatment activities in the context of therapeutic intent:

Thyroid remnant ablation in low-risk patients is typically performed with low ^{131}I activity (e.g., 1.1–1.85 GBq [30–50 mCi]), based on the preponderance of published evidence demonstrating equal effectiveness as compared with higher ^{131}I activities, with lower rates of adverse events (*102–138*). The Federal Drug Administration (FDA) approved the used of rhTSH (Thyrogen®; Genzyme Corp., Cambridge, MA) in combination with 3.7 GBq (100 mCi) ^{131}I for remnant ablation in December 2007 (*68,139,140*).

Adjuvant ^{131}I therapy is performed with 1.85–3.7 GBq (50–100 mCi), with some institutions extending this range to 5.6 GBq (150 mCi); there are no comparison data regarding the effectiveness of 3.7 GBq (100 mCi) vs. 5.6 GBq (150 mCi) for adjuvant treatment, although current guidelines advise that the risk for ^{131}I toxicity increases with therapeutic activity escalation (*141*).

Treatment of known disease is performed with 3.7–5.6 GBq (100–150 mCi) for small-volume locoregional disease and 5.6–7.4 GBq (150–200 mCi) ^{131}I for treatment of advanced locoregional disease and/or small-volume distant metastatic disease. Identification of iodine-avid diffuse metastatic disease may lead to escalation of prescribed therapeutic ^{131}I activity to ≥7.4 GBq (200 mCi), guided by dosimetry calculations (*73,142,143*).

A special circumstance is presented by the use of ^{131}I therapy (3.7 GBq [100 mCi]) for ablation of a remaining thyroid lobe after lobectomy/hemithyroidectomy as an alternative to completion thyroidectomy (*144–146*). Current guidelines propose lobectomy for patients deemed as at low risk for recurrence; however, if the pathology demonstrates a higher risk tumor, then completion thyroidectomy with resection of the contralateral thyroid lobe is recommended, with the goal of facilitating postoperative ^{131}I therapy and long-term surveillance. Therapeutic ^{131}I administration as a substitute for completion thyroidectomy is not recommended routinely (*6*). However, it can be used to eliminate the residual thyroid lobe in highly selected cases, such as patients who had experienced complications during initial surgery (e.g., recurrent laryngeal nerve paralysis), for whom completion thyroidectomy is contraindicated due to other comorbidities, or for patients who decline additional surgery. There are limited data regarding the long-term outcomes of this approach. The data suggest similar clinical outcomes, with a slightly higher proportion of patients with persistently detectable Tg. In a randomized controlled equivalence trial of 136 low-risk DTC patients treated with lobectomy, which compared low vs. high ^{131}I activities in achieving successful ablation of the remaining lobe, the remnant ablation success rate was significantly higher (75% success rate) using 3.7 GBq (100 mCi) as compared with 1.1 GBq (30 mCi) (54% ablation success rate). Mild-to-moderate short-term neck pain was more frequently reported in the high-activity group (66%) than in the low-activity group (51%). Prednisone treatment for neck pain was used more frequently in the high-activity group (36%) than in the low-activity group (*147*).

I. Dosimetry-Guided ^{131}I Therapy

There are 2 approaches for individualization of ^{131}I therapy based on dosimetry calculations: (1) blood or bone marrow dosimetry–based methods, primarily targeting *safety*; and (2) lesion dosimetry–based methods, primarily targeting *efficacy*. Of these, the classic blood-based method is more widely used and permits calculation of the MTA that can be administered to an individual patient without risk of severe hematopoietic toxicity. (The complete online version of the guideline contains a detailed discussion of blood- and lesion-based dosimetry methods.)

J. Radioiodine Toxicity: Acute and Chronic Side Effects of Radioiodine Therapy and Possible Risk of Subsequent Primary Malignancies

Therapeutic ^{131}I administration carries a risk for acute and chronic side effects and a small risk of possible

subsequent primary malignancies. (The complete online version of the guideline contains a detailed discussion of these risks.)

V. THYROID HORMONE THERAPY AND SURVEILLANCE STRATEGY

After ^{131}I therapy patients receive T4 therapy with the goal of TSH suppression, depending on patients' risk stratification (0.1–0.3 mU/L for patients with regional metastases and <0.1 mU/L for patients with distant metastases) (*6*). A recent consensus statement by the American, British, and European thyroid associations recommends that T4/T3 therapy should be considered under specific circumstances and for selected patients, especially hypothyroid patients without residual thyroid function and those with persistent symptoms of impaired well-being and cognitive dysfunction despite adequate T4 doses (*148*).

Serum Tg measurement is employed for monitoring DTC status after primary therapy. However, the usefulness of following Tg is limited in patients who have TgAbs because the serum Tg levels can be underestimated when using immunometric assays (*52*). In these patients the trend of TgAb levels over time can serve as a surrogate tumor marker (*29*). Immune memory in patients with a background of thyroid autoimmune disease accounts for the slow decline of TgAb levels after initial DTC treatment, and levels should be interpreted with caution for at least 6 mo after ^{131}I therapy (*51*). During long-term surveillance the TSH suppression target is adjusted, taking into consideration the outcome of primary therapy according to dynamic risk restratification. In patients with a structural incomplete response serum TSH is maintained <0.1 mIU/L indefinitely, while target values of 0.5–2 and 0.1–0.5 mIU/L are adopted in low- to intermediate-risk and in high-risk patients, respectively, with excellent response. Finally, TSH target values of 0.1–0.5 mIU/L are also suggested when post-therapy Tg remains detectable with evidence of structural disease (*6*).

VI. RESPONSE ASSESSMENT AFTER PRIMARY THERAPY

Dynamic risk restratification consists of reassignment of recurrence risk based on response to initial treatment, which is predictive of long-term clinical outcomes (*6*). This is performed during the first 2 y of follow-up after initial therapy (total thyroidectomy followed by ^{131}I therapy) and involves basal and stimulated Tg testing and imaging reevaluation. US is a reliable method for detection of locoregional persistent or recurrent DTC (i.e., thyroid bed and cervical lymph nodes). However, the probability of false-positive results leading to unnecessary and expensive additional procedures is far from negligible. Accordingly, the use of US should be limited (particularly in low-risk DTC) and, in the absence of TgAbs, reserved only for patients with unstimulated serum Tg levels ≥1 ng/mL (*96*). US-guided FNA biopsy with Tg determination in the fluid aspirate is used for Dx confirmation of residual disease in suspicious-appearing cervical lymph nodes identified on anatomic imaging.

In combination with Tg measurement, follow-up DxWBS are helpful for therapy response evaluation and to identify patients with suspected non-iodine–avid metastatic disease (based on elevated basal and/or stimulated Tg and negative WBS), which will prompt further investigation with ^{18}F-FDG PET/CT and/or Dx CT scan for localizing structural persistent disease (*73,149,150*).

The combination of Tg, US, and follow-up DxWBS performed at 1–2 y after primary therapy is used to restratify the risk of recurrence according to patient response to initial therapy for more accurately predicting long-term clinical outcomes. Risk restratification criteria are summarized in Table 4 (*6*).

In patients with excellent response to therapy the risk of disease recurrence is 1%–4%, which for *intermediate-risk patients* (whose initial risk for recurrence is estimated at 36%–43%) and for *high-risk patients* (whose initial risk for recurrence is estimated at 68%–70%) represents a major change in risk when CR to therapy is achieved. The clinical outcomes in patients with biochemical incomplete response are usually good: ~60% have no evidence of disease over long-term follow-up, 20% continue to have persistently abnormal Tg values without structural correlates, and only 20% develop structurally identifiable disease over 5–10-y follow-up. Patients with biochemical indeterminate response generally do well: in 80%–90% of patients the nonspecific biochemical findings either remain stable or resolve over time with T4 suppression therapy alone; however, up to 20% of these patients will eventually develop functional or structural evidence of disease progression and require additional therapies. Patients with structural incomplete response require multidisciplinary management tailored to their disease status (e.g., regional vs. distant metastases, iodine-avid

TABLE 4
Response to Therapy in DTC Patients: Dynamic Risk Stratification Criteria (Modified from [*6*])

Excellent response: No clinical, biochemical, or structural evidence of disease: negative imaging and either suppressed Tg <0.2 ng/mL or stimulated Tg <1 ng/mL
Biochemical incomplete response: Abnormal Tg (i.e., suppressed Tg >1 ng/mL or stimulated Tg >10 ng/mL) or rising anti-Tg antibody levels in the absence of localizable disease (i.e., negative imaging)
Structural incomplete response: Persistent or newly identified locoregional or distant metastases (any Tg value)
Indeterminate response: Nonspecific biochemical (i.e., suppressed Tg 0.2–1 ng/mL or stimulated Tg 1–10 ng/mL or stable/declining anti-Tg antibody levels) or structural findings that cannot be confidently classified as either benign or malignant

Tg = thyroglobulin.

vs. non-iodine–avid disease) (*6*). Depending on the results of such additional treatment patients may be restratified according to the criteria above.

Importantly, dynamic risk restratification has been validated only in patients treated with complete thyroid ablation (i.e., [near-] total thyroidectomy and postoperative ^{131}I therapy). Evidence is not available for patients treated with lobectomy alone or with thyroidectomy without postoperative ^{131}I therapy (*151*). After thyroidectomy, Tg levels are influenced by the amount of thyroid tissue remnant and the TSH level at the time of Tg measurement. Even if decreasing Tg levels may be reassuring, it is difficult to provide general interpretation criteria for serum Tg in such cases. Furthermore, measuring Tg is essentially useless after lobectomy, because Tg levels will not depend on the presence or absence of tumor but rather on the mass of remaining thyroid tissue, current iodine status, and TSH concentration (*152*). Park et al. (*153*) followed 208 low-risk PTC patients postlobectomy over a median of 6.9 y. The levels of Tg and Tg/TSH ratio and the proportions of patients in whom serum Tg levels increased by ≥50% or ≥100% over baseline measurement did not differ significantly in patients with or without recurrence (*153*).

VII. THERAPY OF ADVANCED DISEASE

Distant metastases develop in about 10% of DTC patients, commonly in lungs and less frequently in bone, brain, liver, and skin, and are the main cause of significant symptoms and death (i.e., overall mortality of 65% at 5 y and 75% at 10 y) (*154*). Younger patients and those with single-organ metastases and low disease burden have the best outcomes (*60*). The mainstay of metastatic disease treatment is TSH suppression and repeated courses of ^{131}I treatment as long as the disease remains iodine-avid (*155*). About two-thirds of patients have radioiodine-avid distant metastases, and >40% of these will achieve remission after ^{131}I treatments (*60*). However, a minority of DTC cases lose the ability to concentrate iodine in sufficient quantities to allow therapeutically effective radiation absorbed doses to DTC lesions (i.e., radioiodine-refractory DTC). Determining when a patient will no longer respond to ^{131}I therapy can be challenging, and all factors impacting the patient's specific clinical situation (such as age, tumor histology, initial stage, radioiodine residual avidity, and ^{18}F-FDG avidity) should be carefully considered (*156*). Definitions of radioiodine-refractory DTC have been proposed by several authors (*157–160*), followed by updated classifications of radioiodine-refractory disease (*20,156,161, 162*). Classification of a patient as radioiodine refractory is very important and consequential. If one classifies a patient as radioiodine refractory when, in fact, the patient may respond to a ^{131}I therapy, then that patient has lost the potential benefit of an effective ^{131}I therapy in a situation with limited therapeutic options. However, if patients receive ^{131}I therapy without benefit, not only may they experience unnecessary side effects from an ineffective therapy, but a potentially beneficial alternative therapy is delayed.

The criterion with the best predictive value that a patient has radioiodine-refractory disease and will not respond to another ^{131}I treatment is progression after a short time interval after administration of a maximum safe ^{131}I therapeutic activity. All other criteria have varying degrees of likelihood that the patient is radioiodine refractory and should be cautiously considered, understanding their limitations (*161*). Although exact likelihood ratios cannot be given here for the various criteria that have been used in the past, Figure 5 presents an example of the spectrum of relatively low-to-high likelihoods of 3 criteria for predicting that a patient's metastatic DTC is radioiodine refractory. Nevertheless, the time from ^{131}I treatment to progression (i.e., progression-free survival [PFS]) after optimized ^{131}I treatment is 1 of the most important criteria for predicting radioiodine-refractory DTC. Although in the past disease progression was considered in and of itself indicative of ^{131}I treatment failure (*6*), progression must be considered in light of many factors (Table 5), including length of PFS and amount of ^{131}I activity administered. Caveats guiding classification of a patient's metastatic DTC as radioiodine refractory are also noted in Table 6. Additional management options to be considered prior to classifying a patient's metastatic DTC as radioiodine refractory are presented in Table 7.

Despite a negative DxWBS, administration of ^{131}I therapy should still be considered for obtaining a PT-WBS, which is more sensitive for detectig metastatic disease with reduced (but not absent) ^{131}I-concentrating capacity. Although absence of uptake on a PT-WBS is a stronger indicator of radioiodine-refractory disease, it is not a definitive imaging biomarker for tumor NIS expression in the setting of progressive metastatic disease. Several authors have shown that the timing of a PT-WBS scan after therapeutic ^{131}I administration (e.g., 3–4 d versus 5–7 d) can make the difference in interpretation between a negative and positive PT-WBS (*80,81,83,84,163*). Additional options to be considered before classifying a

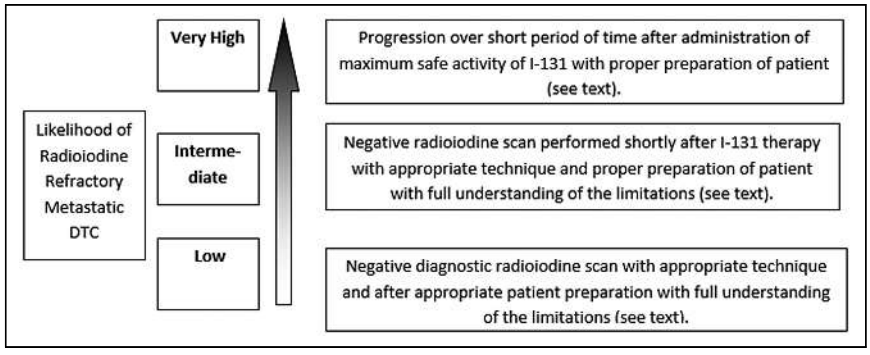

FIGURE 5. Likelihood of radioiodine-refractory differentiated thyroid cancer.

TABLE 5
Additional Considerations Before Assignment of Radioiodine-Refractory Disease Status (*161*)

• Appropriate preparation of patient for diagnostic and/or posttherapy RAI scan (*39*,*177*)
• Results of the diagnostic scan
• Results of the posttherapy scan
• Response to the last ^{131}I therapy
• Criteria for progression
• Time to progression
• Activity of ^{131}I administered for the last ^{131}I therapy
• Total accumulative activity of ^{131}I administered
• Objectives of ^{131}I therapy (e.g., cure, progression-free survival, overall survival, palliation)
• Location and number of metastases. They may be radioiodine avid, but perhaps focal direct therapy (e.g., surgery, XRT, cryotherapy, etc.) may be more effective, warranted, or desired.
• Type, frequency, and severity of side effects of ^{131}I therapy
• Patient's desires (e.g., patient is a "minimalist" or "maximalist") (*200*)

patient's DTC as radioiodine refractory are: (1) refer the patient to a site that performs radioiodine dosimetry and/or frequently manages aggressive and progressive DTC; or (2) help selected patients explore eligibility for participating in a research study offering "resensitizing" or "redifferentiating"

TABLE 6
Caveats Regarding Criteria for Radioiodine-Refractory Metastatic Differentiated Thyroid Cancer (Adapted from [*161*])

• The observation that a patient does not demonstrate radioiodine uptake on a diagnostic scan or posttherapy scan does not necessarily mean that the patient's metastatic disease is radioiodine refractory.
• The observation that a patient does demonstrate radioiodine uptake on a diagnostic scan or posttherapy scan does not necessarily mean that the patient's metastatic disease is responsive to a ^{131}I therapy.
• As the total accumulative activity of administered ^{131}I increases, the likelihood of a response to a subsequent ^{131}I therapy decreases. However, no maximum accumulated threshold of administered ^{131}I activity should designate a patient's metastatic disease as radioiodine refractory.
• One metastatic *lesion* that is classified as *radioiodine refractory* does not necessarily mean the *patient* is now *radioiodine refractory*. Combination therapy of direct focal therapy (e.g., surgery, external-beam radiotherapy, radiofrequency ablation, cryotherapy, embolization, radioisotope embolization) or/with targeted therapy (e.g., tyrosine kinase inhibitors, BRAF inhibitors, etc.) in combination with ^{131}I therapy may benefit the patient.
• Progression, in and of itself, is not a criterion that a ^{131}I therapy has "failed" and that a patient's metastatic disease is "radioiodine refractory." Additional factors, such as duration of progression-free survival and administered activity of ^{131}I are important.

TABLE 7
Additional Options Prior to Radioiodine Refractory Classification

• Consider a "blind" ^{131}I therapy (see text).
• Refer the patient to a site that performs dosimetry.
• Refer the patient to a site that routinely manages metastatic differentiated thyroid cancer.
• Consider exploring the patient's eligibility for participating in a study that offers "resensitizing" or "redifferentiating" agents to see if radioiodine uptake can be reestablished or increased for a potential ^{131}I therapy

agents to determine if radioiodine uptake can be reestablished or increased for a potential ^{131}I therapy (*164*–*167*).

Focally targeted treatment (i.e., resection, vertebroplasty, external-beam radiation therapy, and thermal ablation) can provide local control, provide symptomatic relief, and delay initiation of systemic therapy. These therapies can be used with concurrent ^{131}I or other systemic therapies when targeting progression in a single lesion and may enable continued overall disease control (*168*). Treatment with bisphosphonates or denosumab can delay time to skeletal related events (*169*). However, caution is necessary if using biphosphonates, as there is a risk for osteonecrosis of the jaw, especially in patients treated with intravenous bisphosphonates. Therefore, it is important to evaluate dental health before initiation of such therapy and avoid dental procedures during the therapy (*170*). In cases of confirmed systemic progression of radioiodine-refractory disease, intravenous chemotherapy with doxorubicin was traditionally used, but a partial response was obtained only in a small minority of patients. More recently "targeted" therapies, including multikinase inhibitors (MKIs) (e.g., sorafenib and lenvatinib), have been approved for patients with advanced radioiodine-refractory DTC. These drugs have been shown to induce periods of PFS (rarely remission). However, they do not increase cancer-specific survival and may be associated with significant side effects, such as hypertension, diarrhea, hand/foot skin reactions, rash, fatigue, mucositis, loss of appetite, and weight loss (*154*). It remains unclear which patients will benefit from MKIs in terms of an increase in quality-adjusted life years and optimal time to start therapy, especially in asymptomatic patients. As a rule, molecular-targeted therapies should be started in patients with progression of measurable lesions (as defined radiologically by the Response Evaluation Criteria in Solid Tumors [RECIST]) over the previous 12 mo, taking into consideration tumor burden, disease sites, symptoms, and risk of local complications (*171*). In the setting of clinical trials involving redifferentiation strategy, molecular tumor analysis can direct therapy (e.g., BRAFV600E + → dabrafenib [± trametinib, vemurafenib; BRAF– → trametinib]). Furthermore, identification of NTRK RET fusion could also direct therapy toward selective inhibitors (e.g., selpercatinib).

The biologic mechanisms implicated in radioiodine refractoriness involve gain-of-function mutations in the MAPK-signaling pathway, resulting in reduced NIS and other iodine-metabolizing gene expression. Experimental data showed that MAPK-signaling pathway inhibition using MEK or BRAF inhibitors may restore radioiodine avidity. Subsequent clinical studies demonstrated that mutation-guided treatment using selective MEK inhibitors (selumetinib, trametinib), BRAF inhibitors (dabrafenib, vemurafenib), or a combination of BRAF inhibitor and MEK inhibitor is feasible and represents a promising strategy to redifferentiate radioiodine-refractory DTC, thereby permitting reapplication of ^{131}I therapy. Preliminary data obtained on a small clinical series of 13 patients demonstrated restoration of ^{131}I avidity in 62% of patients who subsequently received ^{131}I treatment (median activity, 7.6 GBq [204.4 mCi]; range, 5.5–9.4 GBq [150–253 mCi]), resulting in durable disease control (median duration >1 y) while not receiving chronic, expensive MKI therapy (*165*). ^{131}I therapy remains the only known cure for metastatic radioidine-sensitive DTC, and the use of a redifferentiating strategy to permit additional ^{131}I treatment for patients with radioiodine-refractory metastatic disease represents a promising therapeutic approach while minimizing exposure to kinase inhibitor therapy.

A. ^{18}F-FDG PET/CT Imaging for Thyroid Cancer

Advances in molecular Dx imaging and the clinical availability of PET/CT systems produced a paradigm shift in the management of thyroid cancer by allowing characterization of tumor biology based on variable uptake patterns of radioiodine and ^{18}F-FDG in metastatic lesions. Feine et al. (*172,173*) described the "flip-flop" phenomenon as opposite radiotracer uptake patterns on radioiodine scintigraphy and ^{18}FDG-PET/CT imaging, recognizing 4 patterns of variable radioiodine/FDG uptake in metastatic disease. *Type I* is characterized by negative ^{131}I/positive FDG uptake and is the most commonly encountered pattern in patients with elevated Tg and negative scintigraphy (i.e., Tg+/scan–), which is found in ~46% cases. *Type II* is characterized by positive ^{131}I/negative FDG uptake and represents the most favorable context for therapeutic ^{131}I administration. *Type III* consists of a combination of type I and II patterns recognized in different metastatic lesions within the same patient due to varying biologic behavior in metastatic foci. *Type IV* is characterized by uptake of both ^{131}I and ^{18}FDG within the same metastatic lesions. The flip-flop phenomenon is not a constant for DTC metastases but rather a variable marker of tumor biology. A prospective study of 122 postthyroidectomy patients with established metastatic DTC who were imaged with both DxWBS and ^{18}FDG-PET/CT showed a general correlation of FDG avidity with lack of iodine avidity; however, the correlation coefficient was only 0.62. For the selected SUV_{max} cutoff value of 4.0, the authors calculated a sensitivity of 75.3% and specificity of 56.7% for identification of non-iodine–avid metastatic disease (*174*). Hence, the decision on whether to perform ^{131}I therapy should not be based on ^{18}F-FDG PET/CT alone. The most common application of PET/CT imaging in DTC is for evaluation of patients with elevated Tg and negative DxWBS (i.e., Tg+/scan–) (*175*).

B. Management Algorithm for Patients with Elevated Tg and Negative DxWBS (Tg+/Scan–)

Although this is frequently seen as 1 syndrome (called TENIS syndrome [Tg elevation, negative iodine scintigraphy]), in fact it represents a wide spectrum of clinical situations (discussed in more detail in the online complete version of the guideline).

Devising a treatment plan may be facilitated by following 4 steps:

Step 1: Rule out false-negative DxWBS and false-positive Tg levels: To evaluate for false-negative DxWBS, the interpreting physician needs to consider: (1) screening for a history of recent iodine load, such as recent administration of radiologic contrast agents or ingestion of kelp, as well as administration of amiodarone, even months to years earlier; (2) confirming compliance with LID as demonstrated by low urinary iodine levels (e.g., spot urine iodine level, spot urine I/Cr, or 24-h urine iodine collection); (3) ascertaining adequate TSH elevation, which is especially important with preparation by THW; (4) excluding heterophilic antibody interference on Tg measurement (prevalence 0.4%–1%) (*176*); (5) confirming correct radiopharmaceutical administration (reviewing documents for appropriate isotope and prescribed activity and reviewing the scan images themselves for inappropriate distribution of radioactivity); (6) confirming technical scan parameters (collimator type, peaking of energy window, table speed for planar scan, time interval for stop position for SPECT acquisition, etc). Although one may assume that all radioiodine scans are performed equally, they are not, and assessment of the quality of the scan is important to minimize false-negative radioiodine scans (*177*).

Step 2: Perform dynamic risk restratification: If the patient has a low risk for disease recurrence, active surveillance is appropriate and may include: (1) physical exam; (2) Tg, TgAb, and TSH testing; and (3) US of the thyroid bed and neck. However, nonradioiodine imaging is indicated when the patient has an intermediate or higher risk for disease recurrence. Other factors noted in Table 8 are relevant to consider.

Step 3: Obtain nonradioiodine imaging: Nonradioiodine imaging studies for metastatic DTC have been divided into 3 tiers: primary, secondary, and tertiary. The primary tier includes: (1) neck US; (2) ^{18}F-FDG PET/CT imaging; and/or (3) CT of the neck, chest, abdomen, and pelvis. These studies can be performed sequentially; however, whenever possible, integrated PET/CT imaging is preferable because it provides both functional and anatomic information. The secondary tier includes: (1) brain MRI; (2) bone scanning (using ^{99m}Tc-methylene disphosphonate [^{99m}Tc-MDP] or ^{18}F-sodium fluoride PET/CT [^{18}F-NaF PET/CT]); and (3) mitochondrial imaging (e.g., ^{99m}Tc-sestamibi, ^{201}Tl, or ^{99m}Tc-tetrofosmin). These studies should primarily be reserved for patients in whom the

TABLE 8
Factors Considered for Management of Elevated Tg and Negative DxWBS (Tg+/Scan–) Patients

• Treatment objectives (i.e., cure, progression-free survival, palliation)
• Time interval since last ^{131}I treatment
• Amount of ^{131}I activity administered for most recent treatment
• Response to most recent ^{131}I treatment (if there has been a previous therapy)
• Total cumulative ^{131}I therapeutic activity
• Frequency and severity of side effects of prior ^{131}I therapies
• Is the patient a minimalist or maximalist regarding benefit vs risk of ^{131}I therapy?
• Comorbidities
• Capabilities of the treating facility

first tier did not reveal metastatic lesions. In the context of advanced DTC, brain MRI is recommended, because patients may have brain metastases in the absence of neurologic signs or symptoms and ^{18}F-FDG PET is not reliable in the brain due to high brain glucose metabolism. Although DTC osseous metastases are typically osteolytic and highly vascularized, bone metastases can occasionally be detected on ^{99m}Tc-MDP bone scintigraphy or ^{18}F-NaF PET/CT when ^{18}F-FDG PET/CT is negative. Although widespread implementation of ^{18}F-FDG PET/CT imaging for evaluation of Tg+/scan– patients replaced routine use of mitochondrial imaging, the different uptake mechanisms of ^{99m}Tc-sestamibi and ^{18}F-FDG in neoplastic cells provides the rationale for selected use of ^{99m}Tc-sestamibi in difficult patients with suspected metastatic disease not identified by other conventional imaging modalities (e.g., negative ^{131}I WBS, US, ^{18}F-FDG PET/CT, and CT) (*79,178*). The tertiary tier includes somatostatin receptor (SSR) imaging with radiolabeled somatostatin analogs (e.g., ^{99m}Tc-depreotide, ^{99m}Tc-EDDA/HYNIC-Tyr3-octreotide [Tektrotyd], ^{111}In-octreotide, and ^{68}Ga-DOTATATE/TOC/NOC). A substantial percentage of aggressive histologic variants of DTC (e.g., Hürthle cell, tall cell, insular variants) associated with locoregionally advanced and/or metastatic DTC exhibit cellular expression of SSR, which can be found independently of glucose transporter overexpression (i.e., in patients with negative ^{18}F-FDG PET/CT imaging) (*79*). SSR PET imaging also often provides complementary information in ^{18}F-FDG+ patients and appears to be especially promising in poorly differentiated and oxyphilic subtypes (i.e., Hürthle cell) metastatic DTC (*179,180*). Peptide-receptor radionuclide therapy using radiolabeled somatostatin analogues has shown promise for treatment of ^{131}I-refractory metastatic DTC, with a demonstrated objective response rate of 20%–60% tumor reduction as determined by radiologic measurements (RECIST) (*181–183*). For the future, some promise is shown in individual cases employing ^{68}Ga–prostate-specific membrane antigen imaging.

Step 4: Customize management to the location and number of the metastases: Once 1 or multiple metastatic sites are identified, one must decide whether tissue biopsy for histologic examination and mutational profile characterization is needed. Focally directed therapy needs to be considered for management of unifocal or oligometastatic disease (e.g., surgical resection, external-beam radiation therapy, alcohol injection, radiofrequency ablation, cryotherapy, embolization, and/or radioisotope embolization). ^{131}I therapy should be considered if doubt is still present regarding ^{131}I refractory status. Systemic and/or combined therapy is recommended for multifocal or widespread metastases.

C. ^{18}F-FDG PET/CT Imaging for Prognosis of Metastatic DTC

Approximately 15%–20% of patients with metastatic DTC and most patients with Hürthle cell thyroid cancer are refractory to radioiodine, and OS for these patients ranges between 2.5 and 4.5 y (*60,158,184*). The prognosis of metastatic DTC is variable, with 2 distinct phenotypes identified: indolent and aggressive (*185,186*). Patients with iodine-avid metastatic DTC tend to have more favorable prognoses, with 10-y survival >90%, whereas non-iodine–avid metastatic DTC has a dire 10-y survival of 10% (*187*). On a molecular level, this is largely driven by genetic patterns, with specific mutations associated with aggressiveness of thyroid cancer disease (*188*). Two studies demonstrated suboptimal predictive value of staging, including the widely used TNM system (*189,190)*. Tg doubling time (Tg-DT) has been identified as a prognostic factor, with Tg-DT < 1 y portending poor prognosis and Tg-DT > 2 y signifying good prognosis (*191*). However, Tg-DT cannot be calculated in the presence of TgAbs, which invalidate Tg measurements, and it cannot inform regarding the metabolic phenotype and spatial distribution of metastatic lesions. There is a large variability in survival time for patients with metastatic DTC, ranging from 1 to 30 y (*186*). The lack of accurate survival estimates for the individual patient has important implications for treatment decisions, especially regarding initiation of targeted MKI therapies (*192,193*). Due to the toxicity profiles of these medications, current National Comprehenisve Cancer Network guidelines advocate active surveillance as standard of care in metastatic disease until evidence of symptomatic or clinically progressive disease as outlined by RECIST (*194,195*).

^{18}F-FDG PET/CT imaging is particularly useful not only for identification and localization of non-iodine–avid metastases but also for predicting the course of disease as aggressive or indolent. ^{18}F-FDG PET/CT has demonstrated prognostic value for survival in metastatic DTC (*196*), predicting a survival disadvantage for patients with positive PET compared with those with negative PET results (*184,197*). Robbins et al. (*184*) demonstrated that in patients with metastatic DTC a positive ^{18}F-FDG PET/CT scan result predicted a 7-fold increased risk of mortality compared with patients who had negative FDG scans.

^{18}F-FDG PET/CT metabolic parameters can help define the volume and biologic variations of metastatic tumor burden.

Specifically, metabolic tumor volume (MTV) and total glycolytic activity (also referred to as total lesion glycolysis [TLG]) have been proposed as imaging biomarkers for prognosis in human solid tumors (*198*). Robbins et al. (*184*) demonstrated that total FDG tumor volume and lesional SUV_{max} correlate with survival. Wang et al. (*196*) noted that an FDG volume >125 mL was associated with worse survival. The metabolic parameters of MTV and TLG obtained with ^{18}F-FDG PET/CT have been used as surrogate markers for tumor burden and biologic aggressiveness for prognosis of OS and PFS in non-iodine–avid metastatic DTC. Higher-than-median MTV and TLG values were associated with worse OS and PFS, with a median OS of only 3.5 y for patients with radioiodine-refractory metastatic DTC (*199*). This information can be used to guide more rapid implementation of newer therapeutic agents for radioiodine-refractory metastatic DTC and enrollment in clinical trials.

VIII. CONCLUSION

DTC is the most common endocrine malignancy, with a rising incidence for the last 30 y. The standard of care for DTC patients is multidisciplinary and involves a risk-stratified approach integrating information from surgical histopathology, genetic markers, postoperative Tg levels, and anatomic/functional imaging studies. Early identification of residual nodal and/or distant metastases is particularly relevant for successful ^{131}I therapy of metastatic disease, because patients who achieve a CR have considerably higher survival rates than patients with structural incomplete responses. Integration of Dx radioiodine scintigraphy in the management algorithm of patients with thyroid cancer should be considered, and further multidiciplinary collaborative studies to assess patient-relevant outcome measures (disease-specific survival, recurrence rates, and PFS) need to be performed.

REFERENCES

1. Surveillance, Epidemiology, and End Results Program. Cancer stat facts: Thyroid Cancer. Bethesda, MD: National Cancer Institute; 2021. Available at: https://seer.cancer.gov/statfacts/html/thyro.html. Accessed on March 7, 2022.
2. Ahn HS, Kim HJ, Kim KH, et al. Thyroid cancer screening in South Korea increases detection of papillary cancers with no impact on other subtypes or thyroid cancer mortality. *Thyroid.* 2016;26(11):1535–1540.
3. Davies L, Morris LG, Haymart M, et al. American Association of Clinical Endocrinologists and American College of Endocrinology Disease State Clinical Review: The increasing incidence of thyroid cancer. *Endocr Pract.* 2015;21(6):686–696.
4. Gulec SA, Ahuja S, Avram A, et al. A joint statement from the American Thyroid Association, the European Association of Nuclear Medicine, the European Thyroid Association, the Society of Nuclear Medicine and Molecular Imaging on current diagnostic and theranostic approaches in the management of thyroid cancer. *Thyroid.* 2021;31(7):1009–1019.
5. Rossi E, Fadda G. Pathology and immunohistochemistry in thyroid tumors. In: *Atlas of Thyroid and Neuroendocrine Tumor Markers.* Giovanella L, ed. New York; NY: Springer International Publishing; 2018:3–12.
6. Haugen BR, Alexander EK, Bible KC, et al. 2015 American Thyroid Association Management Guidelines for Adult Patients with Thyroid Nodules and Differentiated Thyroid Cancer: The American Thyroid Association Guidelines Task Force on Thyroid Nodules and Differentiated Thyroid Cancer. *Thyroid.* 2016;26(1):1–133.
7. Kwak JY, Han KH, Yoon JH, et al. Thyroid imaging reporting and data system for US features of nodules: A step in establishing better stratification of cancer risk. *Radiology.* 2011;260(3):892–899.
8. Russ G, Bonnema SJ, Erdogan MF, Durante C, Ngu R, Leenhardt L. European Thyroid Association Guidelines for Ultrasound Malignancy Risk Stratification of Thyroid Nodules in Adults: The EU-TIRADS. *Eur Thyroid J.* 2017;6(5):225–237.
9. Cibas ES, Ali SZ. The 2017 Bethesda System for Reporting Thyroid Cytopathology. *Thyroid.* 2017;27(11):1341–1346.
10. Giovanella L, Avram AM, Iakovou I, et al. EANM Practice Guideline/SNMMI Procedure Standard for RAIU and Thyroid Scintigraphy. *Eur J Nucl Med Mol Imaging.* 2019;46(12):2514–2525.
11. Zulewski H, Giovanella L, Bilz S, et al. Multidisciplinary approach for risk-oriented treatment of low-risk papillary thyroid cancer in Switzerland. *Swiss Med Wkly.* 2019;149:w14700.
12. Ito Y, Miyauchi A, Oda H. Low-risk papillary microcarcinoma of the thyroid: A review of active surveillance trials. *Eur J Surg Oncol.* 2018;44(3):307–315.
13. Davies L, Roman BR, Fukushima M, Ito Y, Miyauchi A. Patient experience of thyroid cancer active surveillance in Japan. *JAMA Otolaryngol Head Neck Surg.* 2019;145(4):363–370.
14. Miller JE, Al-Attar NC, Brown OH, et al. Location and causation of residual lymph node metastasis after surgical treatment of regionally advanced differentiated thyroid cancer. *Thyroid.* 2018;28(5):593–600.
15. Roh JL, Park JY, Park CI. Total thyroidectomy plus neck dissection in differentiated papillary thyroid carcinoma patients: pattern of nodal metastasis, morbidity, recurrence, and postoperative levels of serum parathyroid hormone. *Ann Surg.* 2007;245(4):604–610.
16. Barczynski M, Konturek A, Stopa M, Nowak W. Prophylactic central neck dissection for papillary thyroid cancer. *Br J Surg.* 2013;100(3):410–418.
17. Piccardo A, Trimboli P, Foppiani L, et al. PET/CT in thyroid nodule and differentiated thyroid cancer patients. The evidence-based state of the art. *Rev Endocr Metab Disord.* 2019;20(1):47–64.
18. Brierley JD, Gospodarowicz MK, Wittekind C. *TNM Classification of Malignant Tumours.* 8th ed. Oxford, UK: John Wiley & Sons, Ltd; 2017.
19. Van Nostrand D. The benefits and risks of I-131 therapy in patients with well-differentiated thyroid cancer. *Thyroid.* 2009;19(12):1381–1391.
20. Tuttle RM, Ahuja S, Avram AM, et al. Controversies, consensus, and collaboration in the use of ^{131}I therapy in differentiated thyroid cancer: A joint statement from the American Thyroid Association, the European Association of Nuclear Medicine, the Society of Nuclear Medicine and Molecular Imaging, and the European Thyroid Association. *Thyroid.* 2019;29(4):461–470.
21. Jonklaas J, Sarlis NJ, Litofsky D, et al. Outcomes of patients with differentiated thyroid carcinoma following initial therapy. *Thyroid.* 2006;16(12):1229–1242.
22. Carhill AA, Litofsky DR, Ross DS, et al. Long-term outcomes following therapy in differentiated thyroid carcinoma: NTCTCS registry analysis 1987–2012. J Clin Endocrinol Metab. 2015;100(9):3270–3279.
23. Sawka AM, Thephamongkhol K, Brouwers M, Thabane L, Browman G, Gerstein HC. Clinical review 170: A systematic review and metaanalysis of the effectiveness of radioactive iodine remnant ablation for well-differentiated thyroid cancer. *J Clin Endocrinol Metab.* 2004;89(8):3668–3676.
24. Ruel E, Thomas S, Dinan M, Perkins JM, Roman SA, Sosa JA. Adjuvant radioactive iodine therapy is associated with improved survival for patients with intermediate-risk papillary thyroid cancer. *J Clin Endocrinol Metab.* 2015;100(4):1529–1536.
25. Yang Z, Flores J, Katz S, Nathan CA, Mehta V. Comparison of survival outcomes following postsurgical radioactive iodine versus external beam radiation in stage IV differentiated thyroid carcinoma. *Thyroid.* 2017;27(7):944–952.
26. Higashi T, Nishii R, Yamada S, et al. Delayed initial radioactive iodine therapy resulted in poor survival in patients with metastatic differentiated thyroid carcinoma: a retrospective statistical analysis of 198 cases. *J Nucl Med.* 2011;52(5):683–689.
27. Hocevar M, Auersperg M, Stanovnik L. The dynamics of serum thyroglobulin elimination from the body after thyroid surgery. *Eur J Surg Oncol.* 1997;23(3):208–210.
28. Mazzaferri EL, Kloos RT. Clinical review 128: Current approaches to primary therapy for papillary and follicular thyroid cancer. *J Clin Endocrinol Metab.* 2001;86(4):1447–1463.
29. Spencer CA. Clinical review: Clinical utility of thyroglobulin antibody (TgAb) measurements for patients with differentiated thyroid cancers (DTC). *J Clin Endocrinol Metab.* 2011;96(12):3615–3627.
30. Xiao J, Yun C, Cao J, et al. A pre-ablative thyroid-stimulating hormone with 30-70 mIU/L achieves better response to initial radioiodine remnant ablation in differentiated thyroid carcinoma patients. *Sci Rep.* 2021;11(1):1348.
31. Lawal IO, Nyakale NE, Harry LM, et al. Higher preablative serum thyroid-stimulating hormone level predicts radioiodine ablation effectiveness in patients with differentiated thyroid carcinoma. *Nucl Med Commun.* 2017;38(3):222–227.
32. Vrachimis A, Riemann B, Mader U, Reiners C, Verburg FA. Endogenous TSH levels at the time of ^{131}I ablation do not influence ablation success, recurrence-free

survival or differentiated thyroid cancer-related mortality. *Eur J Nucl Med Mol Imaging.* 2016;43(2):224–231.
33. Pluijmen MJ, Eustatia-Rutten C, Goslings BM, et al. Effects of low-iodide diet on postsurgical radioiodide ablation therapy in patients with differentiated thyroid carcinoma. *Clin Endocrinol (Oxf).* 2003;58(4):428–435.
34. Kim JY, Kim KR. Dietary iodine intake and urinary iodine excretion in patients with thyroid diseases. *Yonsei Med J.* 2000;41(1):22–28.
35. Lakshmanan M, Schaffer A, Robbins J, Reynolds J, Norton J. A simplified low iodine diet in I-131 scanning and therapy of thyroid cancer. *Clin Nucl Med.* 1988; 13(12):866–868.
36. Katamine S, Mamiya Y, Sekimoto K, et al. Iodine content of various meals currently consumed by urban Japanese. *J Nutr Sci Vitaminol (Tokyo).* 1986;32(5):487–495.
37. World Health Organization. *Urinary Iodine Concentrations for Determining Iodine Status in Populations*. Vitamin and Mineral Nutrition Information System. Technical Report. Geneva, Switzerland: World Health Organization; 2013.
38. Sohn SY, Choi JY, Jang HW, et al. Association between excessive urinary iodine excretion and failure of radioactive iodine thyroid ablation in patients with papillary thyroid cancer. *Thyroid.* 2013;23(6):741–747.
39. Bartel Chair TB, Magerefteh S, Avram AM, et al. SNMMI Procedure Standard for Scintigraphy for Differentiated Thyroid Cancer. *J Nucl Med Technol.* 2020; 48(3):202–209.
40. Lim CY, Kim JY, Yoon MJ, Chang HS, Park CS, Chung WY. Effect of a low iodine diet vs. restricted iodine diet on postsurgical preparation for radioiodine ablation therapy in thyroid carcinoma patients. *Yonsei Med J.* 2015;56(4): 1021–1027.
41. ThyCa: Thyroid Cancer Survivors' Association. *Low-Iodine Cookbook.* 9th ed. Olney, MD: ThyCa: Thyroid Cancer Survivors' Association; 2020. Available from: https://www.thyca.org/download/document/231/Cookbook. Accessed on March 11, 2022.
42. Smith CD, Grondin R, LeMaster W, Martin B, Gold BT, Ain KB. Reversible cognitive, motor, and driving impairments in severe hypothyroidism. *Thyroid.* 2015; 25(1):28–36.
43. Grigsby PW, Siegel BA, Bekker S, Clutter WE, Moley JF. Preparation of patients with thyroid cancer for ^{131}I scintigraphy or therapy by 1–3 weeks of thyroxine discontinuation. *J Nucl Med.* 2004;45(4):567–570.
44. Van Nostrand D WL, Bloom G, Kulkarni KP, eds. *Thyroid Cancer: A Guide for Patients.* Toledo, OH: Keystone Press; 2010.
45. Giovanella L, Duntas LH. Management of endocrine disease: The role of rhTSH in the management of differentiated thyroid cancer: Pros and cons. *Eur J Endocrinol.* 2019;181(4):R133–R145.
46. Potzi C, Moameni A, Karanikas G, et al. Comparison of iodine uptake in tumour and nontumour tissue under thyroid hormone deprivation and with recombinant human thyrotropin in thyroid cancer patients. *Clin Endocrinol (Oxf).* 2006;65(4):519–523.
47. Freudenberg LS, Jentzen W, Petrich T, et al. Lesion dose in differentiated thyroid carcinoma metastases after rhTSH or thyroid hormone withdrawal: ^{124}I PET/CT dosimetric comparisons. *Eur J Nucl Med Mol Imaging.* 2010;37(12):2267–2276.
48. Zanotti-Fregonara P, Hindie E. On the effectiveness of recombinant human TSH as a stimulating agent for ^{131}I treatment of metastatic differentiated thyroid cancer. *Eur J Nucl Med Mol Imaging.* 2010;37(12):2264–2266.
49. Plyku D, Hobbs RF, Huang K, et al. Recombinant human thyroid-stimulating hormone versus thyroid hormone withdrawal in ^{124}I PET/CT-based dosimetry for ^{131}I therapy of metastatic differentiated thyroid cancer. *J Nucl Med.* 2017;58(7): 1146–1154.
50. Clerc J, Verburg FA, Avram AM, Giovanella L, Hindie E, Taieb D. Radioiodine treatment after surgery for differentiated thyroid cancer: a reasonable option. *Eur J Nucl Med Mol Imaging.* 2017;44(6):918–925.
51. Verburg FA, Luster M, Cupini C, et al. Implications of thyroglobulin antibody positivity in patients with differentiated thyroid cancer: A clinical position statement. *Thyroid.* 2013;23(10):1211–1225.
52. Giovanella L, Feldt-Rasmussen U, Verburg FA, Grebe SK, Plebani M, Clark PM. Thyroglobulin measurement by highly sensitive assays: focus on laboratory challenges. *Clin Chem Lab Med.* 2015;53(9):1301–1314.
53. Campenni A, Ruggeri RM, Siracusa M, et al. Early preablation rhTSH-stimulated thyroglobulin predicts outcome of differentiated thyroid cancer (DTC) patients. *Eur J Nucl Med Mol Imaging.* 2021;48(8):2466–2475.
54. Giovanella L, Suriano S, Ceriani L, Verburg FA. Undetectable thyroglobulin in patients with differentiated thyroid carcinoma and residual radioiodine uptake on a postablation whole-body scan. *Clin Nucl Med.* 2011;36(2):109–112.
55. Park EK, Chung JK, Lim IH, et al. Recurrent/metastatic thyroid carcinomas false negative for serum thyroglobulin but positive by posttherapy I-131 whole body scans. *Eur J Nucl Med Mol Imaging.* 2009;36(2):172–179.
56. Matrone A, Gambale C, Piaggi P, et al. Postoperative thyroglobulin and neck ultrasound in the risk restratification and decision to perform ^{131}I ablation. *J Clin Endocrinol Metab.* 2017;102(3):893–902.
57. Schlumberger M, Leboulleux S, Catargi B, et al. Outcome after ablation in patients with low-risk thyroid cancer (ESTIMABL1): 5-year follow-up results of a randomised, phase 3, equivalence trial. *Lancet Diabetes Endocrinol.* 2018;6(8): 618–626.
58. Hindie E, Taieb D, Avram AM, Giovanella L. Radioactive iodine ablation in low-risk thyroid cancer. *Lancet Diabetes Endocrinol.* 2018;6(9):686.
59. Van Nostrand D, Atkins F, Moreau S, et al. Utility of the radioiodine whole-body retention at 48 hours for modifying empiric activity of 131-iodine for the treatment of metastatic well-differentiated thyroid carcinoma. *Thyroid.* 2009;19(10): 1093–1098.
60. Durante C, Haddy N, Baudin E, et al. Long-term outcome of 444 patients with distant metastases from papillary and follicular thyroid carcinoma: benefits and limits of radioiodine therapy. *J Clin Endocrinol Metab.* 2006;91(8):2892–2899.
61. Schmidt D, Linke R, Uder M, Kuwert T. Five months' follow-up of patients with and without iodine-positive lymph node metastases of thyroid carcinoma as disclosed by ^{131}I-SPECT/CT at the first radioablation. *Eur J Nucl Med Mol Imaging.* 2010;37(4):699–705.
62. Chen MK, Yasrebi M, Samii J, Staib LH, Doddamane I, Cheng DW. The utility of I-123 pretherapy scan in I-131 radioiodine therapy for thyroid cancer. *Thyroid.* 2012;22(3):304–309.
63. Song H, Mosci C, Akatsu H, Basina M, Dosiou C, Iagaru A. Diagnostic ^{123}I whole body scan prior to ablation of thyroid remnant in patients with papillary thyroid cancer: Implications for clinical management. *Clin Nucl Med.* 2018; 43(10):705–709.
64. Van Nostrand D, Aiken M, Atkins F, et al. The utility of radioiodine scans prior to iodine 131 ablation in patients with well-differentiated thyroid cancer. *Thyroid.* 2009;19(8):849–855.
65. Wong KK, Sisson JC, Koral KF, Frey KA, Avram AM. Staging of differentiated thyroid carcinoma using diagnostic ^{131}I SPECT/CT. *AJR Am J Roentgenol.* 2010; 195(3):730–736.
66. Sarkar SD, Kalapparambath TP, Palestro CJ. Comparison of ^{123}I and ^{131}I for whole-body imaging in thyroid cancer. *J Nucl Med.* 2002;43(5):632–634.
67. Choe M DG, Spies W, Savas H. A comparison between TSH stimulated diagnostic I-123 and post-therapy I-131 scans in the detection of remnant, loco-regional and distant functioning metastatic disease. Presented at the SNMMI Meeting Mid-Winter Meeting; Orlando, FL, 2018.
68. Genzyme. Thyrogen [package insert]. Cambridge, MA: Genzyme; 2008.
69. Ladenson PW, Braverman LE, Mazzaferri EL, et al. Comparison of administration of recombinant human thyrotropin with withdrawal of thyroid hormone for radioactive iodine scanning in patients with thyroid carcinoma. *N Engl J Med.* 1997;337(13):888–896.
70. Haugen BR, Pacini F, Reiners C, et al. A comparison of recombinant human thyrotropin and thyroid hormone withdrawal for the detection of thyroid remnant or cancer. *J Clin Endocrinol Metab.* 1999;84(11):3877–3885.
71. Avram AM, Fig LM, Frey KA, Gross MD, Wong KK. Preablation 131-I scans with SPECT/CT in postoperative thyroid cancer patients: what is the impact on staging? *J Clin Endocrinol Metab.* 2013;98(3):1163–1171.
72. Avram AM, Esfandiari NH, Wong KK. Preablation 131-I scans with SPECT/CT contribute to thyroid cancer risk stratification and 131-I therapy planning. *J Clin Endocrinol Metab.* 2015;100(5):1895–1902.
73. Avram AM, Rosculet N, Esfandiari NH, et al. Differentiated thyroid cancer outcomes after surgery and activity-adjusted ^{131}I theragnostics. *Clin Nucl Med.* 2019; 44(1):11–20.
74. Klein HA. Radioiodine dilution due to levothyroxine when using recombinant human thyroid-stimulating hormone: case report and discussion. *Clin Nucl Med.* 2011;36(10):899–903.
75. Barbaro D, Boni G, Meucci G, et al. Radioiodine treatment with 30 mCi after recombinant human thyrotropin stimulation in thyroid cancer: effectiveness for postsurgical remnants ablation and possible role of iodine content in L-thyroxine in the outcome of ablation. *J Clin Endocrinol Metab.* 2003;88(9):4110–4115.
76. King Pharmaceuticals, Inc. Cytome [package insert]. Bristol, TN: King Pharmaceuticals, Inc.; 2004.
77. Sisson JC, Dewaraja YK, Wizauer EJ, Giordano TJ, Avram AM. Thyroid carcinoma metastasis to skull with infringement of brain: treatment with radioiodine. *Thyroid.* 2009;19(3):29–303.
78. Wong KK, Zarzhevsky N, Cahill JM, Frey KA, Avram AM. Incremental value of diagnostic ^{131}I SPECT/CT fusion imaging in the evaluation of differentiated thyroid carcinoma. *AJR Am J Roentgenol.* 2008;191(6):1785–1794.
79. Donohoe KJ, Aloff J, Avram AM, et al. Appropriate use criteria for nuclear medicine in the evaluation and treatment of differentiated thyroid cancer. *J Nucl Med.* 2020;61(3):375–396.
80. Salvatori M, Perotti G, Villani MF, et al. Determining the appropriate time of execution of an I-131 post-therapy whole-body scan: comparison between early and late imaging. *Nucl Med Commun.* 2013;34(9):900–908.

81. Hung BT, Huang SH, Huang YE, Wang PW. Appropriate time for post-therapeutic I-131 whole body scan. *Clin Nucl Med.* 2009;34(6):339–342.
82. Sisson JC, Avram AM, Lawson SA, Gauger PG, Doherty GM. The so-called stunning of thyroid tissue. *J Nucl Med.* 2006;47(9):1406–1412.
83. Chong A, Song HC, Min JJ, et al. Improved detection of lung or bone metastases with an I-131 whole body scan on the 7th day after high-dose I-131 therapy in patients with thyroid cancer. *Nucl Med Mol Imaging.* 2010;44(4):273–281.
84. Kodani N, Okuyama C, Aibe N, Matsushima S, Yamazaki H. Utility of additional delayed post-therapeutic ^{131}I whole-body scanning in patients with thyroid cancer. *Clin Nucl Med.* 2012;37(3):264–267.
85. Xue YL, Qiu ZL, Song HJ, Luo QY. Value of ^{131}I SPECT/CT for the evaluation of differentiated thyroid cancer: a systematic review of the literature. *Eur J Nucl Med Mol Imaging.* 2013;40(5):768–778.
86. Schmidt D, Szikszai A, Linke R, Bautz W, Kuwert T. Impact of ^{131}I SPECT/spiral CT on nodal staging of differentiated thyroid carcinoma at the first radioablation. *J Nucl Med.* 2009;50(1):18–23.
87. McDougall IR. 74 MBq radioiodine ^{131}I does not prevent uptake of therapeutic doses of ^{131}I (i.e. it does not cause stunning) in differentiated thyroid cancer. *Nucl Med Commun.* 1997;18(6):505–512.
88. Avram AM, Dewaraja YK. Thyroid cancer radiotheragnostics: The case for activity adjusted ^{131}I therapy. *Clin Transl Imaging.* 2018;6(5):335–346.
89. Van Nostrand D. Surveillance radioiodine whole body scans. In: Wartofsky L, Van Nostrand D, eds. *Thyroid Cancer: A Comprehensive Guide to Clinical Management*, 3rd ed. New York, NY: Springer; 2016:471–474.
90. Banerjee M, Wiebel JL, Guo C, Gay B, Haymart MR. Use of imaging tests after primary treatment of thyroid cancer in the United States: Population based retrospective cohort study evaluating death and recurrence. *BMJ.* 2016;354:i3839.
91. Luster M, Clarke SE, Dietlein M, et al. Guidelines for radioiodine therapy of differentiated thyroid cancer. *Eur J Nucl Med Mol Imaging.* 2008;35(10):1941–1959.
92. Freudenberg LS, Jentzen W, Gorges R, et al. ^{124}I-PET dosimetry in advanced differentiated thyroid cancer: Therapeutic impact. *Nuklearmedizin.* 2007;46(4):121–128.
93. Jentzen W, Nahum AE, Bockisch A, Binse I, Tulchinsky M. Fixed 3.7-GBq ^{131}I activity for metastatic thyroid cancer therapy ignores science and history. *J Nucl Med.* 2017;58(9):1530.
94. Verburg FA, Luster M, Giovanella L, et al. The "reset button" revisited: Why high activity ^{131}I therapy of advanced differentiated thyroid cancer after dosimetry is advantageous for patients. *Eur J Nucl Med Mol Imaging.* 2017;44(6):915–917.
95. Campenni A, Giovanella L, Pignata SA, et al. Undetectable or low (<1 ng/ml) postsurgical thyroglobulin values do not rule out metastases in early stage differentiated thyroid cancer patients. *Oncotarget.* 2018;9(25):17491–17500.
96. Verburg FA, Mader U, Giovanella L, Luster M, Reiners C. Low or undetectable basal thyroglobulin levels obviate the need for neck ultrasound in differentiated thyroid cancer patients after total thyroidectomy and ^{131}I ablation. *Thyroid.* 2018; 28(6):722–728.
97. Maier TM, Schober O, Gerss J, et al. Differentiated thyroid cancer patients more than 60 years old paradoxically show an increased life expectancy. *J Nucl Med.* 2015;56(2):190–195.
98. Verburg FA, Mader U, Reiners C, Hanscheid H. Long-term survival in differentiated thyroid cancer is worse after low-activity initial post-surgical ^{131}I therapy in both high- and low-risk patients. *J Clin Endocrinol Metab.* 2014;99(12):4487–4496.
99. Hindie E, Zanotti-Fregonara P, Keller I, et al. Bone metastases of differentiated thyroid cancer: Impact of early ^{131}I-based detection on outcome. *Endocr Relat Cancer.* 2007;14(3):799–807.
100. Albano D, Bertagna F, Bonacina M, et al. Possible delayed diagnosis and treatment of metastatic differentiated thyroid cancer by adopting the 2015 ATA guidelines. *Eur J Endocrinol.* 2018;179(3):143–151.
101. Verburg FA, Aktolun C, Chiti A, et al. Why the European Association of Nuclear Medicine has declined to endorse the 2015 American Thyroid Association management guidelines for adult patients with thyroid nodules and differentiated thyroid cancer. *Eur J Nucl Med Mol Imaging.* 2016;43(6):1001–1005.
102. McCowen KD, Adler RA, Ghaed N, Verdon T, Hofeldt FD. Low dose radioiodide thyroid ablation in postsurgical patients with thyroid cancer. *Am J Med.* 1976;61(1):52–58.
103. Johansen K, Woodhouse NJ, Odugbesan O. Comparison of 1073 MBq and 3700 MBq iodine-131 in postoperative ablation of residual thyroid tissue in patients with differentiated thyroid cancer. *J Nucl Med.* 1991;32(2):252-4.
104. Logue JP, Tsang RW, Brierley JD, Simpson WJ. Radioiodine ablation of residual tissue in thyroid cancer: relationship between administered activity, neck uptake and outcome. Br J Radiol. 1994;67(803):1127–1131.
105. Bal C, Padhy AK, Jana S, Pant GS, Basu AK. Prospective randomized clinical trial to evaluate the optimal dose of 131 I for remnant ablation in patients with differentiated thyroid carcinoma. *Cancer.* 1996;77(12):2574–2580.
106. Bal CS, Kumar A, Pant GS. Radioiodine dose for remnant ablation in differentiated thyroid carcinoma: a randomized clinical trial in 509 patients. *J Clin Endocrinol Metab.* 2004;89(4):1666–1673.
107. Rosario PW, Reis JS, Barroso AL, Rezende LL, Padrao EL, Fagundes TA. Efficacy of low and high ^{131}I doses for thyroid remnant ablation in patients with differentiated thyroid carcinoma based on post-operative cervical uptake. *Nucl Med Commun.* 2004;25(11):1077–1081.
108. Pilli T, Brianzoni E, Capoccetti F, et al. A comparison of 1850 (50 mCi) and 3700 MBq (100 mCi) 131-iodine administered doses for recombinant thyrotropin-stimulated postoperative thyroid remnant ablation in differentiated thyroid cancer. *J Clin Endocrinol Metab.* 2007;92(9):3542–3546.
109. Cherk MH, Kalff V, Yap KS, Bailey M, Topliss D, Kelly MJ. Incidence of radiation thyroiditis and thyroid remnant ablation success rates following 1110 MBq (30 mCi) and 3700 MBq (100 mCi) post-surgical ^{131}I ablation therapy for differentiated thyroid carcinoma. *Clin Endocrinol (Oxf).* 2008;69(6):957–962.
110. Maenpaa HO, Heikkonen J, Vaalavirta L, Tenhunen M, Joensuu H. Low vs. high radioiodine activity to ablate the thyroid after thyroidectomy for cancer: A randomized study. *PLoS One.* 2008;3(4):e1885.
111. Kukulska A, Krajewska J, Gawkowska-Suwinska M, et al. Radioiodine thyroid remnant ablation in patients with differentiated thyroid carcinoma (DTC): Prospective comparison of long-term outcomes of treatment with 30, 60 and 100 mCi. *Thyroid Res.* 2010;3(1):9.
112. Bal C, Chandra P, Kumar A, Dwivedi S. A randomized equivalence trial to determine the optimum dose of iodine-131 for remnant ablation in differentiated thyroid cancer. *Nucl Med Commun.* 2012;33(10):1039–1047.
113. Caglar M, Bozkurt FM, Akca CK, et al. Comparison of 800 and 3700 MBq iodine-131 for the postoperative ablation of thyroid remnant in patients with low-risk differentiated thyroid cancer. *Nucl Med Commun.* 2012;33(3):268–274.
114. Schlumberger M, Catargi B, Borget I, et al. Strategies of radioiodine ablation in patients with low-risk thyroid cancer. *N Engl J Med.* 2012;366(18):1663–1673.
115. Mallick U, Harmer C, Yap B, et al. Ablation with low-dose radioiodine and thyrotropin alfa in thyroid cancer. *N Engl J Med.* 2012;366(18):1674–1685.
116. Kruijff S, Aniss AM, Chen P, et al. Decreasing the dose of radioiodine for remnant ablation does not increase structural recurrence rates in papillary thyroid carcinoma. *Surgery.* 2013;154(6):1337–1344; discussion 1344–1345.
117. Castagna MG, Cevenini G, Theodoropoulou A, et al. Post-surgical thyroid ablation with low or high radioiodine activities results in similar outcomes in intermediate risk differentiated thyroid cancer patients. *Eur J Endocrinol.* 2013;169(1): 23–29.
118. Cheng W, Ma C, Fu H, et al. Low- or high-dose radioiodine remnant ablation for differentiated thyroid carcinoma: A meta-analysis. *J Clin Endocrinol Metab.* 2013;98(4):1353–1360.
119. Fang Y, Ding Y, Guo Q, Xing J, Long Y, Zong Z. Radioiodine therapy for patients with differentiated thyroid cancer after thyroidectomy: Direct comparison and network meta-analyses. *J Endocrinol Invest.* 2013;36(10):896–902.
120. Valachis A, Nearchou A. High versus low radioiodine activity in patients with differentiated thyroid cancer: A meta-analysis. *Acta Oncol.* 2013;52(6):1055–1061.
121. Han JM, Kim WG, Kim TY, et al. Effects of low-dose and high-dose postoperative radioiodine therapy on the clinical outcome in patients with small differentiated thyroid cancer having microscopic extrathyroidal extension. *Thyroid.* 2014; 24(5):820–825.
122. Zhang Y, Liang J, Yang X, Yang K, Lin Y. Low-dose radioiodine ablation in differentiated thyroid cancer with macroscopic extrathyroidal extension and low level of preablative-stimulated thyroglobulin. *Nucl Med Commun.* 2015;36(6): 553–559.
123. Du P, Jiao X, Zhou Y, et al. Low versus high radioiodine activity to ablate the thyroid after thyroidectomy for cancer: a meta-analysis of randomized controlled trials. *Endocrine.* 2015;48(1):96–105.
124. Joung JY, Choi JH, Cho YY, et al. Efficacy of low-dose and high-dose radioactive iodine ablation with rhTSH in Korean patients with differentiated thyroid carcinoma: The first report in nonwestern countries. *Am J Clin Oncol.* 2016;39(4):374–378.
125. Fatima N, Zaman MU, Zaman A, Zaman U, Tahseen R. Comparable ablation efficiency of 30 and 100 mCi of I-131 for low to intermediate risk thyroid cancers using triple negative criteria. *Asian Pac J Cancer Prev.* 2016;17(3):1115–1118.
126. Ibrahim DR KM, Michael MM, Elsayed ZM. Low-dose versus high-dose radioactive iodine ablation of differentiated thyroid carcinoma: a prospective randomized study. *Int J Cancer Ther Oncol.* 2016;4(4):4415.
127. Shengguang Y, Ji-Eun C, Lijuan HL. I-131 for remnant ablation in differentiated thyroid cancer after thyroidectomy: A meta-analysis of randomized controlled evidence. *Med Sci Monit.* 2016;22:2439–2450.
128. Ben Ghachem T, Yeddes I, Meddeb I, et al. A comparison of low versus high radioiodine administered activity in patients with low-risk differentiated thyroid cancer. *Eur Arch Otolaryngol.* 2017;274(2):655–660.
129. Lv RB, Wang QG, Liu C, et al. Low versus high radioiodine activity for ablation of the thyroid remnant after thyroidectomy in Han Chinese with low-risk differentiated thyroid cancer. *Onco Targets Ther.* 2017;10:4051–7.

130. Ma C, Feng F, Wang S, et al. Chinese data of efficacy of low- and high-dose iodine-131 for the ablation of thyroid remnant. *Thyroid.* 2017;27(6):832–837.
131. Qu Y, Huang R, Li L. Low- and high-dose radioiodine therapy for low-/intermediate-risk differentiated thyroid cancer: A preliminary clinical trial. *Ann Nucl Med.* 2017;31(1):71–83.
132. Seo M, Kim YS, Lee JC, et al. Low-dose radioactive iodine ablation is sufficient in patients with small papillary thyroid cancer having minor extrathyroidal extension and central lymph node metastasis (T3 N1a). *Clin Nucl Med.* 2017;42(11):842–846.
133. Jimenez Londoño GA. Garcia Vicente AM, Sastre Marcos J, et al. Low-dose radioiodine ablation in patients with low-risk differentiated thyroid cancer. *Eur Thyroid J.* 2018;7:218–224.
134. Cai XY, Vijayaratnam N, McEwan AJB, Reif R, Morrish DW. Comparison of 30 mCi and 50 mCi I-131 doses for ablation of thyroid remnant in papillary thyroid cancer patients. *Endocr Res.* 2018;43(1):11–14.
135. Dehbi HM, Mallick U, Wadsley J, Newbold K, Harmer C, Hackshaw A. Recurrence after low-dose radioiodine ablation and recombinant human thyroid-stimulating hormone for differentiated thyroid cancer (HiLo): Long-term results of an open-label, non-inferiority randomised controlled trial. *Lancet Diabetes Endocrinol.* 2019;7(1):44–51.
136. Vardarli I, Weidemann F, Aboukoura M, Herrmann K, Binse I, Gorges R. Longer-term recurrence rate after low versus high dose radioiodine ablation for differentiated thyroid cancer in low and intermediate risk patients: A meta-analysis. *BMC Cancer.* 2020;20(1):550.
137. Li F, Li W, Gray KD, Zarnegar R, Wang D, Fahey TJ 3rd. Ablation therapy using a low dose of radioiodine may be sufficient in low- to intermediate-risk patients with follicular variant papillary thyroid carcinoma. *J Int Med Res.* 2020; 48(11):300060520966491.
138. Dong P, Wang L, Qu Y, Huang R, Li L. Low- and high-dose radioiodine ablation for low-/intermediate-risk differentiated thyroid cancer in China: Large randomized clinical trial. *Head Neck.* 2021;43(4):1311–1320.
139. Thyrogen Prescribing Information. Available from: https://www.accessdata.fda.gov/drugsatfda_docs/label/2014/020898s054lbl.pdf. Accessed on: April 21, 2022.
140. Pacini F, Ladenson PW, Schlumberger M, et al. Radioiodine ablation of thyroid remnants after preparation with recombinant human thyrotropin in differentiated thyroid carcinoma: Results of an international, randomized, controlled study. *J Clin Endocrinol Metab.* 2006;91(3):926–932.
141. Singer MC, Marchal F, Angelos P, et al. Salivary and lacrimal dysfunction after radioactive iodine for differentiated thyroid cancer: American Head and Neck Society Endocrine Surgery Section and Salivary Gland Section Joint Multidisciplinary Clinical Consensus Statement of Otolaryngology, Ophthalmology, Nuclear Medicine and Endocrinology. *Head Neck.* 2020;42(11):3446–3459.
142. Ylli D, Van Nostrand D, Wartofsky L. Conventional radioiodine therapy for differentiated thyroid cancer. *Endocrinol Metab Clin North Am.* 2019;48(1):181–197.
143. Van Nostrand D, Atkins F, Yeganeh F, Acio E, Bursaw R, Wartofsky L. Dosimetrically determined doses of radioiodine for the treatment of metastatic thyroid carcinoma. *Thyroid.* 2002;12(2):121–34.
144. Leblanc G, Tabah R, Liberman M, Sampalis J, Younan R, How J. Large remnant ^{131}I ablation as an alternative to completion/total thyroidectomy in the treatment of well-differentiated thyroid cancer. *Surgery.* 2004;136(6):1275–1280.
145. Santra A, Bal S, Mahargan S, Bal C. Long-term outcome of lobar ablation versus completion thyroidectomy in differentiated thyroid cancer. *Nucl Med Commun.* 2011;32(1):52–58.
146. Barbesino G, Goldfarb M, Parangi S, Yang J, Ross DS, Daniels GH. Thyroid lobe ablation with radioactive iodine as an alternative to completion thyroidectomy after hemithyroidectomy in patients with follicular thyroid carcinoma: long-term follow-up. *Thyroid.* 2012;22(4):369–376.
147. Giovanella L, Piccardo A, Paone G, Foppiani L, Treglia G, Ceriani L. Thyroid lobe ablation with iodine-^{131}I in patients with differentiated thyroid carcinoma: a randomized comparison between 1.1 and 3.7 GBq activities. *Nucl Med Commun.* 2013;34(8):767–770.
148. Jonklaas J, Bianco AC, Cappola AR, et al. Evidence-based use of levothyroxine/liothyronine combinations in treating hypothyroidism: A consensus document. *Eur Thyroid J.* 2021;10(1):10–38.
149. Gonzalez Carvalho JM, Gorlich D, Schober O, et al. Evaluation of ^{131}I scintigraphy and stimulated thyroglobulin levels in the follow up of patients with DTC: A retrospective analysis of 1420 patients. *Eur J Nucl Med Mol Imaging.* 2017; 44(5):744–756.
150. Schleupner MC, Riemann B, Schafers M, Backhaus P, Vrachimis A. Impact of FDG-PET on therapy management and outcome of differentiated thyroid carcinoma patients with elevated thyroglobulin despite negative iodine scintigraphy. *Nuklearmedizin.* 2020;59(5):356–364.
151. Giovanella L, Cosma C, Plebani M. Letter to the editor: what is the role of serum thyroglobulin measurement in patients with differentiated thyroid cancer treated without radioactive iodine? *J Clin Endocrinol Metab.* 2017;102(6):2113–2114.
152. Giovanella L, Clark PM, Chiovato L, et al. Thyroglobulin measurement using highly sensitive assays in patients with differentiated thyroid cancer: A clinical position paper. *Eur J Endocrinol.* 2014;171(2):R33–R46.
153. Park S, Jeon MJ, Oh HS, et al. Changes in serum thyroglobulin levels after lobectomy in patients with low-risk papillary thyroid cancer. *Thyroid.* 2018; 28(8):997–1003.
154. Cabanillas ME, McFadden DG, Durante C. Thyroid cancer. *Lancet.* 2016; 388(10061):2783–2795.
155. Diessl S, Holzberger B, Mader U, et al. Impact of moderate vs stringent TSH suppression on survival in advanced differentiated thyroid carcinoma. *Clin Endocrinol (Oxf).* 2012;76(4):586–592.
156. Giovanella L, Van Nostrand D. Advanced differentiated thyroid cancer: When to stop radioiodine? *Q J Nucl Med Mol Imaging.* 2019;63(3):267–70.
157. Brose MS, Smit J, Capdevila J, et al. Regional approaches to the management of patients with advanced, radioactive iodine-refractory differentiated thyroid carcinoma. *Expert Rev Anticancer Ther.* 2012;12(9):1137–1147.
158. Schlumberger M, Brose M, Elisei R, et al. Definition and management of radioactive iodine-refractory differentiated thyroid cancer. *Lancet Diabetes Endocrinol.* 2014;2(5):356–358.
159. Sacks W, Braunstein GD. Evolving approaches in managing radioactive iodine-refractory differentiated thyroid cancer. *Endocr Pract.* 2014;20(3):263–275.
160. Kiyota N, Robinson B, Shah M, et al. Defining radioiodine-refractory differentiated thyroid cancer: Efficacy and safety of lenvatinib by radioiodine-refractory criteria in the SELECT trial. *Thyroid.* 2017;27(9):1135–1141.
161. Van Nostrand D. Radioiodine refractory differentiated thyroid cancer: Time to update the classifications. *Thyroid.* 2018;28(9):1083–1093.
162. Jin Y, Van Nostrand D, Cheng L, Liu M, Chen L. Radioiodine refractory differentiated thyroid cancer. *Crit Rev Oncol Hematol.* 2018;125:111–120.
163. Lee JW, Lee SM, Koh GP, Lee DH. The comparison of ^{131}I whole-body scans on the third and tenth day after ^{131}I therapy in patients with well-differentiated thyroid cancer: preliminary report. *Ann Nucl Med.* 2011;25(6):439–446.
164. Ho AL, Grewal RK, Leboeuf R, et al. Selumetinib-enhanced radioiodine uptake in advanced thyroid cancer. *N Engl J Med.* 2013;368(7):623–632.
165 Jaber T, Waguespack SG, Cabanillas ME, et al. Targeted therapy in advanced thyroid cancer to resensitize tumors to radioactive iodine. *J Clin Endocrinol Metab.* 2018;103(10):3698–3705.
166. Tepmongkol S, Keelawat S, Honsawek S, Ruangvejvorachai P. Rosiglitazone effect on radioiodine uptake in thyroid carcinoma patients with high thyroglobulin but negative total body scan: A correlation with the expression of peroxisome proliferator-activated receptor-gamma. *Thyroid.* 2008;18(7):697–704.
167. Rothenberg SM, McFadden DG, Palmer EL, Daniels GH, Wirth LJ. Redifferentiation of iodine-refractory BRAF V600E-mutant metastatic papillary thyroid cancer with dabrafenib. *Clin Cancer Res.* 2015;21(5):1028–1035.
168. Giovanella L, Scappaticcio L. Radioiodine therapy of advanced differentiated thyroid cancer: clinical considerations and multidisciplinary approach. *Q J Nucl Med Mol Imaging.* 2019;63(3):229–234.
169. Iniguez-Ariza NM, Bible KC, Clarke BL. Bone metastases in thyroid cancer. *J Bone Oncol.* 2020;21:100282.
170. Lee SH, Chan RC, Chang SS, et al. Use of bisphosphonates and the risk of osteonecrosis among cancer patients: a systemic review and meta-analysis of the observational studies. *Support Care Cancer.* 2014;22(2):553–560.
171. Sabra MM, Sherman EJ, Tuttle RM. Tumor volume doubling time of pulmonary metastases predicts overall survival and can guide the initiation of multikinase inhibitor therapy in patients with metastatic, follicular cell-derived thyroid carcinoma. *Cancer.* 2017;123(15):2955–2964.
172. Feine U, Lietzenmayer R, Hanke JP, Wöhrle H, Müller-Schauenburg W. ^{18}FDG whole-body PET in differentiated thyroid carcinoma. Flipflop in uptake patterns of ^{18}FDG and ^{131}I. [In German]. *Nuklearmedizin.* 1995;34(4):127–134.
173. Feine U, Lietzenmayer R, Hanke JP, Held J, Wöhrle H, Müller-Schauenburg W. Fluorine-18-FDG and iodine-131-iodide uptake in thyroid cancer. *J Nucl Med.* 1996;37(9):1468–1472.
174. Liu M, Cheng L, Jin Y, Ruan M, Sheng S, Chen L. Predicting ^{131}I-avidity of metastases from differentiated thyroid cancer using ^{18}F-FDG PET/CT in postoperative patients with elevated thyroglobulin. *Sci Rep.* 2018;8(1):4352.
175. Silberstein EB. The problem of the patient with thyroglobulin elevation but negative iodine scintigraphy: The TENIS syndrome. *Semin Nucl Med.* 2011;41(2): 113–120.
176. Giovanella L, Treglia G, Ceriani L, Verburg F. Detectable thyroglobulin with negative imaging in differentiated thyroid cancer patients. What to do with negative anatomical imaging and radioiodine scan? *Nuklearmedizin.* 2014;53(1):1–10.
177. Van Nostrand D. Radioiodine imaging for differentiated thyroid cancer: Not all radioiodine images are performed equally. *Thyroid.* 2019;29(7):901–909.
178. Wu D, Ylli D, Gomes Lima CJ, et al. Use of ^{99m}Tc-sestamibi SPECT/CT when conventional imaging studies are negative for localizing suspected recurrence in

differentiated thyroid cancer: A method and a lesson for clinical management. *Endocrine.* 2018;62(1):57–63.
179. Binse I, Poeppel TD, Ruhlmann M, et al. ^{68}Ga-DOTATOC PET/CT in patients with iodine- and ^{18}F-FDG-negative differentiated thyroid carcinoma and elevated serum thyroglobulin. *J Nucl Med.* 2016;57(10):1512–1517.
180. Vrachimis A, Stegger L, Wenning C, et al. ^{68}Ga-DOTATATE PET/MRI and ^{18}F-FDG PET/CT are complementary and superior to diffusion-weighted MR imaging for radioactive-iodine-refractory differentiated thyroid cancer. *Eur J Nucl Med Mol Imaging.* 2016;43(10):1765–1772.
181. Czepczynski R, Matysiak-Grzes M, Gryczynska M, et al. Peptide receptor radionuclide therapy of differentiated thyroid cancer: efficacy and toxicity. *Arch Immunol Ther Exp (Warsz).* 2015;63(2):147–154.
182. Versari A, Sollini M, Frasoldati A, et al. Differentiated thyroid cancer: A new perspective with radiolabeled somatostatin analogues for imaging and treatment of patients. *Thyroid.* 2014;24(4):715–726.
183. Roll W, Riemann B, Schafers M, Stegger L, Vrachimis A. ^{177}Lu-DOTATATE therapy in radioiodine-refractory differentiated thyroid cancer: A single center experience. *Clin Nucl Med.* 2018;43(10):e346–e351.
184. Robbins RJ, Wan Q, Grewal RK, et al. Real-time prognosis for metastatic thyroid carcinoma based on 2-^{18}F-fluoro-2-deoxy-D-glucose-positron emission tomography scanning. *J Clin Endocrinol Metab.* 2006;91(2):498–505.
185. Grebe SK, Hay ID. Prognostic factors and management in thyroid cancer–Consensus or controversy? *West J Med.* 1996;165(3):156–157.
186. Ain KB. Papillary thyroid carcinoma. Etiology, assessment, and therapy. *Endocrinol Metab Clin North Am.* 1995;24(4):711–760.
187. Xing M, Haugen BR, Schlumberger M. Progress in molecular-based management of differentiated thyroid cancer. *Lancet.* 2013;381(9871):1058–1069.
188. Wang W, Larson SM, Tuttle RM, et al. Resistance of ^{18}F-fluorodeoxyglucose-avid metastatic thyroid cancer lesions to treatment with high-dose radioactive iodine. *Thyroid.* 2001;11(12):1169–1175.
189. Brierley JD, Panzarella T, Tsang RW, Gospodarowicz MK, O'Sullivan B. A comparison of different staging systems predictability of patient outcome. Thyroid carcinoma as an example. *Cancer.* 1997;79(12):2414–2423.
190. Sherman SI, Brierley JD, Sperling M, et al. Prospective multicenter study of thyroiscarcinoma treatment: initial analysis of staging and outcome. National Thyroid Cancer Treatment Cooperative Study Registry Group. *Cancer.* 1998;83(5):1012–1021.
191. Miyauchi A, Kudo T, Miya A, et al. Prognostic impact of serum thyroglobulin doubling-time under thyrotropin suppression in patients with papillary thyroid carcinoma who underwent total thyroidectomy. *Thyroid.* 2011;21(7):707–716.
192. Brose MS, Nutting CM, Jarzab B, et al. Sorafenib in radioactive iodine-refractory, locally advanced or metastatic differentiated thyroid cancer: A randomised, double-blind, phase 3 trial. *Lancet.* 2014;384(9940):319–328.
193. Schlumberger M, Tahara M, Wirth LJ, et al. Lenvatinib versus placebo in radioiodine-refractory thyroid cancer. *N Engl J Med.* 2015;372(7):621–630.
194. Carhill AA, Cabanillas ME, Jimenez C, et al. The noninvestigational use of tyrosine kinase inhibitors in thyroid cancer: Establishing a standard for patient safety and monitoring. *J Clin Endocrinol Metab.* 2013;98(1):31–42.
195. Eisenhauer EA, Therasse P, Bogaerts J, et al. New response evaluation criteria in solid tumours: Revised RECIST guideline (version 1.1). *Eur J Cancer.* 2009;45(2):228–247.
196. Wang W, Larson SM, Fazzari M, et al. Prognostic value of ^{18}F-fluorodeoxyglucose positron emission tomographic scanning in patients with thyroid cancer. *J Clin Endocrinol Metab.* 2000;85(3):1107–1113.
197. Robbins RJ, Larson SM. The value of positron emission tomography (PET) in the management of patients with thyroid cancer. Best practice and research. *Clin Endocrinol Metab.* 2008;22(6):1047–1059.
198. Dibble EH, Alvarez AC, Truong MT, Mercier G, Cook EF, Subramaniam RM. ^{18}F-FDG metabolic tumor volume and total glycolytic activity of oral cavity and oropharyngeal squamous cell cancer: Adding value to clinical staging. *J Nucl Med.* 2012;53(5):709–715.
199. Manohar PM, Beesley LJ, Bellile EL, Worden FP, Avram AM. Prognostic value of FDG-PET/CT metabolic parameters in metastatic radioiodine-refractory differentiated thyroid cancer. *Clin Nucl Med.* 2018;43(9):641–647.
200. Groopman J, Hartzband P. *Your Medical Mind: How to Decide What is Right for You.* London, UK: Penguin Books; 2011.

The most powerful words you'll ever hear.

"Thank You."

With your contribution, our profession can continue efforts leading to critical advances in cancer treatments and care.

The **Value Initiative Transformative Leadership Campaign** is the cornerstone for making these efforts a reality for patients of all ages.

The world needs more "thank you's."

Help improve the life of a patient. Lend your support today.

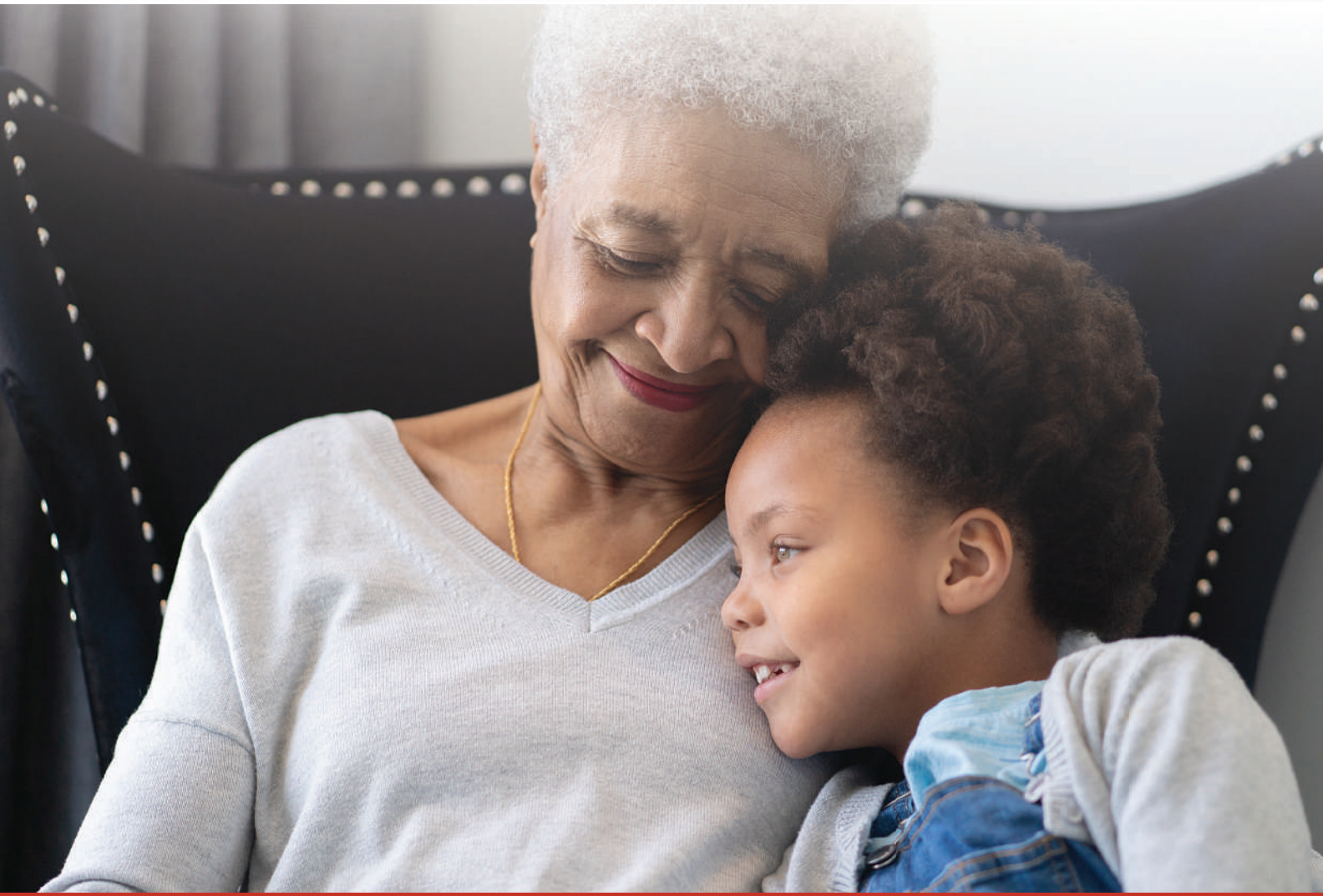

www.snmmi.org/TransformativeLeadership

SNMMI is a 501 (c)(3) tax id 36-2496678. Your donation is tax deductible as per current IRS regulations. Please remember SNMMI in your estate plans.

SNMMI Value Initiative

SOCIETY OF NUCLEAR MEDICINE & MOLECULAR IMAGING

How Many Theranostics Centers Will We Need in the United States?

Johannes Czernin and Jeremie Calais

David Geffen School of Medicine at UCLA, Los Angeles, California

Lutetium-177-PSMA-617 (PLUVICTO) has been approved by the U.S. Food and Drug Administration for patients with prostate-specific membrane antigen (PSMA)–positive metastatic castration-resistant prostate cancer (mCRPC) who have been treated with androgen receptor (AR) pathway inhibition and taxane-based chemotherapy (*1*). This great success was enabled by the design, execution, and results of the VISION trial (*2*) and has been awaited with great excitement by patients, their families, and treatment teams.

We have previously provided some simplified business forecasts for nuclear theranostics (*3*). We are expecting a high demand for prostate-specific membrane antigen (PSMA)–targeted molecular radiotherapy initially—a demand that will further increase as indications expand to earlier disease stages. The randomized phase 2 TheraP trial suggested that ^{177}Lu-PSMA-617 may achieve better prostate-specific antigen responses and progression-free survival than taxanes (cabazitaxel) as second-line therapy in patients with metastatic castration-resistant prostate cancer who progress after docetaxel (*4*). Several other clinical trials exploring the role of PSMA-targeted molecular radiotherapy, ranging from the neoadjuvant setting to the hormone-sensitive setting to first-line therapy for metastatic castration-resistant prostate cancer, are ongoing or about to start (*5*).

Theranostic centers will also take care of patients with thyroid cancer; neuroendocrine tumors, including paraganglioma and pheochromocytoma; and other cancer types in the future.

How and where will we be able to provide the best care for our patients?

First, we must establish competence. Implementing training and accreditation standards is an essential prerequisite. Two articles, one from experts in Australia and the other from the European Association of Nuclear Medicine, the Society of Nuclear Medicine and Molecular Imaging, and the International Atomic Energy Agency, will soon be published in *The Journal of Nuclear Medicine* and provide guidance.

Second, we must create a robust supply chain. Given the limited production capacities that are further at risk by the current geopolitical uncertainties, a robust supply chain of therapeutic isotopes is critically important. Failure to deliver therapies reliably will reliably deliver failure of the approach. This is both a challenge and an opportunity for industry and academia, as new production strategies could be developed jointly.

Third, we must establish a large number of theranostic centers. The incidence of neuroendocrine tumors is increasing, being currently estimated at 12,000–15,000 new cases per year in the United States, with an estimated prevalence of 170,000 cases (*6*). Half the newly diagnosed patients will undergo surgery, but many will experience slowly progressing disease. As a conservative estimate, and assuming that late-stage rather than earlier-stage patients are treated, around 7,500 patients per year might benefit from therapy with ^{177}Lu-DOTATATE (Lutathera; Advanced Accelerator Applications). Patients usually undergo 4 cycles, which translates into 30,000 cycles per year in the United States (Table 1).

Johannes Czernin

Jeremie Calais

Most patients who have end-stage prostate cancer and progress after chemotherapy are potential candidates for PSMA-targeted molecular radiotherapy (~40,000 patients per year) (*7*). PSMA PET screening may exclude 6,000 of these 40,000 patients (15%) from ^{177}Lu-PSMA therapy (*8*). We assume that the 50% of patients who are nonresponding would discontinue treatment after 2 cycles whereas the responders would complete the 4–6 scheduled cycles. Thus, we estimate that 34,000 patients will need a total of around 120,000 treatment cycles.

Taken together, 41,500 patients would require 150,000 treatment cycles of lutetium-based molecular radiotherapy per year for metastatic neuroendocrine tumors and prostate cancer (Table 1). At least 70 treatment sites, each providing 8 cycles per day, would be required to deliver approximately 150,000 cycles (assuming

TABLE 1
Conservative Estimates for Number of Treatment Cycles per Year in United States

Molecular radiotherapy agent	Patients per year	Cycles per year
^{177}Lu-DOTATATE	7,500	30,000 (4 cycles per patient)
^{177}Lu-PSMA	34,000	120,000 (2–6 cycles)
Total	41,500	150,000

DOI: 10.2967/jnumed.122.264144

260 workdays in the United States). Currently, a much lower site capacity is expected. Table 2 provides the number of centers required if each site delivers 2, 4, or 8 cycles per day.

Theranostics have arrived as an important component of precision oncology. Theranostics-based precision oncology requires substantial investments in the supply chain, in training (physicians, nurses, technologists, dosimetrists, radiation safety experts), in site design, in needs assessments, and in operational workflows. Professional organizations need to negotiate appropriate compensation and reimbursement with public and private insurance companies.

TABLE 2
How Many Centers Are Needed in United States to Deliver 150,000 Treatment Cycles per Year?

Cycles per site per day	Cycles per site per year	Centers needed to deliver 150,000 cycles per year*
8	2,088	70
4	1,044	140
2	522	280

*Approximations.

The first year after Food and Drug Administration approval of PSMA-targeted theranostics will inform us about the initial demand for services. However, because of the predicted rapid future growth, we need to get ready now.

REFERENCES

1. U.S. Food and Drug Administration (FDA). FDA approves Pluvicto for metastatic castration-resistant prostate cancer. U.S. FDA website. https://www.fda.gov/drugs/resources-information-approved-drugs/fda-approves-pluvicto-metastatic-castration-resistant-prostate-cancer. Accessed March 28, 2022.
2. Sartor O, de Bono J, Chi KN, et al.; VISION Investigators. Lutetium-177-PSMA-617 for metastatic castration-resistant prostate cancer. *N Engl J Med.* 2021;385:1091–1103.
3. Czernin J, Sonni I, Razmaria A, Calais J. The future of nuclear medicine as an independent specialty. *J Nucl Med.* 2019;60(suppl 2):3S–12S.
4. Hofman MS, Emmett L, Sandhu S, et al.; Trial Investigators and the Australian and New Zealand Urogenital and Prostate Cancer Trials Group. [^{177}Lu]Lu-PSMA-617 versus cabazitaxel in patients with metastatic castration-resistant prostate cancer (TheraP): a randomised, open-label, phase 2 trial. *Lancet.* 2021;397:797–804.
5. Zhang H, Koumna S, Pouliot F, Beauregard JM, Kolinsky M. PSMA theranostics: current landscape and future outlook. *Cancers (Basel).* 2021;13:4023.
6. Dasari A, Shen C, Halperin D, et al. Trends in the incidence, prevalence, and survival outcomes in patients with neuroendocrine tumors in the United States. *JAMA Oncol.* 2017;3:1335–1342.
7. Siegel RL, Miller KD, Fuchs HE, Jemal A. Cancer statistics, 2022. *CA Cancer J Clin.* 2022;72:7–33.
8. Hotta M, Gafita A, Czernin J, Calais J. Outcome of patients with PSMA-PET/CT screen failure by VISION criteria and treated with ^{177}Lu-PSMA therapy: a multicenter retrospective analysis. *J Nucl Med.* March 10, 2022 [Epub ahead of print].

A Letter from Ukraine

March 30th, 2022

Dear All,

My name is Ken Herrmann and I'm a nuclear medicine physician from Germany. I also chair the EANM Oncology and Theranostics Committee.

I am reaching out to you today in my role as Chair of Nuclear Medicine in Essen. We are all shocked about the invasion of your country and the current events in Ukraine. As a native of East Berlin, I am emotionally affected and am reminded of my personal history.

Accordingly, I want to reach out to offer any help for you and/or your families. Please let us know if there is anything we can do.

Currently our hospital is accommodating a number of Ukraine health-care professionals and I want to offer more to help. Please let us know what we can do.

All the best, and we sincerely hope that the war will be over soon.

Ken

Patient treatment in war times. Photograph taken in the waiting room of Clinical Hospital "Feofaniya" in Kyiv, Ukraine (March 2022).

March 30th, 2022

Dear Ken,

Thank you for your support!

Kmetyuk Yaroslav MD, PhD, Head of Radiosurgery, Center Clinical Hospital "Feofaniya"

I am the head of the department of the hospital in Kyiv where PET/CT is performed. I have been living at work since the first day of the war. We provide care to patients with a minimum number of staff. Because of frequent Russian bombings in the area where I live, I have to spend the night in the basement of my clinic. I am also in charge of the radiation therapy department. We did not stop irradiating patients for a single day. PET/CT had to be stopped due to lack of staff. Last week, colleagues were able to move to an area near the clinic and resume operation of the cyclotron and laboratory. I hope we will succeed with the production of FDG soon.

Many cancer patients have remained in Kyiv and need medical care. We do our job, although it is not easy. There are lots of new challenges. Every time the city is bombarded or covered with missile strikes, patients have to go down to the basement on an alarm signal. But it is clear that we cannot interrupt ongoing radiation therapy. I decided for myself that when we start PET, we will not interrupt the scan either. We will not let patients down who have already been injected with radiopharmaceuticals so as not to irradiate others. I understand that this looks ridiculous while under the risk of a nuclear attack.

This war takes the lives of thousands of Ukrainians. Adults and children. We are fighting for our freedom. We are fighting for the lives of our people.

P.S. Thanks for a quick response of EANM on my official letter as Vice-president of the Ukrainian Society of Nuclear Medicine. In the beginning of March, we asked to terminate Russia's EANM membership and provide support to our country.

Best regards,
Pray for us

Kmetyuk Yaroslav MD, PhD
Head of Radiosurgery Center,
Clinical Hospital "Feofaniya"
03680, Kyiv, Ukraine
21, Zabolotnogo st.
Kmetyuk@feofaniya.org

DOI: 10.2967/jnumed.122.264288

Precision Medicine Clinical Trials

A Conversation Between Peter O'Dwyer and Lale Kostakoglu

Peter J. O'Dwyer[1] and Lale Kostakoglu[2]

[1]Department of Medical Oncology, Hospital of the University of Pennsylvania, Philadelphia, Pennsylvania; and [2]Department of Radiology and Medical Imaging, Division of Nuclear Medicine and Molecular Imaging, University of Virginia Health Systems, Charlottesville, Virginia

Lale Kostakoglu, MD, MPH, a professor of Radiology and Chief of Nuclear Medicine and Molecular Imaging in the University of Virginia Health System (Charlottesville, VA), talked with Peter J. O'Dwyer, MD, a professor of Medicine at the University of Pennsylvania (Philadelphia) and a medical oncologist with expertise in gastrointestinal (GI) and pancreatic cancers. Dr. O'Dwyer has been the Group Co-Chair of the ECOG-ACRIN Cancer Research Group since May 2017. ECOG-ACRIN is a membership-based scientific organization that designs and conducts cancer research involving adults who have or are at risk of developing cancer. The network includes more than 1,300 academic and community-based cancer centers and hospitals in the United States and around the world, with approximately 15,000 oncology professionals involved in sponsored research.

Within ECOG-ACRIN, Dr. O'Dwyer co-chairs the landmark National Cancer Institute (NCI) Molecular Analysis for Therapy Choice (MATCH) precision medicine cancer trial. He is the CEO and chair of the Board of Managers of PrECOG, LLC, and president of the ECOG Research and Education Foundation.

Dr. O'Dwyer received his medical degree from the University of Dublin, Trinity College (Ireland), and completed his residency at the Hammersmith Hospital (London, U.K.). After a fellowship at the Baltimore Cancer Research Center (MD), he became a senior investigator in the Division of Cancer Treatment at NCI (Bethesda, MD). He previously led the Developmental Therapeutics Programs at Fox Chase Cancer Center (Philadelphia, PA) and the University of Pennsylvania. He has authored more than 350 scientific articles and participates in numerous national and international organizations.

Dr. Kostakoglu: *Let's start with your inspiring trans-Atlantic experience. Would you like to tell us about your background and the pivotal decisions that shaped your career path?*

Dr. O'Dwyer: That's an interesting question. Actually, my career path has been formed in the United States. I have links with Europe just because many of my colleagues through the years have gone from junior to more mature positions there, and a lot of research is based on personal links. We're fortunate within ECOG-ACRIN to have a strong presence in Europe, South America, Asia, and Canada to establish new member relationships. Particularly in Asia, where South Korea is the most important country for us to focus on right now because we have shared studies there. It's been difficult to go beyond that because of various regulatory issues, particularly in South America. To generate scientific ideas and design new trials, we often collaborate with global research consortia, such as the International Rare Cancers Initiative and others.

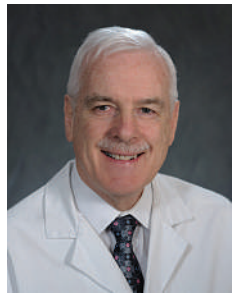

Peter J. O'Dwyer, MD

I think these international interactions really help us focus on the global impact of our studies and assist us in carrying out ECOG-ACRIN's strong commitment to advancing standards of care in broad populations of cancer patients and those at risk. We seek patient diversity in all clinical trials, including African-American patients, patients with Hispanic ethnicity, and Asian groups. For example, our current Tomosynthesis Mammographic Imaging Screening Trial (TMIST) is highly diverse. I think that precision medicine, where we tailor treatment to the individual, is helping us increase awareness of how important it is to include diverse patient populations in our trials to ensure that the results apply to all.

Dr. Kostakoglu: *Thank you so much for that background. Can we talk about your leadership role more specifically now? You're wearing at least 2 hats: 1 as an active researcher in the GI and developmental therapeutics programs at the University of Pennsylvania and the other as the national co-chair of the ECOG-ACRIN group. If we start from developmental therapeutics, could you tell us what this focus fosters and how it integrates translational research with clinical program resources?*

Dr. O'Dwyer: Although I continue to see patients at the Abramson Cancer Center at the University of Pennsylvania, I have relinquished any UPenn leadership roles to focus more on ECOG-ACRIN. But, certainly, developmental therapeutics has informed my approach to clinical research in GI cancers and more broadly. Having had responsibility for an R01-funded research lab for about 20 years, this type of research is my background. Developmental therapeutics programs are the main idea generators for clinical research; our role is to link academic medical centers to a broader community to allow translational research efforts to have maximum impact. Unfortunately, resources from the government are decreasing. Now, more than ever, institutions need to develop partnerships to be able to conduct these studies. We're constantly talking with the senior leadership of the NCI about ways to increase the impact of translational research.

Dr. Kostakoglu: *Shifting the topic to novel therapeutics, we know that owing to the highly adaptive nature of cancers, there is definitely a need for new therapeutic strategies. But what are the principal mechanisms for these novel targeted therapeutics in circumventing the barriers of conventional treatments?*

DOI: 10.2967/jnumed.121.264320

Dr. O'Dwyer: Hormonal interventions for breast cancer were the earliest targeted therapeutics. In the last few years, the major class of targeted therapeutics has been the kinase inhibitors, beginning with imatinib in chronic myeloid leukemia and GI stromal tumors. Now these are standard drugs in most leukemias and lymphomas, as well as the major solid tumors. This class of drug has had an important impact—in reality, the first to get us beyond chemotherapy. As we've learned more about targeted treatments, their clinical use has become more established and more focused on specific genomic characteristics of patients' tumors.

Understanding mechanisms of resistance and then targeting those novel mutations with more specific drugs have induced longer durations of survival than conventional therapies. A good example is the epidermal growth factor receptor inhibitors that have made such a survival difference for patients with lung cancer. An iterative research process to define exactly how lung tumors were escaping control by the earliest kinase inhibitors has allowed the development of even more specific therapeutics with superior outcomes in both activity and toxicity. Another story is about the targeting of BRAF mutations. In some tumors, like melanoma, the effects are astounding, with high rates of durable response and favorable survival and quality of life. But in colon cancer the effects are much less. In fact, as a result of the NCI MATCH trial, an application is under U.S. Food and Drug Administration review for a tumor-agnostic registration for BRAF-mutated tumors, excluding colon cancer.

Dr. Kostakoglu: *That is a nice segue to NCI MATCH, the landmark precision medicine cancer trial. As the co-chair of this trial, could you tell us in what ways MATCH has been successful?*

Dr. O'Dwyer: It certainly is a uniquely effective trial—one that is influencing how we will design and conduct precision medicine studies in the future. Just to put it in context, after about 2 years of planning, in the first 3 months after study initiation, our accrual rate was 8-fold higher than expected. Several aspects worked in the trial's favor. First, at a time when DNA sequencing was expensive and it was unclear how it would be funded, the cost of sequencing was covered by the study. By meeting this need for cancer patients, the trial accrued faster than any other large cooperative group trial ever—6,000 patients enrolled for central screening in 15 months. Another positive was that, despite our concerns about being able to reach patients with rare tumors, 60% of accruals represented uncommon tumors (those other than breast, colorectal, non–small cell lung, or prostate cancer). This is very gratifying to observe, because it allows us to think about precision medicine broadly across tumors. It also shows the value of platform trials for patients with uncommon or rare genomically driven cancers. MATCH results will allow us to identify groups in which a specific treatment will be effective, versus others where different treatment strategies should be developed.

Also important, of course, is that we proved that this type of trial is feasible and that there is broad interest among physicians. At the time of development, the size and scope of MATCH had never been attempted. For the NCI and ECOG-ACRIN, it was an enormous undertaking to develop the infrastructure for a national precision medicine trial across all cancers. As a result of this tremendous effort, NCI MATCH is building a knowledge base and laying the groundwork for future precision medicine initiatives.

As a reminder, this trial continues to offer 2 treatment opportunities (Arm H and Arm Z1M). The other 37 arms are now closed to enrollment, and multiple journals are expected to publish the results of the individual treatment arms. In MATCH, we are looking at single-agent treatments, with the exception of 2 arms that use combinations. We are finding that most of the patients have cooccurring mutations that are known to confer resistance, but we don't currently have a targeted drug for most of the concurrent mutations. This is perhaps the greatest opportunity for the future. We need to think about combinations of targeted therapies with immunotherapy and vaccines to stop the development of drug resistance.

Dr. Kostakoglu: *In that vein, what would be the main drivers of these novel combination treatments? Would you foresee paired resistance?*

Dr. O'Dwyer: We can talk about this at 2 levels. One is that combination precision medicine trials are in development with sponsorship from the NCI. Within ECOG-ACRIN and together with the Alliance for Cancer Clinical Trials, the SWOG Cancer Research Network, and NRG Oncology, we are developing the ComboMATCH trial. This trial's approach is tumor agnostic, much like the original NCI MATCH trial. However, the principle here is to overcome drug resistance to single-agent therapy by developing genomically directed targeted agent combinations. Another suggestion from the MATCH trial is that while hitting certain drug targets may be useful across tumor sites of origin, several are limited to specific tumor types. ComboMATCH will recognize the importance of cancer tissue type specificity in response to targeted therapy by incorporating randomized arms in specific diseases.

ECOG-ACRIN recently expanded our Developmental Therapeutics Committee with a Genomics Subcommittee to develop molecularly informed concepts, particularly combination concepts, to move forward not just through ComboMATCH but also through ECOG-ACRIN and PrECOG. Combination concepts can include immunotherapy, targeted therapies, chemotherapy, or radiation therapy. We hope to do this by actively engaging our industry partners and helping them develop these types of concepts with novel compounds—particularly in areas like rare tumor subtypes.

> "Developmental therapeutics programs are the main idea generators for clinical research; our role is to link academic medical centers to a broader community to allow translational research efforts to have maximum impact."

Another NCI-funded precision medicine trial in development is MyeloMATCH, which targets genomically defined subgroups of acute myeloid leukemia and myelodysplastic syndromes. A further example is iMATCH, which stands for Immunologic MATCH. Both trials are in development with SWOG.

At another level, I think these precision medicine initiatives of the NCI will pave the way for further advancements in the management of particular tumors. Importantly the payors want to see these data. If convincing, the results from these trials are likely to be addressed in National Comprehensive Cancer Network (NCCN) guidelines in the future. These guidelines are essential to the payors as objective evidence for effective treatments.

Dr. Kostakoglu: *These are fascinating trials. In your opinion, will MATCH results lead to paradigm shifts for cancer management in the near future?*

Dr. O'Dwyer: Sure, and these will even have implications for cancer biology. Think about this: We've identified mutations that are associated with cancer development—namely driver mutations, which are critical to tumor survival—but, given that not all

cancers with the mutation respond, the question arises as to whether we have the right definition of driver mutations? To answer that question, we've interrogated the Cancer Genome Atlas (TCGA) and other molecular characterizations of cancer at a broad level. We now can understand how to characterize a driver mutation at the very earliest stage of carcinogenesis. We can ask: What are the other acquired biologic characteristics that could promote therapy resistance? And can we be better at selecting patients who have the best chance of responding to therapy so that we can have a starting point in the clinic based on biologic studies? And, of course, can we detect and intervene to target these mutations as early as possible to prevent cancer ever arising?

Dr. Kostakoglu: *MATCH also has a radiogenomics substudy. How is that study going? It's always challenging to get the tissues and the imaging data to match with them.*

Dr. O'Dwyer: Those studies have been approved, and we are in the process of collecting material and associated data both for histopathologic and for radiomic analysis of CTs, PETs, and MRIs. This project will be a major component of ECOG-ACRIN's data science effort going forward. We are forming a data science committee to analyze how big data can contribute to interpretation of the MATCH results, how they relate to patient outcomes, and also how they relate to the genomics to define patient eligibility for treatments. We see this effort needing to coordinate widely with other platforms (including whole-exome or whole-genome sequencing), as well as radiomic and pathomic characterization of tumors for large data science analyses.

Dr. Kostakoglu: *When do you think these exciting results will be available in the public domain?*

Dr. O'Dwyer: I'm not sure, but I think it will be within a 1- to 2-year time frame, probably not longer than that, because it is really important to get these data out there soon.

Dr. Kostakoglu: *Exactly; can't wait. Changing gears a bit: As one of the national leaders within the National Clinical Trials Network (NCTN), could you just briefly tell us what NCTN is and how it is structured?*

Dr. O'Dwyer: NCTN is a funding instrument from the NCI and a structure under which grants are awarded to individual cooperative groups to conduct clinical trials to prove the efficacy of experimental cancer therapeutics. It's a vital structure for cancer research. What's the difference between the cooperative groups and the NCTN as a whole? The 6 groups themselves are each legally distinct entities with their own separate identities. They include the Alliance for Clinical Trials in Oncology, Canadian Cancer Trials Group, Children's Oncology Group, ECOG-ACRIN Cancer Research Group, NRG Oncology, and SWOG Cancer Research Network.

There are regular meetings among the group chairs. In addition, the group chairs meet regularly with the director and senior leadership of the NCI—collectively known as the "Cabinet." The Cabinet is an important forum in which to establish ways to work together to advance the goals of the NCI director, to accelerate the development of cancer research, and to remove potential barriers going forward. But, of course, NCTN and the group trials that it funds don't exist in a vacuum. They exist in a community-wide competition with clinical trials funded by other entities—with the pharmaceutical and biotech industries being the largest. The NCTN groups have a vision that our trials need to be cutting edge, so we need the most advanced and effective drugs to be in the mix. NCTN provides an important avenue for the groups to access these drugs and include them in our trials, particularly in less common diseases where industry trials could be lacking. Bringing effective treatments faster to cancer patients is really our main mission.

Dr. Kostakoglu: *Talking about that very topic, in a 2021 presentation at the European Society for Medical Oncology, NCTN leadership, including you, reported that NCI-funded randomized trials have generated substantial gains in life years for cancer patients. Could you briefly tell us about that study? I thought the results were fascinating.*

Dr. O'Dwyer: This cross-group study (Clinical and scientific impact of National Cancer Institute: Sponsored clinical trial network group treatment trials. *Ann Oncol.* 2021;32[suppl 5]:S1102–S1110) was initiated by SWOG investigators, and we need to give credit to the actual person who did the work, Joseph Unger, PhD, MS, from the Fred Hutchinson Cancer Research Center (Seattle, WA). The analysis systematically reviewed the survival impact of randomized phase 3 trials funded by NCI from 1980 through 2019. Over the past 40 years, adults in the United States diagnosed with cancer gained 14 million years of additional life thanks to the results of cancer clinical trials conducted by the NCTN. Furthermore, more than 80% of the studies influenced care recommendations and formal guidelines. These results strikingly affirm the importance of doing this type of collective research that contributes significantly to the health care system. Dr. Unger's findings are all the more important in this time of increasing costs of clinical research. The return to the American people of government-funded investment in better cancer care has been remarkably solid—a huge impact.

Dr. Kostakoglu: *These are amazing results. One last (but not least) issue is unnecessary treatment. Your co-chair at ECOG-ACRIN, Mitchell Schnall, MD, PhD, coined the phrase "one man's cure is another man's overtreatment." How do we bring value to targeted treatments and avoid overtreatment? And, of course, could we use molecular imaging as a complementary prognostic or predictive marker?*

Dr. O'Dwyer: Absolutely. The imaging studies in the MATCH trial that we have talked about have real potential to identify populations that are more or less likely to respond. Another recently proposed study would assign risk factors to some cancer patients based on genomic features. There are data to indicate that you can identify high-risk patients using genomic techniques. But imaging features can also be exploited, because they do not always overlap with the genomic features. The idea is to identify patients at the highest risk and initiate appropriately aggressive treatment strategies. With this approach, we could also decrease the number of patients subjected to unnecessary treatments.

This approach to overtreatment dovetails with the need to question the intensity of some therapies being used. ECOG-ACRIN led the definitive Trial Assigning Individualized Options for Treatment (TAILORx), which showed in 2018 that most women with early breast cancer do not benefit from chemotherapy. TAILORx also provided unequivocal evidence supporting the clinical utility of an assay to risk stratify women, leading to changes in NCCN and other treatment guidelines globally.

Within ECOG-ACRIN, multiple active studies are incorporating imaging to be able to stratify risk groups for proper treatment options. I think this type of strategy is going to have important patient outcome implications. You know, ECOG-ACRIN is unique among cooperative groups in that we are charged with developing advanced imaging trials for the NCI's NCTN. This is one of several goals for our expansive Imaging Committee, which is the hub for imaging scientists to engage with the group. The specialty

groups under this committee explore experimental imaging science, immunooncology, quantitative imaging, and radiomics.

Imaging scientists in ECOG-ACRIN develop and conduct trials for early evaluation of new imaging agents and approaches, as well as plans for their broader application, in collaboration with our 12 cancer-type–oriented therapeutic committees. These studies are developed with the help of our Cancer Research Advocates Committee. You know, for a patient who has just been diagnosed with cancer, the idea of decreasing the intensity of care can be frightening—and makes them very hesitant about being part of this type of clinical trial. So there's a complexity here that we're learning about, and our advocates are guiding us in developing ways to help patients understand and partner in this sort of research.

Dr. Kostakoglu: *A closing personal question. Being such a busy person, how do you strike a balance between your family life and work schedule? It's probably very difficult.*

Dr. O'Dwyer: It really is. But I have tremendous support from the best team of people that I have ever worked with. I'm only half of the leadership of ECOG-ACRIN. The other half is Dr. Schnall, group co-chair of ECOG-ACRIN and chair of the Department of Radiology at the University of Pennsylvania. Mitch is obviously a real expert, not just in the imaging field but also in health systems and precision medicine. So it isn't as hard to be organized as one would think. It's very important to be grounded in patient care, because, really, that's where the rubber hits the road. Being too far from patients can lead to unrealistic expectations. Again, this is all collaborative, and it's really a joy and a privilege to be able to work in this setting, both from the perspective of ECOG-ACRIN and the University of Pennsylvania, where I work and collaborate. I also have the good fortune to be married to Naomi Haas, MD, a genitourinary (GU) oncologist, also at the University of Pennsylvania, and co-chair of the ECOG-ACRIN GU Committee. Our mutual understanding of the clinical and research requirements and deadlines makes flexibility essential but allows us also to have a life away from these demands.

Dr. Kostakoglu: *It has been a truly great pleasure talking to you. We have covered myriad exciting topics. And thanks so much again for your time and willingness to share your valuable perspectives.*

Dr. O'Dwyer: Not only do I thank you so much for reaching out but also hope this discussion will be of interest to the readership.

Dr. Kostakoglu: *Thank you so much again for your valuable contribution.*

The VISION Forward: Recognition and Implication of PSMA−/^{18}F-FDG+ mCRPC

Hossein Jadvar

Division of Nuclear Medicine, Department of Radiology, Keck School of Medicine, University of Southern California, Los Angeles, California

Metastatic castration resistant prostate cancer (mCRPC) is incurable. The expression of the transmembrane protein prostate-specific membrane antigen (PSMA) is markedly increased in most mCRPC lesions. PSMA has been recognized as a viable biologic target for imaging and radionuclide therapy (theranostics) in mCRPC. The PET agents ^{68}Ga-PSMA-11 and ^{18}F-DCFPyL have recently been approved for imaging evaluation of patients with suspected metastasis who are candidates for initial definitive therapy and patients with suspected recurrence based on elevated serum prostate-specific antigen level. Radioligand therapy (RLT) with ^{177}Lu-PSMA-617 (^{177}Lu-vipivotide tetraxetan, Pluvicto, Novartis/AAA) was approved on March 23, 2022, based on the favorable results of the VISION trial. It has been recognized that PET imaging of PSMA expression and glucose metabolism (with ^{18}F-FDG) provides a more comprehensive assessment of the tumor burden and heterogeneity. However, there are many unresolved issues that surround whether or not imaging with ^{18}F-FDG PET is advantageous in the clinical setting of PSMA RLT in mCRPR.

Key Words: prostate; cancer; PSMA; FDG; VISION

J Nucl Med 2022; 63:812–815
DOI: 10.2967/jnmt.121.263274

The recently published VISION trial grounded on targeting the prostate-specific membrane antigen (PSMA) and the subsequent approval of ^{177}Lu-PSMA-617 by the Food and Drug Administration (FDA) is a momentous milestone for nuclear medicine, adding to the drive that has been generated over the past decade in the growth of theranostics and radiopharmaceutical therapy in cancer management (*1*). While metastatic castration-resistant prostate cancer (mCRPC) remains incurable despite significant strides in the development of various drug regimens, PSMA-based radioligand therapy (RLT) provides an additional viable option for prolonging life. According to the definition and spirit of theranostics, it is self-evident that the imaging component is an essential partner for assessing the presence, extent, and intensity of the target expression before commencing the therapy companion in the anticipation of favorable response and acceptable biologic and financial toxicities. It is therefore curious to note that the essential step of PSMA imaging in the theranostics process has been a topic of debate (*2,3*). However, in this discussion, my focus is on whether or not imaging with ^{18}F-FDG is needed or desired in the clinical setting of PSMA RLT.

PIVOTAL RELEVANCE OF TUMOR HETEROGENEITY

It is recognized that there is remarkable molecular heterogeneity between neoplastic cells in an individual tumor mass, between primary tumor and its metastases, and among the metastases, although it appears that intraindividual genomic diversity is more limited than interindividual genomic diversity (*4*). The multifeature heterogeneity of mCRPC renders its potential cure exceptionally challenging. It is posited that only when the reality of biologic heterogeneity is taken into full consideration, then there may be opportunities for early suitable therapeutic maneuverers to prolong life substantially, preferably with the least compromise on life quality. We have already encountered the heterogeneity concept in nuclear medicine. An example clinical setting includes patients with metastatic thyroid cancer and a negative radioiodine scan but positive ^{18}F-FDG PET/CT scan. Another similar setting involves patients with neuroendocrine tumors who harbor metastases with discordant somatostatin expression and glucose metabolism. Accordingly, discordance of PSMA expression and ^{18}F-FDG uptake is not unanticipated in mCRPC.

In a recent prospective investigation of a cohort of men with metastatic prostate cancer, there was only 22% concordance between ^{18}F-DCFPyL and ^{18}F-FDG, revealing substantial tumor heterogeneity (*5*). In another study of men with mCRPC undergoing ^{177}Lu-PSMA-617 RLT, at least 1 mismatch PSMA-negative/^{18}F-FDG–positive (PSMA−/^{18}F-FDG+) metastasis was noted in 59% of patients and this mismatch was associated with a significantly shorter overall survival compared with those patients without mismatch lesions (3.3 vs. 6 mo, $P = 0.008$) (*6*). A similar finding was reported in an investigation of 54 men with mCRPC who underwent PSMA PET/CT and ^{18}F-FDG PET/CT at baseline before ^{177}Lu-PSMA-617 RLT. Patients with at least 1 PSMA−/^{18}F-FDG+ metastasis at baseline had significantly lower median overall survival than those without mismatch lesions (6.0 vs. 16.0 mo, $P < 0.001$) (*7*). The Australian investigators noted that in patients who were excluded from the ^{177}Lu-PSMA-617 RLT clinical trial based on metastases with low PSMA expression and high ^{18}F-FDG uptake, the outcome was poor, with a short median survival of only 2.5 mo, even if the patients received additional systemic treatments (*8*). New discordant PSMA−/^{18}F-FDG+ lesions can also develop during ^{177}Lu-PSMA-617. Hartrampf et al. noted that after only 2 cycles of PSMA RLT, new PSMA−/^{18}F-FDG+ metastases developed in 13% of their patients (*9*). The authors paid particular attention to the newly appearing liver metastases. Liver metastases from prostate cancer are not uncommon, being the second most common site (along with lung) after

Received Sep. 27, 2021; revision accepted Dec. 16, 2021.
For correspondence or reprints, contact Hossein Jadvar (jadvar@med.usc.edu).
Published online Dec. 21, 2021.

bone, with a clinically evident macro-metastatic incidence of up to 25% and association with worst prognosis despite therapy (*10,11*). Most liver metastases (~80%) are PSMA-avid and amenable to PSMA RLT (*12*). The lack of sufficient PSMA uptake may be due to either low PSMA expression (e.g., genomic dedifferentiation) or reduced target-to-background ratio in relation to high physiologic hepatic uptake of the radiotracer (e.g., ^{18}F-PSMA-1007). In the investigation by Hartrampf et al., the few PSMA− liver metastases were all ^{18}F-FDG+. Except in 1 case, these lesions were also identified on contrast-enhanced CT. These observations imply that aside from effects of the type of PSMA radiotracer that is used and the available ancillary anatomic imaging information in identifying metastatic lesions, the change in tumor biology early in the PSMA RLT, probably through clonal selection with transdifferentiation from an epithelial phenotype to the more aggressive neuroendocrine phenotype, may affect the efficacy of subsequent RLT cycles and the overall impact on patient outcome (*13*).

WHAT PREDICTS DISCORDANT PSMA–/^{18}F-FDG+ METASTATIC DISEASE?

Chen et al. noted at least 1 PSMA−/^{18}F-FDG+ lesion in 23.2% of their patients with mCRPC who underwent both ^{68}Ga-PSMA-11 PET/CT and ^{18}F-FDG PET/CT. Multivariate regression analysis revealed that dichotomized thresholding of Gleason score (GS) at 8 and serum prostate-specific antigen (PSA) level at 7.9 ng/mL could predict PSMA−/^{18}F-FDG+ mismatch lesions with no mismatch lesions at GS and PSA levels below the threshold levels, 21.7% mismatch with GS $<$ 8 but PSA $\geq$ 7.9 ng/mL, and as high as 61.5% mismatch metastases when both GS and serum PSA level were above the threshold values (*14*). Interestingly, in the M0 CRPC clinical setting, Wang et al. reported that a high Gleason grade group was associated significantly with PSMA−/^{18}F-FDG+ disease. Moreover, they noted that castrate-sensitive metastatic disease was rarely associated with PSMA−/^{18}F-FDG+ lesions (*15*).

Blood parameters (liquid biopsy) may also be helpful as simple predictors of mismatch lesions. Rosar et al. observed that serum neuron-specific enolase (a cytoplasmic enzyme and a marker for tumors of neuroendocrine origin) concentration was significantly and positively associated with ^{18}F-FDG–avid and low PSMA-expressing metastases in patients with mCRPC (*16*). A recent systematic review reported that serum neuron-specific enolase correlates with prognosis in patients with progressive mCRPC (*17*). The LuPSMA trial investigators assessed for prognostic biomarkers that included blood parameters (alkaline phosphatase [ALP], lactate dehydrogenase [LDH]), and imaging (whole-body segmented and quantified tumor volume on PET and EXINI index for bone scan). For ^{18}F-FDG PET/CT, lesions were considered if they displayed SUVs greater than mean hepatic parenchyma uptake plus 2 SDs. For PSMA PET/CT, any lesion with an SUV above 3 was considered. The hazard ratios of prognostic biomarkers for overall survival were 2.6, 2.3, 1.2, 1.1, and 0.89 for ^{18}F-FDG+ tumor volume, bone scan index, LDH, ALP, and mean intensity of PSMA-avid tumor uptake, respectively (*18*). The ^{18}F-FDG+ tumor volume was the most informative prognostic biomarker.

HOW IS A LESION CHARACTERIZED AS PSMA– AND ^{18}F-FDG+?

The definition of PSMA positivity and ^{18}F-FDG negativity is not standardized. The phase 2 LuPSMA trial defined PSMA positivity when the lesion uptake level as measured by maximum SUV (SUV_{max}) was at least 1.5 times greater than liver SUV. Patients with any ^{18}F-FDG+ disease and corresponding PSMA uptake lower than the selected positivity definition were excluded (*19*). With these dual imaging criteria, 16% of the patients were excluded. In the phase 2 TheraP trial, PSMA positivity was defined as an SUV_{max} of at least 20 at a disease site and greater than 10 at all other measurable sites of metastatic disease. Patients were excluded if there were any PSMA−/^{18}F-FDG+ metastases (10% for PSMA− metastases, 18% for ^{18}F-FDG+ metastases) (*20*). Despite differing PSMA positivity definitions in the 2 trials, these maneuvers preselected patients with relatively high PSMA-expressing metastases, which enriched the potential for favorable outcome in patients undergoing ^{177}Lu-PSMA-617 RLT in these 2 clinical trials (PSA reduction of 50% or more from baseline or PSA50 in 57% and 66% of patients for LuPSMA and TheraP, respectively). The strategy was successful and supported additional clinical trials including the recently published pivotal randomized open-label phase 3 VISION trial comparing standard care plus ^{177}Lu-PSMA-617 with standard care alone (*21*).

In the VISION trial, only ^{68}Ga-PSMA-11 PET/CT was performed with the eligibility criteria that the patients harbor at least 1 PSMA+ metastatic lesion (defined as uptake greater than that of liver parenchyma in lesions of any size in any organ system) and no PSMA− lesions (defined as uptake equal to or lower than that of liver parenchyma in any lymph node with a short axis of at least 2.5 cm, in any solid organ lesion with a short axis of at least 1.0 cm, or in any bone lesion with a soft-tissue component of at least 1.0 cm in the short axis). With these imaging selection criteria, 12.6% of patients were excluded after PSMA PET/CT imaging. ^{18}F-FDG PET/CT was not performed. Outcome of PSA50 was noted in 46% of patients. The lower PSA50 in the VISION trial in comparison to those reported in the LuPSMA and TheraP trials may be in part due to the differing imaging-based patient eligibility criteria among the trials. It is probable that at least some patients who were eligible for VISION trial would have been excluded from LuPSMA and TheraP trials. It is interesting to concoct how the results of the VISION trial would have been impacted if the patient eligibility criteria included ^{18}F-FDG PET/CT similar to the LuPSMA and TheraP trials. However, in broader term, it remains to be determined if patients with low PSMA expression and discordant ^{18}F-FDG+ lesions should be excluded from PSMA RLT (*7*).

PROS AND CONS OF ^{18}F-FDG PET/CT INCLUSION IN PSMA RLT

Imaging evaluation of mCRPC with both ^{18}F-FDG and a PSMA radiotracer will provide a more comprehensive assessment of the tumor burden. However, how the levels of PSMA expression and ^{18}F-FDG discordance should impact PSMA RLT management decisions remain an open debate and will need further investigation. It is reasonable to anticipate that patients with tumors that display moderate PSMA expression but with ^{18}F-FDG discordance may be candidates for combination therapy (PSMA RLT plus chemotherapy, immunotherapy, or androgen deprivation therapy (ADT) in patients with polymetastatic disease or PSMA RLT plus stereotactic body radiation therapy with or without ADT in patients with oligometastatic disease). Interim ^{18}F-FDG PET/CT scanning during a course of PSMA RLT may also provide important information on any evolutionary biologic changes of the tumor sites, which may facilitate the tailoring of the subsequent

RLT cycles (in terms of timing and dosage) with or without inclusion of other therapies. Clinical trials may be envisioned to address these matters. In this regard, a standardized method to quantify PSMA PET/CT and ^{18}F-FDG PET/CT scans would be helpful to simplify image analysis and interpretation. A 6-tier image scoring system referred to as Pro-PET score has been proposed, although there has been no external validation (*22*). There are also proposed semiautomated algorithms that can facilitate quantification of total tumor burden on either PSMA PET/CT or ^{18}F-FDG PET/CT (*23–25*).

While there are rational motives to include ^{18}F-FDG PET/CT in PSMA RLT, it renders the entire process more complex from multiple points of view. The scans will likely be performed on 2 separate days, which may be inconvenient to patients. The imaging components of the theranostics will need to be interpreted in combination and results provided in a simple standardized format that can inform clinical decision making. While ^{18}F-FDG PET/CT is covered by the Center for Medicare and Medicaid Services (CMS) under the "subsequent treatment strategy" category for prostate cancer, the coverage for PSMA PET/CT has yet to be instituted. It is also unclear if CMS or insurance agencies would be amenable to pay for 2 PET/CT scans in close temporal proximity for the same indication if the outcome benefit for such diagnostic imaging strategy is unestablished. Notwithstanding, the overall cost of imaging will increase, and cost-utility studies will be needed to decipher whether higher cost and incorporation of combined ^{18}F-FDG PET/CT and PSMA PET/CT results improve patient management and outcome. Aside from the important issues of cost and logistics, and as alluded to above, many questions arise that remain unanswered at this time. It is unclear what treatment strategy may be best to treat patients with PSMA−/^{18}F-FDG+ disease (however, this condition ends up being defined) and if these patients should be excluded from PSMA RLT or if some patients may be included as potential candidates for the therapy if PSMA expression can be primed with intervention (e.g., properly timed and dosed ADT) (Fig. 1).

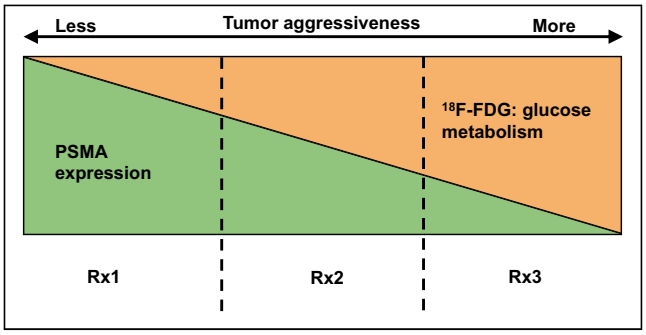

FIGURE 1. Simplified schematic of spectrum of PSMA and ^{18}F-FDG uptake in mCRPC lesions. Tumor aggressiveness generally increases from left to right, although there can be aggressive tumors without marked hypermetabolism (e.g., neuroendocrine phenotype). Prognosis is also poorer as tumor aggressiveness increases. Vertical dashed lines designate yet-to-be-defined borders of PSMA and ^{18}F-FDG avidity of total tumor burden, which may lead to different therapy strategies. RX1 = in tumors with mainly PSMA+ disease, PSMA RLT may be primary choice of therapy; RX2 = in tumors with mixed PSMA and ^{18}F-FDG avidity, combination therapy (PSMA RLT, chemotherapy, immunotherapy, ADT) may be considered; RX3 = in tumors with low or no PSMA expression and discordant ^{18}F-FDG+ disease, non-RLT may be mainstay strategy, although interventions may be instituted to shift tumor phenotype to left for enabling additional therapeutic approaches that may include PSMA RLT.

POTENTIAL STRATEGY FOR FUTURE

The current evidence suggests that at least in the clinical trial settings, incorporation of both PSMA PET/CT and ^{18}F-FDG PET/CT can be informative and potentially impactful. Post hoc analysis of the pertinent data collected from completed clinical trials can also be contributory. Inclusion of various clinical features such as GS, PSA and its kinetics, prior therapies, and relevant blood indicators may also provide the important stratification parameters for justifying the inclusion or exclusion of ^{18}F-FDG PET/CT imaging in the clinical setting of PSMA RLT.

DISCLOSURE

This study was supported in part by grants R21-EB017568 and P30-CA014089 from the U.S. National Institutes of Health. Hossein Jadvar is on the advisory board of Radiomedix, Inc., is a consultant to Bayer and Blue Earth Diagnostics, and is on the speaker's bureau for Lantheus, all unrelated to this submission. No other potential conflict of interest relevant to this article was reported.

REFERENCES

1. U.S. Food and Drug Administration (FDA). FDA approves Pluvicto for metastatic castration-resistant prostate cancer. U.S. FDA website. https://www.fda.gov/drugs/resources-information-approved-drugs/fda-approves-pluvicto-metastatic-castration resistant-prostate-cancer. Accessed May 16, 2022..
2. Srinivas S, Iagaru A. To scan or not to scan: an unnecessary dilemma for PSMA radioligand therapy. *J Nucl Med.* 2021;62:1487–1488.
3. Calais J, Czernin J. PSMA expression assessed by PET imaging is a required biomarker for selecting patients for PSMA-targeted therapy. *J Nucl Med.* 2021;62: 1489–1491.
4. Kumar A, Coleman I, Morrissey C, et al. Substantial interindividual and limited intraindividual genomic diversity among tumors from men with metastatic prostate cancer. *Nat Med.* 2016;22:369–378.
5. Fourquet A, Rosenberg A, Mena E, et al. A comparison of ^{18}F-DCFPyL, ^{18}F-NaF and ^{18}F-FDG PET/CT in a prospective cohort of men with metastatic prostate cancer. *J Nucl Med.* 2021;63: 735–741.
6. Khreish F, Ribbat K, Bartholomä M, et al. Value of combined PET imaging with [^{18}F]FDG and [^{68}Ga]Ga-PSMA-11 in mCRPC patients with worsening disease in [^{177}Lu]Lu-PSMA-617 RLT. *Cancers (Basel).* 2021;13:4134.
7. Michalski K, Ruf J, Goetz C, et al. Prognostic implications of dual tracer PET/CT: PSMA ligand and [^{18}F]FDG PET/CT in patients undergoing [^{177}Lu]PSMA radioligand therapy. *Eur J Nucl Med Mol Imaging.* 2021;48:2024–2030.
8. Thang SP, Violet J, Sandhu S, et al. Poor outcomes for patients with metastatic castration-resistant prostate cancer with low prostate-specific membrane antigen (PSMA) expression deemed ineligible for ^{177}Lu-labeled PSMA radioligand therapy. *Eur Urol Oncol.* 2019;2:670–676.
9. Hartrampf PE, Lapa C, Serfling SE, et al. Development of discordant hypermetabolic prostate cancer lesions in the course of [^{177}Lu]PSMA radioligand therapy and their possible influence on patient outcome. *Cancers (Basel).* 2021;13:4270.
10. Ma B, Wells A, Wei L, Zheng J. Prostate cancer liver metastasis: dormancy and resistance to therapy. *Semin Cancer Biol.* 2021;71:2–9.
11. Singh A, Cheedella NKS, Shakil SA, Gulmi F, Kim DS, Wang JC. Liver metastases in prostate carcinoma represent a relatively aggressive subtype refractory to hormonal therapy and short-term duration response to docetaxel monotherapy. *World J Oncol.* 2015;6:265–269.
12. Damjanovic J, Janssen J-C, Prasad V, et al. ^{68}Ga-PSMA-PET/CT for the evaluation of liver metastases in patients with prostate cancer. *Cancer Imaging.* 2019;19: 37.
13. Bakht MK, Lovnicki JM, Tubman J, et al. Differential expression of glucose transporters and hexokinase in prostate cancer with a neuroendocrine gene signature: a mechanistic perspective for ^{18}F-FDG imaging of PSMA-suppressed tumors. *J Nucl Med.* 2020;61:904–910.
14. Chen R, Wang Y, Zhu Y, et al. The added value of ^{18}F-FDG PET/CT compared to ^{68}Ga-PSMA PET/CT in patients with castration-resistant prostate cancer [abstract]. *J Nucl Med.* April 23, 2021 [Epub ahead of print].
15. Wang B, Liu C, Wei Y, et al. A prospective trial of ^{68}Ga-PSMA and ^{18}F-FDG PET/CT in nonmetastatic prostate cancer patients with an early PSA progression during castration. *Clin Cancer Res.* 2020;26:4551–4558.

16. Rosar F, Ribbat K, Ries M, et al. Neuron-specific enolase has potential value as a biomarker for [^{18}F]FDG/[^{68}Ga]Ga-PSMA-11 PET mismatch findings in advanced mCRPC patients. *EJNMMI Res.* 2020;10:52.
17. Muoio B, Pascale M, Roggero E. The role of serum neuron-specific enolase in patients with prostate cancer: a systematic review of the recent literature. *Int J Biol Markers.* 2018;33:10–21.
18. Ferdinandus J, Violet J, Sandhu S, et al. Prognostic biomarkers in men with metastatic castration-resistant prostate cancer receiving [^{177}Lu]-PSMA-617. *Eur J Nucl Med Mol Imaging.* 2020;47:2322–2327.
19. Hofman MS, Violet J, Hicks RJ, et al. [^{177}Lu]-PSMA-617 radionuclide treatment in patients with metastatic castration-resistant prostate cancer (LuPSMA trial): a single-centre, single-arm, phase 2 study. *Lancet Oncol.* 2018;19:825–833.
20. Hofman MS, Emmett L, Sandhu S, et al; TheraP Trial Investigators and the Australian and New Zealand Urogenital and Prostate Cancer Trials Group. [^{177}Lu]Lu-PSMA-617 versus cabazitaxel in patients with metastatic castration-resistant prostate cancer (TheraP): a randomised, open-label, phase 2 trial. *Lancet.* 2021;397:797–804.
21. Sartor O, de Bono J, Chi KN, et al; VISION Investigators. Lutetium-177-PSMA-617 for metastatic castration-resistant prostate cancer. *N Engl J Med.* 2021;385:1091–1103.
22. Adnan A, Basu S. Concept proposal for a six-tier integrated dual tracer PET-CT (^{68}Ga-PSMA and FDG) image scoring system ('Pro-PET' score) and examining its potential implications in metastatic castration-resistant prostate carcinoma theranostics and prognosis. *Nucl Med Commun.* 2021;42:566–574.
23. O JH, Lim SJ, Wang H, Leal JP, Shu HG, Wahl RL; QIN PET Readers. Quantitation of cancer treatment response by 2-[^{18}F]FDG PET/CT: multi-center assessment of measurement variability using AUTO-PERCIST^{TM}. *EJNMMI Res.* 2021;11:15.
24. Seifert R, Sandach P, Kersting D, et al. Repeatability of ^{68}Ga-PSMA-HBED-CC PET/CT-derived total molecular tumor volume. *J Nucl Med.* 2022;63:746–753.
25. Hammes J, Täger P, Drzezga A. EBONI: a tool for automated quantification of bone metastasis load in PSMA PET/CT. *J Nucl Med.* 2018;59:1070–1075.

Why We Did What We Did: PSMA PET/CT Selection Criteria for the VISION Trial

Phillip H. Kuo[1], Taylor Benson[2], Richard Messmann[2], and Michael Groaning[3]

[1]*Departments of Medical Imaging, Medicine, and Biomedical Engineering, University of Arizona, Tucson, Arizona;* [2]*Novartis Pharmaceuticals Corporation, Basel, Switzerland; and* [3]*Amgen, Thousand Oaks, California*

After years of development and many published studies, prostate-specific membrane antigen–targeted radioligand therapy recently reached a critical milestone on March 23, 2022, with approval of ^{177}Lu-PSMA-617 by the U.S. Food and Drug Administration (*1*). This landmark success heralds a new era of large-scale theranostics for nuclear medicine. This editorial provides the first-hand perspective on the origins of the phase III VISION trial and, specifically, the creation of the imaging criteria for selection of patients for PSMA-targeted therapy.

ENDOCYTE: A PHOENIX RISEN FROM THE ASHES

Endocyte was founded in 1996 to develop small-molecule drug conjugates and imaging agents targeting the folate receptor (*2*). In 2012, Endocyte entered into a license agreement with Merck & Co. for codevelopment of a folate-targeted theragnostic for women with platinum-resistant ovarian cancer. Two years later, Endocyte received a positive opinion for conditional marketing authorization from the Committee for Human Medicinal Products for the combination of the folate-targeted small-molecule drug conjugate and a companion SPECT diagnostic for patient selection. Shortly after, Endocyte withdrew the conditional marketing authorization application because the phase III trial failed the predefined futility analysis. During that same time, Endocyte expanded its portfolio to include prostate-specific membrane antigen (PSMA)–targeted theranostics and initiated a phase I trial investigating a PSMA-targeted small-molecule drug conjugate and ^{99m}Tc-based PSMA-targeted SPECT tracer for prostate cancer (*3*).

While analyzing the failure of the folate-targeted theragnostic trial (*4*), Endocyte restructured the organization and explored in-licensing opportunities. Leveraging of the company's history with theranostics and patient selection experience, along with the growing recognition of the potential of PSMA-targeted radioligand therapy, Endocyte announced the worldwide licensing agreement for ^{177}Lu-PSMA-617 with ABX GmbH in October 2017. The team then quickly worked to initiate the phase III trial "^{177}Lu-PSMA-617 for Metastatic Castration-Resistant Prostate Cancer" (VISION). Endocyte decided to use ^{68}Ga-PSMA-11 PET/CT for patient selection and entered into a supply agreement with Telix to use its PSMA-11 kit for sites that did not have an active ^{68}Ga-PSMA-11 investigational-new-drug authorization. Less than a year after acquisition of PSMA-617, the first patient was enrolled in the VISION study. Along with overall survival, imaging-based progression-free survival was negotiated by Endocyte with the Food and Drug Administration as an alternate primary endpoint. In October 2018, Novartis announced its intent to acquire Endocyte—an event that completed the story of Endocyte's rising from the ashes. On March 23, 2021, Novartis announced the successful results of the VISION trial, approximately 3.5 y after Endocyte's acquisition of the exclusive license for PSMA-617 (*5*).

FORMULATING THE PSMA PET SELECTION CRITERIA

The first decision was whether to even use imaging for patient selection. For example, if imaging excluded only less than 10% of patients, would it be worth the added effort, expense, and complexity to the trial? On the other hand, if selection were too restrictive, patients could be excluded who might otherwise benefit from ^{177}Lu-PSMA-617. After consulting with a variety of opinion leaders, a 10%–20% exclusion rate by imaging was targeted as an optimal compromise between too restrictive and not restrictive enough, which was achieved in the trial. At the time (and arguably still), there were not enough robust data in the public domain to inform a definitive exclusion rate and set expectations based on efficacy outcomes in this patient population using PSMA PET. In addition to the complex task of maximizing the likelihood of successfully reaching efficacy endpoints, one must balance the feasibility and thus reproducibility of the reading criteria. Relating novel criteria to existing, familiar, criteria may improve the likelihood of successful implementation.

The next decision was whether to use PSMA PET alone or to combine PSMA and ^{18}F-FDG PET. At that time, the combination of PSMA and ^{18}F-FDG PET had been advantageously used to evaluate for low PSMA uptake by PSMA PET, as well as for discordant lesions by combining PSMA and ^{18}F-FDG PET (*6*). After careful consideration, it was decided to use PSMA PET/CT in combination with the diagnostic CT, because adding ^{18}F-FDG PET presented potential operational complexity and cost in the execution of a large, global clinical trial. However, when considering patients in a standard-of-care clinical setting, addition of ^{18}F-FDG PET/CT to improve patient selection could save money (*7*). In a large, global clinical trial setting, 2 scans versus 1 scan could increase variability in readings. Future issues with reimbursement of PET could occur with both ^{18}F-FDG and PSMA PET, but PSMA PET was considered more essential given the patent necessity for assessing the PSMA expression of tumors for this targeted therapy.

Received Dec. 7, 2021; revision accepted Jan. 20, 2022.
For correspondence or reprints, contact Phillip H. Kuo (pkuo@email.arizona.edu).
Published online Jan. 27, 2022.

DOI: 10.2967/jnumed.121.263638

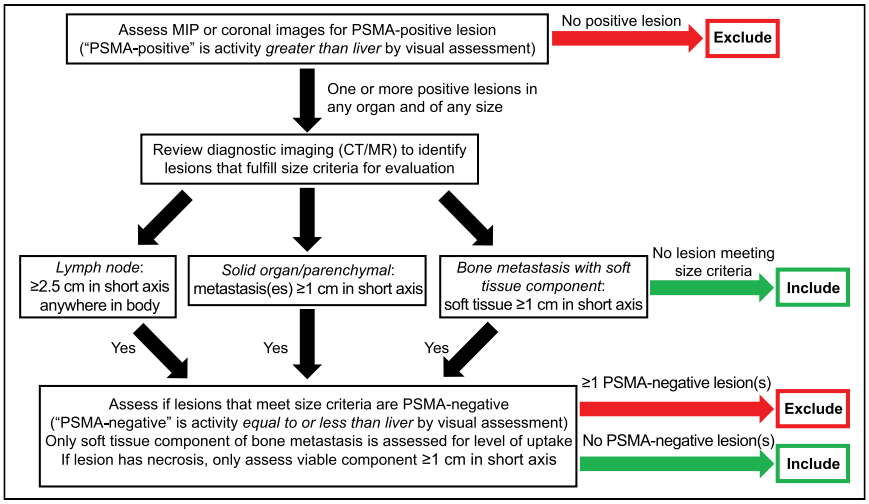

FIGURE 1. Reading methodology of VISION trial for patient selection. MIP = maximum-intensity projection.

A definition for "PSMA-positive" and "PSMA-negative" was created specifically for this trial. In this context, the definition of PSMA positivity was designed not to localize prostate cancer but to identify tumors with sufficient target expression that would likely respond to therapy. The use of an SUV cutoff was not chosen for this global trial given the variability of SUV across clinical sites and the known challenges of standardization and certification. Visual assessment against an appropriate internal reference was chosen. Blood pool was too low as a reference, and using multiples of the blood pool would require measuring SUVs. Spleen was considered, which often has high uptake and thus the possible advantage of a more stringent threshold. Preliminary evaluation of splenic uptake in PSMA PET scans revealed there was too much variability (unpublished data, Phillip H. Kuo, February 2018). Finally, some patients might not have a spleen, which would preclude that as a universal reference organ. The commonly used Deauville criteria for ^{18}F-FDG PET for lymphoma uses the liver as a reproducible visual internal reference standard (*8*). The team defined PSMA positivity as "greater than liver" rather than "equal to or greater than liver" to provide a more stringent selection. Given the prior Endocyte experience with grading levels of activity on folate-receptor imaging, a binary assessment (PSMA positivity or negativity) was chosen.

CT can be used to identify aggressive tumors, which would then be assessed on the PET/CT scan for level of PSMA uptake. To aid with reproducibility, we used the familiar RECIST 1.1 as a foundation. Assessment of anatomic imaging was divided into 3 systems: lymph nodes, solid organs, and skeleton. The need to identify and accurately measure lesions for determination of PSMA status requires high-quality anatomic imaging and careful reads by imagers.

First, the lymph node category was addressed. The ALSYMPCA trial with ^{223}Ra-chloride included patients with lymphadenopathy up to 3 cm in short-axis diameter and showed that benefit in overall survival could be achieved in patients with bone metastases without treating nodes up to 3 cm (*9*). If a patient had extensive, nonnodal disease with intense uptake on PSMA PET but PSMA-negative nodes, we surmised that patients would still likely benefit. Instead of a 3-cm threshold, 2.5 cm in short-axis diameter was ultimately used for greater stringency.

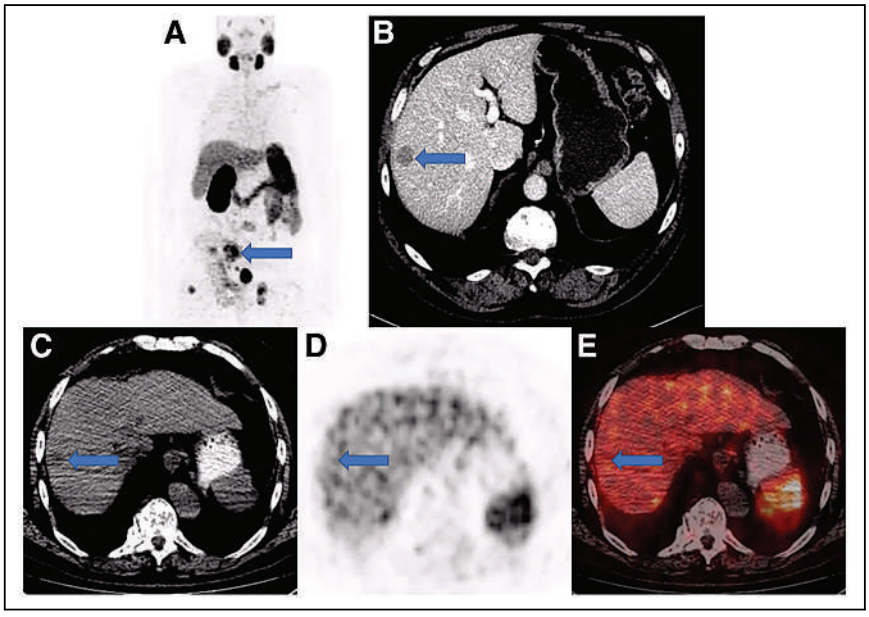

FIGURE 2. Example of patient who would have been excluded by imaging selection criteria used in VISION trial. (A) Anterior maximum-intensity projection from ^{68}Ga-PSMA-11 PET/CT has readily evident PSMA-positive disease, such as in sacrum (arrow); thus, next step is to evaluate diagnostic CT for lesions that fulfill size criteria for possible exclusion. (B) On contrast-enhanced diagnostic CT, 1.8-cm metastasis is identified in right hepatic lobe (arrow). Transaxial low-dose CT (C), PET (D), and PET/CT (E) images show that metastasis (arrows) has activity similar to normal liver, is therefore PSMA-negative, and would result in exclusion. Level of uptake in hepatic metastasis was importantly confirmed in sagittal and coronal planes (not shown) in case of misregistration.

Next, the solid-organ and parenchymal metastases were considered. Like the size criteria for target lesions in RECIST 1.1, only disease at least 1.0 cm in short-axis diameter would be assessed for PSMA status. The need to identify metastases down to 1.0 cm in short-axis diameter emphasizes the need for careful evaluation of the anatomic imaging, since a PSMA-negative metastasis could be more difficult to identify on PET imaging. Unfortunately, at 1.0 cm in short-axis diameter, activity could be underestimated because of the partial-volume effect, but it would be critical to include metastases down to this size given the impact of parenchymal metastases on survival.

Finally, the skeletal system was particularly challenging. Because the patient population in the VISION trial would be previously treated with multiple therapies, it would have been difficult to distinguish between healed, sclerotic metastases and active sclerotic disease on CT. Thus, a focus on aggressive or destructive bone disease with a soft-tissue component was pursued. Like the size criteria for target lesions in RECIST 1.1, the reader would assess only those bone metastases with a soft-tissue component at least 1.0 cm in

short-axis diameter, and only the soft-tissue component would be assessed for level of activity.

The first step in the reading criteria is assessing the PSMA PET images for at least 1 PSMA-positive lesion (of any size) to ensure the presence of targetable disease (Fig. 1). The reader then evaluated the anatomic imaging for lesions that met the size criteria for assessment of PSMA status (Fig. 1). One or more PSMA-negative lesions resulted in exclusion (Figs. 1 and 2). The rationale was that 1 PSMA-negative lesion of adequate size for assessment could represent only a portion of the PSMA-negative disease reservoir that would not respond to PSMA-targeted therapy. This was also important for the imaging-based progression-free-survival endpoint. Theoretically, PSMA-positive disease would respond promptly after the initial cycles of ^{177}Lu-PSMA-617 but even 1 PSMA-negative lesion would continue to grow and, therefore, the sum of the diameters of the target lesions would increase to progression of disease soon after nadir. A major concern was potentially excluding good responders who have high uptake in many lesions except one. Use of cutoffs such as greater than 70%, 80%, or 90% of lesions positive was considered. Prior unpublished Endocyte experience with folate imaging demonstrated that this methodology adds significant variability and complexity to the reading (unpublished data, Phillip H. Kuo et al., October 2013). Ultimately, the original exclusion criterion of one or more PSMA-negative lesions was maintained.

By synthesizing the knowledge of radiotherapeutic trials with prior experience in developing reading criteria for theranostics, novel imaging selection criteria saw their first use in the successful VISION trial. Future correlation with outcomes and advanced PSMA PET analyses are needed to further refine these selection criteria to optimize patient care and management decision algorithms (*10,11*).

DISCLOSURE

Phillip Kuo is an employee of Invicro. He is a consultant or speaker for Amgen, Eisai, Endocyte, GE Healthcare, Novartis, Invicro, Bayer, Chimerix, Fusion Pharma, and UroToday. He is a recipient of research grants from Blue Earth Diagnostics and GE Healthcare. Richard Messmann is an employee of Novartis and previously of Endocyte. Taylor Benson is an employee of Novartis and previously of Endocyte. Michael Groaning is an employee of Amgen and previously of Endocyte and Novartis. No other potential conflict of interest relevant to this article was reported.

ACKNOWLEDGMENT

We thank the entire Endocyte and Novartis teams for their contributions to the VISION trial.

REFERENCES

1. U.S. Food and Drug Administration (FDA). FDA approves Pluvicto for metastatic castration-resistant prostate cancer. U.S. FDA website. https://www.fda.gov/drugs/resources-information-approved-drugs/fda-approves-pluvicto-metastatic-castration-resistant-prostate-cancer. Accessed March 28, 2022.
2. Leamon CP, Low PS. Delivery of macromolecules into living cells: a method that exploits folate receptor endocytosis. *Proc Natl Acad Sci USA.* 1991;88:5572–5576.
3. Phase 1 study of EC1169 in patient with recurrent mCRPC. ClinicalTrial.gov website. https://clinicaltrials.gov/ct2/show/NCT02202447. Posted July 29, 2014. Updated February 7, 2019. Accessed March 8, 2022.
4. Study for women with platinum resistant ovarian cancer evaluating EC145 in combination with Doxil® (PROCEED). ClinicalTrial.gov website. https://clinicaltrials.gov/ct2/show/NCT01170650. Posted July 27, 2010. Updated September 30, 2021. Accessed March 8, 2022.
5. Sartor O, de Bono J, Chi KN, et al. Lutetium-177-PSMA-617 for metastatic castration-resistant prostate cancer. *N Engl J Med.* 2021;385:1091–1103.
6. Hofman MS, Violet J, Hicks RJ, et al. Lu-177-PSMA-617 radionuclide treatment in patients with metastatic castration-resistant prostate cancer (LuPSMA trial): single center, single-arm, phase 2 study. *Lancet Oncol.* 2018;19:825–833.
7. Calais J, Czernin J. PSMA expression assessed by PET imaging is a required biomarker for selecting patients for any PSMA-targeted therapy. *J Nucl Med.* 2021; 62:1489–1491.
8. Barrington SF, Kluge R. FDG PET for therapy monitoring in Hodgkin and non-Hodgkin lymphomas. *Eur J Nucl Med Mol Imaging.* 2017;44(suppl 1):97–110.
9. Parker C, Nilsson S, Heinrich D, et al. Alpha emitter radium-223 and survival in metastatic prostate cancer. *N Engl J Med.* 2013;369:213–223.
10. Srinivas S, Iagaru A. To scan or not to scan: an unnecessary dilemma for PSMA radioligand therapy. *J Nucl Med.* 2021;62:1487–1488.
11. Herrmann K, Krause BJ. Nuclear Medicine Theranostics Comes of Age. *Lancet Oncol.* 2021;22:1497–1498.

The Importance of Training, Accreditation, and Guidelines for the Practice of Theranostics: The Australian Perspective

Sze Ting Lee[1–4], Louise M. Emmett[5,6], David A. Pattison[7,8], Michael S. Hofman[9–11], Dale L. Bailey[12], Melissa J. Latter[7,8], Roslyn J. Francis [13,14], and Andrew M. Scott[1–4]

[1]Department of Molecular Imaging and Therapy, Austin Health, Melbourne, Victoria, Australia; [2]Tumour Targeting Laboratory, Olivia Newton-John Cancer Research Institute, Melbourne, Victoria, Australia; [3]Department of Medicine, University of Melbourne, Melbourne, Victoria, Australia; [4]School of Cancer Medicine, La Trobe University, Melbourne, Victoria, Australia; [5]Department of Theranostics and Nuclear Medicine, St. Vincent's Hospital, Sydney, New South Wales, Australia; [6]St. Vincent's Clinical School, University of New South Wales, Sydney, New South Wales, Australia; [7]Department of Nuclear Medicine and Specialised PET Services, Royal Brisbane and Women's Hospital, Brisbane, Queensland, Australia; [8]School of Medicine, University of Queensland, Brisbane, Queensland, Australia; [9]Molecular Imaging and Therapeutic Nuclear Medicine, Peter MacCallum Cancer Centre, Melbourne, Victoria, Australia; [10]Prostate Cancer Theranostics and Imaging Centre of Excellence, Peter MacCallum Cancer Centre, Melbourne, Victoria, Australia; [11]Sir Peter MacCallum Department of Oncology, University of Melbourne, Melbourne, Victoria, Australia; [12]Department of Nuclear Medicine, Royal North Shore Hospital, Sydney, New South Wales, Australia; [13]Department of Nuclear Medicine, Sir Charles Gairdner Hospital, Perth, Western Australia, Australia; and [14]Medical School, University of Western Australia, Perth, Western Australia, Australia

In nuclear medicine, theranostics is a burgeoning development that is rapidly being implemented worldwide. There is an increasing need to provide a multidisciplinary framework to the practice of theranostics, ensuring that patients receive this treatment safely and are secure in the knowledge that their health-care practitioners are adequately trained. Nuclear medicine experts in Australia have taken the initiative of producing a set of theranostic guidelines relevant to Australian medical practice. These guidelines encompass specialist qualifications, patient care, radiopharmaceutical production, radiation safety, and dosimetry. We propose adaptation of these guidelines by other countries, and we promote standards of practice leading to optimal clinical outcomes for patients receiving theranostic treatments.

Key Words: molecular imaging; general oncology; radionuclide therapy; guidelines; theranostics; training

J Nucl Med 2022; 63:819–822
DOI: 10.2967/jnumed.122.263996

Theranostics is the buzzword of the century in nuclear medicine, denoting cell targets with paired imaging and therapeutic radionuclides. Theranostic imaging is used to guide subsequent therapy by demonstrating that a cellular target is expressed at a sufficient concentration for a targeted radionuclide treatment to work. The concept embodies precision medicine targeting the right treatment for the right patient at the right time. Although most often utilized in oncology, it also has potential applications in neurology and cardiovascular disease.

Received Feb. 8, 2022; revision accepted Mar. 22, 2022.
For correspondence or reprints, contact Andrew M. Scott (andrew.scott@austin.org.au).
Published online Apr. 7, 2022.

Several landmark theranostic papers have been published in recent years (*1–4*). The success of these trials and subsequent implications for management of these radionuclide treatments in patients have driven increasing demand for this form of treatment, not just from the treating oncology specialists but from the patients themselves, especially in this digital age with patients connecting via social media. The other consequence of this success is increasing involvement of small to large pharmaceutical companies in theranostic research and development.

Although this treatment approach is being rolled out in both developed and developing countries around the world, there are few consensus statements on the overall safe practice of theranostics. There are individual best-practice statements and guidelines (*5,6*), and the International Atomic Energy Agency has developed a "Training Curriculum for Nuclear Medicine Physicians" document (*7*). This technical document states that there should be an understanding of the general principles of treatment using radiopharmaceuticals and unsealed radioactive sources, including the theranostic approach for personalized medicine. Unfortunately, it was not within the scope of that document to expand on the specifics required in order to be accredited for the practice of theranostics. The Nuclear Medicine Global Initiative on Theranostics, of the Society of Nuclear Medicine and Molecular Imaging, is currently working on a universal approach to the practice of theranostics.

In Australia, the peak body of nuclear medicine medical practitioners—the Australasian Association of Nuclear Medicine Specialists (AANMS)—has produced a position statement on the practice of theranostics in Australia (*8*). This statement was produced in conjunction with representatives from the multidisciplinary membership of the Australia and New Zealand Society of Nuclear Medicine, including medical physicists, radiopharmaceutical scientists, nurses, and nuclear medicine technologists. This position statement provides a consensus on recommendations regarding the care of patients receiving theranostic therapy and to support the provision of safe, high-quality, targeted care by qualified professionals. These

recommendations include identifying the optimal workplace and facility requirements for the production and administration of a radiopharmaceutical, establishing specialist training requirements, and establishing patient workflow and multidisciplinary team requirements. The recommendations cover some essential prerequisites for the practice of theranostics, including the qualifications of a theranostic specialist; appropriate patient selection for theranostic treatment; and individualized treatment plans and departmental requirements, including radiopharmaceutical production and quality control, radiopharmaceutical administration, and discharge requirements.

This position statement outlines common concepts that need to be understood by theranostic specialists. A wide range of theranostic therapies is currently available, with more on the horizon. The most important components of theranostics that were considered in the development of these guidelines include acknowledging the differences and complexities involved in managing patients, developing a good understanding of the breadth of treatments available, and aiming for a strong multidisciplinary approach to patient management. There is also an inherent need to understand the patient's objectives with regard to treatment and to ensure that patient consultation is an essential component of determining optimal patient management.

SYNOPSIS OF AANMS POSITION STATEMENT

The Theranostic Specialist

In the AANMS position statement, a theranostic specialist is defined as a qualified nuclear medicine specialist trained in the practice of theranostics by the Committee for Joint College Training in Nuclear Medicine, which oversees nuclear medicine training in Australia, with representation from the Royal Australasian College of Physicians and the Royal Australian and New Zealand College of Radiologists. To obtain accreditation in theranostics, a qualified nuclear medicine specialist in Australia needs to meet specified accreditation and training requirements as outlined in this paper. PET and SPECT interpretation is fundamental to determining suitability for treatment, dosimetry, and response assessment for theranostic practice, and nuclear medicine provides this expertise. In Australia, nuclear medicine training includes a wide range of adult and pediatric imaging with radiopharmaceuticals; radionuclide therapy, including thyroid cancer; and radiation protection principles and legislative requirements for administering radiopharmaceuticals. The requirement for subaccreditation in theranostics within our specialty group recognizes the importance of advanced training and experience in this emerging area and the lead role of nuclear medicine in this field.

NOTEWORTHY

- The rapid expansion of theranostic services requires guidelines for safe practice.
- The practice of theranostics requires a multidisciplinary approach involving the referrer and service providers, including dosimetry and radiopharmacy.
- Medical practitioners providing theranostic services should be appropriately trained and credentialled.

The Patient

Clinical consultation is an essential step in the proper evaluation of a patient's suitability for radionuclide therapy, including a full clinical assessment of the patient's medical condition and evaluation of the appropriate molecular imaging studies for the theranostic agent to be given. Careful imaging assessment underpins the decision-making process regarding the appropriateness of radionuclide therapy for each patient. This imaging must also be performed in an appropriate time frame relevant to the condition being treated in order to minimize disease progression or transformation, which may impact treatment efficacy. Again, this imaging should be performed in a multidisciplinary setting that enables accurate and shared discussion of all imaging results and clinical aspects of patient care. If treatment is recommended, the patient must be told the practical aspects and logistics of treatment, including any potential side effects and complications, management of the side effects, and long-term complications. Any radiation protection issues relevant to the patient and family members must also be communicated. Once fully informed, the patient can decide whether to proceed with treatment, and written informed consent must be obtained.

After treatment, there should be a follow-up assessment with the treating theranostic specialist according to local institutional practice, with assessment of toxicities, imaging results, and pathology results, as needed, to determine whether the patient remains suitable for further cycles of radionuclide therapy and, if so, whether any dose modifications are required. There should be ongoing multidisciplinary involvement, with shared care between the referring oncology specialist and the theranostic specialists throughout treatment, to ensure optimal holistic disease management. This aspect is particularly important in patients with more aggressive disease and pain control requirements. Shared care can involve alternating visits between the oncology and theranostic specialists (such as at 3-wk intervals). A multidisciplinary team, also known as a tumor board, may also be of value, not only at treatment onset but at seminal stages of treatment (particularly at premature cessation and when any complications arise) and to consider or coordinate other therapies, if appropriate.

Radiopharmaceutical Production

Depending on the relevant local regulations, radiopharmaceuticals may be produced by a central radiopharmacy or a local hospital-based radiopharmaceutical laboratory. The AANMS guidelines cover the specific requirements, and in alignment with our local regulatory requirements in Australia, the radiopharmaceutical can be manufactured in a departmental radiopharmacy by a trained radiopharmaceutical scientist using appropriate standard operating procedures (SOP) under good laboratory practices adopted for continued process control and high-quality standards. When applicable, radiopharmaceuticals should be prepared according to regulatory and monograph guidelines. The entire manufacturing process should be documented on a batch record or worksheet, and staff training and compliance with this procedure should be recorded. Deviations from this procedure should be documented according to site protocols. A risk-based approach to process validation should be completed before radiopharmaceuticals are prepared for human use.

Equipment used in the manufacturing and quality control testing of radiopharmaceuticals should be certified at installation and then checked routinely to ensure reliability in operation. Ongoing maintenance-and-use logs for critical equipment are also recommended.

Radiopharmaceutical production in commercial radiopharmacies is performed under good-manufacturing-practice guidelines.

The final review of product quality remains the responsibility of the administering theranostic specialist.

Medical Radiation and Dosimetry

Good radiation safety practices both within the department and in the general population must be maintained according to local regulations. The development of SOPs would commonly involve a medical physicist and radiation safety officers. For outpatient treatments, the medical physicist's advice is used to decide when patients can be released from the treating facility to their home, another residence, or back to the hospital ward. Once released, patients need to be aware of the radiation protection guidelines to be followed and for what period these apply. This advice can be given by a theranostic medical specialist, a trained medical physicist, or a nuclear medicine technologist. Any departure from normal procedures, such as a spill or an extravasated injection, will require an objective assessment of the likely implications and expert knowledge of the procedures that should be undertaken to mitigate the effect on patients. The medical physicist also plays a critical role in assisting with dosimetry and individual dose planning, as required.

Sites should have specific guidelines for each radiotherapeutic administration, with site-specific medical, nursing, and technologist protocols, as each group will often have important roles in supervising the patient before, during, and after treatment and may coordinate care arrangements. Nursing staff will also administer any required premedications for the specific radionuclide therapy and any necessary preparatory infusions (e.g., amino acids).

All departments should have SOP guidelines for delivery of therapeutic radiopharmaceuticals, to ensure absolute safety of the staff, patients, and general public.

All SOPs developed should be endorsed by both the medical physicist involved in the delivery of care at that site and the theranostic medical specialists directly responsible for care at the treatment facility. In Australia, a qualified nuclear medicine medical physics specialist accredited with the Australasian College of Physical Scientists and Engineers in Medicine must oversee this endorsement, either actively or through the use of an SOP.

TRAINING AND ACCREDITATION

All medical specialists seeking to establish proficiency in theranostics are required to achieve the following skills during their training program: understanding of the physiology and radiation physics used in theranostics, including understanding of the radiobiology of therapeutic nuclear medicine; patient selection (including molecular imaging assessment and correlation) and preparation; understanding of the standard-of care-therapies for different cancer subtypes; understanding of how theranostic treatments fit optimally with other cancer treatment options and when it is most appropriate for theranostics to be administered in each patient journey (the right treatment for the right patient at the right time) based on existing evidence; understanding of the indications, contraindications, and management of adverse events; and radiation protection of the patient, staff, and general public.

The AANMS document has provided some requirements for 2-level accreditation. These include a variety of live and case-based learnings, with a range of therapies and documentation for both prospective and retrospective training. In recognition of prior practice, a legacy provision category has been developed for current nuclear medicine specialists who wish to apply for credentialling according to the level they have reached over the last 3 y—either general accreditation or advanced accreditation.

General Accreditation

Completion of the minimum additional training requirements or legacy provisions for specialists in nuclear medicine will qualify the applicant for general accreditation, allowing participation in providing theranostic services. These requirements are experience with more than 50 therapies by initial consultations or administrations within the last 3 y, participation in multidisciplinary discussion of more than 50 cases, and ongoing participation in relevant continuous professional development activities (e.g., conferences or courses).

Advanced Accreditation

Practitioners who have extensive experience may apply for advanced accreditation. Advanced accredited specialists will be allowed to provide training and are a requirement for site accreditation. Advanced accredited specialists must have clinical experience that encompasses more than 120 therapy initial consultations or administrations within the last 3 y, participation in multidisciplinary discussion of more than 100 cases, ongoing participation in relevant continuous professional development activities (e.g., conferences or courses), and participation in recognized research in the field.

The training site requirements are also outlined, but the minimum level includes the presence of an accredited theranostic specialist onsite during delivery of the therapy, and other necessary staff. There should be an updated protocol manual that describes general provisions for administration of radionuclide therapies and for each specific therapy offered, including the roles of medical, radiopharmaceutical scientist, physicist, nursing, and administrative staff and the protocols for radiopharmaceutical dispensing, labeling, and disposal (as required). Regular multidisciplinary team meetings that encompass all theranostic applications used at the site are also important.

THERANOSTIC COMMITTEE

The committee will aim to promote a collaborative and consistent model of theranostic training and service delivery, with a multidisciplinary representation from the Australia and New Zealand Society of Nuclear Medicine, the relevant colleges or stakeholders, and a patient representative. The committee's role is to formulate and review guidelines for training in theranostics, provide and review suitable training courses, advise on theranostic research initiatives, and advise the government on theranostics. Training courses in theranostics do not necessarily supplant experiential training, which is the most important aspect in the provision of theranostics.

CONCLUSION

Although theranostics has increasing importance in the future of nuclear medicine, there is a constant need to ensure that delivery is by the most qualified specialists in the field, which in Australia are the appropriately trained nuclear medicine specialists. The AANMS position statement is the first local foray into addressing this issue but can be adapted to the requirements of any jurisdiction across the world.

DISCLOSURE

No potential conflict of interest relevant to this article was reported.

REFERENCES

1. Strosberg J, El-Haddad G, Wolin E, et al. Phase 3 trial of ^{177}Lu-DOTATATE for midgut neuroendocrine tumors. *N Engl J Med.* 2017;376:125–135.
2. Hofman MS, Violet J, Hicks RJ, et al. [^{177}Lu]-PSMA-617 radionuclide treatment in patients with metastatic castration-resistant prostate cancer (LuPSMA trial): a single-centre, single-arm, phase 2 study. *Lancet Oncol.* 2018;19:825–833.
3. Hofman MS, Emmett L, Sandhu S, et al. [^{177}Lu]Lu-PSMA-617 versus cabazitaxel in patients with metastatic castration-resistant prostate cancer (TheraP): a randomised, open-label, phase 2 trial. *Lancet.* 2021;397:797–804.
4. Sartor O, de Bono J, Chi KN, et al. Lutetium-177–PSMA-617 for metastatic castration-resistant prostate cancer. *N Engl J Med.* 2021;385:1091–1103.
5. Hicks RJ, Kwekkeboom DJ, Krenning E, et al. ENETS consensus guidelines for the standards of care in neuroendocrine neoplasia: peptide receptor radionuclide therapy with radiolabeled somatostatin analogues. *Neuroendocrinology.* 2017;105:295–309.
6. *IAEA Human Health Series No. 20: Practical Guidance on Peptide Receptor Radionuclide Therapy (PRRNT) in Neuroendocrine Tumours.* International Atomic Energy Agency; 2013. Publication 1560.
7. Training curriculum for nuclear medicine physicians. IAEA website. https://www-pub.iaea.org/MTCD/Publications/PDF/TE-1883web.pdf. Published 2019. Accessed April 11, 2022.
8. Australasian Association of Nuclear Medicine Specialists (AANMS) position statement on practice of theranostics in Australia. Australasian Association of Nuclear Medicine Specialists website. https://aanms.org.au/wp-content/uploads/2021/07/AANMS-Theranostics-Position-Statement-2021.pdf. Published February 2021. Accessed April 11, 2022.

Prostate Cancer Treatment: ^{177}Lu-PSMA-617 Considerations, Concepts, and Limitations

Oliver Sartor[1] and Ken Herrmann[2]

[1]*Tulane University School of Medicine, Tulane Cancer Center, New Orleans, Louisiana; and* [2]*University of Duisburg–Essen and German Cancer Consortium, University Hospital Essen, Essen, Germany*

Learning Objectives: On successful completion of this activity, participants should be able to describe (1) selection criteria employed in the VISION trial; (2) the VISION trial in the context of other therapies for advanced prostate cancer; and (3) an overview of newer phase III protocols using radiopharmaceuticals in the treatment of advanced prostate cancer.

Financial Disclosure: Dr. Sartor is a consultant/advisor for Advanced Accelerator Applications (AAA), Amgen, Astellas, AstraZeneca, Bayer, Blue Earth Diagnostics, Inc., Bavarian Nordic, Bristol Myers Squibb, Clarity Pharmaceuticals, Clovis, Constellation, Curium, Dendreon, EMD Serono, Fusion, Isotopen Technologien Meunchen, Janssen, JNJ, Myovant, Myriad, Noria Therapeutics, Inc., Novartis, Noxopharm, Nucligen, Progenics, POINT Biopharma, Pfizer, Sanofi, Tenebio, Telix, and Theragnostics; has investment interest in Clarity, Lantheus, Noria, Ratio, Nucligen, and Telix; and is an investigator for Advanced Accelerator Applications, Amgen, AstraZeneca, Bayer, Constellation, Endocyte, Invitae, Janssen, Lantheus, Merck, POINT, Biopharma, Progenics, and Tenebio. Dr. Herrmann is a consultant to AAA, AstraZeneca, Bayer Healthcare, JNJ, Novartis, Curium, and Amgen; receives personal fees from Bayer, Sofie Biosciences, SIRTEX, Adacap, Curium, Endocyte, BTG, IPSEN, Siemens Healthineers, GE Healthcare, Amgen, Novartis, ymabs, Aktis Oncology, Theragnostics, Pharma15, Debiopharm, AstraZeneca, and Janssen; received a grant from BTG; received nonfinancial support from ABX; and received other support from Sofie Biosciences. The authors of this article have indicated no other relevant relationships that could be perceived as a real or apparent conflict of interest.

CME Credit: SNMMI is accredited by the Accreditation Council for Continuing Medical Education (ACCME) to sponsor continuing education for physicians. SNMMI designates each *JNM* continuing education article for a maximum of 2.0 AMA PRA Category 1 Credits. Physicians should claim only credit commensurate with the extent of their participation in the activity. For CE credit, SAM, and other credit types, participants can access this activity through the SNMMI website (http://www.snmmilearningcenter.org) through June 2025.

The phase III VISION trial using ^{177}Lu-PSMA-617 has significant implications for the field of theranostics and broad repercussions for the clinical management of prostate cancer. Metastatic prostate cancer is a rapidly evolving field with a complex landscape that has multiple established therapies, including chemotherapies, hormonal therapies, immunotherapies, radiopharmaceuticals, and targeted therapies. The current landscape was created by an important series of pivotal phase III trials, typically with an overall-survival endpoint. To best understand the VISION trial (performed on patients with metastatic castration-resistant prostate cancer), it is essential to have a thorough understanding of the key decisions that underpinned the design, as well as the context of those decisions. Here, we describe critical elements of the VISION phase III trial and how those elements will shape regulatory decision making and clinic practice. Inclusion and exclusion criteria were carefully crafted, as were treatments, assessments, and endpoints. The results of the VISION trial were impressive, with clear improvements in survival for patients having few treatment alternatives. Besides the significant progress, there are also significant limitations. ^{177}Lu-PSMA-617 treatments will have far-reaching implications for prostate cancer. Food and Drug Administration approval was granted March 23, 2022, on the basis of the VISION data.

Key words: prostate cancer; castration-resistant; PSMA; theranostics; clinical trials

J Nucl Med 2022; 63:823–829
DOI: 10.2967/jnumed.121.262413

The Food and Drug Administration (FDA) approval of ^{177}Lu-PSMA-617 on March 23, 2022, provided an excellent opportunity to understand the context of this new therapy in prostate cancer and to dissect the key design elements for the pivotal phase III VISION trial (*1*).

Prostate cancer has a multiplicity of life-prolonging treatments utilized in the metastatic setting. In general, treatment of metastatic prostate cancer is subdivided into either metastatic castration-sensitive prostate cancer or metastatic castration-resistant prostate cancer (mCRPC) (Fig. 1). For metastatic castration-sensitive prostate cancer, the use of androgen deprivation therapy (ADT) in the form of luteinizing hormone–releasing hormone analogues (e.g., leuprolide, goserelin, triptorelin, degarelix, and relugolix) or orchiectomy has long been utilized, and additional review of older studies is not warranted. More recently, ADT plus docetaxel chemotherapy has been shown to prolong survival in metastatic castration-sensitive prostate cancer (*2,3*), as has ADT plus a novel androgen receptor pathway inhibitor (ARPI): either abiraterone, enzalutamide, or apalutamide (*4–7*). Abiraterone, apalutamide, and enzalutamide are ARPIs that either block the androgen receptor (enzalutamide/enzalutamide) or block androgen synthesis (abiraterone). Today, the use of ADT monotherapy is not typically indicated for those with metastatic castration-sensitive prostate cancer. Two recent phase III studies indicated that ADT plus docetaxel plus abiraterone (*8*) or ADT plus docetaxel plus darolutamide (another androgen receptor antagonist) (*9*) is superior to ADT plus docetaxel.

Table 1 summarizes all life-prolonging trials in men with mCRPC. In 2004, docetaxel was the first agent to prolong survival in phase III mCRPC trials (*10,11*). The androgen axis inhibitors abiraterone and enzalutamide have both been shown to be life-prolonging whether given in the first-line mCRPC setting or in the postdocetaxel mCRPC setting (*12–15*). Cabazitaxel is FDA-approved

Received Jan. 13, 2022; revision accepted Apr. 7, 2022.
For correspondence or reprints, contact Oliver Sartor (osartor@tulane.edu).

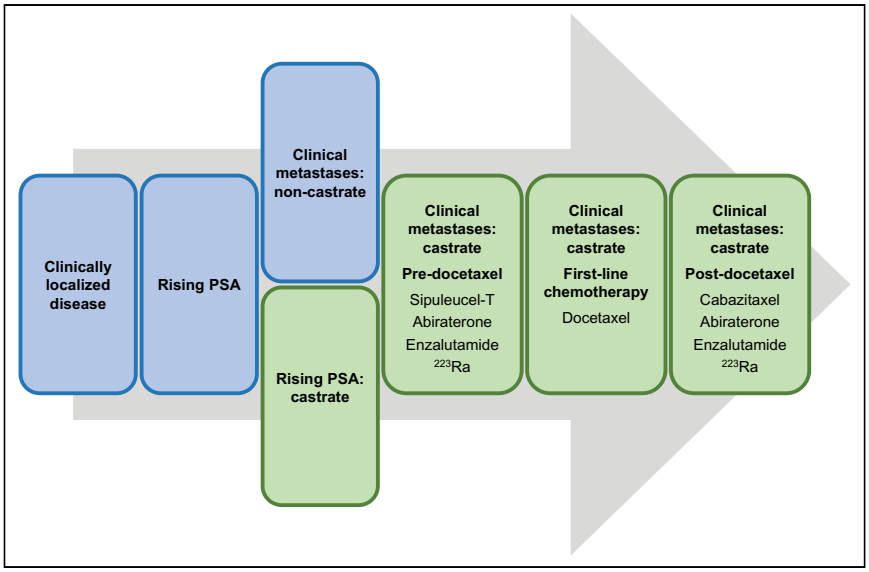

FIGURE 1. Schema of clinical disease state model of prostate cancer before VISION. (Adapted from (*33*).)

in the postdocetaxel setting of mCRPC (*16*) but has also been shown to be active in the post-ARPI and postdocetaxel setting (*17*). The use of ^{223}Ra-dichloride has been shown to be life-prolonging in the pre- or postdocetaxel setting (*18*). Sipuleucel-T, an immunotherapy, has been shown to prolong survival in asymptomatic or minimally symptomatic mCRPC patients (predominantly before chemotherapy) (*19*). Those men with mCRPC and homologous recombination repair defects (such as BRCA1 and BRCA2) live longer after ARPI or after ARPI/docetaxel (*20*).

The VISION trial was clearly conducted in the post-ARPI and posttaxane mCRPC setting, and the recent regulatory approval of ^{177}Lu-PSMA-617 clearly follows the VISION eligibility criteria.

THERANOSTICS

There have been tremendous improvements in theranostics and targeted radiopharmaceuticals over the past decade, and what once was an obscure area of oncology has now emerged as a key component in developmental therapeutics (*21*). Traditional pharmaceutical companies were slow to embrace this field given the early scientific successes that were commercial failures (*22*). It is hard to make investments in a field when the dividends from that investment are difficult to realize. Reasons for commercial failure have been discussed, but reimbursement and the competitive landscape are clearly features of importance.

Though it is debatable when radiopharmaceuticals were embraced in broader cancer circles, the clear success of ^{223}Ra-dichloride in prolonging overall survival (OS) in mCRPC was a catalyst for investment and further research (*18*). Earlier studies leading to FDA approval for ^{89}Sr-chloride and ^{153}Sm-lexidronam demonstrated only palliative benefit (*23–25*). The success of ^{223}Ra-dichloride, followed by success in treating neuroendocrine tumors with ^{177}Lu-DOTATATE (*26*), has been key for commercial involvement (Table 2). Key to regulatory approval is the pivotal trial design and execution. In this article, the design elements for the VISION trial (*1*) will be emphasized, with some explanatory details where controversy existed (Fig. 2). As in any trial design, there are many choices to be made, and these choices as a whole shape the way patients are included, treated, followed, and assessed.

TABLE 1
Anticancer Therapeutic Radiopharmaceuticals Currently Approved by Regulators in United States

Agent	Trade name	Year of FDA approval	Primary endpoint	Indication
^{89}Sr-chloride	Metastron (GE Healthcare)	1993	Pain/analgesics	Painful skeletal metastases
^{153}Sm-lexidronam	Quadramet (Dow Chemical Co.)	1997	Pain/analgesics	Painful osteoblastic metastases
^{90}Y-ibritumomab tiuxetan	Zevalin (Acrotech Biopharma)	2002	Tumor response rate	Low-grade or follicular lymphoma
^{131}I-tositumomab	Bexxar (GlaxoSmithKline)	2003	Tumor response rate	Low-grade or follicular lymphoma
^{223}Ra-dichloride	Xofigo (Bayer)	2013	OS	mCRPC
^{177}Lu-DOTATATE	Lutathera (Advanced Accelerator Applications)	2018	Progression-free survival	Select neuroendocrine tumors
^{131}I-iobenguane	Azedra (Progenics Pharmaceuticals)	2018	Lower blood pressure and tumor response rate	Select pheochromocytoma or paraganglioma
^{177}Lu-PSMA-617	Pluvictoa (Advanced Accelerator Applications)	2022	OS and rPFS	PSMA PET-positive mCRPC after ARPI and taxane

PSMA = prostate-specific membrane antigen.

TABLE 2
Life-Prolonging Phase III Trials in mCRPC

Trial	Front-line mCRPC
TAX 327	Docetaxel/prednisone vs. mitoxantrone/prednisone (*10*)
SWOG 9916	Docetaxel plus estramustine vs. mitoxantrone/prednisone (*11*)
IMPACT	Sipuleucel-T vs. nonactivated immune cell control (*19*)
COU-AA-302	Abiraterone/prednisone vs. placebo/prednisone (*13*)
ALSYMPCA	SOC ± ^{223}Ra (*18*)
PREVAIL	Enzalutamide vs. placebo (*15*)
	After docetaxel
TROPIC	Cabazitaxel/prednisone vs. mitoxantrone/prednisone (*16*)
COU-AA- 301	Abiraterone/prednisone vs. placebo/prednisone (*12*)
AFFIRM	Enzalutamide vs. placebo (*14*)
ALSYMPCA	SOC ± ^{223}Ra (*18*)
	After ARPI or ARPI plus docetaxel in HRR mutated subset only
PROfound	Olaparib vs. abiraterone or enzalutamide (*20*)
	After ARPI and DOCETAXEL)
CARD	Cabazitaxel vs. abiraterone or enzalutamide (*17*)
VISION	SOC ± PSMA-617 ^{177}Lu

HRR = homologous recombination repair.

VISION STUDY DESIGN ENDPOINTS

First, the phase III VISION trial was explicitly designed for regulatory approval. As such, the endpoints were endpoints that the FDA and other regulatory bodies had previously accepted in the course of successful studies on advanced prostate cancer. The trial was originally designed with a single primary endpoint of OS. The OS endpoint is considered to be the gold standard when assessing outcomes in advanced cancer and has a long, successful track record in mCRPC space, having been previously used for approvals of docetaxel, cabazitaxel, sipuleucel-T, ^{223}Ra-dichloride, abiraterone, and enzalutamide (*27*). After the VISION trial had been designed and initiated, a second alternate primary endpoint was added, radiographic progression-free survival (rPFS) or death from any cause. This image-based endpoint was in accordance with guidelines created by the Prostate Cancer Working Group 3 (*28*). This secondary endpoint had been accepted by the FDA as a primary endpoint in the olaparib pivotal trial (*29*). Both the OS and the rPFS endpoints are calculated from the time of randomization (not treatment). The assessment of rPFS is rigorous and must be in accord with clearly defined time lines and methodologies (conventional imaging, not PET scans). The rPFS endpoint, as specified by the Prostate Cancer Working Group 3, was previously found to be strongly associated with OS in mCRPC. PET imaging has not been shown to be a response biomarker, and the relationship between PSMA PET imaging and OS is not validated.

Secondary endpoints in the VISION trial included several traditional analyses favored by the FDA. These endpoints were designed to capture supportive data regarding the activity of the experimental drug relative to the control group. Key secondary endpoints included time to symptomatic skeletal events or death, radiographic objective response using criteria established by RECIST 1.1, and disease control rate as assessed by RECIST 1.1. Symptomatic skeletal events included first use of external-beam radiation therapy to relieve skeletal symptoms, new symptomatic pathologic vertebral or nonvertebral bone fractures, spinal cord compression, or tumor-related orthopedic surgical intervention as previously used in ALSYMPCA (*18*). In addition, other endpoints included a confirmed prostate-specific antigen (PSA) response of 50% or more, and health-related quality-of-life assessments utilizing

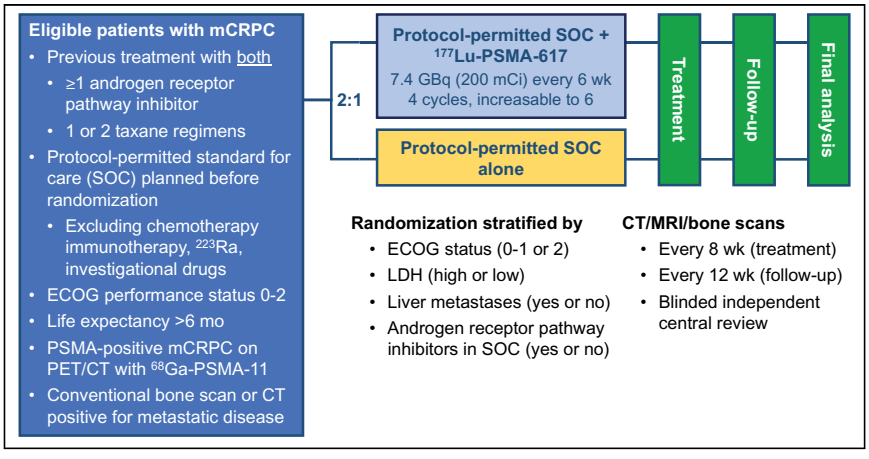

FIGURE 2. Protocol schema for VISION trial. ECOG = Eastern Cooperative Oncology Group; LDH = lactate dehydrogenase.

the Functional Assessment of Cancer Therapy–Prostate; the Brief Pain Inventory–Short Form; and the EuroQol 5-Dimension, 5-Level Questionnaire. Adverse events were assessed by the National Cancer Institute Common Terminology Criteria for Adverse Events, version 5.0. Importantly, none of these were unfamiliar endpoints. Symptomatic skeletal events are particularly helpful in bone-dominant cancer such as prostate, and symptomatic skeletal event assessments played a key role in the ^{223}Ra approval. The various additional criteria have been standardized and accepted in multiple phase III trials. The use of familiar endpoints that are clinically relevant and readily interpretable is a key feature in regulatory decision making. Health-related quality-of-life measurements are more key for certain countries than for others, but all regulators want to ensure that health-related quality-of-life parameters are not adversely affected by treatments. Of note, PSA is not sufficient for regulatory action despite being the most commonly reported end point in a multiplicity of trials. PSMA PET is not validated as a surrogate for OS and must be viewed only in exploratory terms.

VISION ELIGIBILITY CRITERIA

All patients enrolled in VISION had to have mCRPC as determined by conventional imaging (i.e., bone scanning and CT or MRI). Progression at the time of trial entry was required to be documented by PSA or imaging-based criteria. The serum PSA minimum was 2.0 ng/mL. All patients were required to have a castration level of testosterone and to have had disease progression after the use of taxane-based chemotherapy (typically docetaxel) and a novel hormone (i.e., abiraterone or enzalutamide). A variety of other prior treatments, such as olaparib, were allowed but not required. Patients were allowed to have up to 2 prior taxane-based chemotherapies. There was no limit to the number of prior hormonal manipulations. The actual patients enrolled had previously received multiple prior therapies, and very few patients had simply received docetaxel and a novel hormone.

The inclusion criteria for the VISION trial also required the use of PSMA PET imaging (using ^{68}Ga-PSMA-11 concomitantly with a nondiagnostic unenhanced CT scan) within 1–4 wk of therapeutic ^{177}Lu-PSMA injection. PSMA PET/CT imaging was allowed only after all other screening criteria for eligibility had been met. The PSMA PET/CT images were read centrally and, importantly, with positive and negative selection criteria. All patients were required to have at least 1 PSMA PET–positive metastatic lesion. No size criteria were specified for the PET-positive lesion. PSMA positivity was determined relative to liver uptake; in other words, the metastatic lesion had to have uptake greater than that in the liver. A diagnostic-grade contrast-enhanced CT scan of the chest, abdomen, and pelvis (or contrast-enhanced MRI) and total-body bone scintigraphy were also required at baseline. A key feature of the selection criteria by PET/CT imaging involved those metastatic lesions that had PSMA uptake less than liver uptake (deemed PSMA PET–negative). Patients were excluded from trial entry if they had PET-negative visceral lesions (liver or lung) at least 1.0 cm in diameter, PSMA PET–negative lytic bone lesions measuring at least 1.0 cm, or PET-negative lymph nodes measuring at least 2.5 cm. Though ^{18}F-FDG PET was not utilized, many of these PSMA-negative lesions conjecturally would have ^{18}F-FDG PET positivity.

The lack of ^{18}F-FDG PET in VISION has met with some discussion. Potentially, the use of ^{18}F-FDG PET would have improved the number of responding patients (*30,31*). In many countries, it is difficult to obtain 2 distinct PET imaging studies, and the requirement of 2 PET imaging studies was debated in the VISION design phase. The decision was made to forego ^{18}F-FDG PET imaging for practical purposes. That decision in retrospect is viewed favorably by many treating physicians, given the unequivocally positive OS outcomes in the VISION trial. That said, there is no question that optimal imaging may eventually prove to have better results. However, optimal imaging is yet to be established in definitive trials with an OS outcome. Thus, until data are presented to the contrary, it is likely that regulators will adopt a PSMA PET–only entry criterion similar to the VISION trial for those being treated with PSMA-targeted radiopharmaceuticals.

In addition to the inclusion criteria for VISION, there were several elements in the exclusion criteria worthy of note. These include patients with bone superscans, poor performance status, and significant degrees of bone marrow suppression. Previous treatment with any of the following within 6 mo of randomization was not allowed: ^{89}Sr, ^{153}Sm, ^{186}Re, ^{188}Re, ^{223}Ra, or hemibody irradiation. Previous PSMA-targeted radioligand therapy was not allowed. Patients with superscans on their bone scintigraphy cannot be evaluated for bone scan progression, hence their exclusion.

Timing of assessments included a PSMA PET scan (^{68}Ga PSMA-11 was used exclusively) 1–4 wk before protocol-defined treatments began; diagnostic CT or MRI (of the chest, abdomen, and pelvis) and total-body bone scintigraphy were conducted within 4 wk of treatment. Investigators were to specify the standard-of-care (SOC) treatment before randomization (given that novel hormone use was a stratification variable). Bone and CT scans were scheduled every 8 wk ($\pm$4 d) after the first dose of isotope for the first 24 wk then every 12 wk thereafter through the end of treatment. It is critical to note that even if the doses of isotope were delayed, tumor assessments were required to stay on the proper imaging schedule.

VISION STRATIFICATIONS, RANDOMIZATION, AND TREATMENTS

Simple randomization can fail when treated patients are unbalanced for critical features known to influence prognosis. The use of stratification overcomes this potential issue. The 4 stratification factors included in the VISION trial were serum lactate dehydrogenase ($>$260 IU/$\leq$260 IU), liver metastases (yes/no), Eastern Cooperative Oncology Group performance status score (0–1/2), and inclusion of a novel hormone (typically enzalutamide or abiraterone), as treatment in the protocol permitted SOC. Lactate dehydrogenase, liver metastatic disease, and Eastern Cooperative Oncology Group performance status are known to be of prognostic importance in multiple phase III mCRPC trials, hence their use here. Life-prolonging hormonal therapy (abiraterone and enzalutamide typically) as a stratification factor was used to ensure balance in this potentially important variable.

Eligible patients were randomized in a 2:1 fashion favoring the isotopic treatment plus SOC over SOC alone. The dose and duration of treatment for ^{177}Lu-PSMA-617 were not a simple decision. Much of the prior data were collected after using various doses for variable durations at variable intervals. The dose for VISION was strongly influenced after evidence was initially provided from a phase II prospective Australian trial (*30*). In that single-arm, single-center trial, a median dose of 7.5 MBq of ^{177}Lu-PSMA-617 was administered every 6 wk up to 4 doses. The outcomes

demonstrated clear efficacy, with manageable toxicity. The VISION trial utilized a planned dosing schema of 7.4 MBq (200 mCi) per dose (fixed dosing being easier to manage logistically than a weight-based dose) given for a planned 4 cycles. However, clinicians at their discretion could administer up to 6 cycles. The criteria for administering 6 cycles included an assessment of response (radiologic and PSA) and clinical benefit after the fourth dose. In addition, the patient should have had residual disease on CT with contrast, MRI, or bone scanning and have shown good tolerance to the prior ^{177}Lu-PSMA-617 treatments. The use of 6 cycles of therapy was controversial to some given the lack of efficacy or safety data in prior trials.

The control group to be utilized in VISION generated considerable discussion at the time of the design. Should an SOC be specified? Should there be an SOC with or without ^{177}Lu-PSMA-617 or an SOC versus ^{177}Lu-PSMA-617? Should chemotherapy be given in the control group? What about ^{223}Ra-dichloride? Was it ethical to allow additional hormonal therapy after prior hormonal therapy had initially failed to control the disease? What control treatment would be acceptable for both clinicians and patients?

A key decision point was to require 1 taxane treatment but allow up to 2 prior taxane treatments in the inclusion criteria. Second-line taxane chemotherapy with cabazitaxel was known to be life-prolonging, but nothing had ever been shown to prolong survival after 2 prior chemotherapies. Thus, every patient who wanted to receive 2 lines of chemotherapy could receive those therapies and still be eligible, unlike the TheraP trial (*31*). There is no effective third-line chemotherapy, thus rendering moot a decision about mandating third-line chemotherapy in the control group. Also, from a practical perspective, most mCRPC patients never receive 2 chemotherapies before they succumb to the disease. In fact, many patients never receive any chemotherapy before they die (*32*). Prostate cancer patient are often chemotherapy-averse, in part because of their advanced age. Thus, to require patients in the control arm to receive a therapy that in real-world settings is not typically utilized seemed inappropriate.

Some data suggested that PSMA expression could be upregulated by the use of hormonal agents such as enzalutamide. Thus, the combination of a novel hormonal agent and the PSMA-targeted agent could potentially have synergistic implications, and novel hormonal agents were allowed as part of SOC. Such synergism had not been proven in clinical trials. In addition, there were no known adverse interactions regarding novel hormones and ^{177}Lu-PSMA-617. Taken together, the use of SOC with or without ^{177}Lu-PSMA-617 was deemed the optimal design. This mirrors the use of SOC with or without ^{223}Ra-dichloride in the phase III ALSYMPCA trial. ALSYMPCA clearly met with regulatory success. Steroids, bisphosphonates, and other bone-health agents, as well as external-beam radiation, were allowed as part of SOC in the final VISION design. Chemotherapy as an SOC was excluded, not only because patients could receive 1 or 2 taxane-based chemotherapies before protocol treatment if they so desired but also because combining ^{177}Lu-PSMA-617 with chemotherapy was not known to be safe. Similar safety concerns excluded use of ^{223}Ra-dichloride or poly(adenosine diphosphate ribose) polymerase inhibitors such as olaparib.

No crossover from the control group to the isotopic group was planned, but after the trial reported positive results, those in the control group meeting eligibility criteria were allowed to receive ^{177}Lu-PSMA-617 in a compassionate-use manner. Few patients were eligible for this compassionate use.

VISION STATISTICAL ANALYSIS PLAN

The statistical analysis plan was originally conceived to be an assessment of OS with 750 patients. The median survival in the control group was estimated to be 10 mo. The experimental group was projected to have a median OS of 13.7 mo (thus generating a hazard ratio [HR] of 0.7306 after 489 events). The trial originally had 2 interim analyses for OS, and rPFS was a secondary endpoint. The statistical plan had 90% power and a 1-sided type 1 error rate of 0.025. A stratified Cox proportional hazards regression model was planned for OS analysis, with a single covariate for randomized treatment and stratification for the 4 variables noted above.

The statistical analysis plan was later revised (effective March 2019) with FDA assent because of high levels of dropout in the control arm at selected sites. At that time, to overcome concerns regarding clinical trial conduct at these locations, certain clinical trial sites were closed to further accrual and additional site-education procedures were implemented at the remaining sites. The control group discontinuation rate was 56% (47/84 patients) before the March 2019 revisions and 16.3% afterward. This rate clearly indicates the importance of the site-culling and education efforts. Of the sites closed to accrual, all site principal investigators were nuclear medicine–focused and had suboptimal multidisciplinary care systems. One of the key missives in the trial site educational enhancements was to incorporate multidisciplinary care for each patient. Multidisciplinary care is optimal for VISION-type patients given the multiplicity of potential complications in caring for those with far-advanced prostate cancer.

The statistical analysis plan invoked after March 2019 assessed both rPFS and OS as coprimary endpoints and allowed for different populations for OS and rPFS assessments given that patients with poor follow-up were not expected to have timely radiographic assessments. Only patients enrolled after March 9, 2019, were assessed for rPFS (n = 557). The estimated sample size was increased to 814. After revisions, the OS assumptions were unchanged (median, 10 and 13.7 mo). The median rPFS assumptions were 4 and 6 mo for the control and experimental arms, respectively. The overall significance level for the trial was 0.025 (1-sided), allocated between the 2 coprimary endpoints. This approach provided the trial with 84% power to detect an HR of 0.67 for rPFS at a 1-sided significance level of 0.004, after 364 events, and also provided the trial with 90% power to detect an HR of 0.73 for OS at a 1-sided significance level of 0.025. The analysis of OS was to occur after 508 deaths. If both rPFS and OS were positive, sequential testing on key secondary endpoints could occur (time to symptomatic skeletal events, RECIST 1.1 response rate, and disease control rate by RECIST 1.1).

VISION PATIENT CHARACTERISTICS

In total, 1,179 patients were screened, and 1,003 (85.1%) had a ^{68}Ga-PSMA-11 PET/CT scan meeting the study-eligibility definition. Of the 1,003 patients, 954 (95.1%) had at least 1 PSMA-positive metastatic lesion, and 87 (8.7%) had at least 1 PSMA-negative metastatic lesion that excluded them from the VISION trial. The eligibility criteria for PSMA imaging were not met in 126 of the 1,003 patients (12.6%), either because there was no PSMA-positive lesions or there was at least 1 exclusionary PSMA-negative lesion. Thus, 869 patients of those scanned with PSMA PET/CT (86.6%) qualified for the study. Eight patients had missing PSMA results and could not be classified. The fact that

nearly 87% of the scanned patients qualified for the study was somewhat surprising and indicates a high level of leniency in determining who was eligible for the study. In the TheraP Australian randomized phase II study, only 68.7% of scanned patients met the criteria for enrollment (*31*). The TheraP group used a double-PET strategy, with both PSMA PET/CT and ^{18}F-FDG PET/CT in the selection criteria.

In total, 831 patients were actually randomized in the VISION trial. Prior treatments were extensively used before the protocol therapy was applied. Of the 831 randomized patients, 342 (41.2%) had received 2 taxane-based chemotherapies (all, of course, had received at least one, as this was an inclusion criterion), and 406 (48.7%) had received 2 or more novel hormonal agents (typically abiraterone and enzalutamide). Use of these agents was well balanced between arms. Median PSA was 74.6 ng/mL in the SOC arm and 77.5 ng/mL in the SOC-plus-isotopic arm. The median time since diagnosis was 7.0 and 7.3 y in the SOC and experimental arms, respectively. Bone metastases were present in 91.4% of SOC patients and 91.5% of experimentally treated patients. Liver metastases were annotated in 13.6% and 11.4% of the randomized patients, respectively.

VISION RESULTS

The median follow-up was 20.9 mo. The endpoints of VISION were well discussed in the primary article (*1*). The OS was clearly positive, with an HR of 0.62 (95% CI, 0.52–0.74; $P < 0.001$). Median survival was 11.3 mo in the SOC arm and 15.3 mo in the SOC–plus–^{177}Lu-PSMA-617 arm. Of the 831 (63.8%) patients, 530 died at the time of the VISION OS analysis, indicating a sufficiently mature trial. For rPFS, the median in the SOC arm was 3.4 mo, versus 8.7 mo in the SOC–plus–^{177}Lu-PSMA-617 arm (HR, 0.40; 99.2% CI, 0.29–0.57; $P < 0.001$). A sensitivity analysis of the rPFS population for OS ($n = 581$) yielded an HR of 0.63 for OS (95% CI, 0.51–0.79). Some have pointed out that the VISION trial likely would have been positive even without PSMA PET/CT selection given the strong HRs and CIs. Analysis of various appropriately powered subsets all revealed positive trends for rPFS and OS. Patients with liver metastases are a special case in which the HR CIs overlapped 1.0 (HR, 0.87; 95% CI, 0.53–1.43), but the subset was clearly underpowered given the small percentage of patients enrolled who had a liver metastasis.

All secondary endpoints analyzed to date have also been positive. Time to symptomatic skeletal events or death was improved by the isotopic treatment (11.5 vs. 6.8 mo; HR, 0.50; 95% CI, 0.40–0.62; $P < 0.001$). RECIST complete response rate by independent central review (among 248 patients with measurable disease at baseline) was 9.2% in the experimental group and 0.0% in the SOC group. Partial responses were annotated in 41.8% of the isotopic-plus-SOC group and 9.2% of the SOC-alone group. Complete-plus-partial responses were 51% versus 9.2%, an impressively high complete response plus partial response rate compared with other mCRPC trials. The CARD trial, similarly conducted on patients progressing after both docetaxel and a novel hormone, reported a RECIST complete response plus partial response of 37.0% for cabazitaxel (*17*). Abiraterone reported a RECIST complete response plus partial response of 14% in the COU-301 trial (postdocetaxel mCRPC) (*12*). PSA responses of at least 50% (confirmed) were found in 46.0% in the experimental arm and 7.1% of the SOC-alone arm. For comparison's sake, in the CARD trial, 35.7% of cabazitaxel patients had a confirmed PSA decline of at least 50%, and 29% of abiraterone patients had a confirmed PSA decline of at least 50%. It is hard to find trials comparable to VISION given the extensive prior treatments administered to these patients. Regardless, the data from these very heavily pretreated patients compare favorably with other postdocetaxel trials on mCRPC.

Health-related quality-of-life (total score for Functional Assessment of Cancer Therapy–Prostate) and pain assessments (pain intensity on Brief Pain Inventory–Short Form) both favor the use of ^{177}Lu-PSMA-617 plus SOC versus SOC alone. The time to deterioration of the Functional Assessment of Cancer Therapy–Prostate total score was 5.7 versus 2.2 mo (HR, 0.54; 95% CI, 0.45–0.66). The time to pain deterioration was 5.9 versus 2.2 mo (HR, 0.52; 95% CI, 0.43–0.63). These patient-centric reports confirm the clinical relevance of the VISION findings. Both OS and health-related quality of life were improved in those treated with ^{177}Lu-PSMA-617 plus SOC.

Treatment-emergent adverse events (Common Terminology Criteria for Adverse Events, version 5.0) were assessed in VISION for an unequal duration when comparing the 2 arms (7.56 mo in the experimental arm vs. 2.07 mo for SOC). An unequal duration of follow-up is known to influence the frequency of adverse events. Some investigators advocate that adverse event rates be corrected for the duration of observation (events per month). The most common adverse events reported in the isotopic arm were fatigue (43.1%), dry mouth (38.8%), nausea (35.3%), anemia (31.8%), and back pain (23.4%). All except dry mouth are potentially disease-related, but there is no doubt that rates were higher in the experimental arm. The control group rates were fatigue (22.9%), dry mouth (0.5%), nausea (16.6%), anemia (13.2%), and back pain (14.6%). Adverse events leading to a reduction in ^{177}Lu dosing were present in 5.7% of patients. Adverse events that led to discontinuation of ^{177}Lu dosing were present in 11.9% of patients. This side effect profile was anticipated given the prior experience with the agent.

LIMITATIONS

The use of ^{177}Lu-PSMA-617 plus SOC compared favorably with SOC at all endpoints. There is no doubt that these patients with far-advanced disease and few choices benefited from the experimental treatment. That said, there is much we do not know. What are the optimal PSMA PET criteria for selection of patients? Do patients with low-SUV lesions respond less favorably than those with high-SUV lesions? Although PSMA PET criteria are debatable, these authors favor keeping the PSMA PET/CT in order to exclude patients unlikely to respond. All patients were planned to have 4 cycles of therapy, and up to 6 were allowed. No PSMA retreatments were allowed. What if there is disease progression during the first 2 or 3 cycles of therapy? Should more be given? Is PSA a reliable marker of response or progression? What about patients with clear pain relief but no PSA decline? Do we give more drug? When should therapies be stopped? How many doses of isotope are optimal? What is the optimal dose of the isotope? What is the optimal frequency of administration? Should we be using PSMA PET/CT as a response criterion? What if the PSMA PET reveals no more disease after 2 cycles? Do we need to give more therapy? What about earlier phases of disease? What is the role of SOC (if any) when given in combination with ^{177}Lu-PSMA-617? Is there a meaningful and clinically relevant

upregulation of PSMA expression when using abiraterone or enzalutamide?

There are many questions that arise despite a positive phase III trial, and many questions remain unanswered. More answers may emerge from additional VISION analyses, and many more analyses will be performed. Many of these questions will require new clinical studies, but pivotal trials are expensive and difficult to execute; definitive answers are not going to be readily forthcoming.

FUTURE PHASE III TRIALS

Additional phase III trials with ^{177}Lu-PSMA-617 are being performed now. These include the PSMAfore trial (NCT04689828) and the PSMAddition trial (NCT04720157). The PSMAfore trial will enroll 450 patients with chemotherapy-naïve mCRPC and has an endpoint of rPFS. Crossover will be allowed. ^{177}Lu-PSMA-617 will be compared with a second novel hormone in those previously treated with at least 1 novel hormone (abiraterone, enzalutamide, apalutamide, or darolutamide). The PSMAddition trial will also have rPFS as a primary endpoint and will enroll patients with metastatic hormone-sensitive prostate cancer. ^{177}Lu-PSMA-617 will be used in combination with ADT and a novel hormone of investigator choice. Docetaxel will not be allowed. PSMAddition will enroll approximately 1,126 patients and will use rPFS as a primary endpoint. Crossover will be allowed.

Other phase III trials with PSMA-targeted therapies will soon have randomization under way. The ^{177}Lu-PSMA I&T agent (also called ^{177}Lu-PNT2002) will be evaluated in SPLASH (NCT04647526) in a setting similar to PSMAfore. Similarly, ^{177}Lu-PSMA I&T will be evaluated in the ECLIPSE trial.

Even more phase III trials are being contemplated. Simply stated, ^{177}Lu-PSMA-617 is an active agent that can provide tumor responses and enhance health-related quality of life in patients with advanced prostate cancer. Additional concepts potentially leading to regulatory approvals are eagerly anticipated. Careful trial design and execution using established endpoints will be key.

REFERENCES

1. Sartor O, de Bono J, Chi KN, et al. Lutetium-177-PSMA-617 for metastatic castration-resistant prostate cancer. *N Engl J Med.* 2021;385:1091–1103.
2. Sweeney CJ, Chen YH, Carducci M, et al. Chemohormonal therapy in metastatic hormone-sensitive prostate cancer. *N Engl J Med.* 2015;373:737–46.
3. James ND, Sydes MR, Clarke NW, et al. Addition of docetaxel, zoledronic acid, or both to first-line long-term hormone therapy in prostate cancer (STAMPEDE): survival results from an adaptive, multiarm, multistage, platform randomised controlled trial. *Lancet.* 2016;387:1163–1177.
4. James ND, de Bono JS, Spears MR, et al. Abiraterone for prostate cancer not previously treated with hormone therapy. *N Engl J Med.* 2017;377:338–351.
5. Fizazi K, Tran N, Fein L, et al. Abiraterone plus prednisone in metastatic, castration-sensitive prostate cancer. *N Engl J Med.* 2017;377:352–360.
6. Chi KN, Agarwal N, Bjartell A, et al. Apalutamide for metastatic, castration-sensitive prostate cancer. *N Engl J Med.* 2019;381:13–24.
7. Davis ID, Martin AJ, Stockler MR, et al. Enzalutamide with standard first-line therapy in metastatic prostate cancer. *N Engl J Med.* 2019;381:121–131.
8. Fizazi K, Galceran JC, Foulon S, et al. A phase III trial with a 2x2 factorial design in men with de novo metastatic castration-sensitive prostate cancer: overall survival with abiraterone acetate plus prednisone in PEACE-1. *Ann Oncol.* 2021; 32(suppl 5): S1283–S1346.
9. Smith MR, Hussain M, Saad F, et al. Darolutamide and survival in metastatic, hormone-sensitive prostate cancer. *N Engl J Med.* 2022;386:1132–1142.
10. Tannock IF, de Wit R, Berry WR, et al. Docetaxel plus prednisone or mitoxantrone plus prednisone for advanced prostate cancer. *N Engl J Med.* 2004;351:1502–1512.
11. Petrylak DP, Tangen CM, Hussain MH, et al. Docetaxel and estramustine compared with mitoxantrone and prednisone for advanced refractory prostate cancer. *N Engl J Med.* 2004;351:1513–1520.
12. de Bono JS, Logothetis CJ, Molina A, et al. Abiraterone and increased survival in metastatic prostate cancer. *N Engl J Med.* 2011;364:1995–2005.
13. Ryan CJ, Smith MR, de Bono JS, et al. Abiraterone in metastatic prostate cancer without previous chemotherapy. *N Engl J Med.* 2013;368:138–148.
14. Scher HI, Fizazi K, Saad F, et al. Increased survival with enzalutamide in prostate cancer after chemotherapy. *N Engl J Med.* 2012;367:1187–1197.
15. Beer TM, Armstrong AJ, Rathkopf DE, et al. Enzalutamide in metastatic prostate cancer before chemotherapy. *N Engl J Med.* 2014;371:424–433.
16. de Bono JS, Oudard S, Ozguroglu M, et al. Prednisone plus cabazitaxel or mitoxantrone for metastatic castration-resistant prostate cancer progressing after docetaxel treatment: a randomised open-label trial. *Lancet.* 2010;376:1147–1154.
17. de Wit R, de Bono J, Sternberg CN, et al. Cabazitaxel versus abiraterone or enzalutamide in metastatic prostate cancer. *N Engl J Med.* 2019;381:2506–2518.
18. Parker C, Nilsson S, Heinrich D, et al. Alpha emitter radium-223 and survival in metastatic prostate cancer. *N Engl J Med.* 2013;369:213–223.
19. Kantoff PW, Higano CS, Shore ND, et al. Sipuleucel-T immunotherapy for castration-resistant prostate cancer. *N Engl J Med.* 2010;363:411–422.
20. Hussain M, Mateo J, Fizazi K, et al. Survival with olaparib in metastatic castration-resistant prostate cancer. *N Engl J Med.* 2020;383:2345–2357.
21. Herrmann K, Kraus BJ, Hadaschik B, et al. Nuclear medicine theranostics comes of age. *Lancet Oncol.* 2021;22:1497–1498.
22. Green DJ, Press OW. Whither radioimmunotherapy: to be or not to be? *Cancer Res.* 2017;77:2191–2196.
23. Porter AT, McEwan AJ, Powe JE, et al. Results of a randomized phase-III trial to evaluate the efficacy of strontium-89 adjuvant to local field external beam irradiation in the management of endocrine resistant metastatic prostate cancer. *Int J Radiat Oncol Biol Phys.* 1993;25:805–813.
24. Sartor O, Reid RH, Hoskin PJ, et al. Samarium-153-lexidronam complex for treatment of painful bone metastases in hormone-refractory prostate cancer. *Urology.* 2004;63:940–945.
25. Serafini AN, Houston SJ, Resche I, et al. Palliation of pain associated with metastatic bone cancer using samarium-153 lexidronam: a double-blind placebo-controlled clinical trial. *J Clin Oncol.* 1998;16:1574–1581.
26. Strosberg J, El-Haddad G, Wolin E, et al. Phase 3 trial of ^{177}Lu-dotatate for midgut neuroendocrine tumors. *N Engl J Med.* 2017;376:125–135.
27. Sartor O, de Bono JS. Metastatic prostate cancer. *N Engl J Med.* 2018;378: 645–657.
28. Scher HI, Morris MJ, Stadler WM, et al. Trial design and objectives for castration-resistant prostate cancer: updated recommendations from the prostate cancer clinical trials working group 3. *J Clin Oncol.* 2016;34:1402–1418.
29. de Bono J, Mateo J, Fizazi K, et al. Olaparib for metastatic castration-resistant prostate cancer. *N Engl J Med.* 2020;382:2091–2102.
30. Hofman MS, Violet J, Hicks RJ, et al. [^{177}Lu]-PSMA-617 radionuclide treatment in patients with metastatic castration-resistant prostate cancer (LuPSMA trial): a single-centre, single-arm, phase 2 study. *Lancet Oncol.* 2018;19:825–833.
31. Hofman MS, Emmett L, Sandhu S, et al. [^{177}Lu]Lu-PSMA-617 versus cabazitaxel in patients with metastatic castration-resistant prostate cancer (TheraP): a randomised, open-label, phase 2 trial. *Lancet.* 2021;397:797–804.
32. George DJ, Sartor O, Miller K, et al. Treatment patterns and outcomes in patients with metastatic castration-resistant prostate cancer in a real-world clinical practice setting in the United States. *Clin Genitourin Cancer.* 2020;18:284–294.
33. Scher HI, Heller G. Clinical states in prostate cancer: toward a dynamic model of disease progression. *Urology.* 2000;55:323–327.

Tau Beats Amyloid in Predicting Brain Atrophy in Alzheimer Disease: Implications for Prognosis and Clinical Trials

Maura Malpetti[1,2], Renaud La Joie[1], and Gil D. Rabinovici[1,3]

[1]*Memory and Aging Center, Department of Neurology, Weill Institute for Neurosciences, University of California, San Francisco, San Francisco, California;* [2]*Department of Clinical Neurosciences, University of Cambridge, Cambridge, United Kingdom; and* [3]*Department of Radiology and Biomedical Imaging, University of California, San Francisco, San Francisco, California*

Several biomarkers have emerged in the past few decades to quantify pathologic brain changes related to Alzheimer disease (AD). In particular, PET radiotracers that bind selectively to amyloid-β plaques and tau neurofibrillary tangles have advanced AD research and drug development by enabling the detection and quantification of the neuropathologic lesions that define AD in living people.

Among amyloid-β PET tracers, ^{11}C-Pittsburgh compound B was the first to be developed, followed by ^{18}F-labeled tracers approved for clinical use (i.e., ^{18}F-florbetapir, ^{18}F-florbetaben, and ^{18}F-flutametamol). Cumulative evidence has demonstrated the diagnostic utility of amyloid PET in differentiating AD from nonamyloid neurodegenerative diseases (*1,2*). However, amyloid PET retention begins 2 decades before the onset of clinical symptoms and reaches a relative plateau throughout most of the neocortex early in the evolution of AD (before, or coincident with, early clinical symptoms). As a result, the distribution and burden of amyloid correlate poorly with disease stage or clinical measures in symptomatic patients and do not colocalize with markers of regional neurodegeneration (*3,4*).

^{18}F-flortaucipir was the first PET tracer to show high affinity and selectivity for AD neurofibrillary tangles, followed by next-generation tau tracers such as ^{18}F-MK6240, ^{18}F-RO948, ^{18}F-PI2620, ^{18}F-GTP1, and ^{18}F-PM-PBB3. ^{18}F-flortaucipir is, to date, the only tau PET tracer to receive Food and Drug Administration approval for clinical use in the United States. ^{18}F-flortaucipir PET distinguishes AD from other underlying neuropathologies, including non-AD tauopathies to which the tracer shows a low binding affinity (*5–8*). In contrast to the early widespread distribution of amyloid PET binding, tau PET signal originates in the entorhinal cortex and other medial temporal regions. In the presence of amyloid, signal progressively spreads into the inferior temporal gyrus, followed by the lateral occipital cortex, posterior cingulate/precuneus, lateral temporoparietal regions, and, finally, prefrontal cortex. This evolution is similar (though not identical) to Braak neuropathologic staging of tau neurofibrillary tangles and closely colocalizes with brain atrophy and hypometabolism patterns as measured by MRI or ^{18}F-FDG PET (*3,9*). Increasing spread of tau is associated with clinical impairment (*10–12*), with the tau PET binding topography associated with domain-specific cognitive deficits (*13,14*) and distinct AD clinical variants (*9,15,16*),

The relationships between amyloid and tau PET and clinical measures largely replicate clinicopathologic studies showing that the stage and extent of neurofibrillary tau tangles are strongly associated with antemortem clinical status and cognitive deficits (*17,18*), whereas amyloid neuropathology correlates weakly with antemortem clinical impairment. Moreover, the regional distribution of neurofibrillary tau tangles after death also relates to distinct clinical presentations and syndromes (*19*), whereas amyloid-β plaque distribution generally does not. Postmortem pathology and in vivo imaging evidence together suggest a spatial and temporal decoupling between amyloid-β plaque accumulation and neurodegeneration, whereas neurofibrillary tangles are more closely associated with regional neurodegeneration and clinical impairment. These observations support the hypothesis that amyloid-β may influence neuronal integrity only indirectly by facilitating tau spreading (*20*), leading to synaptic and cell loss and ultimately translating into cognitive and functional decline.

In cross-sectional multimodal imaging studies along the clinical AD spectrum, tau accumulation has also been observed in areas without overt neurodegeneration (*3,9,15,21*). These findings support the hypothesis that tau elevation may locally precede neurodegeneration, which would be a downstream event in the cascade associated with AD. Such hypotheses are reinforced by significant associations between baseline tau PET patterns and prospective MRI atrophy (*22,23*). A recent study by La Joie et al. (*22*) showed that in patients with clinically mild AD, the burden and regional distribution of tau pathology at baseline, as measured with ^{18}F-flortaucipir PET, can forecast the severity and topography of prospective brain atrophy over the following 15 mo. In contrast, neither the severity nor the topography of amyloid PET was found to be informative of atrophy progression. At a group level, regional tau PET uptake at baseline explained more than 40% of unique variance in atrophy at follow-up, even when corrected for baseline cortical thickness, versus 3% of variance explained by regional amyloid PET. Importantly, the close association between baseline tau PET and subsequent atrophy was found not only at the group level but also in each individual patient (Fig. 1). In line with this finding, tau PET also correlates strongly with retrospective longitudinal atrophy (years preceding PET) in both cognitively unimpaired individuals and patients with clinical AD (*24,25*).

Tau PET is a sensitive predictor not only of structural brain changes in AD but also of prospective cognitive decline. Several

Received Jan. 29, 2022; revision accepted Mar. 10, 2022.
For correspondence or reprints, contact Maura Malpetti (mm2243@medschl.cam.ac.uk).

DOI: 10.2967/jnumed.121.263694

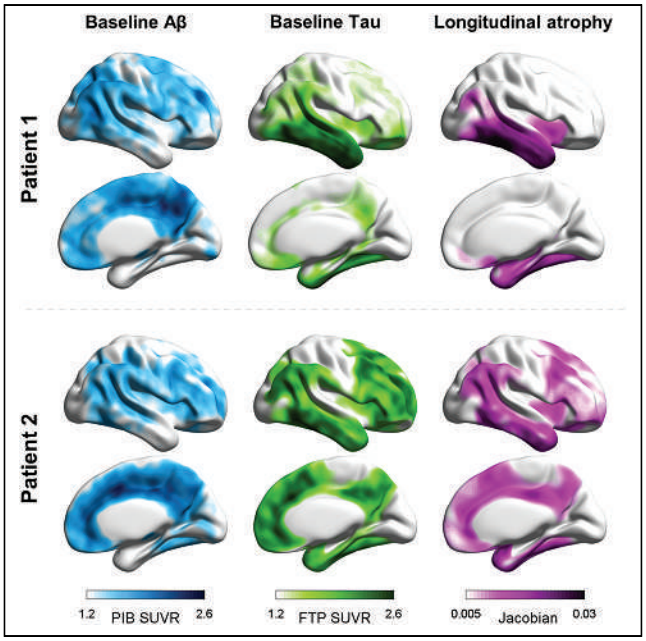

FIGURE 1. Single-subject amyloid and tau PET patterns at baseline and cortical atrophy over time. (Left and middle) ^{11}C-Pittsburgh compound B (PIB) and ^{18}F-flortaucipir (FTP) PET SUV ratio maps, respectively, with higher values indicate more severe pathology. (Right) Patterns derived from prospective longitudinal structural MRI scans after PET, with positive Jacobians indicating shrinkage over time. Patient 1 is 71-y-old with mild AD dementia; patient 2 is 61-y-old with mild AD dementia.

studies have described strong associations between baseline tau PET and cognitive changes over time across the AD clinical spectrum. In head-to-head comparisons, tau PET binding in temporoparietal regions outperformed amyloid PET and structural MRI measures in predicting cognitive decline (*26–28*), especially in patients at early AD stages (*26*). This result was replicated by local and multicenter studies using different tau PET tracers (i.e., ^{18}F-flortaucipir and ^{18}F-RO948), retrospective and prospective longitudinal cognitive assessments, and participants with different severities of impairment. These converging findings suggest that tau PET is a promising prognostic tool for predicting cognitive decline and that tau pathology may be the main driver of neurodegeneration and cognitive symptoms.

Tau PET may play an important role in future precision medicine approaches to AD care by enabling prediction of specific neurodegeneration and cognitive trajectories in individual patients. A recent study that evaluated tau PET patterns in a large, multisite dataset (n = 1,612) revealed substantial variability across patients, highlighting 4 distinct spatiotemporal patterns, each associated with specific demographic and clinical features (*29*). This heterogeneity highlights the limitations of a one-size-fits-all approach to predicting tau, neurodegeneration, or clinical change. Furthermore, individual factors modify the relationship between tau accumulation and cognition, with younger age, female sex, higher educational attainment, and higher baseline cortical thickness all associated with increased resistance against the deleterious effect of pathology on cognitive performance (*30*). Some studies suggest that the relationship between tau, neurodegeneration, and cognition may also vary with race and ethnicity as proxies for social determinants of health (*31*), though much more work on diverse cohorts is needed to better understand these relationships. Finally, the development of biomarkers that measure common non-AD pathologies (e.g., vascular lesions, TDP43, and α-synuclein aggregates) will be critical for achieving a more adequate prognosis, as these processes are highly prevalent in patients with AD (*32*) and contribute significantly to neurodegeneration and cognitive decline.

Plasma biomarkers have recently emerged as promising and accessible biomarkers for tau pathology in AD (*33*). Plasma p-tau 181, p-tau 217, and p-tau 231 increase in early stages of AD, discriminate patients with AD from those with non-AD conditions, and show moderate correlations with tau PET uptake (*34,35*). Although plasma p-tau measures Aβ-induced changes in tau phosphorylation and secretion, tau PET measures the overall burden and topographic distribution of neurofibrillary tangles. Therefore, plasma p-tau measurements and tau PET provide additive and complementary information on tau pathology and prognosis. In a recent head-to-head study, baseline plasma p-tau 217 best predicted longitudinal increases in tau PET in preclinical AD, whereas baseline tau PET was the better predictor in symptomatic patients (*36*). Future work will determine whether baseline patterns of tau PET can also predict domain-specific changes in cognition (e.g., medial temporal tau predicting changes in episodic memory, or occipital tau predicting changes in visuospatial function).

The close relationship between tau burden, prospective neurodegeneration, and consequent clinical decline is particularly important in the development of novel AD therapies. Effective treatments for AD may ultimately require combination therapies targeting both amyloid-β and tau pathology as well as other elements of AD pathophysiology. Antitau therapies could be effective in preventing synaptic loss and atrophy, thus slowing clinical decline, whereas antiamyloid therapies in early stages could prevent tau spreading. Thus, tau PET may be a good tool to stratify patients in clinical trials of disease-modifying therapies, with personalized estimations of neurodegeneration and cognitive trajectories, enhancing the chance to identify the best time window and the cohort in which a given therapy can be most effective. In a recent phase 2 trial of donanemab (*37*), a monoclonal antibody targeting the pyroglutamate epitope on Aβ plaques, ^{18}F-flortaucipir PET was used to limit trial inclusion to patients with intermediate tau deposition. This innovative approach to patient stratification shifts the focus from amyloid to tau pathology, enabling more accurate prediction of clinical progression. Including patients with an intermediate amount of tau pathology addresses the concern that antiamyloid therapies may not be beneficial at advanced disease stages (high tau) but also reduces the risk of including patients who may not progress clinically during the course of the trial (low tau). In the trial, significant amyloid PET lowering by donanemab was associated with slower tau PET progression in the frontal and temporal cortices and with modestly slower cognitive and functional decline compared with placebo. This successful trial foreshadows a future in which tau PET may have an important role in establishing eligibility and evaluating response to novel disease-modifying therapies. However, future clinical trials also need to evaluate alternative tau PET tracers, which may be more sensitive than ^{18}F-flortaucipir PET for early Braak tau stages in order to ensure the inclusion of patients with early AD-tau pathology, as these patients may benefit most from antiamyloid and other therapeutic approaches.

In conclusion, tau PET is a highly promising tool that will likely play an important role in future precision medicine approaches to AD care. Tau PET is both highly specific for AD neuropathology and (in contrast to amyloid PET) strongly associated with neurodegeneration and clinical outcomes. Further work is needed to fully

leverage the potential of tau PET to predict individual patient trajectories, understand the complex pathophysiology of the disease, and ultimately accelerate the development of effective therapies.

DISCLOSURE

Gil Rabinovici receives research support from Avid Radiopharmaceuticals, GE Healthcare, Genentech, and Life Molecular Imaging. He has received consultation fees from Eli Lilly, Roche, and Genentech. He serves on a data safety monitoring board for Johnson & Johnson and as an associate editor for JAMA Neurology. No other potential conflict of interest relevant to this article was reported.

REFERENCES

1. Rabinovici GD, Gatsonis C, Apgar C, et al. Association of amyloid positron emission tomography with subsequent change in clinical management among Medicare beneficiaries with mild cognitive impairment or dementia. *JAMA.* 2019;321:1286–1294.
2. Ossenkoppele R, Jansen WJ, Rabinovici GD, et al. Prevalence of amyloid PET positivity in dementia syndromes: a meta-analysis. *JAMA.* 2015;313:1939–1949.
3. Iaccarino L, La Joie R, Edwards L, et al. Spatial relationships between molecular pathology and neurodegeneration in the Alzheimer's disease continuum. *Cereb Cortex.* 2021;31:1–14.
4. La Joie R, Perrotin A, Barré L, et al. Region-specific hierarchy between atrophy, hypometabolism, and 2-amyloid (Aβ) load in Alzheimer's disease dementia. *J Neurosci.* 2012;32:16265–16273.
5. Ossenkoppele R, Rabinovici GD, Smith R, et al. Discriminative accuracy of [^{18}F]flortaucipir positron emission tomography for Alzheimer disease vs other neurodegenerative disorders. *JAMA.* 2018;320:1151–1162.
6. Jack CR, Wiste HJ, Botha H, et al. The bivariate distribution of amyloid-β and tau: relationship with established neurocognitive clinical syndromes. *Brain.* 2019;142:3230–3242.
7. Fleisher AS, Pontecorvo MJ, Devous MD, et al. Positron emission tomography imaging with [^{18}F]flortaucipir and postmortem assessment of Alzheimer disease neuropathologic changes. *JAMA Neurol.* 2020;77:829–839.
8. Soleimani-Meigooni DN, Iaccarino L, La Joie R, et al. ^{18}F-flortaucipir PET to autopsy comparisons in Alzheimer's disease and other neurodegenerative diseases. *Brain.* 2020;143:3477–3494.
9. Ossenkoppele R, Schonhaut DR, Schöll M, et al. Tau PET patterns mirror clinical and neuroanatomical variability in Alzheimer's disease. *Brain.* 2016;139:1551–1567.
10. Schöll M, Lockhart SN, Schonhaut DR, et al. PET imaging of tau deposition in the aging human brain. *Neuron.* 2016;89:971–982.
11. Maass A, Landau S, Baker S, et al. Comparison of multiple tau PET measures as biomarkers in aging and Alzheimer's disease. *Neuroimage.* 2017;157:448–463.
12. Lowe VJ, Wiste HJ, Senjem ML, et al. Widespread brain tau and its association with ageing, Braak stage and Alzheimer's dementia. *Brain.* 2018;141:271–287.
13. Bejanin A, Schonhaut DR, La Joie R, et al. Tau pathology and neurodegeneration contribute to cognitive impairment in Alzheimer's disease. *Brain.* 2017;140:3286–3300.
14. Ossenkoppele R, Smith R, Ohlsson T, et al. Associations between tau, Aβ, and cortical thickness with cognition in Alzheimer disease. *Neurology.* 2019;92:e601–e612.
15. Whitwell JL, Graff-Radford J, Tosakulwong N, et al. Imaging correlations of tau, amyloid, metabolism, and atrophy in typical and atypical Alzheimer's disease. *Alzheimers Dement.* 2018;14:1005–1014.
16. Josephs KA, Tosakulwong N, Graff-Radford J, et al. MRI and flortaucipir relationships in Alzheimer's phenotypes are heterogeneous. *Ann Clin Transl Neurol.* 2020;7:707–721.
17. Nelson PT, Alafuzoff I, Bigio EH, et al. Correlation of Alzheimer disease neuropathologic changes with cognitive status: a review of the literature. *J Neuropathol Exp Neurol.* 2012;71:362–381.
18. Serrano-Pozo A, Qian J, Muzikansky A, et al. Thal amyloid stages do not significantly impact the correlation between neuropathological change and cognition in the Alzheimer disease continuum. *J Neuropathol Exp Neurol.* 2016;75:516–526.
19. Petersen C, Nolan AL, de Paula França Resende E, et al. Alzheimer's disease clinical variants show distinct regional patterns of neurofibrillary tangle accumulation. *Acta Neuropathol (Berl).* 2019;138:597–612.
20. Busche MA, Hyman BT. Synergy between amyloid-β and tau in Alzheimer's disease. *Nat Neurosci.* 2020;23:1183–1193.
21. Harrison TM, La Joie R, Maass A, et al. Longitudinal tau accumulation and atrophy in aging and Alzheimer disease. *Ann Neurol.* 2019;85:229–240.
22. La Joie R, Visani AV, Baker SL, et al. Prospective longitudinal atrophy in Alzheimer's disease correlates with the intensity and topography of baseline tau PET. *Sci Transl Med.* 2020;12:1–13.
23. Scott MR, Hampton OL, Buckley RF, et al. Inferior temporal tau is associated with accelerated prospective cortical thinning in clinically normal older adults. *Neuroimage.* 2020;220:116991.
24. LaPoint MR, Chhatwal JP, Sepulcre J, Johnson KA, Sperling RA, Schultz AP. The association between tau PET and retrospective cortical thinning in clinically normal elderly. *Neuroimage.* 2017;157:612–622.
25. Das SR, Xie L, Wisse LEM, et al. Longitudinal and cross-sectional structural magnetic resonance imaging correlates of AV-1451 uptake. *Neurobiol Aging.* 2018;66:49–58.
26. Ossenkoppele R, Smith R, Mattsson-Carlgren N, et al. Accuracy of tau positron emission tomography as a prognostic marker in preclinical and prodromal Alzheimer disease: a head-to-head comparison against amyloid positron emission tomography and magnetic resonance imaging. *JAMA Neurol.* 2021;78:961–971.
27. Hanseeuw BJ, Betensky RA, Jacobs HIL, et al. Association of amyloid and tau with cognition in preclinical Alzheimer disease: a longitudinal study. 2019;76:915–924.
28. Malpetti M, Kievit RA, Passamonti L, et al. Microglial activation and tau burden predict cognitive decline in Alzheimer's disease. *Brain.* 2020;143:1588–1602.
29. Vogel JW, Young AL, Oxtoby NP, et al. Four distinct trajectories of tau deposition identified in Alzheimer's disease. *Nat Med.* 2021;27:871–881.
30. Ossenkoppele R, Lyoo CH, Jester-Broms J, et al. Assessment of demographic, genetic, and imaging variables associated with brain resilience and cognitive resilience to pathological tau in patients with Alzheimer disease. *JAMA Neurol.* 2020;77:632–642.
31. Gleason CE, Zuelsdorff M, Gooding DC, et al. Alzheimer's disease biomarkers in Black and non-Hispanic White cohorts: a contextualized review of the evidence. *Alzheimers Dement.* December 6, 2021 [Epub ahead of print].
32. Spina S, La Joie R, Petersen C, et al. Comorbid neuropathological diagnoses in early versus late-onset Alzheimer's disease. *Brain.* 2021;144:2186–2198.
33. Hampel H, O'Bryant SE, Molinuevo JL, et al. Blood-based biomarkers for Alzheimer disease: mapping the road to the clinic. *Nat Rev Neurol.* 2018;14:639–652.
34. Thijssen EH, La Joie R, Strom A, et al. Plasma phosphorylated tau 217 and phosphorylated tau 181 as biomarkers in Alzheimer's disease and frontotemporal lobar degeneration: a retrospective diagnostic performance study. *Lancet Neurol.* 2021;20:739–752.
35. Ashton NJ, Pascoal TA, Karikari TK, et al. Plasma p-tau231: a new biomarker for incipient Alzheimer's disease pathology. *Acta Neuropathol (Berl).* 2021;141:709–724.
36. Leuzy A, Smith R, Cullen NC, et al. Biomarker-based prediction of longitudinal tau positron emission tomography in Alzheimer disease. *JAMA Neurol.* 2022;79:149–158.
37. Mintun MA, Lo AC, Duggan Evans C, et al. Donanemab in early Alzheimer's disease. *N Engl J Med.* 2021;384:1691–1704.

Pretherapeutic Comparative Dosimetry of ^{177}Lu-rhPSMA-7.3 and ^{177}Lu-PSMA I&T in Patients with Metastatic Castration-Resistant Prostate Cancer

Benedikt Feuerecker[1–3], Maythinee Chantadisai[1], Anne Allmann[1], Robert Tauber[4], Jakob Allmann[1], Lisa Steinhelfer[1], Isabel Rauscher[1], Alexander Wurzer[5], Hans-Jürgen Wester[5], Wolfgang A. Weber[1,2], Calogero d'Alessandria*[1], and Matthias Eiber*[1,2]

[1]*Department of Nuclear Medicine, School of Medicine, Technical University of Munich, München, Germany;* [2]*Partnersite München, German Cancer Consortium (DKTK), Heidelberg, Germany;* [3]*Department of Radiology, School of Medicine, Technical University of Munich, München, Germany;* [4]*Department of Urology, School of Medicine, Technical University of Munich, München, Germany; and* [5]*Department of Pharmaceutical Radiochemistry, Technical University of Munich, Garching, Germany*

Radiohybrid prostate-specific membrane antigen (rhPSMA) ligands allow for labeling with ^{18}F and radiometals for endoradiotherapy. rhPSMA-7.3 has been designated as a lead compound with promising preclinical data for ^{177}Lu-rhPSMA-7.3, which has shown higher tumor uptake than ^{177}Lu-PSMA I&T. In this retrospective analysis, we compared pretherapeutic clinical dosimetry data of both PSMA ligands. **Methods:** Six patients with metastatic castration-resistant prostate cancer underwent both ^{177}Lu-rhPSMA-7.3 and ^{177}Lu-PSMA I&T pretherapeutic dosimetry. Whole-body scintigraphy was performed at 1 h, 4 h, 24 h, 48 h, and 7 d after injection. Regions of interest covering the whole body, organs, bone marrow, and tumor lesions were drawn for each patient. Absorbed doses for individual patients and pretherapeutic applications were calculated using OLINDA/EXM. To facilitate the comparison of both ligands, we introduced the therapeutic index (TI), defined as the ratio of mean pretherapeutic doses to tumor lesions over relevant organs at risk. **Results:** Mean whole-body pretherapeutic effective doses for ^{177}Lu-rhPSMA-7.3 and ^{177}Lu-PSMA I&T were 0.12 ± 0.07 and 0.05 ± 0.03 Sv/GBq, respectively. Mean absorbed organ doses for ^{177}Lu-rhPSMA-7.3 and ^{177}Lu-PSMA I&T were, for example, 1.65 ± 0.28 and 0.73 ± 0.18 Gy/GBq for the kidneys, 0.19 ± 0.09 and 0.07 ± 0.03 Gy/GBq for the liver, 2.35 ± 0.78 and 0.80 ± 0.41 Gy/GBq for the parotid gland, and 0.67 ± 0.62 and 0.30 ± 0.27 Gy/GBq for the bone marrow, respectively. Tumor lesions received mean absorbed doses of ^{177}Lu-rhPSMA-7.3 and ^{177}Lu-PSMA I&T of 6.44 ± 6.44 and 2.64 ± 2.24 Gy/GBq, respectively. The mean TIs for the kidneys were 3.7 ± 2.2 and 3.6 ± 2.2 for ^{177}Lu-rhPSMA-7.3 and ^{177}Lu-PSMA I&T, respectively, and those for the bone marrow were 15.2 ± 10.2 and 15.1 ± 10.2 for ^{177}Lu-rhPSMA-7.3 and ^{177}Lu-PSMA I&T, respectively. **Conclusion:** Pretherapeutic clinical dosimetry confirmed preclinical results of mean absorbed doses for tumors that were 2–3 times higher for ^{177}Lu-rhPSMA-7.3 than for ^{177}Lu-PSMA I&T. Absorbed doses to normal organs also tended to be higher for ^{177}Lu-rhPSMA-7.3, resulting overall in similar average TIs for both radiopharmaceuticals with considerable interpatient variability. ^{177}Lu-rhPSMA-7.3 has promise for a therapeutic efficacy similar to that of ^{177}Lu-PSMA I&T at smaller amounts of injected activity, simplifying radiation safety measurements (especially for large patient numbers or dose escalation regimens).

Key Words: ^{177}Lu-rhPSMA-7.3; ^{177}Lu-PSMA I&T; dosimetry; mCRPC; prostate cancer; PSMA

J Nucl Med 2022; 63:833–839
DOI: 10.2967/jnumed.121.262671

Treatment of metastatic castration-resistant prostate cancer (mCRPC) remains challenging. ^{177}Lu-PSMA radioligand therapy (RLT) is an option with a variety of different prostate-specific membrane antigen (PSMA) ligands developed in recent years (*1*). Several prospective and retrospective studies proved that ^{177}Lu-PSMA (using either PSMA-617 or PSMA I&T) had substantial antitumor effects (*2,3*). Most recently, the VISION trial showed longer median radiographic progression-free survival (8.7 vs. 3.4 mo) and overall survival (15.3 vs. 11.3 mo) for ^{177}LuPSMA-617 versus the standard of care, respectively, in PSMA-positive mCRPC after the use of taxane and next-generation androgen receptor signaling inhibitor agents (*4*).

For the assessment of new radiopharmaceuticals, dosimetry is essential to link the potential range of injected activities with therapeutic responses and possible side effects. For example, PSMA ligands can exhibit intense tracer accumulation in some normal organs, such as the kidneys. Dosimetric results have been published for the theranostic DOTA-conjugated PSMA ligands ^{177}Lu-PSMA-DKFZ-617 and ^{177}Lu-PSMA I&T (*5*), including both pretherapeutic (*6*) and posttherapeutic (*7–10*) evaluations.

Recently, a class of radiohybrid PSMA (rhPSMA) ligands were developed. They are theranostic agents allowing both fluorination and labeling with radiometals (*11–14*). Preclinical data have proposed that the single diastereoisomer ^{18}F-rhPSMA-7.3 is the most promising clinical candidate (*15,16*). ^{18}F-rhPSMA-7.3 is currently in 2 phase 3 trials for PET imaging of primary (NCT04186819) and recurrent (NCT04186845) prostate cancers. Most recently, promising preclinical data on ^{177}Lu-rhPSMA-7.3 in comparison to ^{177}Lu-PSMA I&T were published (*16*).

Here, we present a retrospective analysis exploring the potential of ^{177}Lu-rhPSMA-7.3 in comparison to ^{177}Lu-PSMA I&T for endoradiotherapy in mCRPC. We used pretherapeutic comparative dosimetry data for normal organs and tumor lesions.

Received Jun. 1, 2021; revision accepted Aug. 26, 2021.
For correspondence or reprints, contact Benedikt Feuerecker (benedikt.feuerecker@tum.de).
*Contributed equally to this work.
Published online Sep. 16, 2021.

MATERIALS AND METHODS

Patients and Rationale for Comparative Dosimetry

According to current German guidelines, mCRPC patients after chemotherapy and novel antiandrogen therapy can be considered for ^{177}Lu-PSMA RLT after interdisciplinary tumor board discussion (*17*). All patients in the presented analysis had undergone chemotherapy and novel antiandrogen therapy before ^{177}Lu-PSMA.

Patients were informed that there are no approved PSMA-targeted therapies but that preliminary preclinical and clinical data support the antitumor activity of ^{177}Lu-PSMA I&T. Additionally, information about preclinical data showing higher uptake of ^{18}F-rhPSMA-7.3 and higher absorbed doses of ^{177}Lu-rhPSMA-7.3 in tumors (*14,16*), indicating higher radiation doses to tumor tissue of ^{177}Lu-rhPSMA-7.3 than of ^{177}Lu-PSMA I&T for clinical use, was provided.

Patients were offered pretherapeutic administration of both ^{177}Lu-PSMA I&T and ^{177}Lu-rhPSMA-7.3 to determine tumor and normal organ doses. Subsequent treatment was then performed with the agent that showed favorable tumor-to-normal organ dose ratios or with ^{177}Lu-PSMA I&T if the differences in the tumor-to-normal organ dose ratios were similar. ^{177}Lu-PSMA I&T and ^{177}Lu-rhPSMA-7.3 were prepared in compliance with the German Medicinal Products Act, AMG §13 2b, and after informing the responsible regulatory body (Government of Oberbayern, Germany). The institutional review board of the Technical University of Munich approved the retrospective scientific analysis of the dosimetry data (115/18 S-KK).

Between April 2018 and November 2020, 6 patients agreed to undergo these dosimetric investigations. Patient characteristics are presented in Supplemental Table 1 (supplemental materials are available at http://jnm.snmjournals.org). The approach was based on the rationale of individual selection of the optimal ligand for a specific patient to offer the possibility of benefit from higher tumor uptake, as recent preclinical data indicated (*16*).

Definitions of Therapeutic Index (TI) and Relative TI (rTI)

To assess the potential antitumor effect in relation to organs at risk of ^{177}Lu-PSMA I&T versus ^{177}Lu-rhPSMA-7.3, a TI was calculated. It was defined as the mean radiation dose to tumor lesions divided by the radiation dose to relevant organs at risk. As the kidneys and bone marrow are the most relevant organs, we report the TI for the kidneys and the TI for the bone marrow (*4*). The respective rTI was defined as the ratio of the TI of ^{177}Lu-rhPSMA-7.3 to the TI of ^{177}Lu-PSMA I&T, with a value of greater than 1 indicating a distribution favoring ^{177}Lu-rhPSMA-7.3.

Pretherapeutic Dosimetry, Image Analysis, and Dosimetric Calculations

The mean applied pretherapeutic activities were 1,066 ± 83 MBq (range, 1,000–1,243 MBq) for ^{177}Lu-PSMA I&T and 1,012 ± 51 MBq (range, 917–1,083 MBq) for ^{177}Lu-rhPSMA-7.3. Activity was injected over approximately 1 min and was followed by a saline flush. Specific activities were 47.5 GBq/0.59 μmol for ^{177}Lu-PSMA I&T and 47.5 GBq/0.61 μmol for ^{177}Lu-rhPSMA-7.3. The mean time period between application of both agents was 172 h (range, 166–190 h). Whole-body scintigraphy was performed at least 1 h, 4 h, 24 h, 48 h, and 7 d after administration.

Individual patient absorbed doses for the whole body, kidneys, liver, parotid, submandibular, and lacrimal glands, tumor lesions, and red bone marrow were estimated on the basis of the MIRD scheme, as recommended in the European Association of Nuclear Medicine Dosimetry Committee Guidelines. Absorbed organ and tumor doses for each cycle were calculated using OLINDA/EXM (*18–20*). Details on the regions of interest (ROIs) for scintigraphy and the volume calculations for PET are given in the supplemental data (e.g., Supplemental Table 2).

Statistical Analysis

All continuous data reported are expressed as mean ± SD and range. A nonpaired *t* test followed by Welch correction was performed to compare means. Statistical analyses were conducted using GraphPad Prism (version 5.0; GraphPad Software).

RESULTS

Qualitative ^{177}Lu-PSMA I&T and ^{177}Lu-rhPSMA-7.3 Biodistributions on Pretherapeutic Scintigraphy

Physiologic uptake was seen in the lacrimal, parotid, and submandibular glands, kidneys, and small intestine; uptake was less pronounced in the liver and spleen. Uptake in excess of the background was also seen for multiple tumor lesions, with progressive accumulation up to 24–48 h after injection for ^{177}Lu-PSMA I&T and ^{177}Lu-rhPSMA-7.3 (Fig. 1). Delayed whole-body images (up to 7 d after therapy) exhibited long-term retention of ^{177}Lu-PSMA I&T and ^{177}Lu-rhPSMA-7.3 in the metastases, with nearly no residual uptake in normal organs.

Pretherapeutic Dosimetry of Normal Organs

The mean whole-body pretherapeutic effective dose for ^{177}Lu-rhPSMA-7.3 was 0.117 Gy (0.12 ± 0.07 Sv/GBq), and that for ^{177}Lu-PSMA I&T was 0.054 Gy (0.05 ± 0.03 Sv/GBq). The mean absorbed organ doses for ^{177}Lu-rhPSMA-7.3 and ^{177}Lu-PSMA I&T were 1.65 ± 0.28 and 0.73 ± 0.18 Gy/GBq, respectively, for the kidneys; 0.19 ± 0.09 and 0.07 ± 0.03 Gy/GBq, respectively, for the liver; 2.35 ± 0.78 and 0.80 ± 0.41 Gy/GBq for the parotid glands, respectively; 2.10 ± 0.86 and 0.67 ± 0.31 Gy/GBq for the submandibular glands, respectively; and 5.29 ± 2.16 and 1.92 ± 0.80 Gy/GBq for the lacrimal glands, respectively (Supplemental Table 3). Figure 2 and Supplemental

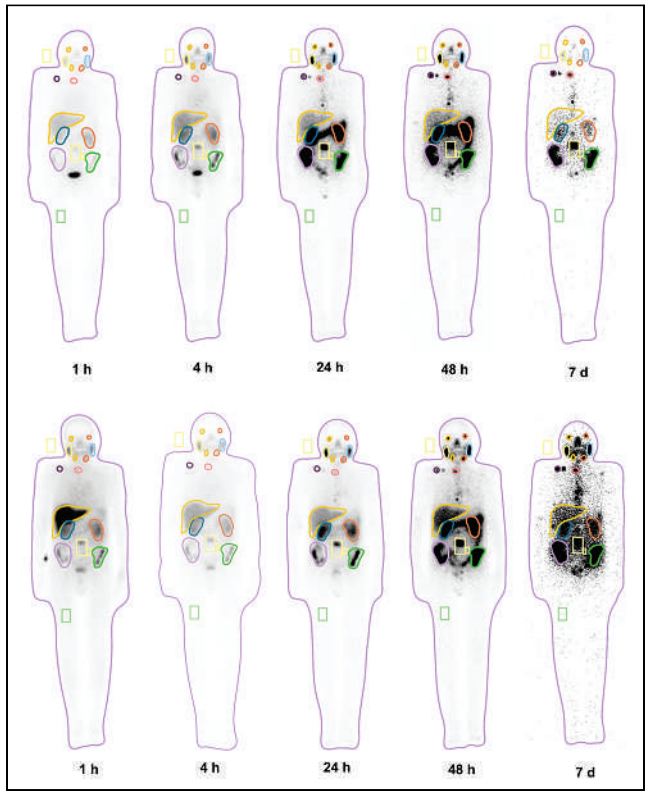

FIGURE 1. Examples of ROIs in 1 patient for ^{177}Lu-PSMA I&T (top) and ^{177}Lu-rhPSMA-7.3 (bottom).

Figs. 1 and 2 display mean organ doses, individual organ doses, and individual percentage injected doses.

Pretherapeutic Dosimetry of Bone Marrow

When ROIs were placed in the thigh regions, red bone marrow absorbed doses were 0.67 ± 0.62 Gy/GBq for ^{177}Lu-rhPSMA-7.3 and 0.30 ± 0.27 Gy/GBq for ^{177}Lu-PSMA I&T. Data for bone marrow dosimetry obtained with ROIs next to the lumbar spine for correction are presented in Supplemental Tables 3 and 4.

Pretherapeutic Dosimetry of Tumor Lesions

A total of 21 representative lesions were analyzed (14 bone and 7 lymph node metastases). Mean and individual sizes of individual tumor lesions are given in the supplemental materials and Supplemental Table 2.

The pretherapeutic mean absorbed doses of tumor lesions were 6.44 ± 6.44 Gy/GBq (range, 0.66–29.25 Gy/GBq) for ^{177}Lu-rhPSMA-7.3 and 2.64 ± 2.24 Gy/GBq (range, 0.38–9.80 Gy/GBq) for ^{177}Lu-PSMA I&T. The pretherapeutic mean absorbed doses for bone and lymph node metastases were 4.09 ± 2.57 and 11.14 ± 8.83 Gy/GBq, respectively, for ^{177}Lu-rhPSMA-7.3 and 1.70 ± 1.13 and 4.51 ± 2.69 Gy/GBq, respectively, for ^{177}Lu-rhPSMA-7.3 (Table 1). Figure 2 and Supplemental Figs. 1–3 display mean tumor doses, individual tumor doses, and individual percentage injected doses.

TI and rTI

The mean TIs for the kidneys were 3.7 ± 2.2 for ^{177}Lu-rhPSMA-7.3 and 3.6 ± 2.2 for ^{177}Lu-PSMA I&T. Intraindividual comparisons of ^{177}Lu-rhPSMA-7.3 and ^{177}Lu-PSMA I&T revealed a higher TIs for the kidneys in 2 patients for ^{177}Lu-rhPSMA-7.3 (patient 2: 5.1 vs. 3.7; patient 4: 1.6 vs. 1.1) and in 1 patient for ^{177}Lu-PSMA I&T (patient 6: 2.9 vs. 4.3). In 3 patients, no clear differences were seen (patient 1: 1.5 vs. 1.6; patient 3: 7.8 vs. 7.9; patient 5: 3.1 vs. 3.1). Consequently, the rTI for the kidneys was greater than 1 in patients 2 and 4 and less than or equal to 1 in all other patients. The individual TIs and the rTIs are shown in Figures 3A and 3B, respectively.

When ROIs in the thigh were used, the mean TIs for the bone marrow were 15.2 ± 10.2 for ^{177}Lu-rhPSMA-7.3 and 15.1 ± 10.2 for ^{177}Lu-PSMA I&T. Intraindividual comparisons of ^{177}Lu-rhPSMA-7.3 and ^{177}Lu-PSMA I&T revealed that ^{177}Lu-rhPSMA-7.3 showed higher TIs for the bone marrow in 4 patients (patient 1: 2.8 vs. 2.7; patient 2: 25.5 vs. 21.3; patient 3: 28.4 vs. 27.5; patient 4: 10.6 vs. 9.8). In 1 patient, no clear difference was measured (patient 5: 3.4 vs. 3.4), and in another patient, ^{177}Lu-PSMA I&T showed a higher TI for the bone marrow (patient 6: 20.3 vs. 25.7).

DISCUSSION

We presented data on pretherapeutic radiation dosimetry for normal organs and tumor lesions for ^{177}Lu-rhPSMA-7.3 and ^{177}Lu-PSMA I&T in 6 mCRPC patients. Quantitative analyses revealed, on average, an absorbed dose to tumor lesions of ^{177}Lu-rhPSMA-7.3 that was 2.4 times higher than that of ^{177}Lu-PSMA I&T. This finding is in line with recent preclinical data demonstrating a 2.6-fold difference (*16*). However, in our clinical investigation, absorbed doses to normal organs were also 2–3 times higher (e.g., 2.3 for the kidneys, 2.9 for the parotid glands, and 2.2 for the bone marrow). Notably, these relationships substantially differed at the patient level.

Because of controversies about the extrapolation of preclinical evaluations, pretherapeutic clinical dosimetry is important (*21*). Currently, dosimetry for PSMA ligands focuses on absorbed doses delivered to normal organs, primarily the kidneys but also the salivary glands as the most relevant organs at risk. Despite numerically high absorbed doses to the salivary and parotid glands, clinically relevant toxicity has only been anecdotally reported and has been mainly transient (*22*). Although red bone marrow dosing is essential, its methodology is prone to errors—for example, as a result of the frequent presence of extensive bone metastases. Nevertheless, bone marrow toxicity even in the presence of extensive osseous metastases is not a frequent side effect (*4,23*).

rhPSMA ligands belong to a new class of fully theranostic agents (*16*). They allow the use of radiochemical twins, such as ^{19}F/^{177}Lu-rhPSMA or ^{18}F/^{nat}Lu-rhPSMA, for potential pretherapeutic PET-based imaging and subsequent PSMA RLT (*24*). Recently published promising preclinical data demonstrated that the radiohybrid ^{19}F/^{177}Lu-rhPSMA-7.3 is a suitable candidate for clinical translation because of similar clearance kinetics and radiation doses but superior tumor uptake and retention compared with ^{177}Lu-PSMA I&T (*16*). Using this approach, our aim was to investigate ^{177}Lu-rhPSMA-7.3 by comparing it to ^{177}Lu-PSMA I&T as the established agent for PSMA RLT, allowing us to maximize the absorbed radiation dose to tumor lesions and to minimize the absorbed radiation dose to relevant organs at risk.

When differences in radiation doses to normal organs are investigated, the kidneys are usually regarded as dose-limiting organs at risk. Pretherapeutic kidney doses in our 6 mCRPC patients were 2.3 times higher with ^{177}Lu-PSMA-7.3 than with ^{177}Lu-PSMA I&T. Regarding potential radiation damage, currently either 23 Gy with a 5% probability of late kidney damage within 5 y or 28 Gy with a 50% probability of late kidney damage within 5 y is used (*25*). For ^{177}Lu-PSMA I&T and ^{177}Lu-PSMA-617, severe kidney toxicity has been described as a side effect in only a few patients (*26*). However, care must be taken given the limited overall survival of late-stage mCRPC patients. Kabaskal et al. calculated a maximum activity of 32.9 GBq to achieve a 23-Gy kidney dose report for ^{177}Lu-PSMA-617 using pretherapeutic dosimetry (*10*). For ^{177}Lu-rhPSMA-7.3, our mean data would

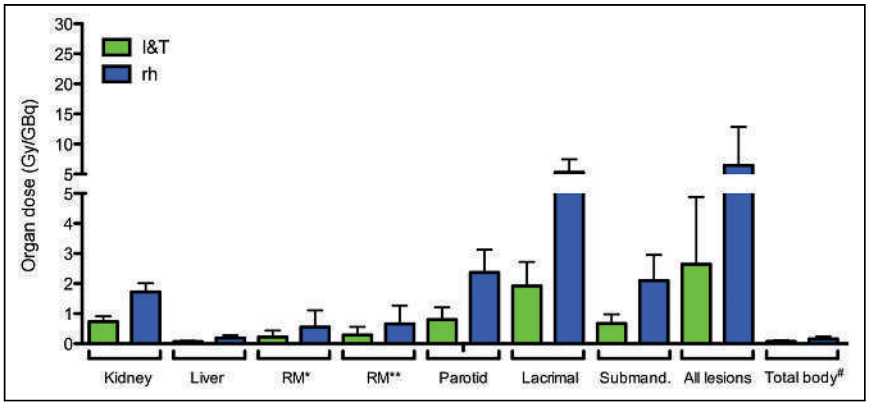

FIGURE 2. Mean organ doses (Gy/GBq) for kidneys, liver, parotid, lacrimal, and submandibular (Submand.) glands, and tumor lesions and total-body doses (Sv/GBq) determined with ^{177}Lu-PSMA I&T (I&T) and ^{177}Lu-rhPSMA-7.3 (rh) for all patients. Individual patient organ doses are shown in Supplemental Figs. 1–3. RM = red bone marrow. RM* = using an ROI for correction next to the lumbar spine (n = 4); RM** = using an ROI in the thigh (n = 6); #Sv/GBq.

TABLE 1
Effective Doses for Tumor and Ratios to Effective Doses for Kidney and Bone Marrow

			^{177}Lu-rhPSMA-7.3 (rh)			^{177}Lu-PSMA I&T (I&T)					
Patient	Tumor no.	Tumor site	Tumor dose (mGy/MBq)	TI for kidneys	TI for bone marrow	Tumor dose (mGy/MBq)	TI for kidneys	TI for bone marrow	Ratio of tumor rh to tumor I&T	rTI for kidneys	rTI for bone marrow*
1	1	B	3.00	1.91	3.63	1.31	2.07	3.45	2.30	0.92	1.05
	2	B	1.58	1.01	1.91	0.73	1.16	1.94	2.16	0.87	0.99
2	1	B	4.05	2.33	11.60	1.38	1.71	9.82	2.95	1.36	1.18
	2	B	6.94	3.99	19.90	2.31	2.88	16.51	3.00	1.39	1.21
	3	LN	29.25	16.81	83.81	9.80	12.20	70.00	2.98	1.38	1.20
	4	B	2.81	1.62	8.05	0.88	1.09	6.27	3.20	1.48	1.28
	5	B	1.53	0.88	4.37	0.52	0.65	3.72	2.94	1.35	1.18
3	1	LN	16.15	11.97	43.42	5.15	10.42	35.99	3.14	1.15	1.21
	2	LN	14.00	10.37	37.63	5.93	12.01	41.49	2.36	0.86	0.91
	3	B	1.56	1.16	4.20	0.73	1.47	5.07	2.15	0.79	0.83
4	1	B	2.21	1.24	8.24	0.92	0.97	8.45	2.40	1.28	0.98
	2	LN	3.46	1.94	12.91	1.22	1.28	11.19	2.84	1.52	1.15
5	1	B	6.88	3.23	3.55	2.79	2.96	3.26	2.47	1.09	1.09
	2	B	6.67	3.13	3.44	3.00	3.18	3.51	2.22	0.99	0.98
	3	B	5.92	2.78	3.05	2.69	2.85	3.14	2.20	0.98	0.97
	4	B	9.49	4.46	4.89	4.37	4.63	5.11	2.17	0.96	0.96
	5	B	3.91	1.84	2.02	1.82	1.93	2.13	2.15	0.95	0.95
6	1	B	0.66	0.50	3.38	0.38	0.66	4.00	1.72	0.75	0.85
	2	LN	8.05	6.05	41.28	4.66	8.06	48.54	1.73	0.75	0.85
	3	LN	3.38	2.54	17.32	1.93	3.33	20.06	1.75	0.76	0.86
	4	LN	3.71	2.79	19.03	2.89	5.00	30.10	1.28	0.56	0.63
Mean ± SD for all			6.44 ± 6.44†	3.93 ± 4.07‡	16.08 ± 19.79‡	2.64 ± 2.24	3.83 ± 3.58	15.89 ± 18.28	2.39	1.05	1.01
Mean ± SD for B			4.09 ± 2.57§	2.15 ± 1.17‡	5.87 ± 4.68‡	1.70 ± 1.13	2.02 ± 1.11	5.46 ± 3.76	2.43	1.08	1.03
Mean ± SD for LN			11.14 ± 8.83‡	7.50 ± 5.27‡	36.49 ± 22.49‡	4.51 ± 2.69	7.47 ± 4.03	36.77 ± 17.90	2.30	1.00	0.97

*Results for red marrow dosimetry using ROI placed in thigh.
†$P = 0.02$.
‡Not significant.
§$P = 0.007$.
B = bone; LN = lymph node.
Data for all patients are presented for individual tumor lesions and grouped by tumor lesion type.

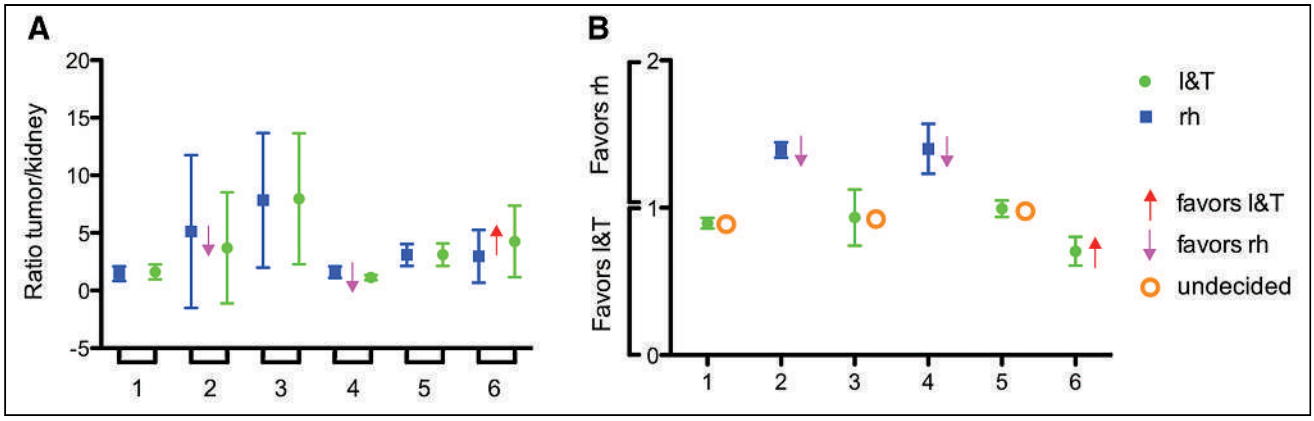

FIGURE 3. TIs (A) and rTIs (B) for tumor-to-kidney ratio for each individual patient. Values of >1 indicate favorable biodistribution for ^{177}Lu-rhPSMA-7.3 (rh) compared with ^{177}Lu-PSMA I&T (I&T) and vice versa. Two patients had favorable distribution of ^{177}Lu-rhPSMA-7.3, 1 patient had favorable distribution of ^{177}Lu-PSMA I&T, and in 3 patients no clear preference was observed.

indicate the option to apply approximately 17 GBq on the basis of a mean of 1.65 Gy/GBq. However, this lower activity would achieve similar absorbed tumor doses. It remains to be decided which activity levels and timing of cycles will be pursued in any potential clinical development of ^{177}Lu-rhPSMA-7.3. Nevertheless, we believe that the presented data might inform potential future study protocols.

Notably, given the results of the VISION trial, bone marrow toxicity is a rare but relevant side effect (*4*). In our retrospective study, the radiation delivery to the bone marrow was 2.2 times higher for ^{177}Lu-rhPSMA-7.3. The relative TI of 1.2, integrating absorbed doses to both tumors and bone marrow, suggests only a slight improvement over ^{177}Lu-PSMA I&T.

However, the calculation of red bone marrow doses is complex when based on scintigraphic images. For example, in 2 of our patients, radiation exposure of the bone marrow was probably overestimated because of the presence of tumor lesions in the ROI. Nevertheless, although important for absolute values, the ratio between ^{177}Lu-rhPSMA-7.3 and ^{177}Lu-PSMA I&T was probably less affected. Our results for bone marrow dosimetry showed mean absorbed doses of 0.67 ± 0.62 mGy/MBq for ^{177}Lu-rhPSMA-7.3 and 0.30 ± 0.27 mGy/MBq for ^{177}Lu-PSMA I&T. These doses resulted in a favorable tumor-to-bone marrow index in 3 patients. The absolute values were substantially higher than those reported in the literature for ^{177}Lu-PSMA-617, but the difference can be mainly explained by the different methods (thigh vs. lumbar spine correction) (*7,8*).

It is important to emphasize that the absorbed dose limits for solid organs are based on conventionally fractionated external-beam therapy and cannot necessarily be directly applied to low-dose-rate radiation (*27*). Patients without risk factors for kidney disease might tolerate a renal biologic equivalent dose up to 40 Gy, on the basis of experience with radiopeptide treatment of neuroendocrine tumors (*28*). However, dosimetry is an important but not the only factor for determining the safety of a radionuclide treatment. As observed in a similar setting comparing somatostatin agonist and antagonist treatments, disproportionately higher hematotoxicity was observed with the somatostatin antagonist, with up to 57% of patients experiencing grade 4 hematotoxicity after 2 cycles (*29*).

High variability of absorbed doses was observed in tumor lesions, similar to data reported for ^{177}Lu-PSMA I&T (*5*) and ^{177}Lu-PSMA-617 (*8,30–32*). The broad range might be partially attributable to the fact that our patients had only a few lesions. Similar to organ dosimetry, the relationship of the absorbed doses of both ligands is a more reliable parameter than the absolute values. Okamoto et al. and Baum et al. reported absorbed doses between 0.22 and 12.0 Gy/GBq and between 0.02 and 78 Gy/GBq, respectively, for ^{177}Lu-PSMA I&T (*5,33*). For ^{177}Lu-PSMA-617, Violet et al. reported mean absorbed doses of 5.28 Gy/GBq for bone metastases and 3.91 Gy/GBq for lymph node metastases (*32*).

Integrating all the previously discussed data for organs and tumor lesions, we calculated the TI for the kidneys in all patients (Fig. 3). Ultimately, 2 patients were treated with ^{177}Lu-rhPSMA-7.3, as pretherapeutic dosimetry indicated a clear advantage. In 1 patient, ^{177}Lu-PSMA I&T was used, given its clearly favorable profile. In the remaining 3 patients, the TI did not favor either of the 2 PSMA ligands. On the basis of the TI for the bone marrow, 3 patients had a favorable profile for ^{177}Lu-rhPSMA-7.3 and 3 patients had a favorable profile for ^{177}Lu-PSMA I&T.

Our analyses warrant some discussion on how the different characteristics of ^{177}Lu-rhPSMA-7.3 can be exploited. Potential options for a drug development program would be the application of similar activities, as recommended for ^{177}Lu-PSMA I&T and ^{177}Lu-PSMA-617, which would lead to higher absorbed tumor doses and potential efficacy (*34*). This approach could be feasible given the so-far low toxicity profile of ^{177}Lu-PSMA in general, with reported injected activities of up to 2 doses of 11 GBq of ^{177}Lu-PSMA-617 (applied within 1 wk) (*35*). However, long-term toxicity for the kidneys of ^{177}Lu-PSMA in general is unclear, and even the potential dose limits are controversial. Alternatively, similar tumor and organ doses with a smaller amount of activity and subsequently with a lower cost could be achieved, especially when non–carrier-added ^{177}Lu is used for treatment (*36*). In the context of an expected large number of patients to be treated with PSMA RLT in the future, smaller amounts of ^{177}Lu would also improve practical aspects (e.g., radioactive material program licensing, improved radiation safety for involved medical personnel).

Our retrospective analysis has limitations. First, only a small number of patients could be analyzed. Second, numerous factors can impair the accuracy of PET and planar dosimetry and can lead to a decreased correlation of the 2 modalities. Overlay in planar scintigraphy can lead to an overestimation of the absorbed dose, and further errors can occur for volumetric assessment (*8,37*). We tried to minimize such errors by adjusting the volume of interest using information from PET for the anatomic configuration of the lesions. However, especially for bone lesions, anatomic delineation can be

difficult. Third, our dosimetry analyses for the bone marrow were prone to substantial challenges, as described earlier. As an alternative, we applied an additional method, using correction from tissue adjacent to the tissue in the thigh. In principle, this method is used in clinical dosimetry. However, as discussed earlier, it usually results in higher absorbed doses (less background to be subtracted in the thigh than adjacent to the lumbar spine), and no data are available in the literature to compare it with other PSMA ligands. Fourth, our pretherapeutic dosimetry using 1 GBq of ^{177}Lu-rhPSMA-7.3 and ^{177}Lu-PSMA I&T might already have achieved some therapeutic effect. Given the higher tumor doses delivered by ^{177}Lu-rhPSMA-7.3, the dosimetry of subsequent ^{177}Lu-PSMA I&T might be more affected than the dosimetry of ^{177}Lu-rhPSMA-7.3 after ^{177}Lu-PSMA I&T. We tried to minimize this bias by alternating the sequence of pretherapeutic applications.

CONCLUSION

Pretherapeutic clinical dosimetry confirmed preclinical results, with mean absorbed doses for tumors of ^{177}Lu-rhPSMA-7.3 that were 2–3 times higher than those of ^{177}Lu-PSMA I&T. Absorbed doses to normal organs increased at different levels, including the bone marrow. The newly introduced TI allowed for individual adjustment of absorbed tumor doses for the kidneys and the bone marrow as organs at risk. For the kidneys, it identified 2 of 6 patients with a clearly favorable biodistribution of ^{177}Lu-rhPSMA-7.3 compared with ^{177}Lu-PSMA I&T and a similar profile in 3 of 6 patients. For the bone marrow, a favorable profile was observed in 3 of 6 patients for ^{177}Lu-rhPSMA-7.3 and in 3 of 6 patients for ^{177}Lu-PSMA I&T. ^{177}Lu-rhPSMA-7.3 holds promise for a therapeutic effect similar to that of ^{177}Lu-PSMA I&T at lower absorbed doses and offers potential economical and radiation safety benefits.

DISCLOSURE

H.-J. Wester, A. Wurzer, and M. Eiber have applied for a patent for rhPSMA. H.-J. Wester is founder, shareholder, and advisory board member of Scintomics GmbH, Fuerstenfeldbruck, Germany. W.A. Weber reports prior consulting activities for Blue Earth Diagnostics Ltd. M. Eiber reports prior consulting activities for Blue Earth Diagnostics Ltd., Novartis, Telix, Progenics, Bayer, Point Biopharma, and Janssen. No other potential conflict of interest relevant to this article was reported.

KEY POINTS

QUESTION: Are the biodistribution, dosimetry, and therapeutic efficacy of ^{177}Lu-rhPSMA-7.3 and ^{177}Lu-PSMA I&T comparable?

PERTINENT FINDINGS: In mCRPC, pretherapeutic organ and tumor absorbed doses for ^{177}Lu-rhPSMA-7.3 were higher than those for ^{177}Lu-PSMA I&T, whereas the TI was equal to the mean for the kidney absorbed dose. Using ^{177}Lu-rhPSMA-7.3 could lead to the same therapeutic effect without higher nephrotoxicity and with smaller amounts of radioactivity.

IMPLICATIONS FOR PATIENT CARE: Pretherapeutic data indicate higher tumor absorbed doses for ^{177}Lu-rhPSMA-7.3 in radioligand treatment, a finding that should be explored in prospective clinical studies.

REFERENCES

1. Lütje S, Heskamp S, Cornelissen AS, et al. PSMA ligands for radionuclide imaging and therapy of prostate cancer: clinical status. *Theranostics.* 2015;5:1388–1401.
2. Heck MM, Tauber R, Schwaiger S, et al. Treatment outcome, toxicity, and predictive factors for radioligand therapy with ^{177}Lu-PSMA-I&T in metastatic castration-resistant prostate cancer. *Eur Urol.* 2019;75:920–926.
3. Hofman MS, Violet J, Hicks RJ, et al. [^{177}Lu]-PSMA-617 radionuclide treatment in patients with metastatic castration-resistant prostate cancer (LuPSMA trial): a single-centre, single-arm, phase 2 study. *Lancet Oncol.* 2018; 19:825–833.
4. Morris MJ, De Bono JS, Chi KN, et al. Phase III study of lutetium-177-PSMA-617 in patients with metastatic castration-resistant prostate cancer (VISION) [abstract LBA4]. *J Clin Oncol.* 2021;39(suppl).
5. Okamoto S, Thieme A, Allmann J, et al. Radiation dosimetry for ^{177}Lu-PSMA I&T in metastatic castration-resistant prostate cancer: absorbed dose in normal organs and tumor lesions. *J Nucl Med.* 2017;58:445–450.
6. Kabasakal L, AbuQbeitah M, Aygun A, et al. Pre-therapeutic dosimetry of normal organs and tissues of ^{177}Lu-PSMA-617 prostate-specific membrane antigen (PSMA) inhibitor in patients with castration-resistant prostate cancer. *Eur J Nucl Med Mol Imaging.* 2015;42:1976–1983.
7. Kratochwil C, Giesel FL, Stefanova M, et al. PSMA-targeted radionuclide therapy of metastatic castration-resistant prostate cancer with ^{177}Lu-labeled PSMA-617. *J Nucl Med.* 2016;57:1170–1176.
8. Delker A, Fendler WP, Kratochwil C, et al. Dosimetry for ^{177}Lu-DKFZ-PSMA-617: a new radiopharmaceutical for the treatment of metastatic prostate cancer. *Eur J Nucl Med Mol Imaging.* 2016;43:42–51.
9. Hohberg M, Eschner W, Schmidt M, et al. Lacrimal glands may represent organs at risk for radionuclide therapy of prostate cancer with [^{177}Lu]DKFZ-PSMA-617. *Mol Imaging Biol.* 2016;18:437–445.
10. Kabasakal L, Toklu T, Yeyin N, et al. Lu-177-PSMA-617 prostate-specific membrane antigen inhibitor therapy in patients with castration-resistant prostate cancer: stability, bio-distribution and dosimetry. *Mol Imaging Radionucl Ther.* 2017;26: 62–68.
11. Eiber M, Kroenke M, Wurzer A, et al. ^{18}F-rhPSMA-7 PET for the detection of biochemical recurrence of prostate cancer after radical prostatectomy. *J Nucl Med.* 2020;61:696–701.
12. Kroenke M, Wurzer A, Schwamborn K, et al. Histologically confirmed diagnostic efficacy of ^{18}F-rhPSMA-7 PET for N-staging of patients with primary high-risk prostate cancer. *J Nucl Med.* 2020;61:710–715.
13. Oh SW, Wurzer A, Teoh EJ, et al. Quantitative and qualitative analyses of biodistribution and PET image quality of a novel radiohybrid PSMA, ^{18}F-rhPSMA-7, in patients with prostate cancer. *J Nucl Med.* 2020;61:702–709.
14. Wurzer A, Di Carlo D, Schmidt A, et al. Radiohybrid ligands: a novel tracer concept exemplified by ^{18}F- or ^{68}Ga-labeled rhPSMA inhibitors. *J Nucl Med.* 2020;61: 735–742.
15. Wurzer A, Parzinger M, Konrad M, et al. Preclinical comparison of four [^{18}F, (nat)Ga]rhPSMA-7 isomers: influence of the stereoconfiguration on pharmacokinetics. *EJNMMI Res.* 2020;10:149.
16. Yusufi N, Wurzer A, Herz M, et al. Comparative preclinical biodistribution, dosimetry and endoradiotherapy in metastatic castration-resistant prostate cancer using ^{19}F/^{177}Lu-rhPSMA-7.3 and ^{177}Lu-PSMA I&T. *J Nucl Med.* 2021;62: 1106–1111.
17. O'Sullivan GJ, Carty FL, Cronin CG. Imaging of bone metastasis: an update. *World J Radiol.* 2015;7:202–211.
18. Siegel JA, Thomas SR, Stubbs JB, et al. MIRD Pamphlet No. 16: techniques for quantitative radiopharmaceutical biodistribution data acquisition and analysis for use in human radiation dose estimates. *J Nucl Med.* 1999;40(suppl):37S–61S.
19. Hindorf C, Glatting G, Chiesa C, Linden O, Flux G; Committee ED. EANM dosimetry committee guidelines for bone marrow and whole-body dosimetry. *Eur J Nucl Med Mol Imaging.* 2010;37:1238–1250.
20. Stabin MG, Sparks RB, Crowe E. OLINDA/EXM: the second-generation personal computer software for internal dose assessment in nuclear medicine. *J Nucl Med.* 2005;46:1023–1027.
21. Blaickner M, Baum RP. Relevance of PET for pretherapeutic prediction of doses in peptide receptor radionuclide therapy. *PET Clin.* 2014;9:99–112.
22. Heck MM, Retz M, D'Alessandria C, et al. Systemic radioligand therapy with ^{177}Lu labeled prostate specific membrane antigen ligand for imaging and therapy in patients with metastatic castration resistant prostate cancer. *J Urol.* 2016;196: 382–391.
23. Gafita A, Fendler WP, Hui W, et al. Efficacy and safety of ^{177}Lu-labeled prostate-specific membrane antigen radionuclide treatment in patients with diffuse bone marrow involvement: a multicenter retrospective study. *Eur Urol.* 2020;78:148–154.

24. Wester HJ, Schottelius M. PSMA-targeted radiopharmaceuticals for imaging and therapy. *Semin Nucl Med.* 2019;49:302–312.
25. Emami B, Lyman J, Brown A, et al. Tolerance of normal tissue to therapeutic irradiation. *Int J Radiat Oncol Biol Phys.* 1991;21:109–122.
26. Gallyamov M, Meyrick D, Barley J, Lenzo N. Renal outcomes of radioligand therapy: experience of ^{177}lutetium–prostate-specific membrane antigen ligand therapy in metastatic castrate-resistant prostate cancer. *Clin Kidney J.* 2019;13:1049–1055.
27. Dale R, Carabe-Fernandez A. The radiobiology of conventional radiotherapy and its application to radionuclide therapy. *Cancer Biother Radiopharm.* 2005; 20:47–51.
28. Bodei L, Cremonesi M, Ferrari M, et al. Long-term evaluation of renal toxicity after peptide receptor radionuclide therapy with ^{90}Y-DOTATOC and ^{177}Lu-DOTATATE: the role of associated risk factors. *Eur J Nucl Med Mol Imaging.* 2008;35:1847–1856.
29. Reidy-Lagunes D, Pandit-Taskar N, O'Donoghue JA, et al. Phase I trial of well-differentiated neuroendocrine tumors (NETs) with radiolabeled somatostatin antagonist ^{177}Lu-satoreotide tetraxetan. *Clin Cancer Res.* 2019;25:6939–6947.
30. Fendler WP, Reinhardt S, Ilhan H, et al. Preliminary experience with dosimetry, response and patient reported outcome after ^{177}Lu-PSMA-617 therapy for metastatic castration-resistant prostate cancer. *Oncotarget.* 2017;8:3581–3590.
31. Scarpa L, Buxbaum S, Kendler D, et al. The ^{68}Ga/^{177}Lu theragnostic concept in PSMA targeting of castration-resistant prostate cancer: correlation of SUVmax values and absorbed dose estimates. *Eur J Nucl Med Mol Imaging.* 2017;44:788–800.
32. Violet J, Jackson P, Ferdinandus J, et al. Dosimetry of ^{177}Lu-PSMA-617 in metastatic castration-resistant prostate cancer: correlations between pretherapeutic imaging and whole-body tumor dosimetry with treatment outcomes. *J Nucl Med.* 2019;60:517–523.
33. Baum RP, Kulkarni HR, Schuchardt C, et al. ^{177}Lu-labeled prostate-specific membrane antigen radioligand therapy of metastatic castration-resistant prostate cancer: safety and efficacy. *J Nucl Med.* 2016;57:1006–1013.
34. Kratochwil C, Fendler WP, Eiber M, et al. EANM procedure guidelines for radionuclide therapy with ^{177}Lu-labelled PSMA-ligands (^{177}Lu-PSMA-RLT). *Eur J Nucl Med Mol Imaging.* 2019;46:2536–2544.
35. Tagawa ST, Niaz MJ, Osborne J, et al. Phase I/II dose-escalation trial of fractionated dose ^{177}Lu-J591 plus ^{177}Lu-PSMA-617 for metastatic castration-resistant prostate cancer (mCRPC) [abstract TPS339]. *J Clin Oncol.* 2019;37(suppl).
36. Tarasov VA, Andreev OI, Romanov EG, Kuznetsov RA, Kupriyanov VV, Tselishchev IV. Production of no-carrier added lutetium-177 by irradiation of enriched ytterbium-176. *Curr Radiopharm.* 2015;8:95–106.
37. Afshar-Oromieh A, Malcher A, Eder M, et al. PET imaging with a [^{68}Ga]gallium-labelled PSMA ligand for the diagnosis of prostate cancer: biodistribution in humans and first evaluation of tumour lesions. *Eur J Nucl Med Mol Imaging.* 2013; 40:486–495.

Effects of ^{225}Ac-Labeled Prostate-Specific Membrane Antigen Radioligand Therapy in Metastatic Castration-Resistant Prostate Cancer: A Meta-Analysis

Dong Yun Lee and Yong-il Kim

Department of Nuclear Medicine, Asan Medical Center, University of Ulsan College of Medicine, Seoul, Republic of Korea

Prostate-specific membrane antigen (PSMA), overexpressed in prostate cancer, has become a popular target for radionuclide-based theranostic applications in the advanced stages of prostate cancer. We conducted a meta-analysis of the therapeutic effects of PSMA-targeting α-therapy (^{225}Ac-PSMA radioligand therapy [RLT]) in patients with metastatic castration-resistant prostate cancer (mCRPC). **Methods:** A systematic search was performed using the keywords "mCRPC," "^{225}Ac-PSMA," and "alpha therapy." Therapeutic responses were analyzed as the pooled proportions of patients with more than a 50% prostate-specific antigen (PSA) decline and any PSA decline. Survival outcomes were analyzed by estimating summary survival curves for progression-free survival and overall survival. Adverse events were analyzed as the pooled proportions of patients with xerostomia and severe hematotoxicity (anemia, leukocytopenia, and thrombocytopenia). **Results:** Nine studies with 263 patients were included in our meta-analysis. The pooled proportions of patients with more than a 50% PSA decline and any PSA decline were 60.99% (95% CI, 54.92%–66.83%) and 83.57% (95% CI, 78.62%–87.77%), respectively. The estimated mean progression-free survival and mean overall survival were 9.15 mo (95% CI, 6.69–11.03 mo) and 11.77 mo (95% CI, 9.51–13.49 mo), respectively. The pooled proportions of patients with adverse events were 62.81% (95% CI, 39.34%–83.46%) for xerostomia, 14.39% (95% CI, 7.76%–22.63%) for anemia, 4.12% (95% CI, 0.97%–9.31%) for leukocytopenia, and 7.18% (95% CI, 2.70%–13.57%) for thrombocytopenia. **Conclusion:** In our study, around 61% of patients had more than a 50% PSA decline and 84% of patients had any PSA decline after ^{225}Ac-PSMA RLT. The common adverse events in ^{225}Ac-PSMA RLT were xerostomia in 63% of patients and severe hematotoxicity in 4%–14% of patients.

Key Words: ^{225}Ac; radioligand therapy; prostate-specific membrane antigen; prostate-specific antigen; xerostomia

J Nucl Med 2022; 63:840–846
DOI: 10.2967/jnumed.121.262017

The increasing worldwide incidence of prostate cancer is inevitable because of the increasing number of elderly men (*1*). The end-stage form of prostate cancer, known as metastatic castration-resistant prostate cancer (mCRPC), is a progressive disease with limited therapeutic options despite androgen deprivation therapy (*2*). Although several treatment options such as second-generation antiandrogen therapy, taxane-based chemotherapy, and ^{223}Ra are available, a novel treatment approach is necessary given the devastating and lethal course of mCRPC (*3*).

Prostate-specific membrane antigen (PSMA) is a type II membrane glycoprotein overexpressed in prostate carcinoma, and it has been recognized as a reliable biomarker reflecting disease burden in dedifferentiated and castration-resistant prostate cancer (*4,5*). Targeting PSMA with diagnostic and therapeutic radionuclide allows the use of the theranostic approach in patients with recurrent or metastatic prostate cancer (*6*). Recently, the first PSMA-targeting diagnostic radiotracer, ^{68}Ga-PSMA-11, was approved by the U.S. Food and Drug Administration, providing the foundation for PSMA-based theranostics.

PSMA-based radioligand therapy (RLT) with ^{177}Lu, a β-ray–emitting therapeutic radionuclide, has been used in European countries since 2015 for compassionate use in patients with mCRPC (*7,8*). Since then, several studies have reported positive results when using ^{177}Lu-PSMA RLT (*9,10*). However, up to 30%–40% of patients were found to be refractory to ^{177}Lu-PSMA RLT during clinical trials and showed hematotoxicity, which limits dose escalation (*11*).

α-particle–emitting radionuclides, which have higher energy transfer rates and shorter pathlengths, have attracted great attention as an alternative to β-ray–emitting radionuclides for PSMA-based RLT (*12*). ^{225}Ac has been the first choice as an α-particle–emitting radionuclide in recent experimental PSMA-based RLT for managing patients with mCRPC (*13–21*). However, given the limited availability of ^{225}Ac coupled with the unstructured clinical setting in these exploratory studies, there is a lack of strong evidence to guide physicians in managing patients with mCRPC using α-particle–emitting RLT. In this context, we conducted a meta-analysis to estimate the therapeutic response, survival outcome, and adverse event of patients with mCRPC who received ^{225}Ac-PSMA RLT.

MATERIALS AND METHODS

Data Search and Study Selection

A systematic search of PubMed, Embase, the Cochrane Library, CINAHL, and Web of Science was conducted on June 10, 2021. The searching keywords were as follows: "metastatic castration-resistant prostate cancer (mCRPC)," "actinium-225 (^{225}Ac) prostate-specific membrane antigen (PSMA)," and "alpha therapy." Studies that reported the therapeutic response according to the prostate-specific antigen (PSA) evaluation, survival outcome, or adverse event of patients with mCRPC who received ^{225}Ac-PSMA RLT were selected. The search was restricted to publications between 2000 and 2021 written in English. Therapeutic responses were confined to more than a 50% PSA decline or any PSA decline after ^{225}Ac-

Received Jan. 26, 2021; revision accepted Aug. 20, 2021.
For correspondence or reprints, contact Yong-il Kim (kyi821209@naver.com).
Published online Sep. 9, 2021.

PSMA RLT. Abstracts, dosimetry/synthesis-related articles, case reports, reviews, editorials, and articles with fewer than 5 patients were not included. When multiple studies were published from the same group, studies with a completely different patient population were included to avoid duplication. Two reviewers independently screened the literature and unanimously selected eligible studies for final inclusion. The protocol of this study was registered in the International Prospective Register of Systematic Reviews (PROSPERO; registration no. CRD42021226139). Institutional review board approval was not required for this meta-analysis because it evaluated published studies.

Data Extraction and Quality Assessment

Publication-related clinical data were extracted from the included articles, and the following information was recorded: first author, year of publication, imaging indication of RLT, number of patients, α-particle–emitting RLT agent, therapeutic dose, therapy cycle, median PSA, median alkaline phosphatase, prechemotherapy (%), prior ^{177}Lu-PSMA (%), prior ^{233}Ra (%), time of PSA evaluation after RLT, therapeutic response, survival outcome, duration of survival follow-up, and adverse events. Two reviewers evaluated each article according to the Newcastle–Ottawa Scale for scoring the quality of nonrandomized studies in meta-analysis (*22*). This quality scale was categorized into 3 groups (selection, comparability, and outcome) with a perfect score of 8. A maximum of 3 scores could be awarded for selection and outcome, and a maximum of 2 scores could be given for comparability. In cases of discrepancy, 2 reviewers made a consensus decision.

Statistical Analysis

Forest plots were generated to evaluate the effects of ^{225}Ac-PSMA RLT. Therapeutic responses were analyzed as the pooled proportions of patients with more than a 50% PSA decline and any PSA decline, with 95% CIs. Survival outcomes were analyzed by estimating summary survival curves with random effects for progression-free survival (PFS) and overall survival (OS) using the MetaSurv package in R (*23*). Survival data were read from the Kaplan–Meier curves using the Engauge Digitizer (http://markummitchell.github.io/engauge-digitizer/) (*24*). Adverse events were analyzed as the pooled proportions of patients with xerostomia and severe hematotoxicity (anemia, leukocytopenia, and thrombocytopenia) with 95% CI. Meta-regression analysis was performed to determine the effect of median PSA, median alkaline phosphatase, prechemotherapy, prior ^{177}Lu-PSMA, and prior ^{223}Ra on the therapeutic response and adverse events. Finally, funnel plots were generated to visually investigate publication bias, and the Egger test was used to evaluate the asymmetry of the funnel plots (*25,26*). Heterogeneity between the studies (for therapeutic responses and adverse events) was assessed by I^2 statistics and χ^2 tests (*27*). The fixed-effects model was used when I^2 was not more than 50% and P was at least 0.1 (Cochran Q test), and the random-effects model was used when I^2 was more than 50% or P was less than 0.1 (Cochran Q test). Statistical analyses were performed mainly using MedCalc, version 19.1.7, for Microsoft Windows. Comprehensive Meta-analysis Software, Version 3, was used for meta-regression.

A P value less than 0.05 was considered statistically significant.

RESULTS

Study Characteristics

Through electronic database searches, we identified 220 records (Supplemental Tables 1–5; supplemental materials are available at http://jnm.snmjournals.org), and 112 records remained after removing duplicates. Of these, 42 records were excluded on the basis of the title and abstract because of the use of diagnostic radiotracers for PSMA ($n = 4$), the use of other therapeutic radiotracers ($n = 21$), in vitro and in vivo preclinical studies ($n = 7$), and no association with RLT or PSMA ($n = 10$). After a thorough analysis of the full text of the remaining 70 articles, 61 articles were excluded because of an association with dosimetry, safety, or physics ($n = 11$); association with synthesis/chemistry ($n = 3$); being published as case report/review/editorial ($n = 44$); and inadequate data ($n = 3$). Finally, 9 studies with 263 patients were included in our meta-analysis (*13–19*) (Fig. 1). No qualifying study was missed after hand-searching by the reviewers.

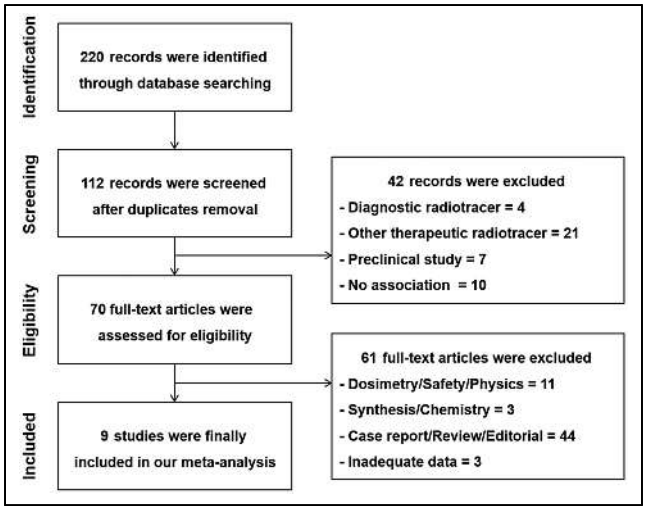

FIGURE 1. Flowchart of study selection process.

Seven of the 9 studies were conducted under a retrospective design (*13,15–19,21*), and 2 studies were conducted prospectively (*14,20*). ^{225}Ac-PSMA-617 was administered in 8 studies (*13–15, 17–21*) and ^{225}Ac-PSMA-I&T was used in 1 study (*16*) as α-particle–emitting RLT agents. The therapeutic dose range per cycle was reported in 3 studies as 1.5–13 MBq (*13,16,17*), and the total number of treatment cycles ranged from 1 to 8. The median level of baseline PSA was 57.2–331 ng/mL, and the follow-up time for PSA evaluation was 2–6 wk after RLT. Therapeutic responses were reported in all 9 studies involving 263 patients (*13–21*), and survival outcomes were identified for 200 patients in 6 of the studies (*13–15,17,19,20*). Adverse events were documented in 8 studies involving 225 patients, which included xerostomia and severe hematotoxicity (*13–20*) (Table 1). Quality assessment of all 9 studies was performed, and the scores of the Newcastle–Ottawa Scale ranged from 6 to 8 (Table 2).

Therapeutic Response

The pooled proportion of patients with more than a 50% PSA decline was 60.99% after ^{225}Ac-PSMA RLT using a random-effects model (95% CI, 54.92%–66.83%), and the I^2 statistic was 25.25% ($P = 0.219$; Cochran Q test). The pooled proportion of patients with any PSA decline was 83.57% after ^{225}Ac-PSMA RLT using a fixed-effects model (95% CI, 78.62%–87.77%), and the I^2 statistic was 0.00% ($P = 0.844$; Cochran Q test) (Fig. 2; Table 3).

Survival Outcome

The estimated mean PFS was 9.15 mo (median PFS, 7.78 mo) after ^{225}Ac-PSMA RLT using a random-effects model (95% CI, 6.69–11.03 mo), and the I^2 statistic was 7.29%. The estimated mean OS was 11.77 mo (median OS, 11.85 mo) after ^{225}Ac-PSMA RLT using a random-effects model (95% CI, 9.51–13.49 mo), and the I^2 statistic was 0.00% (Fig. 3; Table 3).

TABLE 1
Baseline Characteristics of Included Studies

Author	Year	Imaging indication of RLT	Patients (*n*)	α-RLT agent	Median/mean therapeutic dose per cycle	Median cycles of therapy	Median PSA* (ng/ml)	Median ALP* (U/L)	No. of pre-chemotherapy	No. of prior ^{177}Lu-PSMA	No. of prior ^{223}Ra	Time of PSA evaluation after RLT	Therapeutic response	Survival outcome†	Median duration of survival follow-up (mo)	Adverse events
Feuerecker	2021	Uptake higher than liver in PSMA ligand PET/CT	26	^{225}Ac-PSMA-617	9 MBq (range, 4–13 MBq)	2 (range, 1–6)	331 (142–682)	200 (143–517)	25 (96%)	26 (100%)	6 (23%)	After 6 wk	>50% of PSA decline, any PSA decline	PFS (16), OS (16)	6.4	Xerostomia, hematotoxicity
Rosar	2021	Not mentioned	15	^{225}Ac-PSMA-617	2.7 ± 1.1 MBq	2 (range, 1–6)	272 (58–3389)	115 (8–1659)	10 (67%)	0 (0%)	3 (20%)	After 6 ± 2 wk	>50% of PSA decline, any PSA decline	PFS (14), OS (12)	19.4	Xerostomia, hematotoxicity
Sen	2021	^{68}Ga-PSMA-11 uptake ≥ ^{68}Ga-PSMA-11 uptake in parotid glands	38	^{225}Ac-PSMA-617	100 kBq/kg	2 (range, 2–5)	147 (4.9–1400)	(−)	38 (100%)	9 (24%)	2 (5%)	After 2 wk	>50% of PSA decline, any PSA decline	PFS (26), OS (22)	14	Xerostomia, hematotoxicity
Zacherl	2021	Sufficient PSMA expression on ^{18}F-PSMA-1007 PET/CT	14	^{225}Ac-PSMA-I&T	7.8 MBq (range, 6.0–8.5 MBq)	Range, 1–5	112 (20.5–818)	143 (67–695)	12 (86%)	11 (79%)	2 (14%)	After 4 wk	>50% of PSA decline, any PSA decline	(−)	5.9	Xerostomia, hematotoxicity
Khreish	2020	Uptake higher than normal liver uptake on ^{68}Ga-PSMA-11 PET/CT	20	^{225}Ac-PSMA-617	5.3 MBq (range, 1.5–7.9 MBq)	1	215 (6–5547)	160 (53-–917)	18 (90%)	20 (100%)	4 (20%)	After 2-4 wk	>50% of PSA decline, any PSA decline	PFS (16), OS (9)	5.5	Xerostomia, hematotoxicity
Satapathy	2020	Tracer-avid lesion on ^{68}Ga-PSMA-11 PET/CT, with SUV_{max} of lesion being ≥1.5 times greater than that of normal liver	11	^{225}Ac-PSMA-617	100 kBq/kg	(−)	158 (35–840)	(−)	10 (91%)	5 (45%)	0 (0%)	After 6 wk	>50% of PSA decline, any PSA decline	(−)	(−)	Xerostomia, hematotoxicity
Sathekge	2020	Uptake greater than twice normal physiologic liver uptake on ^{68}Ga-PSMA-11 PET/CT	73	^{225}Ac-PSMA-617	(−)	3 (range, 1–8)	57.2	154	27 (37%)	14 (19%)	0 (0%)	After 4 wk	>50% of PSA decline, any PSA decline	PFS (23), OS (13)	9	Xerostomia, hematotoxicity
Yadav	2020	Intense PSMA expression on ^{68}Ga-PSMA-11 PET/CT ≥ liver	28	^{225}Ac-PSMA-617	100 kBq/kg	3 (range, 1–7)	222.2 (47–443.2)	(−)	24 (86%)	15 (54%)	0 (0%)	After 2 wk	>50% of PSA decline, any PSA decline	PFS (8), OS (6)	10	Xerostomia, hematotoxicity
Kratochwil	2018	^{68}Ga-PSMA-11 PET/CT–positive or ^{99m}Tc-MIP-1427 scan–positive lesion with higher uptake than liver	40	^{225}Ac-PSMA-617	100 kBq/kg	3–5	169	181	35 (88%)	0 (0%)	9 (23%)	After 4 wk	>50% of PSA decline, any PSA decline	(−)	(−)	(−)

*Data in parentheses are range or interquartile range.
†Data in parentheses are number of events.
α-RLT = α-particle-emitting RLT; ALP = alkaline phosphatase.

TABLE 2
Quality Assessment of Included Studies Using Newcastle-Ottawa Scale

Author	Selection	Comparability	Outcome	Score
Feuerecker	⋆⋆⋆	⋆⋆	⋆⋆	7
Rosar	⋆⋆⋆	⋆	⋆⋆⋆	7
Sen	⋆⋆⋆	⋆	⋆⋆⋆	7
Zacherl	⋆⋆⋆	⋆	⋆⋆	6
Khreish	⋆⋆⋆	⋆	⋆⋆⋆	7
Satapathy	⋆⋆⋆	⋆	⋆⋆	6
Sathekge	⋆⋆⋆	⋆⋆	⋆⋆⋆	8
Yadav	⋆⋆⋆	⋆	⋆⋆⋆	7
Kratochwil	⋆⋆⋆	⋆	⋆⋆⋆	7

3 or 4 stars in Selection column AND 1 or 2 stars in Comparability column AND 2 or 3 stars in Outcome column = good quality; 2 stars in Selection column AND 1 or 2 stars in Comparability column AND 2 or 3 stars in Outcome column = fair quality; and 0 or 1 star in Selection column OR 0 star in Comparability column OR 0 or 1 star in Outcome column = poor quality.

Adverse Event

The pooled proportion of patients with xerostomia grade 1 or 2 was 62.81% after ^{225}Ac-PSMA RLT using a random-effects model (95% CI, 39.34%–83.46%), and the I^2 statistic was 92.04% ($P < 0.0001$; Cochran Q test). The pooled proportion of patients with anemia grade 3 or 4 was 14.39% after ^{225}Ac-PSMA RLT using a random-effects model (95% CI, 7.76%–22.63%), and the I^2 statistic was 59.32% ($P = 0.016$; Cochran Q test). The pooled proportion of patients with leukocytopenia grade 3 or 4 was 4.12% after ^{225}Ac-PSMA RLT using a random-effects model (95% CI, 0.97%–9.31%), and the I^2 statistic was 58.47% ($P = 0.018$; Cochran Q test). The pooled proportion of patients with thrombocytopenia grade 3 or 4 was 7.18% after ^{225}Ac-PSMA RLT using a random-effects model (95% CI, 2.70%–13.57%), and the I^2 statistic was 58.83% ($P = 0.017$; Cochran Q test) (Fig. 4; Table 4).

Meta-Regression

Meta-regression analysis for the therapeutic response showed no significant results (Supplemental Table 6). However, the results were significant for adverse events in terms of median PSA (leukocytopenia), median alkaline phosphatase (xerostomia and leukocytopenia), prechemotherapy (anemia and thrombocytopenia), prior ^{177}Lu-PSMA (leukocytopenia), and prior ^{223}Ra (leukocytopenia) (Table 5).

Publication Bias

Visual investigation of the funnel plots showed no evidence of publication bias for the therapeutic responses and adverse events of ^{225}Ac-PSMA RLT. Egger tests also demonstrated no evidence of funnel plot asymmetry (Fig. 5; Supplemental Fig. 1).

DISCUSSION

We investigated the effects of ^{225}Ac-PSMA RLT in patients with mCRPC through a meta-analysis. Around 61% of patients achieved more than a 50% PSA decline, and 84% of patients demonstrated any PSA decline after ^{225}Ac-PSMA RLT. The estimated mean PFS and mean OS were approximately 9 and 12 mo, respectively. Xerostomia grade 1 or 2 was observed in 63% of patients, and severe hematotoxicity was noted in approximately 4%–14% of patients.

In comparison with β-ray–emitting radionuclides, α-particle– emitting radionuclides offer several theoretic advantages (*12,28*). First, the relatively short range of penetration allows the selective killing of targeted tumor tissues while minimizing unwanted damage in the surrounding normal tissues. Second, higher-linear-energy transfer delivers intensive radiation to cancer cells, resulting in more effective DNA strand breakage and reducing the development of treatment resistance.

According to the Prostate Cancer Clinical Trials Working Group 3, the response to therapy of mCRPC patients should be assessed on the basis of PSA changes, and the commonly defined parameter is more than a 50% PSA

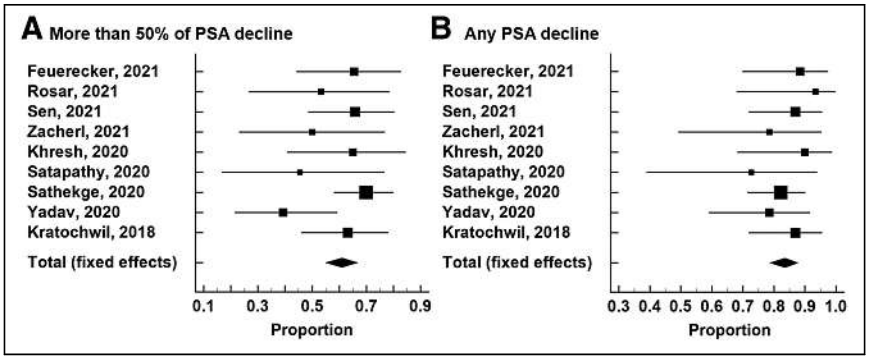

FIGURE 2. Forest plot for therapeutic responses after ^{225}Ac-PSMA RLT: more than 50% PSA decline (A) and any PSA decline (B).

TABLE 3
Summary of Therapeutic Responses and Survival Outcomes After ^{225}Ac-PSMA RLT

Therapeutic response and survival outcome	No. of studies	Model	Pooled estimate	95% CI of pooled estimate	I^2 (%)
>50% PSA decline	9	Fixed effects	60.99%	54.92%–66.83%	25.25
Any PSA decline	9	Fixed effects	83.57%	78.62%–87.77%	0.00
Mean PFS	6	Random effects	9.15 mo	6.69–11.03 mo	7.29
Mean OS	6	Random effects	11.77 mo	9.51–13.49 mo	0.00

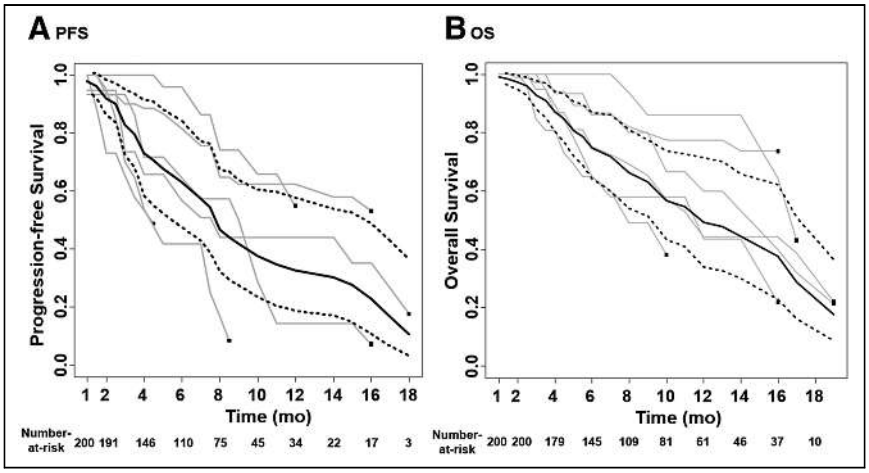

FIGURE 3. Survival outcome estimation after ^{225}Ac-PSMA RLT: PFS (A) and OS (B).

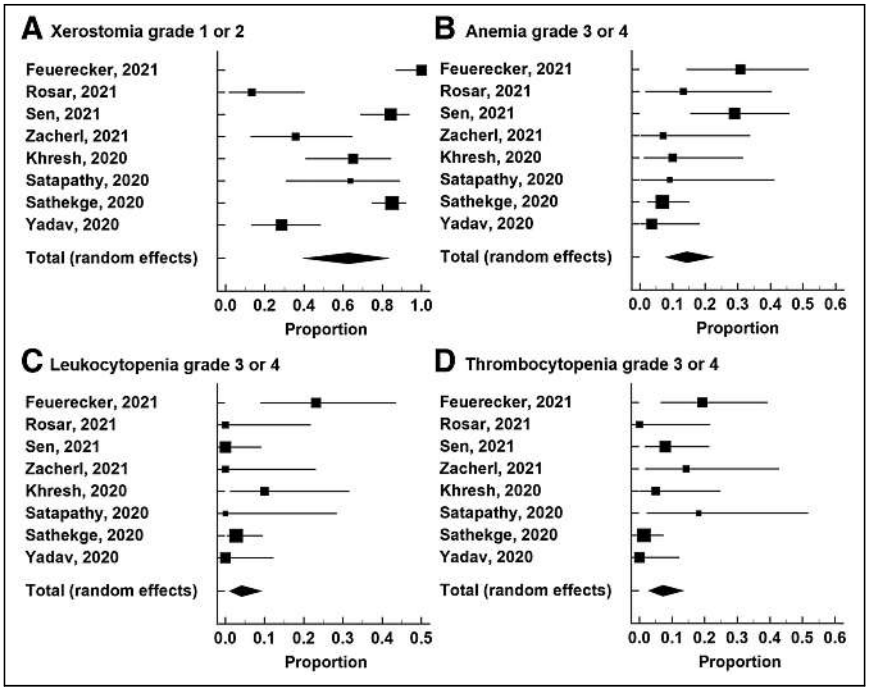

FIGURE 4. Forest plot for adverse events after ^{225}Ac-PSMA RLT: xerostomia grade 1 or 2 (A), anemia grade 3 or 4 (B), leukocytopenia grade 3 or 4 (C), and thrombocytopenia grade 3 or 4 (D).

decline (*29*). In our study, 61% (95% CI, 55%–67%) of patients showed more than a 50% PSA decline, which is higher than the response in a previous meta-analysis for ^{177}Lu-PSMA RLT (46%; 95% CI, 40%–53%) (*30*) and a previous phase 2 clinical trial of ^{177}Lu-PSMA-617 (57%) (*31*). As survival is an important marker in mCRPC patients, the secondary outcomes of our study were PFS and OS after ^{225}Ac-PSMA RLT. The median PFS (8 mo) and median OS (12 mo) in our study were similar to those (11 mo and 14 mo, respectively) in a previous meta-analysis of ^{177}Lu-PSMA RLT (*30*).

Despite the encouraging therapeutic response and survival of patients who received ^{225}Ac-PSMA RLT, dose reduction or discontinuation of the therapy is often required (*32*). Xerostomia is a major adverse event in ^{225}Ac-PSMA RLT (*33*), and our results revealed an incidence rate of 63% (95% CI, 39%–83%). A study highlighted the beneficial effects of sialendoscopy with steroid injection on salivary gland function after ^{225}Ac-PSMA RLT (*34*); however, it is an invasive procedure. Another study suggested that ^{225}Ac-PSMA/^{177}Lu-PSMA tandem therapy could improve salivary gland function (*17*). Therefore, more techniques are needed in addition to ^{225}Ac-PSMA RLT to protect salivary gland function (*35*). In a previous phase 2 clinical trial of ^{177}Lu-PSMA-617, the incidence rate of xerostomia grade 1 or 2 was 87%, which is similar to the incidence rate (63%; 95% CI, 39%–83%) in our study (*31*). Severe hematotoxicity is another common adverse event of ^{225}Ac-PSMA RLT in previous studies (*36*), and our study showed anemia grade 3 or 4 in 14% of cases (95% CI, 8%–23%), leukocytopenia grade 3 or 4 in 4% of cases (95% CI, 1%–9%), and thrombocytopenia grade 3 or 4 in 7% of cases (95% CI, 3%–14%). The incidence rates are similar to those in previous studies of ^{177}Lu-PSMA RLT (*10,30,37*). According to meta-regression analysis, tumor burden and previous damage to bone marrow and

TABLE 4
Summary of Adverse Events After ^{225}Ac-PSMA RLT

Adverse event	No. of studies	Model	Pooled proportion	95% CI of pooled proportion	I^2 (%)
Xerostomia grade 1 or 2	8	Random-effects	62.81%	39.34%–83.46%	92.04
Anemia grade 3 or 4	8	Random-effects	14.39%	7.76%–22.63%	59.32
Leukocytopenia grade 3 or 4	8	Random-effects	4.12%	0.97%–9.31%	58.47
Thrombocytopenia grade 3 or 4	8	Random-effects	7.18%	2.70%–13.57%	58.83

TABLE 5
Results of Meta-Regression Analysis for Adverse Event

Adverse event	Variable	No. of studies	Regression coefficient	*P*
Xerostomia grade 1 or 2	Median PSA	8	−0.0028	0.6448
	Median ALP	5	0.0700	0.0012*
	Prechemotherapy (%)	8	0.0049	0.8613
	Prior ^{177}Lu-PSMA (%)	8	0.0112	0.4814
	Prior ^{223}Ra (%)	8	−0.0061	0.9181
Anemia grade 3 or 4	Median PSA	8	0.0043	0.2482
	Median ALP	5	0.0194	0.0747
	Prechemotherapy (%)	8	0.0244	0.0235*
	Prior ^{177}Lu-PSMA (%)	8	0.0031	0.7643
	Prior ^{223}Ra (%)	8	0.0404	0.2761
Leukocytopenia grade 3 or 4	Median PSA	8	0.0092	0.0016*
	Median ALP	5	0.0352	0.0050*
	Prechemotherapy (%)	8	0.0237	0.2148
	Prior ^{177}Lu-PSMA (%)	8	0.0265	0.0013*
	Prior ^{223}Ra (%)	8	0.0990	0.0013*
Thrombocytopenia grade 3 or 4	Median PSA	8	0.0045	0.2505
	Median ALP	5	0.0216	0.2520
	Prechemotherapy (%)	8	0.0392	0.0208*
	Prior ^{177}Lu-PSMA (%)	8	0.0153	0.0937
	Prior ^{223}Ra (%)	8	0.0415	0.2755

*$P < 0.05$.
ALP = alkaline phosphatase.

salivary glands might adversely affect the toxicity of ^{225}Ac-PSMA RLT. Future studies should consider tumor burden and previous therapy history. Moreover, patient-based dosimetry is required to reduce adverse events and increase the antitumor activity of ^{225}Ac-PSMA RLT.

There were some limitations in this study. The included studies were few in number and had different patient profiles, and the therapeutic doses and cycles of ^{225}Ac-PSMA RLT were somewhat different. Differences in patient profiles likely contributed to the observed heterogeneity, which limits the generalizability of the pooled outcome estimates beyond the reported studies and requires careful interpretation, especially in the aspect of adverse events. Moreover, patient-based analyses could not be performed because of a lack of data on individual patients. In the future, prospective, randomized, multicenter clinical trials are needed to confirm the effects of ^{225}Ac-PSMA RLT.

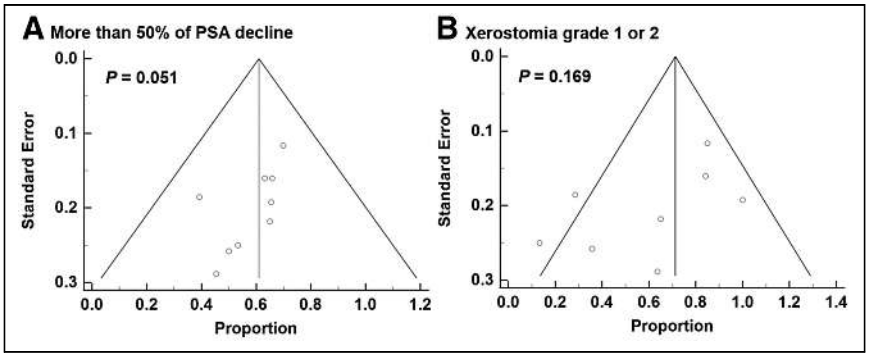

FIGURE 5. Funnel plot and Egger test for publication bias assessment: more than 50% PSA decline (A) and xerostomia grade 1 or 2 (B).

CONCLUSION

^{225}Ac-PSMA RLT may be an effective treatment option for patients with mCRPC. Our meta-analysis revealed that approximately 61% of patients (95% CI, 55%–67%) showed more than a 50% PSA decline and that 84% of patients (95% CI, 79%–88%) showed any PSA decline after ^{225}Ac-PSMA RLT. Among mCRPC patients who received ^{225}Ac-PSMA RLT, xerostomia (63% of patients; 95% CI, 39%–83%) was the most common adverse event, followed by severe hematotoxicity (4%–14% of patients; 95% CI, 1%–23%).

DISCLOSURE

No potential conflict of interest relevant to this article was reported.

ACKNOWLEDGMENTS

We thank Seonok Kim, Msc (Department of Clinical Epidemiology and Biostatistics, Asan Medical Center) for statistical analysis of survival outcomes.

KEY POINTS

QUESTION: What are the effects of ^{225}Ac-PSMA RLT in patients with mCRPC?

PERTINENT FINDINGS: More than a 50% PSA decline and any PSA decline were observed in about 61% (95% CI, 55%–67%) and 84% (95% CI, 79%–88%), respectively of patients after ^{225}Ac-PSMA RLT. The estimated mean PFS and mean OS were about 9 mo (95% CI, 7–11 mo) and 12 mo (95% CI, 10–13 mo), respectively. Xerostomia was the most common adverse event (63%; 95% CI = 39-83%), followed by severe anemia (14%; 95% CI, 6%–23%), severe leukocytopenia (4%; 95% CI, 1-9%), and severe thrombocytopenia (7%; 95% CI, 3%–14%).

IMPLICATIONS FOR PATIENT CARE: PSMA-targeted α-therapy using ^{225}Ac-PSMA may be a novel therapeutic option for mCRPC patients.

REFERENCES

1. Global Burden of Disease Cancer Collaboration; Fitzmaurice C, Allen C, Barber RM, et al. Global, regional, and national cancer incidence, mortality, years of life lost, years lived with disability, and disability-adjusted life-years for 32 cancer groups, 1990 to 2015: a systematic analysis for the global burden of disease study. *JAMA Oncol.* 2017;3:524–548.
2. Kessel K, Seifert R, Weckesser M, et al. Molecular analysis of circulating tumor cells of metastatic castration-resistant prostate cancer patients receiving ^{177}Lu-PSMA-617 radioligand therapy. *Theranostics.* 2020;10:7645–7655.
3. Marshall CH, Antonarakis ES. Emerging treatments for metastatic castration-resistant prostate cancer: immunotherapy, PARP inhibitors, and PSMA-targeted approaches. *Cancer Treat Res Commun.* 2020;23:100164.
4. Maurer T, Eiber M, Schwaiger M, Gschwend JE. Current use of PSMA-PET in prostate cancer management. *Nat Rev Urol.* 2016;13:226–235.
5. Siva S, Udovicich C, Tran B, Zargar H, Murphy DG, Hofman MS. Expanding the role of small-molecule PSMA ligands beyond PET staging of prostate cancer. *Nat Rev Urol.* 2020;17:107–118.
6. Bashir U, Tree A, Mayer E, et al. Impact of Ga-68-PSMA PET/CT on management in prostate cancer patients with very early biochemical recurrence after radical prostatectomy. *Eur J Nucl Med Mol Imaging.* 2019;46:901–907.
7. Weineisen M, Schottelius M, Simecek J, et al. Ga-68- and Lu-177-labeled PSMA I&T: optimization of a PSMA-targeted theranostic concept and first proof-of-concept human studies. *J Nucl Med.* 2015;56:1169–1176.
8. Kratochwil C, Giesel FL, Stefanova M, et al. PSMA-targeted radionuclide therapy of metastatic castration-resistant prostate cancer with Lu-177-labeled PSMA-617. *J Nucl Med.* 2016;57:1170–1176.
9. Kim YJ, Kim YI. Therapeutic responses and survival effects of ^{177}Lu-PSMA-617 radioligand therapy in metastatic castrate-resistant prostate cancer: a meta-analysis. *Clin Nucl Med.* 2018;43:728–734.
10. Rahbar K, Ahmadzadehfar H, Kratochwil C, et al. German multicenter study investigating ^{177}Lu-PSMA-617 radioligand therapy in advanced prostate cancer patients. *J Nucl Med.* 2017;58:85–90.
11. Hofman MS, Violet J, Hicks RJ, et al. [Lu-177]-PSMA-617 radionuclide treatment in patients with metastatic castration-resistant prostate cancer (LuPSMA trial): a single-centre, single-arm, phase 2 study. *Lancet Oncol.* 2018;19:825–833.
12. Parker C, Lewington V, Shore N, et al. Targeted alpha therapy, an emerging class of cancer agents: a review. *JAMA Oncol.* 2018;4:1765–1772.
13. Feuerecker B, Tauber R, Knorr K, et al. Activity and adverse events of actinium-225-PSMA-617 in advanced metastatic castration-resistant prostate cancer after failure of lutetium-177-PSMA. *Eur Urol.* 2021;79:343–350.
14. Rosar F, Krause J, Bartholomä M, et al. Efficacy and safety of [^{225}Ac]Ac-PSMA-617 augmented [^{177}Lu]Lu-PSMA-617 radioligand therapy in patients with highly advanced mCRPC with poor prognosis. *Pharmaceutics.* 2021;13:722.
15. Sen I, Thakral P, Tiwari P, et al. Therapeutic efficacy of ^{225}Ac-PSMA-617 targeted alpha therapy in patients of metastatic castrate resistant prostate cancer after taxane-based chemotherapy. *Ann Nucl Med.* 2021;35:794–810.
16. Zacherl MJ, Gildehaus FJ, Mittlmeier L, et al. First clinical results for PSMA targeted alpha therapy using ^{225}Ac-PSMA-I&T in advanced mCRPC patients. *J Nucl Med.* 2021;62:669–674.
17. Khreish F, Ebert N, Ries M, et al. ^{225}Ac-PSMA-617/^{177}Lu-PSMA-617 tandem therapy of metastatic castration-resistant prostate cancer: pilot experience. *Eur J Nucl Med Mol Imaging.* 2020;47:721–728.
18. Satapathy S, Mittal BR, Sood A, et al. Health-related quality-of-life outcomes with actinium-225-prostate-specific membrane antigen-617 therapy in patients with heavily pretreated metastatic castration-resistant prostate cancer. *Indian J Nucl Med.* 2020;35:299–304.
19. Sathekge M, Bruchertseifer F, Vorster M, et al. Predictors of overall and disease-free survival in metastatic castration-resistant prostate cancer patients receiving Ac-225-PSMA-617 radioligand therapy. *J Nucl Med.* 2020;61:62–69.
20. Yadav MP, Ballal S, Bal C. Efficacy and safety of ^{225}Ac-PSMA-617 targeted alpha therapy in metastatic castration-resistant prostate cancer patients. *Theranostics.* 2020;10:9364–9377.
21. Kratochwil C, Bruchertseifer F, Rathke H, et al. Targeted alpha-therapy of metastatic castration-resistant prostate cancer with ^{225}Ac-PSMA-617: swimmer-plot analysis suggests efficacy regarding duration of tumor control. *J Nucl Med.* 2018;59:795–802.
22. Zeng X, Zhang Y, Kwong JS, et al. The methodological quality assessment tools for preclinical and clinical studies, systematic review and meta-analysis, and clinical practice guideline: a systematic review. *J Evid Based Med.* 2015;8:2–10.
23. Combescure C, Foucher Y, Jackson D. Meta-analysis of single-arm survival studies: a distribution-free approach for estimating summary survival curves with random effects. *Stat Med.* 2014;33:2521–2537.
24. Parmar MK, Torri V, Stewart L. Extracting summary statistics to perform meta-analyses of the published literature for survival endpoints. *Stat Med.* 1998;17:2815–2834.
25. Sterne JA, Egger M. Funnel plots for detecting bias in meta-analysis: guidelines on choice of axis. *J Clin Epidemiol.* 2001;54:1046–1055.
26. Egger M, Davey Smith G, Schneider M, Minder C. Bias in meta-analysis detected by a simple, graphical test. *BMJ.* 1997;315:629–634.
27. Higgins JP, Thompson SG, Deeks JJ, Altman DG. Measuring inconsistency in meta-analyses. *BMJ.* 2003;327:557–560.
28. De Vincentis G, Gerritsen W, Gschwend JE, et al. Advances in targeted alpha therapy for prostate cancer. *Ann Oncol.* 2019;30:1728–1739.
29. Scher HI, Morris MJ, Stadler WM, et al. Trial design and objectives for castration-resistant prostate cancer: updated recommendations from the prostate cancer clinical trials working group 3. *J Clin Oncol.* 2016;34:1402–1418.
30. Yadav MP, Ballal S, Sahoo RK, Dwivedi SN, Bal C. Radioligand therapy with ^{177}Lu-PSMA for metastatic castration-resistant prostate cancer: a systematic review and meta-analysis. *AJR.* 2019;213:275–285.
31. Hofman MS, Violet J, Hicks RJ, et al. [^{177}Lu]-PSMA-617 radionuclide treatment in patients with metastatic castration-resistant prostate cancer (LuPSMA trial): a single-centre, single-arm, phase 2 study. *Lancet Oncol.* 2018;19:825–833.
32. Kratochwil C, Bruchertseifer F, Rathke H, et al. Targeted α-therapy of metastatic castration-resistant prostate cancer with ^{225}Ac-PSMA-617: dosimetry estimate and empiric dose finding. *J Nucl Med.* 2017;58:1624–1631.
33. Kratochwil C, Haberkorn U, Giesel FL. ^{225}Ac-PSMA-617 for therapy of prostate cancer. *Semin Nucl Med.* 2020;50:133–140.
34. Rathke H, Kratochwil C, Hohenberger R, et al. Initial clinical experience performing sialendoscopy for salivary gland protection in patients undergoing ^{225}Ac-PSMA-617 RLT. *Eur J Nucl Med Mol Imaging.* 2019;46:139–147.
35. Langbein T, Chaussé G, Baum RP. Salivary gland toxicity of PSMA radioligand therapy: relevance and preventive strategies. *J Nucl Med.* 2018;59:1172–1173.
36. Lawal IO, Bruchertseifer F, Vorster M, Morgenstern A, Sathekge MM. Prostate-specific membrane antigen-targeted endoradiotherapy in metastatic prostate cancer. *Curr Opin Urol.* 2020;30:98–105.
37. Violet J, Sandhu S, Iravani A, et al. Long-term follow-up and outcomes of retreatment in an expanded 50-patient single-center phase II prospective trial of ^{177}Lu-PSMA-617 theranostics in metastatic castration-resistant prostate cancer. *J Nucl Med.* 2020;61:857–865.

Head-to-Head Comparison of ^{68}Ga-PSMA-11 PET/CT and mpMRI with a Histopathology Gold Standard in the Detection, Intraprostatic Localization, and Determination of Local Extension of Primary Prostate Cancer: Results from a Prospective Single-Center Imaging Trial

Ida Sonni[1], Ely R. Felker[2], Andrew T. Lenis[3], Anthony E. Sisk[4], Shadfar Bahri[1,5], Martin Allen-Auerbach[1,5], Wesley R. Armstrong[1], Voraparee Suvannarerg[2,6], Teeravut Tubtawee[2,7], Tristan Grogan[8], David Elashoff[8], Matthias Eiber[1,9], Steven S. Raman[2], Johannes Czernin[1,5,10], Robert E. Reiter*[3,5,10], and Jeremie Calais*[1,5,10]

[1]Ahmanson Translational Theranostics Division, Department of Molecular and Medical Pharmacology, David Geffen School of Medicine, UCLA, Los Angeles, California; [2]Department of Radiology, David Geffen School of Medicine, UCLA, Los Angeles, California; [3]Department of Urology, UCLA, Los Angeles, California; [4]Department of Pathology, David Geffen School of Medicine, UCLA, Los Angeles, California; [5]Institute of Urologic Oncology, David Geffen School of Medicine, UCLA, Los Angeles, California; [6]Department of Radiology, Faculty of Medicine, Siriraj Hospital, Mahidol University, Bangkok, Thailand; [7]Department of Radiology, Prince of Songkla University, Hat Yai, Thailand; [8]Department of Medicine Statistics Core, UCLA, Los Angeles, California; [9]Department of Nuclear Medicine, Klinikum Rechts der Isar, Technical University of Munich, Munich, Germany; and [10]Jonsson Comprehensive Cancer Center, UCLA, Los Angeles, California

The role of prostate-specific membrane antigen (PSMA)–targeted PET in comparison to multiparametric MRI (mpMRI) in the evaluation of intraprostatic cancer foci is not well defined. The aim of our study was to compare the diagnostic performance of ^{68}Ga-PSMA-11 PET/CT (PSMA PET/CT), mpMRI, and PSMA PET/CT + mpMRI using 3 independent masked readers for each modality and with histopathology as the gold standard in the detection, intraprostatic localization, and determination of local extension of primary prostate cancer. **Methods:** Patients with intermediate- or high-risk prostate cancer who underwent PSMA PET/CT as part of a prospective trial (NCT03368547) and mpMRI before radical prostatectomy were included. Each imaging modality was interpreted by 3 independent readers who were unaware of the other modality result. A central majority rule was applied (2:1). Pathologic examination of whole-mount slices was used as the gold standard. Imaging scans and whole-mount slices were interpreted using the same standardized approach on a segment level and a lesion level. A "neighboring" approach was used to define imaging–pathology correlation for the detection of individual prostate cancer foci. Accuracy in determining the location, extraprostatic extension (EPE), and seminal vesicle invasion (SVI) of prostate cancer foci was assessed using receiver-operating-characteristic curve analysis. Interreader agreement was calculated using intraclass correlation coefficient analysis. **Results:** The final analysis included 74 patients (14 [19%] with intermediate risk and 60 [81%] with high risk). The cancer detection rate (lesion-based analysis) was 85%, 83%, and 87% for PSMA PET/CT, mpMRI, and PSMA PET/CT + mpMRI, respectively. The change in AUC was statistically significant between PSMA PET/CT + mpMRI and the 2 imaging modalities alone for delineation of tumor localization (segment-based analysis) ($P < 0.001$) but not between PSMA PET/CT and mpMRI ($P = 0.093$). mpMRI outperformed PSMA PET/CT in detecting EPE ($P = 0.002$) and SVI ($P = 0.001$). In the segment-level analysis, intraclass correlation coefficient analysis showed moderate reliability among PSMA PET/CT and mpMRI readers using a 5-point Likert scale (range, 0.53–0.64). In the evaluation of T staging, poor reliability was found among PSMA PET/CT readers and poor to moderate reliability was found for mpMRI readers. **Conclusion:** PSMA PET/CT and mpMRI have similar accuracy in the detection and intraprostatic localization of prostate cancer foci. mpMRI performs better in identifying EPE and SVI. For the T-staging evaluation of intermediate to high-risk prostate cancer, mpMRI should still be considered the imaging modality of reference. Whenever available, PSMA PET/MRI or the coregistration or fusion of PSMA PET/CT and mpMRI (PSMA PET/CT + mpMRI) should be used as it improves tumor extent delineation.

Key Words: PSMA PET/CT; prostate cancer; mpMRI; staging; T staging

J Nucl Med 2022; 63:847–854
DOI: 10.2967/jnumed.121.262398

Prostate cancer is the most common solid-organ malignancy in men, accounting for over 190,000 new diagnoses and over 33,000 deaths in 2020 (*1*). Distant extrapelvic staging in patients with unfavorable intermediate- and high-risk disease with cross-sectional imaging and bone scanning is recommended to guide initial therapy (*2,3*).

Current methods used to locally stage prostate cancer and identify the precise location of foci of disease rely on the results of systematic or targeted biopsies and multiparametric MRI (mpMRI). Although targeted biopsies have considerably improved the identification of clinically significant prostate cancer and even allowed for the tracking of biopsy cores over time, there is still over a 30% chance of missing

Received Apr. 18, 2021; revision accepted Sep. 26, 2021.
For correspondence or reprints, contact Ida Sonni (isonni@mednet.ucla.edu).
*Contributed equally to this work.
Guest Editor: Todd Peterson, Vanderbilt University
Published online Oct. 14, 2021.

clinically significant prostate cancer in men with multifocal disease (*4*). Further, in a cohort of men selected as candidates for focal therapy who underwent radical prostatectomy, nearly half had unidentified bilateral disease and would have been inadequately treated (*5*). Therefore, additional and perhaps complementary methods are needed to better characterize and identify clinically significant prostate cancer foci.

Prostate-specific membrane antigen (PSMA) is a transmembrane cell-surface protein overexpressed in prostate cancer cells relative to most other tissues (*6*). ^{68}Ga-PSMA-11 PET/CT (PSMA PET/CT) has been shown in prospective studies to be highly sensitive and specific for the identification of biochemically recurrent disease and to improve staging in patients with newly diagnosed disease (*7–9*). Previous studies comparing PSMA PET and mpMRI in the local staging of prostate cancer had overall discordant results. Although some studies found PSMA PET/CT to be superior to mpMRI (*10–12*), others showed no significant differences (*13,14*).

The goal of the current analysis was to compare the diagnostic performance of PSMA PET/CT, mpMRI, and the combination of the two (PSMA PET/CT + mpMRI) in the detection, intraprostatic localization, and determination of local extension of primary prostate cancer, with histopathology as the gold standard, using 3 masked independent readers for each modality.

MATERIALS AND METHODS

Study Design and Patient Population

We report here the results of an exploratory endpoint of a prospective trial conducted at UCLA (NCT03368547). The primary outcome of the trial was to evaluate the diagnostic performance (sensitivity, specificity, positive predictive value, and negative predictive value) of PSMA PET/CT for the detection of regional nodal metastases compared with histopathology at radical prostatectomy in patients with intermediate- to high-risk prostate cancer. The results of the primary endpoint analysis were the foundation of a new-drug application for ^{68}Ga-PSMA-11 (*15*) and will be reported separately.

For the current study, patients with biopsy-proven intermediate- or high-risk prostate cancer by NCCN (*16*) and enrolled in the pivotal trial were included in the analysis if they underwent initial staging with both PSMA PET/CT and mpMRI at our institution and subsequently underwent radical prostatectomy. Patients treated with androgen deprivation therapy were excluded from the analysis. The study was done under an investigational-new-drug approval protocol (IND 130649) and was approved by the local institutional review board (approval 16-001684).

mpMRI Image Acquisition

mpMRI was performed on a 3-T MRI system (Magnetom Trio, Skyra, or Verio; Siemens Medical Systems) using a standardized protocol with pelvic external phased-array coils. The mpMRI protocol included conventional multiplanar T2-weighted turbo spin-echo imaging, diffusion-weighted imaging, axial unenhanced T1-weighted imaging, and axial 3-dimensional fast-field echo dynamic contrast-enhanced imaging, as described previously (*17*). In addition, a small–field-of-view 3-dimensional axial turbo spin-echo T2-weighted sequence was performed using spatial and chemical-shift encoded excitation (SPACE; Siemens Healthcare), as described in detail previously (*17,18*).

PSMA PET/CT Image Acquisition

PSMA PET/CT images were acquired after intravenous injection of a median of 192.4 MBq of ^{68}Ga-PSMA-11 (interquartile range, 185–203.5 MBq) and a median uptake time of 61.5 min (interquartile range, 58–67 min) using a Biograph 64 or mCT PET/CT scanner (Siemens Medical Systems) (axial field of view, 22.1 cm). ^{68}Ga-PSMA-11 (Glu-NH-CO-NH-Lys-(Ahx)-[^{68}Ga(HBEDCC)]) was used as the PSMA ligand (*19*) and was obtained from the Biomedical Cyclotron Facility at UCLA. Oral and intravenous CT contrast media were administered unless contraindicated. A 5-mm slice thickness was used for the CT scan. All PET images acquired from pelvis to vertex were corrected for attenuation, dead time, random events, and scatter. The time per bed position was based on patient weight (*20*).

Image Analysis

For the purpose of this exploratory endpoint analysis, the PSMA PET/CT and mpMRI were read independently by 3 board-certified nuclear medicine physicians (with 4, 4, and 1 y of experience in interpreting PSMA PET/CT, that is, ~250 scans/y, and 19, 7, and 7 y of experience in interpreting oncologic PET/CT, that is, ~1,000 scans/y) and 3 radiologists (with 5, 5, and 12 y of experience in prostate mpMRI, that is, ~1,000 scans/y) using OsiriX and DynaCAD software, respectively (*21*).

All readers were aware of the presence of biopsy-proven prostate cancer but not of any other demographic, clinical, pathology, or imaging information. The readers were masked to the PSMA PET/CT and mpMRI clinical reports and to the other readers' findings. A standardized approach was used for imaging interpretation, assessing the presence, location, and size of prostate cancer foci (lesions) within the prostate. The analysis was conducted on an individual-lesion level and on a segment level.

Segment-Level Analysis (Prostate Cancer Localization). The prostate was divided into 12 segments using orthogonal axial planes for PSMA PET/CT and oblique axial planes for mpMRI: base, mid gland, and apex, defined as the upper, middle, and lower thirds, respectively, of the prostate; right/left and anterior/posterior were defined on axial views by a vertical line (sagittal plane) and horizontal line (coronal plane), respectively, passing through the center of the prostate (Fig. 1). The 12 segments used in this analysis represented a compromise between the 41 sectors used in the Prostate Imaging Reporting and Data System (PI-RADS) score and the sextants used for PSMA PET in previous studies (*12,22*). All PSMA PET/CT and mpMRI readers assigned each segment a score using a 5-point Likert scale (PSMA score, resembling scores using PSMA-RADS version 1.0 (*23,24*) and PI-RADS version 2.1 (*25*), respectively) based on the overall likelihood of prostate cancer. Each reader's 5-point scores were further converted into a binary score (1 and 2 = negative for cancer; 3, 4, and 5 = positive for cancer).

Lesion-Level Analysis (Prostate Cancer Detection). A maximum of 3 prostate cancer lesions was listed for each patient and described as the index, secondary, and tertiary lesions. Each reader recorded lesion size and other parameters (i.e., SUV_{max} for PSMA PET/CT and diffusion-weighted imaging PI-RADS score for mpMRI) to aid in the overall interpretation.

T Staging. The presence of bilateral intraprostatic disease, seminal vesicle invasion (SVI [T3b]), and extraprostatic extension (EPE [T3a]) was assessed visually in a binary manner (*26*).

Majority Rule and Central Reads. One lead investigator collected the imaging and pathology reads and conducted the final analysis. A central majority rule (2:1) was used to obtain the final reads for PSMA PET/CT and mpMRI. On a segment level, lesion level, and T-staging level, positivity for cancer involvement in the individual segment, lesion, or T level was considered present if at least 2 of 3 readers described it as positive for cancer.

PSMA PET/CT + mpMRI. PSMA PET/CT + mpMRI findings were obtained by combining the central majority reads from the 2 imaging modalities. If a segment, lesion, or T-level finding was described as positive on only 1 imaging modality (only on PET or mpMRI), it was automatically considered positive on PSMA PET/CT + mpMRI.

Histopathology Analysis

Whole-mount slices (tissue sections of 5 mm, histologic sections cut at 5 μm) were read by a genitourinary pathologist (with 7 y of whole-mount

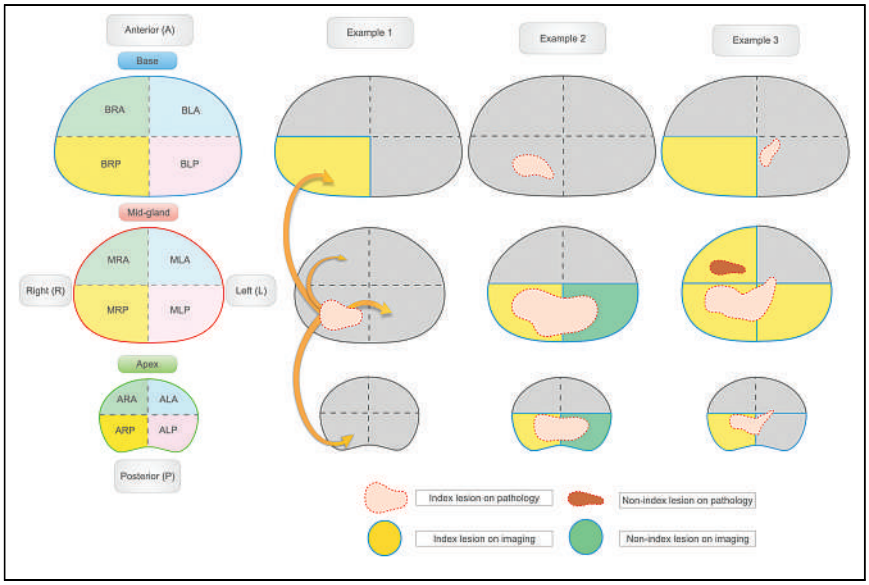

FIGURE 1. Prostate segmentation template and imaging–pathology correspondence for lesion-based analysis. Twelve-segment subdivision of prostate gland was used for standardized reads (left). Examples are shown of imaging–pathology correlation for lesion-level analysis using neighboring approach. Arrows indicate adjacent or neighboring segments. (Example 1) One lesion described on pathology as involving segment MRP, and 1 lesion identified by imaging as involving segment BRP. Imaging–pathology correlation: true-positive finding because BRP and MRP are neighboring segments. (Example 2) One large lesion described on pathology as involving segments ARP, MRP, BRP, ALP, and MLP, and 2 lesions identified by imaging (lesion 1, involving ARP and MRP [yellow segments], and lesion 2, involving ALP and MLP [green segments]). Imaging–pathology correlation: true-positive because one single lesion was described on pathology and correctly identified as cancer by imaging, even though described differently. (Example 3) Two lesions described on pathology (lesion 1, involving ALP, MLP, BLP, ALA, MLA, ARP, and MRP [pink lesion], and lesion 2, involving MRA [red lesion]), and 1 large lesion described by imaging as involving segments ARP, MRP, MLP, BRP, and MRA. Imaging–pathology correlation: 2 true-positive findings because 2 lesions were described on pathology, and both were described as cancer on imaging.

experience) who was masked to all imaging results using the lesion- and segment-level approach. Each lesion was assessed for the presence, location, and size of cancer foci and for the Gleason grade.

Benign prostatic lesions were not considered and were excluded from the detection analysis.

Imaging–Pathology Correlation

To define imaging–pathology correspondence on a lesion level, an adaptation of a previously described approach was used (Fig. 1) (*27*). This "neighboring" approach did not take into account the number of lesions and allowed the location correspondence to involve the immediately adjacent segments. This approach was used to overcome possible interpretation errors due to misregistration or misalignment deriving from deformation and shrinkage during fixation, commonly happening during whole-mount slice preparation (*28*), or due to use of different orientations by PSMA PET/CT, mpMRI, and pathologic examination of whole-mount slices (prostatectomy specimen cross section) to define the prostate base, mid-gland, and apical regions.

Statistical Analysis

Patient characteristics and study variables were summarized using mean and SD, median and interquartile range, or frequency and percentage, as appropriate. The diagnostic performance of PSMA PET/CT, mpMRI, and PSMA PET/CT + mpMRI were compared with histopathologic analysis on a lesion level and a segment level. Receiver-operating-characteristic curves and area under the receiver-operating-characteristic curves (AUCs) were obtained along with 95% CIs. AUC CI changes and *P* values were determined using the DeLong test.

Interrater agreement was calculated using the intraclass correlation coefficient (ICC) with the 2-way random-effects model, using absolute-agreement and single-measure options. Statistical analyses were performed using SPSS (version 25; IBM), and *P* values of less than 0.05 were considered statistically significant.

RESULTS

Patient Population

Between January 2017 and November 2019, 398 patients were enrolled in the trial. Seventy-four patients were included in the final analysis of this study (study flowchart in Fig. 2). The mean time was 43 d (SD, 39.9 d; range, −31 to 123 d) between PSMA PET/CT and mpMRI, 54.1 d (SD, 35.9 d; range, 6–180 d) between PSMA PET/CT and radical prostatectomy, and 100.8 d (SD, 53.4 d; range, 3–288 d) between mpMRI and radical prostatectomy. In 44 of 74 patients (59%), the mpMRI was performed before the biopsy, whereas all PSMA PET/CT scans were obtained after confirmation of a positive biopsy. Patient characteristics are summarized in Table 1.

Prostate Cancer Localization (Segment-Based Analysis)

In total, 425 of 888 segments (48%) were positive for cancer by pathologic examination. PSMA PET/CT, mpMRI, and PSMA PET/CT + mpMRI found cancer (majority reads) in 310 (35%), 314 (35%), and 405 (46%) segments, respectively. The results of the segment-level analysis and the receiver-operating-characteristic curve analysis per reader and per imaging modality are shown in Figures 3A and 3B. In total, 408 of 888 segments (46%) were described as harboring clinically significant prostate cancer (Gleason score $> 3 + 3 = 6$). The results of a subanalysis including only clinically significant lesions are shown in Supplemental Figure 1 (supplemental materials are available at http://jnm.snmjournals.org).

The AUCs for PSMA PET/CT, mpMRI, and PSMA PET/CT + mpMRI were 0.7 (sensitivity, 0.84; specificity, 0.55), 0.73 (sensitivity, 0.86; specificity, 0.59), and 0.77 (sensitivity, 0.77; specificity, 0.71), respectively. The change in AUC was statistically significant between PSMA PET/CT + mpMRI and the 2 imaging modalities alone ($P < 0.001$) but not between PSMA PET/CT and mpMRI ($P = 0.093$).

The AUCs for readers 1, 2, and 3 were 0.69, 0.69, and 0.66, respectively, using the PSMA score and 0.71, 0.72, and 0.71, respectively, using the PI-RADS score.

ICC analysis showed moderate reliability (*29*) among PSMA PET/CT and mpMRI readers using the 5-point Likert scale (PSMA PET/CT: reader 1/reader 2, 0.63; reader 1/reader 3, 0.53; and reader 2/reader 3, 0.64) (mpMRI: reader 1/reader 2, 0.61; reader 1/reader 3, 0.55; and reader 2/reader 3, 0.55).

Prostate Cancer Detection (Lesion-Based Analysis)

Pathologic examination of whole-mount slices identified 109 prostate cancer foci (74, 32, and 3 index, secondary, and tertiary lesions, respectively). Using the majority reads, PSMA PET/CT

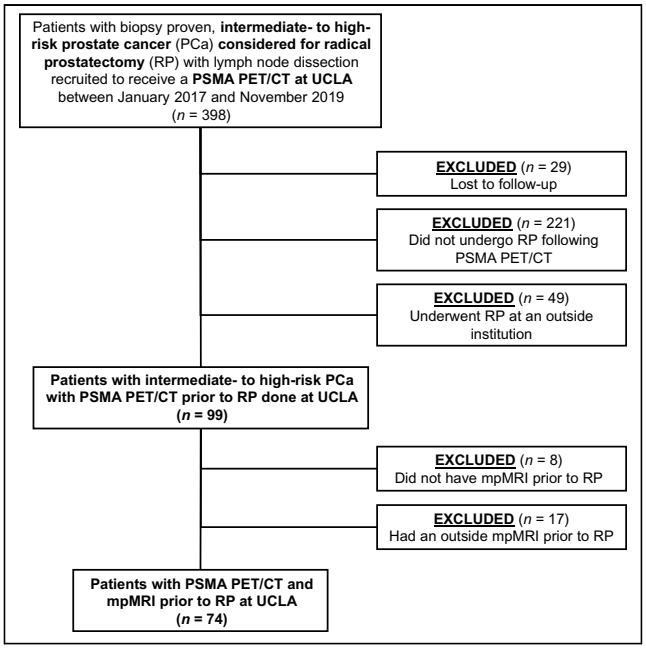

FIGURE 2. Study flowchart.

identified 111 lesions (74, 33, and 4 index, secondary, and tertiary lesions, respectively) and mpMRI identified 91 (74, 16, and 1 index, secondary, and tertiary lesions, respectively). The results of the lesion-level analysis and detection rates for all cancerous lesions are shown in Table 2. Individual readers' results are shown in Supplemental Table 1.

The detection rate was 85%, 83%, and 87% for PSMA PET/CT, mpMRI, and PSMA PET/CT + mpMRI, respectively. PSMA PET/CT identified 4 lesions (1 primary and 3 secondary) missed by mpMRI, whereas mpMRI identified 2 lesions (1 primary and 1 secondary) missed by PSMA PET/CT (Supplemental Table 2). Differences in detection rates between PSMA PET/CT and mpMRI were not statistically significant. The addition of PSMA PET/CT did not provide significant increases in detection rates over mpMRI alone.

Two separate subanalyses excluding small cancerous lesions (≤0.5 cm on histopathologic analysis) and lesions with a Gleason score of 3 + 3 = 6 were conducted.

Twelve of 109 lesions (11%) were graded as having a Gleason score of 3 + 3 = 6 (10 secondary lesions and 2 tertiary lesions). The overall detection rate excluding these lesions was 95% for PSMA PET/CT + mpMRI (vs. 92% for both PSMA PET/CT and mpMRI alone).

The detection rates for clinically significant lesions are summarized in Table 2.

Five of 109 lesions (5%) measured 0.5 cm or less on histopathologic analysis. Three of the 5 were not detected by either imaging modality, 1 of the 5 was identified by both, and 1 of the 5 was identified by mpMRI and PSMA PET/CT.

Figure 4 and Supplemental Figure 2 show examples of a PSMA PET/CT image, an mpMRI image, and a whole-mount slice from our cohort.

T Staging

Histopathologic examination detected bilateral disease in 37 of 74 patients (50%), SVI in 25 of 74 (34%), and EPE in 43 of 74 (58%). By majority reads, although mpMRI had a higher AUC than PSMA PET/CT for the detection of bilateral disease (0.65 vs. 0.54), this difference was not significantly different (DeLong test, $P = 0.138$) (Fig. 3). mpMRI had a better AUC than PSMA PET/CT for detection of EPE (0.79 vs. 0.59, $P = 0.002$) or SVI (0.84 vs. 0.63, $P = 0.001$). The use of PSMA PET/CT + mpMRI did not provide statistically significantly improvements over mpMRI alone.

Poor reliability was found among readers for PSMA PET/CT in the evaluation of bilaterality (ICC, 0.344), EPE (ICC, 0.203), and SVI (ICC, 0.081); moderately strong reliability was found among mpMRI readers for bilaterality (ICC, 0.693) and EPE (ICC, 0.580), and poor reliability was found for SVI (ICC, 0.305).

TABLE 1
Patient Characteristics

Characteristic	Data
No. of patients	74
Median age (y)	65 (IQR, 60–69)
Median PSA (ng/mL)	11.1 (IQR, 7.5–21.5)
Initial PSA (ng/mL)	
<10	29 (39%)
10–20	26 (35%)
>20	19 (26%)
D'Amico risk classification	
Intermediate risk	14 (19%)
High risk	60 (81%)
Presurgical Gleason grade	
3 + 3 = 6	1 (1%)
3 + 4 = 7	14 (20%)
3 + 5 = 8	2 (2%)
4 + 3 = 7	13 (19%)
4 + 4 = 8	24 (34%)
4 + 5 = 9	19 (27%)
5 + 4 = 9	1 (1%)

IQR = interquartile range; PSA = prostate-specific antigen level.

DISCUSSION

Using the majority reads of 3 masked independent readers for each imaging modality, our single-center study including 74 patients with intermediate- to high-risk prostate cancer found that PSMA PET/CT and mpMRI performed similarly in the detection and intraprostatic localization of primary prostate cancer, whereas mpMRI was superior for determining the T stage. The combined use of PSMA PET/CT and mpMRI improved tumor extent delineation (segment-level analysis) and allowed the identification of multifocal lesions but did not significantly improve the detection rates (lesion-level analysis) of the 2 modalities alone.

Current clinical guidelines (*2,30*) still recommend the use of cross-sectional imaging (CT or MRI) with bone scanning for extraprostatic distant staging in patients with intermediate- to high-risk prostate cancer. Several studies showed PSMA PET/CT to be superior to conventional imaging in the evaluation of N and M stage (*7–9,31–34*), but its added value in the definition of

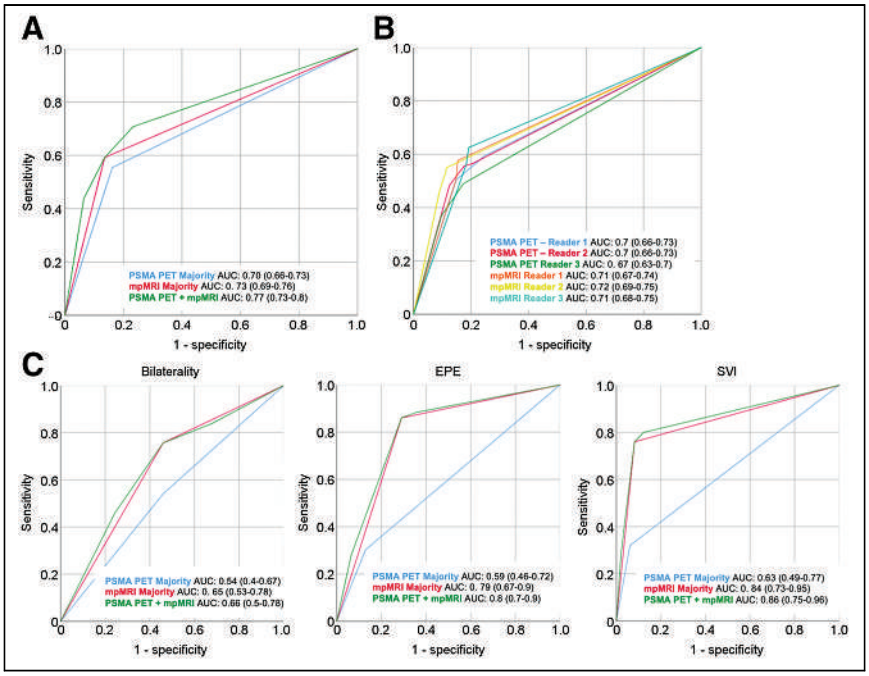

FIGURE 3. Prostate cancer localization (segment-based analysis) and T3 staging. (A and B) Receiver-operating-characteristic curves for segment-level analysis obtained for PSMA PET/CT and mpMRI majority reads (A) and using 1–5 PSMA and PI-RADS score for each individual reader (B). Graphs show change in AUC between PSMA PET/CT and mpMRI (95% CI, −0.01 to 0.07; P = 0.093), between PSMA PET/CT + mpMRI and PSMA PET/CT (95% CI, 0.05–0.1; $P < 0.001$), and between PSMA PET/CT + mpMRI and mpMRI (95% CI, 0.03–0.06; $P < 0.001$). (C) Receiver-operating-characteristic curves for PSMA PET/CT and mpMRI majority reads in evaluation of T staging. Graphs show change in AUC for bilateral disease (0.65 vs. 0.54, DeLong test, P = 0.138), change in AUC for EPE (0.79 vs. 0.59; 95% CI, 0.08–0.32; P = 0.002), and change in AUC for SVI (0.84 vs. 0.63; 95% CI, 0.09–0.33; P = 0.001).

T stage and in intraprostatic tumor localization is still controversial. The goal of our analysis was to compare the 2 imaging modalities in the definition of local disease and to evaluate whether the combination of the two provides any significant advantage. In this setting, the current literature shows discordant results, mostly due to small cohorts, different study designs, and different approaches in defining the imaging–pathology correlation. Unlike previous studies, the current work included a relatively large cohort of prospectively selected patients and involved a standardized approach to the correlation analysis of image findings and whole-mount pathology findings. An additional analysis on T staging was conducted, as well as a subanalysis on lesions with lower Gleason grades (3 + 3 = 6). In our study, PSMA PET/CT allowed the detection of 4 lesions missed by mpMRI (4/109 lesions [4%]) but also misclassified more lesions as prostate cancer (higher number of false-positives) at the expense of the positive predictive value. In a future study, we will conduct an additional analysis specifically looking at lesions negative on both imaging modalities, discordant cases, and the histopathologic features of these tumor foci.

The segment-level analysis for localization of prostate cancer foci did not show significant differences between PSMA PET/CT and mpMRI. Conversely, the addition of PSMA PET/CT to mpMRI significantly increased the number of segments detected, indicating that PSMA PET/CT improves the definition of tumor extent and can be an important aid in guiding the initial therapeutic approach (*5*). However, to confirm this finding, further investigation is needed.

The results were obtained using a neighboring approach to evaluate imaging–pathology correlation, which was applied to overcome the intrinsic limitation of the lack of registration between imaging and pathology. The use of PSMA PET/CT + mpMRI allowed the detection of 99% of primary lesions and 69% of secondary lesions, with an overall detection rate of 87% (vs. 85% and 83% for PSMA PET/CT and mpMRI alone, respectively) for all lesions, and 95% (vs. 92% for both PSMA PET/CT and mpMRI alone) for clinically significant lesions (Supplemental Table 2). On the basis of the improved performance of the combined PSMA PET/CT + mpMRI information, we recommend that discordant cases in clinical practice be evaluated in consensus between PET/CT and MRI readers or by a multidisciplinary prostate cancer tumor board. A lesion detected on only one of the modalities should be considered suggestive of cancer. Whenever possible, the PSMA PET/CT and mpMRI images should be coregistered using the CT and MRI prostate contours as a reference.

mpMRI performed significantly better than PSMA PET/CT in the definition of T stage, that is, SVI (T3b) and EPE (T3a), but not in the detection of bilateral disease (T2c). This finding is attributable mainly to the poor interreader agreement among the 3 PET readers for T staging, probably because of the lack of standardized criteria for T-staging evaluation by PSMA PET/CT. In contrast, since the correct definition of the locoregional extension of prostate cancer relies strongly on visualization of anatomic detail, the well-established higher soft-tissue contrast, higher spatial resolution, and multiplanar capability of mpMRI represent an advantage over CT and led to good agreement among the 3 MRI readers for T staging. However, interrater reliability was also poor for mpMRI readers in the evaluation of SVI. These results contrast with those of a previously published study involving 54 patients; in that study, PSMA PET/CT showed a higher sensitivity for the definition of EPE but not for SVI (*35*).

Intraprostatic tumor detection and localization by PSMA PET/CT relies largely on the PSMA PET signal because of the poor tissue contrast of CT. Consequently, lesion localization is highly dependent on the SUV visual scaling threshold used while interpreting the scans. The readers did not receive any specific recommendation on a fixed SUV threshold, as interpretation should be done by adapting the scaling to the background signal. This lack of a recommendation represents a source of interreader variability, but despite this inherent limitation for PSMA PET/CT, the segment-level analysis for localization of prostate cancer foci did not show significant differences from mpMRI.

Several studies showed that the combined use of PSMA PET/CT and mpMRI provides the best diagnostic accuracy overall (*10,14*). In light of the recent advent of PET/MRI, a growing body of literature is now available using PSMA PET/MRI, which has been shown by several groups to outperform each modality alone (*22,28,36–38*). However, the limited number of PET/MRI scanners available worldwide

TABLE 2
Prostate Cancer Detection Rates (Lesion-Based Analysis)

Parameter	All lesions			Clinically significant lesions		
	PSMA PET/CT	mpMRI	PSMA PET/CT + mpMRI	PSMA PET/CT	mpMRI	PSMA PET/CT + mpMRI
Index lesion (n = 74)	72 (97%)	72 (97%)	73 (99%)	72 (97%)	72 (97%)	73 (99%)
Secondary lesion (n = 32)	21 (66%)	19 (59%)	22 (69%)	18 (81%)	18 (81%)	19 (86%)
Tertiary lesion (n = 3)	0 (0%)	0 (0%)	0 (0%)	0 (0%)	0 (0%)	0 (0%)
Overall (detection rate)	93 (85%)	91 (83%)	95 (87%)	90 (93%)	90 (93%)	92 (95%)
Positive predictive value	97%	100%	—	94%	100%	—

Clinically significant lesions exclude lesions with Gleason score of 3 + 3 = 6. Differences in detection rate between PSMA PET/CT and mpMRI were not statistically significant.

and the associated high costs still limit its widespread use in clinical practice. The well-established superiority of PSMA PET/CT in N and M staging, combined with an enhanced ability to determine T stage and local extension with mpMRI, highlights the complementary role of each imaging modality and underscores the diagnostic potential of PSMA PET/MRI. If available, PSMA PET/MRI should be considered the modality of choice in the initial evaluation of patients with advanced prostate cancer. When a hybrid PET/MRI scanner is not available, the PSMA PET/CT and mpMRI images acquired separately should be coregistered using a reproducible multimodality DICOM image-fusion tool. If this is not possible, mpMRI remains the imaging modality of reference for the evaluation of T stage.

The main limitations of the study are the lack of coregistration between PSMA PET/CT, mpMRI, and pathology and the absence of the use of a 3-dimensional custom mold (*39–41*). To compensate for this inaccurate imaging–pathology correlation, we used a neighboring approach. Another limitation is that the interval between mpMRI and radical prostatectomy was not homogeneous, ranging between 3 and 288 d, raising the potential issue of inherent tumor changes over time. Additionally, sources of bias include the lack of negative controls in the cohort, as all imaging readers were aware of the presence of biopsy-proven high- to intermediate-risk prostate cancer, and patient selection, as we cannot rule out the exclusion of patients with a positive mpMRI result and a negative biopsy result from the final cohort. Thus, the PPV should be interpreted with caution. Finally, since we included only patients with intermediate- and high-risk disease, we were not able to address the clinical question of whether PSMA PET/CT can bring a significant added value to mpMRI in the initial staging of a heterogeneous population of patients with prostate cancer, including patients with less aggressive disease.

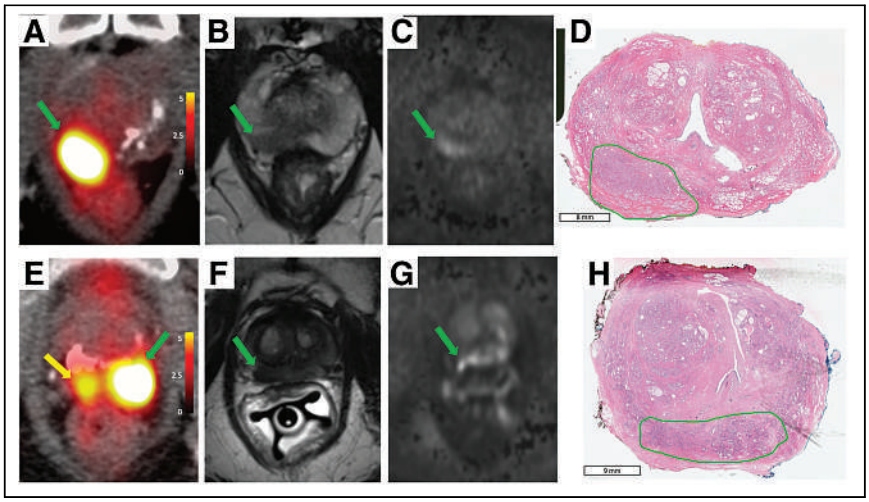

FIGURE 4. Two case examples from our cohort. (A–D) A 68-y-old patient (patient 4) with biopsy-proven prostate cancer with Gleason score of 3 + 4 = 7 and PSA of 8.6 ng/mL at time of PSMA PET/CT. Transverse PSMA PET/CT image (A), T2-weighted MR image (B), and high b-value diffusion-weighted MR image (C) show right-posterior mid-gland lesion (arrows). Whole-mount slice (D) shows 1 lesion, with Gleason score of 4 + 3 = 7, in same segment (contoured in green), and lesion showed EPE. There was good imaging–pathology correspondence (true-positive finding for both imaging modalities). All 6 readers correctly identified and described lesion. (E–H) A 69-y-old patient (patient 5) with biopsy-proven prostate cancer with Gleason score of 3 + 4 = 7 and PSA of 11.4 ng/mL at time of PSMA PET/CT. Transverse PSMA PET/CT image (E) shows 2 foci of increased PSMA uptake in right-posterior apex (yellow arrow) and left-posterior apex (green arrow). PSMA reader 1 correctly described 1 lesion involving left- and right-posterior apex; PSMA readers 2 and 3 described left and right foci as 2 separate lesions. T2-weighted MR image (F) shows hypointense lesion, and diffusion-weighted image (G) shows diffusion restriction in right- and left-posterior apex (arrow). All MRI readers correctly described only 1 lesion. Whole-mount slice (H) shows 1 lesion encompassing both right- and left-posterior apex (contoured in green) with EPE. This is an example of same lesion being described differently by PSMA PET/CT and whole-mount slice (true-positive finding for both imaging modalities).

CONCLUSION

In our study using the majority reads of 3 masked independent readers for each modality, both PSMA PET/CT and mpMRI performed well in the detection and intraprostatic localization of intermediate- to high-risk primary prostate cancer, whereas mpMRI had superior performance in the definition of T stage (T2c, T3). The combined use of PSMA PET/CT and mpMRI improved tumor extent delineation. Our findings highlight the complementarity of the 2 imaging modalities.

DISCLOSURE

Johannes Czernin is a board member of Sofie Biosciences and a founder of Trethera Therapeutics. Jeremie Calais reports prior consulting activities outside the submitted work for Advanced Accelerator Applications, Blue Earth Diagnostics, Curium Pharma, GE Healthcare, Janssen, POINT Biopharma, Progenics, Radiomedix, and Telix Pharmaceuticals. He is the recipient of grants from the Prostate Cancer Foundation (2020 Young Investigator Award 20YOUN05), the Society of Nuclear Medicine and Molecular Imaging (2019 Molecular Imaging Research Grant for Junior Academic Faculty), the Philippe Foundation Inc. (New York, USA), and the ARC Foundation (France) (International Mobility Award SAE20160604150). No other potential conflict of interest relevant to this article was reported.

KEY POINTS

QUESTION: How does PSMA PET/CT perform in the local evaluation of primary prostate cancer in comparison to mpMRI, and is there an additional value in the combined use of both PSMA PET/CT and MRI in comparison to mpMRI alone?

PERTINENT FINDINGS: The 2 imaging modalities showed similar accuracy in the detection and localization of intraprostatic lesions, whereas mpMRI performed better in the definition of EPE and SVI. The combined use of the two leads to better cancer localization but did not significantly improve detection rates.

IMPLICATIONS FOR PATIENT CARE: In this study, the addition of PSMA PET/CT to mpMRI did not significantly change local staging in patients with intermediate- to high-risk prostate cancer.

REFERENCES

1. Siegel RL, Miller KD, Jemal A. Cancer statistics, 2020. *CA Cancer J Clin.* 2020; 70:7–30.
2. Mottet N, Bellmunt J, Bolla M, et al. EAU-ESTRO-SIOG guidelines on prostate cancer. Part 1: screening, diagnosis, and local treatment with curative intent. *Eur Urol.* 2017;71:618–629.
3. Sanda MG, Cadeddu JA, Kirkby E, et al. Clinically localized prostate cancer: AUA/ASTRO/SUO guideline. Part I: risk stratification, shared decision making, and care options. *J Urol.* 2018;199:683–690.
4. Johnson DC, Raman SS, Mirak SA, et al. Detection of individual prostate cancer foci via multiparametric magnetic resonance imaging. *Eur Urol.* 2019;75: 712–720.
5. Johnson DC, Yang JJ, Kwan L, et al. Do contemporary imaging and biopsy techniques reliably identify unilateral prostate cancer? Implications for hemiablation patient selection. *Cancer.* 2019;125:2955–2964.
6. Silver DA, Pellicer I, Fair WR, Heston WD, Cordon-Cardo C. Prostate-specific membrane antigen expression in normal and malignant human tissues. *Clin Cancer Res.* 1997;3:81–85.
7. Hofman MS, Lawrentschuk N, Francis RJ, et al. Prostate-specific membrane antigen PET-CT in patients with high-risk prostate cancer before curative-intent surgery or radiotherapy (proPSMA): a prospective, randomised, multicentre study. *Lancet.* 2020;395:1208–1216.
8. Hope TA, Goodman JZ, Allen IE, Calais J, Fendler WP, Carroll PR. Metaanalysis of ^{68}Ga-PSMA-11 PET accuracy for the detection of prostate cancer validated by histopathology. *J Nucl Med.* 2019;60:786–793.
9. Lenis AT, Pooli A, Lec PM, et al. Prostate-specific membrane antigen positron emission tomography/computed tomography compared with conventional imaging for initial staging of treatment-naïve intermediate- and high-risk prostate cancer: a retrospective single-center study. *Eur Urol Oncol.* September 18, 2020 [Epub ahead of print].
10. Rhee H, Thomas P, Shepherd B, et al. Prostate specific membrane antigen positron emission tomography may improve the diagnostic accuracy of multiparametric magnetic resonance imaging in localized prostate cancer. *J Urol.* 2016; 196:1261–1267.
11. Berger I, Annabattula C, Lewis J, et al. ^{68}Ga-PSMA PET/CT vs. mpMRI for locoregional prostate cancer staging: correlation with final histopathology. *Prostate Cancer Prostatic Dis.* 2018;21:204–211.
12. Donato P, Roberts MJ, Morton A, et al. Improved specificity with ^{68}Ga PSMA PET/CT to detect clinically significant lesions "invisible" on multiparametric MRI of the prostate: a single institution comparative analysis with radical prostatectomy histology. *Eur J Nucl Med Mol Imaging.* 2019; 46:20–30.
13. Kalapara AA, Nzenza T, Pan HYC, et al. Detection and localisation of primary prostate cancer using ^{68}gallium prostate-specific membrane antigen positron emission tomography/computed tomography compared with multiparametric magnetic resonance imaging and radical prostatectomy specimen pathology. *BJU Int.* 2020; 126:83–90.
14. Chen M, Zhang Q, Zhang C, et al. Combination of ^{68}Ga-PSMA PET/CT and multiparametric MRI improves the detection of clinically significant prostate cancer: a lesion-by-lesion analysis. *J Nucl Med.* 2019;60:944–949.
15. Gallium Ga 68 PSMA-11 injection, for intravenous use. Food and Drug Administration website. https://www.accessdata.fda.gov/drugsatfda_docs/label/2020/212642s000lbl.pdf. Published 2020. Revised December 2020. Accessed March 22. 2022.
16. Schaeffer E, Srinivas S, Antonarakis ES, et al. NCCN guidelines insights: prostate cancer, version 1.2021. *J Natl Compr Canc Netw.* 2021;19:134–143.
17. Tan N, Lin WC, Khoshnoodi P, et al. In-bore 3-T MR-guided transrectal targeted prostate biopsy: prostate imaging reporting and data system version 2-based diagnostic performance for detection of prostate cancer. *Radiology.* 2017;283:130–139.
18. Natarajan S, Marks LS, Margolis DJ, et al. Clinical application of a 3D ultrasound-guided prostate biopsy system. *Urol Oncol.* 2011;29:334–342.
19. Eder M, Schäfer M, Bauder-Wüst U, et al. ^{68}Ga-complex lipophilicity and the targeting property of a urea-based PSMA inhibitor for PET imaging. *Bioconjug Chem.* 2012;23:688–697.
20. Halpern BS, Dahlbom M, Quon A, et al. Impact of patient weight and emission scan duration on PET/CT image quality and lesion detectability. *J Nucl Med.* 2004; 45:797–801.
21. Rosset A, Spadola L, Ratib O. OsiriX: an open-source software for navigating in multidimensional DICOM images. *J Digit Imaging.* 2004;17:205–216.
22. Eiber M, Weirich G, Holzapfel K, et al. Simultaneous ^{68}Ga-PSMA HBED-CC PET/MRI improves the localization of primary prostate cancer. *Eur Urol.* 2016;70: 829–836.
23. Rowe SP, Pienta KJ, Pomper MG, Gorin MA. Proposal for a structured reporting system for prostate-specific membrane antigen-targeted PET imaging: PSMA-RADS version 1.0. *J Nucl Med.* 2018;59:479–485.
24. Rowe SP, Pienta KJ, Pomper MG, Gorin MA. PSMA-RADS version 1.0: a step towards standardizing the interpretation and reporting of PSMA-targeted PET imaging studies. *Eur Urol.* 2018;73:485–487.
25. Turkbey B, Rosenkrantz AB, Haider MA, et al. Prostate imaging reporting and data system version 2.1: 2019 update of prostate imaging reporting and data system version 2. *Eur Urol.* 2019;76:340–351.
26. Paner GP, Stadler WM, Hansel DE, Montironi R, Lin DW, Amin MB. Updates in the eighth ed. of the tumor-node-metastasis staging classification for urologic cancers. *Eur Urol.* 2018;73:560–569.
27. Turkbey B, Pinto PA, Mani H, et al. Prostate cancer: value of multiparametric MR imaging at 3 T for detection–histopathologic correlation. *Radiology.* 2010; 255:89–99.
28. Hicks RM, Simko JP, Westphalen AC, et al. Diagnostic accuracy of ^{68}Ga-PSMA-11 PET/MRI compared with multiparametric MRI in the detection of prostate cancer. *Radiology.* 2018;289:730–737.
29. Koo TK, Li MY. A guideline of selecting and reporting intraclass correlation coefficients for reliability research. *J Chiropr Med.* 2016;15:155–163.
30. Lam TBL, MacLennan S, Willemse PM, et al. EAU-EANM-ESTRO-ESUR-SIOG prostate cancer guideline panel consensus statements for deferred treatment with curative intent for localised prostate cancer from an international collaborative study (DETECTIVE study). *Eur Urol.* 2019; 76:790–813.
31. Kim SJ, Lee SW, Ha HK. Diagnostic performance of radiolabeled prostate-specific membrane antigen positron emission tomography/computed tomography for primary lymph node staging in newly diagnosed intermediate to high-risk prostate cancer patients: a systematic review and meta-analysis. *Urol Int.* 2019; 102:27–36.

32. Koschel S, Murphy DG, Hofman MS, Wong LM. The role of prostate-specific membrane antigen PET/computed tomography in primary staging of prostate cancer. *Curr Opin Urol.* 2019;29:569–577.
33. Perera M, Papa N, Roberts M, et al. Gallium-68 prostate-specific membrane antigen positron emission tomography in advanced prostate cancer: updated diagnostic utility, sensitivity, specificity, and distribution of prostate-specific membrane antigen-avid lesions—a systematic review and meta-analysis. *Eur Urol.* 2020;77:403–417.
34. Zacho HD, Nielsen JB, Haberkorn U, Stenholt L, Petersen LJ. ^{68}Ga-PSMA PET/CT for the detection of bone metastases in prostate cancer: a systematic review of the published literature. *Clin Physiol Funct Imaging.* October 29, 2017 [Epub ahead of print].
35. Chen M, Zhang Q, Zhang C, et al. Comparison of ^{68}Ga-prostate-specific membrane antigen (PSMA) positron emission tomography/computed tomography (PET/CT) and multi-parametric magnetic resonance imaging (MRI) in the evaluation of tumor extension of primary prostate cancer. *Transl Androl Urol.* 2020;9:382–390.
36. Grubmüller B, Baltzer P, Hartenbach S, et al. PSMA ligand PET/MRI for primary prostate cancer: staging performance and clinical impact. *Clin Cancer Res.* 2018; 24:6300–6307.
37. Muehlematter UJ, Burger IA, Becker AS, et al. Diagnostic accuracy of multiparametric MRI versus ^{68}Ga-PSMA-11 PET/MRI for extracapsular extension and seminal vesicle invasion in patients with prostate cancer. *Radiology.* 2019; 293:350–358.
38. Thalgott M, Düwel C, Rauscher I, et al. One-stop-shop whole-body ^{68}Ga-PSMA-11 PET/MRI compared with clinical nomograms for preoperative T and N staging of high-risk prostate cancer. *J Nucl Med.* 2018;59:1850–1856.
39. Priester A, Natarajan S, Khoshnoodi P, et al. Magnetic resonance imaging underestimation of prostate cancer geometry: use of patient specific molds to correlate images with whole mount pathology. *J Urol.* 2017;197: 320–326.
40. Priester A, Wu H, Khoshnoodi P, et al. Registration accuracy of patient-specific, three-dimensional-printed prostate molds for correlating pathology with magnetic resonance imaging. *IEEE Trans Biomed Eng.* 2019;66: 14–22.
41. Wu HH, Priester A, Khoshnoodi P, et al. A system using patient-specific 3D-printed molds to spatially align in vivo MRI with ex vivo MRI and whole-mount histopathology for prostate cancer research. *J Magn Reson Imaging.* 2019;49:270–279.

^{18}F-DCFPyL PET Acquisition, Interpretation, and Reporting: Suggestions After Food and Drug Administration Approval

Hong Song[1], Andrei Iagaru[1], and Steven P. Rowe[2]

[1]*Division of Nuclear Medicine and Molecular Imaging, Department of Radiology, Stanford University, Stanford, California; and*
[2]*Division of Nuclear Medicine and Molecular Imaging, Department of Radiology and Radiological Science, Johns Hopkins University, Baltimore, Maryland*

Recently, ^{18}F-DCFPyL was approved by the Food and Drug Administration for evaluation before definitive therapy and for biochemical recurrence. Here, we focus on the key data that justify the clinical use of ^{18}F-DCFPyL, as well as those aspects of protocol implementation and image interpretation that are important to the nuclear medicine physicians and radiologists who will interpret ^{18}F-DCFPyL PET/CT and PET/MRI scans.

^{18}F-DCFPYL

^{18}F-DCFPyL is a urea-based small-molecule inhibitor of prostate-specific membrane antigen (PSMA) that was developed at Johns Hopkins University in the wake of promising results with a first-generation PSMA PET tracer, ^{18}F-DCFBC (*1,2*). Although the idea for urea-based agents for prostate cancer PET can be traced back to the 1990s, the field began to take off in earnest with the preclinical evaluation of the first PSMA PET agent, ^{11}C-DCMC (also known as ^{11}C-MCG), in 2002 (*3*), followed by its evaluation in an experimental model of prostate cancer, alongside the radiohalogen, ^{125}I-DCIT, in 2005 (*4*). Radiometal agents targeting PSMA were initially described a few years later (*5*).

Initial clinical evaluation of ^{18}F-DCFPyL demonstrated high tumor uptake, comparable to that of ^{68}Ga-PSMA-11 and improved relative to ^{18}F-DCFBC, as well as favorable clearance, with normal-tissue distribution resulting in a radiation dose within the limits required by the Food and Drug Administration (*6*). Semiquantitative and quantitative studies have confirmed the consistency and repeatability of ^{18}F-DCFPyL uptake in normal organs and in metastatic prostate cancer, with the distribution being only minimally altered by variability in tumor burden (*7*).

In newly diagnosed, high-risk prostate cancer, accurate staging is crucial to guide appropriate treatment decisions. The phase II/III prospective, multicenter OSPREY trial, which accrued 252 patients with high-risk prostate cancer into a cohort undergoing radical prostatectomy with extended pelvic lymph node dissection, reported very similar performance for ^{18}F-DCFPyL, with median specificity of 97.9% and sensitivity of 40.3% among 3 central reviewers (*8*). Compared with conventional imaging modalities, ^{18}F-DCFPyL PET/CT has shown improved diagnostic performance, with similar sensitivity (40%) but a 3-fold higher positive predictive value for detecting pelvic nodal metastasis. Those findings were comparable to observations for ^{68}Ga-PSMA-11 PET (*9*). In brief, for initial staging of prostate cancer, both imaging specialists and clinicians should be aware that any finding of focal uptake in a pelvic lymph node is almost certainly representative of true-positive disease but that a subset of patients with small-volume pelvic nodal involvement will have a false-negative scan result.

In the setting of biochemical recurrence, ^{18}F-DCFPyL PET has a high rate of lesion detection after primary definitive therapy. In a cohort of the phase II/III OSPREY study, ^{18}F-DCFPyL PET/CT had a sensitivity of 95.8% and a positive predictive value of 81.9% for extraprostatic lesions in 93 patients with radiologic evidence of recurrent or metastatic prostate cancer on conventional imaging (*8*).The phase III CONDOR study further established the utility of ^{18}F-DCFPyL for prostate cancer biochemical recurrence (*10*), by leveraging a novel composite truth standard referred to as correct localization rate. In 208 men with uninformative conventional imaging results and a median prostate-specific antigen level of 0.8 ng/mL, the detection efficiency among 3 central reviewers was 59%–66%, with a correct localization rate of 84.8%–87.0%. Most importantly, 63.9% of the patients had changes in management after ^{18}F-DCFPyL PET. In several separate prospective studies evaluating ^{18}F-DCFPyL-PET in biochemical recurrence, the overall detection rate was found to be 80.2% and increased with rising prostate-specific antigen (*11–15*). Biochemical recurrence is likely to be the most common indication for ^{18}F-DCFPyL PET, and most scans will have positive findings if they are read with the appropriate level of sensitivity.

An indication of increasing interest among many clinicians is the identification of oligometastatic disease to guide metastasis-directed therapy. A post hoc analysis of the prospective ORIOLE trial found that those men who had all ^{18}F-DCFPyL–avid lesions treated by stereotactic body radiation therapy had improved progression-free survival and distant-metastasis–free survival relative to those men who had only a subset of avid lesions treated (*16*). Careful communication between the interpreting radiologist or nuclear medicine physician and the oncology team will be necessary to ensure that maximum value for detecting and treating oligometastatic disease is realized.

^{18}F-DCFPYL PET VERSUS OTHER PSMA-TARGETING PET RADIOPHARMACEUTICALS

PSMA-targeted PET imaging can be performed with multiple compounds. Overall, for prostate cancer biochemical recurrence,

Received Aug. 1, 2021; revision accepted Sep. 9, 2021.
For correspondence or reprints, contact Andrei Iagaru (aiagaru@stanford.edu).
Published online Sep. 16, 2021.

DOI: 10.2967/jnumed.121.262989

PSMA-targeted PET imaging demonstrated a detection rate and positive predictive value higher than those of any other imaging modality (CT, bone scanning, MRI, ^{11}C-choline PET, ^{18}F-fluciclovine PET) (*17–20*). ^{68}Ga-PSMA-11 is the most widely studied PSMA agent. Clinical trials of ^{68}Ga-PSMA-11 (*21–23*) or ^{18}F-DCFPyL (*8,10*) with large cohorts have shown excellent and comparable detection rates in both prostate cancer staging and biochemical recurrence. Few studies directly compared ^{18}F-DCFPyL and ^{68}Ga-PSMA-11. Hammes et al. found no differences in uptake between ^{18}F-DCFPyL and ^{68}Ga-PSMA-11 in bone tissue not affected by osseous metastasis in 21 patients with biochemical recurrence, suggestive of similar negative predictive value (*24*). In a small cohort of 14 patients with biochemical recurrence, ^{18}F-DCFPyL PET detected more lesions than ^{68}Ga-PSMA-11 did, with a significantly higher mean SUV_{max} and tumor-to-background ratio (*25*). The higher SUV_{max} of detected lesions on ^{18}F-DCFPyL PET could be clinically relevant in detecting small lesions such as lymph nodes. One advantage of ^{18}F-DCFPyL over ^{68}Ga-PSMA-11 is that ^{18}F-DCFPyL can be commercially produced and distributed, making it widely available to prostate cancer patients, potentially leading to a paradigm change in clinical management of prostate cancer. However, cyclotron-produced ^{68}Ga will allow for wider availability of ^{68}Ga-PSMA-11 as well. An in-depth review of other ^{18}F-labeled PSMA targeting agents was previously published (*26*).

IMAGING PROTOCOLS

Both PET/CT and PET/MRI systems have been used for ^{18}F-DCFPyL PET imaging. For prostate cancer patients, the same protocol has been used for both primary staging and biochemical recurrence. Patients do not need to fast before ^{18}F-DCFPyL injection. They are instructed to drink water (1–2 glasses) to ensure adequate hydration before receiving the ^{18}F-DCFPyL, and they are encouraged to void frequently for the first few hours after ^{18}F-DCFPyL administration to reduce radiation exposure. No diuresis is necessary, although for some patients it may be helpful to clear radioactive urine out of the ureters to decrease equivocal findings.

A fixed ^{18}F-DCFPyL dose of 333 MBq has been used. Images are typically acquired from the mid thighs to vertex. For PET/CT, either low-dose CT or diagnostic CT with intravenous or oral contrast medium is performed for attenuation correction and anatomic correlation at the start of the ^{18}F-DCFPyL acquisition. For PET/MRI, pelvic multiparametric MRI is performed after ^{18}F-DCFPyL administration, with simultaneous pelvic PET acquired between 45 and 60 min. Fast whole-body MRI is then performed, followed by a whole-body PET acquisition between 60 and 120 min.

No differences in lesion uptake were observed between patients who fasted at least 6 h before ^{18}F-DCFPyL injection and patients who did not fast, although fasting resulted in higher uptake in the submandibular gland, liver, and spleen (*27*). Forced diuresis with furosemide reduced the intensity of ^{18}F-DCFPyL uptake in the ureters, kidneys, and bladder, especially at 120 min after injection with late diuresis at 85 min (*28*). However, forced diuresis could interrupt the PET acquisition or require catherization in patients with incontinence, leading to a risk of infection and urinary discomfort and slowing the technologist workflow. Wondergem et al. found that ^{18}F-DCFPyL PET/CT detected more lesions with significantly higher lesion uptake at 120 min than at 60 min after ^{18}F-DCFPyL administration in 65 prostate cancer patients (*29*). The choice between 60 and 120 min for the interval between injection and imaging will have to be a nuanced decision based on logistical considerations (e.g., number of available dosing rooms or PET center workflow limitations) versus the apparent improved yield for subtle lesions at a more delayed time point, especially for pelvic lymph node and prostate bed detection.

IMAGE INTERPRETATION

^{18}F-DCFPyL has intense physiologic uptake in normal tissues such as the salivary glands, lacrimal glands, kidneys, ureters, and bladder, as well as moderate uptake in the liver, spleen, and proximal bowel. Knowledge of normal-tissue distribution and uptake is important since aggressive windowing may be required to detect small lesions within and adjacent to normal tissues with high uptake. Because of ^{18}F-DCFPyL excretion through the urinary system, lesion detection in the prostate bed and pelvis may be limited, especially in primary staging, and readers will need to be diligent in appropriately windowing and using multiplanar reformatted images to maximize sensitivity for subtle local tumors or recurrences.

Typical patterns of local recurrence and metastatic spread of prostate cancer include the prostate bed; the regional lymph nodes, with extension to the retroperitoneal and extrapelvic lymph nodes; osseous metastases; and other soft-tissue metastases such as the lungs, adrenal glands, liver, or dura when widespread metastatic disease has occurred. Mild uptake in atypical locations for prostate cancer metastases should be interpreted with caution. In addition, caution is needed when interpreting ^{18}F-DCFPyL uptake in bone lesions, especially solitary bone lesions, since PSMA uptake has been shown in both posttraumatic foci and many benign bone lesions. Generally, ^{18}F-DCFPyL is considered superior to bone scanning for lesion detection (*18*), and ^{18}F-DCFPyL has sensitivity nearly identical to that of ^{18}F-NaF, although the specificity of these findings was not assessed (*30*).

PEARLS AND PITFALLS

Although PSMA-based PET imaging has high positive predictive values, PSMA is known to be expressed in normal tissues at physiologic levels, in benign processes, and in some other malignancies. Interpretation of ^{18}F-DCFPyL PET finding should therefore be done with consideration of patient history, findings on other imaging modalities, and common pitfalls. Although a complete discussion of potential interpretive pitfalls is beyond the scope of this text, the reader is encouraged to review more extensive discussions (*31,32*). An in-depth discussion of PSMA PET in nonprostate malignancies has been previously published (*33*).

The peripheral ganglia are one of the most common sites for ^{18}F-DCFPyL accumulation; up to 97% of patients can have uptake in at least one peripheral ganglion, often in the lumbar and cervical dorsal root ganglia, the cervicothoracic and stellate ganglia, or the celiac ganglia. Most peripheral ganglia are located at anatomic sites clearly separated from common nodal stations, except the celiac ganglia, which can be misinterpreted as retroperitoneal lymph nodes. The celiac ganglia are near the celiac trunk origin and are typically linear, with mild ^{18}F-DCFPyL uptake, whereas metastatic lymph nodes are usually round with high ^{18}F-DCFPyL uptake.

Another common pitfall for PSMA PET is uptake in healing fractures or benign bone lesions. In fact, Chen et al. showed that most solitary rib lesions with PSMA uptake on ^{68}Ga-PSMA-11 PET have mild uptake and are benign (*34*). Other commonly encountered benign bone lesions such as Paget disease, fibrous dysplasia, hemangioma, and avascular necrosis have been reported

to have uptake with ^{18}F-DCFPyL or ^{68}Ga-PSMA-11. Correlation with findings on other imaging modalities such as radiography, CT, or MRI using bone marrow sequences is crucial for correctly identifying these benign lesions.

Pulmonary metastases in prostate cancer can occur, often with late metastatic disease, although there is a cohort of men with an underlying genetic profile that predisposes to recurrence in the lung. Several case reports have shown PSMA uptake in a selection of benign pulmonary pathologies, such as granulomatous disease and sarcoidosis, bronchiectasis, tuberculosis, and pneumoconiosis. PSMA uptake in isolated, symmetric pulmonary lesions without other typical sites of prostate cancer metastasis needs to be interpreted with caution and correlated with patient history, the results of other imaging modalities, and histologic sampling in select cases.

The fact that PSMA PET radiopharmaceuticals have no increased uptake in the central nervous system may facilitate the detection of brain metastases. However, ^{68}Ga-PSMA-11 uptake in subacute stroke may mimic brain metastasis. Other benign neurogenic tumors with PSMA uptake include meningioma, schwannoma, paraganglioma, and neurofibroma.

Benign soft-tissue pathologies were also reported to have increased ^{18}F-DCFPyL uptake, such as splenic hemangioma, adrenal adenoma, cylindroma, and elastofibroma dorsi.

Besides benign pathologies, PSMA uptake is increased in other malignancies, often related to accumulation of PSMA in neovascular endothelial cells, as opposed to tumor epithelial cells. Several case reports and case series have described ^{18}F-DCFPyL uptake in renal cell carcinoma, follicular lymphoma, differentiated thyroid cancer, and primary peripheral primitive neuroectodermal tumors. Knowing the patient history and the metastatic pattern of different malignancies can help establish the differential diagnosis of these lesions.

STRUCTURED REPORTING FOR ^{18}F-DCFPYL PET

Structured reports with standardized formats, categorization of findings, and interpretations are essential to improve communication with referring clinicians and promote consistency. The report should be clear, concise, complete, and clinically relevant. The final report should identify the patient and indicate the reason for the study, such as primary staging, evaluation of biochemical recurrence, or evaluation of treatment response. Relevant clinical history should be noted, including whether the patient has other malignancies or recent treatment with antihormonal therapy and whether imaging studies are available for comparison; if such studies are available, the procedure should be noted, including the radiopharmaceutical activity, whether intravenous or oral contrast medium was used, if applicable, and the imaging acquisition protocol. The findings should include the anatomic location, size, and intensity of PET uptake, preferably in SUV_{max} relevant to a normal-tissue reference such as blood pool, liver, or parotid gland uptake, as well as associated CT or MRI findings such as bone sclerosis. The final impression should have reasonable and clinically relevant conclusions and appropriate recommendations.

Several guidelines and interpretation standards have been proposed for PSMA-based PET reporting to improve accuracy and reproducibility among readers. The European Association of Nuclear Medicine and the Society of Nuclear Medicine and Molecular Imaging issued joint procedure guidelines and standardized interpretation criteria for prostate cancer imaging (*35,36*) proposing that all areas of increased radiotracer uptake higher than adjacent background uptake, in sites not expected to show physiologic uptake, are to be reported as anomalous. Anomalous sites of uptake are categorized as pathologic, anomalous, uncertain, nonpathologic, or normal on the basis of anatomic location, degree of uptake, and relevant clinical information. The final summary should identify the study results as normal or abnormal, and the question asked in the study indication should be addressed directly.

The Prostate Cancer Molecular Imaging Standardized Evaluation (PROMISE) criteria (*37*) proposed that lesions with an SUV_{mean} higher than that of liver are considered typical of prostate cancer. Each lesion is classified as positive, negative, or equivocal, and then a molecular imaging TNM classification is provided with consideration of clinical information and other imaging findings. The final diagnosis is positive, equivocal, or negative, with a 5-point-scale diagnostic level of certainty. The Food and Drug Administration recently approved aPROMISE, a machine learning tool developed to assist with image classification and reporting.

The PSMA Reporting and Data System (RADS) (*38*) proposed that lesions be classified into a 5-point scale, with higher numbers representing increasing likelihood of prostate cancer. The classification is based on the level of PSMA uptake, lesion sites that are typical or atypical of metastatic prostate cancer, and findings on corresponding anatomic imaging. The overall scan score is derived from the corresponding highest PSMA-RADS score assigned to individual detected lesions. This approach is likely most useful for patients with a limited number of lesions, such as in biochemical recurrence or oligometastatic disease.

Toriihara et al. compared these 3 proposed criteria in terms of interreader, intrareader, and intercriteria agreement and found good reproducibility of the 3 criteria in evaluating ^{68}Ga-PSMA-11 PET. However, there are interreader disagreements that suggest the need for further work to harmonize or improve the criteria (*39*). More recently, the European Association of Nuclear Medicine proposed standardized reporting guidelines, E-PSMA (*40*), based on a modified Delphi consensus process. Individual findings are classified as benign, probably benign, or equivocal; probable prostate cancer; or definite evidence of prostate cancer on the basis of PSMA uptake and an anatomic site of disease typical or atypical of prostate cancer. In addition, PSMA PET findings are classified as prostate and prostate bed, regional lymph nodes, or distant metastases on the basis of the molecular imaging TNM regional classification.

FUTURE DEVELOPMENTS

Recently, the phase III VISION trial showed that ^{177}Lu-PSMA-617 significantly improved radiographic progression-free survival in patients with metastatic castration-resistant prostate cancer (*41*). ^{68}Ga-PSMA-11 PET was used in the trial to screen PSMA-positive patients dependent on uptake relative to liver. Screening ^{18}F-DCFPyL PET for ^{177}Lu-PSMA-617 treatment is expected to provide similar sensitivity and specificity on the basis of prior clinical trials of these 2 agents, though additional clinical confirmation may be needed. Future use will likely include ^{18}F-DCFPyL biopsy guidance in men with suspected prostate cancer. ^{18}F-DCFPyL PET may be used to identify or better contour small tumors than does standard-of-care MRI and guide nonconventional focal therapies such as high-intensity focused ultrasound and cryosurgery in local recurrence after radiotherapy in the absence of metastatic disease (*42*). In the setting of castration-resistant prostate cancer, Fendler et al. showed that PSMA PET was able to detect distant metastases in 54.5% of

patients whose disease was classified as nonmetastatic by conventional imaging (*43*). Other indications for ^{18}F-DCFPyL PET may potentially include assessing treatment response after systemic therapy (*44*).

CONCLUSION

PSMA-targeted PET with ^{18}F-DCFPyL will be transformative within the prostate cancer imaging domain, as it is the first widely commercially available PSMA PET agent with approval from a major regulatory body. Radiologists and nuclear medicine physicians who will interpret ^{18}F-DCFPyL PET scans should be aware of the clinical data that have driven approval, as well as the potential interpretive pitfalls associated with this novel type of PET scan. Important points for interpreting physicians and referring clinicians to be aware of include, first, that ^{18}F-DCFPyL has moderate sensitivity but very high specificity for the identification of involved pelvic lymph nodes in patients undergoing primary staging; second, that ^{18}F-DCFPyL has excellent detection efficiency in patients with biochemical recurrence, even at low prostate-specific antigen values; and third, that ^{18}F-DCFPyL PET may be helpful in guiding therapy for patients with oligometastatic disease. Uptake of ^{18}F-DCFPyL in benign lesions, as well as in the neovasculature of nonprostate malignancies, should be understood, and all sites of uptake on a ^{18}F-DCFPyL PET scan should be interpreted in the context of the clinical scenario and known routes of spread of metastatic disease. Structured reporting frameworks are valuable in improving interpretive reliability and consistency.

DISCLOSURE

Progenics Pharmaceuticals provided ^{18}F-DCFPyL to Stanford University as part of a Research Access Program. Under a license agreement between Progenics (a wholly owned subsidiary of Lantheus) and the Johns Hopkins University, the University is entitled to royalties on an invention described in this article. This arrangement has been reviewed and approved by the Johns Hopkins University in accordance with its conflict-of-interest policies. Steven Rowe is a consultant for, and has received research funding from, Progenics. Andrei Iagaru is an unpaid consultant for Progenics. No other potential conflict of interest relevant to this article was reported.

REFERENCES

1. Chen Y, Pullambhatla M, Foss CA, et al. 2-(3-{1-carboxy-5-[(6-[^{18}F]fluoro-pyridine-3-carbonyl)-amino]-pentyl}-ureido)-pentanedioic acid, [^{18}F]DCFPyL, a PSMA-based PET imaging agent for prostate cancer. *Clin Cancer Res.* 2011;17:7645–7653.
2. Mease RC, Dusich CL, Foss CA, et al. *N*-[*N*-[(*S*)-1,3-dicarboxypropyl]carbamoyl]-4-[^{18}F]fluorobenzyl-L-cysteine, [^{18}F]DCFBC: a new imaging probe for prostate cancer. *Clin Cancer Res.* 2008;14:3036–3043.
3. Pomper MG, Musachio JL, Zhang J, et al. ^{11}C-MCG: synthesis, uptake selectivity, and primate PET of a probe for glutamate carboxypeptidase II (NAALADase). *Mol Imaging.* 2002;1:96–101.
4. Foss CA, Mease RC, Fan H, et al. Radiolabeled small-molecule ligands for prostate-specific membrane antigen: in vivo imaging in experimental models of prostate cancer. *Clin Cancer Res.* 2005;11:4022–4028.
5. Banerjee SR, Foss CA, Castanares M, et al. Synthesis and evaluation of technetium-99m- and rhenium-labeled inhibitors of the prostate-specific membrane antigen (PSMA). *J Med Chem.* 2008;51:4504–4517.
6. Szabo Z, Mena E, Rowe SP, et al. Initial evaluation of [^{18}F]DCFPyL for prostate-specific membrane antigen (PSMA)-targeted PET imaging of prostate cancer. *Mol Imaging Biol.* 2015;17:565–574.
7. Li X, Rowe SP, Leal JP, et al. Semiquantitative parameters in PSMA-targeted PET imaging with ^{18}F-DCFPyL: variability in normal-organ uptake. *J Nucl Med.* 2017;58:942–946.
8. Pienta KJ, Gorin MA, Rowe SP, et al. A phase 2/3 prospective multicenter study of the diagnostic accuracy of prostate specific membrane antigen PET/CT with ^{18}F-DCFPyL in prostate cancer patients (OSPREY). *J Urol.* 2021;206:52–61.
9. Yaxley JW, Raveenthiran S, Nouhaud FX, et al. Outcomes of primary lymph node staging of intermediate and high risk prostate cancer with ^{68}Ga-PSMA positron emission tomography/computerized tomography compared to histological correlation of pelvic lymph node pathology. *J Urol.* 2019;201:815–820.
10. Morris MJ, Rowe SP, Gorin MA, et al. Diagnostic performance of ^{18}F-DCFPyL-PET/CT in men with biochemically recurrent prostate cancer: results from the CONDOR phase III, multicenter study. *Clin Cancer Res.* 2021;27:3674–3682.
11. Song H, Harrison C, Duan H, et al. Prospective evaluation of ^{18}F-DCFPyL PET/CT in biochemically recurrent prostate cancer in an academic center: a focus on disease localization and changes in management. *J Nucl Med.* 2020;61:546–551.
12. Rousseau E, Wilson D, Lacroix-Poisson F, et al. A prospective study on ^{18}F-DCFPyL PSMA PET/CT imaging in biochemical recurrence of prostate cancer. *J Nucl Med.* 2019;60:1587–1593.
13. Rowe SP, Campbell SP, Mana-Ay M, et al. Prospective evaluation of PSMA-targeted ^{18}F-DCFPyL PET/CT in men with biochemical failure after radical prostatectomy for prostate cancer. *J Nucl Med.* 2020;61:58–61.
14. Mena E, Lindenberg ML, Turkbey IB, et al. ^{18}F-DCFPyL PET/CT imaging in patients with biochemically recurrent prostate cancer after primary local therapy. *J Nucl Med.* 2020;61:881–889.
15. Crocerossa F, Marchioni M, Novara G, et al. Detection rate of prostate specific membrane antigen tracers for positron emission tomography/computerized tomography in prostate cancer biochemical recurrence: a systematic review and network meta-analysis. *J Urol.* 2021;205:356–369.
16. Phillips R, Shi WY, Deek M, et al. Outcomes of observation vs stereotactic ablative radiation for oligometastatic prostate cancer: the ORIOLE phase 2 randomized clinical trial. *JAMA Oncol.* 2020;6:650–659.
17. Hofman MS, Lawrentschuk N, Francis RJ, et al. Prostate-specific membrane antigen PET-CT in patients with high-risk prostate cancer before curative-intent surgery or radiotherapy (proPSMA): a prospective, randomised, multicentre study. *Lancet.* 2020;395:1208–1216.
18. Rowe SP, Macura KJ, Mena E, et al. PSMA-based [^{18}F]DCFPyL PET/CT is superior to conventional imaging for lesion detection in patients with metastatic prostate cancer. *Mol Imaging Biol.* 2016;18:411–419.
19. Calais J, Fendler WP, Herrmann K, Eiber M, Ceci F. Comparison of ^{68}Ga-PSMA-11 and ^{18}F-fluciclovine PET/CT in a case series of 10 patients with prostate cancer recurrence. *J Nucl Med.* 2018;59:789–794.
20. Hicks RM, Simko JP, Westphalen AC, et al. Diagnostic accuracy of ^{68}Ga-PSMA-11 PET/MRI compared with multiparametric MRI in the detection of prostate cancer. *Radiology.* 2018;289:730–737.
21. Fendler WP, Calais J, Eiber M, et al. Assessment of ^{68}Ga-PSMA-11 PET accuracy in localizing recurrent prostate cancer: a prospective single-arm clinical trial. *JAMA Oncol.* 2019;5:856–863.
22. Ceci F, Castellucci P, Graziani T, et al. ^{68}Ga-PSMA-11 PET/CT in recurrent prostate cancer: efficacy in different clinical stages of PSA failure after radical therapy. *Eur J Nucl Med Mol Imaging.* 2019;46:31–39.
23. Maurer T, Gschwend JE, Rauscher I, et al. Diagnostic efficacy of ^{68}gallium-PSMA positron emission tomography compared to conventional imaging for lymph node staging of 130 consecutive patients with intermediate to high risk prostate cancer. *J Urol.* 2016;195:1436–1443.
24. Hammes J, Hohberg M, Tager P, et al. Uptake in non-affected bone tissue does not differ between [^{18}F]-DCFPyL and [^{68}Ga]-HBED-CC PSMA PET/CT. *PLoS One.* 2018;13:e0209613.
25. Dietlein M, Kobe C, Kuhnert G, et al. Comparison of [^{18}F]DCFPyL and [^{68}Ga]Ga-PSMA-HBED-CC for PSMA-PET imaging in patients with relapsed prostate cancer. *Mol Imaging Biol.* 2015;17:575–584.
26. Werner RA, Derlin T, Lapa C, et al. ^{18}F-labeled, PSMA-targeted radiotracers: leveraging the advantages of radiofluorination for prostate cancer molecular imaging. *Theranostics.* 2020;10:1–16.
27. Wondergem M, van der Zant FM, Vlottes PW, Knol RJJ. Effects of fasting on ^{18}F-DCFPyL uptake in prostate cancer lesions and tissues with known high physiologic uptake. *J Nucl Med.* 2018;59:1081–1084.
28. Wondergem M, van der Zant FM, Rafimanesh-Sadr L, Knol RJJ. Effect of forced diuresis during ^{18}F-DCFPyL PET/CT in patients with prostate cancer: activity in

ureters, kidneys and bladder and occurrence of halo artefacts around kidneys and bladder. *Nucl Med Commun.* 2019;40:652–656.
29. Wondergem M, van der Zant FM, Knol RJJ, Lazarenko SV, Pruim J, de Jong IJ. ^{18}F-DCFPyL PET/CT in the detection of prostate cancer at 60 and 120 minutes: detection rate, image quality, activity kinetics, and biodistribution. *J Nucl Med.* 2017;58:1797–1804.
30. Rowe SP, Li X, Trock BJ, et al. Prospective comparison of PET imaging with PSMA-targeted ^{18}F-DCFPyL versus Na^{18}F for bone lesion detection in patients with metastatic prostate cancer. *J Nucl Med.* 2020;61:183–188.
31. Sheikhbahaei S, Afshar-Oromieh A, Eiber M, et al. Pearls and pitfalls in clinical interpretation of prostate-specific membrane antigen (PSMA)-targeted PET imaging. *Eur J Nucl Med Mol Imaging.* 2017;44:2117–2136.
32. Sheikhbahaei S, Werner RA, Solnes LB, et al. Prostate-specific membrane antigen (PSMA)-targeted PET imaging of prostate cancer: an update on important pitfalls. *Semin Nucl Med.* 2019;49:255–270.
33. Salas Fragomeni RA, Amir T, Sheikhbahaei S, et al. Imaging of nonprostate cancers using PSMA-targeted radiotracers: rationale, current state of the field, and a call to arms. *J Nucl Med.* 2018;59:871–877.
34. Chen MY, Franklin A, Yaxley J, et al. Solitary rib lesions showing prostate-specific membrane antigen (PSMA) uptake in pre-treatment staging ^{68}Ga-PSMA-11 positron emission tomography scans for men with prostate cancer: benign or malignant? *BJU Int.* 2020;126:396–401.
35. Fendler WP, Eiber M, Beheshti M, et al. ^{68}Ga-PSMA PET/CT: joint EANM and SNMMI procedure guideline for prostate cancer imaging: version 1.0. *Eur J Nucl Med Mol Imaging.* 2017;44:1014–1024.
36. Fanti S, Minozzi S, Morigi JJ, et al. Development of standardized image interpretation for ^{68}Ga-PSMA PET/CT to detect prostate cancer recurrent lesions. *Eur J Nucl Med Mol Imaging.* 2017;44:1622–1635.
37. Eiber M, Herrmann K, Calais J, et al. Prostate Cancer Molecular Imaging Standardized Evaluation (PROMISE): proposed miTNM classification for the interpretation of PSMA-ligand PET/CT. *J Nucl Med.* 2018;59:469–478.
38. Rowe SP, Pienta KJ, Pomper MG, Gorin MA. PSMA-RADS version 1.0: a step towards standardizing the interpretation and reporting of PSMA-targeted PET imaging studies. *Eur Urol.* 2018;73:485–487.
39. Toriihara A, Nobashi T, Baratto L, et al. Comparison of 3 interpretation criteria for ^{68}Ga-PSMA11 PET based on inter- and intrareader agreement. *J Nucl Med.* 2020; 61:533–539.
40. Ceci F, Oprea-Lager DE, Emmett L, et al. E-PSMA: the EANM standardized reporting guidelines v1.0 for PSMA-PET. *Eur J Nucl Med Mol Imaging.* 2021;48:1626–1638.
41. Morris MJ, De Bono JS, Chi KN, et al. Phase III study of lutetium-177-PSMA-617 in patients with metastatic castration-resistant prostate cancer (VISION) [abstract]. *J Clin Oncol.* 2021;39(suppl):LBA4.
42. Schaeffer E, Srinivas S, Antonarakis ES, et al. NCCN guidelines insights: prostate cancer, version 1.2021. *J Natl Compr Canc Netw.* 2021;19:134–143.
43. Fendler WP, Weber M, Iravani A, et al. Prostate-specific membrane antigen ligand positron emission tomography in men with nonmetastatic castration-resistant prostate cancer. *Clin Cancer Res.* 2019;25:7448–7454.
44. Grubmüller B, Rasul S, Baltzer P, et al. Response assessment using [^{68}Ga]Ga-PSMA ligand PET in patients undergoing systemic therapy for metastatic castration-resistant prostate cancer. *Prostate.* 2020;80:74–82.

PET with a ^{68}Ga-Labeled FAPI Dimer: Moving Toward Theranostics

Muhsin H. Younis[1], Xiaoli Lan[2,3], and Weibo Cai[1]

[1]*Departments of Radiology and Medical Physics, University of Wisconsin–Madison, Madison, Wisconsin;* [2]*Department of Nuclear Medicine, Union Hospital, Tongji Medical College, Huazhong University of Science and Technology, Wuhan, China; and* [3]*Hubei Key Laboratory of Molecular Imaging, Wuhan, China*

See the associated article on page 862.

In recent years, quinoline-based fibroblast activation protein (FAP) inhibitors (FAPIs; e.g., FAPI-04 and FAPI-46) have shown promising results in the diagnosis of cancer and various other diseases, making them the hot spot of much productive research (*1*). However, one major issue is that these FAPI molecules have a relatively short tumor retention time, which may hamper the use of FAPI molecules for targeted radionuclide therapy applications. In this issue of *The Journal of Nuclear Medicine,* a novel dimeric FAPI molecule, ^{68}Ga-DOTA-2P(FAPI)$_2$, was designed and synthesized by Zhao et al. (*2*). This intriguing work moves the field forward by addressing an important issue in the development and optimization of FAPI-based tracers, that is, how to increase uptake and tracer retention in tumors for potential therapeutic or theranostic applications. Taking advantage of the multivalency effect, the dimeric FAPI tracer ^{68}Ga-DOTA-2P(FAPI)$_2$ demonstrated significantly higher tumor uptake in mouse tumor models than did ^{68}Ga-FAPI-46. More importantly, results from patient-derived xenograft models, healthy volunteers, and cancer patients also indicated that ^{68}Ga-DOTA-2P(FAPI)$_2$ has better tumor uptake and longer tumor retention time than ^{68}Ga-FAPI-46. Therefore, ^{68}Ga-DOTA-2P(FAPI)$_2$ could be a promising tracer for both diagnostic imaging and targeted radionuclide therapy (when ^{68}Ga is replaced by therapeutic isotopes such as ^{177}Lu, ^{90}Y, or ^{225}Ac) in malignant tumors with high FAP expression.

In general, FAPI-based radiotracers are a promising avenue for research in nuclear medicine. On the basis of the currently available data for lesion detection, the sensitivity of most FAPI-based PET/CT for all lesions falls in the range of 85%–100%, which is comparable to or even superior to that of ^{18}F-FDG PET/CT (*3*,*4*). FAPI-based tracers are especially superior for detecting gastrointestinal cancer, nasopharyngeal cancer, liver cancer, peritoneal carcinomatosis, and brain tumors. As part of this study (*2*), ^{68}Ga-DOTA-2P(FAPI)$_2$ PET/CT imaging in 3 cancer patients (1 with thyroid cancer, 1 with nasopharyngeal cancer, and 1 with hepatocellular carcinoma) showed a rapid and stable accumulation of the tracer in tumorous lesions. Tumor uptake of ^{68}Ga-DOTA-2P(FAPI)$_2$ in most lesions was significantly higher than that of ^{68}Ga-FAPI-46, leading to clearer visualization of primary lesions and metastases.

However, the relatively high level of physiologic uptake of ^{68}Ga-DOTA-2P(FAPI)$_2$ that was observed in the blood pool, thyroid, liver, and pancreas was not the case in previous FAPI-based PET/CT imaging. The high background uptake of ^{68}Ga-DOTA-2P(FAPI)$_2$ in these normal organs may result in relatively low tumor-to-background ratios, which may affect the lesion detection rate of ^{68}Ga-DOTA-2P(FAPI)$_2$ PET/CT in these organs. Therefore, from our perspective, monomeric FAPI-based tracers (e.g., ^{68}Ga-FAPI-04 and FAPI-46) are still recommended for diagnostic imaging purposes because of the rapid blood clearance and low background uptake, whereas DOTA-2P(FAPI)$_2$ may be more suitable for labeling with ^{177}Lu, ^{90}Y, or ^{225}Ac for future therapeutic applications. For the latter, the delayed blood pool radioactivity of radiolabeled DOTA-2P(FAPI)$_2$ may contribute to a relatively high bone marrow toxicity. As such, dosimetry estimation for major organs should be carefully investigated for safety dose limitation, when DOTA-2P(FAPI)$_2$ is labeled with ^{177}Lu or ^{90}Y or, potentially, α-emitters (e.g., ^{225}Ac or ^{213}Bi).

The applications of FAPI-based PET tracers are certainly not limited to lesion detection. Many investigators and stakeholders in the field would agree that the two other most advisable uses are the selection of cancer patients for treatments involving FAP-targeted radionuclide therapy and the quantitative and noninvasive monitoring of patients receiving such therapies. Considering that the next logical step is to explore the therapeutic efficacy of ^{177}Lu-DOTA-2P(FAPI)$_2$, ^{68}Ga-DOTA-2P(FAPI)$_2$ or ^{68}Ga-FAPI-46 PET/CT should certainly be investigated for precisely selecting the patients who will most likely benefit from FAP-targeted radionuclide therapy. Regarding therapeutic response monitoring, several studies have reported that ^{68}Ga-FAPI-04 PET/CT may be useful for evaluating the treatment response to chemotherapy (*5*,*6*). However, another study revealed that fibrosis induced by radiation exhibited high uptake of ^{68}Ga-FAPI-04 (*7*). Thus, FAPI-based PET/CT might be problematic in differentiating between residual or recurrent disease and postradiation inflammatory reactions. Consequently, the real potential of FAPI-based PET/CT in therapeutic response monitoring needs to be studied and confirmed with well-designed clinical investigations.

In the radioligand binding study, the half-maximal inhibitory concentration (IC_{50}) values for the monomeric and dimeric FAPI were

Received Oct. 18, 2021; revision accepted Nov. 1, 2021.

For correspondence or reprints contact Xiaoli Lan (xiaoli_lan@hust.edu.cn) or Weibo Cai (wcai@uwhealth.org).

Published online Nov. 5, 2021.

DOI: 10.2967/jnumed.121.263292

comparable (2.06 ± 1.84 nM vs. 3.68 ± 1.82 nM) (*2*). To our knowledge, if the dimerization can allow for simultaneous binding to 2 FAPs, then it should be observed (i.e., reflected by significantly different IC_{50} values) in this in vitro assay. However, increased avidity was not observed, meaning that only 1 FAPI is actually binding to FAP at any given time. We speculate that the distance between the 2 FAPI molecules in DOTA-2P$(FAPI)_2$ may not be enough to enable simultaneous binding. Nonetheless, the binding of 1 FAPI motif to FAP will increase the local concentration of a second FAPI motif in the vicinity. The locally enhanced FAPI concentration may explain the higher tumor uptake and retention of ^{68}Ga-DOTA-2P$(FAPI)_2$ than that of ^{68}Ga-FAPI-46. To further improve FAP-targeting capability, the distance between 2 (or more) FAPI molecules needs to be determined, optimized, and leveraged so that they can enable simultaneous binding of multiple FAPs. To the best of our knowledge, no dimer or multimer of FAPI has been reported to date, making this the first example. However, we predict that increasingly more such studies will soon appear in the literature.

This elegant and comprehensive study (*2*), which spans the entire translational spectrum of new tracer synthesis, in vitro characterization, preclinical investigation in patient-derived xenograft models, and pilot studies in healthy volunteers and cancer patients, is a prime example of translational research in the modern era. The head-to-head comparison between ^{68}Ga-DOTA-2P$(FAPI)_2$ and ^{68}Ga-FAPI-46 was also thorough, including blocking and histology studies to confirm FAP specificity in vivo, which provided invaluable information. The encouraging results of this work strongly suggest that future investigation into the anticancer therapeutic applications of a ^{177}Lu-labeled FAPI dimer or multimer such as ^{177}Lu-DOTA-2P$(FAPI)_2$ in patient-derived xenograft models is warranted, to explore whether multivalency could enhance the therapeutic efficacy when compared with a ^{177}Lu-labeled FAPI monomer (e.g., FAPI-46 or FAPI-04). If this investigation is proven to be successful, pilot clinical studies of ^{177}Lu-DOTA-2P$(FAPI)_2$ or other optimized multimeric FAPI ligands can follow.

In comparison to ^{177}Lu-FAPI-46, which has been clinically tested (*8*), a ^{177}Lu-labeled dimeric FAPI will likely be more efficacious, because of its higher uptake and longer retention time in the tumor tissue. Additionally, it could even compare with ^{177}Lu-FAP-2286, a novel FAP-targeting molecule with a cyclic peptide binding motif, which was reported to have a longer tumor retention time by Baum et al. (*9*) and hence could be useful to treat diverse adenocarcinomas. In addition, shortening the interval between treatments, increasing the radioactivity dose administered, or using α-emitters (e.g., ^{225}Ac, ^{213}Bi, or ^{211}At) may further enhance the therapeutic efficacy of FAP-targeted radionuclide therapy. Recently, Xu et al. (*10*) reported 2 albumin binder-conjugated FAPI molecules derived from FAPI-04, which is another strategy to improve tumor uptake and retention time for therapeutic or diagnostic applications. Named as TEFAPI-06 and TEFAPI-07, both molecules have been successfully labeled with ^{68}Ga, ^{86}Y, and ^{177}Lu (*10*). Comparison of dimeric FAPI ligands to these molecules, and perhaps the combination of albumin binders and multimerization of FAPI ligands, are both possible promising avenues for future research.

Without any doubt, FAPI-based imaging and therapy of cancer and various other diseases has been a highly vibrant research field over the last several years. New preclinical and clinical studies appear in the literature virtually every week. We look forward to future studies and rapid translation of the most promising FAPI ligands into the clinical arena to benefit (cancer) patients. The recent development and commercial availability of PET/CT systems with a long axial field of view and total-body imaging capability can also play an important role in the development and translation of novel FAPI-based PET tracers, since it can enable unprecedented, facile evaluation of the whole-body distribution and pharmacokinetic profiles of radiotracers.

DISCLOSURE

Financial support was received from the National Natural Science Foundation of China (81630049 and 82030052), the University of Wisconsin–Madison, and the National Institutes of Health (P30CA014520).Weibo Cai is a scientific advisor, stockholder, and grantee of Focus-X Therapeutics, Inc. No other potential conflict of interest relevant to this article was reported.

REFERENCES

1. Altmann A, Haberkorn U, Siveke J. The latest developments in imaging of fibroblast activation protein. *J Nucl Med.* 2021;62:160–167.
2. Zhao L, Niu B, Fang J, et al. Synthesis, preclinical evaluation, and a pilot clinical PET imaging study of ^{68}Ga-labeled FAPI dimer. *J Nucl Med.* 2022;63:862–868.
3. Chen H, Pang Y, Wu J, et al. Comparison of [^{68}Ga]Ga-DOTA-FAPI-04 and [^{18}F]FDG PET/CT for the diagnosis of primary and metastatic lesions in patients with various types of cancer. *Eur J Nucl Med Mol Imaging.* 2020;47:1820–1832.
4. Sollini M, Kirienko M, Gelardi F, et al. State-of-the-art of FAPI-PET imaging: a systematic review and meta-analysis. *Eur J Nucl Med Mol Imaging.* 2021;48:4396–4414.
5. Zhao L, Pang Y, Zheng H, et al. Clinical utility of [^{68}Ga]Ga-labeled fibroblast activation protein inhibitor (FAPI) positron emission tomography/computed tomography for primary staging and recurrence detection in nasopharyngeal carcinoma. *Eur J Nucl Med Mol Imaging.* 2021;48:3606–3617.
6. Zhao L, Chen S, Lin L, et al. [^{68}Ga]Ga-DOTA-FAPI-04 improves tumor staging and monitors early response to chemoradiotherapy in a patient with esophageal cancer. *Eur J Nucl Med Mol Imaging.* 2020;47:3188–3189.
7. Chen H, Zhao L, Ruan D, et al. Usefulness of [^{68}Ga]Ga-DOTA-FAPI-04 PET/CT in patients presenting with inconclusive [^{18}F]FDG PET/CT findings. *Eur J Nucl Med Mol Imaging.* 2021;48:73–86.
8. Assadi M, Rekabpour SJ, Jafari E, et al. Feasibility and therapeutic potential of ^{177}Lu–fibroblast activation protein inhibitor–46 for patients with relapsed or refractory cancers. *Clin Nucl Med.* 2021;46:e523–e530.
9. Baum RP, Schuchardt C, Singh A, et al. Feasibility, biodistribution and preliminary dosimetry in peptide-targeted radionuclide therapy (PTRT) of diverse adenocarcinomas using ^{177}Lu-FAP-2286: first-in-human results. *J Nucl Med.* June 24, 2021 [Epub ahead of print].
10. Xu M, Zhang P, Ding J, et al. Albumin binder–conjugated fibroblast activation protein inhibitor radiopharmaceuticals for cancer therapy. *J Nucl Med.* September 30, 2021 [Epub ahead of print].

Synthesis, Preclinical Evaluation, and a Pilot Clinical PET Imaging Study of ^{68}Ga-Labeled FAPI Dimer

Liang Zhao*[1,2], Bo Niu*[3], Jianyang Fang*[4], Yizhen Pang[1], Siyang Li[3], Chengrong Xie[5], Long Sun[1], Xianzhong Zhang[4], Zhide Guo[4], Qin Lin[2], and Haojun Chen[1]

[1]*Department of Nuclear Medicine and Minnan PET Center, The First Affiliated Hospital of Xiamen University, Xiamen, China;* [2]*Department of Radiation Oncology, The First Affiliated Hospital of Xiamen University, Xiamen, China;* [3]*School of Medicine, Xiamen University, Xiamen, China;* [4]*State Key Laboratory of Molecular Vaccinology and Molecular Diagnostics and Center for Molecular Imaging and Translational Medicine, School of Public Health, Xiamen University, Xiamen, China; and* [5]*Fujian Provincial Key Laboratory of Chronic Liver Disease and Hepatocellular Carcinoma, Xiamen, China*

See an invited perspective on this article on page 860.

J Nucl Med 2022; 63:862–868
DOI: 10.2967/jnumed.121.263016

Cancer-associated fibroblasts (CAFs) are crucial components of the tumor microenvironment. Fibroblast activation protein (FAP) is overexpressed in CAFs. FAP-targeted molecular imaging agents, including the FAP inhibitors (FAPIs) 04 and 46, have shown promising results in tumor diagnosis. However, these molecules have a relatively short tumor-retention time for peptide-targeted radionuclide therapy applications. We aimed to design a ^{68}Ga-labeled FAPI dimer, ^{68}Ga-DOTA-2P(FAPI)$_2$, to optimize the pharmacokinetics and evaluate whether this form is more effective than its monomeric analogs. **Methods:** ^{68}Ga-DOTA-2P(FAPI)$_2$ was synthesized on the basis of the quinoline-based FAPI variant (FAPI-46), and its binding properties were assayed in CAFs. Preclinical pharmacokinetics were determined in FAP-positive patient-derived xenografts using small-animal PET and biodistribution experiments. The effective dosimetry of ^{68}Ga-DOTA-2P(FAPI)$_2$ was evaluated in 3 healthy volunteers, and PET/CT imaging of ^{68}Ga-FAPI-46 and ^{68}Ga-DOTA-2P(FAPI)$_2$ was performed on 3 cancer patients. **Results:** ^{68}Ga-DOTA-2P(FAPI)$_2$ was stable in phosphate-buffered saline and fetal bovine serum for 4 h. The FAPI dimer showed high affinity and specificity for FAP in vitro and in vivo. The tumor uptake of ^{68}Ga-DOTA-2P(FAPI)$_2$ was approximately 2-fold stronger than that of ^{68}Ga-FAPI-46 in patient-derived xenografts, whereas healthy organs showed low tracer uptake and fast body clearance. The effective dose of ^{68}Ga-DOTA-2P(FAPI)$_2$ was 1.19E−02 mSv/MBq, calculated using OLINDA. Finally, the PET/CT scans of the 3 cancer patients revealed higher intratumoral uptake of ^{68}Ga-DOTA-2P(FAPI)$_2$ than of ^{68}Ga-FAPI-46 in all tumor lesions (SUV_{max}, 8.1–39.0 vs. 1.7–24.0, respectively; $P < 0.001$). **Conclusion:** ^{68}Ga-DOTA-2P(FAPI)$_2$ has increased tumor uptake and retention properties compared with ^{68}Ga-FAPI-46, and it could be a promising tracer for both diagnostic imaging and targeted therapy of malignant tumors with positive expression of FAP.

Key Words: fibroblast activation protein; cancer-associated fibroblasts; FAPI dimer; patient-derived xenografts; PET imaging

Cancer-associated fibroblasts (CAFs) are crucial components of the tumor microenvironment and can constitute over half the mass in various types of tumor. According to previous reports, CAFs play important roles in tumor growth, immune suppression, and cancer invasion (*1,2*). Thus, CAFs may be promising targets for tumor diagnosis and therapy. Fibroblast activation protein (FAP) is overexpressed in the CAFs of numerous epithelial carcinomas and weakly expressed in healthy tissues, therefore representing an attractive target for cancer research. The past few years have witnessed an expansion of research on FAP-targeted molecular imaging in tumor diagnosis (*3–5*).

Recently, there has been growing application of FAP targeting, from diagnostic imaging to peptide-targeted radionuclide therapy (PTRT) (*6–10*). However, the reports on PTRT are based mainly on peptides of the FAP inhibitors (FAPIs) 04 and 46, which showed a relatively short tumor-retention time in preclinical models and human subjects (*10–12*). Another FAPI variant, FAP-2286, has been studied in PTRT to improve tumor-retention time (*13*). Moreover, mouse models used to evaluate the pharmacokinetics of FAPI variants were cancer cell–derived xenografts in previous research (*7,10,11*). When xenotransplanted, cancer cell-derived xenografts adequately recruit mouse fibroblasts during tumor growth; thus, they are highly suitable for direct tracer comparisons (*14*). However, patient-derived xenografts (PDXs), established by direct implantation of fresh surgical tissue fragments into immunodeficient mice, could be more attractive because they retain the tumor environment and molecular signature of the corresponding parental tumor compared with that of cancer cell-derived xenografts (*15*). However, the potential of PDXs for PET imaging of CAFs has rarely been investigated.

The polyvalency effect has been applied to develop multimeric peptides to enhance the tumor-targeting efficacy of the tracers and improve the quality of in vivo imaging (*16,17*). Moreover, adding an amphiphilic polyethylene glycol linker (PEGylation) has been widely used to improve the in vivo kinetics of various pharmaceuticals (*16,18*). In the present study, we designed and synthesized a novel FAPI dimer with 2 mini-PEG spacers (11-amino-3,6,9-trioxaundecanoic acid, with 3 ethylene oxide units) between the 2 FAPI motifs in the homodimeric peptides, denoted as DOTA-2P(FAPI)$_2$. The novel dimeric FAP-targeted molecule was labeled with the positron-emitting

Received Aug. 8, 2021; revision accepted Sep. 22, 2021.
For correspondence or reprints, contact Haojun Chen (leochen0821@foxmail.com) or Zhide Guo (gzd666888@xmu.edu.cn).
*Contributed equally to this work.
Published online Sep. 23, 2021.

radionuclide ^{68}Ga (^{68}Ga-DOTA-2P(FAPI)$_2$) for PET imaging. We present the results of ^{68}Ga-DOTA-2P(FAPI)$_2$ testing in PDX models, healthy volunteers, and cancer patients. We hypothesized that the dimeric FAPI is more effective than monomeric analogs in terms of tumor uptake and tumor-retention time.

MATERIALS AND METHODS

Chemistry and Radiochemistry

The vender information concerning chemicals, cells, reagents, synthesis procedure, high-performance liquid chromatography, liquid chromatography-mass spectrometry, and the flow diagram of DOTA-2P(FAPI)$_2$ is provided in the supplemental materials and Supplemental Figure 1 (supplemental materials are available at http://jnm.snmjournals.org).

FAPI variants were radiolabeled by adjusting a mixture of 50 μg (56.4 nmol) of FAPI-46 or 50 μg (25.3 nmol) of DOTA-2P(FAPI)$_2$, and 4 mL of ^{68}Ga solution (1.3 GBq in 0.6 M HCl) to pH 3.3–3.6 with 1 mL of sodium acetate (0.25M in water; total volume of reaction, 5 mL). After being heated to 100°C for 15 min, the product was isolated by a C18 Sep-Pak cartridge (WAT020515; Waters) using ethanol (0.5 mL) as the eluent. Quality control of the radiosynthesis was performed using ultraviolet and radio–high-performance liquid chromatography (details presented in the supplemental materials).

The radiolabeled compound was incubated in phosphate-buffered saline and fetal bovine serum (FBS) at 37°C for 1, 2, and 4 h to measure the in vitro stability. Then, 0.5 mL of acetonitrile was added to remove plasma proteins from the serum after the sample was centrifuged at 1, 2, and 4 h. Finally, the radiochemical purities were analyzed using radio–high-performance liquid chromatography.

PDX Model Establishment

Written informed consent was obtained from all patients, and the research protocol was approved by the Clinical Research Ethics Committee of the First Affiliated Hospital of Xiamen University (ID KYZ-2017-001). All animal care and experimental procedure were reviewed and approved by the Animal Care and Use Committee of the Xiamen University Laboratory Animal Center (ID XMULAC20170063). The establishment of PDX models was based on our previous protocols, detailed in the supplemental materials (*19*).

Western Blot and Histopathologic Staining

Western blot analysis was performed in CAFs and the Huh7 cell line to select cells expressing FAP. CAFs or Huh7 cells were cultured in RPMI 1640 or Dulbecco modified Eagle medium containing 10% FBS at 37°C in 5% CO_2. Western blotting and histopathologic staining were performed as described in the supplemental materials according to our previous protocol (*20*).

Radioligand Binding Studies

Radioligand binding studies included cell uptake, cell uptake blocking, and FAP binding assay. CAFs expressing FAP were seeded in 24-well plates with 1640 medium containing 10% FBS and cultivated for 48 h to a density of approximately 80% before the experiments. The medium was replaced with 1640 medium without FBS. ^{68}Ga-DOTA-2P(FAPI)$_2$ or ^{68}Ga-FAPI-46 or ^{68}Ga-DOTA-2P(FAPI)$_2$ with 11.3 nmol of unlabeled FAPI-46 (for the blocking experiment) was added to the 24-well plates and incubated for the scheduled times (10, 30, 60, 90, and 120 min). The FAP-binding assays were performed by simultaneous exposure to unlabeled FAPI variants (1.27×10^{-4} to 10^{-13} M for ^{68}Ga-DOTA-2P(FAPI)$_2$; 2.83×10^{-4} to 10^{-13} M for ^{68}Ga-FAPI-46) and radiolabeled compounds for 60 min. The inhibitory concentration of 50% was calculated by fitting the data by nonlinear regression using GraphPad Prism. In each step of the experiments, the cells were washed twice with 1 mL of phosphate-buffered saline. Finally, CAFs were lysed with 0.5 mL of 1 M NaOH for radioactivity counting (counts per minute), examined in a γ-counter. Each independent experiment was repeated 3 times.

PET Imaging and Biodistribution Study in Hepatocellular Carcinoma (HCC)-PDX Models

The products of ^{68}Ga-DOTA-2P(FAPI)$_2$ and ^{68}Ga-FAPI-46 were diluted to a concentration of 74 MBq/mL, and 7.4 MBq (bout 0.1 mL) of ^{68}Ga-DOTA-2P(FAPI)$_2$ or ^{68}Ga-FAPI-46 were intravenously injected into HCC-PDXs ($n = 3$ for each group). All PET scans were conducted using an Inveon small-animal PET scanner (Siemens Preclinical Solution). Dynamic and static PET imaging procedures are provided in the supplemental materials.

In the biodistribution study, the products of ^{68}Ga-DOTA-2P(FAPI)$_2$ and ^{68}Ga-FAPI-46 were diluted to a concentration of 14.8 MBq/mL. HCC-PDX mice were injected with the same batch of 1.48-MBq ^{68}Ga-DOTA-2P(FAPI)$_2$ and killed at different times (1 and 4 h after injection; $n = 3$ for each time point). The main organs and tumors were isolated, weighed, and analyzed. The biodistribution in the ^{68}Ga-FAPI-46 group (1.48 MBq) and the blocking group (^{68}Ga-DOTA-2P(FAPI)$_2$ [1.48 MBq] with 30 nmol of unlabeled FAPI-46) was also evaluated for comparison. The radioactivity (counts per minute) was measured with a γ-counter.

PET Imaging in Healthy Volunteers and Cancer Patients

The clinical study was registered at ClinicalTrials.gov (NCT04941872). The Clinical Research Ethics Committee of the First Affiliated Hospital of Xiamen University approved the study, and all subjects gave written informed consent. Safety data were collected before and 4 h after injection of ^{68}Ga-DOTA-2P(FAPI)$_2$, including vital signs (blood pressure, heart rate, respiratory frequency, and temperature) and adverse events. The scan and reconstruction procedures are presented in the supplemental materials according to a previously described protocol (*21*). Time–activity curve fitting and subsequent dose calculations were performed using OLINDA/EXM, version 1.1 (*22*).

Statistical Analysis

All quantitative data are expressed as mean ± SD. All statistical analyses were conducted using SPSS, a statistical analysis software program (version 22.0; IBM). One-way ANOVA, Student *t*-testing, and Wilcoxon matched-pairs signed-rank testing were used to compare means. Statistical significance was set at a P value of less than 0.05.

RESULTS

Synthesis and Radiolabeling

The dimer of FAPI-46 with 2 PEG_3 groups and the chelator DOTA were synthesized (Fig. 1; Supplemental Fig. 1). Subsequently, 2 radioligands were prepared as controls and tests: ^{68}Ga-FAPI-46, first reported by Loktev et al. (*3*), and ^{68}Ga-DOTA-2P(FAPI)$_2$, the dimer of FAPI-46. ^{68}Ga-DOTA-2P(FAPI)$_2$ and ^{68}Ga-FAPI-46 were radiolabeled at an average specific activity of 37 and 16.5 GBq/μmol, respectively, with more than 95% radiochemical purity after purification (Supplemental Figs. 2A and 2B).

The stability of ^{68}Ga-DOTA-2P(FAPI)$_2$ was evaluated in phosphate-buffered saline and FBS at 1, 2, and 4 h after incubation. High-performance liquid chromatography analysis results showed that ^{68}Ga-DOTA-2P(FAPI)$_2$ had high stability for up to 4 h, with no significant demetalation observed in either phosphate-buffered saline (92.78%) or FBS (97.80%) (Supplemental Figs. 2C and 2D).

Cell-Based Experiments

The binding properties of FAPI variants were first verified and evaluated in a FAP-expressing cell line. Western blotting results revealed

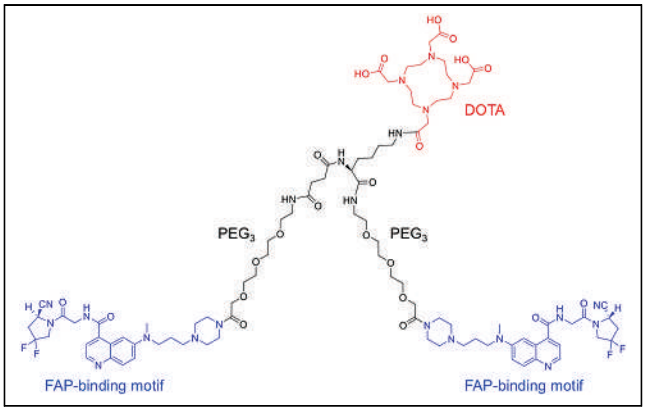

FIGURE 1. Chemical structure of DOTA-2P(FAPI)$_2$.

that FAP was highly expressed in CAFs and negatively expressed in Huh7 cells (Fig. 2A). Since FAP is expressed on the CAF surface, ^{68}Ga-DOTA-2P(FAPI)$_2$ and ^{68}Ga-FAPI-46 could bind to FAP rapidly. Uptake of ^{68}Ga-FAPI-46 reached approximately 1.5% after 10 min of incubation and then slightly increased until 120 min. The uptake pattern of ^{68}Ga-DOTA-2P(FAPI)$_2$ was similar; however, the uptake value was approximately double. Regarding the cell uptake–blocking experiment, the FAPI-46 precursor could significantly block binding between ^{68}Ga-DOTA-2P(FAPI)$_2$ and FAP (Fig. 2B). The mean ± SD and error of the inhibitory concentrations of 50% were 2.06 ± 1.84 nM and 1.06 nM, respectively, for the monomer and 3.68 ± 1.82 nM and 1.05 nM, respectively, for the dimer (Figs. 2C and 2D). The comparable inhibitory concentrations of 50% for DOTA-2P(FAPI)$_2$ and FAPI-46 suggest that the dimerization of the FAPI structure has a minimal effect on the receptor-binding avidity.

HCC-PDX Establishment and Validation

Two different groups of HCC-PDXs were successfully established, denoted as HCC-PDX-1 and HCC-PDX-2. The 2 groups had different clinical data (patient 1: male, T1aN0M0, poorly differentiated HCC; patient 2: male, T1bN0M0, moderately differentiated HCC), both with high levels of FAP expression (Supplemental Fig. 3). Both groups showed histopathologic characteristics (FAP, Ki-67, and hematoxylin and eosin; Supplemental Fig. 3) consistent with their corresponding primary HCC and were chosen as the experimental models to evaluate the in vivo behavior of ^{68}Ga-DOTA-2P(FAPI)$_2$.

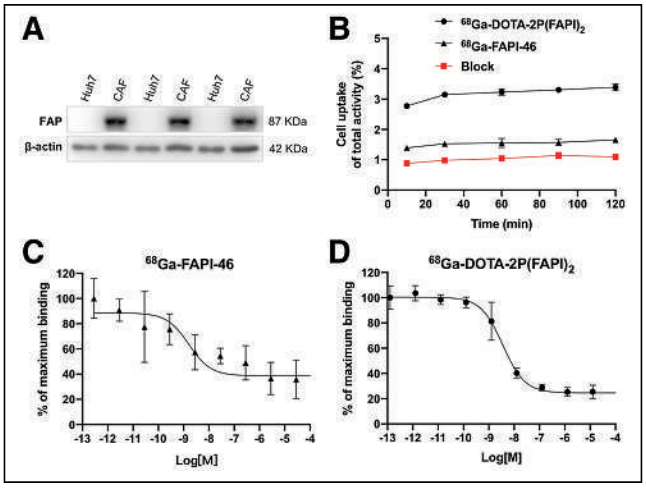

FIGURE 2. (A) FAP expression in Huh7 cells and CAFs assayed using Western blotting. (B) Cell uptake assay of ^{68}Ga-DOTA-2P(FAPI)$_2$, ^{68}Ga-FAPI-46, and blocking experiment on CAFs (n = 3). (C) Inhibition of ^{68}Ga-FAPI-46 binding to FAP on CAFs by unlabeled FAPI-46 (2.83×10^{-4} to 10^{-13} M; n = 3). (D) Inhibition of ^{68}Ga-DOTA-2P(FAPI)$_2$ binding to FAP on CAFs by unlabeled FAPI-46 (1.27×10^{-4} to 10^{-13} M; n = 3).

Small-Animal PET Studies

In HCC-PDX-1, both radiotracers were absorbed strongly by the tumor at 0.5 h after injection, and the uptake decreased relatively slowly until 4 h (Fig. 3). However, tumor uptake of ^{68}Ga-DOTA-2P(FAPI)$_2$ was significantly higher than that of ^{68}Ga-FAPI-46. The detailed percentage injected dose (%ID)/g in tumor for both tracers from small-animal PET are shown in Supplemental Figure 4A. Other organs demonstrated low nonspecific binding that quickly decreased (Supplemental Figs. 4B and 4E), resulting in a low background signal and favorable tumor-to-background ratios. For a comprehensive investigation of the early pharmacokinetics of ^{68}Ga-DOTA-2P(FAPI)$_2$, 60-min dynamic PET was performed on HCC-PDX-1. The tumor accumulation of ^{68}Ga-DOTA-2P(FAPI)$_2$ was rapid, and the time dependency of the FAPI dimer uptake was similar to that of other FAPI tracers. In contrast, the heart, kidney, and liver uptake showed sharp elimination (Fig. 3). Regarding ^{68}Ga-DOTA-2P(FAPI)$_2$ PET in HCC-PDX-2, tumor accumulation was rapid. Slightly decreased tumor uptake was observed from 30 min to 1 h, and it then remained constant between 1 and 4 h (Fig. 4A; Supplemental Fig. 5), similarly to that in HCC-PDX-1. The 60-min dynamic PET was also performed on HCC-PDX-2 (Supplemental Fig. 6).

Target specificity was evaluated by simultaneous administration of unlabeled FAPI-46 as a competitor with ^{68}Ga-DOTA-2P(FAPI)$_2$. Tumor uptake 1 h after injection was greatly suppressed by blocking in HCC-PDX-1 and HCC-PDX-2, and radiotracer clearance in most organs was faster than that without blocking (Fig. 4B). The uptake values of the tumor and key organ with or without competitor are presented in Supplemental Figures 4F and 5F.

Organ Distribution in HCC-PDX-1

The biodistribution of ^{68}Ga-FAPI-46 in HCC-PDX-1 was determined by ex vivo counting in tissues collected 1 and 4 h after injection (Fig. 5A). At 1 h after injection, ^{68}Ga-FAPI-46 accumulated mainly in the tumor (4.60 ± 1.12 %ID/g) and kidney (4.42 ± 0.97 %ID/g), and the tumor-to-kidney ratio was 1.05 ± 0.18. Four hours after injection, ^{68}Ga-FAPI-46 in the blood, heart, liver, lung,

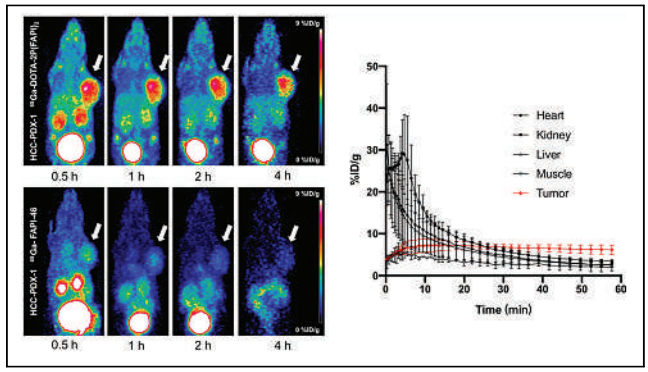

FIGURE 3. Representative static PET imaging of ^{68}Ga-DOTA-2P(FAPI)$_2$ (left top) and ^{68}Ga-FAPI-46 (left bottom) in HCC-PDX-1, and dynamic time–activity curves of ^{68}Ga-DOTA-2P(FAPI)$_2$ (right) in heart, kidney, liver, muscle, and tumor tissues.

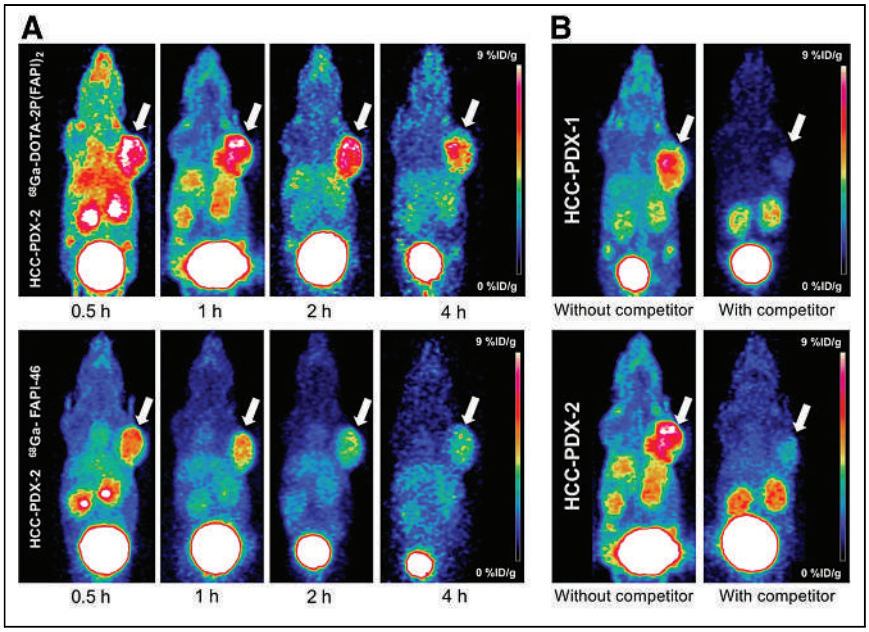

FIGURE 4. (A) Representative static PET imaging of ^{68}Ga-DOTA-2P(FAPI)$_2$ and ^{68}Ga-FAPI-46 in HCC-PDX-2. (B) Representative static PET imaging of ^{68}Ga-DOTA-2P(FAPI)$_2$ in HCC-PDX-1 and HCC-PDX-2 with and without simultaneous injection of unlabeled FAPI-46 as competitor 1 h after administration.

and spleen decreased sharply, whereas tumor uptake was steady (3.81 ± 0.18 %ID/g).

The biodistribution of ^{68}Ga-DOTA-2P(FAPI)$_2$ was also assessed in the same PDX model by comparison (Fig. 5B). Consistently with the PET findings, ^{68}Ga-DOTA-2P(FAPI)$_2$ demonstrated higher uptake in the tumor than did ^{68}Ga-FAPI-46, 1 h after injection (8.97 ± 0.32 vs. 4.60 ± 1.12 %ID/g, $P = 0.003$) and 4 h after injection (7.61 ± 0.64 vs. 3.81 ± 0.18 %ID/g, $P = 0.001$). The organ uptake of ^{68}Ga-DOTA-2P(FAPI)$_2$ was slightly greater than that of ^{68}Ga-FAPI-46 both 1 and 4 h after injection. As a result, ^{68}Ga-DOTA-2P(FAPI)$_2$ had a higher tumor-to-kidney ratio than did ^{68}Ga-FAPI-46 (1.60 ± 0.26 vs. 1.05 ± 0.18, $P = 0.039$, 1 h after injection), although the difference was not significant 4 h after injection (1.33 ± 0.29 vs. 0.95 ± 0.09, $P = 0.093$).

Regarding the blocking group, a dramatic decrease in radioactivity was detected in most organs (Fig. 5B), and the tumor uptake decreased most significantly (8.97 ± 0.32 vs. 1.07 ± 0.19 %ID/g 1 h after injection, $P < 0.001$, Student t test; 7.61 ± 0.64 vs. 1.14 ± 0.15 %ID/g 4 h after injection, $P = 0.002$, Student t test).

Additional biodistribution and PET studies were performed to rule out the effect of molar activity on comparative experiments between FAPI dimer and FAPI-46. The amount of precursor administered was 23 μg (25.9 nmol) for FAPI-46 and 50 μg (25.3 nmol) for DOTA-2P(FAPI)$_2$, resulting in the same specific activity for ^{68}Ga-FAPI-46 and ^{68}Ga-FAPI dimer. Under these circumstances, the results from the biodistribution study demonstrated that ^{68}Ga-FAPI dimer had higher tumor uptake than did ^{68}Ga-FAPI-46 (8.45 ± 2.19 vs. 4.03 ± 0.69 %ID/g; $P = 0.029$, Student t test, Supplemental Fig. 7). Similar results were observed from the PET imaging study (Supplemental Fig. 8).

Adverse Events

All observed vital signs (including blood pressure, heart rate, and body temperature) remained normal during the injection and at the 4-h follow-up. No individuals reported any adverse events.

Dosimetry Estimate

The dosimetry reports and a representative figure for 3 healthy volunteers are shown in Table 1 and Figure 6, respectively. There was no time dependency of tracer uptake, showing that the tracer distribution was not obviously changing after 10 min. The effective dose of ^{68}Ga-DOTA-2P(FAPI)$_2$ was 1.19E−02 mSv/MBq, calculated using OLINDA. The organ with the highest effective dose was the thyroid (3.11E−03 mSv/MBq), followed by the liver (1.65E−03 mSv/MBq) and lungs (1.36E−03 mSv/MBq). Overall, the effective dose of ^{68}Ga-DOTA-2P(FAPI)$_2$ was comparable to the effective doses of ^{68}Ga-FAPI-02 (1.80E−02 mSv/MBq) and ^{68}Ga-FAPI-04 (1.64E−02 mSv/MBq) (*4*) and higher than the effective dose of ^{68}Ga-FAPI-46 (7.80E−03 mSv/MBq) (*23*).

^{68}Ga-DOTA-2P(FAPI)$_2$ PET Imaging in Cancer Patients

^{68}Ga-FAPI-46 and ^{68}Ga-DOTA-2P(FAPI)$_2$ PET/CT scans were performed after 60 min of intravenous administration in 3 patients: one with nasopharyngeal nonkeratinized undifferentiated carcinoma and wild diffuse bone metastases after chemoradiotherapy and immunotherapy; one with papillary thyroid carcinoma and wild diffuse lymph node metastases after total thyroidectomy and multiple cycles of radioiodine treatment; and one with HCC, who was treatment-naïve. Representative PET images of these 3 patients after administration of ^{68}Ga-FAPI-46 and ^{68}Ga-DOTA-2P(FAPI)$_2$ are shown in Figure 7 and Supplemental Figures 9 and 10. In the patient with metastatic thyroid cancer, ^{68}Ga-DOTA-2P(FAPI)$_2$ accumulated mainly in the tumor, pancreas, submandibular glands, and blood pool. Interestingly, the activity of

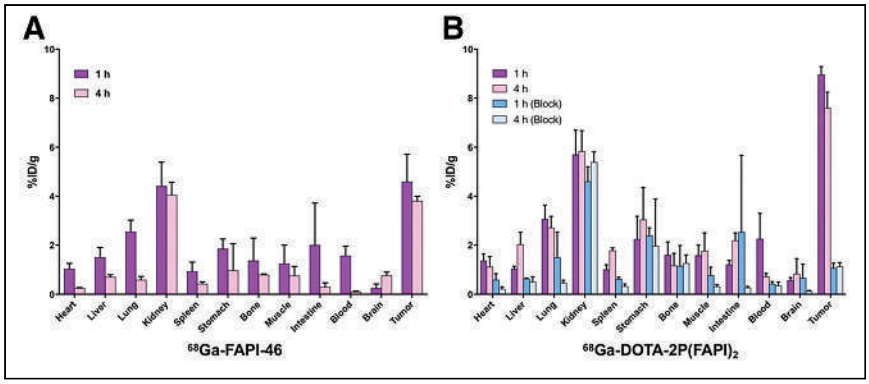

FIGURE 5. (A) Ex vivo biodistribution of ^{68}Ga-FAPI-46 in HCC-PDX-1, 1 and 4 h after injection (n = 3/group). (B) Ex vivo biodistribution of ^{68}Ga-DOTA-2P(FAPI)$_2$ in HCC-PDX-1, 1 and 4 h after injection, with and without coadministration of unlabeled FAPI-46 as blocking agent (n = 3/group).

TABLE 1
^{68}Ga-DOTA-2P(FAPI)$_2$ Dosimetry Summary of Effective Doses Using OLINDA/EXM, Version 1.1

Target organ	Mean (mSv/MBq)	SD (mSv/MBq)
Adrenal glands	7.98E−05	3.04E−05
Brain	3.16E−05	1.96E−05
Breasts	6.36E−05	1.09E−05
Gallbladder wall	—	—
Lower large intestine wall	9.22E−04	2.33E−04
Small intestine	5.18E−05	1.84E−05
Stomach wall	7.12E−04	3.16E−05
Upper large intestine wall	2.79E−05	1.13E−05
Heart wall	—	—
Kidneys	1.01E−04	4.96E−05
Liver	1.65E−03	4.12E−04
Lungs	1.36E−03	4.59E−04
Muscle	4.19E−05	2.07E−05
Ovaries	5.94E−04	1.06E−04
Pancreas	7.61E−04	8.05E−04
Red marrow	1.12E−03	1.33E−04
Osteogenic cells	6.47E−05	6.87E−06
Skin	1.22E−05	2.32E−06
Spleen	1.58E−04	9.12E−05
Thymus	9.64E−06	4.47E−06
Thyroid	3.11E−03	4.68E−04
Urinary bladder wall	1.04E−03	5.22E−04
Uterus	1.27E−05	6.00E−06
Effective dose equivalent	1.69E−02	1.92E−03
Effective dose	1.19E−02	9.45E−04

FAPI dimer in the blood pool remained at a high level (SUV_{max}, 8.3) 4 h after injection. All tumor lesions were clearly visible because of the favorable tumor-to-background ratios. In the lesion-to-lesion comparison, the dimer uptake in 21 lesions (from 3 patients) was higher than monomer uptake (SUV_{max} 1 h after injection, 8.1–39.0 vs. 1.7–24.0, respectively; $P < 0.001$ by Wilcoxon matched-pairs signed-rank test; mean SUV_{max}, 15.3 vs. 23.9; Supplemental Table 1). In addition, the ^{68}Ga-2P(FAPI)$_2$ uptake in tumors was slightly decreased from 1 to 4 h (SUV_{max} 1 h after injection, 8.1–39.0; SUV_{max} 4 h after injection, 6.6–35.0).

DISCUSSION

With a burst of preclinical and clinical research on quinoline-based FAPI variants, 2 main hurdles remain: improving the tumor retention time and finding the appropriate preclinical models. Since FAP is overexpressed mainly in CAFs and not in tumor cells, the tumor cell-line transfected with human or murine FAP could not reflect the tumor microenvironment (*3,7*). In contrast, PDXs can reliably reproduce a patient's parental tumor for histopathology and genetics (*15*). Therefore, PDXs are suitable models for studying tumor biology, including the microenvironment and patient sensitivity to target agents. Despite an increasing number of case

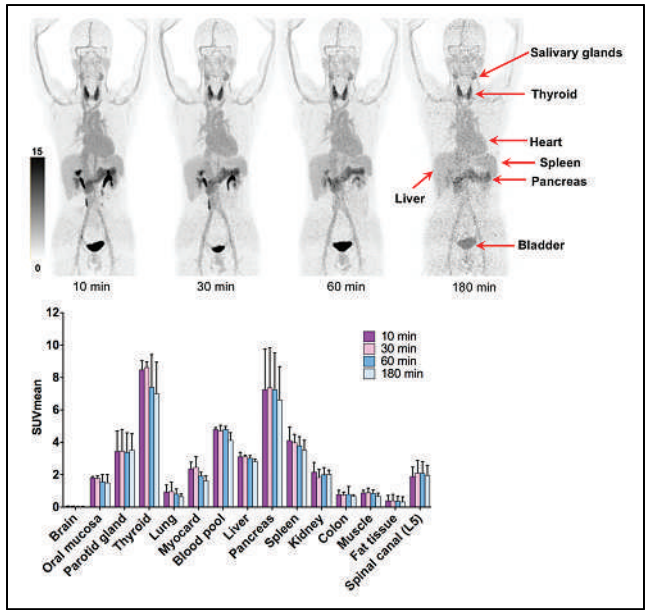

FIGURE 6. ^{68}Ga-DOTA-2P(FAPI)$_2$, 10, 30, 60, and 180 min after injection, in healthy volunteers (top), and SUV_{mean} of healthy organs at different time points (bottom).

studies (*6–9*) and 2 clinical trials with a small patient population (*13,24*) for FAP-based PTRT, basic research on this topic is rare (*10*). In the present study, PDXs derived from HCC could maintain the principal histopathologic characterization of the human tumor, confirming the robustness of this model for testing the properties of the new FAPI variant.

With FAPI being a pan-cancer target, labeling of FAPI monomers with different imaging isotopes has shown impressive results in several tumor diagnoses (*3–5,25*); however, the pharmacokinetics with fast clearance from blood and short retention in tumors are problematic for PTRT application. Thus, structural modification of FAPI for optimizing tumor uptake and tumor retention time for PTRT is another key research direction.

On the basis of the polyvalent effect, multimeric peptides can help improve tumor-targeting efficacy and generate higher-quality in vivo imaging. This strategy has been widely used in the development of multimeric Arg-Gly-Asp (RGD) peptides (*16,17*). Indeed, given that the distance between 2 FAPI motifs in DOTA-2P(FAPI)$_2$ may not be long enough, it is unlikely that they would bind to 2 adjacent FAP sites simultaneously. However, the binding of one FAPI motif to FAP will significantly increase the local concentration of a second FAP motif in the vicinity of FAP sites. The locally enhanced FAPI concentration may explain the increased tumor uptake of radiolabeled FAPI dimers compared with their monomeric analogs. Similar findings were observed in the studies of radiolabeled RGD dimers (*26*). Nonetheless, although tetrameric and octameric peptides possess higher receptor-binding affinity and higher tumor uptake than their dimeric and monomeric counterparts, they also have substantially higher background activity, especially in the kidney (*27*). Therefore, dimeric peptides seem to be an optimal choice because of their increased tumor uptake and favorable pharmacokinetics (*27*). PEGylation is another widely used strategy to improve the in vivo pharmacokinetics of radiotracers. According to previous reports of studies in which PEGylated RGD peptides were labeled with different isotopes, PEGylation improved the labeling yield and in vivo pharmacokinetics (*16,18*). However,

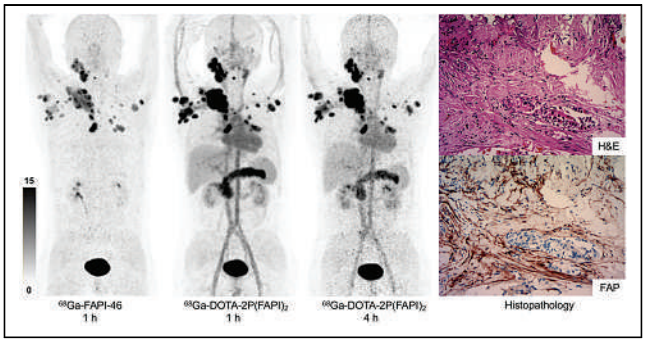

FIGURE 7. ^{68}Ga-FAPI-46, 1 h after injection, and ^{68}Ga-DOTA-2P(FAPI)$_2$, 1 and 4 h after injection, in patient with metastatic thyroid cancer. Hematoxylin and eosin (H&E) staining and FAP immunohistochemistry staining showed high FAP expression in tumor stroma (×100).

PEGylation also induces hydrophilicity and increases kidney uptake, partially explaining the high initial kidney uptake compared with other FAPI derivatives. In this study, we designed and synthesized a novel FAPI dimer with 2 mini-PEG spacers between the FAPI motifs in homodimeric peptides. The in vitro binding assays demonstrated that DOTA-2P(FAPI)$_2$ had specific and high binding affinity to FAP expressed on CAFs, revealing that the polyvalent strategy did not compromise its FAP-binding affinity.

After radiolabeling with ^{68}Ga, the FAPI dimers exhibited improved in vivo pharmacokinetics and enhanced tumor uptake compared with the FAPI monomer. Dynamic PET scans in the 2 HCC-PDX groups showed prominent tumor uptake and predominant organ clearance. After the tracers were applied to static PET scans, ^{68}Ga-DOTA-2P(FAPI)$_2$ demonstrated higher tumor uptake than ^{68}Ga-FAPI-46 at all time points examined in both PDXs. In the small-animal PET imaging study, higher initial (30 min after injection) kidney and liver uptake was observed for ^{68}Ga-DOTA-2P(FAPI)$_2$ than for FAPI-monomers, including ^{68}Ga-FAPI-04, ^{68}Ga-FAPI-46, and ^{18}F-FGlc-FAPI (*14*). However, the kidney and liver uptake was quickly eliminated at 60 min after injection in PET imaging and the biodistribution study. The high initial kidney uptake and rapid renal clearance may be attributed to the insertion of 2 PEG groups, which improved the hydrophilic properties (*16,18*). Nevertheless, the main organ uptake should be carefully estimated for safety-dose limitations when FAPI dimer is labeled with ^{177}Lu for targeted radionuclide therapy. The FAP specificity of ^{68}Ga-DOTA-2P(FAPI)$_2$ was strongly confirmed by effective uptake inhibition in the presence of unlabeled FAPI-46 in cell-uptake, PET, and biodistribution experiments.

It was reported that the FAP-blocking dose (cold mass of FAPI) in one mouse was 30 nmol (*7,11*). Since the specific activity of FAPI dimer and FAPI-46 was 37 GBq/μmol and 16.5 GBq/μmol, respectively, in this study, a dose of 7.4 MBq of ^{68}Ga-FAPI-46 (0.45 nmol, hot and cold mass) or ^{68}Ga-FAPI dimer (0.2 nmol, hot and cold mass) per mouse for PET imaging may have minimal impact on tumor uptake. Therefore, there is no effect of the different injected cold mass of the radiotracers that might have caused the significant differences in tumor uptake. Moreover, additional PET imaging and biodistribution experiments have been performed to rule out the effect of molar activity on all comparative experiments of dimeric and monomeric inhibitors.

The encouraging results of the in vitro and mouse studies led to the clinical translation of FAPI dimer into human subjects. The radiation dose deposition of ^{68}Ga-DOTA-2P(FAPI)$_2$ in healthy organs was estimated using the PET data of 3 healthy volunteers at 4 time points. The average effective whole-body dose was 1.19E−02 mSv/MBq. This estimate is comparable to the previously reported effective doses of ^{68}Ga-FAPI-02 and ^{68}Ga-FAPI-04 (1.80E−02 and 1.64E−02 mSv/MBq, respectively), and higher than that of ^{68}Ga-FAPI-46 (7.80E−03 mSv/MBq) (*4,23*).

Regarding clinical diagnosis, ^{68}Ga-DOTA-2P(FAPI)$_2$ PET/CT imaging in the patients showed a rapid and stable accumulation of the dimer in tumorous lesions, consistent with the results of animal experiments. Tumor uptake in most lesions was significantly higher with ^{68}Ga-DOTA-2P(FAPI)$_2$ than with ^{68}Ga-FAPI-46, leading to visualization of primary lesions and metastases more clearly. Interestingly, retention of the tracer in the patient blood pool remained high 4 h after injection, in contrast to mouse findings. The prolonged retention in the blood pool may make DOTA-2P(FAPI)$_2$ an attractive tracer for PTRT applications. Although the PET/CT results were encouraging in patients, high physiologic uptake in the thyroid and pancreas should be noted. Nevertheless, DOTA-2P(FAPI)$_2$ labeling with ^{68}Ga demonstrated favorable data in cells, mice, and patients. For future development, especially for antitumor therapeutic applications, labeling of the ligand with therapeutic radionuclides such as ^{177}Lu and ^{90}Y should be considered to compare the FAPI dimer with the monomer.

CONCLUSION

^{68}Ga-DOTA-2P(FAPI)$_2$ provides better tumor uptake and longer tumor retention than does ^{68}Ga-FAPI-46 and could be a promising tracer for both diagnostic imaging and targeted radionuclide therapy in malignant tumors with positive FAP expression. Further work to optimize the pharmacokinetics of DOTA-2P(FAPI)$_2$ and evaluate its antitumor efficacy after labeling with therapeutic isotopes should be envisaged.

DISCLOSURE

This work was funded by the National Natural Science Foundation of China (grants 82071961, 81901805, and 81772893) and by the key medical and health projects in Xiamen (grant 3502Z20191104). No other potential conflict of interest relevant to this article was reported.

ACKNOWLEDGMENTS

We gratefully acknowledge Dr. Dongyan Shen (The First Affiliated Hospital of Xiamen University, Xiamen University, China) for providing the CAFs.

KEY POINTS

QUESTION: How can tumor uptake and retention of the FAP-targeting molecular agents be optimized?

PERTINENT FINDINGS: In a pilot clinical cancer imaging study, ^{68}Ga-DOTA-2P(FAPI)$_2$ was synthesized as a FAPI dimer and tested for its pharmacokinetic properties. Its tumor uptake was higher than that of monomeric FAPIs in vitro, in vivo, and in cancer patients.

IMPLICATIONS FOR PATIENT CARE: Because ^{68}Ga-DOTA-2P(FAPI)$_2$ shows improved tumor uptake and retention properties, it could be a promising candidate tracer for both diagnostic imaging and targeted therapy of malignant tumors with positive FAP expression.

REFERENCES

1. Gaggioli C, Hooper S, Hidalgo-Carcedo C, et al. Fibroblast-led collective invasion of carcinoma cells with differing roles for RhoGTPases in leading and following cells. *Nat Cell Biol.* 2007;9:1392–1400.
2. Lakins MA, Ghorani E, Munir H, Martins CP, Shields JD. Cancer-associated fibroblasts induce antigen-specific deletion of CD8 (+) T cells to protect tumour cells. *Nat Commun.* 2018;9:948.
3. Loktev A, Lindner T, Burger EM, et al. Development of fibroblast activation protein-targeted radiotracers with improved tumor retention. *J Nucl Med.* 2019;60: 1421–1429.
4. Giesel FL, Kratochwil C, Lindner T, et al. ^{68}Ga-FAPI PET/CT: biodistribution and preliminary dosimetry estimate of 2 DOTA-containing FAP-targeting agents in patients with various cancers. *J Nucl Med.* 2019;60:386–392.
5. Chen H, Pang Y, Wu J, et al. Comparison of [^{68}Ga]Ga-DOTA-FAPI-04 and [^{18}F]FDG PET/CT for the diagnosis of primary and metastatic lesions in patients with various types of cancer. *Eur J Nucl Med Mol Imaging.* 2020;47:1820–1832.
6. Ballal S, Yadav MP, Kramer V, et al. A theranostic approach of [^{68}Ga]Ga-DOTA.SA.FAPi PET/CT-guided [^{177}Lu]Lu-DOTA.SA.FAPi radionuclide therapy in an end-stage breast cancer patient: new frontier in targeted radionuclide therapy. *Eur J Nucl Med Mol Imaging.* 2021;48:942–944.
7. Lindner T, Loktev A, Altmann A, et al. Development of quinoline-based theranostic ligands for the targeting of fibroblast activation protein. *J Nucl Med.* 2018;59: 1415–1422.
8. Lindner T, Altmann A, Kramer S, et al. Design and development of ^{99m}Tc-labeled FAPI tracers for SPECT imaging and ^{188}Re therapy. *J Nucl Med.* 2020;61:1507–1513.
9. Kratochwil C, Giesel FL, Rathke H, et al. [^{153}Sm]samarium-labeled FAPI-46 radioligand therapy in a patient with lung metastases of a sarcoma. *Eur J Nucl Med Mol Imaging.* 2021;48:3011–3013.
10. Watabe T, Liu Y, Kaneda-Nakashima K, et al. Theranostics targeting fibroblast activation protein in the tumor stroma: ^{64}Cu- and ^{225}Ac-labeled FAPI-04 in pancreatic cancer xenograft mouse models. *J Nucl Med.* 2020;61:563–569.
11. Loktev A, Lindner T, Mier W, et al. A tumor-imaging method targeting cancer-associated fibroblasts. *J Nucl Med.* 2018;59:1423–1429.
12. Assadi M, Rekabpour SJ, Jafari E, et al. Feasibility and therapeutic potential of ^{177}Lu-fibroblast activation protein inhibitor-46 for patients with relapsed or refractory cancers: a preliminary study. *Clin Nucl Med.* 2021;46:e523–e530.
13. Baum RP, Schuchardt C, Singh A, et al. Feasibility, biodistribution and preliminary dosimetry in peptide-targeted radionuclide therapy (PTRT) of diverse adenocarcinomas using ^{177}Lu-FAP-2286: first-in-human results. *J Nucl Med.* June 24, 2021 [Epub ahead of print].
14. Toms J, Kogler J, Maschauer S, et al. Targeting fibroblast activation protein: radiosynthesis and preclinical evaluation of an ^{18}F-labeled FAP inhibitor. *J Nucl Med.* 2020;61:1806–1813.
15. Hidalgo M, Amant F, Biankin AV, et al. Patient-derived xenograft models: an emerging platform for translational cancer research. *Cancer Discov.* 2014;4:998–1013.
16. Lang L, Li W, Guo N, et al. Comparison study of [^{18}F]FAl-NOTA-PRGD2, [^{18}F]FPPRGD2, and [^{68}Ga]Ga-NOTA-PRGD2 for PET imaging of U87MG tumors in mice. *Bioconjug Chem.* 2011;22:2415–2422.
17. Li ZB, Cai W, Cao Q, et al. ^{64}Cu-labeled tetrameric and octameric RGD peptides for small-animal PET of tumor alpha$_v$beta$_3$ integrin expression. *J Nucl Med.* 2007; 48:1162–1171.
18. Wu Z, Li ZB, Chen K, et al. MicroPET of tumor integrin alpha$_v$beta$_3$ expression using ^{18}F-labeled PEGylated tetrameric RGD peptide (^{18}F-FPRGD4). *J Nucl Med.* 2007;48:1536–1544.
19. Zhao L, Chen H, Guo Z, et al. Targeted radionuclide therapy in patient-derived xenografts using ^{177}Lu-EB-RGD. *Mol Cancer Ther.* 2020;19:2034–2043.
20. Chen H, Zhao L, Fu K, et al. Integrin alpha$_v$beta$_3$-targeted radionuclide therapy combined with immune checkpoint blockade immunotherapy synergistically enhances anti-tumor efficacy. *Theranostics.* 2019;9:7948–7960.
21. Chen H, Zhao L, Ruan D, et al. Usefulness of [^{68}Ga]Ga-DOTA-FAPI-04 PET/CT in patients presenting with inconclusive [^{18}F]FDG PET/CT findings. *Eur J Nucl Med Mol Imaging.* 2021;48:73–86.
22. Stabin MG, Sparks RB, Crowe E. OLINDA/EXM: the second-generation personal computer software for internal dose assessment in nuclear medicine. *J Nucl Med.* 2005;46:1023–1027.
23. Meyer C, Dahlbom M, Lindner T, et al. Radiation dosimetry and biodistribution of ^{68}Ga-FAPI-46 PET imaging in cancer patients. *J Nucl Med.* 2020;61:1171–1177.
24. Jokar N, Velikyan I, Ahmadzadehfar H, et al. Theranostic approach in breast cancer: a treasured tailor for future oncology. *Clin Nucl Med.* 2021;46:e410–e420.
25. Wang S, Zhou X, Xu X, et al. Clinical translational evaluation of Al^{18}F-NOTA-FAPI for fibroblast activation protein-targeted tumour imaging. *Eur J Nucl Med Mol Imaging.* 2021;48:4259–4271.
26. Liu S. Radiolabeled cyclic RGD peptides as integrin alpha$_v$beta$_3$-targeted radiotracers: maximizing binding affinity via bivalency. *Bioconjug Chem.* 2009;20: 2199–2213.
27. Li ZB, Chen K, Chen X. ^{68}Ga-labeled multimeric RGD peptides for microPET imaging of integrin alpha$_v$beta$_3$ expression. *Eur J Nucl Med Mol Imaging.* 2008; 35:1100–1108.

Diagnostic Performance of ^{124}I-Metaiodobenzylguanidine PET/CT in Patients with Pheochromocytoma

Manuel Weber[1,2], Jochen Schmitz[1,2], Ines Maric[1,2], Kim Pabst[1,2], Lale Umutlu[2,3], Martin Walz[4], Ken Herrmann[1,2], Christoph Rischpler[1,2], Frank Weber[2,5], Walter Jentzen[1,2], Sarah Theurer[2,6], Thorsten D. Poeppel[7], Nicole Unger*[2,8], and Wolfgang P. Fendler*[1,2]

[1]*Department of Nuclear Medicine, University Hospital Essen, Essen, Germany;* [2]*German Cancer Consortium, Essen, Germany;* [3]*Department of Diagnostic and Interventional Radiology and Neuroradiology, University Hospital Essen, Essen, Germany;* [4]*Department of Surgery and Center of Minimally Invasive Surgery, Evangelische Kliniken Essen–Mitte, Academic Teaching Hospital of University Duisburg–Essen, Essen, Germany;* [5]*Department of General, Visceral, and Transplantation Surgery, Section of Endocrine Surgery, University of Duisburg–Essen, Essen, Germany;* [6]*Institute of Pathology, University Hospital Essen, University Duisburg–Essen, Essen, Germany;* [7]*Nuklearmedizin, MVZ CDT Strahleninstitut, Cologne, Germany; and* [8]*Division of Laboratory Research, Department of Endocrinology and Metabolism, University Hospital Essen, University Duisburg–Essen, Essen, Germany*

$^{123/131}$I-metaiodobenzylguanidine (MIBG) scintigraphy has shown a high specificity for imaging pheochromocytoma and paraganglioma, but with low sensitivity because of low spatial resolution. ^{124}I-MIBG PET may be able to overcome this limitation and improve the staging of patients with (suspected) pheochromocytoma. **Methods:** We analyzed the sensitivity, specificity, and positive and negative predictive values of ^{124}I-MIBG PET in 43 consecutive patients with suspected (recurrence of) pheochromocytoma using histopathologic (n = 25) and clinical validation (n = 18) as the standard of truth. Furthermore, we compared the detection rate of ^{124}I-MIBG PET versus contrast-enhanced (CE) CT on a per-patient and per-lesion basis in 13 additional patients with known metastatic malignant pheochromocytoma. **Results:** ^{124}I-MIBG PET/CT was positive in 19 (44%) of 43 patients with suspected pheochromocytoma. The presence of pheochromocytoma was confirmed in 22 (51%) of 43. ^{124}I-MIBG PET/CT sensitivity, specificity, and positive and negative predictive values were 86%, 100%, 100%, and 88%, respectively. ^{124}I-MIBG PET was positive in 11 (85%) of 13 patients with malignant pheochromocytoma. Combined ^{124}I-MIBG PET and CE CT detected 173 lesions, of which 166 (96%) and 118 (68%) were visible on ^{124}I-MIBG PET and CE CT, respectively. **Conclusion:** ^{124}I-MIBG PET detects pheochromocytoma with high accuracy at initial staging and a high detection rate at restaging. Future assessment of ^{124}I-MIBG PET for treatment guidance, including personalized ^{131}I-MIBG therapy, is warranted.

Key Words: ^{124}I-MIBG PET; pheochromocytoma; theranostics

J Nucl Med 2022; 63:869–874
DOI: 10.2967/jnumed.121.262797

Metaiodobenzylguanidine (MIBG), or iobenguane, is an analog of the adrenergic neurotransmitter norepinephrine and shows uptake in sympathetically innervated tissues such as the heart and salivary glands and tumors that express norepinephrine transporters (*1*). Because of high accumulation and retention in sympathicomedullary tissue, ^{123}I/^{131}I-MIBG scintigraphy has been used for decades in the imaging of pheochromocytoma and paraganglioma, as well as in many neural crest tumors, with reported sensitivities and specificities of between 80% and 100% (*2–4*). The sensitivity is hampered considerably by a low spatial resolution, making the assessment of small lesions particularly challenging (*5*). Because of superior technology and workflows, PET expanded rapidly (*6*) and is now the standard imaging modality for most cancer entities, including pretherapeutic imaging in patients with neuroendocrine tumors (*7*) and prostate cancer (*8,9*). In patients with pheochromocytoma and paraganglioma, somatostatin receptor–targeted PET (*10–12*) and ^{18}F-flubrobenguane (*13*) have shown a high specific uptake and a high sensitivity. However, ^{124}I-MIBG PET comes with several potential advantages.

The similarity in its biodistribution to that of ^{123}I-MIBG allows for the translation of current concepts for image interpretation (e.g., SIOPEN [International Society of Paediatric Oncology European Neuroblastoma] and curie), protocols, and medications established by use of ^{123}I-MIBG scintigraphy (*14,15*).

Furthermore, ^{124}I-MIBG PET potentially combines the high specificity of MIBG imaging with the high sensitivity (*5,16*) and better quantification of PET tracers (*17–19*) and thereby addresses major shortcomings of current γ-emitting compounds.

In addition, the long ^{124}I half-life (4.18 d) allows for the assessment of pharmacokinetics by performing imaging and blood tests at multiple time points (*18,20–23*). Following the theranostic principle, the sister compound ^{131}I-labeled MIBG is applied for radionuclide therapy. In light of the recent Food and Drug Administration approval of ^{131}I-MIBG (*24*) for the treatment of unresectable, locally advanced, and metastatic pheochromocytoma and paraganglioma, pretherapeutic ^{124}I-MIBG PET can provide valuable information on absorbed doses to the tumor and organs at risk and thereby lay the foundation for personalized dosimetry and activity escalation. The potential of the theranostic pair ^{124}I/^{131}I to improve efficacy and mitigate toxicity has previously been shown in the treatment of patients with differentiated thyroid cancer (*20,21,23,25*) and in a case report on ^{124}I/^{131}I-MIBG (*18*).

The aim of this retrospective study was to assess the diagnostic performance of ^{124}I-MIBG PET in patients with suspected pheochromocytoma and in patients with metastatic malignant

Received Jul. 6, 2021; revision accepted Sep. 8, 2021.
For correspondence and reprints, contact Manuel Weber (manuel.weber@uk-essen.de).
*Contributed equally to this work.
Published online Sep. 23, 2021.

pheochromocytoma (MMP) before ^{131}I-MIBG therapy. With this intent, we analyzed the optimal imaging time point with regard to tumor uptake, the accuracy in comparison to CT, and the rate of upstaging by use of ^{124}I-MIBG PET in patients with MMP.

MATERIALS AND METHODS

Study Design and Participants

We screened our institutional database for patients who, between March 2005 and March 2017, underwent ^{124}I-MIBG PET/CT for suspected recurrence of adrenal pheochromocytoma and who had sufficient follow-up data for validation. The primary endpoint in these patients was the diagnostic performance, defined as sensitivity, specificity, and negative and positive predictive value. Validation was performed histopathologically or—when histopathology was not available—by an experienced, board-certified endocrinologist on the basis of clinical and laboratory parameters. Secondary endpoints were the diagnostic power of quantitative assessment using SUV_{peak} for differentiating between patients for whom the suspected pheochromocytoma was confirmed versus those for whom it was ruled out. A subgroup analysis was performed for patients who met the criteria for an indeterminate adrenal mass (size > 10 mm and Hounsfield units [HU] > 10 on non–contrast-enhanced [NC] CT).

For a second analysis, we included patients with known metastatic MMP. The primary metric in this cohort was the lesion detection rate of ^{124}I-MIBG PET using the sum of all detected lesions in conjunction with coacquired contrast-enhanced (CE) CT as the reference standard. The protocol was approved by the Ethics Commission of the University of Duisburg–Essen medical faculty (protocol 20-9656-BO).

^{124}I-MIBG Synthesis

^{124}I-MIBG was manually prepared by the substitution of non–carrier-added ^{124}I-iodine to MIBG. The labeling was performed via copper(I)-assisted isotopic iodine/iodine exchange. ^{124}I-iodine was purchased from PerkinElmer LAS in the form of sodium iodide (^{124}I) as 0.02N NaOH solution. Glacial acetic acid (Merck KGaA) was used as the solvent for all other reactants. Typically, 100–130 MBq of the ^{124}I solution were transferred into a testing tube, 10 μL of a sodium disulfite solution (4 mg/mL) were added, and the mixture was reduced to dryness using a rotating evaporator. A 40-μL volume of a solution containing 100 μg of metaiodobenzylguanidine (Sigma-Aldrich) and 1.5 μL of Cu(I)Cl (0.1 M; Merck KGaA) was added to the residue. The mixture was then heated in the stoppered testing tube at 160°C for 10 min. After the subsequent reduction to dryness, the raw product was resolved in 80–100 μL of hydrochloric acid (0.01 M, aqueous; Sigma-Aldrich) and the volume was injected into a high-performance liquid chromatography system (Waters) for purification. The semipreparative high-performance liquid chromatography was performed isocratically using a LiChroCART 250-4 column (Purospher RP-18, 5 μm; Merck) with radioactivity and ultraviolet detection (254 nm), the eluent being an aqueous solution of NaH_2PO_4 (1.38 g/L) and acetonitrile, 9:1 (v/v). The product peak (retention time, 13 min; activity channel) was collected in a round-bottom flask, and the volume was reduced to dryness and formulated in 5 mL of phosphate-buffered saline. The volume was collected into a syringe and passed through a 0.22-μm filter (Millex GV; Millipore) directly into a sterile vial (Cis-Bio), yielding 50–70 MBq of formulated ^{124}I-MIBG. Quality control testing of the product was performed using a high-performance liquid chromatography system identical to that for the semipreparative run. Purity was determined to be between 98% and 100%

Imaging Protocol

PET/CT was performed on a Siemens Duo (n = 40, 71%), Siemens Biograph mCT (n = 15, 27%), or Siemens Biograph mMR (n = 1, 2%) at 4 h (n = 26), 1 d (n = 53), 2 d (n = 33), and 4 or 5 d (n = 11) after the administration of a mean activity of 49.8 (interquartile range, 48.3–53.0) MBq of ^{124}I-MIBG. The emission time was 3 min 30 s per bed position for PET/CT and 8 min for PET/MRI. Attenuation correction was performed with the coacquired CT or MRI scan.

Image Analysis

SUV_{peak} was measured in the 5 lesions displaying the highest tracer uptake for each MMP patient at all imaging time points, with the aim of identifying the imaging time point with the highest average SUV_{peak} and tumor-to-background ratio, with SUV_{mean} liver as the reference background.

The ^{124}I-MIBG PET/CT images of all preoperative or recurrent pheochromocytomas at this time point were then read by a masked central reader, and pathologic findings were categorized by anatomic region (adrenal gland, bones, or viscera, including distant lymph nodes). The size, SUV_{peak}, and HU of the adrenal masses on the NC CT images were measured. The CE CT and ^{124}I-MIBG PET/CT images were anonymized separately and read by a masked reader, with at least 2 wk elapsing between reading sessions to avoid recall bias.

Statistical Analysis

The accuracy of ^{124}I-MIBG PET is reported by descriptive statistics. For an indeterminate adrenal mass, separate analyses were performed using the NC CT criteria (>10 HU and >10 mm) versus combined ^{124}I-MIBG PET and NC CT criteria (^{124}I-MIBG PET–positive or adrenal mass >10 HU and >10 mm). The detection rate for patients with MMP was defined as the fraction of ^{124}I-MIBG PET–positive lesions among all lesions for CE CT and ^{124}I-MIBG PET/CT combined. Statistical analysis was performed using SPSS Statistics, version 26 (IBM Corp.). Mann–Whitney U testing was performed to determine the statistical significance of SUV_{peak} between patients with and without pheochromocytoma. A receiver-operating-characteristic curve, with area under the curve as a metric, was used to determine the predictive potential of SUV_{peak} for the diagnosis of pheochromocytoma, after the exclusion of 1 patient for whom images were acquired 2 d after the administration of ^{124}I-MIBG. The Youden J statistic was used to identify the optimal cutoff for the diagnosis of pheochromocytoma based on the SUV_{peak} for all patients and separately for patients with an indeterminate adrenal mass.

RESULTS

Patient Cohort

Fifty-six consecutive patients were eligible. In 43 of 56 patients ^{124}I-MIBG PET was performed for suspected pheochromocytoma because of an elevated catecholamine metabolite level, an unclear renal mass, or the clinical appearance; 4 of these were examined because of suspected recurrence after initial resection. Patient characteristics are given in Table 1. The mean patient age was 51.8 y (range, 20–74 y); 25 patients (58%) were female, and 18 (42%) were male. Three patients (7%) had multiple endocrine neoplasia type IIA, and one (2%) had neurofibromatosis type 1. The mean levels for metanephrine and normetanephrine were 180.9 pg/mL (range, 15–1,377 pg/mL) and 313.8 pg/mL (range, 28–2,358 pg/mL), respectively.

In 13 patients, ^{124}I-MIBG PET/CT was performed for known MMP. The mean patient age was 50.9 y (range, 17–80 y). Seven (54%) of these 13 patients were female, and 6 (46%) were male.

An overview of the MMP patient characteristics is provided in Table 2.

TABLE 1
Characteristics of Patients Who Underwent ^{124}I-MIBG PET for Suspected Pheochromocytoma

Characteristic	Data
Mean age (y)	51.8 (range, 20–74)
Sex (*n*)	
Male	18 (42%)
Female	25 (58%)
Catecholamine metabolites (pg/mL)	
Normetanephrines (plasma)	313.8 (28–2,358)
Metanephrines (plasma)	180.8 (15–1,377)
Mean size of adrenal mass (mm)	30 (range, 6–82)
Associated genetic syndrome (*n*)	
Multiple endocrine neoplasia IIA	3 (7%)
Neurofibromatosis	1 (2%)

^{124}I-MIBG Tumor Uptake

The mean SUV_{peak} across all lesions was 13.0, 13.3, 12.0, and 9.2 after 4 h, 1 d, 2 d, and 4 or 5 d, respectively. The tumor-to-background ratio at 4 h, 1 d, 2 d, and 4 or 5 d was 1.4, 6.2, 4.9, and 7.6, respectively. Because of the highest tumor SUV_{peak} and the highest number of available data points 1 d after ^{124}I-MIBG injection, this time point was used for the subsequent accuracy analyses. In 3 patients, for whom ^{124}I-MIBG PET/CT was not performed 1 d after injection, 2-d images were used instead. Figure 1 shows the mean SUV_{peak} across all measured lesions and the mean tumor-to-background ratio over time.

TABLE 2
Characteristics of Patients Who Underwent ^{124}I-MIBG PET for Known Metastatic MMP

Characteristic	Data
Mean age (y)	50.9 (range, 17–81)
Sex (*n*)	
Male	6 (46%)
Female	7 (54%)
Tumor sites per patient (*n*)	
Adrenal gland	3 (23%)
Regional lymph nodes	5 (38%)
Bones	6 (46%)
Visceral, including distant lymph nodes	6 (46%)

^{124}I-MIBG PET Accuracy for Suspected Pheochromocytoma

^{124}I-MIBG PET was positive in 19 (44%) of 43 patients with suspected pheochromocytoma and negative in 24 (56%). In 1 of the 19 patients with positive findings on ^{124}I-MIBG PET, a local lymph node metastasis was detected. Twenty-five of the 43 patients had adrenal masses with a density of more than 10 HU on NC CT; in 22 of these, the respective masses were more than 10 mm.

The suspicion of pheochromocytoma was confirmed by the reference standard in 22 (51%) of the 43 patients and ruled out in 21 (49%). Histopathology was available in all cases with confirmed pheochromocytoma and in 3 (14%) of 21 cases in which the presence of pheochromocytoma was ruled out. Of the 22 patients with pheochromocytoma, 21 (95%) had unilateral involvement and 1 (5%) had bilateral involvement. In 18 (42%) of the 43 patients, the presence of pheochromocytoma was excluded on the basis of clinical records and repeated assessment of serum and urine catecholamine metabolites.

An overview of the diagnostic performance of ^{124}I-MIBG PET is provided in Table 3. Imaging was positive in 19 of 22 patients with confirmed pheochromocytoma and negative in 21 of 21 patients in whom the presence of pheochromocytoma was ruled out, resulting in a sensitivity and specificity of 86% and 100%, respectively.

In all patients with positive findings on ^{124}I-MIBG PET, pheochromocytoma was histopathologically confirmed, whereas 3 patients with a negative ^{124}I-MIBG PET result would later be diagnosed with pheochromocytoma, leading to a positive predictive value and negative predictive value of 100% and 88%, respectively.

NC CT was available for 36 patients. Of the 25 patients with adrenal masses greater than 10 HU, pheochromocytoma was confirmed in 18 and ruled out in 7; of the 11 patients with adrenal masses less than 10 HU, pheochromocytoma was confirmed in 1 and ruled out in 10, leading to a sensitivity, specificity, positive predictive value, and negative predictive value of 95%, 59%, 72%, and 91%, respectively.

Using an additional size threshold of 10 mm did not affect sensitivity but improved specificity, positive predictive value, and negative predictive value to 76%, 82%, and 93%, respectively.

Combined ^{124}I-MIBG PET and NC CT criteria improved the sensitivity to 100%, specificity to 76%, negative predictive value to 100%, and positive predictive value to 84%.

Pheochromocytomas had a significantly higher SUV_{peak} than did unaffected adrenal glands (11.8 vs. 3.5, $P < 0.001$). The area under the curve for the SUV_{peak}-based identification of pheochromocytoma was 0.88, with the optimal cutoff being 5.4. Subgroup analysis of all patients with adrenal lesions having a density higher than 10 HU showed an area under the curve of 0.90 (sensitivity, 68%; specificity, 100%) for classification into pheochromocytoma versus nonpheochromocytoma. Separate subgroup analyses of all patients with an

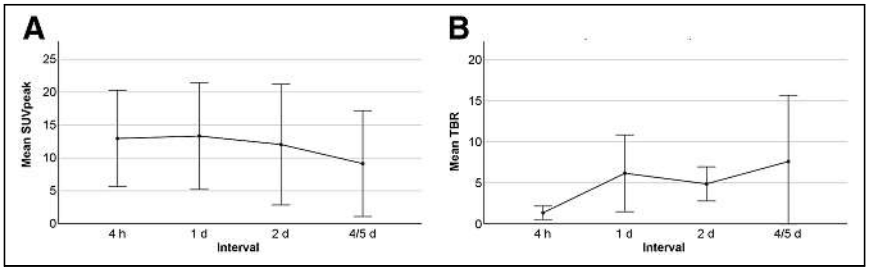

FIGURE 1. Simple error bar with 95% CI plotting mean tumor SUV_{peak} (A) and tumor SUV_{peak}/tumor SUV_{mean} (B) for all measured lesions in ^{124}I-MIBG PET–positive MMP patients (n = 11) over time.

TABLE 3
Diagnostic Performance of ^{124}I-MIBG PET, NC CT, and Combined ^{124}I-MIBG PET and NC CT in Patients

Modality	Tumor present		Tumor absent		Diagnostic metrics				
	Scan+	Scan−	Scan+	Scan−	Sen	Spe	PPV	NPV	Acc
^{124}I-MIBG PET	19	3	0	21	86%	100%	100%	88%	93%
^{124}I-MIBG PET (NC CT available)	17	2	0	17	89%	100%	100%	89%	94%
HU > 10	18	7	1	10	95%	59%	72%	91%	78%
HU > 10; size > 10 mm	18	4	1	13	95%	76%	82%	93%	86%
^{124}I-MIBG PET + NC CT	21	0	4	13	100%	76%	83%	100%	89%

Sen = sensitivity; Spe = specificity; Acc = accuracy.

indeterminate adrenal mass (HU > 10 and size > 10 mm; $n = 22$) showed an SUV_{peak} of 8.5 versus 2.9 ($P < 0.001$), resulting in an area under the curve of 0.90 (sensitivity, 72%; specificity, 100%) with an optimal cutoff of 7.0. Figure 2 gives an overview of the SUV_{peak} of patients for whom pheochromocytoma was confirmed versus those for whom it was ruled out.

^{124}I-MIBG PET Detection Rate for Metastatic Pheochromocytoma

In the 13 patients with known MMP lesions, increased focal ^{124}I-MIBG uptake was observed in 11 (85%). Combined CE CT and ^{124}I-MIBG PET detected 173 lesions, of which 166 (96%) showed increased ^{124}I-MIBG uptake, whereas 118 lesions (67%) were detected on standalone CE CT. This led to upstaging from M1a to M1c disease in 1 patient (8%) and migration from oligometastatic disease (>5 tumor sites) (*26*) in 3 (23%).

In 5 of these patients, additional ^{68}Ga-DOTATOC PET/CT was performed. ^{68}Ga-DOTATOC–positive/^{124}I-MIBG PET–negative lesions were found in 2 patients, and ^{68}Ga-DOTATOC–negative/^{124}I-MIBG PET–positive lesions were found in 1 patient. In the remainder, ^{68}Ga-DOTATOC PET and ^{124}I-MIBG PET yielded identical results with regard to lesion detection, but tumor-specific uptake was higher on ^{124}I-MIBG PET. Figure 3 shows an example MMP patient with positive ^{124}I-MIBG PET/CT results.

DISCUSSION

The present study reports high ^{124}I-MIBG PET accuracy at initial staging and a high detection rate at restaging in the—so far, to our knowledge—largest published cohort of patients with (suspected) pheochromocytoma.

Image acquisition 1 d after ^{124}I-MIBG PET demonstrated the highest SUV_{peak}, and subsequent analyses were performed at this time point.

The reported sensitivity of the present study is comparable to that reported for $^{123/131}$I-MIBG scintigraphy studies, and the specificity is close to the higher end of reported values (*4,27–30*). Sensitivity similar to that of $^{123/131}$I-MIBG is unexpected, as the spatial resolution of PET imaging when compared with scintigraphy might translate into a higher accuracy. Interestingly, patients with false-negative ^{124}I-MIBG PET results did not have particularly small pheochromocytomas (3.0, 2.2, and 4.0 cm) when compared with the mean size of all resected pheochromocytomas (3.5 cm), implying that biology and norepinephrine transporter expression, rather than spatial resolution, are critical for lesion detection.

In line with the published literature, NC CT–based assessment has shown a high sensitivity, with only 1 false-negative finding, but at the expense of a low specificity.

Because ^{124}I-MIBG PET enables coacquisition of CE CT, NC CT, or MRI, the diagnostic performance might be improved over that of ^{123}I-MIBG scintigraphy, taking advantage of the high specificity of functional imaging and the high sensitivity of morphologic imaging. Therefore, complementary information from ^{124}I-MIBG PET might be of added value in the workup of unclear adrenal lesions when prior diagnostic imaging is inconclusive and to rule out or confirm metastatic spread before local treatment. In our cohort, visual interpretation of ^{124}I-MIBG images was superior to semiquantitative assessment for the diagnosis of pheochromocytoma. Further studies should assess the potential diagnostic value of ^{124}I-MIBG kinetics in the diagnostic workup of adrenal lesions suggestive of pheochromocytoma. Because of an increase in tumor-to-background ratio over time, images acquired at late time points might aide the differentiation of tumor uptake from physiologic uptake in equivocal lesions.

^{124}I-MIBG PET/CT has also shown a high diagnostic performance in patients with MMP, demonstrating additional lesions compared with standalone CE CT in 7 (54%) of 13 patients, with TNM upstaging in 1 patient (8%) and stage migration from oligometastatic disease (*26*) to disseminated disease in

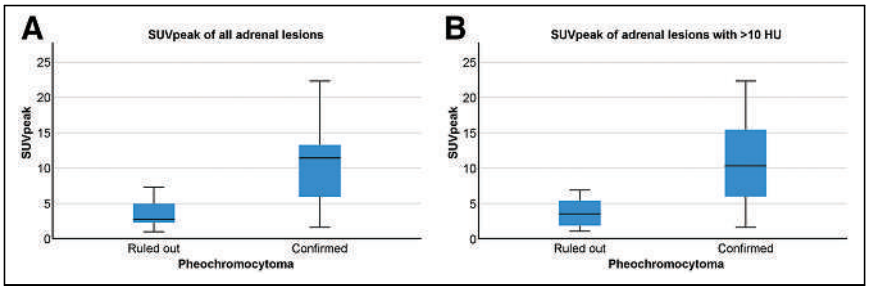

FIGURE 2. Adrenal SUV_{peak} for all patients (A) and patients with indeterminate adrenal masses (B) for whom pheochromocytoma was confirmed vs. those for whom it was ruled out.

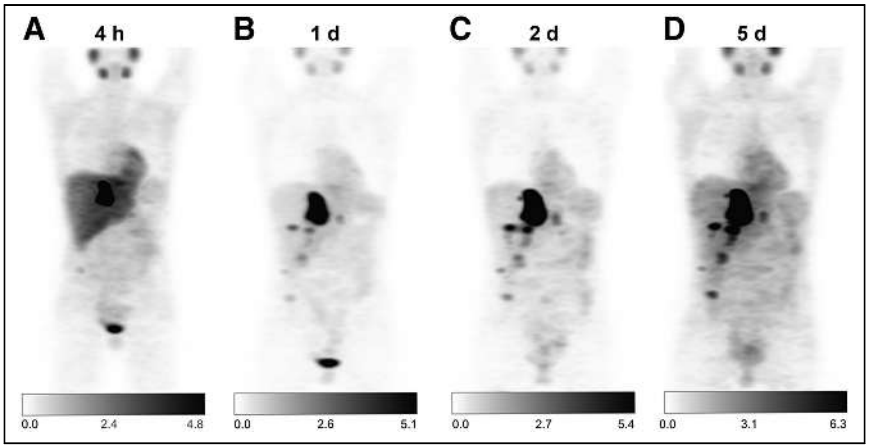

FIGURE 3. Example patient with metastatic MMP who underwent ^{124}I-MIBG PET/CT before planned radionuclide therapy. At 4 h (A), 1 d (B), 2 d (C), and 5 d (D) after image acquisition, dosimetry-derived activity of 20 GBq of ^{131}I-MIBG was administered, leading to lesion-absorbed doses of between 110 and 320 Gy and progression-free survival of 54 mo.

3 (23%). The high detection rate may impact patient staging, implementation of local treatment, and response assessment of systemic or local treatment. Detection of additional tumor sites might also prevent locoregional therapies in disseminated disease when little benefit is to be expected.

In light of the 2018 Food and Drug Administration approval of ^{131}I-MIBG radionuclide therapy for MIBG-positive unresectable, locally advanced or metastatic pheochromocytoma and paraganglioma, ^{124}I-MIBG PET/CT furthermore carries great potential for radionuclide therapy planning.

The long half-life or superior quantification of ^{124}I-MIBG PET/CT when compared with $^{123/131}$I-MIBG scintigraphy facilitates an improved assessment of uptake intensity and kinetics (*18,20,31–34*). Pretherapeutic dosimetry of tumor lesions and organs at risk enables personalized dosimetry with the goal of maximizing tumor response while keeping toxicity levels acceptable. The potential of personalized dosimetry for ^{131}I therapy has previously been described in the context of differentiated thyroid cancer (*25,35,36*), but data on pheochromocytoma are scarce (*18,34,37*). In our cohort, 85% of patients with known MMP were MIBG-positive. In 2 patients with at least 1 ^{124}I-MIBG–negative lesion, intense ^{68}Ga-DOTATOC uptake was observed in all lesions, underpinning the theranostic potential of ^{68}Ga-/^{177}Lu-/^{90}Y-labeled somatostatin analogs (*38*). Prior small retrospective studies identified radiopeptide as a potential treatment option, leading to response rates of up to 50% and disease control rates of up to 100% (*39–42*).

Limitations of this study include the retrospective design and the small sample, as well as the absence of an adrenal-specific CT protocol and MR tomography.

CONCLUSION

^{124}I-MIBG PET detects pheochromocytoma with high accuracy at the initial work-up of adrenal masses and at restaging of metastatic disease. Accuracy was similar to that previously reported for $^{123/131}$I-MIBG scintigraphy. Future studies on the impact of ^{124}I-MIBG PET on locoregional treatment and personalized ^{131}I-MIBG therapy, as well as a head-to-head comparison with $^{123/131}$I-MIBG scintigraphy, are warranted.

DISCLOSURE

Manuel Weber reports fees from Boston Scientific (speakers bureau) outside the submitted work. Ken Herrmann reports personal fees from Bayer, SIRTEX, Adacap, Curium, Endocyte, IPSEN, Siemens Healthineers, GE Healthcare, Amgen, Novartis, and ymabs; personal fees and other fees from Sofie Biosciences; nonfinancial support from ABX; and grants and personal fees from BTG outside the submitted work. Wolfgang P. Fendler reports fees from Calyx (consultant), RadioMedix (image review), Bayer (speakers bureau), and Parexel (image review) outside the submitted work. No other potential conflict of interest relevant to this article was reported.

KEY POINTS

QUESTION: What is the diagnostic performance of ^{124}I-MIBG PET in patients with known or suspected pheochromocytoma?

PERTINENT FINDINGS: ^{124}I-MIBG PET has a higher accuracy than NC CT in suspected pheochromocytoma and detects additional lesions in patients with known metastatic pheochromocytoma.

IMPLICATIONS FOR PATIENT CARE: ^{124}I-MIBG PET is a promising imaging technique that can provide information additional to that from cross-sectional imaging and thereby complement the diagnostic workup in patients with known or suspected pheochromocytoma.

REFERENCES

1. Vallabhajosula S, Nikolopoulou A. Radioiodinated metaiodobenzylguanidine (MIBG): radiochemistry, biology, and pharmacology. *Semin Nucl Med.* 2011;41:324–333.
2. Wiseman GA, Pacak K, O'Dorisio MS, et al. Usefulness of ^{123}I-MIBG scintigraphy in the evaluation of patients with known or suspected primary or metastatic pheochromocytoma or paraganglioma: results from a prospective multicenter trial. *J Nucl Med.* 2009;50:1448–1454.
3. Bomanji J, Bouloux PM, Levison DA, et al. Observations on the function of normal adrenomedullary tissue in patients with phaeochromocytomas and other paragangliomas. *Eur J Nucl Med.* 1987;13:86–89.
4. Shapiro B, Copp JE, Sisson JC, Eyre PL, Wallis J, Beierwaltes WH. Iodine-131 metaiodobenzylguanidine for the locating of suspected pheochromocytoma: experience in 400 cases. *J Nucl Med.* 1985;26:576–585.
5. Aboian MS, Huang SY, Hernandez-Pampaloni M, et al. ^{124}I-MIBG PET/CT to monitor metastatic disease in children with relapsed neuroblastoma. *J Nucl Med.* 2021;62:43–47.
6. Vaz SC, Oliveira F, Herrmann K, Veit-Haibach P. Nuclear medicine and molecular imaging advances in the 21st century. *Br J Radiol.* 2020;93:20200095.
7. Hofman MS, Kong G, Neels OC, Eu P, Hong E, Hicks RJ. High management impact of Ga-68 DOTATATE (GaTate) PET/CT for imaging neuroendocrine and other somatostatin expressing tumours. *J Med Imaging Radiat Oncol.* 2012;56:40–47.
8. Hofman MS, Lawrentschuk N, Francis RJ, et al. Prostate-specific membrane antigen PET-CT in patients with high-risk prostate cancer before curative-intent surgery or radiotherapy (proPSMA): a prospective, randomised, multicentre study. *Lancet.* 2020;395:1208–1216.

9. Hofman MS, Emmett L, Sandhu S, et al. [^{177}Lu]Lu-PSMA-617 versus cabazitaxel in patients with metastatic castration-resistant prostate cancer (TheraP): a randomised, open-label, phase 2 trial. *Lancet.* 2021;397:797–804.
10. Kroiss A, Putzer D, Frech A, et al. A retrospective comparison between ^{68}Ga-DOTA-TOC PET/CT and ^{18}F-DOPA PET/CT in patients with extra-adrenal paraganglioma. *Eur J Nucl Med Mol Imaging.* 2013;40:1800–1808.
11. Kroiss A, Putzer D, Decristoforo C, et al. ^{68}Ga-DOTA-TOC uptake in neuroendocrine tumour and healthy tissue: differentiation of physiological uptake and pathological processes in PET/CT. *Eur J Nucl Med Mol Imaging.* 2013;40:514–523.
12. Kroiss AS, Uprimny C, Shulkin BL, et al. ^{68}Ga-DOTATOC PET/CT in the localization of metastatic extra-adrenal paraganglioma and pheochromocytoma compared with ^{18}F-DOPA PET/CT. *Rev Esp Med Nucl Imagen Mol.* 2019;38:94–99.
13. Kessler L, Schlitter AM, Kronke M, et al. First experience using ^{18}F-flubrobenguane PET imaging in patients with suspected pheochromocytoma or paraganglioma. *J Nucl Med.* 2021;62:479–485.
14. Lewington V, Lambert B, Poetschger U, et al. ^{123}I-mIBG scintigraphy in neuroblastoma: development of a SIOPEN semi-quantitative reporting, method by an international panel. *Eur J Nucl Med Mol Imaging.* 2017;44:234–241.
15. Ady N, Zucker JM, Asselain B, et al. A new ^{123}I-MIBG whole body scan scoring method: application to the prediction of the response of metastases to induction chemotherapy in stage IV neuroblastoma. *Eur J Cancer.* 1995;31A:256–261.
16. Beijst C, de Keizer B, Lam M, Janssens GO, Tytgat GAM, de Jong H. A phantom study: should ^{124}I-mIBG PET/CT replace ^{123}I-mIBG SPECT/CT? *Med Phys.* 2017;44:1624–1631.
17. Hicks RJ, Hofman MS. Is there still a role for SPECT-CT in oncology in the PET-CT era? *Nat Rev Clin Oncol.* 2012;9:712–720.
18. Huang SY, Bolch WE, Lee C, et al. Patient-specific dosimetry using pretherapy [^{124}I]m-iodobenzylguanidine ([^{124}I]mIBG) dynamic PET/CT imaging before [^{131}I]mIBG targeted radionuclide therapy for neuroblastoma. *Mol Imaging Biol.* 2015;17:284–294.
19. Beijst C, Kist JW, Elschot M, et al. Quantitative comparison of ^{124}I PET/CT and ^{131}I SPECT/CT detectability. *J Nucl Med.* 2016;57:103–108.
20. Jentzen W, Bockisch A, Ruhlmann M. Assessment of simplified blood dose protocols for the estimation of the maximum tolerable activity in thyroid cancer patients undergoing radioiodine therapy using ^{124}I. *J Nucl Med.* 2015;56:832–838.
21. Pettinato C, Monari F, Nanni C, et al. Usefulness of ^{124}I PET/CT imaging to predict absorbed doses in patients affected by metastatic thyroid cancer and treated with ^{131}I. *Q J Nucl Med Mol Imaging.* 2012;56:509–514.
22. Plyku D, Hobbs RF, Huang K, et al. Recombinant human thyroid-stimulating hormone versus thyroid hormone withdrawal in ^{124}I PET/CT-based dosimetry for ^{131}I therapy of metastatic differentiated thyroid cancer. *J Nucl Med.* 2017;58:1146–1154.
23. Ruhlmann M, Sonnenschein W, Nagarajah J, Binse I, Herrmann K, Jentzen W. Pretherapeutic ^{124}I dosimetry reliably predicts intratherapeutic blood kinetics of ^{131}I in patients with differentiated thyroid carcinoma receiving high therapeutic activities. *Nucl Med Commun.* 2018;39:457–464.
24. Pryma DA, Chin BB, Noto RB, et al. Efficacy and safety of high-specific-activity ^{131}I-MIBG therapy in patients with advanced pheochromocytoma or paraganglioma. *J Nucl Med.* 2019;60:623–630.
25. Klubo-Gwiezdzinska J, Van Nostrand D, Atkins F, et al. Efficacy of dosimetric versus empiric prescribed activity of ^{131}I for therapy of differentiated thyroid cancer. *J Clin Endocrinol Metab.* 2011;96:3217–3225.
26. Hellman S, Weichselbaum RR. Oligometastases. *J Clin Oncol.* 1995;13:8–10.
27. Furuta N, Kiyota H, Yoshigoe F, Hasegawa N, Ohishi Y. Diagnosis of pheochromocytoma using [^{123}I]-compared with [^{131}I]-metaiodobenzylguanidine scintigraphy. *Int J Urol.* 1999;6:119–124.
28. Rufini V, Troncone L, Valentini AL, Danza FM. A comparison of scintigraphy with radioiodinated MIBG and CT in localizing pheochromocytomas [in Italian]. *Radiol Med (Torino).* 1988;76:466–470.
29. Mozley PD, Kim CK, Mohsin J, Jatlow A, Gosfield E III, Alavi A. The efficacy of iodine-123-MIBG as a screening test for pheochromocytoma. *J Nucl Med.* 1994; 35:1138–1144.
30. Van Der Horst-Schrivers AN, Jager PL, Boezen HM, Schouten JP, Kema IP, Links TP. Iodine-123 metaiodobenzylguanidine scintigraphy in localising phaeochromocytomas: experience and meta-analysis. *Anticancer Res.* 2006;26: 1599–1604.
31. Kolbert KS, Pentlow KS, Pearson JR, et al. Prediction of absorbed dose to normal organs in thyroid cancer patients treated with ^{131}I by use of ^{124}I PET and 3-dimensional internal dosimetry software. *J Nucl Med.* 2007;48:143–149.
32. Sgouros G, Hobbs RF, Atkins FB, Van Nostrand D, Ladenson PW, Wahl RL. Three-dimensional radiobiological dosimetry (3D-RD) with ^{124}I PET for ^{131}I therapy of thyroid cancer. *Eur J Nucl Med Mol Imaging.* 2011;38(suppl 1):S41–S47.
33. Jentzen W, Freudenberg L, Eising EG, Sonnenschein W, Knust J, Bockisch A. Optimized ^{124}I PET dosimetry protocol for radioiodine therapy of differentiated thyroid cancer. *J Nucl Med.* 2008;49:1017–1023.
34. Seo Y, Gustafson WC, Dannoon SF, et al. Tumor dosimetry using [^{124}I]m-iodobenzylguanidine microPET/CT for [^{131}I]m-iodobenzylguanidine treatment of neuroblastoma in a murine xenograft model. *Mol Imaging Biol.* 2012;14:735–742.
35. Hartung-Knemeyer V, Nagarajah J, Jentzen W, et al. Pre-therapeutic blood dosimetry in patients with differentiated thyroid carcinoma using 124-iodine: predicted blood doses correlate with changes in blood cell counts after radioiodine therapy and depend on modes of TSH stimulation and number of preceding radioiodine therapies. *Ann Nucl Med.* 2012;26:723–729.
36. Weber M, Binse I, Nagarajah J, Bockisch A, Herrmann K, Jentzen W. The role of ^{124}I PET/CT lesion dosimetry in differentiated thyroid cancer. *Q J Nucl Med Mol Imaging.* 2019;63:235–252.
37. Lee CL, Wahnishe H, Sayre GA, et al. Radiation dose estimation using preclinical imaging with ^{124}I-metaiodobenzylguanidine (MIBG) PET. *Med Phys.* 2010;37: 4861–4867.
38. Han S, Suh CH, Woo S, Kim YJ, Lee JJ. Performance of ^{68}Ga-DOTA-conjugated somatostatin receptor-targeting peptide PET in detection of pheochromocytoma and paraganglioma: a systematic review and metaanalysis. *J Nucl Med.* 2019;60: 369–376.
39. Puranik AD, Kulkarni HR, Singh A, Baum RP. Peptide receptor radionuclide therapy with ^{90}Y/^{177}Lu-labelled peptides for inoperable head and neck paragangliomas (glomus tumours). *Eur J Nucl Med Mol Imaging.* 2015;42:1223–1230.
40. Zovato S, Kumanova A, Dematte S, et al. Peptide receptor radionuclide therapy (PRRT) with ^{177}Lu-DOTATATE in individuals with neck or mediastinal paraganglioma (PGL). *Horm Metab Res.* 2012;44:411–414.
41. Kong G, Grozinsky-Glasberg S, Hofman MS, et al. Efficacy of peptide receptor radionuclide therapy for functional metastatic paraganglioma and pheochromocytoma. *J Clin Endocrinol Metab.* 2017;102:3278–3287.
42. Forrer F, Riedweg I, Maecke HR, Mueller-Brand J. Radiolabeled DOTATOC in patients with advanced paraganglioma and pheochromocytoma. *Q J Nucl Med Mol Imaging.* 2008;52:334–340.

The Added Value of ^{68}Ga-FAPI PET/CT in Patients with Head and Neck Cancer of Unknown Primary with ^{18}F-FDG–Negative Findings

Bingxin Gu[1–4], Xiaoping Xu[1–4], Ji Zhang[1–4], Xiaomin Ou[5], Zuguang Xia[6], Qing Guan[7], Silong Hu[1–4], Zhongyi Yang[1–4], and Shaoli Song[1–4]

[1]Department of Nuclear Medicine, Fudan University Shanghai Cancer Center, Shanghai, China; [2]Department of Oncology, Shanghai Medical College, Fudan University, Shanghai, China; [3]Center for Biomedical Imaging, Fudan University, Shanghai, China; [4]Shanghai Engineering Research Center of Molecular Imaging Probes, Shanghai, China; [5]Department of Radiation Oncology, Fudan University Shanghai Cancer Center, Shanghai, China; [6]Department of Medical Oncology, Fudan University Shanghai Cancer Center, Shanghai, China; and [7]Department of Head and Neck Surgery, Fudan University Shanghai Cancer Center, Shanghai, China

^{18}F-FDG PET/CT plays an important role in locating the primary tumor for patients with head and neck cancer of unknown primary (HNCUP). Nevertheless, in some cases it can be challenging to locate the primary malignancy on ^{18}F-FDG PET/CT scans. Because ^{68}Ga-radiolabeled fibroblast activation protein inhibitor (FAPI) PET/CT has promising results in detecting different tumor entities, our study aimed to evaluate the performance of ^{68}Ga-FAPI PET/CT for detecting the primary tumor in HNCUP patients with negative ^{18}F-FDG findings. **Methods:** Eighteen patients (16 men and 2 women; median age, 55 y; age range, 24–72 y) with negative ^{18}F-FDG findings were enrolled in this study. All patients underwent ^{18}F-FDG and ^{68}Ga-FAPI PET/CT within 1 wk. Biopsy and histopathologic examinations were performed in the sites with positive ^{68}Ga-FAPI PET/CT findings. **Results:** ^{68}Ga-FAPI PET/CT detected the primary tumor in 7 of 18 patients (38.89%). Among these 7 patients, primary tumor sites included the nasopharynx (n = 1), palatine tonsil (n = 2), submandibular gland (n = 2), and hypopharynx (n = 2). The primary tumors showed moderate to intensive uptake of ^{68}Ga-FAPI (mean SUV_{max}, 8.79; range, 2.60–16.50) and excellent tumor–to–contralateral normal-tissue ratio (mean SUV_{max} ratio, 4.50; range, 2.17–8.21). In lesion-based analysis, 65 lymph nodes and 17 bone metastatic lesions were identified. The mean SUV_{max} of lymph node metastases was 9.05 ± 5.29 for ^{18}F-FDG and 9.08 ± 4.69 for ^{68}Ga-FAPI (P = 0.975); the mean SUV_{max} of bone metastases was 8.11 ± 3.00 for ^{18}F-FDG and 6.96 ± 5.87 for ^{68}Ga-FAPI (P = 0.478). The mean tumor-to-background ratios of lymph node and bone metastases were 10.65 ± 6.59 versus 12.80 ± 8.11 (P = 0.100) and 9.08 ± 3.35 versus 9.14 ± 8.40 (P = 0.976), respectively. **Conclusion:** We present the first evidence, to our knowledge, of a diagnostic role of ^{68}Ga-FAPI PET/CT in HNCUP. Our study demonstrated that ^{68}Ga-FAPI PET/CT has the potential to improve the detection rate of primary tumor in HNCUP patients with negative ^{18}F-FDG findings. Moreover, ^{68}Ga-FAPI had a performance in assessing metastases similar to that of ^{18}F-FDG.

Key Words: ^{68}Ga-FAPI; head and neck; cancer of unknown primary; metastases

J Nucl Med 2022; 63:875–881
DOI: 10.2967/jnumed.121.262790

Head and neck cancer of unknown primary (HNCUP) is defined as a metastatic disease in the cervical lymph nodes with an unidentifiable primary tumor (*1*), even after a thorough diagnostic workup according to the National Comprehensive Cancer Network (*2*) and American Society of Clinical Oncology guidelines (*3*). HNCUP constitutes 1%–5% of all head and neck cancers (*4,5*). Squamous cell carcinoma (SCC) is the most common pathologic type of HNCUP, and approximately 90% of these cases are associated with human papillomavirus (*1*). The most frequent primary site of HNCUP is the oropharynx, accounting for 80%–90% (*6*). However, factors such as small tumor volume, hidden location, slow growth rate, and tumor involution hinder primary site identification (*7*). The absence of primary tumor identification may result in uncertain treatment decisions and increasing psychologic burden for patients with HNCUP (*8*).

Medical imaging plays an important role in oncology, particularly in tumor location (*9*). Conventional imaging modalities, CT and MRI, can provide plentiful anatomic information about primary and metastatic malignancies. However, the detection rates of the primary site for these 2 imaging modalities range from 9% to 23% in HNCUP (*10–12*). PET/CT, a typical molecular imaging modality, outperforms CT and MRI in identifying the primary tumor, with a detection rate of 25%–69% using ^{18}F-FDG (*13–16*). Nevertheless, some limitations hamper the application of ^{18}F-FDG PET/CT in primary tumor identification for HNCUP (*17,18*). First, physiologic ^{18}F-FDG uptake can be seen in any lymphatic structure (especially Waldeyer's ring), salivary glands, and brown fat. Second, uptake in the symmetric vocal cords and neck muscles is commonly seen if the patient talks or coughs during the uptake period. Third, infection and chronic inflammation (e.g., nasopharyngitis, amygdalitis, and gingivitis) can also result in high ^{18}F-FDG uptake. These limitations may lead to false-positive findings, with a rate of 16%–25% (*4,13,16*). Last, false-negative ^{18}F-FDG uptake can be seen in small, mucinous, well-differentiated, and necrotic lesions (*18*). Therefore, novel specific radiopharmaceuticals with low background uptake in the head and neck, which may better improve the detection rate of the primary tumor in HNCUP, are in urgent need.

Received Jun. 28, 2021; revision accepted Sep. 21, 2021.
For correspondence or reprints, contact Shaoli Song (shaoli-song@163.com) or Zhongyi Yang (yangzhongyi21@163.com).
Published online Sep. 30, 2021.

Cancer-associated fibroblasts (CAFs), accounting for high proportion of most solid tumor mass, play a vital role in tumor growth, migration, and progression (*19*). The major feature discriminating CAFs from normal fibroblasts is the overexpression of fibroblast activation protein (FAP) (*20*). The presence of FAP was observed on a variety of epithelial and mesenchymal malignancies (*21,22*). Recently, ^{68}Ga-radiolabeled fibroblast activation protein inhibitor (FAPI), a novel FAP-targeted PET tracer, has shown great value in the diagnosis of diverse carcinomas (*23,24*). Furthermore, studies (*25,26*) have demonstrated that ^{68}Ga-FAPI revealed high uptake in primary tumors and low background noise in the head and neck region. These promising findings indicate that ^{68}Ga-FAPI could serve as a potential alternative to ^{18}F-FDG for the assessment of head and neck cancers.

Thus, the aim of this study was to investigate the value of ^{68}Ga-FAPI PET/CT for identifying the primary tumor of ^{18}F-FDG–negative HNCUP.

MATERIALS AND METHODS

Patient Selection

For patients whose primary tumor could not be identified by thorough medical history, clinical examination, medical imaging (e.g., contrast-enhanced CT, contrast-enhanced MRI, ultrasound, and ^{18}F-FDG PET/CT), and endoscopy, ^{68}Ga-FAPI PET/CT was recommended, based on the decision of a multidisciplinary team in head and neck cancer (Fig. 1A). In addition to patients in whom ^{18}F-FDG findings were negative for localizing the primary tumor, ^{68}Ga-FAPI PET/CT was also recommended to patients in whom ^{18}F-FDG findings were positive for localizing the primary tumor who had undergone a biopsy that resulted in a negative finding. To further investigate the role of ^{68}Ga-FAPI PET/CT in HNCUP, inclusion criteria were as follows: adult patients (age $>$ 18 and $<$ 80 y); pathology-confirmed metastatic cervical carcinoma by fine-needle aspiration; conventional imaging modalities (e.g., contrast-enhanced CT, contrast-enhanced MRI, or ultrasound) could not provide positive finding of primary tumor; both ^{18}F-FDG and ^{68}Ga-FAPI PET/CT were performed. The exclusion criteria were patients with lymphomas or non–head and neck original cancers, confirmed by immunohistochemistry; patients with both positive ^{18}F-FDG and ^{68}Ga-FAPI PET/CT findings for primary tumors, including anaplastic thyroid carcinoma, lymphoepithelioma-like carcinoma, and biopsy-negative but clinically diagnosed nasopharyngeal carcinoma; patients with 2 or more malignant tumors history; and patients unwilling to undergo ^{18}F-FDG or ^{68}Ga-FAPI PET/CT. ^{18}F-FDG PET/CT reported negatively for localization of primary tumor in patients with HNCUP would be regarded as negative ^{18}F-FDG PET/CT findings. This prospective study was approved by Fudan University Shanghai Cancer Center Institutional Review Board (ID 2004216-25) conducted in accordance with the 1964 Declaration of Helsinki and its later amendments or comparable ethical standards, and all subjects signed an informed consent form.

Radiopharmaceuticals and PET/CT Scanning Procedure

^{18}F-FDG was produced automatically using the Explora FDG_4 module with cyclotron (Siemens CTI RDS Eclips ST) in our center. DOTA-FAPI-04 (Jiangsu Huayi Technology Co., Ltd.) was radiolabeled with ^{68}Ga solution (elution from the ^{68}Ge generator IGG100, Eckert & Ziegler) according to the procedure of Lindner et al. (*27*). The radiochemical purities of ^{18}F-FDG and ^{68}Ga-FAPI were both more than 95%.

^{18}F-FDG PET/CT was performed first, and ^{68}Ga-FAPI PET/CT imaging was then performed within 1 wk. For ^{18}F-FDG PET/CT scanning, patients fasted at least 6 h, maintaining venous blood glucose levels under 10 mmol/L before ^{18}F-FDG administration. This fasting process was not necessary for ^{68}Ga-FAPI PET/CT scanning. After injection of with 260.64 ± 40.81 MBq of ^{18}F-FDG or 143.71 ± 16.19 MBq of ^{68}Ga-FAPI, patients were kept in a quiet environment for approximately 60 min before examination. All images were obtained on a Biograph mCT Flow scanner (Siemens Medical Solutions). PET image datasets were reconstructed iteratively using an ordered-subset expectation maximization iterative reconstruction by applying CT data for attenuation correction. Two experienced nuclear medicine physicians independently analyzed and interpreted the images masked, and they reached a consensus in the case of inconsistency.

Increased radioactivity of primary and metastatic lesions compared with the muscle background uptake was defined as being positive, verified by biopsy or follow-up. For quantitative analysis, maximum or mean of SUV (SUV_{max} or SUV_{mean}) normalized to body weight was manually computed for primary and metastatic lesions and healthy tissues by drawing a 3-dimensional volume of interest. Meanwhile, the SUV_{max} ratio for primary tumor was defined as the quotient of the SUV_{max} of primary tumor and the contralateral normal tissue, and tumor-to-background ratio (TBR) for primary and metastatic lesions was calculated according to the formula $TBR = tSUV_{max}/bSUV_{mean}$, where $tSUV_{max}$ is the SUV_{max} of the tumor lesion, and $bSUV_{mean}$ is the SUV_{mean} of muscle. The size of primary and metastatic lesions was measured by CT.

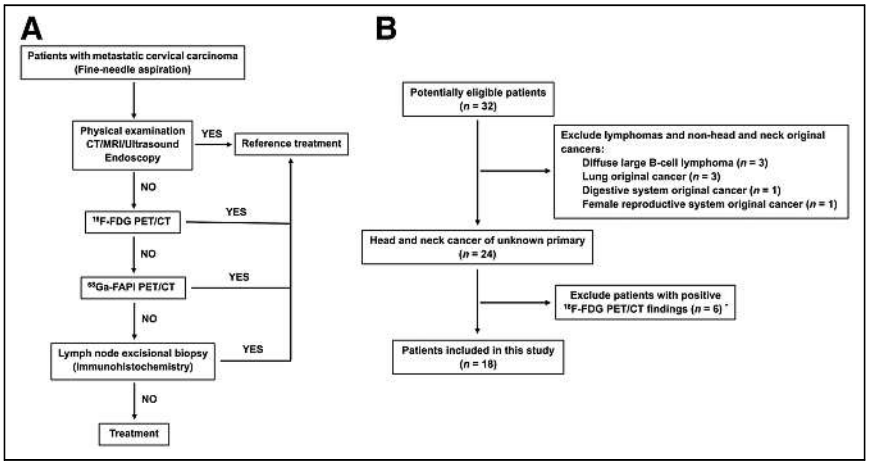

FIGURE 1. Flowchart of diagnostic workup (A) and patient selection (B). "YES" means the primary tumor was identified by these techniques and further confirmed by pathology, and "NO" indicates these techniques could not identify the primary tumor. *^{68}Ga-FAPI PET/CT could also identify the primary tumor in these patients.

Statistical Analysis

All statistical analyses were performed using SPSS 25.0 (IBM). Means with SDs or medians with ranges were used to describe continuous characteristics. To compare the uptake of ^{18}F-FDG and ^{68}Ga-FAPI in metastatic lesions, 2-sample *t* tests were used. Two-tailed *P* values less than 0.05 were considered statistically significant.

RESULTS

Patients

A total of 32 patients were enrolled consecutively from our center from June 2020 to February 2021, and 18 patients were included for further analysis according to the inclusion and exclusion criteria (Fig. 1B). The basic clinical characteristics are presented in Table 1. Among the included 18 patients (16 men and 2 women; median age, 55 y;

TABLE 1
Patients Characteristics

Patient	Sex	Age (y)	EBV-DNA status	HPV status	p16 status	Pathologic type of cervical lymph node
1	M	52	P	U	U	SCC
2	M	63	N	P	P	SCC
3	M	58	N	P	P	SCC
4	M	50	N	U	U	AC
5	M	41	U	P	P	AC
6	M	55	N	U	U	SCC
7	M	54	N	N	N	SCC
8	M	72	N	U	U	SCC
9	M	61	N	P	N	SCC
10	M	47	N	N	P	SCC
11	M	62	N	N	N	SCC
12	F	55	P	N	N	SCC
13	M	63	N	U	U	SCC
14	F	67	N	U	U	SCC
15	M	40	N	P	P	SCC
16	M	24	N	N	N	SCC
17	M	55	N	U	U	SCC
18	M	51	U	P	P	SCC

EBV-DNA = Epstein-Barr virus DNA; HPV = human papillomavirus; P = positive; U = unknown; N = negative; AC = adenocarcinoma.

age range, 24–72 y), 2 (11.11%) were infected with Epstein-Barr virus, 6 (33.33%) were infected with human papillomavirus, 16 (88.89%) were pathologically diagnosed with cervical lymph node SCC, and 2 (11.11%) had adenocarcinoma.

Comparison of ^{18}F-FDG and ^{68}Ga-FAPI PET/CT in Metastatic Lesions

A total of 65 lymph node and 17 bone metastases were detected by both ^{18}F-FDG and ^{68}Ga-FAPI PET/CT (Fig. 2, Table 2, and Supplemental Table 1 [supplemental materials are available at http://jnm.snmjournals.org]). Both tracers showed intensive uptake in lymph node and bone metastases. The mean SUV_{max} of lymph node metastases was 9.05 ± 5.29 for ^{18}F-FDG and 9.08 ± 4.69 for ^{68}Ga-FAPI (P = 0.975). The TBR for ^{68}Ga-FAPI was a slightly higher than that for ^{18}F-FDG (12.80 ± 8.11 vs. 10.65 ± 6.59, respectively); however, the difference was not significant (P = 0.100). For bone metastases, the mean SUV_{max} was 8.11 ± 3.00 for ^{18}F-FDG and 6.96 ± 5.87 for ^{68}Ga-FAPI (P = 0.478), and the mean TBR values were 9.08 ± 3.35 and 9.14 ± 8.40 (P = 0.976), respectively. Generally, no significant uptake difference was observed between ^{18}F-FDG and ^{68}Ga-FAPI in lymph node and bone metastases, indicating that ^{68}Ga-FAPI PET/CT had a performance similar to that of ^{18}F-FDG PET/CT in assessing metastases of head and neck cancers.

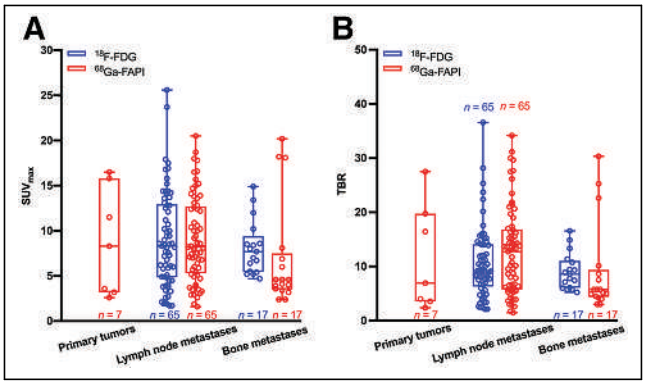

FIGURE 2. Box plots of SUV_{max} (A) and TBR (B) on ^{18}F-FDG versus ^{68}Ga-FAPI PET/CT.

^{68}Ga-FAPI PET/CT Imaging Results of Primary Tumors

Primary tumors in 7 of 18 (38.89%) patients with ^{18}F-FDG–negative results were identified by ^{68}Ga-FAPI PET/CT and pathologically confirmed by subsequent biopsy. ^{68}Ga-FAPI PET/CT showed a higher detection rate in adenocarcinoma (2/2, 100%) than in SCC (5/16, 31.25%). Primary sites included the nasopharynx (n = 1), palatine tonsil (n = 2) (Fig. 3), submandibular gland (n = 2) (Fig. 4), and hypopharynx (n = 2) (Supplemental Fig. 1 and Table 3).

American Joint Committee on Cancer (AJCC) TNM stages for the 7 patients with ^{18}F-FDG–negative results ranged from I to IVC (eighth edition of the AJCC TNM staging system) (*28*). The smallest primary tumor size detected by ^{68}Ga-FAPI PET/CT was 5 × 3 mm. The mean SUV_{max} of ^{68}Ga-FAPI for primary tumors was 8.79 (range, 2.60–16.50), and the mean TBR value was 11.50 (range, 2.36–27.50). When compared with the contralateral normal tissue, the primary tumor showed a remarkably higher uptake of ^{68}Ga-FAPI, with a mean SUV_{max} ratio of 4.50 (range, 2.17–8.21).

TABLE 2
Comparison of Metastatic Lesions on ^{18}F-FDG and ^{68}Ga-FAPI PET/CT in 18 Patients with HNCUP

Patient	Metastases		Range of metastases size (mm)	^{18}F-FDG		^{68}Ga-FAPI		*P*	
	Location	No.		SUV_{max}	TBR	SUV_{max}	TBR	SUV_{max}	TBR
1	LN	3	7–8	5.27 ± 1.29	4.39 ± 1.07	2.27 ± 0.91	2.06 ± 0.82		
2	LN	2	7–20	6.55 ± 0.92	7.28 ± 1.02	7.10 ± 0.42	5.92 ± 0.35		
3	LN	2	10–16	8.10 ± 1.84	9.00 ± 2.04	14.40 ± 0.85	20.57 ± 1.21		
4	LN	16	7–22	10.78 ± 3.13	11.98 ± 3.48	13.69 ± 4.19	22.81 ± 6.98		
	Bone	1	N/A	8.00	8.89	18.20	30.33		
5	LN	8	4–8	2.70 ± 1.07	3.38 ± 1.33	9.41 ± 2.40	11.77 ± 3.00		
	Bone	1	N/A	8.60	10.75	20.20	25.25		
6	LN	2	17–22	5.60 ± 4.24	8.00 ± 6.06	5.35 ± 0.92	5.94 ± 1.02		
7	LN	1	17	7.60	8.44	12.80	14.22		
8	LN	1	38	25.60	36.57	15.20	19.00		
9	LN	4	7–17	15.78 ± 1.61	13.15 ± 1.34	3.83 ± 1.32	4.25 ± 1.47		
10	LN	1	27	7.30	9.13	3.10	2.58		
11	LN	2	13–20	15.35 ± 3.61	19.19 ± 4.51	5.60 ± 2.69	8.00 ± 3.84		
12	LN	3	13–21	10.80 ± 5.17	18.00 ± 8.62	5.63 ± 3.82	8.05 ± 5.46		
13	LN	1	10	6.20	8.86	8.60	9.56		
14	LN	8	5–11	6.81 ± 4.30	11.35 ± 7.17	7.60 ± 3.31	8.44 ± 3.68		
15	LN	1	5	2.10	2.63	2.90	3.63		
16	LN	3	12–26	12.63 ± 2.29	14.04 ± 2.55	11.87 ± 3.27	14.83 ± 4.08		
	Bone	15	N/A	8.08 ± 3.19	8.98 ± 3.55	5.33 ± 3.86	6.66 ± 4.83		
17	LN	3	10–19	8.80 ± 1.28	8.00 ± 1.16	7.60 ± 0.50	15.20 ± 1.00		
18	LN	4	4–18	11.08 ± 9.02	11.08 ± 9.02	7.58 ± 3.51	9.47 ± 4.39		
Sum	LN	65	4–26	9.05 ± 5.29	10.65 ± 6.59	9.08 ± 4.69	12.80 ± 8.11	0.975	0.100
	Bone	17	N/A	8.11 ± 3.00	9.08 ± 3.35	6.96 ± 5.87	9.14 ± 8.40	0.478	0.976

PET semiquantitative parameters were presented as means with SD.
TBR = tumor-to-background ratio; LN = lymph node; N/A = not applicable.

DISCUSSION

Identifying the primary tumor remains a concern for patients with HNCUP, though the development in imaging, endoscopy, and pathology techniques has progressed quickly. When no positive findings are obtained using noninvasive procedures, invasive diagnostic procedures such as tonsillectomy are then performed; these invasive procedures have a risk of bleeding or infection (*5*). Thus, noninvasive methods may be needed for improving the detection rate of primary tumor in HNCUP patients. This study investigated the performance of ^{68}Ga-FAPI PET/CT in identifying the primary tumor of ^{18}F-FDG–negative HNCUP. Our results demonstrated that ^{68}Ga-FAPI can dramatically improve the detection rate of primary tumor in HNCUP patients compared with ^{18}F-FDG. Furthermore, ^{68}Ga-FAPI may show a performance similar to ^{18}F-FDG in assessing metastases.

In the current study, the detection rate of the primary tumor by ^{68}Ga-FAPI PET/CT was 38.89% (7/18). Notably, these patients all exhibited false-negative ^{18}F-FDG PET/CT findings. Sites of false-negative ^{18}F-FDG PET/CT findings included the nasopharynx, palatine tonsil, submandibular gland, and hypopharynx; these sites are different from previously reported observations that the tonsil was the most frequent false-negative location (*16*). Recently, Serfling et al. (*26*) reported ^{68}Ga-FAPI PET/CT showed a better visual detection of the malignant primary in Waldeyer's tonsillar ring than ^{18}F-FDG PET/CT. However, the representative cases could provide positive findings of the primary site by ^{18}F-FDG PET/CT alone in terms of HNCUP. Another study demonstrated that an SUV_{max} ratio of ^{18}F-FDG uptake between tonsils of ≥1.6 could be regarded as malignancy and used to guide biopsy (*29*). In this study, 2 patients were diagnosed with palatine tonsil carcinoma by tonsillectomy. Puzzlingly, ^{18}F-FDG PET/CT revealed no visual difference between right and left palatine tonsils in both cases. Furthermore, the SUV_{max} ratios of ^{18}F-FDG uptake were all approximately equivalent to 1.00 (1.07 and 1.04 for patients 2 and 3, respectively), which was mistaken as physiologic uptake. By contrast, ^{68}Ga-FAPI PET/CT showed intensive uptake in the tumor site and low uptake in the normal site, resulting in a visual difference (SUV_{max} ratio = 3.46 and 8.21, respectively). In line with our results, Syed et al. (*25*) demonstrated high ^{68}Ga-FAPI avidity within tumorous lesions and low background uptake in healthy tissues of the head and neck region, again emphasizing the potential role of ^{68}Ga-FAPI PET/CT in detecting palatine tonsil carcinoma, particularly in patients with ^{18}F-FDG–negative results.

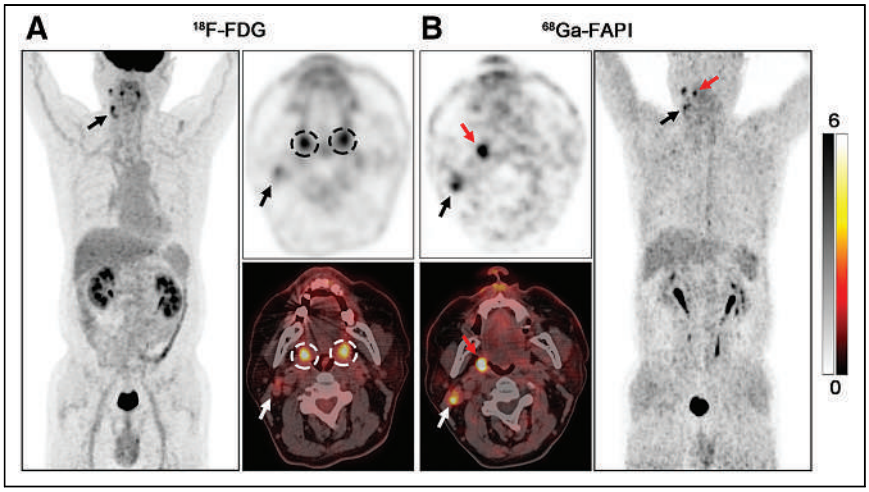

FIGURE 3. PET/CT scans with ^{18}F-FDG (A) and ^{68}Ga-FAPI (B) in 63-y-old male patient (patient 2) with metastatic SCC of right neck. ^{18}F-FDG PET/CT was negative for detection of primary. Increased uptake of ^{18}F-FDG was detected in palatine tonsils of both right and left sides (A, black and white dashed circles; SUV_{max} = 6.40 and 6.00, respectively), resulting an SUV_{max} ratio of 1.07. On ^{68}Ga-FAPI PET/CT, there was asymmetric fullness with intensive uptake in right palatine tonsil (B, red arrow; SUV_{max} = 8.30), whereas low background uptake was seen in left palatine tonsil (SUV_{max} ratio = 3.46). Subsequent tonsillectomy confirmed SCC. Black and white arrows indicate metastatic lymph nodes.

In addition to high-grade physiologic uptake in the head and neck, small lesion size was the major reason for the false-negative ^{18}F-FDG findings due to the partial-volume effect and low tumor glucose metabolic activity (*30,31*). In the current study, ^{18}F-FDG PET/CT missed 3 of 7 primary tumors because of their small size (diameter < 10 mm). Encouragingly, ^{68}Ga-FAPI PET/CT revealed moderate uptake (SUV_{max} = 2.60, 3.20, and 3.60 for patients 1, 6, and 7, respectively) and a clearly visual difference (SUV_{max} ratio = 2.17, 2.91, and 3.27, respectively) in these primary tumors with small size, which was consistent with previous research (*24*). ^{68}Ga-FAPI uptake is primarily based on the expression of FAP on CAFs in a solid tumor microenvironment, and even small T1 stage primary tumors could show a moderate FAP expression (*26*). Thus, to reduce the false-negative results by ^{18}F-FDG PET/CT, ^{68}Ga-FAPI could serve as an alternative tracer for identifying small primary tumors.

Most of the research focuses on SCC, as it is the most frequent pathologic type of HNCUP (*3–5*). However, other pathologic types, such as adenocarcinoma and neuroendocrine carcinoma, may cause diagnostic difficulties in clinical practice because of the lack of information regarding these pathologic types. Moreover, for cervical metastatic adenocarcinoma, diagnostic resection of the salivary gland is not recommended even after thorough noninvasive investigations. Furthermore, salivary gland cancers show a paucity of ^{18}F-FDG avidity (*32*), which was proven again in our study (patients 4 and 5). Several non–^{18}F-FDG radiopharmaceuticals, for example, ^{18}F-fluorothymidine, ^{68}Ga-DOTA-somatostatin analogs, and ^{18}F-fluoromisonidazole, are recommended for detecting the primary tumor of HNCUP (*33*). However, these tracers are too specific to identify all types of head and neck cancers. Promisingly, recent studies have demonstrated ^{68}Ga-FAPI can evaluate a broad spectrum of malignancies, including adenocarcinoma, neuroendocrine carcinoma, and well-differentiated carcinoma (*23,24*). In this study, ^{68}Ga-FAPI showed intensive uptake in the submandibular gland (SUV_{max} = 16.50 and 15.80, respectively), providing sufficient information following surgery. Notably, ^{68}Ga-FAPI had a higher detection rate in adenocarcinoma (2/2, 100%) than SCC (5/16, 31.25%) of HNCUP, indicating that ^{68}Ga-FAPI was more sensitive to adenocarcinoma. However, further research with larger sample sizes is needed to verify this result.

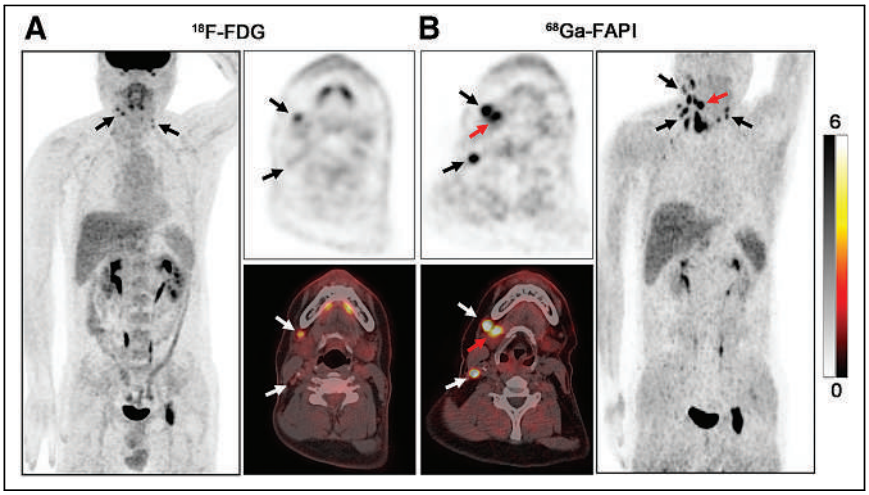

FIGURE 4. PET/CT scans with ^{18}F-FDG (A) and ^{68}Ga-FAPI (B) in a 41-y-old male patient (patient 5) with metastatic adenocarcinoma of right neck. ^{18}F-FDG PET/CT was negative for detection of primary. On ^{68}Ga-FAPI PET/CT, there was intensive uptake in right submandibular gland (B, red arrow; SUV_{max} = 15.80), whereas low background uptake was seen in left submandibular gland (SUV_{max} ratio = 6.87). Subsequent surgery confirmed salivary ductal carcinoma. Black and white arrows indicate metastatic lymph nodes.

Regarding the detection of regional and distant metastases, the performance of ^{68}Ga-FAPI PET/CT varies among different studies (*24,26*). In our study, ^{68}Ga-FAPI PET/CT showed a performance ($P > 0.05$) similar to that of ^{18}F-FDG PET/CT in detecting both lymph node and bone metastases. Because radiation therapy is one of the most important modalities of treating HNCUP, the advantages of ^{68}Ga-FAPI PET/CT in both primary tumors and metastases may play a vital role in gross tumor volume delineation.

There are some limitations in this study. The main limitation is the relatively small number of patients and that the number of pathologic types is imbalanced. In the future, larger population cohort studies with more cancer types need to be considered. Additionally, immunohistochemistry for FAP expression of primary tumors and metastases is lacking. Hence, FAPI imaging and FAP expression control studies are also necessary in the future.

TABLE 3
Primary Tumor Characteristics and Semiquantitative Parameters of ^{68}Ga-FAPI PET/CT

Patient	TNM	Primary tumor location	Pathologic type	Tumor size (mm)	^{68}Ga-FAPI		
					SUV_{max}	TBR	SUV_{max} ratio
1	T1N1M0 Stage II	Nasopharynx top wall	NDSCC	6 × 5	2.60	2.36	2.17
2	T1N1M0 Stage I	Palatine tonsil right side	SCC	11 × 10	8.30	6.92	3.46
3	T1N1M0 Stage I	Palatine tonsil right side	SCC	13 × 10	11.50	16.43	8.21
4	T2N2M1 Stage IVC	Submandibular gland right side	SDC	23 × 20	16.50	27.50	4.58
5	T1N2M1 Stage IVC	Submandibular gland right side	SDC	17 × 13	15.80	19.75	6.87
6	T1N1M0 Stage III	Hypopharynx posterior wall	SCC	5 × 3	3.20	3.56	2.91
7	T1N1M0 Stage III	Sinus piriformis right side	SCC	6 × 5	3.60	4.00	3.27

NDSCC = nonkeratinizing differentiated squamous cell carcinomas; SDC = salivary ductal carcinoma.

CONCLUSION

This study demonstrated that ^{68}Ga-FAPI PET/CT can improve the detection rate of the primary tumor in HNCUP patients with negative ^{18}F-FDG findings. Furthermore, for evaluating metastatic lesions, ^{68}Ga-FAPI PET/CT showed a performance similar to that of ^{18}F-FDG PET/CT. Because an improved detection rate is necessary in HNCUP, future research on more patients with HNCUP should be considered to evaluate the clinical value of ^{68}Ga-FAPI PET/CT.

DISCLOSURE

This work was funded by National Natural Science Foundation of China (grants 81771861, 81971648, and 81901778) and Shanghai Anticancer Association Program (grant no. HYXH2021004). No other potential conflict of interest relevant to this article was reported.

ACKNOWLEDGEMENT

We thank the head and neck cancer multidisciplinary team in our center for the great help to our work.

KEY POINTS

QUESTION: Does ^{68}Ga-FAPI PET/CT have value for identifying the primary tumor in HNCUP patients with ^{18}F-FDG–negative results?

PERTINET FINDINGS: In this prospective study, ^{68}Ga-FAPI PET/CT improved the detection rate (38.89%) of the primary tumor in HNCUP patients with negative ^{18}F-FDG findings.

IMPLICATIONS FOR PATIENT CARE: Our study provides a new strategy for identifying the primary tumor in patients with HNCUP, which may change their treatment decisions.

REFERENCES

1. Kennel T, Garrel R, Costes V, Boisselier P, Crampette L, Favier V. Head and neck carcinoma of unknown primary. *Eur Ann Otorhinolaryngol Head Neck Dis.* 2019; 136:185–192.
2. Pfister DG, Spencer S, Adelstein D, et al. Head and neck cancers, version 2.2020, NCCN clinical practice guidelines in oncology. *J Natl Compr Canc Netw.* 2020; 18:873–898.
3. Maghami E, Ismaila N, Alvarez A, et al. Diagnosis and management of squamous cell carcinoma of unknown primary in the head and neck: ASCO guideline. *J Clin Oncol.* 2020;38:2570–2596.
4. Galloway TJ, Ridge JA. Management of squamous cancer metastatic to cervical nodes with an unknown primary site. *J Clin Oncol.* 2015;33:3328–3337.
5. Moy J, Li R. Approach to the patient with unknown primary squamous cell carcinoma of the head and neck. *Curr Treat Options Oncol.* 2020;21:93.
6. Keller LM, Galloway TJ, Holdbrook T, et al. p16 status, pathologic and clinical characteristics, biomolecular signature, and long-term outcomes in head and neck squamous cell carcinomas of unknown primary. *Head Neck.* 2014;36: 1677–1684.
7. Golusinski P, Di Maio P, Pehlivan B, et al. Evidence for the approach to the diagnostic evaluation of squamous cell carcinoma occult primary tumors of the head and neck. *Oral Oncol.* 2019;88:145–152.
8. Arosio AD, Pignataro L, Gaini RM, Garavello W. Neck lymph node metastases from unknown primary. *Cancer Treat Rev.* 2017;53:1–9.
9. Junn JC, Soderlund KA, Glastonbury CM. Imaging of head and neck cancer with CT, MRI, and US. *Semin Nucl Med.* 2021;51:3–12.
10. Regelink G, Brouwer J, de Bree R, et al. Detection of unknown primary tumours and distant metastases in patients with cervical metastases: value of FDG-PET versus conventional modalities. *Eur J Nucl Med Mol Imaging.* 2002;29:1024–1030.
11. Freudenberg LS, Fischer M, Antoch G, et al. Dual modality of ^{18}F-fluorodeoxyglucose-positron emission tomography/computed tomography in patients with cervical carcinoma of unknown primary. *Med Princ Pract.* 2005;14:155–160.
12. Waltonen JD, Ozer E, Hall NC, Schuller DE, Agrawal A. Metastatic carcinoma of the neck of unknown primary origin: evolution and efficacy of the modern workup. *Arch Otolaryngol Head Neck Surg.* 2009;135:1024–1029.
13. Rusthoven KE, Koshy M, Paulino AC. The role of fluorodeoxyglucose positron emission tomography in cervical lymph node metastases from an unknown primary tumor. *Cancer.* 2004;101:2641–2649.
14. Zhu L, Wang N. ^{18}F-fluorodeoxyglucose positron emission tomography-computed tomography as a diagnostic tool in patients with cervical nodal metastases of unknown primary site: a meta-analysis. *Surg Oncol.* 2013;22:190–194.
15. Lee JR, Kim JS, Roh JL, et al. Detection of occult primary tumors in patients with cervical metastases of unknown primary tumors: comparison of ^{18}F-FDG PET/CT with contrast-enhanced CT or CT/MR imaging-prospective study. *Radiology.* 2015;274:764–771.
16. Liu Y. FDG PET/CT for metastatic squamous cell carcinoma of unknown primary of the head and neck. *Oral Oncol.* 2019;92:46–51.
17. Goel R, Moore W, Sumer B, Khan S, Sher D, Subramaniam RM. Clinical practice in PET/CT for the management of head and neck squamous cell cancer. *AJR.* 2017;209:289–303.

18. Szyszko TA, Cook GJR. PET/CT and PET/MRI in head and neck malignancy. *Clin Radiol.* 2018;73:60–69.
19. Kuzet SE, Gaggioli C. Fibroblast activation in cancer: when seed fertilizes soil. *Cell Tissue Res.* 2016;365:607–619.
20. Koczorowska MM, Tholen S, Bucher F, et al. Fibroblast activation protein-alpha, a stromal cell surface protease, shapes key features of cancer associated fibroblasts through proteome and degradome alterations. *Mol Oncol.* 2016;10:40–58.
21. Rettig WJ, Garin-Chesa P, Beresford HR, Oettgen HF, Melamed MR, Old LJ. Cell-surface glycoproteins of human sarcomas: differential expression in normal and malignant tissues and cultured cells. *Proc Natl Acad Sci USA.* 1988;85: 3110–3114.
22. Scanlan MJ, Raj BK, Calvo B, et al. Molecular cloning of fibroblast activation protein alpha, a member of the serine protease family selectively expressed in stromal fibroblasts of epithelial cancers. *Proc Natl Acad Sci USA.* 1994;91: 5657–5661.
23. Kratochwil C, Flechsig P, Lindner T, et al. ^{68}Ga-FAPI PET/CT: tracer uptake in 28 different kinds of cancer. *J Nucl Med.* 2019;60:801–805.
24. Chen H, Pang Y, Wu J, et al. Comparison of [^{68}Ga]Ga-DOTA-FAPI-04 and [^{18}F] FDG PET/CT for the diagnosis of primary and metastatic lesions in patients with various types of cancer. *Eur J Nucl Med Mol Imaging.* 2020;47:1820–1832.
25. Syed M, Flechsig P, Liermann J, et al. Fibroblast activation protein inhibitor (FAPI) PET for diagnostics and advanced targeted radiotherapy in head and neck cancers. *Eur J Nucl Med Mol Imaging.* 2020;47:2836–2845.
26. Serfling S, Zhi Y, Schirbel A, et al. Improved cancer detection in Waldeyer's tonsillar ring by ^{68}Ga-FAPI PET/CT imaging. *Eur J Nucl Med Mol Imaging.* 2021;48: 1178–1187.
27. Lindner T, Loktev A, Altmann A, et al. Development of quinoline-based theranostic ligands for the targeting of fibroblast activation protein. *J Nucl Med.* 2018;59: 1415–1422.
28. Amin MB, Edge SB, Greene FL, et al. *AJCC Cancer Staging Manual.* 8th ed. New York: Springer; 2017.
29. Pencharz D, Dunn J, Connor S, et al. Palatine tonsil SUVmax on FDG PET-CT as a discriminator between benign and malignant tonsils in patients with and without head and neck squamous cell carcinoma of unknown primary. *Clin Radiol.* 2019; 74:165.e17–165.e23.
30. Redondo-Cerezo E, Martinez-Cara JG, Jimenez-Rosales R, et al. Endoscopic ultrasound in gastric cancer staging before and after neoadjuvant chemotherapy: a comparison with PET-CT in a clinical series. *United European Gastroenterol J.* 2017; 5:641–647.
31. Spadafora M, Pace L, Evangelista L, et al. Risk-related ^{18}F-FDG PET/CT and new diagnostic strategies in patients with solitary pulmonary nodule: the ITALIAN multicenter trial. *Eur J Nucl Med Mol Imaging.* 2018;45:1908–1914.
32. Wong WL. PET-CT for staging and detection of recurrence of head and neck cancer. *Semin Nucl Med.* 2021;51:13–25.
33. Eisenmenger LB. Non-FDG radiopharmaceuticals in head and neck PET imaging: current techniques and future directions. *Semin Ultrasound CT MR.* 2019;40:424–433.

Pretreatment Levels of Soluble Tumor Necrosis Factor Receptor 1 and Hepatocyte Growth Factor Predict Toxicity and Overall Survival After ^{90}Y Radioembolization: Potential Novel Application of Biomarkers for Personalized Management of Hepatotoxicity

Matthew M. Cousins*[1], Theresa P. Devasia*[1], Christopher M. Maurino[1], Justin Mikell[1], Matthew J. Schipper[1], Ravi K. Kaza[2], Theodore. S. Lawrence[1], Kyle C. Cuneo†[1], and Yuni K. Dewaraja†[2]

[1]*Department of Radiation Oncology, University of Michigan, Ann Arbor, Michigan; and* [2]*Department of Radiology, University of Michigan, Ann Arbor, Michigan*

Liver function may be negatively affected by radiation for treatment of hepatic malignancy. Pretreatment blood cytokine levels are biomarkers for prediction of toxicity and survival after external-beam radiation therapy. We hypothesized that cytokines may also predict outcomes after radioembolization, enabling a biomarker-driven personalized approach to treatment. **Methods:** Pretherapy blood samples from patients enrolled on a prospective protocol evaluating ^{90}Y radioembolization for management of intrahepatic malignancy were analyzed for 2 cytokines selected on the basis of prior studies in stereotactic body radiotherapy, soluble tumor necrosis factor receptor 1 (sTNFR1) and hepatocyte growth factor (HGF), via enzyme-linked immunosorbent assay, and key dosimetric parameters were derived from posttreatment ^{90}Y PET/CT imaging. Toxicity was defined as a change in albumin–bilirubin score from baseline to follow-up (3–6 mo after treatment). Associations of cytokine levels, dose metrics, and baseline liver function with toxicity and overall survival were assessed. **Results:** Data from 43 patients treated with ^{90}Y radioembolization for primary (48.8% [21/43]) or secondary (51.2% [22/43]) malignancy were assessed. Examined dose metrics and baseline liver function were not associated with liver toxicity; however, levels of sTNFR1 ($P = 0.045$) and HGF ($P = 0.005$) were associated with liver toxicity in univariate models. Cytokines were the only predictors of toxicity in multivariable models including dose metrics and prior liver-directed therapy. sTNFR1 (hazard ratio, 12.3; 95% CI, 3.5–42.5, $P < 0.001$) and HGF (hazard ratio, 7.5; 95% CI, 2.4–23.1, $P < 0.001$) predicted overall survival, and findings were similar when models were controlled for absorbed dose and presence of metastatic disease. **Conclusion:** Pretreatment cytokine levels predict liver toxicity and overall survival. These pathways can be targeted with available drugs, an advantage over previously studied dose metrics and liver function tests. Interventions directed at the TNFα-axis should be considered in future studies for prevention of liver toxicity, and HGF should be explored further to determine whether its elevation drives toxicity or indicates ongoing liver regeneration after prior injury.

Key Words: inflammation; cytokines; liver; toxicity

J Nucl Med 2022; 63:882–889
DOI: 10.2967/jnumed.121.262447

Radioembolization with microspheres containing ^{90}Y is an established approach for treatment of malignancies involving the liver (*1*). A pretreatment ^{99m}Tc-macroaggregated albumin scan is used to assess for enteric and pulmonary shunting before treatment with glass microspheres administered to achieve a dose to the targeted liver of 80–150 Gy (*2*). This approach currently relies on calculations that include perfused liver mass and pulmonary shunt fraction, but recent data suggest that the use of more personalized dosimetry can result in improved response rates with low rates of toxicity (*3–7*).

Side effects of radioembolization have been well characterized and include lung toxicity, gastrointestinal toxicity, and hepatotoxicity (*8*). Multiple studies have found that baseline liver function and dosimetry predict hepatotoxicity after radioembolization, suggesting that both should be considered for risk reduction (*6,7,9,10*). In contrast, our group and others have previously found that uninvolved liver absorbed dose does not correlate with toxicity (*11,12*). Though there remains some debate as to the importance of dose for toxicity prediction, it is important to consider other factors that show promise for prediction of liver toxicity after stereotactic body radiotherapy (SBRT) that might be applied to benefit patients receiving radioembolization.

Studies of liver toxicity after SBRT have shown that pretreatment levels of hepatocyte growth factor (HGF) and tumor necrosis factor receptor 1 (TNFR1) in soluble form (sTNFR1) predict hepatic injury after treatment (*13–15*). Additionally, baseline cytokine levels and inflammation-related lab values predict overall survival, suggesting even broader potential application of pretreatment lab-based studies (*14,16*). However, the linkage between these markers and overall survival has multiple potential explanations (e.g., relationships between markers and baseline liver status, risk of liver toxicity, local disease progression, systemic disease, or comorbid conditions). We have previously proposed that select cytokines portend an inflammatory state that could be targeted with the goal of reducing toxicity after radiation (*13*). Prior studies of hepatotoxicity and

Received Apr. 16, 2021; revision accepted Aug. 20, 2021.
For correspondence, contact Kyle C. Cuneo (kcuneo@med.umich.edu).
*Contributed equally to this work.
†Contributed equally to this work.
Published online Sep. 9, 2021.

survival after radioembolization have focused on dose metrics and liver function assessment, but some have considered blood cytokine levels (*17–19*). To date, no study—to our knowledge—has simultaneously considered dose metrics, liver function, and biomarkers. We hypothesized that hepatotoxicity and overall survival after ^{90}Y radioembolization may be predicted by baseline cytokine levels and that these biomarkers might guide personalized treatment.

MATERIALS AND METHODS

Study Population, Sample Collection, and Storage

Individuals with hepatic malignancy slated to receive treatment via ^{90}Y radioembolization (TheraSphere; BTG International Ltd.) at the University of Michigan University Hospital (March 2017 to February 2020) who met eligibility criteria (ability to undergo imaging, follow-up at the University of Michigan, and informed consent) were enrolled prospectively into an Institutional Review Board–approved research study (UMCC 2016.090; HUM00118705) that included a blood draw and ^{90}Y PET/CT imaging. Participants provided written informed consent. Blood samples were collected before radioembolization; serum and plasma were prepared and stored (−80°C) until analysis, which was performed in March 2020 in 1 batch after the last patient was enrolled.

Treatment

Before ^{90}Y treatment, each patient underwent a ^{99m}Tc-macroaggregated albumin scan to assess for shunting. The treating team adhered to standard guidelines for delivery of 80–150 Gy to the entirety of the treated liver lobe (40/43 lobar treatments; 3/43 selective treatments). Dose selection but not treatment strategy (selective vs. lobar) depended on disease histology, lung shunt, and baseline liver function. To achieve target doses, administered activities 0.5–12.6 GBq were delivered using microspheres with specific activity 107–1542 Bq/sphere.

Imaging and Segmentation

Posttreatment ^{90}Y PET/CT imaging reconstruction, registration, and segmentation were as described previously (*12*) and are summarized here. PET/CT imaging was performed within about 2 h (average, 2.5 h; range, 1–5 h) of radioembolization, with an acquisition time of about 30 min over a field encompassing the liver and portions of the thorax. Lesion contours segmented on pretreatment diagnostic CT or MRI by an experienced radiologist were transferred to ^{90}Y PET/CT after rigid registration (MIM Software), with fine adjustment of location, guided by PET and CT, when misregistration was evident. A total of 1–5 lesions larger than 2 cm^3 were segmented per patient. For the current study, liver segmentation was performed on the CT portion of PET/CT using deep learning–based tools (MIM Software). The liver volume minus the sum of segmented lesions (including a 1-cm expansion zone around each lesion to account for PET resolution) constituted the nontumoral liver volume that included the noninjected lobe (Fig. 1).

Dose Variables

Voxel dosimetry was performed by coupling the quantitative ^{90}Y PET/CT images with explicit Monte Carlo radiation transport as described previously (*12*). Voxels within lesions and nontumoral liver were scaled by volume-dependent recovery coefficients for a mean-value partial-volume correction (*12*). The following liver dose metrics were collected for the entire nontumoral liver volume: mean liver physical absorbed dose (MLD), mean liver biologically effective dose (BED; α/β, 2.5 Gy; cell repair constant, 0.28 h^{-1} (*6*)), BED to radiation delivered at 2 Gy/fraction, maximum dose to the coldest xx% (DCxx), and maximum dose to the coldest 700 cm^3 (DC700cc). DCxx and DC700cc were expressed as BED for DCxx (BEDCxx) and for DC700cc (BEDC700cc), respectively (*20*). As a surrogate for macroscopic nonuniformity, we calculated (DC10 − DC90)/DC50 and DC10 − DC90. Some patients received multiple treatments.

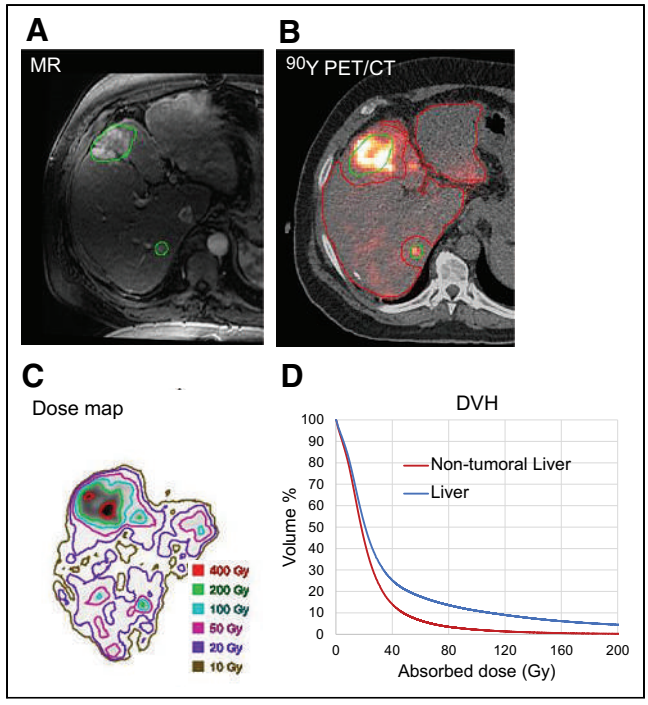

FIGURE 1. Example baseline MRI (A) and ^{90}Y PET/CT (B) after treatment (3.2 GBq) are shown. Lesion contours (green) were defined on MRI and applied to coregistered PET/CT. Nontumoral liver (red) accounts for 1-cm expansion around lesions to address PET resolution. Dose map (C) and DVH (D) are provided for treatment with MLD 24 Gy and DC90 48 Gy.

When time between treatment was 90 d or less, dose values were generated using the summed PET/CT dose map from both treatments (Supplemental Fig. 1; supplemental materials are available at http://jnm.snmjournals.org). In this case, before summation the 2 dose maps were aligned on the basis of a CT–CT rigid registration (MIM Software) with manual fine-tuning. Summation of dosimetric data for treatments given no more than 90 d apart was performed because it was felt that 90 d constitutes a first portion of the radiation response likely lasting at least 7–9 mo as shown in the literature on radiation-induced liver injury and in studies of hypertrophy after radioembolization (*21,22*). Therefore, it is less likely that this 90-d period would be sufficient for significant recovery to occur before the second injury. Dose metrics from the first treatment were used if time between treatments was more than 90 d.

Toxicity Assessment

Previous work has established albumin–bilirubin (ALBI) score [0.66 × $\log_{10}$bilirubin (μmol/L) − 0.085 × albumin (g/L)] as a measure of liver function (*23*). The difference between ALBI score at baseline and a follow-up assessment at 3–6 mo was defined as ΔALBI. A positive ΔALBI is indicative of worsening liver function, considered the toxicity outcome in the current work. Additionally, relevant laboratory-based assessments were collected using Common Terminology Criteria for Adverse Events, version 5, within 6 mo of treatment for alanine aminotransferase, aspartate aminotransferase, alkaline phosphatase, and total bilirubin.

Cytokine Quantification

HGF (serum) and sTNFR1 (plasma) were quantified in appropriate specimens using Quantikine enzyme-linked immunosorbent assay kits (R&D Systems): DRT100 (sTNFR1) and DHG00B (HGF). Assays were performed according to manufacturer recommendations without variation. After assay development, absorbance data were collected and analyzed using a Synergy HT plate reader and Gen5 software,

respectively, (BioTek Instruments). Cytokine concentrations were determined through comparison to standards.

Statistical Methods

Correlations among the nontumoral liver dose metrics were measured using the Pearson correlation coefficient (ρ). Cytokine values were log-transformed because of outliers. Univariate associations of ΔALBI and each of the dose metrics, HGF, and sTNFR1 were assessed using scatterplots. On the basis of the scatterplots, linear trends were identified. Univariate linear models with dose metrics, cytokines, or baseline disease factors were constructed. Multivariable models using the cytokines, dose metrics, and clinical factors were constructed. The association between cytokines and overall survival was assessed. Kaplan–Meier curves of overall survival stratified by median values of each cytokine were constructed and compared using the log-rank test. Univariate Cox proportional hazards models were fit to quantify the effect of cytokines on risk of death. The Harrell c-index was used to quantify the predictive accuracy of survival models. Analyses were completed using R, version 4.0.3.

RESULTS

Overview

Data were available from 43 patients with a median age 65.0 y (range, 37.0–82.0) treated with ^{90}Y radioembolization for hepatocellular carcinoma (37.2% [16/43]), cholangiocarcinoma (11.6% [5/43]), or metastatic (51.2% [22/43]) malignancy (Table 1). Most patients (62.8% [27/43]) had a pretreatment Child–Pugh score of 5. Toxicity outcome assessments included 34/43 (79.1%) patients with available ΔALBI. The median follow-up for toxicity was 6.0 mo. Most patients (82.4% [28/34]) had a positive ΔALBI, signifying worsening liver function. Six-month Common Terminology Criteria for Adverse Events, version 5, grade toxicity data for liver-associated laboratory studies are provided in Supplemental Table 1. Median follow-up for survival was 10.9 mo, and 25 of 43 patients died during follow-up.

Absorbed Dose and Toxicity

Dose metrics are summarized in Table 1. Assessments included evaluation of relationships between dose metrics themselves and relationships between dose metrics and ΔALBI. Strong pairwise correlations were noted for MLD, BED, and BED to radiation delivered at 2 Gy/fraction ($\rho > 0.8$, Supplemental Table 2). BEDC10, BEDC30, BEDC90, and BEDC700cc also strongly correlated with DC10, DC30, DC90, and DC700cc, respectively ($\rho > 0.96$, Supplemental Table 2). Simple linear fits demonstrated the greatest positive associations between 3 dose metrics in particular (MLD, DC700cc, and DC90) and ΔALBI (Supplemental Fig. 2); however, none of these associations were statistically significant (Table 2). Only MLD and DC90 were selected for multivariable modeling because of strong relationships that were noted between dose metrics and the identification of a subset of metrics, including MLD and DC90, with the strongest associations with ΔALBI. The effect of dose heterogeneity on toxicity was also examined, and neither of 2 measures of dose uniformity that we evaluated, (DC10 − DC90)/DC50 or DC10 − DC90, were associated with toxicity (Table 2).

TABLE 1
Summary of Patient Characteristics, Radiation Dose, and Outcomes

Variable	Summary
n	43
Age at ^{90}Y (y)	65.0 (37.0–82.0)
Female sex	17 (39.5)
White race	38 (88.4)
Baseline cirrhosis	16 (37.2)
Cancer details	—
Primary	21 (48.8)
HCC	16 (37.2)
Metastatic	22 (51.2)
Treatment history	—
Prior liver-directed therapy	15 (34.9)
Prior systemic therapy	26 (60.0)
Two ^{90}Y treatments	14 (32.6)
Baseline liver scores	—
Child–Pugh	—
5	27 (62.8)
6	11 (25.6)
7	1 (2.3)
8	Not applicable
9	1 (2.3)
Unavailable	3 (7.0)
MELD-NA	9.0 (6.4–18.7)
Baseline ALBI	−2.70 (−3.38 to −1.28)
Dose metrics (Gy)	—
Mean dose	50.2 (1.2–132.1)
Mean BED	145.1 (1.3–770.5)
DC10	0.9 (0.0–40.0)
DC90	128.7 (1.7–345.1)
DC700cc	15.7 (0.2–203.1)
Baseline cytokines (pg/mL)	—
sTNFR1	1,736.5 (924.4–5,518.0)
HGF	2,557.7 (1,328.1–6,876.2)
Outcomes	—
Toxicity follow-up (mo)	6.0 (3.0–6.0)
ΔALBI (*n* = 34)	0.3 (−0.3 to 1.9)
Positive ΔALBI (*n* = 34)	28 (82.4)
Overall survival follow-up (mo)	10.9 (1.2–41.8)
Number of deaths	25 (58.1)

Continuous factors are summarized as median and range; and categoric factors are summarized as number and percentage.

Cytokines and Toxicity

Higher baseline levels of sTNFR1 and HGF were associated with a larger ΔALBI (Fig. 2). Formal models were constructed to characterize relationships between cytokine levels at baseline and toxicity as measured by ΔALBI. Baseline HGF ($P = 0.005$) and sTNFR1 ($P = 0.045$) were significantly associated with greater liver toxicity (Table 2). Metastatic disease, baseline ALBI score, baseline cirrhosis, number of prior liver-directed therapies, and number of prior systemic therapies were not significantly associated with toxicity.

TABLE 2
Univariate Linear Models for ΔALBI

Model	Covariate	Coefficient	R^2	95% CI LB	95% CI UB	*P*
1	MLD	0.001	0.004	−0.004	0.006	0.737
2	BED	0.000	0.0001	−0.001	0.001	0.951
3	DC10	0.001	0.0002	−0.017	0.018	0.940
4	DC30	−0.001	0.001	−0.009	0.007	0.866
5	DC90	0.001	0.028	−0.001	0.003	0.348
6	DC700cc	0.001	0.004	−0.002	0.003	0.734
7	DC10 − DC90	−0.001	0.029	−0.003	0.001	0.333
8	(DC10 − DC90)/DC50	0.001	0.013	−0.002	0.005	0.524
9	Log(sTNFR1)	0.477	0.119	0.029	0.925	0.045
10	Log(HGF)	0.572	0.222	0.201	0.944	0.005
11	Pre-^{90}Y liver therapies (*n*)	−0.020	0.002	−0.171	0.130	0.792
12	Cirrhosis	0.195	0.044	−0.122	0.513	0.236
13	Metastatic	−0.082	0.008	−0.400	0.236	0.615
14	Baseline ALBI score	0.014	0.0001	−0.385	0.413	0.947
15	Baseline Child–Pugh = 6	0.077	0.005	−0.307	0.462	0.696
	Baseline Child–Pugh = 7	−0.006		−0.968	0.956	0.990
16	Pre-^{90}Y systemic therapies (*n*)	−0.087	0.042	−0.232	0.058	0.247

LB = lower bound; UB = upper bound.

After discovering that a subset of the selected cytokines predicted toxicity, multivariable toxicity models incorporating select dose metrics, cytokines, and clinical covariates were constructed (Table 3). HGF ($P < 0.002$) and sTNFR1 ($P < 0.030$) were significant predictors of toxicity, when models were adjusted for baseline ALBI score, receipt of prior liver-directed therapy, and either MLD or DC90. Models with DC700cc demonstrated similar findings (Supplemental Table 3). Relationships among cytokines were assessed to determine whether they provide independent information. Baseline HGF and sTNFR1 correlated positively ($\rho = 0.50$, Supplemental Table 4); when a multivariable toxicity model including both cytokines was constructed, only HGF was significant (Supplemental Table 5).

Cytokines and Overall Survival

After determining that cytokine levels were associated with toxicity, we examined cytokines for prediction of overall survival. Baseline sTNFR1 ($P = 0.010$; Fig. 3A) and HGF ($P = 0.011$; Fig. 3B) above the median for each cytokine were associated with worse survival. Median overall survival was 33.3 mo (95% CI [10.9, not applicable (NA)]) and 10.9 mo (95% CI [5.9, NA]) for those with baseline sTNFR1 concentration below versus above the median, respectively (Table 4). Median overall survival was 33.3 mo (95% CI [10.9, NA]) and 9.8 mo (95% CI [6.4, NA]) for those with baseline HGF concentrations below versus above the median, respectively (Table 4).

Continuous models found that elevated levels of sTNFR1 (HR, 12.3; $P < 0.001$; c-index, 0.71) and HGF (HR, 7.5; $P < 0.001$; c-index, 0.69) were significantly associated with increased risk of death (Table 5). No dose metrics predicted survival (Supplemental Table 6). In multivariable models adjusting for DC90 or MLD and metastatic disease, sTNFR1 and HGF were strong predictors of survival ($P < 0.001$).

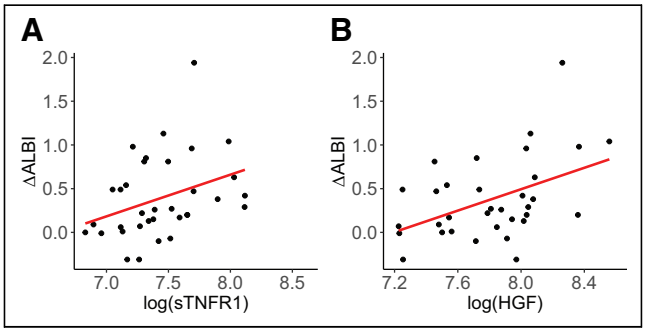

FIGURE 2. Scatterplots of log-transformed sTNFR1 (A) and HGF (B) vs. ΔALBI. Solid red line represents simple linear fit.

DISCUSSION

In the current study, we show that baseline elevations in HGF and sTNFR1 levels predict liver toxicity and overall survival after ^{90}Y radioembolization for management of hepatic malignancy, validating our previous findings in the setting of SBRT (*13,14*). Levels of these soluble signaling molecules appear to be more important for prediction of toxicity than radiation dose and even baseline liver function in patients with both primary and secondary hepatic malignancy. With additional studies, these biomarkers could be used to guide patient care in the pretreatment setting by providing valuable prognostic information regarding both toxicity and overall survival. As signaling through both entities is targetable, our findings support future trials of interventions in the pretreatment setting for prevention of hepatotoxicity after radioembolization.

Many have implicated TNFα as a potential mediator of inflammatory signals that result in liver injury (*24,25*). TNFR1 is a

TABLE 3
Multivariable Linear Models for ΔALBI

Model	Covariate	Coefficient	95% CI LB	95% CI UB	*P*
1	MLD	0.003	−0.002	0.008	0.319
	Log(sTNFR1)	0.622	0.099	1.145	0.027
	Baseline ALBI score	−0.166	−0.583	0.251	0.442
	Prior liver-directed therapy	−0.026	−0.362	0.311	0.883
2	MLD	0.003	−0.001	0.008	0.181
	Log(HGF)	0.709	0.285	1.133	0.003
	Baseline ALBI score	−0.143	−0.514	0.229	0.458
	Prior liver-directed therapy	0.079	−0.246	0.405	0.636
3	DC90	0.002	−0.0004	0.004	0.124
	Log(sTNFR1)	0.628	0.132	1.125	0.019
	Baseline ALBI score	−0.081	−0.493	0.331	0.702
	Prior liver-directed therapy	−0.034	−0.359	0.290	0.837
4	DC90	0.002	−0.00003	0.004	0.064
	Log(HGF)	0.706	0.306	1.106	0.002
	Baseline ALBI score	−0.045	−0.414	0.324	0.813
	Prior liver-directed therapy	0.065	−0.245	0.375	0.686

LB = lower bound; UB = upper bound.

ubiquitously expressed plasma membrane–associated molecule that transduces extracellular signals into the intracellular environment (*26*). The soluble form of TNFR1 (sTNFR1) is released constitutively, but sTNFR1 shedding increases with exposure to TNFα (*27–29*). Elevated sTNFR1 levels are associated with liver inflammation (*30*). Two key preclinical studies linked radiation to liver injury mediated by the TNFα axis. First, when hepatocytes were irradiated in the presence of TNFα, higher levels of apoptotic cell death were observed (*31*). Second, hepatocyte apoptosis was prevented in irradiated cells when they were treated with antisense oligonucleotides against TNFR1 in the presence of TNFα (*32*). Therefore, sTNFR1 represents a stable analyte for assessment of TNFα signaling that has previously been linked to liver toxicity after SBRT (*13*) and for the first time has been linked to liver toxicity after ^{90}Y radioembolization in the current study.

HGF was also predictive of liver toxicity after SBRT, as previously shown by our group and others (*14,15*). The mechanism through which one might explain these relationships is less clear. c-MET, the major downstream signaling target of HGF, is a receptor tyrosine kinase (*33*), and HGF signaling through this molecule is mitogenic, driving regeneration after liver injury or resection (*34–36*). However, there is some disagreement in the literature as to whether c-MET promotes hepatocyte recovery or fibrosis (*37,38*). HGF-MET signaling has also been linked to unfavorable tumor characteristics, including metastasis and invasion (*33*).

Our finding that sTNFR1 and HGF predicted liver toxicity after ^{90}Y radioembolization presents multiple potential opportunities for personalized medicine. Food and Drug Administration–approved small-molecule inhibitors targeting the TNFα axis and c-MET, the signaling partner of HGF (*39,40*), should be considered in future clinical trials for prevention of toxicity. The fact that these signaling entities (sTNFR1 and HGF) might be targeted for potential therapeutic gain constitutes a major advantage over biomarkers or scores that can direct only treatment adaptation or avoidance. However, further study of HGF is needed before targeting this entity to ensure that HGF is driving toxicity and not simply elevated in the setting of liver recovery (*18*).

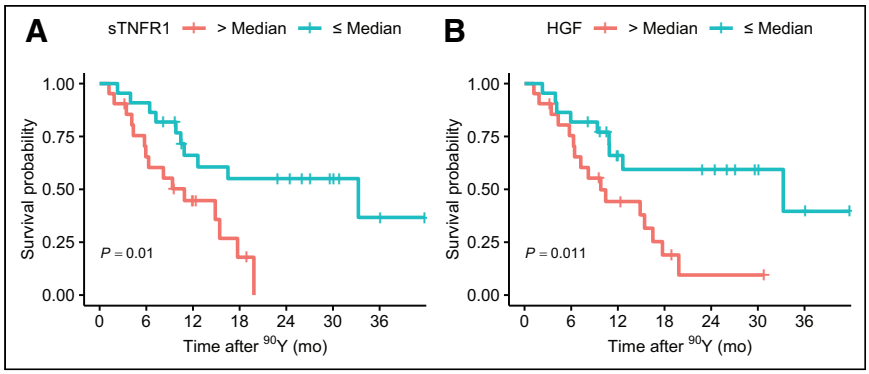

FIGURE 3. Kaplan–Meier curves for overall survival stratified by median value of sTNFR1 (A) and HGF (B) with log-rank *P* value.

The impact of dose on liver toxicity after radioembolization has been widely discussed in the ^{90}Y literature (*6*). We did not note associations between dose and toxicity, though others have shown the presence (*10*) or absence (*11,12*) of such relationships. One explanation for this difference is that our sample included a nearly even mixture of those with primary and secondary malignancy with generally good liver function. Additionally, our sample size was small. Despite our findings, we

TABLE 4
Median Overall Survival Estimates, 95% CIs, and Number of Deaths by Median Values of Each Cytokine

Cytokine	Median overall survival (mo)	95% CI LB	95% CI UB	Deaths (*n*)	Deaths (*n*)
sTNFR1 ≤ median	33.3	10.9	NA	10	45.5
sTNFR1 > median	10.9	5.9	NA	15	71.4
HGF ≤ median	33.3	10.9	NA	9	40.9
HGF > median	9.8	6.4	NA	16	76.2

LB = lower bound; UB = upper bound.

encourage continued efforts toward more personalized dosimetry to balance disease control and toxicity given positive results in recent studies (*5,9*).

Relationships between signaling molecules and overall survival are more difficult to explain than the toxicity relationships reviewed above. It is important to consider nonliver or nononcologic disease states along with liver disease, cancer status, and treatment toxicity as potential explanations for both increases in cytokines and worse survival. Regardless of the potential mechanistic explanations, these relationships are significant and should be evaluated in future studies with the goal of applying their prognostic power to guide clinical decision making.

There are several weaknesses of this work that we would like to note. The study was relatively small and was conducted at a single institution, suggesting that analyses might have been underpowered and that a limited number of treatment scenarios might have been captured. Though care was taken in registration of images and segmentation, it is not possible to eliminate the impact of misregistration on dosimetric calculations. The impact of misregistration and the use of rigid registration for dose accumulation are limitations of the study. Though beyond the scope of this study, additional studies are needed to determine the value of deformable registration for ^{90}Y and if changes in technique (e.g., higher exposure, use of contrast) of the CT of PET/CT are necessary to yield accurate deformable maps from a diagnostic quality scan to CT of PET/CT that is performed without contrast and with low mAs. Respiratory motion effects might also impact dosimetric calculations, though mean nontumoral liver dose, which is the dose metric we focus on in the current paper, has been shown to be insensitive to respiratory motion up to 4 cm in a simple phantom study (*41*). Furthermore, although we evaluated macroscale level heterogeneity indices, the impact of dose deposition nonuniformity at the microscale level (*42,43*) was not evaluated because of the challenges of doing this with resolution capabilities of PET. Despite these limitations, this study validates prior work in SBRT demonstrating the importance of cytokines for toxicity prediction after liver irradiation. When combined with prior work demonstrating relationships between disease response and ^{90}Y PET

TABLE 5
Univariate and Multivariable Cox Proportional Hazards Model Results for Overall Survival

Model	Covariate	HR	95% CI LB	95% CI UB	*P*	c-index
1	Log(sTNFR1)	12.27	3.54	42.53	<0.001	0.71
2	Log(HGF)	7.48	2.42	23.08	<0.001	0.69
3	MLD (Gy)	0.99	0.98	1.01	0.403	0.58
4	DC90 (Gy)	0.99	0.99	1.00	0.383	0.55
5	Log(sTNFR)	18.76	4.95	71.14	<0.001	0.71
	Metastatic	2.27	0.87	5.93	0.093	
	DC90 (Gy)	0.99	0.99	1.00	0.521	
6	Log(HGF)	15.32	3.93	59.74	<0.001	0.72
	Metastatic	2.98	1.01	8.81	0.049	
	DC90 (Gy)	0.99	0.99	1.00	0.516	
7	Log(sTNFR)	19.32	5.12	72.86	<0.001	0.70
	Metastatic	2.36	0.92	6.05	0.075	
	MLD (Gy)	0.99	0.98	1.01	0.348	
8	Log(HGF)	15.60	4.05	60.14	<0.001	0.72
	Metastatic	3.22	1.05	9.90	0.042	
	MLD (Gy)	0.99	0.98	1.01	0.426	

LB = lower bound; UB = upper bound.

dosimetry (*12*), the findings of the current study hold great promise for personalized treatment planning. This study will inform larger clinical studies in the SBRT and radioembolization spaces to select and validate biomarker cut points to facilitate their use in patient selection and to test approaches to directly target processes driving liver damage in those at higher risk for toxicity.

CONCLUSION

HGF and sTNFR1 levels before ^{90}Y radioembolization predict both posttreatment hepatotoxicity and overall survival. These findings support larger studies to identify cutoffs for signaling molecules, a clinical trial of TNF axis inhibitors for prevention of liver toxicity, and further preclinical examination of the relationship between HGF and liver toxicity. These data will facilitate the development of novel biomarker-based approaches for prediction and intervention to address hepatotoxicity after radioembolization, an improvement over using only dosimetry and liver function assessments that have been the focus of hepatotoxicity prevention efforts to date.

DISCLOSURE

This work was supported by the National Institutes of Health (1R01EB022075 to Yuni Dewaraja) and a University of Michigan Comprehensive Cancer Center Support grant (3P30CA046592). No other potential conflict of interest relevant to this article was reported.

ACKNOWLEDGMENT

We thank Joel Whitfield for assistance with cytokine quantification.

KEY POINTS

QUESTION: Do baseline cytokine levels predict liver toxicity or overall survival in those treated with ^{90}Y radioembolization for hepatic malignancy to enable a novel biomarker-driven personalized approach to treatment?

PERTINENT FINDINGS: Pretreatment HGF and sTNFR1 levels predicted liver toxicity and overall survival, while ^{90}Y PET/CT–derived absorbed dose metrics did not.

IMPLICATIONS FOR PATIENT CARE: With further study and validation, HGF or sTNFR1 might be used for pretreatment patient stratification or treatment adaptation to avoid toxicity. Interventional trials of TNFα axis–modifying agents and c-MET inhibitors should be considered.

REFERENCES

1. Salem R, Gabr A, Riaz A, et al. Institutional decision to adopt Y90 as primary treatment for hepatocellular carcinoma informed by a 1,000-patient 15-year experience. *Hepatology.* 2018;68:1429–1440.
2. TheraSphere® Yttrium-90 Glass Microspheres. Package insert. BTG; undated.
3. Salem R, Padia SA, Lam M, et al. Clinical and dosimetric considerations for Y90: recommendations from an international multidisciplinary working group. *Eur J Nucl Med Mol Imaging.* 2019;46:1695–1704.
4. Strigari L, Sciuto R, Rea S, et al. Efficacy and toxicity related to treatment of hepatocellular carcinoma with ^{90}Y-SIR Spheres: radiobiologic considerations. *J Nucl Med.* 2010;51:1377–1385.
5. Garin E, Tselikas L, Guiu B, et al. Personalised versus standard dosimetry approach of selective internal radiation therapy in patients with locally advanced hepatocellular carcinoma (DOSISPHERE-01): a randomised, multicentre, open-label phase 2 trial. *Lancet Gastroenterol Hepatol.* 2021;6:17–29.
6. Cremonesi M, Chiesa C, Strigari L, et al. Radioembolization of hepatic lesions from a radiobiology and dosimetric perspective. *Front Oncol.* 2014;4:210.
7. Chiesa C, Mira M, Maccauro M, et al. Radioembolization of hepatocarcinoma with ^{90}Y glass microspheres: development of an individualized treatment planning strategy based on dosimetry and radiobiology. *Eur J Nucl Med Mol Imaging.* 2015;42:1718–1738.
8. Riaz A, Awais R, Salem R. Side effects of yttrium-90 radioembolization. *Front Oncol.* 2014;4:198.
9. Garin E, Palard X, Rolland Y. Personalised dosimetry in radioembolisation for HCC: impact on clinical outcome and on trial design. *Cancers (Basel).* 2020;12:1557.
10. Chiesa C, Mira M, Bhoori S, et al. Radioembolization of hepatocarcinoma with ^{90}Y glass microspheres: treatment optimization using the dose-toxicity relationship. *Eur J Nucl Med Mol Imaging.* 2020;47:3018–3032.
11. Kappadath SC, Mikell J, Balagopal A, Baladandayuthapani V, Kaseb A, Mahvash A. Hepatocellular carcinoma tumor dose response after ^{90}Y-radioembolization with glass microspheres using ^{90}Y-SPECT/CT-based voxel dosimetry. *Int J Radiat Oncol Biol Phys.* 2018;102:451–461.
12. Dewaraja YK, Devasia T, Kaza RK, et al. Prediction of tumor control in ^{90}Y radioembolization by logit models with PET/CT-based dose metrics. *J Nucl Med.* 2020;61:104–111.
13. Cousins MM, Morris E, Maurino C, et al. TNFR1 and the TNFα axis as a targetable mediator of liver injury from stereotactic body radiation therapy. *Transl Oncol.* 2021;14:100950.
14. Cuneo KC, Devasia T, Sun Y, et al. Serum levels of hepatocyte growth factor and CD40 ligand predict radiation-induced liver injury. *Transl Oncol.* 2019;12:889–894.
15. Hong TS, Grassberger C, Yeap BY, et al. Pretreatment plasma HGF as potential biomarker for susceptibility to radiation-induced liver dysfunction after radiotherapy. *NPJ Precis Oncol.* 2018;2:22.
16. Lo C-H, Lee H-L, Hsiang C-W, et al. Pretreatment neutrophil-to-lymphocyte ratio predicts survival and liver toxicity in patients with hepatocellular carcinoma treated with stereotactic ablative radiation therapy. *Int J Radiat Oncol Biol Phys.* 2021;109:474–484.
17. Seidensticker M, Powerski M, Seidensticker R, et al. Cytokines and ^{90}Y-radioembolization: relation to liver function and overall survival. *Cardiovasc Intervent Radiol.* 2017;40:1185–1195.
18. Fernandez-Ros N, Iñarrairaegui M, Paramo JA, et al. Radioembolization of hepatocellular carcinoma activates liver regeneration, induces inflammation and endothelial stress and activates coagulation. *Liver Int.* 2015;35:1590–1596.
19. Wickremesekera JK, Chen W, Cannan RJ, Stubbs RS. Serum proinflammatory cytokine response in patients with advanced liver tumors following selective internal radiation therapy (SIRT) with ^{90}yttrium microspheres. *Int J Radiat Oncol Biol Phys.* 2001;49:1015–1021.
20. Miften M, Vinogradskiy Y, Moiseenko V, et al. Radiation dose-volume effects for liver SBRT. *Int J Radiat Oncol Biol Phys.* 2021;110:196–205.
21. Teo JY, Allen JC Jr, Ng DC, et al. A systematic review of contralateral liver lobe hypertrophy after unilobar selective internal radiation therapy with Y90. *HPB (Oxford).* 2016;18:7–12.
22. Lawrence TS, Robertson JM, Anscher MS, Jirtle RL, Ensminger WD, Fajardo LF. Hepatic toxicity resulting from cancer treatment. *Int J Radiat Oncol Biol Phys.* 1995;31:1237–1248.
23. Johnson PJ, Berhane S, Kagebayashi C, et al. Assessment of liver function in patients with hepatocellular carcinoma: a new evidence-based approach—the ALBI grade. *J Clin Oncol.* 2015;33:550–558.
24. Küsters S, Tiegs G, Alexopoulou L, et al. In vivo evidence for a functional role of both tumor necrosis factor (TNF) receptors and transmembrane TNF in experimental hepatitis. *Eur J Immunol.* 1997;27:2870–2875.
25. Yang YM, Seki E. TNFα in liver fibrosis. *Curr Pathobiol Rep.* 2015;3:253–261.
26. Holbrook J, Lara-Reyna S, Jarosz-Griffiths H, McDermott M. Tumour necrosis factor signalling in health and disease. *F1000Res.* 2019;8:F1000.
27. Aderka D, Sorkine P, Abu-Abid S, et al. Shedding kinetics of soluble tumor necrosis factor (TNF) receptors after systemic TNF leaking during isolated limb perfusion: relevance to the pathophysiology of septic shock. *J Clin Invest.* 1998;101:650–659.
28. Pinckard JK, Sheehan KC, Arthur CD, Schreiber RD. Constitutive shedding of both p55 and p75 murine TNF receptors in vivo. *J Immunol.* 1997;158:3869–3873.
29. Xia M, Xue SB, Xu CS. Shedding of TNFR1 in regenerative liver can be induced with TNF alpha and PMA. *World J Gastroenterol.* 2002;8:1129–1133.
30. Abiru S, Migita K, Maeda Y, et al. Serum cytokine and soluble cytokine receptor levels in patients with non-alcoholic steatohepatitis. *Liver Int.* 2006;26:39–45.
31. Christiansen H, Saile B, Neubauer-Saile K, et al. Irradiation leads to susceptibility of hepatocytes to TNF-alpha mediated apoptosis. *Radiother Oncol.* 2004;72:291–296.

32. Huang XW, Yang J, Dragovic AF, Zhang H, Lawrence TS, Zhang M. Antisense oligonucleotide inhibition of tumor necrosis factor receptor 1 protects the liver from radiation-induced apoptosis. *Clin Cancer Res*. 2006;12:2849–2855.
33. Gherardi E, Birchmeier W, Birchmeier C, Vande Woude G. Targeting MET in cancer: rationale and progress. *Nat Rev Cancer*. 2012;12:89–103.
34. Matsumoto K, Nakamura T. Hepatocyte growth factor: molecular structure, roles in liver regeneration, and other biological functions. *Crit Rev Oncog*. 1992;3:27–54.
35. Efimova EA, Glanemann M, Nussler AK, et al. Changes in serum levels of growth factors in healthy individuals after living related liver donation. *Transplant Proc*. 2005;37:1074–1075.
36. Ishiki Y, Ohnishi H, Muto Y, Matsumoto K, Nakamura T. Direct evidence that hepatocyte growth factor is a hepatotrophic factor for liver regeneration and has a potent antihepatitis effect in vivo. *Hepatology*. 1992;16:1227–1235.
37. Giebeler A, Boekschoten MV, Klein C, et al. c-Met confers protection against chronic liver tissue damage and fibrosis progression after bile duct ligation in mice. *Gastroenterology*. 2009;137:297–308.
38. Krawczyk M, Zimmermann S, Hess G, et al. Panel of three novel serum markers predicts liver stiffness and fibrosis stages in patients with chronic liver disease. *PLoS One*. 2017;12:e0173506.
39. Puccini A, Marín-Ramos NI, Bergamo F, et al. Safety and tolerability of c-MET inhibitors in cancer. *Drug Saf*. 2019;42:211–233.
40. Chiang GT, Glaser RL. Clinical review: GP2015 (proposed biosimilar to US-licensed Enbrel). Food and Drug Administration website. https://www.fda.gov/media/105952/download. Published November 5, 2015. Accessed February 22, 2022.
41. Siman W, Mawlawi OR, Mikell JK, Mourtada F, Kappadath SC. Effects of image noise, respiratory motion, and motion compensation on 3D activity quantification in count-limited PET images. *Phys Med Biol*. 2017;62:448–464.
42. Pasciak AS, Abiola G, Liddell RP, et al. The number of microspheres in Y90 radioembolization directly affects normal tissue radiation exposure. *Eur J Nucl Med Mol Imaging*. 2020;47:816–827.
43. d'Abadie P, Hesse M, Jamar F, Lhommel R, Walrand S. ^{90}Y TOF-PET based EUD reunifies patient survival prediction in resin and glass microspheres radioembolization of HCC tumours. *Phys Med Biol*. 2018;63:245010.

Pitfalls and Common Findings in ^{68}Ga-FAPI PET: A Pictorial Analysis

Lukas Kessler[1,2], Justin Ferdinandus[1,2], Nader Hirmas[1,2], Fadi Zarrad[1,2], Michael Nader[1,2], David Kersting[1,2], Manuel Weber[1,2], Sandra Kazek[1,2], Miriam Sraieb[1,2], Rainer Hamacher[2,3], Katharina Lueckerath[1,2], Lale Umutlu[2,4], Wolfgang P. Fendler[1,2], and Christoph Rischpler[1,2]

[1]Department of Nuclear Medicine, University Hospital Essen, University of Duisburg–Essen, Essen, Germany; [2]German Cancer Consortium, University Hospital Essen, University of Duisburg–Essen, Essen, Germany; [3]Department of Medical Oncology, West German Cancer Center, University Hospital Essen, University of Duisburg–Essen, Essen, Germany; and [4]Institute of Diagnostic and Interventional Radiology, University Hospital Essen, University of Duisburg–Essen, Essen, Germany

Fibroblast activation protein inhibitor (FAPI) PET/CT is a new tool in the diagnostic workup of cancer. With a growing volume of applications, pitfalls and common findings need to be considered for ^{68}Ga-FAPI PET/CT image interpretation. The aim of this study was to summarize common findings and report pitfalls in ^{68}Ga-FAPI PET/CT. **Methods:** Ninety-one patients underwent whole-body PET/CT with either FAPI-04 ($n = 25$) or FAPI-46 ($n = 66$). Findings were rated in a consensus session of 2 experienced readers. Pitfalls and common findings were defined as focal or localized uptake above the background level and categorized as unspecific or nonmalignant and grouped into degenerative, muscular, scarring/wound-healing, uterine, mammary gland, and head-and-neck findings. The frequency of findings was reported on a per-patient and per-group basis, and SUV_{max}, SUV_{mean}, and SUV_{peak} were measured. **Results:** Non–tumor-specific uptake was found in 81.3% of patients. The most frequent finding was uptake in degenerative lesions (51.6%), with a mean SUV_{max} of 7.7 ± 2.9, and head-and-neck findings (45.1%). Except for the salivary glands, the uptake values did not differ between 10 and 60 min after injection in most findings. Uterine uptake was found in most women (66.7%), with a mean SUV_{max} of 12.2 ± 7.3, and uptake correlated negatively with age (SUV_{max}, $r = -0.6$, $P < 0.01$; SUV_{peak}, $r = -0.57$, $P < 0.01$; SUV_{mean}, $r = -0.58$, $P < 0.01$). **Conclusion:** Pitfalls include non–tumor-specific ^{68}Ga-FAPI uptake in degenerative lesions, muscle, the head and neck, scarring, the mammary glands, or the uterus. Here, we summarize the findings to help readers avoid common mistakes at centers introducing ^{68}Ga-FAPI PET/CT.

Key Words: cancer imaging; FAPI; fibroblast activation protein; PET; pitfalls

J Nucl Med 2022; 63:890–896
DOI: 10.2967/jnumed.121.262808

Fibroblast-activation protein (FAP) is a protein commonly expressed in cancer-associated fibroblasts, which are present in the stroma of 80%–90% of all cancers. Mediators produced by carcinoma-associated fibroblasts influence tumor cells on many levels by promoting tumor angiogenesis, migration, and proliferation (*1,2*). In normal fibroblasts, the structurally similar enzyme dipeptidyl peptidase 4 is expressed, whereas FAP is not expressed (*3,4*). On this basis, a metaanalysis of 15 studies proved that FAP overexpression in solid tumors is associated with a poor outcome and is distinctly present in tumor cells compared with normal tissue (*5*). Therefore, FAP has become a highly promising target for novel cancer therapeutics and diagnostics.

In 2018, Loktev et al. showed that DOTA-containing FAP inhibitors (FAPIs) can be coupled with ^{68}Ga and used for PET imaging of multiple tumor entities, such as breast, colon, lung, and pancreatic cancer (*6*). Since then, clinical evidence has been growing for FAP-targeted PET.

TABLE 1
Patient Characteristics

Characteristic	Data
Overall	91
Age (y)	
Mean	57.4 (SD, 13.3)
Median	58.0 (range, 18.0–83.0)
Sex	
Female	42 (46.2%)
Male	49 (53.8%)
Oncologic diagnosis	76
Pancreatic cancer	28 (36.8%)
Sarcoma	16 (21.1%)
Lung cancer	10 (13.2%)
Other	22 (28.9%)
Nononcologic diagnosis	15
CAD	10 (66.7%)
Atrial fibrillation	3 (20.0%)
Other	2 (13.3%)
FAP radiotracer	
FAPI04	25 (27.5%)
FAPI46	66 (72.5%)

CAD = coronary artery disease.
Data are number followed by percentage in parentheses, except for age.

Received Jul. 1, 2021; revision accepted Aug. 20, 2021.
For correspondence and reprints, contact Lukas Kessler (lukas.kessler@uk-essen.de).
Published online Oct. 7, 2021.

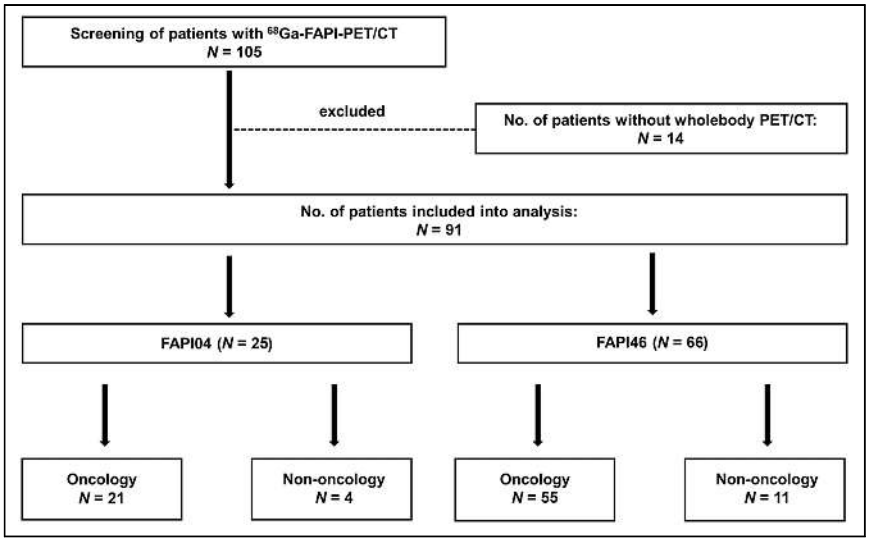

FIGURE 1. Patient selection flowchart.

It was recently shown that ^{68}Ga-FAPI PET can identify tumor lesions in various malignancies, with clinically beneficial tracer kinetics and lower tracer-to-background ratios than for ^{18}F-FDG (*7–10*). Furthermore, ^{68}Ga-FAPI showed a biodistribution similar to that of ^{18}F-FDG, with lower background uptake (*7*). Because tracer kinetics are independent from blood glucose levels, dietary arrangements are not needed for adequate imaging. Although promising data on this new radiotracer are increasing, false-positive results have been increasingly observed as well, such as in fibrotic or scar tissue (*7*). Recently, cases of nonmalignant diseases with FAPI uptake have been emerging, leading to questioning of the initially proclaimed tumor specificity (*11–17*).

After the introduction of a novel radiotracer, various potential pitfalls emerge over time and need to be summarized for the imaging community. Challenging findings have been reported in the past, such as for prostate-specific membrane antigen PET, for which a variety of false-positive findings have been found (*18,19*).

The aim of this study was to evaluate the frequency and intensity of common unspecific uptake patterns or pitfalls in ^{68}Ga-FAPI PET/CT in oncologic and nononcologic patients. We present data from our single-center retrospective study.

MATERIALS AND METHODS

Patients

One hundred five patients who underwent clinically indicated ^{68}Ga-FAPI PET/CT with either FAPI-04 or FAPI-46 between October 2018 and July 2020 were screened for eligibility. Only patients who had undergone wholebody PET/CT were included in the analysis, which led to the exclusion of 14 patients. All patients were referred for ^{68}Ga-FAPI PET/CT by treating physicians because of diagnostic challenges in oncologic and nononcologic diseases. All reported investigations were conducted in accordance with the Helsinki Declaration and with national regulations. The retrospective analysis was approved by the local Ethics Committee (permits 20-9485-BO and 20-9777-BO). Radiolabeling and administration of ^{68}Ga-FAPI-04 and ^{68}Ga-FAPI-46 complied with national and regional regulations for unproven interventions.

Image Acquisition

PET scans were obtained on a PET/CT system (Biograph mCT or Vision; Siemens). Two scans were performed approximately 10 and 60 min after injection. The injected activity of ^{68}Ga-FAPI was 149.7 ± 37.9 MBq. All PET images were iteratively reconstructed (Vision: 4 iterations, 5 subsets, 220 × 220 matrix, gaussian filtering of 5 mm; mCT: 3 iterations and 21 subsets) with time-of-flight information, using the dedicated software of the manufacturer (syngo MI.PET/CT; Siemens). Low-dose CT was acquired for attenuation correction (30 mAs, 120 keV, 512 × 512 matrix, 3-mm slice thickness) in cases of CT imaging.

Image Evaluation

Unspecific or nontumor findings were defined as findings not related to the respective disease or the purpose of the scan. Findings were rated in a consensus session by 2 experienced nuclear medicine physicians, with availability of all clinical and imaging information, and were reported along with SUV, SUV_{max}, SUV_{peak}, and SUV_{mean} 10 min and 60 min after tracer injection. Equivocal findings that could not clearly be discriminated from tumor or malignant lesions were not measured. Findings were grouped in major categories: degenerative findings, scarring and wound healing, focal or localized muscle uptake, mammary gland uptake, uterine uptake, and head-and-neck uptake (e.g., salivary glands, extraocular muscles, and dental foci).

TABLE 2
Pitfalls Listed Separately for Categories and Groups

Pitfall	All (n = 91)	FAPI-04 (n = 25)	FAPI-46 (n = 66)	P
Unspecific or non–tumor-specific findings	74 (81.3%)	17 (68.0%)	57 (86.4%)	0.06
Bone degenerative lesions	47 (51.6%)	8 (32.0%)	39 (59.1%)	0.41
Focal or localized muscle uptake	26 (28.6%)	7 (28.0%)	19 (28.8%)	0.99
Scarring or wound healing	18 (19.8%)	4 (16.0%)	14 (21.2%)	0.77
Mammary glands	7 (7.7%)	2 (8.0%)	5 (7.6%)	0.99
Uterus (n = 36)	24 (66.7%)	7 (19.4%)	17 (47.2%)	0.99
Head and neck (dental uptake, salivary glands, nasal mucosa)	41 (45.1%)	11 (44.0%)	30 (45.5%)	0.99

Data are number followed by percentage in parentheses.

TABLE 3
Radioligand Uptake in Pitfall Lesions at 60 Minutes After Injection

Pitfall lesion	SUV_{max}	SUV_{peak}	SUV_{mean}
Degenerative lesions			
Mean	7.7 (2.9)	4.3 (1.8)	4.3 (1.8)
Median	8.0 (3.1–17.3)	4.2 (2.1–11.5)	4.1 (1.1–9)
Focal or localized muscle uptake			
Mean	6.1 (2.2)	4.2 (1.4)	3.6 (1.5)
Median	5.45 (2.14–10.6)	3.8 (1.6–7.4)	3.25 (1.27–7.1)
Scarring and wound healing			
Mean	7.7 (3.3)	4.8 (1.9)	4.6 (1.9)
Median	7.6 (2.42–13.3)	5.0 (1.92–7.5)	4.7 (1.62–7.0)
Mammary glands			
Mean	4.5 (1.5)	2.6 (0.8)	2.7 (0.8)
Median	4.3 (2.3–7.25)	2.5 (1.5–3.9)	2.6 (1.2–3.8)
Uterine uptake			
Mean	12.2 (7.3)	9.6 (5.7)	7.5 (4.7)
Median	10.2 (4.2–31.2)	7.3 (3.8–24.6)	5.6 (2.2–19.3)
Salivary glands			
Mean	3.2 (0.2)	2.4 (0.2)	2.1 (0.3)
Median	3.1 (3.1–3.5)	2.4 (2.3–2.6)	2.1 (1.8–2.3)
Pancreatic uptake			
Mean	9.7 (6.0)	6.5 (4.9)	6.3 (4.0)
Median	8.8 (3.0–17.0)	5.45 (2.0–12.3)	5.75 (1.8–10.9)

Data in parentheses are SD or range.

SUV parameters were calculated by 3-dimensional volumes of interest using e.soft software (Siemens) at a 50% isocontour. The unspecific background in the blood pool (aortic vessel content), liver, and muscle was quantified with a circular 2-cm-diameter sphere.

Statistical Analysis

Statistical analyses were performed using Prism (version 9.1.0; GraphPad Software). Quantitative values were expressed as mean ± SD or as median and range when appropriate. Data were tested for a gaussian distribution using Shapiro–Wilk testing. When there was a gaussian distribution, paired Student *t* testing was used. Nonparametric data were compared using a Mann–Whitney *U* test. For bivariate correlation analyses, Spearman or Pearson correlation coefficients were calculated. For comparison of distribution, contingency testing using the Fisher exact test was used. All statistical tests were performed 2-sided, and a *P* value of less than 0.05 was considered to indicate statistical significance.

RESULTS

Patient characteristics are given in Table 1. In total, 91 patients were included in the analysis, primarily with a diagnosis of cancer (83.5%). Twenty-five patients (27.5%) were scanned with ^{68}Ga-FAPI-04, and 66 patients (82.5%) were scanned with ^{68}Ga-FAPI-46 (Fig. 1).

In most patients (81.3%), there was at least one reported finding that was rated as not related to the respective disease and

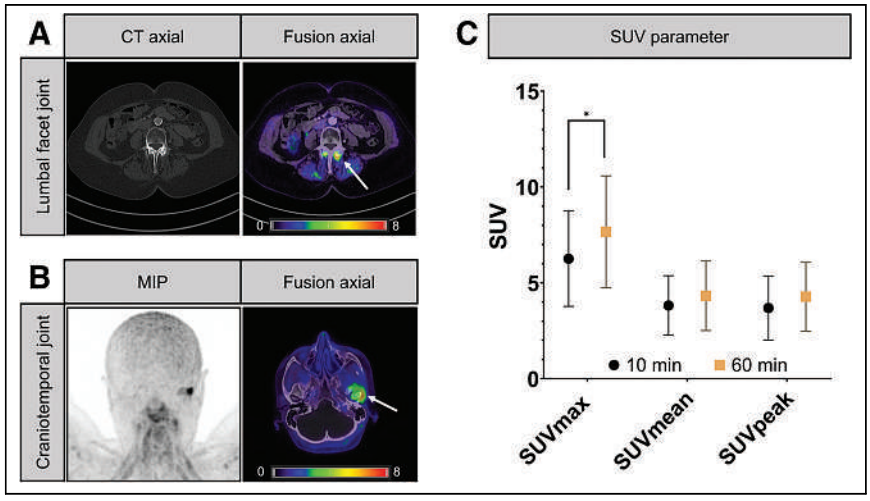

FIGURE 2. Degenerative lesions, associated mostly with joints and osteophytes. (A and B) Increased uptake of lumbar facet joints (A) and craniotemporal joint (B). (C) Uptake values showing wide range of intensity and significant increase in SUV_{max} (6.3 ± 2.5 vs. 7.7 ± 2.9, $P = 0.04$) from 10 to 60 min after injection. MIP = maximum-intensity projection.

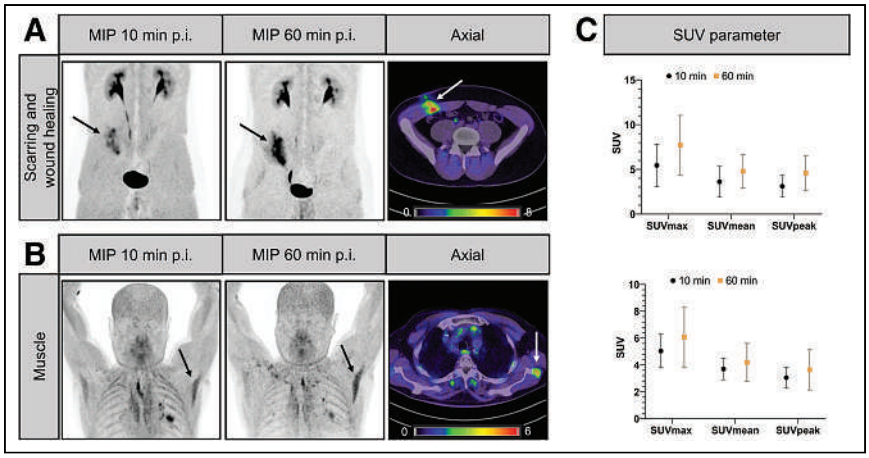

FIGURE 3. Scarring, wound healing, and muscle uptake. (A) Focal uptake along access route after surgical or interventional procedures can be observed, such as after tumor resection of round cell sarcoma of right abdominal wall. (B) Localized, isolated increased uptake is observed in larger muscles and tendon insertions. (C) Both findings show stable uptake values over 60 min. MIP = maximum-intensity projection; p.i. = after injection.

therefore categorized as unspecific. Comparison of distributions showed no statistically significant differences in findings between ^{68}Ga-FAPI-04 and ^{68}Ga-FAPI-46 (Table 2). A detailed description of uptake locations for degenerative, muscle, and scar/wound healing is given in Supplemental Table 1 (supplemental materials are available at http://jnm.snmjournals.org). Uptake values for the categories are shown in Table 3, and ^{68}Ga-FAPI-04 and ^{68}Ga-FAPI-46 uptake for the respective categories is additionally discriminated in Supplemental Table 2. Here, we will discuss the findings and pitfalls by category.

Degenerative Pitfalls

Common pitfall findings were degenerative lesions, mostly associated with joints and vertebral bones (51.6%), with no significant difference between ^{68}Ga-FAPI-04 and ^{68}Ga-FAPI-46 ($P = 0.41$) (Table 2). The lesions showed focal uptake with a mean SUV_{max} of 7.7 ± 2.9 (Table 3). Figure 2 depicts a case of uptake in the facet joints of the lumbar vertebrae with degenerative features on CT (Fig. 2A), as well as a case of focal uptake in the left temporomandibular joint (Fig. 2B). SUV parameters showed a significant increase in SUV_{max} (mean SUV_{max}, 6.3 ± 2.5 vs. 7.7 ± 2.9, $P = 0.04$) but no difference between early and late imaging timepoints for SUV_{mean} and SUV_{peak} (mean SUV_{peak}, 3.8 ± 1.6 vs. 4.3 ± 1.8, $P = 0.19$; mean SUV_{mean}, 3.7 ± 1.7 vs. 4.3 ± 1.8, $P = 0.14$) (Fig. 2C).

Scarring/Wound Healing and Muscle Uptake

Focal or localized muscle uptake was observed in 28.6%, with a mean SUV_{max} of 6.1 ± 2.2, and uptake in scars or wound-healing processes was found in 19.8%, with a mean SUV_{max} of 7.7 ± 3.3 (Tables 2 and 3). Sites with a predilection for muscle uptake were larger muscle groups such as the quadriceps femoris muscle, latissimus dorsi muscle, triceps muscle, and autochthone muscles. SUV parameters did not differ between early and late imaging either in muscle uptake findings (mean SUV_{max}, 5.0 ± 1.3 vs. 6.1 ± 2.2, $P = 0.06$) or in scarring and wound-healing processes (mean SUV_{max}, 5.4 ± 2.4 vs. 7.7 ± 3.3, $P = 0.08$) (Fig. 3).

Head-and-Neck Pitfalls

In 41 patients (45.1%), uptake could be found in the head and neck, most frequently localized in the extraocular muscles, the salivary glands, the oral or nasal mucosa, or focally in the teeth (Fig. 4, top panel). The salivary glands showed a significant decrease in uptake from early to late imaging timepoints (SUV_{max}, 6.0 ± 1.2 vs. 3.2 ± 0.2; SUV_{mean}, 4.4 ± 0.8 vs. 2.4 ± 0.2; SUV_{peak}, 3.7 ± 0.7 vs. 2.1 ± 0.3 [$P < 0.05$]). Uptake in the extraocular muscle and teeth was stable between 10 and 60 min after injection (Fig. 4, middle and bottom panels).

Uterine and Mammary Findings

Intense, variable uptake in the uterus occurred in 66.7% of all female patients ($n = 36$; posthysterectomy patients excluded) (SUV_{max} 60 min after injection, 12.2 ± 7.3; range, 4.2–31.2). Younger women, in particular, showed higher uptake in the uterus, with a negative correlation between SUV parameters and age (SUV_{max}, $r = -0.6$, $P < 0.01$; SUV_{peak}, $r = -0.57$, $P < 0.01$;

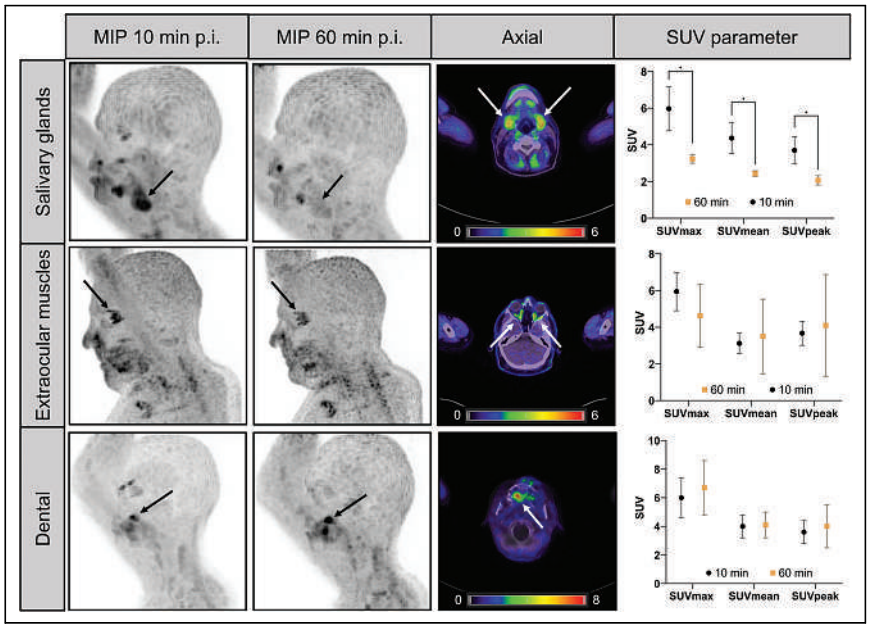

FIGURE 4. Head-and-neck findings. Salivary glands show significant decrease in uptake from 10 to 60 min after injection ($P < 0.05$). Few patients have increased uptake in extraocular muscles. Dental foci are often reported most likely linked to chronic inflammatory processes. MIP = maximum-intensity projection; p.i. = after injection

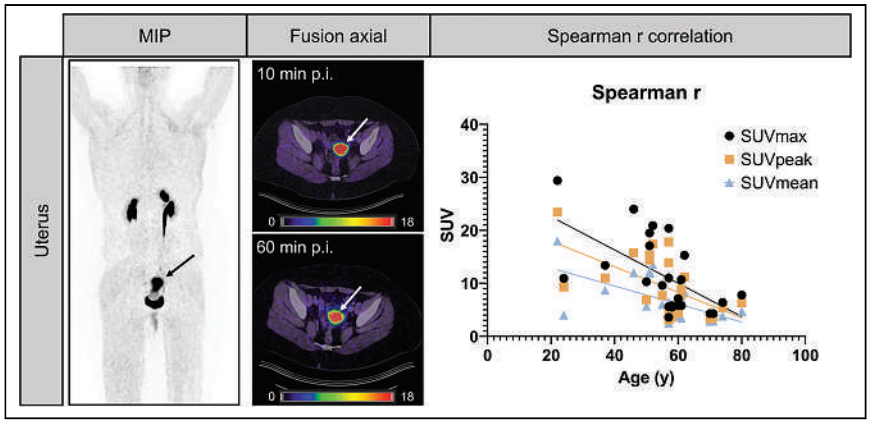

FIGURE 5. Uterine findings. Of female patients (posthysterectomy patients excluded), 66.7% showed fibroblast activation of uterus. Uterine uptake has moderate to strong negative correlation with age (SUV_{max}, $r = -0.6$, $P < 0.01$; SUV_{peak}, $r = -0.57$, $P < 0.01$; SUV_{mean}, $r = -0.58$, $P < 0.01$), possibly linked to menopausal shrinkage. MIP = maximum-intensity projection; p.i. = after injection.

SUV_{mean}, $r = -0.58$, $P < 0.01$) (Fig. 5). As depicted in Figure 6, few patients (7.7%) showed increased uptake in the mammary glands; uptake was stable over 60 min, with a mean SUV_{max} of 4.5 ± 1.5 at 60 min after injection. Age ranged from 24 to 67 y in these female patients.

DISCUSSION

FAP-directed ^{68}Ga-FAPI PET/CT is a novel modality introduced for imaging of various entities. Recent studies have demonstrated comparable or even increased detection rates in comparison with ^{18}F-FDG PET/CT, such as in pancreatic cancer, sarcoma, and hepatic malignancies (*9,10,20*). In the interpretation of ^{68}Ga-FAPI PET/CT scans, the readers—especially at centers to which this technology was recently introduced—need to be informed about common findings and potential pitfalls. This pictorial analysis aimed to summarize ^{68}Ga-FAPI PET/CT uptake patterns and common interpretation pitfalls that were recorded in our retrospective database.

Further, we aimed to report uptake intensity, location, and frequency of occurrence. In our opinion, such a report is of great importance in avoiding misdiagnosis, as this novel modality will soon become more widespread.

We found that unspecific or nontarget uptake can be observed in degenerative, traumatic, inflammatory, and physiologic processes, and we were able to show that non–tumor-specific or unspecific uptake is present in most patients at a variety of locations, but especially in degenerative spine conditions. In our cohort, uterine uptake was noted in 66.7% of women and showed a decrease in intensity with age. Hypothetically, this is due to the decreased FAP expression of the endometrium after menopause, as is supported by proteomic data and PET data on the FAP expression of the endometrium before and after menopause (*16,21,22*). This decreased expression might pose an important pitfall and limitation in the use of ^{68}Ga-FAPI PET/CT for local staging of gynecologic cancers and should be take into consideration, but larger cohorts are needed to verify this finding.

Furthermore, we observed in nearly half of patients non–tumor-related uptake in the head-and-neck region. Interestingly, the salivary glands showed a decrease in tracer retention within the first hour after injection, but a thorough literature review did not reveal the underlying mechanism. This observation might reflect unspecific tracer accumulation, which should be considered when patients with head-and-neck cancer are being imaged; these tumors might benefit from use of later imaging timepoints. Additionally, intense uptake in the extraocular muscles was noted in 9% of the patients; however, these patients had no medical history of major ocular disorders and, to date, no specific data on FAP expression in these muscles is available.

Previous studies demonstrated decreasing uptake in pancreatitis and other, unspecified, inflammatory diseases (*9,17,23*). In contrast, in our study dental foci of active inflammation showed increased uptake over time, possibly due to unspecific uptake in surrounding edema.

Numerous studies provide data on FAP overexpression in carcinoma-associated fibroblasts and in various other processes, such as fibrosis, inflammatory atheromata, and osteoarthritis (*24–27*). FAP is overexpressed by myofibroblasts in tissue remodeling, wound healing, and fibrotic tissue (*28*). This phenomenon has already been found by our group and others that studied patients after myocardial infarction using ^{68}Ga-FAPI PET/CT (*29–31*). In those patients, ^{68}Ga-FAPI uptake matched

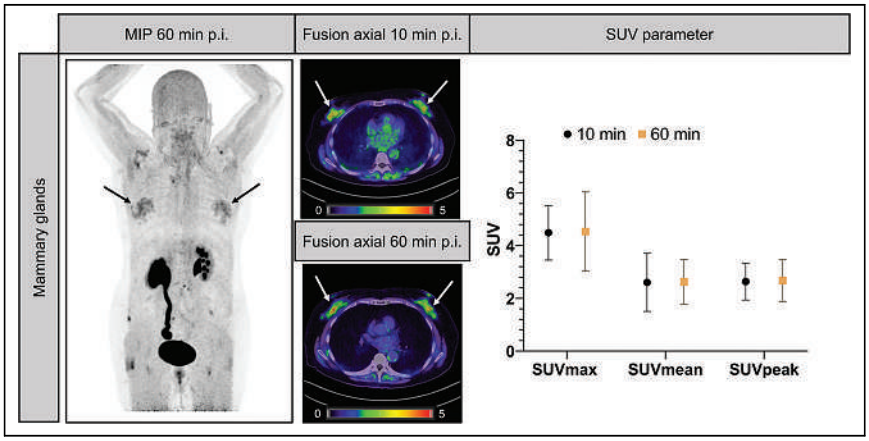

FIGURE 6. Mammary gland findings. Rarely, patients showed increased uptake in mammary tissue (7.7%). Uptake was reported in middle-aged women and one man with gynecomastopathy. Additionally, other non–tumor-specific uptake around shoulder and hip joints can be seen, as well as tracer accumulation in urinary tract. MIP = maximum-intensity projection; p.i. = after injection.

the affected myocardium, most likely due to ongoing remodeling processes, and agrees with scientific evidence on fibroblast activation after ischemia (*32,33*).

Pitfalls may originate from specific uptake through an increased FAP expression level and mechanisms of unspecific uptake, including edema, tracer extravasation, and some inflammatory disorders. Future studies should aim to thoroughly validate positive ^{68}Ga-FAPI PET/CT findings via immunohistochemical FAP expression (*10,34*).

Our study comes with several limitations. Our single-center analysis consisted of a heterogeneous cohort with various oncologic and nononcologic diseases and at different disease stages. In addition, we analyzed 2 different FAPI tracers, which might have different frequencies of certain pitfalls, although such differences were not observed in our cohort. Lastly, the list of common findings we have reported here is not intended to be exhaustive and cannot give proper answers about the underlying pathophysiologic processes. Future studies should elucidate disease- and tracer-specific pitfalls and common findings. Because the implementation of ^{68}Ga-FAPI PET is expanding, it is important to share pitfalls and common findings now, especially for centers that have recently introduced this new technology.

CONCLUSION

Here, we have reported non–tumor-specific ^{68}Ga-FAPI uptake—especially in degenerative lesions, wound healing, muscles, and the uterus—as a potential pitfall in the interpretation of ^{68}Ga-FAPI PET/CT images. This report will help readers improve the accuracy of image interpretation at centers that have recently begun using ^{68}Ga-FAPI PET/CT. Our work can be seen as an initial guide to the reporting of ^{68}Ga-FAPI PET/CT, a novel and rapidly expanding imaging modality.

DISCLOSURE

Wolfgang Fendler reports fees from BTG (consultant), Calyx (consultant), RadioMedix (image reader), Bayer (speakers bureau), and Parexel (image reader) outside the submitted work. Rainer Hamacher is supported by the Clinician Scientist Program of the University Medicine Essen Clinician Scientist Academy (UMEA), sponsored by the faculty of medicine and Deutsche Forschungsgemeinschaft (DFG), and has received travel grants from Lilly, Novartis, and PharmaMar, as well as fees from Lilly outside the submitted work. Lukas Kessler is a consultant for BTG and AAA and received fess from Sanofi outside the submitted work. Justin Ferdinandus has received a Junior Clinician Scientist Stipend granted by the University Duisburg–Essen. Manuel Weber is a consultant for Boston Scientific and received fees outside the submitted work. Christoph Rischpler reports grants and other fees from Pfizer; other fees from Alnylam, GE, Siemens, and Advanced Accelerator Applications; and personal fees from Pharmtrace outside the submitted work. Katharina Lueckerath reports paid consulting activities for Sofie Biosciences/iTheranostics and funding from AMGEN outside the submitted work. No other potential conflict of interest relevant to this article was reported.

KEY POINTS

QUESTION: Is there an association between ^{68}Ga-FAPI uptake intensity and FAP expression in bone and soft-tissue sarcomas, and what is the diagnostic performance of ^{68}Ga-FAPI PET in sarcoma patients?

PERTINENT FINDINGS: We observed an association between ^{68}Ga-FAPI uptake intensity and immunohistochemical FAP expression in sarcomas and showed ^{68}Ga-FAPI PET to have high accuracy in sarcoma patients.

IMPLICATIONS FOR PATIENT CARE: ^{68}Ga-FAPI PET has diagnostic utility for patients with sarcoma and future implications in FAP-targeted therapies.

REFERENCES

1. Koczorowska MMM, Tholen S, Bucher F, et al. Fibroblast activation protein-α, a stromal cell surface protease, shapes key features of cancer associated fibroblasts through proteome and degradome alterations. *Mol Oncol.* 2016;10:40–58.
2. Kalluri R. The biology and function of fibroblasts in cancer. *Nat Rev Cancer.* 2016;16:582–598.
3. Rettig WJ, Garin-Chesa P, Beresford HR, Oettgen HF, Melamed MR, Old LJ. Cell-surface glycoproteins of human sarcomas: differential expression in normal and malignant tissues and cultured cells. *Proc Natl Acad Sci USA.* 1988;85:3110–3114.
4. Niedermeyer J, Garin-Chesa P, Kriz M, et al. Expression of the fibroblast activation protein during mouse embryo development. *Int J Dev Biol.* 2001;45:445–447.
5. Liu F, Qi L, Liu B, et al. Fibroblast activation protein overexpression and clinical implications in solid tumors: a meta-analysis. *PLoS One.* 2015;10:e0116683.
6. Loktev A, Lindner T, Burger E-M, et al. Development of fibroblast activation protein–targeted radiotracers with improved tumor retention. *J Nucl Med.* 2019;60:1421–1429.
7. Giesel FL, Kratochwil C, Lindner T, et al. ^{68}Ga-FAPI PET/CT: biodistribution and preliminary dosimetry estimate of 2 DOTA-containing FAP-targeting agents in patients with various cancers. *J Nucl Med.* 2019;60:386–392.
8. Kratochwil C, Flechsig P, Lindner T, et al. ^{68}Ga-FAPI PET/CT: tracer uptake in 28 different kinds of cancer. *J Nucl Med.* 2019;60:801–805.
9. Röhrich M, Naumann P, Giesel FL, et al. Impact of ^{68}Ga-FAPI PET/CT imaging on the therapeutic management of primary and recurrent pancreatic ductal adenocarcinomas. *J Nucl Med.* 2021;62:779–786.
10. Kessler L, Ferdinandus J, Hirmas N, et al. ^{68}Ga-FAPI as a diagnostic tool in sarcoma: data from the ^{68}Ga-FAPI PET prospective observational trial. *J Nucl Med.* 2022;63:89–95.
11. Lin R, Lin Z, Zhang J, Yao S, Miao W. Increased ^{68}Ga-FAPI-04 uptake in Schmorl node in a patient with gastric cancer. *Clin Nucl Med.* 2021;46:700–702.
12. Can C, Gündoğan C, Güzel Y, Kaplan İ, Kömek H. ^{68}Ga-FAPI uptake of thyroiditis in a patient with breast cancer. *Clin Nucl Med.* 2021;46:683–685.
13. Liu H, Chen Z, Yang X, Fu W, Chen Y. Increased ^{68}Ga-FAPI uptake in chronic cholecystitis and degenerative osteophyte. *Clin Nucl Med.* 2021;46:601–602.
14. Gündoğan C, Güzel Y, Can C, Alabalik U, Kömek H. False-positive ^{68}Ga-fibroblast activation protein-specific inhibitor uptake of benign lymphoid tissue in a patient with breast cancer. *Clin Nucl Med.* 2021;46:e433–e435.
15. Wu J, Liu H, Ou L, Jiang G, Zhang C. FAPI uptake in a vertebral body fracture in a patient with lung cancer. *Clin Nucl Med.* 2021;46:520–522.
16. Dendl K, Koerber SA, Adeberg S, et al. Physiological FAP-activation in a postpartum woman observed in oncological FAPI-PET/CT. *Eur J Nucl Med Mol Imaging.* 2021;48:2059–2061.
17. Ferdinandus J, Kessler L, Hirmas N, et al. Equivalent tumor detection for early and late FAPI-46 PET acquisition. *Eur J Nucl Med Mol Imaging.* 2021;48:3221–3227.
18. Rischpler C, Beck TI, Okamoto S, et al. ^{68}Ga-PSMA-HBED-CC uptake in cervical, celiac, and sacral ganglia as an important pitfall in prostate cancer PET imaging. *J Nucl Med.* 2018;59:1406–1411.
19. Sheikhbahaei S, Afshar-Oromieh A, Eiber M, et al. Pearls and pitfalls in clinical interpretation of prostate-specific membrane antigen (PSMA)-targeted PET imaging. *Eur J Nucl Med Mol Imaging.* 2017;44:2117–2136.

20. Shi X, Xing H, Yang X, et al. Fibroblast imaging of hepatic carcinoma with ^{68}Ga-FAPI-04 PET/CT: a pilot study in patients with suspected hepatic nodules. *Eur J Nucl Med Mol Imaging.* 2021;48:196–203.
21. Uhlén M, Fagerberg L, Hallstrom BM, et al. Tissue-based map of the human proteome. *Science.* 2015;347:1260419-1260419.
22. Dendl K, Koerber SA, Finck R, et al. ^{68}Ga-FAPI-PET/CT in patients with various gynecological malignancies. *Eur J Nucl Med Mol Imaging.* 2021;48:4089–4100.
23. Schmidkonz C, Rauber S, Atzinger A, et al. Disentangling inflammatory from fibrotic disease activity by fibroblast activation protein imaging. *Ann Rheum Dis.* 2020;79:1485–1491.
24. Wang XM. Fibroblast activation protein and chronic liver disease. *Front Biosci.* 2008;13:3168–3180.
25. Milner JM, Kevorkian L, Young DA, et al. Fibroblast activation protein alpha is expressed by chondrocytes following a pro-inflammatory stimulus and is elevated in osteoarthritis. *Arthritis Res Ther.* 2006;8:R23.
26. Brokopp CE, Schoenauer R, Richards P, et al. Fibroblast activation protein is induced by inflammation and degrades type I collagen in thin-cap fibroatheromata. *Eur Heart J.* 2011;32:2713–2722.
27. Kelly T, Huang Y, Simms AE, Mazur A. Fibroblast activation protein-α. In: *International Review of Cell and Molecular Biology*. Elsevier; 2012:83–116.
28. Scharl M, Huber N, Lang S, Fürst A, Jehle E, Rogler G. Hallmarks of epithelial to mesenchymal transition are detectable in Crohn's disease associated intestinal fibrosis. *Clin Transl Med.* 2015;4:1–9.
29. Kessler L, Kupusovic J, Ferdinandus J, et al. Visualization of fibroblast activation after myocardial infarction using ^{68}Ga-FAPI PET. *Clin Nucl Med.* 2021;46:807–813.
30. Diekmann J, Koenig T, Zwadlo C, et al. Molecular imaging identifies fibroblast activation beyond the infarct region after acute myocardial infarction. *J Am Coll Cardiol.* 2021;77:1835–1837.
31. Zhu W, Guo F, Wang Y, Ding H, Huo L. ^{68}Ga-FAPI-04 accumulation in myocardial infarction in a patient with neuroendocrine carcinoma. *Clin Nucl Med.* 2020; 45:1020–1022.
32. Varasteh Z, Mohanta S, Robu S, et al. Molecular imaging of fibroblast activity after myocardial infarction using a ^{68}Ga-labeled fibroblast activation protein inhibitor, FAPI-04. *J Nucl Med.* 2019;60:1743–1749.
33. Tillmanns J, Hoffmann D, Habbaba Y, et al. Fibroblast activation protein alpha expression identifies activated fibroblasts after myocardial infarction. *J Mol Cell Cardiol.* 2015;87:194–203.
34. Shi X, Xing H, Yang X, et al. Comparison of PET imaging of activated fibroblasts and ^{18}F-FDG for diagnosis of primary hepatic tumours: a prospective pilot study. *Eur J Nucl Med Mol Imaging.* 2021;48:1593–1603.

Imaging PD-L1 Expression in Melanoma Brain Metastases

Sridhar Nimmagadda

Russell H. Morgan Department of Radiology and Radiological Science, Sidney Kimmel Comprehensive Cancer Center and Bloomberg–Kimmel Institute for Cancer Immunotherapy, Department of Pharmacology and Molecular Sciences, and Division of Clinical Pharmacology, Department of Medicine, Johns Hopkins University School of Medicine Baltimore, Maryland

See the associated article on page 899.

Brain metastases, often originating from melanoma, lung cancer, or breast cancer, are the most common tumor in the brain and are associated with a dismal prognosis (*1*). Nearly 12% of patients with melanoma develop brain metastases, leading to a reduction in median survival to less than 9 mo. Brain metastases pose a significant challenge for treatment, as the disease state is highly refractory and central nervous system penetration of drugs across an intact blood–brain barrier is poor (*1*). Therapeutics targeting immune checkpoint proteins have shown intracranial activity in melanoma brain metastases, indicating an immune-active microenvironment (*1*). However, a deeper insight into the genetic and immunologic underpinnings of brain metastases and their response to immune system–targeted therapies is needed to overcome potential resistance mechanisms. Programmed death ligand 1 (PD-L1) is an immune checkpoint protein that is abundantly expressed by tumors (*2*). In this issue of *The Journal of Nuclear Medicine,* Nienhuis et al. characterize the changes in PD-L1 expression in brain and extracranial metastases in melanoma patients receiving immune checkpoint therapy (*3*).

Unlike conventional treatment methods, immune checkpoint therapeutics target the immune system. Efficacy can then be independent of tumor histology and genetic alterations, thus providing durable benefits in a variety of cancer types (*2*). Among the targets, the immune checkpoint proteins cytotoxic T-lymphocyte–associated antigen 4, programmed death 1, and its ligand PD-L1 are the best characterized, with several inhibitors receiving approvals from the Food and Drug Administration (*2*). Long-term treatment benefits are observed in a small percentage of patients when these inhibitors are given as single-agent therapy (*4*). Durable benefits have been observed in a higher percentage of patients when different checkpoint inhibitor combinations are used or when checkpoint inhibitors are combined with chemotherapy, targeted therapy, or radiotherapy (*2*,*5*).

Enrichment of patients to further improve the outcomes of cancer immunotherapy is based on high tumor PD-L1 expression, tumor mutation burden, and DNA mismatch repair deficiency (*6*). To date, PD-L1 detection by immunohistochemistry received several Food and Drug Administration approvals as a complementary or companion diagnostic. However, the current landscape of PD-L1 immunohistochemistry as a predictive biomarker is complex (*7*). Although issues pertaining to the use of multiple antibody clones and staining platforms have been addressed by the Blueprint project, immunohistochemistry assays do not fully capture the heterogeneity in PD-L1 expression within and across patients (*7*). Moreover, immune responses are atypical, are unpredictable, and differ on the basis of tumor type, thus needing real-time noninvasive imaging analysis of changes in the tumor microenvironment.

Radiolabeled analogs of several anti-PD-L1 antibodies have been investigated to noninvasively quantify PD-L1 levels in preclinical tumor models and in cancer patients (*7*). Results from early clinical studies show that PD-L1 radiotracer uptake can readily be detected by PET and is highly heterogeneous within and across patients (*7*). The PET tracer used by Nienhuis et al., ^{18}F-BMS-986192, possesses the advantage of being labeled with ^{18}F, a radionuclide with a favorable energy profile and half-life, and exhibits faster pharmacokinetics facilitating image acquisition at 60 min for rapid PD-L1 quantification. ^{18}F-BMS-986192 is an engineered small adnectin protein with a dissociation constant of less than 35 pM for PD-L1 (*8*). It exhibited PD-L1–specific uptake in human tumor xenografts in vivo and concordance with PD-L1 immunohistochemistry staining in non–small cell lung cancer (NSCLC) tissues ex vivo (*8*). Heterogeneous ^{18}F-BMS-986192 uptake was observed within and between melanoma patients in this study, similarly to previous studies on NSCLC (*9*). Although ^{18}F-BMS-986192 uptake was significantly higher in NSCLC tumors for lesions with at least 50% tumor PD-L1 expression measured by immunohistochemistry, as compared with lesions with less than 50% expression (*9*), the sensitivity of the radiotracer in quantifying PD-L1 level as a continuous variable remains to be established for sustained use in melanoma. Nearly 35% of melanoma tumors exhibit PD-L1 tumor proportion scores of less than 50% (*6*), and PD-L1 expression on tumor cells is lower in melanoma than in other cancers, including NSCLC and renal cell carcinoma (*6*). Establishing the sensitivity of PD-L1 imaging agents is needed to further guide clinical decisions, as most melanoma trials have used a cut point of 5% PD-L1 positivity whereas NSCLC trials used 50%.

Although some homogeneity is observed in spatially and temporally separated brain metastasis in their genetic and immunologic profile, they are highly divergent from extracranial metastases (*10*). No significant differences in PD-L1 expression between melanoma brain and extracranial metastases were observed in that study, however (*10*). Although no significant differences were observed in

Received Oct. 22, 2021; revision accepted Nov. 1, 2021.

For correspondence or reprints, contact Sridhar Nimmagadda (snimmag1@jh.edu).

Published online Nov. 5, 2021.

DOI: 10.2967/jnumed.121.263209

baseline ^{18}F-BMS-986192 uptake between brain and extracranial metastases (mostly lung), a trend toward lower radiotracer uptake in brain metastases could be observed, perhaps because of the poor blood–brain barrier permeability of the radiotracer. In contrast, on treatment, ^{18}F-BMS-986192 scans showed significantly lower uptake of the radiotracer in brain metastases than in extracranial metastases. ^{18}F-BMS-986192 uptake was also observed to be heterogeneous within brain metastases, as could be explained by the fact that some brain metastases can disrupt the blood–brain barrier. The absence of correlative immunohistochemistry data or prior validation of the tracer to detect variable PD-L1 levels makes it difficult to interpret these observations. Combining imaging studies with tissue biomarker analyses, when feasible, would provide a deeper understanding of the organ-specific immune contexture and its relationship to imaging measurements and move us toward developing composite biomarkers.

In this report, the authors observed that lesions with high baseline ^{18}F-BMS-986192 uptake, when corrected for blood-pool activity, respond well to nivolumab or ipilimumab-plus-nivolumab therapy. This observation is in line with prior clinical studies establishing that PD-L1 expression in the melanoma tumor microenvironment is a predicter of response to immune checkpoint therapeutics (*11*). Timing the imaging studies during treatment to capture the transient kinetics of immunologic effects is challenging, however. Early on-treatment biopsies collected at 1.4 mo in melanoma patients showed a highly statistically significant increase in PD-L1 levels in responders, compared with nonresponders (*12*). In this study, authors observed that radiotracer uptake in metastases at 6 wk after treatment positively correlates with tumor size at follow-up at 12 wk. Because of the nature of the study and lack of cross validation, it is difficult to discern the underlying factors contributing to increased radiotracer uptake, which include tumor progression, pseudo progression due to an influx of immune cells, and the resulting PD-L1 induction. The challenge here again will be to ensure optimal imaging times and cross correlation of imaging measures with immunohistochemistry.

Despite the dramatic improvements in advanced melanoma treatments and outcomes, brain metastases remain a significant challenge. Brain metastases are diagnosed in nearly 60% of patients with advanced melanoma and often show isolated progression, although disease is controlled in extracranial metastases. Noninvasively quantifying PD-L1 and other relevant biomarkers in the tumor microenvironment and establishing a relationship to response, as shown here, will play an important role in improving the efficacy of immunotherapy for this patient group.

DISCLOSURE

Sridhar Nimmagadda is supported by the Allegheny Health Network–Johns Hopkins Cancer Research Fund, NIH 1R01CA236616, and NIH P41EB024495; is a consultant for and receives funding from Precision Molecular Inc.; and is a coinventor on a pending U.S. patent covering PD-L1 imaging agents and as such is entitled to a portion of any licensing fees and royalties generated by the technology. This arrangement has been reviewed and approved by the Johns Hopkins University in accordance with its conflict-of-interest policies. No other potential conflict of interest relevant to this article was reported.

REFERENCES

1. Berghoff AS, Venur VA, Preusser M, Ahluwalia MS. Immune checkpoint inhibitors in brain metastases: from biology to treatment. *Am Soc Clin Oncol Educ Book.* 2016;35:e116–e122.
2. Topalian SL, Drake CG, Pardoll DM. Immune checkpoint blockade: a common denominator approach to cancer therapy. *Cancer Cell.* 2015;27:450–461.
3. Nienhuis PH, Antunes IF, Glaudemans A, et al. ^{18}F-BMS986192 PET imaging of PD-L1 in metastatic melanoma patients with brain metastases treated with immune checkpoint inhibitors: a pilot study. *J Nucl Med.* 2022;63:899–905.
4. Schadendorf D, Hodi FS, Robert C, et al. Pooled analysis of long-term survival data from phase II and phase III trials of ipilimumab in unresectable or metastatic melanoma. *J Clin Oncol.* 2015;33:1889–1894.
5. Larkin J, Chiarion-Sileni V, Gonzalez R, et al. Five-year survival with combined nivolumab and ipilimumab in advanced melanoma. *N Engl J Med.* 2019;381:1535–1546.
6. Huang RSP, Haberberger J, Severson E, et al. A pan-cancer analysis of PD-L1 immunohistochemistry and gene amplification, tumor mutation burden and microsatellite instability in 48,782 cases. *Mod Pathol.* 2021;34:252–263.
7. Nimmagadda S. Quantifying PD-L1 expression to monitor immune checkpoint therapy: opportunities and challenges. *Cancers (Basel).* 2020;12:3173.
8. Donnelly DJ, Smith RA, Morin P, et al. Synthesis and biologic evaluation of a novel ^{18}F-labeled adnectin as a PET radioligand for imaging PD-L1 expression. *J Nucl Med.* 2018;59:529–535.
9. Niemeijer AN, Leung D, Huisman MC, et al. Whole body PD-1 and PD-L1 positron emission tomography in patients with non-small-cell lung cancer. *Nat Commun.* 2018;9:4664.
10. Fischer GM, Jalali A, Kircher DA, et al. Molecular profiling reveals unique immune and metabolic features of melanoma brain metastases. *Cancer Discov.* 2019;9:628–645.
11. Lipson EJ, Forde PM, Hammers HJ, Emens LA, Taube JM, Topalian SL. Antagonists of PD-1 and PD-L1 in cancer treatment. *Semin Oncol.* 2015;42:587–600.
12. Chen PL, Roh W, Reuben A, et al. Analysis of immune signatures in longitudinal tumor samples yields insight into biomarkers of response and mechanisms of resistance to immune checkpoint blockade. *Cancer Discov.* 2016;6:827–837.

^{18}F-BMS986192 PET Imaging of PD-L1 in Metastatic Melanoma Patients with Brain Metastases Treated with Immune Checkpoint Inhibitors: A Pilot Study

Pieter H. Nienhuis[1], Inês F. Antunes[1], Andor W.J.M. Glaudemans[1], Mathilde Jalving[2], David Leung[3], Walter Noordzij[1], Riemer H.J.A. Slart[1,4], Erik F.J. de Vries[1], and Geke A.P. Hospers[2]

[1]Department of Nuclear Medicine and Molecular Imaging, Medical Imaging Center, University of Groningen, University Medical Center Groningen, Groningen, The Netherlands; [2]Department of Medical Oncology, University of Groningen, University Medical Center Groningen, Groningen, The Netherlands; [3]Bristol Myers Squibb, Princeton, New Jersey; and [4]Faculty of Science and Technology, Department of Biomedical Photonic Imaging, University of Twente, Enschede, The Netherlands

See an invited perspective on this article on page 897.

Immune checkpoint inhibitors (ICIs) targeting programmed cell death protein-1 (PD-1)/programmed cell death ligand-1 (PD-L1) frequently induces tumor response in metastatic melanoma patients. However, tumor response often takes months and may be heterogeneous. Consequently, additional local treatment for nonresponsive metastases may be needed, especially in the case of brain metastases. Noninvasive imaging may allow the characterization of (brain) metastases to predict response. This pilot study uses ^{18}F-BMS986192 PET for PD-L1 expression to explore the variability in metastatic tracer uptake and its relation to tumor response, with a special focus on brain metastases. **Methods:** Metastatic melanoma patients underwent whole-body ^{18}F-BMS986192 PET/CT scanning before and 6 wk after starting ICI therapy. ^{18}F-BMS986192 uptake was measured in healthy tissues, organs, and tumor lesions. Tumor response was evaluated at 12 wk using CT of the thorax/abdomen and MRI of the brain. RECIST, version 1.1, was used to define therapy response per patient. Response per lesion was measured by the percentage change in lesion diameter. Toxicity was assessed according to Common Terminology Criteria for Adverse Events, version 4.0. **Results:** Baseline ^{18}F-BMS986192 PET/CT was performed in 8 patients, with follow-up scans in 4 patients. The highest tracer uptake was observed in the spleen, bone marrow, kidneys, and liver. Tracer uptake in tumor lesions was heterogeneous. In total, 42 tumor lesions were identified at baseline, with most lesions in the lungs ($n = 21$) and brain ($n = 14$). Tracer uptake was similar between tumor locations. ^{18}F-BMS986192 uptake in lesions at baseline, corrected for blood-pool activity, was negatively correlated with the change lesion diameter at response evaluation ($r = -0.49$, $P = 0.005$), both in intra- and extracerebral lesions. Receiver-operating-characteristic analysis demonstrated that ^{18}F-BMS986192 uptake can discriminate between responding and nonresponding lesions with an area under the curve of 0.82. At the follow-up scan, an increased ^{18}F-BMS986192 uptake compared with baseline scan was correlated with an increased lesion diameter at response evaluation. In the follow-up ^{18}F-BMS986192 PET scan of 2 patients, ICI-related toxicity (thyroiditis and colitis) was detected. **Conclusion:** In this pilot study, ^{18}F-BMS986192 PET showed heterogeneous uptake in intra- and extracerebral metastatic lesions in melanoma patients. Baseline ^{18}F-BMS986192 uptake was able to predict an ICI treatment–induced reduction in lesion volume, whereas the follow-up PET scan allowed the detection of treatment-induced toxicity.

Key Words: PET; PD-L1 expression; metastatic melanoma; brain metastasis; immune checkpoint inhibition

J Nucl Med 2022; 63:899–905
DOI: 10.2967/jnumed.121.262368

Immune checkpoint inhibitors (ICIs) targeting the programmed cell death protein-1 (PD-1)/programmed cell death ligand-1 (PD-L1) axis or cytotoxic T-lymphocyte–associated protein 4 (CTLA-4) receptor, either as monotherapy or as combined treatment, have shown response rates of approximately 40%–60% in patients with metastatic melanoma, with progression-free and overall survival (*1–8*).

However, it often takes months before response to ICI treatment can be detected, and lesions may respond in a heterogeneous manner. Some lesions may respond, whereas other lesions may not respond or display pseudoprogression (*9*). Consequently, some fast-growing lesions may require additional treatment. Data from the Dutch National Cancer Registry show that 22% (876/3,959) of metastatic melanoma patients underwent surgery for nonresponding metastases in addition to systemic treatment with ICI (*10*). Moreover, approximately 30% of metastatic melanoma patients develop brain metastases. Brain metastases are considered as a risky location because they carry a high risk for developing central nervous system failure and mortality (*11*). Therefore, local treatment with radiotherapy or resection is often considered in patients with brain metastases.

Before starting ICI therapy, it is difficult to determine which lesions will respond and which lesions will require additional treatment. Immunohistochemistry on biopsy samples only provides information about a small fraction of a single tumor lesion and is, therefore, unable to address intra- and intertumoral heterogeneity, thus limiting the value of immunohistochemistry to predict response. In patients with metastatic melanoma, known to be a high heterogenic responding tumor, PD-1 immunohistochemistry staining on biopsies was not a good predictor of response to ICI and hence is not used in clinical practice (*12*).

Received Mar. 29, 2021; revision accepted Aug. 24, 2021.
For correspondence or reprints, contact Geke A.P. Hospers (g.a.p.hospers@umcg.nl).
Published online Sep. 9, 2021.

Whole-body PET imaging with a PD-L1–targeting tracer may have added value in detecting heterogenic expression of the drug target for anti–PD-1 therapy. Detection of low levels of PD-L1 expression may be predictive for nonresponding lesions that will require additional treatment. PET imaging of PD-L1 expression in non–small cell lung cancer, bladder cancer, and triple-negative breast cancer has shown that the intensity of the PET signal correlates with tumor response to ICI (*13,14*). The same approach could also be used to address the heterogeneity of metastatic tumor lesions in melanoma. This might especially be of importance for the characterization of brain lesions. PET imaging of PD-L1 expression may thus be a viable noninvasive diagnostic tool for lesion characterization and response prediction in metastatic melanoma patients.

This pilot study investigated the intensity and variability of PD-L1 expression using ^{18}F-BMS986192 PET in metastatic tumor lesions of melanoma patients, including patients with brain metastases. As secondary objectives, we explored whether ^{18}F-BMS986192 uptake was related to tumor response and whether enhanced tracer uptake in major organs was related to immune-related toxicity.

MATERIALS AND METHODS

Patient Population

Patients 18 y or older with stage IV metastatic melanoma who were eligible for treatment with ICI were recruited into the study. Patients with brain metastases were preferably included. Patients with suspected brain metastases could be treated with stereotactic radiotherapy before the start of the ICI therapy; however, these irradiated lesions were not included in the analyses. Other inclusion criteria were the presence of measurable disease according to RECIST, version 1.1; an Eastern Cooperative Oncology Group performance status of 0–1; and an adequate hematologic and end-organ function (*15*). The main exclusion criteria were preexisting autoimmune disease and treatment with immunosuppressive medication.

This study was approved by the Medical Ethical Committee (METc) of the University Medical Center Groningen (UMCG), delegated by the Central Committee on Research Involving Human Subjects, and was registered at ClinicalTrials.gov (ClinicalTrials.gov identifier NCT03520634) and METC 2016/646 (EUDRACT no. 2015-004920-67 with site-specific amendment 6). All patients provided written informed consent.

Study Design

This single-center imaging study with the ^{18}F-BMS986192 tracer was performed at the UMCG, The Netherlands. Patients received either nivolumab (anti–PD-1) or a combination of nivolumab and ipilimumab (anti–CTLA-4). The combination therapy consisted of 4 cycles of ipilimumab and nivolumab every 3 wk, followed by nivolumab monotherapy. Included patients were all treated with an ICI. The study intervention was a ^{18}F-BMS986192 PET scan at baseline and 6 wk after treatment initiation.

Production of ^{18}F-BMS-986192

The azide precursor BMT-180478 and the adnectin BMT-192920, both required for the on-site preparation of the PET tracer ^{18}F-BMS986192, were kindly provided by Brystol Myers Squibb (Supplemental Fig. 1; supplemental materials are available at http://jnm.snmjournals.org). The final PET tracer ^{18}F-BMS-986192 was produced in a Good Manufacturing Practices–compliant automated synthesis module according to the previously published protocol (*16*). The radiochemical purity of ^{18}F-BMS986192 was always more than 95%, and the molar activity always exceeded 3.000 GBq/mmol.

^{18}F-BMS-986192 PET Acquisition and Analysis

Patients received an intravenous bolus injection of approximately 185 MBq (range, 182–192 MBq) of ^{18}F-BMS986192. PET images were acquired 60 min after tracer injection on a Biograph mCT64 or mCT40 camera (Siemens Medical Systems). Whole-body PET scans (head to toe; 12 bed positions, 3 min per bed position) were acquired together with a low-dose CT scan. Vital signs (blood pressure and heart rate) were measured before, 10 min after the injection of ^{18}F-BMS986192, and immediately after the PET/CT scan. Patients remained under observation for 120 min after tracer injection.

All PET scans were reconstructed according to the European Association of Nuclear Medicine (EANM) Research Ltd. (EARL) criteria and analyzed using Syngo.via VB30 software (Siemens) (*17*). For quantification of ^{18}F-BMS986192 uptake, volumes of interest (VOIs) were manually drawn around the visible tumor lesions in the PET scan. For PET-negative lesions, the VOI was drawn around the tumor lesion on the CT or MRI scan that was manually aligned with the PET scan.

Tracer uptake in healthy tissues and lymphoid tissues (lung, thoracic aorta, spleen, liver, bone marrow, tonsils, parotid glands, thyroid, and axillary and inguinal lymph nodes) was measured to assess any toxicity-related increase in tracer uptake, using manually drawn VOIs. Tracer uptake was corrected for body weight and injected dose and expressed as SUVs (SUV_{max}, SUV_{mean}, and SUV_{peak} for tumor lesions and SUV_{mean} for normal tissues) consistent with EANM guidelines for ^{18}F tracers in tumors (*18*). Because the SUV may be influenced by patient-specific characteristics, such as tracer metabolism and clearance, tumor-to-blood ratios (TBRs) were calculated using the VOI of the lesion and the thoracic aorta $\left(\text{TBR} = \frac{\text{Tumor SUV}}{\text{Blood-pool SUVmean}}\right)$ (*19*).

Response Evaluation

Response to therapy was evaluated according to RECIST, version 1.1 (*15*). Contrast-enhanced chest–abdominal CT and gadolinium-enhanced MRI brain scans were obtained at baseline and week 12 as part of routine patient care.

Tumor lesions that were scanned on MR or CT at baseline but not at follow-up were excluded from response evaluation. To evaluate response per tumor lesion, the percentage change of the diameter at follow-up compared with baseline was calculated. Tumor lesions with a long-axis diameter smaller than 10 mm and lymph node lesions with a short-axis diameter smaller than 15 mm were excluded from response analysis.

Adverse events induced by the ICI treatment were assessed at each outpatient visit, using the National Cancer Institute Common Terminology Criteria for Adverse Events version 4.0 and reported in this study until the 12-wk tumor response evaluation.

Statistical Analysis

Patients were evaluated for tracer biodistribution analysis if they underwent at least 1 ^{18}F-BMS986192 PET scan. An assessment of the normality of data was performed using the Shapiro–Wilk test. Differences in tracer uptake between the baseline and on-treatment ^{18}F-BMS986192 PET scans were analyzed using a paired *t* test. Correlations between parameters were calculated using the Spearman correlation test. *P* values of less than 0.05 were considered statistically significant. PET data are expressed as median with interquartile range for nonnormally distributed data and are expressed as mean with SD for normally distributed data.

Receiver-operating-characteristic (ROC) analyses were calculated to determine the ^{18}F-BMS986192 uptake value that best differentiated between responding and nonresponding lesions. Statistical analyses were performed using GraphPad Prism 8.0.1 software for Microsoft Windows.

RESULTS

A total of 10 patients were included in this study, 8 of whom underwent baseline ^{18}F-BMS986192 PET/CT imaging before starting anti–PD-1 therapy (Table 1). In the remaining 2 patients, no

TABLE 1
Patient Characteristics

Characteristic	*n*
No. of patients included	10
No. of evaluable patients*	8
No. of lesions on PET	47
No. of evaluable lesions†	42
No. of lesions ≥ 10 mm at baseline (CT or MRI)	32
Median patient age at baseline (y)	62
No. of females (*n*)	3 (38)
No. of PET scans per patient (*n*)	
1	4 (50)
2	4 (50)
Immunotherapy regimen (*n*)	
Anti-CTLA4 + Anti-PD-1	5 (62)
Anti-PD1	3 (38)
No. of patients by treatment response (RECIST, version 1.1) (*n*)	
Complete response	0 (0)
Partial response	2 (25)
Stable disease	2 (25)
Progressive disease	4 (50)

*Including 6 patients with brain metastases.
†Lesions that were detected at baseline and follow-up by MR or CT imaging.
Data in parentheses are percentages.

PET scans could be obtained due to rapid clinical progression. In 4 patients, the on-treatment ^{18}F-BMS986192 PET/CT scan was obtained between 41 and 55 d (mean, 42) after starting anti–PD-1 therapy. No ^{18}F-BMS986192–related side effects occurred within the observation period of 120 min after tracer injection.

Biodistribution of ^{18}F-BMS986192

The biodistribution of ^{18}F-BMS986192 was evaluated in healthy tissues at baseline. High tracer uptake at baseline was observed in the spleen (SUV_{mean}, 15.9 ± 8.7), bone marrow (SUV_{mean}, 6.9 ± 1.5), and liver (SUV_{mean}, 4.7 ± 2.4). Patients with a follow-up scan ($n = 4$) did not show significant changes in uptake in healthy tissues compared with the baseline PET scan, except for tonsil uptake, which was significantly higher at baseline than at follow-up (Wilcoxon signed-rank test, $P = 0.002$) (Fig. 1).

Variability in ^{18}F-BMS986192 Uptake in Metastatic Lesions

Of the 42 evaluable tumor lesions, 21 were located in the lungs; 14 in the brain; 2 in soft tissue; and 1 each in bone, mediastinum, peritoneum, adrenal gland, and lymph node. Examples of PET images of a brain and lung lesion are depicted in Figure 2. The variability in uptake is shown in Figure 3 and Supplemental Figures 2 and 3. No significant differences were observed in ^{18}F-BMS986192 uptake between lung and brain lesions ($P = 0.06$). One bone lesion was excluded from analyses because its VOI could not be sufficiently separated from the high bone marrow uptake nearby, resulting in an uptake value 6 SDs higher than the other metastatic lesions.

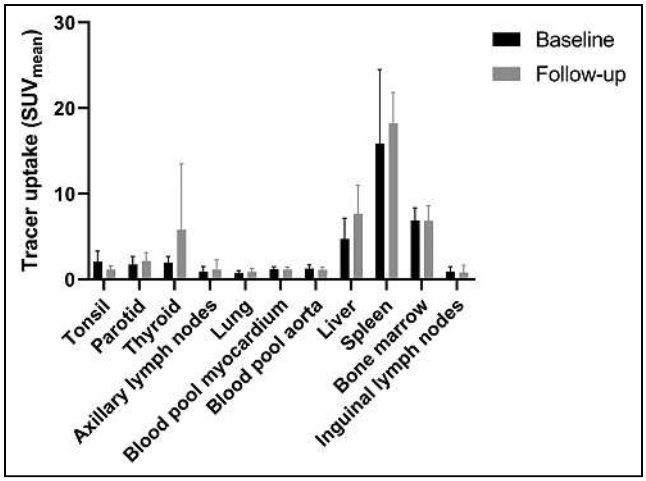

FIGURE 1. Biodistribution of ^{18}F-BMS986192 at baseline ($n = 8$) and follow-up ($n = 4$). In the patients with follow-up scans, ^{18}F-BMS986192 uptake in the tonsil was significantly higher at baseline than at follow-up (Wilcoxon signed rank test, $P = 0.002$). There were no other differences in ^{18}F-BMS986192 uptake between baseline and follow-up.

Association Between Baseline Tumor Uptake and Response to Therapy

After the exclusion of small tumor lesions (median diameter, 5 mm; range, 4–9 mm), 32 lesions (8 brain lesions) remained for response evaluation. The percentage change in lesion diameter was not associated with the baseline tracer uptake parameters SUV_{max} ($r = -0.15$, $P = 0.42$), SUV_{mean} ($r = -0.17$, $P = 0.34$), or SUV_{peak} ($r = -0.18$, $P = 0.31$).

When correcting for differences in tracer availability, using the tracer uptake in the blood pool as reference, we observed a significant correlation between baseline tumor-to-blood ratio and change in tumor lesion size (Fig. 4). This negative association was seen when calculating a TBR from the SUV_{max} ($r = -0.43$, $P = 0.014$), SUV_{mean} ($r = -0.44$, $P = 0.012$), or SUV_{peak} ($r = -0.49$, $P = 0.005$) of the tumor and SUV_{mean} of the blood pool. The same negative association was observed when only analyzing the intracerebral (brain) lesions, but this association was statistically not significant ($r = -0.54$, $P = 0.17$).

Discrimination of Responding and Nonresponding Tumors

ROC analysis was performed to assess the optimal tracer uptake value for predicting an ICI-induced reduction in tumor diameter. When a TBR derived from SUV_{peak} of the lesion and SUV_{mean} of the aortic blood pool was used, ROC analysis resulted in an area under the curve of 0.82 ($P = 0.006$). A TBR cutoff value of 1.3 resulted in a sensitivity of 89% (95% CI, 57%–99%) and a specificity of 78% (95% CI, 58%–90%) for discriminating a tumor decreasing in size from a tumor increasing in size (Fig. 5).

Follow-up ^{18}F-BMS986192 Scan and Response to Therapy

Four patients (50%) with a total of 19 metastases underwent a follow-up ^{18}F-BMS986192 scan at 6 wk. A paired *t* test revealed no differences in tumor ^{18}F-BMS986192 uptake between baseline and follow-up scans. Figure 6A shows the individual differences in tumor ^{18}F-BMS986192 uptake between baseline and follow-up for the brain and lung lesions in these 4 patients. ^{18}F-BMS986192 uptake was significantly lower in the brain lesions than the lung lesions, both at baseline and on-treatment ($P = 0.004$ and 0.05, respectively). No differences were observed in the mean lesion size of these brain and lung lesions.

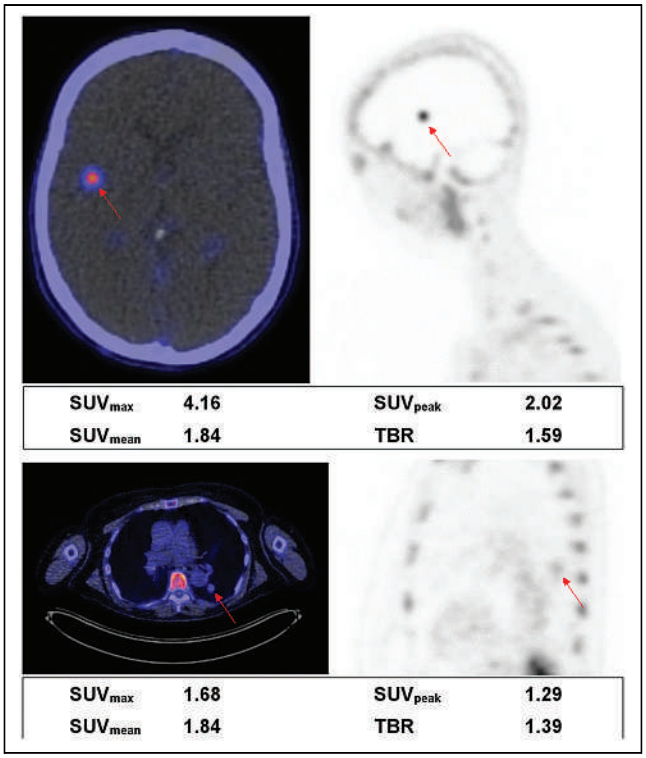

FIGURE 2. Examples of a brain lesion (top) and a lung lesion (bottom). Fused PET/CT transverse images (left) and PET sagittal images (right) are shown. Semiquantitative measurements are reported underneath images. TBR is calculated as lesion SUV_{peak} divided by SUV_{mean} in aortic blood pool.

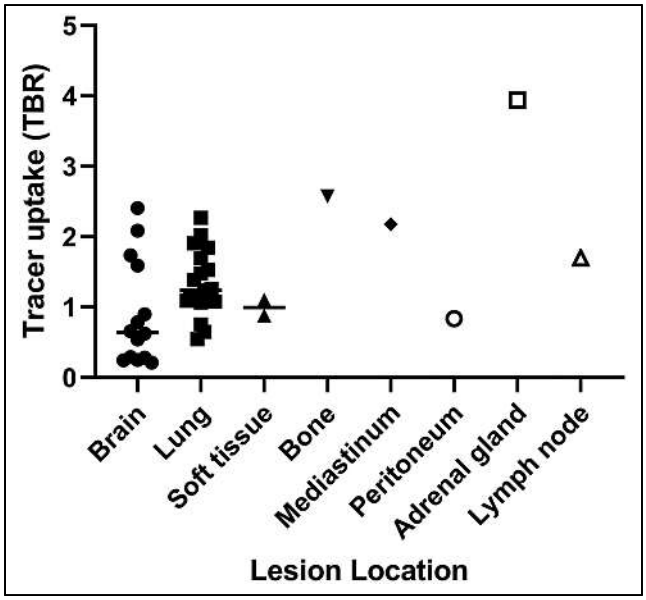

FIGURE 3. Baseline ^{18}F-BMS986192 tracer uptake measured as TBR derived from SUV_{peak} of lesion and SUV_{mean} of aortic blood pool. Median group value is reported as a line. No significant difference was found between mean values of brain and lung lesions (Mann–Whitney *U* test, $P = 0.06$). Analysis included 42 tumor lesions (21 lung; 14 brain; 2 soft-tissue; and 1 each in bone, mediastinum, peritoneum, adrenal gland, and lymph node lesions) in 8 patients.

Fourteen of the 19 metastases on follow-up scans were larger than 10 mm at baseline. A significant correlation between the change in ^{18}F-BMS986192 uptake (TBR) and the change in tumor size between the baseline and follow-up was observed ($r = 0.79$, $P = 0.0007$; Fig. 6B).

Assessment of Toxicity: Increased Uptake of ^{18}F-BMS986192

Follow-up ^{18}F-BMS986192 scans were also evaluated for ICI-related toxicity. One patient developed ICI-related hyperthyroidism, another patient colitis. The follow-up PET scan of the patient with ICI-related hyperthyroidism showed increased uptake in the thyroid (Fig. 7). This diagnosis was substantiated by blood thyroid-stimulating hormone levels of 0.007 mU/L (normal, 0.5–4 mU/L) and free T4 levels of 37.2 pmol/L (normal, 11–19.5 pmol/L). The patient who developed ICI-related colitis 1 d after the PET scan showed a different bowel uptake pattern at the second scan compared with the first scan, but solely based on the PET scan a definitive diagnosis of colitis could not be settled.

DISCUSSION

To our knowledge, this is the first study to investigate ^{18}F-BMS986192 PET imaging before and during ICI therapy in patients with metastatic melanoma, including patients with brain metastases. We found heterogeneous uptake of ^{18}F-BMS986192 in metastatic lesions at all locations, which is in line with a heterogeneous response to ICI therapy that is often observed in melanoma patients. Interestingly, we observed that high baseline ^{18}F-BMS986192 uptake in lesions, corrected for blood-pool uptake, correlated with response to ICI treatment. The same trend was found for brain lesions, which is an important finding because nonresponding brain lesions often require additional treatment. Additionally, increased ^{18}F-BMS-986192 uptake in tumor lesions at the follow-up ^{18}F-BMS986192 PET scan at week 6 was correlated with tumor progression at 12 wk.

Within a single patient with metastatic melanoma, different metastatic lesions may respond variably to ICI therapy. This variability in response to ICI is both in terms of the change in the lesion volume and the time it takes a lesion to show response (*20*). Because of this variability in response to ICI, additional local treatment is often necessary on nonresponding metastatic melanoma lesions

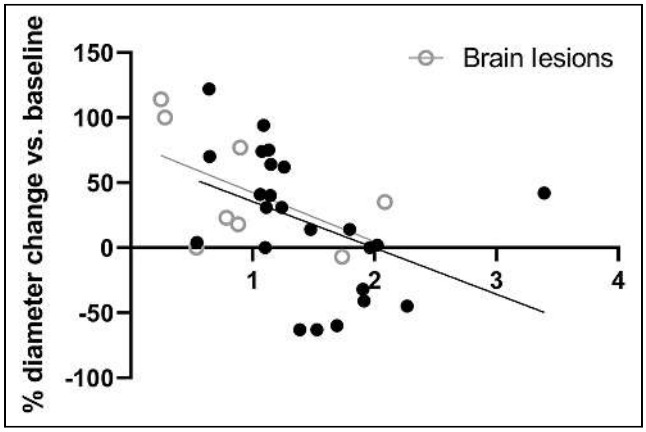

FIGURE 4. Association of TBR, derived from SUV_{peak} of lesion and SUV_{mean} of aortic blood pool, and relative (%) diameter change of lesions (Spearman rank, $r = -0.43$, $P = 0.014$). From all 8 patients, each circle represents 1 lesion. Only lesions larger than 10 mm at baseline were included in this analysis ($n = 32$). ○ = brain lesions ($n = 8$).

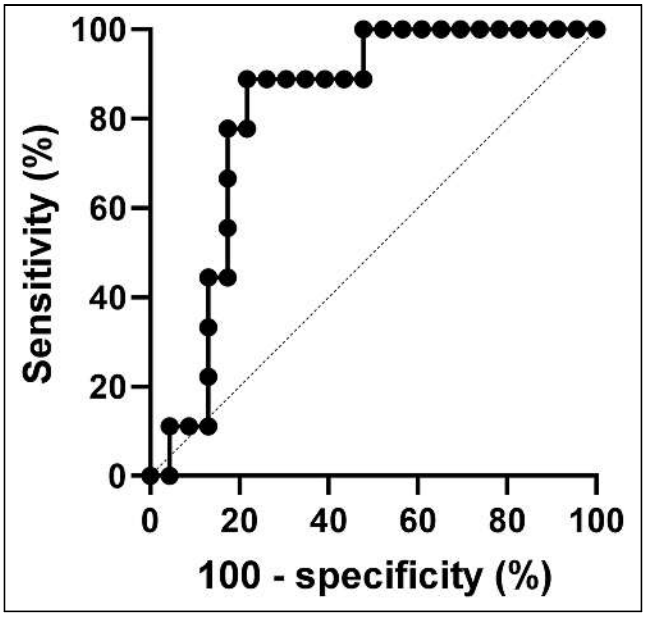

FIGURE 5. ROC curve of TBR of lesion, showing sensitivity and specificity for discriminating between tumors increasing or decreasing in diameter. Area under the curve is 0.82 ($P = 0.006$).

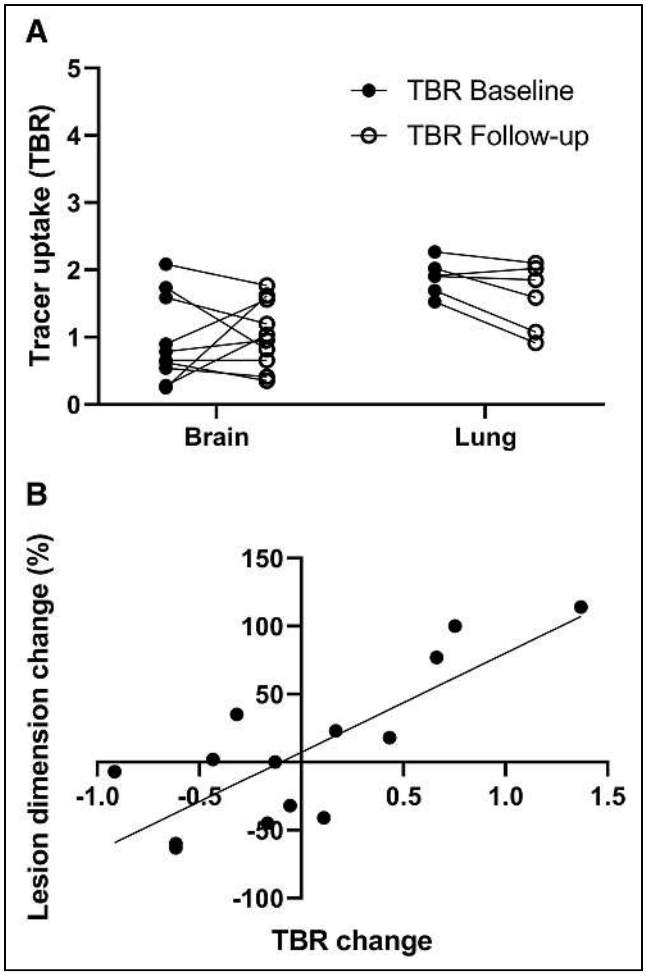

FIGURE 6. (A) ^{18}F-BMS986192 uptake for brain and lung lesions at baseline and follow-up (4 patients, 16 lesions). Tracer uptake is reported as TBR. Significant differences in tracer uptake were observed between brain and lung lesions, both at baseline and at follow-up (Wilcoxon signed rank test, $P = 0.004$ and 0.05, respectively). (B) Association between change in lesion size and change in TBR of follow-up ^{18}F-BMS986192 scan compared with baseline ($TBR_{follow\text{-}up} - TBR_{baseline}$) (4 patients, 14 lesions). Significant positive correlation was found between increasing TBR and increasing lesion diameter (Spearman rank, $r = 0.79$, $P = 0.0007$).

(*10*). High immunohistochemistry PD-L1 expression in a metastatic lesion is associated with a favorable response to ICI therapy. Importantly, metastatic melanoma patients with low PD-L1 expression in a lesion may also respond to ICI therapy (*12*). Therefore, immunohistochemistry PD-L1 expression on biopsies is not used in clinical practice to predict a patient's response to ICI therapy.

Discriminating between the different types of cells that may express PD-L1 in a metastatic melanoma lesion, such as malignant melanocytes, monocytes, and macrophages, may be important for ICI therapy response prediction (*21*). For example, pretreatment PD-L1 expression on macrophages was associated with favorable response to ICI therapy, whereas pretreatment PD-L1 expression on malignant melanocytes did not show any association with response (*22*). Although whole-body PD-L1 PET cannot differentiate between the PD-L1 expression of different cellular compositions, it may be useful to visualize PD-L1 expression in different lesions and predicting response per tumor lesion to ICI. Moreover, lesions with low PD-L1 expression on PET may indicate those lesions that need additional local treatment.

In our study, high ^{18}F-BMS986192 uptake was observed in lymphoid tissues, such as the spleen and bone marrow. This is suggestive for PD-L1 targeting of the tracer ^{18}F-BMS986192, as these organs contain high levels of PD-L1–expressing immune cells. Additionally, the follow-up ^{18}F-BMS986192 PET scan showed an increased PD-L1 uptake in 2 patients with ICI-induced toxicity (thyroiditis and colitis), which may be a sign of inflammation with an increase in PD-L1–expressing immune cells.

The correlation of PD-L1 uptake in tumor lesions at baseline with response to treatment found in our study is comparable with a study in non–small lung cancer. That study demonstrated that both ^{18}F-BMS-986192 (PD-L1) and ^{89}Zr-nivolumab (PD-1) PET imaging could predict response on a lesion level (*13*). In addition, in our study the second ^{18}F-BMS986192 scan during ICI treatment at week 6 performed in 4 patients found an increased ^{18}F-BMS986192 uptake correlating significantly with increased tumor size at follow-up at 12 wk. This positive correlation can be explained by the fact that responding lesions have fewer PD-L1–expressing tumor cells, resulting in a reduction in ^{18}F-BMS986192 uptake. On the other hand, a higher tracer uptake at week 6 in nonresponding tumors at week 12 might theoretically be due to either a higher cell density or an increased expression of PD-L1 per cell. PET cannot discriminate between these options. It is described that high PD L1–expressing tumor cells is related to a higher density of PD-1 tumor–associated T cells (*23*). Therefore, a delayed immune influx in PD-L1–upregulated tumor lesions at week 6 could be responsible for pseudoprogression at week 12. Unfortunately, our pilot study was unable to record any late response to immune checkpoint inhibition therapy as by that time these patients had already switched to another form of treatment. Moreover, technical aspects may have contributed to the correlation between the change in tumor size and the change in tracer uptake. A reduction in tumor size could also lead to a

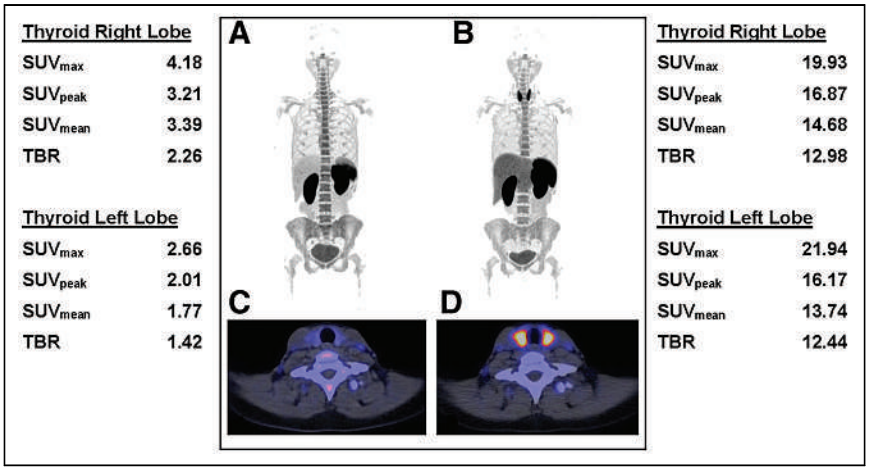

FIGURE 7. ^{18}F-BMS986192 -L1 PET/CT scans of 2 patients who developed ICI-related toxicity. (A–D) ^{18}F-BMS986192 scans of patient who developed ICI-related thyroiditis with increased uptake on treatment (B and D) compared with baseline (A and C). Semiquantitative measurements are shown for baseline scan (left) and the follow-up scan (right). TBR was calculated by dividing thyroid SUV_{peak} by SUV_{mean} in aortic blood pool.

stronger partial-volume effect (spill-out effect), which would also lead to the reduction in ^{18}F-BMS986192 uptake.

Protein-based PET tracers targeting PD-L1 do not accumulate in normal brain tissue (*13,14*), because proteins usually cannot cross the intact blood–brain barrier. The inability of large proteins to enter the brain could be part of the cause of the mixed response of brain metastases to treatment with ICI. Brain metastases can disrupt the blood–brain barrier, but this is not always the case. Niemeijer et al. demonstrated that uptake of the protein-based PD-L1 tracers ^{18}F-BMS-986192 and ^{89}Zr-DFO-nivolumab was observed in some, but not all, untreated brain metastases in 2 non–small lung cancer patients (*13*). In our study, the ^{18}F-BMS986192 uptake in brain metastases was also heterogeneous. Moreover, ^{18}F-BMS986192 uptake in brain metastases showed a relation with response, although this correlation was not statistically significant, but this may be due to the sample size.

In this study, a ^{18}F-labeled adnectin was used to target PD-L1 protein expression. In contrast to PET with the ^{89}Zr-linked antibody tracer ^{89}Zr-DFO-atezolizumab, ^{18}F-BMS986192 PET provides the opportunity to acquire the PET scan 1 h after tracer injection, and thus the examination can be completed within a single visit, which is highly convenient for the patient. Imaging on the same day as tracer injection is especially important for patients with brain metastases, where it is often essential to start treatment without delay. In addition, ^{18}F-BMS986192 PET exposes the patients to a much lower radiation dose, allowing the acquisition of multiple ^{18}F-BMS986192 PET examinations in the same patients within a short time frame. Moreover, it should be emphasized that the tumor accumulation of ^{18}F-BMS986192 and most ^{89}Zr-labeled antibody tracers is based on slightly different mechanisms. ^{18}F-BMS986192 uptake in the tumor is the result of reversible receptor binding and thus reflect receptor expression (*24*). The uptake of ^{89}Zr-labeled antibody tracers, on the other hand, is the result of receptor binding, followed by receptor internalization, and thus represents receptor turnover, more than receptor expression. The lower radiation burden, the fast tracer kinetics, and the uptake mechanism of ^{18}F-BMS986192 make this tracer better suited for pharmacokinetics and pharmacodynamics studies than the ^{89}Zr-labeled antibody tracers.

CONCLUSION

PET imaging with ^{18}F-BMS986192 PET shows heterogeneous PD-L1 expression in brain and lung metastases of melanoma patients. The ^{18}F-BMS986192 tumor uptake correlates with response on a per-lesion basis, with the same trend found in both intracerebral and extracerebral lesions. ICI-related toxicity can be detected at an early stage, before clinical symptoms appear. The preliminary results of this pilot study warrant further evaluation of ^{18}F-BMS986192 PET as a noninvasive imaging tool for assessment of PD-L1 expression in (brain) tumor lesions and prediction of ICI therapy response.

DISCLOSURE

Geke A.P. Hospers has a paid consulting/advisory board role with Amgen, Roche, MSD, BMS, Pfizer, Novartis, and Pierre Fabry (paid to the institution [University Medical Center Groningen]) and has received a research grant (BMS and Seerave, paid to the institution [University Medical Center Groningen]). Mathilde Jalving has a paid advisory role with AstraZeneca and MSD (paid to the institution [University Medical Center Groningen]).

KEY POINTS

QUESTION: Is variability of PD-L1 PET tracer uptake in metastatic melanoma lesions related to tumor response on ICIs, particularly in brain metastases?

PERTINENT FINDINGS: In this pilot study, ^{18}F-BMS986192 PET showed heterogeneous uptake in intra- and extracerebral metastatic lesions in melanoma patients. Baseline ^{18}F-BMS986192 uptake was able to predict an ICI-induced reduction in lesion volume.

IMPLICATIONS FOR PATIENT CARE: In melanoma patients, PD-L1 PET imaging may identify which metastatic lesions require local treatment in addition to ICIs.

REFERENCES

1. Ascierto PA, Long GV, Robert C, et al. survival outcomes in patients with previously untreated BRAF wild-type advanced melanoma treated with nivolumab therapy: three-year follow-up of a randomized phase 3 trial. *JAMA Oncol.* 2019;5: 187–194.
2. Robert C, Long GV, Brady B, et al. Nivolumab in previously untreated melanoma without BRAF mutation. *N Engl J Med.* 2015;372:320–330.
3. Topalian SL, Sznol M, McDermott DF, et al. Survival, durable tumor remission, and long-term safety in patients with advanced melanoma receiving nivolumab. *J Clin Oncol.* 2014;32:1020–1030.
4. Weber JS, D'Angelo SP, Minor D, et al. Nivolumab versus chemotherapy in patients with advanced melanoma who progressed after anti-CTLA-4 treatment (CheckMate 037): a randomised, controlled, open-label, phase 3 trial. *Lancet Oncol.* 2015;16:375–384.
5. Schachter J, Ribas A, Long GV, et al. Pembrolizumab versus ipilimumab for advanced melanoma: final overall survival results of a multicentre, randomised, open-label phase 3 study (KEYNOTE-006). *Lancet.* 2017;390: 1853–1862.

6. Ascierto PA, Del Vecchio M, Robert C, et al. Ipilimumab 10 mg/kg versus ipilimumab 3 mg/kg in patients with unresectable or metastatic melanoma: a randomised, double-blind, multicentre, phase 3 trial. *Lancet Oncol.* 2017;18:611–622.
7. Robert C, Thomas L, Bondarenko I, et al. Ipilimumab plus dacarbazine for previously untreated metastatic melanoma. *N Engl J Med.* 2011;364:2517–2526.
8. Hodi FS, Chiarion-Sileni V, Gonzalez R, et al. Nivolumab plus ipilimumab or nivolumab alone versus ipilimumab alone in advanced melanoma (CheckMate 067): 4-year outcomes of a multicentre, randomised, phase 3 trial. *Lancet Oncol.* 2018;19:1480–1492.
9. Wolchok JD, Hoos A, O'Day S, et al. Guidelines for the evaluation of immune therapy activity in solid tumors: Immune-related response criteria. *Clin Cancer Res.* 2009;15:7412–7420.
10. Blankenstein SA, Aarts MJB, van den Berkmortel FWPJ, et al. Surgery for unresectable stage IIIC and IV melanoma in the era of new systemic therapy. *Cancers (Basel).* 2020;12:1176.
11. Noh T, Walbert T. Brain metastasis: clinical manifestations, symptom management, and palliative care. *Handb Clin Neurol.* 2018;149:75–88.
12. Santos-Briz A, Cañueto J, del Carmen S, et al. Value of PD-L1, PD-1, and CTLA-4 expression in the clinical practice as predictors of response to nivolumab and ipilimumab in monotherapy in patients with advanced stage melanoma. *Am J Dermatopathol.* 2021;43:423–428.
13. Niemeijer AN, Leung D, Huisman MC, et al. Whole body PD-1 and PD-L1 positron emission tomography in patients with non-small-cell lung cancer. *Nat Commun.* 2018;9:4664.
14. Bensch F, van der Veen EL, Lub-de Hooge MN, et al. ^{89}Zr-atezolizumab imaging as a non-invasive approach to assess clinical response to PD-L1 blockade in cancer. *Nat Med.* 2018;24:1852–1858.
15. Eisenhauer EA, Therasse P, Bogaerts J, et al. New response evaluation criteria in solid tumours: Revised RECIST guideline (version 1.1). *Eur J Cancer.* 2009;45:228–247.
16. Donnelly DJ, Adam Smith R, Morin P, et al. Synthesis and biologic evaluation of a novel ^{18}F-labeled adnectin as a PET radioligand for imaging PD-L1 expression. *J Nucl Med.* 2018;59:529–535.
17. Kaalep A, Sera T, Oyen W, et al. EANM/EARL FDG-PET/CT accreditation - summary results from the first 200 accredited imaging systems. *Eur J Nucl Med Mol Imaging.* 2018;45:412–422.
18. Boellaard R, Delgado-Bolton R, Oyen WJGG, et al. FDG PET/CT: EANM procedure guidelines for tumour imaging: version 2.0. *Eur J Nucl Med Mol Imaging.* 2015;42:328–354.
19. Hofheinz F, Bütof R, Apostolova I, et al. An investigation of the relation between tumor-to-liver ratio (TLR) and tumor-to-blood standard uptake ratio (SUR) in oncological FDG PET. *EJNMMI Res.* 2016;6:19.
20. Persigehl T, Lennartz S, Schwartz LH. IRECIST: how to do it. *Cancer Imaging.* 2020;20:2.
21. Tang F, Zheng P. Tumor cells versus host immune cells: whose PD-L1 contributes to PD-1/PD-L1 blockade mediated cancer immunotherapy? *Cell Biosci.* 2018;8:34.
22. Toki MI, Merritt CR, Wong PF, et al. High-plex predictive marker discovery for melanoma immunotherapy-treated patients using digital spatial profiling. *Clin Cancer Res.* 2019;25:5503–5512.
23. Kandl TJ, Sagiv O, Curry JL, et al. High expression of PD-1 and PD-L1 in ocular adnexal sebaceous carcinoma. *Oncoimmunology.* 2018;7:e1475874.
24. Stutvoet TS, van der Veen EL, Kol A, et al. Molecular imaging of PD-L1 expression and dynamics with the adnectin-based PET tracer ^{18} F-BMS-986192. *J Nucl Med.* 2020;61:1839–1844.

^{18}F-FDG PET/CT for Posttreatment Surveillance Imaging of Patients with Stage III Merkel Cell Carcinoma

Sonia Mahajan[1], Christopher A. Barker[2], Audrey Mauguen[3], Sandra P. D'Angelo[4], Randy Yeh[1], and Neeta Pandit-Taskar[1]

[1]*Molecular Imaging & Therapy Service, Medicine, Memorial Sloan Kettering Cancer Center, New York;* [2]*Department of Radiation Oncology, Medicine, Memorial Sloan Kettering Cancer Center, New York;* [3]*Department of Epidemiology and Biostatistics, Memorial Sloan Kettering Cancer Center, New York; and* [4]*Department of Medicine, Memorial Sloan Kettering Cancer Center, New York*

The purpose of this study was to investigate the diagnostic and prognostic value of ^{18}F-FDG PET/CT for surveillance imaging in patients treated for stage III Merkel cell carcinoma (MCC). **Methods:** This retrospective study included 61 consecutive stage III MCC patients who were clinically asymptomatic and underwent surveillance ^{18}F-FDG PET/CT. Findings were correlated with either pathology or clinical/imaging follow-up. The median follow-up period was 4.8 y. Statistical analyses were performed. **Results:** ^{18}F-FDG PET/CT detected unsuspected recurrences in 33% patients (20/61) with lesion-based sensitivity, specificity, and accuracy of 92%, 93%, and 93%, respectively. The mean ± SD SUV for malignant and benign lesions was 7.5 ± 3.9 and 3.8 ± 2.0, respectively. Unknown distant metastases, as first recurrence site, were noted in 12 of 61 patients. Those with positive disease on ^{18}F-FDG PET/CT within 1 y of definitive treatment had relatively worse overall survival ($P < 0.0001$). After adjustment on stage, risk of death increased with a higher SUV_{max} (hazard ratio for 1 unit = 1.17; $P = 0.006$) and with a higher number of positive lesions on ^{18}F-FDG PET/CT (hazard ratio for 1 additional lesion = 1.60; $P < 0.001$). **Conclusion:** Postdefinitive treatment surveillance ^{18}F-FDG PET/CT scanning detects unsuspected recurrences and has prognostic value. Inclusion of ^{18}F-FDG PET/CT within the first 6 mo after definitive treatment would be appropriate for surveillance and early detection of recurrence. Our data merit further studies to evaluate the prognostic implications.

Key Words: ^{18}F-FDG PET/CT; Merkel cell carcinoma; recurrence; PET; surveillance; prognosis

J Nucl Med 2022; 63:906–911
DOI: 10.2967/jnumed.121.262882

Merkel cell carcinoma (MCC) is a rare aggressive cutaneous malignancy of neuroendocrine origin that has shown increasing incidence in the United States, with a reported increase of 95% during the years 2000–2013 (*1,2*). Patient survival depends on the stage of disease at diagnosis (*3–5*), with stage III MCC noted for higher metastatic potential and decreased survival than stages I and II (5-y cumulative incidence [CI] of death, 10%–15%) and substage IIIa having higher disease-specific survival than substage IIIb (5-y CI of death, 22% for IIIa and 53% for IIIb) (*4,6*).

After definitive therapy, recurrences occur in approximately 25%–50% of patients, with a median time to recurrence of about 8 mo, and 90% recurrences occur within 2 y *(3,6–9)*. Follow-up is therefore imperative in MCC, especially in higher stage disease. National Comprehensive Cancer Network (NCCN) guidelines recommend routine follow-up visits every 3–6 mo for 3 y and every 6–12 mo thereafter (*3*). Complete physical examination including skin and lymph node assessment is the mainstay. Currently, ^{18}F-FDG PET/CT is not integrated in the routine follow-up. Imaging with contrast-enhanced CT and MRI is used, as clinically warranted on a case-by-case basis (*3,10,11*).

The overall sensitivity and specificity of ^{18}F-FDG PET/CT for detecting primary or metastatic MCC ranges from 86% to 100% and 89% to 100%, respectively (*10,12–19*), and impact on management has been noted in up to 45% of patients (*13,18–22*). Prior studies have limited data on surveillance, include small number of patients and surveillance scans, lack pathologic correlation, and have variable disease stage and clinical status of patients. The aim of this study was to evaluate diagnostic and prognostic performance of surveillance ^{18}F-FDG PET/CT scans obtained at least 1 mo after definitive treatment in asymptomatic patients with stage III MCC.

MATERIALS AND METHODS

This was an institutional review board–approved single-institution retrospective study, performed in compliance with Health Insurance Portability and Accountability Act regulations, and the requirement to obtain informed consent was waived. A total of 61 patients treated for stage III MCC who underwent surveillance ^{18}F-FDG PET/CT imaging as part of standard of care were included. Staging was performed at the time of diagnosis, according to American Joint Committee of Cancer guidelines, eighth edition (*23*). Stage III disease included patients with suspected lymph node involvement either positive only on sentinel lymph node biopsy in patients with known primary (stage IIIA known primary), positive on clinical examination in patients with unknown primary (stage IIIA unknown primary), or positive on clinical examination and confirmed by pathology (stage IIIB) (*23*). Patients were not on active treatment at the time of the scan, were without any evidence or suspicion of disease as per the clinical assessment of referring physicians, and had a minimum interval of at least 1 mo since the completion of first definitive treatment. Electronic medical records were reviewed for clinicopathologic data, and mean follow-up duration was 4.8 y.

After 6 h of fasting and preinjection serum blood glucose of <200 mg/dL, patients were intravenously injected with 370–555 MBq of 18F-FDG. Whole-body scans were acquired 60–90 min after injection from vertex to toes, with patients supine. Low-dose (120–140 kV, 80 mA) CT scans with oral contrast were obtained and used for attenuation correction of PET images. All images were reviewed on a PACS workstation using the VCAR imaging suite (AW Suite 2, GE Healthcare). Maximum SUVs, normalized to body weight, were determined.

Received Jul. 12, 2021; revision accepted Sep. 25, 2021.
For correspondence or reprints, contact Neeta Pandit-Taskar (pandit-n@mskcc.org).
Published online Oct. 7, 2021.

A total of 221 ^{18}F-FDG PET/CT scans were reviewed. Location, size, and SUV of 107 suspicious lesions were noted. Histopathologic correlation was available for 30 lesions as standard of reference, and clinical/imaging follow-up (≥6 mo) was performed for the remaining 77 lesions. Findings were classified as true-positive for recurrence/metastasis if confirmed by either positive histopathology from biopsies/resections or presence of detectable lesion at corresponding site on follow-up imaging showing increase in SUV or size. Comparison of findings was performed in 28 pairs of PET/CT and CT/MRI (limited regions/areas) scans acquired within 1 mo.

Statistical Methods

Sensitivity, specificity, positive predictive value (PPV), negative predictive value (NPV), and accuracy with 95% CIs were calculated, using pathology and clinical/imaging follow-up as a reference standard. Time to recurrence was defined as time from the end of primary treatment to first recurrence detected on ^{18}F-FDG PET/CT, confirmed pathologically or clinically; alive patients without recurrences were censored at their last date of follow-up, and deaths before recurrence were considered as competing risk. Cumulative rates of recurrence were calculated using the Aalen–Johansen estimator. Overall survival was defined from first surveillance PET/CT scan to date of death; alive patients were censored at their last date of follow-up. A Kaplan–Meier curve was used to estimate survival rates. Landmark analyses were used to compare survival, based on scan positivity at 3, 6, and 12 mo (i.e., events occurring before the landmark time were excluded, and the time was calculating from the landmark time). Survival curves were compared with a log-rank test. Cox-proportional hazards model were used for univariable/multivariable analysis to assess prognostic value of PET parameters. Scan positivity, lesion SUV, number of lesions, and disease substage were correlated with survival. Factors with a P value < 0.20 in univariate analysis were entered in multivariate analysis, and a backward variable selection was done. Adjusted hazard ratios (HRs) are presented, along with 95% CI. Statistical analysis was performed using R, version 3.5.0 (R Core Team).

RESULTS

Patient Characteristics

Patient, scan, and tumor characteristics are described in Table 1. The median interval between end of treatment and first surveillance ^{18}F-FDG PET/CT scan was 3.7 mo (range, 1.1–23.3 mo). The time interval between consecutive scans predominantly ranged between 1.5 mo and 1.6 y, usually based on the clinician's discretion.

TABLE 1
Patient, Tumor, and ^{18}F-FDG PET/CT Scan Characteristics

Characteristic	Data
No. of patients	61
Sex (*n*)	
Male	44 (72%)
Female	17 (28%)
Mean age (±SD) at the time of diagnosis (y)	69 ± 13.0 (range, 25–93)
Site of primary disease (*n*)	
Cheek/chin	5 (8.1%)
Ear/eyelid/nose	4 (6.6%)
Forehead/scalp	5 (8.1%)
Neck node	2 (3.3%)
Axilla	4 (6.6%)
Back/chest	2 (3.3%)
Groin	11 (18.0%)
Buttocks	10 (16.3%)
Finger/hand	2 (3.3%)
Forearm/elbow/arm	8 (13.2%)
Knee/leg/thigh	8 (13.2%)
Stage of primary disease at diagnosis (*n*)	
Stage IIIA (known primary)	23 (37%)
Stage IIIA (unknown primary)	20 (33%)
Stage IIIB	18 (30%)
Prior treatment received (*n*)	
Surgery	20 (33%)
Surgery + chemotherapy/ radiation/chemoradiation	38 (62%)
Chemoradiation	3 (5%)
Number of ^{18}F-FDG PET/CT scans	221
Scans performed per patient (*n*)	
1–4	43
5–10	18

^{18}F-FDG PET/CT Scan-Based Analysis

Of 221 ^{18}F-FDG PET/CT scans, 39 showed ^{18}F-FDG–positive foci. Pathology confirmed recurrent MCC in 15 of 39 scans, and clinical/imaging follow-up confirmed recurrence in another 11 scans. Incidental second malignancy was detected in 1 scan. Overall, true-positive findings were seen in 27 scans (12%, 27/221). False-positive findings were seen in 12 scans (5%, 12/221) and confirmed on pathology in 2 and on clinical/imaging follow-up in 10 scans. A total of 182 ^{18}F-FDG PET/CT scans were negative for recurrent disease, of which 4 of the 221 (2%) were falsely negative, all confirmed on pathology. The remaining 178 scans (81%, 178/221) were true-negative based on clinical/imaging follow-up.

Lesion-Based Analysis

A total of 107 sites of abnormal ^{18}F-FDG avidity were noted (Fig. 1), for which pathology confirmed disease in 24 sites and clinical/imaging follow-up confirmed in 68 sites. False-positive ^{18}F-FDG uptake was seen in 15 sites, including nasal and axillary cutaneous sites (confirmed on pathology), pelvic fracture, rib fracture, 9 reactive neck and mediastinal nodes, and cutaneous sites in thigh and foot (confirmed on clinical/imaging follow-up). Two lesions were thought to be benign but were later confirmed as recurrent disease on pathology—lung infiltrates and neck node. Two in-transit metastases in the thigh and arm were also missed on ^{18}F-FDG PET/CT because they were below PET resolution and too small to characterize.

Overall SUV_{mean} ± SD for ^{18}F-FDG–avid malignant and benign lesions was 7.5 ± 3.9 (range, 1.7–18.9) and 3.8 ± 2.0 (range, 1.6–6.0), respectively; for local recurrence, 6.5 ± 4.1 (range, 1.7–18.9); and for distant metastases 8.0 ± 3.7 (range, 2.3–18.0). Mean SUV for ^{18}F-FDG–avid distant nodes was 7.1 (range, 2.3–12.7) and for osseous lesions 8.2 (range, 4.0–13.4). Mean size of ^{18}F-FDG–avid distant nodal metastases was 1.3 cm in short axis (range, 0.6–2.1 cm). SUV_{mean} ± SD for false-positive findings was 3.7 ± 1.2 (range, 1.6–6.0). On the basis of the ROC curve, the optimal cutoff SUV of 5.4 was associated with a low sensitivity of 54.9% but high specificity of 91.4% (Fig. 2).

Lesion-based sensitivity, specificity, PPV, NPV, and accuracy of PET/CT scan, calculated on the basis of correlation either

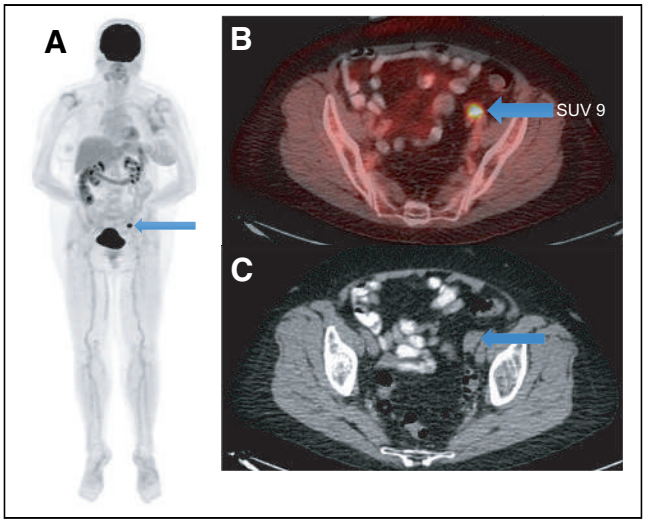

FIGURE 1. Asymptomatic 70-y-old woman with left arm MCC (s/p excision, left axillary lymphadenectomy, radiation to axilla) underwent surveillance ^{18}F-FDG PET/CT scan 3.3 mo after treatment. ^{18}F-FDG PET/CT (A; maximum-intensity projection, arrow) scan revealed solitary focal ^{18}F-FDG uptake in left pelvis (B; fused PET/CT, SUV 9, arrow) in a nodular soft-tissue-density lesion in left adnexa (C; axial CT, arrow). USG pelvis showed solid mass in left ovary measuring 1.8 x 1.4 x 1.6 cm, corresponding to site of abnormality on ^{18}F-FDG PET/CT. Patient underwent salpingo-oophorectomy and pathology was positive for MCC. s/p = status post; USG = ultrasound.

with pathology or with clinical/imaging follow-up, was 92%, 93%, 86%, 96%, and 93%, respectively, whereas scan-based sensitivity, specificity, PPV, NPV, and accuracy was 90%, 94%, 69%, 98%, and 93%, respectively.

Patient-Based Evaluation

Overall, 20 patients had relapse detected on ^{18}F-FDG PET/CT. The cumulative rate of detecting recurrences was 8.2% (95% CI, 1.3, 15.1%) within 3 mo, 16.4% (95% CI, 7.1, 25.7%) within 6 mo, and 26.2% (95% CI, 15.2, 37.3%) within 12 mo after definitive treatment. Local or locoregional relapse at or adjacent to the site of primary was seen in 8 patients, with a median interval of 4.5 mo (range,1.1–14.7 mo) from the end of treatment; disease sites included cutaneous/subcutaneous lesions in extremities (number of patients, n = 4); nodal disease in posterior auricular, inguinal, and axillary region (n = 3); and cutaneous lesion in leg with inguinal node (n = 1). Four of these 8 patients subsequently developed distant metastases. Distant metastasis, as first site of recurrence, was seen in 12 of the total 61 patients, with median interval of 7.2 mo from the end of treatment (range, 3.0–41.9 mo).

^{18}F-FDG PET/CT findings led to implementation of treatment in 20 patients (33%, 20/61). Surgery only was performed in 4 patients including excision of cutaneous/subcutaneous lesions in extremities (number of patients, n = 3) and bilateral salpingo-oophorectomy (n = 1). Radiation only was performed in 7 patients, with sites including retroperitoneal/pelvic nodes (n = 4), pancreas (n = 1), vertebrae (n = 1), mediastinal node, and subcutaneous thigh lesion (n = 1). Chemotherapy only was administered in 3 patients, whereas 2 patients received both chemotherapy and radiation therapy to osseous sites and 1 patient received chemotherapy and radiation therapy to subcutaneous/skin lesions in lower extremities in 2 different settings. Two patients received surgery followed by radiation therapy in axilla and groin, whereas 1 patient received immunotherapy.

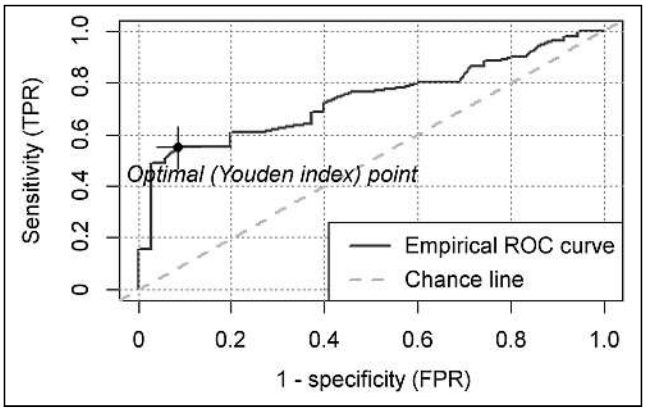

FIGURE 2. Receiver-operating-characteristic (ROC) curve for benign versus malignant lesion prediction based on SUV_{max}. FPR = false-positive rate; TPR = true-positive rate.

Comparison with CT/MRI

Comparison with 28 CT/MRI scans and PET/CT scans was available in 17 of 61 patients (28%). Of 28 CT/MRI scans, 7 showed suspicious findings. Of 7 scans, 6 were true-positives as confirmed by histology in 4 and clinical follow-up in 2. A false-positive finding was seen in 1 CT scan, confirmed on clinical follow-up that demonstrated a borderline enlarged inguinal node (non-^{18}F-FDG–avid) in a patient with primary disease in the groin. Two findings were falsely negative on CT, including biopsy-proven in-transit metastases in thigh (non-^{18}F-FDG–avid) and inguinal node (^{18}F-FDG–avid) positive for recurrence in imaging follow-up. Two findings including a lung nodule and bone lesion, suspicious on ^{18}F-FDG PET/CT and positive for recurrent disease on clinical/imaging follow-up, were outside the regional field of view of the CT/MRI scan.

Prognostic Analyses

Mean follow-up duration was 4.8 y (range, 8 mo–18 y) after first surveillance ^{18}F-FDG PET/CT. Among the 43 patients with negative scan results at 3 mo, 7 (16%) had a positive scan result later. Among the 41 patients with negative scan results at 6 mo, 5 (12%) had a positive scan result later. Among the 39 patients with negative scan results at 12 mo, 3 (8%) had a positive scan result later. Surveillance of patients is represented in the swimmer plot demonstrating the time points of ^{18}F-FDG PET/CT scan positivity and the follow-up duration (Fig. 3). Most of the recurrences developed within 1.5 y after the end of primary treatment. On the basis of the timing of the scan, statistical analysis revealed better overall survival (OS) in patients with a negative ^{18}F-FDG PET/CT scan result, as compared with patients with positive scan result, within 3 mo ($P < 0.0001$), 6 mo ($P < 0.0001$), and 12 mo after treatment ($P < 0.0001$) (Fig. 4).

Univariable statistical analysis showed that the risk of death increased with a positive surveillance ^{18}F-FDG PET/CT scan result, higher SUV, and higher number of ^{18}F-FDG–avid lesions (Table 2). Multivariable analysis showed that risk of death was increased with higher SUV (HR for 1 unit = 1.17; 95% CI, 1.05 to 1.31; P = 0.006) and number of ^{18}F-FDG–avid lesions (HR for 1 additional lesion = 1.60; 95% CI, 1.25 to 2.04; $P < 0.001$) and was decreased for patients with stage IIIA (unknown primary) compared with stage IIIA (known primary) (HR = 0.09; 95% CI, 0.01 to 0.99, Table 2). ^{18}F-FDG PET/CT scan positivity was not evaluated in the multivariable model as we used a summary of the number of positive lesions.

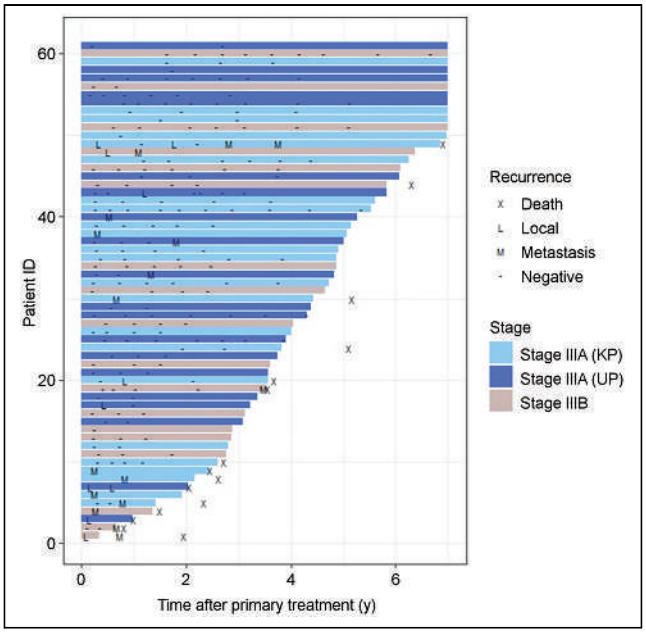

FIGURE 3. Swimmer plot illustrating information about local and distant recurrences, confirmed on pathology, during follow-up on surveillance ^{18}F-FDG PET/CT scans since end of primary treatment for all included stage IIIA known primary (KP), IIIA unknown primary (UP), and IIIB MCC patients (n = 61).

DISCUSSION

In this study, ^{18}F-FDG PET/CT showed high sensitivity and specificity of 92% and 93%, respectively, to detect recurrent MCC lesions in local as well as distant sites. Overall, 12% (27/221) of surveillance ^{18}F-FDG PET/CT scans were true-positive for recurrence, and 81% were true-negative. ^{18}F-FDG PET/CT results contributed to implementation of treatments in 33% (20/61) patients. We also assessed the prognostic significance of ^{18}F-FDG PET/CT, specifically in patients treated for stage III disease, which, to our knowledge, has never been reported before.

On the basis of our results, early inclusion of ^{18}F-FDG PET/CT within the first 6 mo after definitive treatment is suitable to initiate imaging surveillance in stage III MCC patients. Although none of our patients had clinically evident disease after receiving definitive treatment, unexpected true-positive ^{18}F-FDG PET/CT findings were detected in local or locoregional nodes in 13% (8/61) patients at a median interval of 4.5 mo after treatment; all patients had normal-appearing skin and negative clinical nodal exam. Additionally, unexpected findings were seen in distant organs including ovaries, pancreas, bone, and distant lymph nodes in 20% (12/61) of patients at a median interval of 7.2 mo after treatment. Only a few prior studies have partly evaluated follow-up ^{18}F-FDG PET/CT in MCC, with relapse noted in 7%–15% scans and overall impact on management seen in 20%–32% patients (*10,12–13,16,18,20–21*). However, these studies were limited due to small patient cohort, small number of surveillance PET/CT scans included, variable disease stage, unclear clinical status of the patient at the time of scanning, and varying indications for including ^{18}F-FDG PET/CT scans, for example, monitoring treatment response, clinically suspected recurrence, or ongoing surveillance (*16,18,20,22*).

We also observed that most recurrences developed within 1.5 y after definitive treatment, and ^{18}F-FDG PET/CT enabled identification of unsuspected disease relapse, leading to appropriate treatment

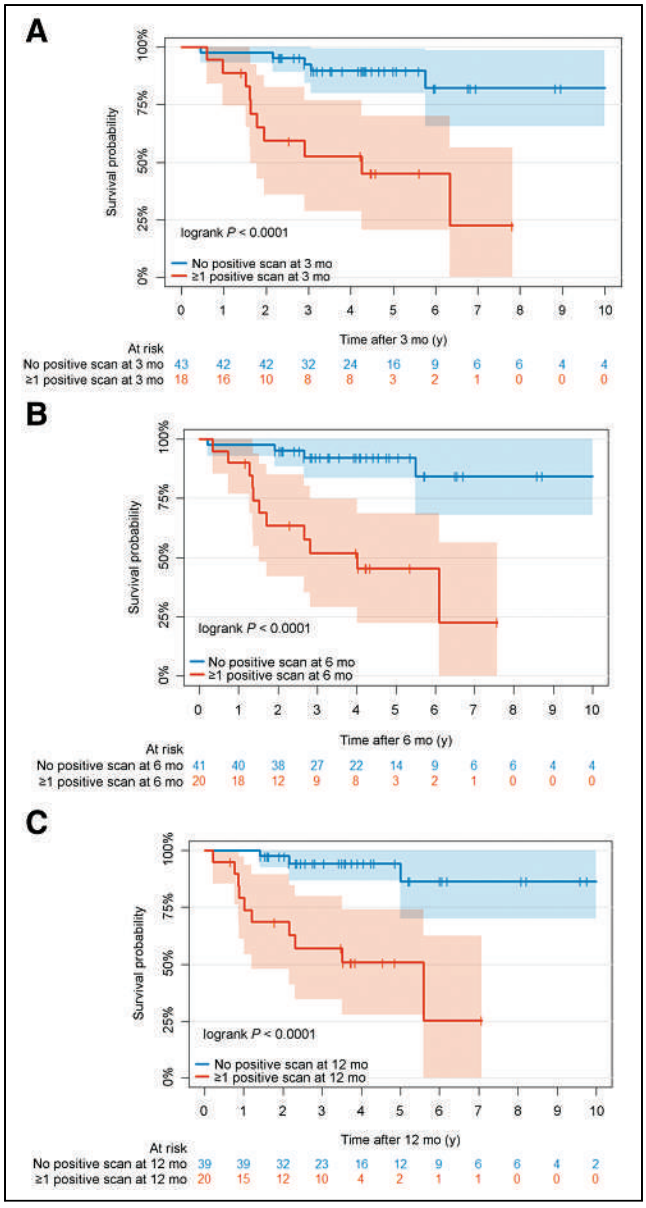

FIGURE 4. OS of patients based on findings and timing of ^{18}F-FDG PET/CT scan (A, at 3-mo; B, at 6 mo, and C, at 12 mo after definitive treatment, respectively).

planning. This invites further studies, preferably of a prospective nature, to evaluate the appropriate time intervals of performing surveillance imaging in the initial posttreatment years. On the basis of our data, surveillance ^{18}F-FDG PET/CT scans obtained within the first 6 mo of end of definitive treatment and follow-up scans spaced at intervals of 6–9 mo for at least 2 y may be beneficial, considering that most recurrences are detected within the first 2 y of diagnosis (*3,6–9*). Currently, there is no consensus on follow-up surveillance imaging of asymptomatic patients after treatment completion. Another study has shown slightly different results with longer mean time to recurrence of 15.3 mo, which may have been due to variable disease stage of included patients (*18*). A few studies that demonstrated median time to recurrence of 6–9 mo have not clearly explained the imaging modality used to detect recurrence (*3,24–27*).

The OS of patients with recurrence detected on ^{18}F-FDG PET/CT was significantly reduced compared with patients with negative

TABLE 2
Univariate and Multivariate Prognostic Models for OS

Variable	Univariate			Multivariate		
	HR	95% CI	*P*	HR	95% CI	*P*
^{18}F-FDG PET/CT scan, positive	15.7	4.34, 56.5	<0.001	—	—	—
SUV_{max} (for 1 unit)	1.27	1.17, 1.39	<0.001	1.17	1.05, 1.31	0.006
No. of positive lesions (for 1 lesion)	1.45	1.27, 1.64	<0.001	1.60	1.25, 2.04	<0.001
Stage			0.16			0.05
IIIA (KP)	Ref.			Ref.		
IIIA (UP)	0.27	0.06, 1.27		0.09	0.01, 0.99	
IIIB	0.86	0.28, 2.64		0.38	0.08, 1.94	

KP = known primary; Ref. = reference; UP = unknown primary.

^{18}F-FDG PET/CT scan results. It is of interest that the chances of developing recurrence decreased with increasing elapsed time from the end of treatment. In our cohort, 16%, 12%, and 8% of patients who had negative ^{18}F-FDG PET/CT scan results at 3, 6, and 12 mo after treatment, respectively, developed recurrences. In addition, the OS of patients was negatively impacted by a higher number of ^{18}F-FDG–avid lesions and higher SUV, suggesting higher disease burden; this higher disease burden has often been reported in other malignancies as well (*28*). To our knowledge, none of the prior studies in the literature has demonstrated the prognostic role of surveillance ^{18}F-FDG PET/CT scans in MCC patients. In the study by TROG (Trans Tasman Radiation Oncology Group), postradiation-treatment ^{18}F-FDG PET/CT scans were acquired at 9 wk after the end of radiation therapy in patients with ongoing systemic treatment. The study showed positive findings in 5 of 41 patients (12%) and no impact on patient survival at 3 y (*16*). The nonsignificant results were attributed to small number of patients with positive PET findings and early intervention with salvage treatment (*16*).

In our study, ^{18}F-FDG PET/CT showed false-positive findings in 8 patients, mainly in cutaneous sites and reactive lymph nodes with relatively low-grade uptake. These false-positive findings can be explained by overexpression of glucose transporters in infectious/inflammatory etiology (*29*). Histopathologic correlation is therefore needed to confirm disease in sites that appear equivocal on ^{18}F-FDG PET/CT. Compared with CT/MRI, ^{18}F-FDG PET/CT scanning detected disease in sites that were outside the conventional imaging field of view and in nodes that were not suspicious by size criteria on CT/MRI. The in-transit metastases were falsely negative on both conventional and metabolic imaging, perhaps related to the small size.

Our study is limited by retrospective design; variable timing of initiation, and continuation, of surveillance imaging; as well as the lack of pathologic correlation for all lesions. We did not study the cost–benefit analysis of performing ^{18}F-FDG PET/CT scans for surveillance as it was beyond the scope of the current study; however, the risk–benefit ratio will need evaluation in future studies to understand the economic impact.

CONCLUSION

Surveillance whole-body ^{18}F-FDG PET/CT is a sensitive imaging modality in posttreatment follow-up of asymptomatic stage III MCC patients. Our data indicate that initiating surveillance ^{18}F-FDG PET/CT within 6 mo after completion of definitive treatment in stage III MCC may be useful in early detection of recurrence. Further scans spaced at intervals of 6–9 mo for at least 2 y may be beneficial. Larger prospective studies may help further validate these findings.

DISCLOSURE

This research was funded in part through the NIH/NCI Cancer Center Support Grant P30 CA008748. No other potential conflict of interest relevant to this article was reported.

KEY POINTS

QUESTION: What is the diagnostic and prognostic value of ^{18}F-FDG PET/CT in surveillance imaging of stage III MCC patients?

PERTINENT FINDINGS: In this retrospective study, 61 posttreatment stage III MCC patients were included who were clinically asymptomatic, and ^{18}F-FDG PET/CT detected unsuspected recurrent disease in 33% patients, with a high sensitivity and specificity of 92% and 93%, respectively. Risk of death was increased with higher number of ^{18}F-FDG–avid lesions ($P < 0.001$) and higher lesion SUV ($P = 0.006$) on ^{18}F-FDG PET/CT. Patients with recurrent disease on ^{18}F-FDG PET/CT, within 1 year of definitive treatment, had relatively worse OS ($P < 0.0001$).

IMPLICATIONS FOR PATIENT CARE: Early implementation of surveillance ^{18}F-FDG PET/CT in patients with stage III MCC allows detection of unsuspected recurrences, leading to appropriate treatment planning, and has a potential prognostic role.

REFERENCES

1. Becker JC. Merkel cell carcinoma. *Ann Oncol.* 2010;21:vii81–vii85.
2. Paulson KG, Park SY, Vandeven NA, et al. Merkel cell carcinoma: current US incidence and projected increases based on changing demographics. *J Am Acad Dermatol.* 2018;78:457–463.e2.
3. Guidelines NCCN. Merkel cell carcinoma. Version 1.2020. Available from NCCNorg website. https://www.nccn.org/professionals/physician_gls/pdf/mcc.pdf. Accessed March 7, 2022.
4. Fields RC, Busam KJ, Chou JF, et al. Five hundred patients with Merkel cell carcinoma evaluated at a single institution. *Ann Surg.* 2011;254:465–473.

5. Becker JC, Stang A, DeCaprio JA, et al. Merkel cell carcinoma. *Nat Rev Dis Primers.* 2017;3:17077.
6. Fields RC, Busam KJ, Chou JF, et al. Recurrence after complete resection and selective use of adjuvant therapy for stage I through III Merkel cell carcinoma. *Cancer.* 2012;118:3311–3320.
7. Miller SJ, Alam M, Andersen J, et al. Merkel cell carcinoma. *J Natl Compr Canc Netw.* 2009;7:322–332.
8. Lewis CW, Qazi J, Hippe DS, et al. Patterns of distant metastases in 215 Merkel cell carcinoma patients: Implications for prognosis and surveillance. *Cancer Med.* 2020;9:1374–1382.
9. Kouzmina M, Koljonen V, Leikola J, et al. Frequency and locations of systemic metastases in Merkel cell carcinoma by imaging. *Acta Radiol Open.* 2017;6: 2058460117700449.
10. Peloschek P, Novotny C, Mueller-Mang C, et al. Diagnostic imaging in Merkel cell carcinoma: lessons to learn from 16 cases with correlation of sonography, CT, MRI and PET. *Eur J Radiol.* 2010;73:317–323.
11. Anderson SE, Beer KT, Banic A, et al. MRI of Merkel cell carcinoma: histologic correlation and review of the literature. *AJR.* 2005;185:1441–1448.
12. Belhocine T, Pierard GE, Fruhking J, et al. Clinical added-value of ^{18}FDG PET in neuroendocrine-Merkel cell carcinoma. *Oncol Rep.* 2006;16:347–352.
13. Maury G, Dereure O, Du-Thanh A, Goulart DM, Guillot B. Interest of ^{18}F-FDG PET-CT scanning for staging and management of Merkel cell carcinoma: a retrospective study of 15 patients. *J Eur Acad Dermatol Venereol.* 2011;25:1420–1427.
14. Treglia G, Kakhki VR, Giovanella L, Sadeghi R. Diagnostic performance of fluorine-18-fluorodeoxyglucose positron emission tomography in patients with Merkel cell carcinoma: a systematic review and meta-analysis. *Am J Clin Dermatol.* 2013; 14:437–447.
15. George A, Girault S, Testard A, et al. The impact of ^{18}F-FDG-PET/CT on Merkel cell carcinoma management: a retrospective study of 66 scans from a single institution. *Nucl Med Commun.* 2014;35:282–290.
16. Poulsen M, Macfarlane D, Veness M, et al. Prospective analysis of the utility of 18-F FDG PET in Merkel cell carcinoma of the skin: A Trans Tasman Radiation OncologyGroup Study, TROG 09:03. *J Med Imaging Radiat Oncol.* 2018;62:412–419.
17. Siva S, Byrne K, Seel M, et al. ^{18}F-FDG PET provides high-impact and powerful prognostic stratification in the staging of Merkel cell carcinoma: a 15-year institutional experience. *J Nucl Med.* 2013;54:1223–1229.
18. Hawryluk EB, O'Regan KN, Sheehy N, et al. Positron emission tomography/computed tomography imaging in Merkel cell carcinoma: a study of 270 scans in 97 patients at the Dana-Farber/Brigham and Women's Cancer Center. *J Am Acad Dermatol.* 2013;68:592–599.
19. Concannon R, Larcos GS, Veness M. The impact of ^{18}F-FDG PET-CT scanning for staging and management of Merkel cell carcinoma: results from Westmead Hospital, Sydney, Australia. *J Am Acad Dermatol.* 2010;62:76–84.
20. Byrne K, Siva S, Chait L, et al. 15-year experience of ^{18}F-FDG PET imaging in response assessment and restaging after definitive treatment of Merkel cell carcinoma. *J Nucl Med.* 2015;56:1328–1333.
21. Ben-Haim S, Garkaby J, Primashvili N, et al. Metabolic assessment of Merkel cell carcinoma: the role of ^{18}F-FDG PET/CT. *Nucl Med Commun.* 2016;37: 865–873.
22. López Prior V, Llombart Cussac B. The role of ^{18}F-FDG PET/CT in the management of Merkel cell carcinoma: The experience of 51 studies in our institution. *Rev Esp Med Nucl Imagen Mol.* 2021;40:139–148.
23. Merkel cell carcinoma. In: Edge SB, Byrd DR, Compton CC, Fritz AG, Greene FL, Trotti A, eds. *AJCC Cancer Staging Manual.* 7th ed. Springer; 2010;315–324.
24. Santamaria-Barria JA, Boland GM, Yeap BY, Nardi V, Dias-Santagata D, Cusack JC. Merkel cell carcinoma: 30-year experience from a single institution. *Ann Surg Oncol.* 2013;20:1365–1373.
25. Kaae J, Hansen AV, Biggar RJ, et al. Merkel cell carcinoma: incidence, mortality and risk of other cancers. *J Natl Cancer Inst.* 2010;102:793–801.
26. Grotz TE, Tarantola T, Otley CC, Weaver AL, McGree ME, Jakub JW. Natural history of Merkel cell carcinoma following locoregional recurrence. *Ann Surg Oncol.* 2012;19:2556–2562.
27. Allen PJ, Bowne WB, Jaques DP, Brennan MF, Busam K, Coit DG. Merkel cell carcinoma: prognosis and treatment of patients from a single institution. *J Clin Oncol.* 2005;23:2300–2309.
28. Bastiaannet E, Hoekstra OS, de Jong JR, Brouwers AH, Suurmeijer AJ, Hoekstra HJ. Prognostic value of the standardized uptake value for ^{18}F-fluorodeoxyglucose in patients with stage IIIB melanoma. *Eur J Nucl Med Mol Imaging.* 2012;39: 1592–1598.
29. Mochizuki T, Tsukamoto E, Kuge Y, et al. FDG uptake and glucose transporter subtype expressions in experimental tumor and inflammation models. *J Nucl Med.* 2001;42:1551–1555.

Combined PARP1-Targeted Nuclear Contrast and Reflectance Contrast Enhance Confocal Microscopic Detection of Basal Cell Carcinoma

Aditi Sahu[1], Jose Cordero[1,2], Xiancheng Wu[1,3], Susanne Kossatz[4–6], Ucalene Harris[1], Paula Demetrio Desouza Franca[4], Nicholas R. Kurtansky[1], Niasia Everett[1], Stephen Dusza[1], Jilliana Monnier[1,7], Piyush Kumar[8], Christi Fox[9], Christian Brand[10], Sheryl Roberts[4], Kivanc Kose[1], William Phillips[1], Erica Lee[1], Chih-Shan Jason Chen[1], Anthony Rossi[1], Kishwer Nehal[1], Melissa Pulitzer[1], Caterina Longo[11,12], Allan Halpern[1], Thomas Reiner[4,13,14], Milind Rajadhyaksha*[1], and Manu Jain*[1]

[1]Dermatology Service, MSKCC, New York, New York; [2]Medical Sciences Campus, University of Puerto Rico, San Juan, Puerto Rico; [3]SUNY Upstate Medical University, Syracuse, New York; [4]Department of Radiology, MSKCC, New York, New York; [5]Department of Nuclear Medicine, University Hospital Klinikum Rechts der Isar and Central Institute for Translational Cancer Research, Technical University Munich, Munich, Germany; [6]Department of Chemistry, Technical University Munich, Munich, Germany; [7]Dermatology Department and Skin Cancer Department, La Timone Hospital, AP-HM, Aix-Marseille University, Marseille, France; [8]Department of Environmental Medicine and Public Health, Icahn School of Medicine at Mt. Sinai, New York, New York; [9]Caliber Imaging and Diagnostics, Rochester, New York; [10]Summit Biomedical Imaging, New York, New York; [11]Department of Dermatology, University of Modena and Reggio Emilia, Modena, Italy; [12]Azienda Unità Sanitaria Locale–IRCCS di Reggio Emilia, Centro Oncologico ad Alta Tecnologia Diagnostica-Dermatologia, Reggio Emilia, Italy; [13]Department of Radiology, Weill Cornell Medical College, New York, New York; and [14]Chemical Biology Program, MSKCC, New York, New York

Reflectance confocal microscopy (RCM) with endogenous backscattered contrast can noninvasively image basal cell carcinomas (BCCs) in skin. However, BCCs present with high nuclear density, and the relatively weak backscattering from nuclei imposes a fundamental limit on contrast, detectability, and diagnostic accuracy. We investigated PARPi-FL, an exogenous nuclear poly(adenosine diphosphate ribose) polymerase (PARP1)–targeted fluorescent contrast agent, and fluorescence confocal microscopy toward improving BCC diagnosis. **Methods:** We tested PARP1 expression in 95 BCC tissues using immunohistochemistry, followed by PARPi-FL staining in 32 fresh surgical BCC specimens. The diagnostic accuracy of PARPi-FL contrast was evaluated in 83 surgical specimens. The optimal parameters for permeability of PARPi-FL through intact skin was tested ex vivo on 5 human skin specimens and in vivo in 3 adult Yorkshire pigs. **Results:** We found significantly higher PARP1 expression and PARPi-FL binding in BCCs than in normal skin structures. Blinded reading of RCM–and–fluorescence confocal microscopy images by 2 experts demonstrated a higher diagnostic accuracy for BCCs with combined fluorescence and reflectance contrast than for RCM alone. Optimal parameters (time and concentration) for PARPi-FL transepidermal permeation through intact skin were successfully determined. **Conclusion:** Combined fluorescence and reflectance contrast may improve noninvasive BCC diagnosis with confocal microscopy.

Key Words: basal cell carcinoma; cancer diagnosis; reflectance confocal microscopy; nuclear contrast; fluorescence confocal microscopy; in vivo

J Nucl Med 2022; 63:912–918
DOI: 10.2967/jnumed.121.262600

Received May 18, 2021; revision accepted Aug. 26, 2021.
For correspondence or reprints, contact Manu Jain (jainm@mskcc.org).
*Contributed equally to this work.
Published online Oct. 14, 2021.

Basal cell carcinomas (BCCs) occur with high incidence rates of more than 4 million in the United States, Europe, and Australia every year (*1*). Diagnosis is based on dermoscopy followed by biopsy and histopathology. BCCs can manifest as superficial, nodular, infiltrative, and micronodular subtypes (*2*). Although dermoscopy provides high sensitivity (80%–100%), the specificity remains low and variable (32%–90%), particularly for lesions lacking distinct pigmentation or vascular patterns (so-called pink lesions) (*3–5*). This lower specificity leads to approximately 3–5 benign lesions being biopsied for every detected malignancy, which translates to roughly 12–15 million biopsies annually (*6*). The specificity for BCC diagnosis has recently been improved with reflectance confocal microscopy (RCM).

RCM is a noninvasive high-resolution, label-free, quasihistopathologic imaging technique that shows cellular-level morphology and architecture in skin to a depth of 200 μm (*7–9*). RCM is based on the detection of singly backscattered light from subsurface optical sections (*10–13*). RCM detects BCCs with sensitivity of 76%–94% and specificity of 54%–95% (*14–16*). When combined with dermoscopy, RCM provides approximately 50% higher specificity, with a resulting approximately 2-times drop in the benign-to-malignant biopsy ratio compared with dermoscopy alone (*17–19*). Although the use of RCM has improved diagnostic accuracy at the bedside, the backscattered contrast imposes a fundamental limit for BCC diagnosis. Because of weak backscatter from intranuclear chromatin, nucleus-dense BCCs appear dark relative to the surrounding dermis. But nucleus-dense normal structures (hair follicles, lower basal cell layer of epidermis) also appear dark, thus mimicking BCCs (*16,20*). This limitation may be overcome with an exogenous molecule-targeted fluorescence nuclear contrast agent and fluorescence confocal microscopy (FCM) imaging.

PARPi-FL is a newly developed small-molecular (620 Da), poly-(adenosine diphosphate ribose) polymerase (PARP1)–targeted

fluorescent reporter (*21*). PARPi-FL is BODIPY-FL (Molecular Probes) conjugated to the PARP inhibitor olaparib, possessing the strong PARP1 specificity of olaparib (*21,22*) and the strong fluorescence properties of BODIPY-FL, and has shown specific nuclear labeling and tumor imaging (*23,24*). The Food and Drug Administration accorded investigational-new-drug status to PARPi-FL, and a phase I/II trial is in progress (NCT03085147) for imaging oral cancers in patients (*25,26*). Higher intranuclear accumulation in tumors, rapid tissue permeation (4.6 μm/s (*27*)), safety, and detectability deeper in tissue makes PARPi-FL attractive for BCC diagnosis.

However, for in vivo use in patients, 2 central questions must be addressed: can the exogenous PARPi-FL nuclear contrast improve diagnostic accuracy for BCCs, and can PARPi-FL be quickly and effectively delivered transepidermally to BCCs in the dermis through intact skin? We report the results of our investigation on PARP1 expression, PARPi-FL staining, and permeability in this article (Fig. 1).

MATERIALS AND METHODS

Sample Collection

PARP1 expression was investigated on formalin-fixed, paraffin-embedded specimens. For experiments on PARPi-FL staining, surgically excised fresh discarded BCCs and normal specimens were collected after Mohs surgeries. For the permeability experiments, large (5 × 5 cm) specimens of normal breast skin were collected at the end of mastectomies. All samples were collected under various institutional review board–approved protocols.

PARP1 Expression in BCCs

Two adjacent thin (5 μm) formalin-fixed, paraffin-embedded sections were obtained for PARP1 immunohistochemistry and hematoxylin and eosin (H&E) staining. PARP1 immunohistochemistry was performed according to a previously described procedure (*24*). We used an anti-PARP1 rabbit monoclonal antibody (46D11; Cell Signaling Technology) at 0.4 μg/mL, followed by a biotinylated goat anti-rabbit IgG (PK6106; Vector Labs) at a 1:200 dilution.

Quantification of PARP1 Expression

Immunohistochemistry-stained and H&E-stained sections were digitally scanned (Aperio ScanScope Slide Scanner; Leica Biosystems). BCCs and surrounding normal structures—hair follicles, sebaceous glands, and epidermis—were annotated by a pathologist using different color codes. PARP1 was quantified using the Aperio Positive Pixel Count Algorithm (Leica Biosystems) (*28*). Thresholding was performed on the diaminobenzidine PARP1-positive area, and total area was determined by hematoxylin-stained area. PARP1 positivity (integrated positive pixel area/total annotated area) was computed in each field of view. Thresholds, hue, and saturation were kept constant for all specimens.

PARPi-FL Staining and Nuclear PARP1 Specificity in Thin Tissue Sections

Fresh discarded BCC tissues were serial-sectioned into four 10-μm frozen sections for PARPi-FL staining, H&E staining, PARP1 immunofluorescence testing, and isotype IgG control (Supplemental Fig. 1A; supplemental materials are available at http://jnm.snmjournals.org). For PARPi-FL staining, tissue sections were stained with 100 nM PARPi-FL (in 30% polyethylene glycol) for 5 min using Hoechst 33342 (Invitrogen), 0.002 mg/mL, as a nuclear counterstain. Immunofluorescence was tested using a previously described procedure (*23*). We used anti-PARP1 antibody (rabbit polyclonal IgG, SC-7150, 1:200 dilution; Santacruz Biotechnology) and isotype control (normal rabbit IgG, 1:200 dilution; Santacruz Biotechnology), and we used AlexaFluor 568 (goat-antirabbit, A21076, 1:1,000 dilution; Invitrogen Molecular Probes) as the secondary antibody. The slides were scanned using a Mirax Slide Scanner (3DHISTECH). For selected tissues, 10–15 PARPi-FL images were also acquired with a commercial microscope (LSM880; Carl Zeiss Microscopy LLC) in tumor and normal areas. Analysis for fluorescence intensity and area positivity on the microscopic images was performed using a batch code implemented in FIJI. Thresholding was performed for PARPi-FL signal, and total nuclear area was calculated using Hoechst 33342 to calculate normalized intensity and area positivity. Analysis was done on an image level and a case level (average of multiple images).

PARPi-FL Staining in Thick Fresh BCC specimens

Specimens were stained with PARPi-FL (250 nM PARPi-FL in 30% polyethylene glycol

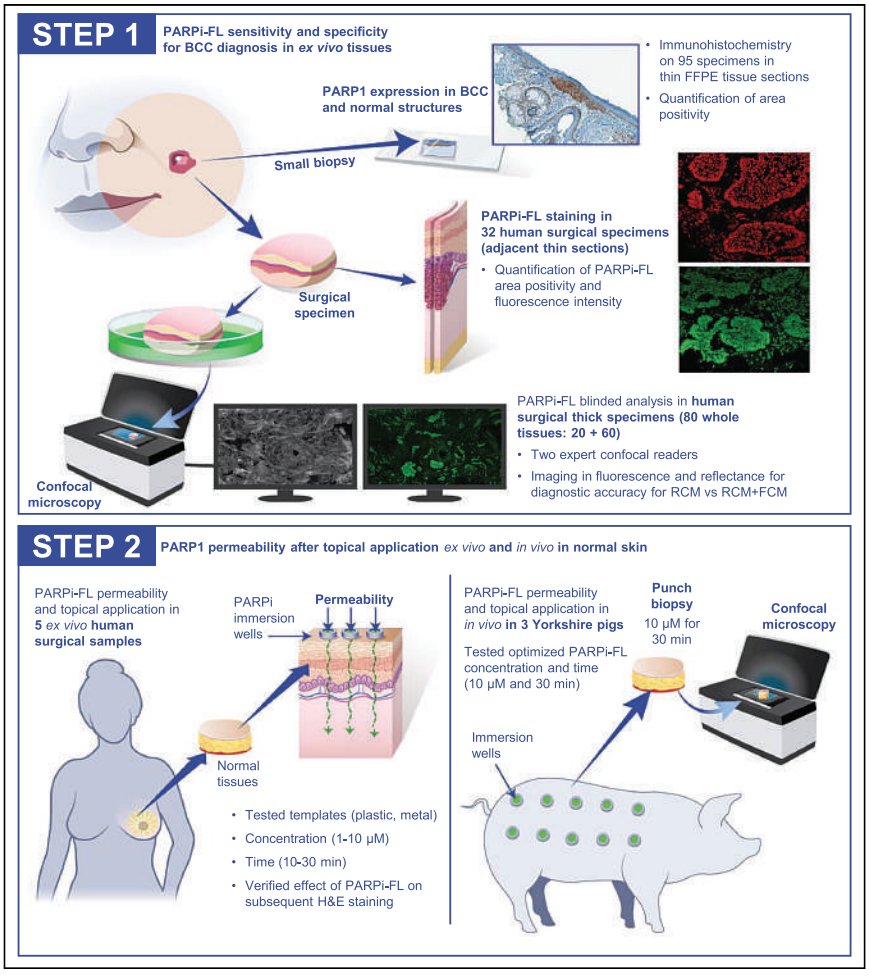

FIGURE 1. Summary of experiments undertaken in study. FFPE = formalin-fixed, paraffin-embedded. FCM = fluorescence confocal microscopy; RCM = reflectance confocal microscopy.

300/phosphate-buffered saline for 10 min, followed by 10 min in 30% polyethylene glycol 300/phosphate-buffered saline) and imaged using a benchtop research ex vivo RCM-and-FCM prototype microscope (Vivascope-2500; Caliber Imaging and Diagnostics) simultaneously in both fluorescence (488 nm) and reflectance (785 nm) modes (Supplemental Fig. 1B). RCM and FCM mosaicking to display up to a 12 × 12 mm field of view encompassing the entire tissue was performed and used for the blinded study.

Blinded Reader Evaluation

The blinded reading study was performed by 2 expert confocal readers. Training was on a subset of RCM and FCM mosaics with an equal number of BCC-positive and BCC-negative cases (i.e., equal prevalence for BCCs and normal skin). Depending on the specimen size, each mosaic was divided into either 2 or 4 submosaics to facilitate reading. The diagnosis was evaluated both at a mosaic (case) level and at an individual submosaic (quadrant) level. Both readers were provided with matched RCM and FCM mosaics for each specimen. The RCM mosaic was evaluated, followed by the matched FCM mosaic to compare BCC diagnostic accuracy on RCM and with added PARPi-FL contrast in RCM and FCM. Readers evaluated BCC presence or absence, nuclear staining (on FCM), and overall diagnostic quality. Blinded analysis results were compared with the corresponding H&E results to compute sensitivity, specificity, positive predictive value, and negative predictive value at a case level and a quadrant level.

Effect of PARPi-FL on Subsequent Histopathology

Normal and BCC tissues were bisected such that one piece was immersed in PARPi-FL (1 μM) and the other in polyethylene glycol–phosphate-buffered saline (control) for 30 min, respectively. Both pieces were separately submitted in formalin for H&E histopathology evaluation. Sections were digitally scanned and read in a blinded manner by 2 pathologists to grade the staining quality of cytoplasm, nucleus, and collagen; diagnostic acceptability or unacceptability; and BCC presence or absence and subtype.

Permeability and Transepidermal Delivery in Ex Vivo Tissue

The mastectomy specimens were processed to remove adipose tissue and blood without disrupting stratum corneum integrity. Tissues were placed on a flat corkboard and gently wiped with an alcohol pad (Webcol alcohol preps; Covidien) and allowed to dry. PARPi-FL was applied topically on the stratum corneum using plastic and metal templates, which served as PARPi-FL reservoirs (Supplemental Fig. 1C). Additionally, in some specimens, a PARPi-FL–saturated gauze (1 μM) followed by a Tegaderm patch (3M Medical) was pinned onto the skin to maintain uniform pressure, to mimic topical application and occlusion in vivo. Ranges of PARPi-FL concentrations (1–10 μM) and application times (10–30 min) were tested. After experiment completion, a 5-mm punch biopsy (MediChoice biopsy punches; Owens and Minor) was performed. Each biopsy sample was bisected and dipped in Hoechst 33342 (Invitrogen) (diluted to 0.002 mg/mL in chilled phosphate-buffered saline) for nuclear counterstaining. The tissues were mounted on their lateral surface for imaging with a confocal microscope (Zeiss LSM880 system [×20/0.8 numerical aperture [NA]]) using 405-nm (Hoechst 33342) and 488-nm (PARPi-FL) wavelengths. The raw files were qualitatively visualized in FIJI.

Permeability and Transepidermal Delivery In Vivo

Topical application and permeability were tested in vivo in adult female Yorkshire pigs obtained under a protocol approved by the institutional animal care and use committee. The pigs were anesthetized using inhalational 5% isoflurane. An area of the flank approximately 46 cm (18 in) in length was selected, shaved, and gently swabbed with ethanol. Any local irritation (confirmed visually) from shaving was allowed to subside before PARPi-FL application. Within this area, 2 sets of rows comprising 5 sites each were marked for the well placement to deliver either PARPi-FL or saline and to perform biopsies (Supplemental Fig. 1D). The application sites were spaced 2 cm apart (edge-to-edge) to prevent cross contamination. Each well (or template) (Everbilt; Home Depot Product Authority, LLC) measured 0.95-cm ($^3/_8$-in) in diameter and was attached to the selected site using an adhesive (Dermabond Advanced; Ethicon US, LLC) in which 1 mL of 10 μM PARPi-FL or saline solution was left for 30 min. Subsequently, ten 8-mm punch biopsies were performed on each pig. The biopsy samples were bisected; one piece was submitted for H&E staining, and the other was promptly imaged using the benchtop ex vivo RCM-and-FCM microscope (Vivascope-2500; Caliber ID). The biopsy samples were processed for histopathology.

Statistical Analysis

Analyses were conducted using Prism (version 8.0; GraphPad), Stata (version 14.2; Stata Corp.), and R (version 2020; R Core Team) with the "rel" package (*29*) to calculate agreement statistics and the "ggplot2" package (*30*) to produce figures. Inferential unpaired-sample comparisons were assessed by the Mann–Whitney *U* test. PARPi-FL intensity and area positivity were converted by a natural log transform because the raw data were right-skewed. Associations of transformed variables with clinical outcomes were analyzed with receiver-operating-characteristic curves. A blinded experiment was conducted to assess diagnostic accuracy using RCM images and RCM-and-FCM images by 2 expert readers. Interrater agreement on the presence of cellular-level features, diagnosis subtyping, and binarized tissue quality assessments was quantified according to Gwet AC1 because of the high marginal imbalance in the sample, in addition to overall percentage agreement. For the effect of PARPi-FL on histopathology, agreement between pathologists was quantified according to Gwet AC1. Statistical significance was determined with an α value of 0.05. Unless stated otherwise, data are presented as mean ± SD, and significance is specified.

RESULTS

PARP1 Expression in BCC and Normal Skin Structures

In 95 specimens, we found PARP1 expression in BCCs (the superficial, nodular, infiltrative, and micronodular subtypes) and in normal structures (Fig. 2A; Supplemental Fig. 2). Higher area positivity was observed in tumors (47.89% ± 21.4), followed by hair follicles, epidermis, and sebaceous glands ($P < 0.001$) (Fig. 2B). The value of 0.927 for area under the curve (AUC) indicates successful discrimination of tumor from normal areas on the basis of PARP1 area positivity (Fig. 2C).

PARPi-FL Staining and PARP1 Immunofluorescence in Thin BCC Sections

In 32 thin BCC sections, PARPi-FL uptake in nuclei correlated with PARP1 expression, confirmed by PARP1 immunofluorescence (Figs. 3A and 3B; Supplemental Figs. 3A and 3B). The fluorescence intensity and area positivity in 394 images (from 32 tissues) demonstrated significantly higher intensity and area positivity in tumors than in normal tissue ($P < 0.01$) with both imagewise and casewise analyses (Fig. 3C; Supplemental Fig. 3C). Similar trends were observed in nontransformed data (Supplemental Figs. 3D and 3E). Area positivity differentiated tumor from normal tissue with higher accuracy (AUC, 0.96) than did fluorescence intensity (AUC, 0.68) (Fig. 3D).

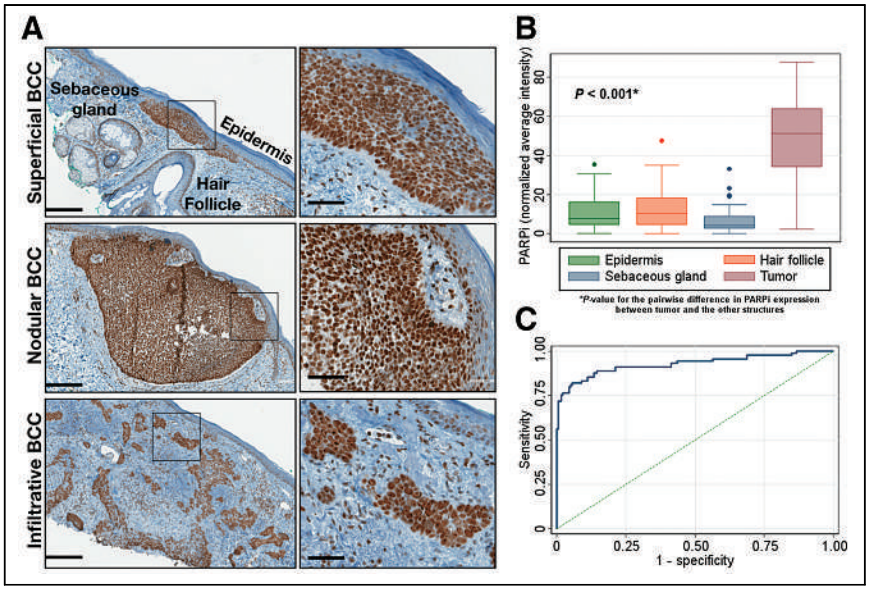

FIGURE 2. Expression of PARP1 is higher in BCCs than in normal skin structures. (A) Representative images of PARP1 expression show high expression in superficial, nodular, and infiltrative BCC, as compared with epidermis, hair follicles, and sebaceous glands. (B) PARP1 area positivity in immunohistochemistry samples ($n = 95$) shows significantly higher positivity in tumors. (C) Receiver-operating-characteristic curve to differentiate tumor from normal skin structures yields AUC of 0.83.

PARPi-FL Staining for Improving BCC Diagnosis in an Ex Vivo Blinded Study

In 83 fresh surgical specimens, PARPi-FL enhanced the visualization of small BCC tumors that otherwise were invisible in the corresponding RCM mosaic, as confirmed on H&E-stained sections (Fig. 4A; Supplemental Fig. 4). Of the 166 RCM and FCM mosaics, 44 were used for training. The blinded evaluation was performed on the remaining 122 mosaics; however, only cases with acceptable diagnostic quality were analyzed. We found higher sensitivity and moderately better specificity in the RCM-and-FCM images than in the RCM-alone images (Figs. 4B and 4C).

Transepidermal Delivery of PARPi-FL Through Intact Skin in Fresh Ex Vivo Human Specimens

In 5 ex vivo normal mastectomy specimens, we tested topical application of PARPi-FL at various concentrations and application times (Fig. 5). We detected PARPi-FL staining in the nuclei of the basal cells of the epidermis and dermal cells, confirming successful permeability. Optimal staining with high nuclear specificity and intensity was observed for the 10 μM PARPi-FL concentration when applied for 30 min. These parameters were selected for in vivo testing in pigs.

Transepidermal Delivery of PARPi-FL in an In Vivo Pig Model

In 3 adult Yorkshire pigs, we verified PARPi-FL permeability in vivo in normal skin after topical application of 10 μM PARPi-FL for 30 min (Fig. 6; Supplemental Fig. 5). Positive nuclear staining in the epidermal basal cell layer was consistently observed in PARPi-FL–treated sites and was absent from the control sites, confirming the permeability and detectability of PARPi-FL after in vivo application. No significant histopathologic differences were noticeable between the PARPi-FL–treated and control groups (Fig. 6; Supplemental Fig. 6).

DISCUSSION

Our results suggest that the addition of exogenous PARPi-FL fluorescence contrast to endogenous reflectance contrast improves noninvasive diagnosis of BCCs. PARP1 proved to be an excellent biomarker; we found consistently higher PARP1 expression in all BCC subtypes than in normal skin structures. Across the 95 specimens investigated, 90% of BCCs had homogeneous PARP1 staining, especially in the superficial and infiltrative subtypes. Some heterogeneous PARP1 expression was observed in a few nodular BCCs (<10%), specifically in the variants with nodular–cystic changes and squamous differentiation (Supplemental Fig. 2E).

We confirmed specific nuclear labeling correlating with PARP1 expression in nucleated tissue areas of tumors, basal epidermal layers in epidermis, hair follicles, and sebaceous glands (Figs. 3A and 3B; Supplemental Figs. 3A and 3B). We used area positivity and intensity parameters to quantitatively confirm PARPi-FL nuclear fluorescence in tumors, as compared with normal nucleated structures—an issue that often confounds BCC diagnosis in vivo. Although both parameters were higher in tumors,

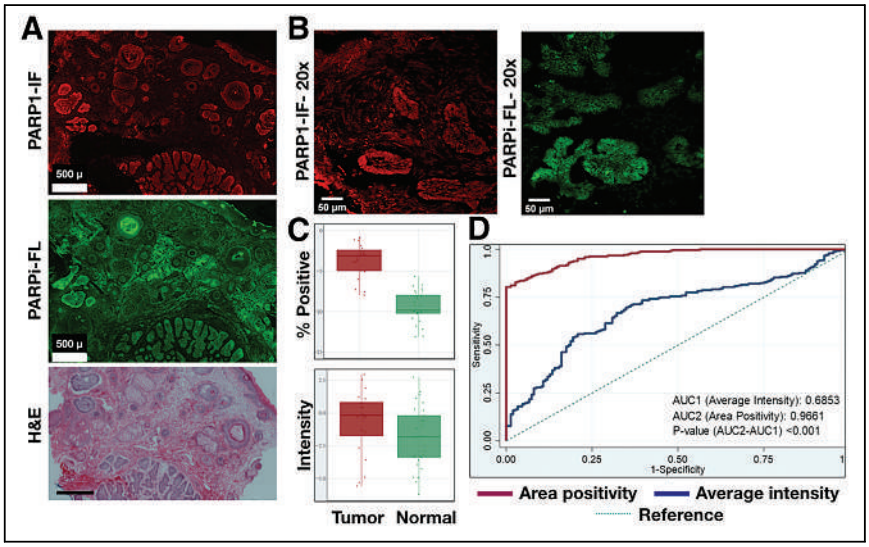

FIGURE 3. Nucleus-specific PARPi-FL staining observed in BCC tissues. (A) Representative images showing successful PARPi-FL nuclear staining in tumor and normal tissue. (B) PARPi-FL nuclear uptake and spatial correlation with nuclear PARP1 in nucleated areas verified in high-resolution images (×20). (C) Higher average intensity and area positivity in tumors than in normal structures in casewise analysis (right) ($P < 0.001$ for percentage area positivity and imagewise intensity). (D) Area positivity better discriminates tumor and normal tissue than does fluorescence intensity (AUC, 0.96 vs. 0.68)

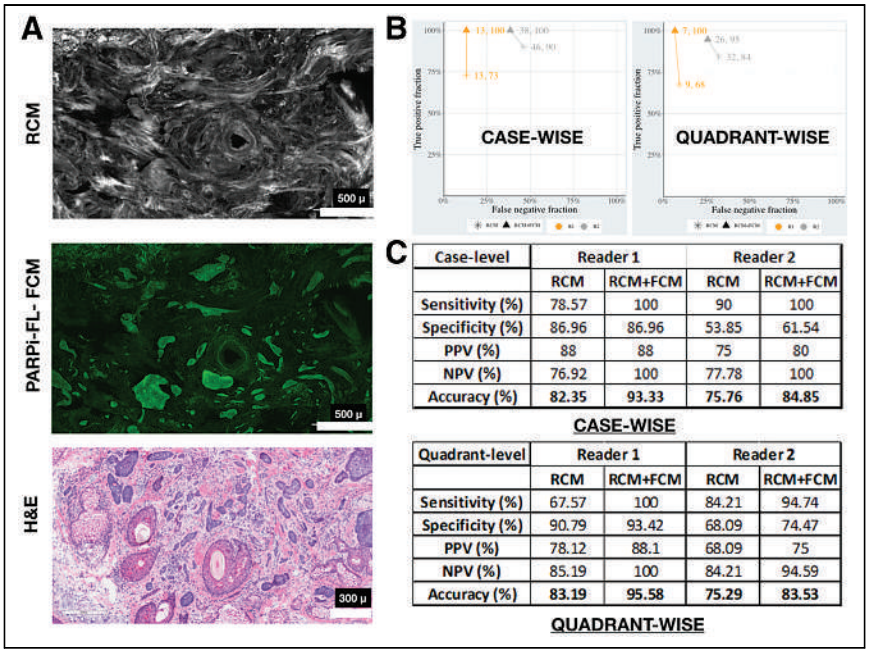

C

Case-level	Reader 1		Reader 2	
	RCM	RCM+FCM	RCM	RCM+FCM
Sensitivity (%)	78.57	100	90	100
Specificity (%)	86.96	86.96	53.85	61.54
PPV (%)	88	88	75	80
NPV (%)	76.92	100	77.78	100
Accuracy (%)	82.35	93.33	75.76	84.85

CASE-WISE

Quadrant-level	Reader 1		Reader 2	
	RCM	RCM+FCM	RCM	RCM+FCM
Sensitivity (%)	67.57	100	84.21	94.74
Specificity (%)	90.79	93.42	68.09	74.47
PPV (%)	78.12	88.1	68.09	75
NPV (%)	85.19	100	84.21	94.59
Accuracy (%)	83.19	95.58	75.29	83.53

QUADRANT-WISE

FIGURE 4. PARPi-FL contrast in FCM images improves BCC diagnostic accuracy over RCM alone. (A) PARPi-FL contrast improves visualization of BCCs, as compared with RCM alone, as confirmed on H&E images. (B and C) Higher sensitivity in RCM-and-FCM images and moderate increase in specificity found in blinded evaluation in both casewise and quadrantwise analysis. NPV = negative predictive value; PPV = positive predictive value.

only area positivity could successfully differentiate tumor from normal structures with a high accuracy (Fig. 3D). We acknowledge that none of these parameters would have utility in clinical practice (as Hoechst 33342 or other nuclear dyes cannot be applied on patients); however, PARPi-FL staining would enhance the cellular and morphologic details that help aid an expert RCM reader to differentiate BCCs from normal structures and improve the diagnosis. This improvement was also demonstrated through the blinded analysis performed by 2 expert RCM readers—an analysis in which PARPi-FL contrast, when combined with RCM, boosted the diagnostic accuracy, as compared with RCM alone. In general, nuclear staining was observed in most tissues; only 5 of 62 (8%) tissues had minimal or no nuclear staining in tumor or normal structures. This finding was in contrast to PARP1 expression, with only 1.1% of specimens showing low or negative expression. A higher rate of inconsistent nuclear staining could be attributed to the delays in fresh tissue handling, since PARP1 can rapidly degrade in excised tissues. Despite some heterogeneity in PARPi-FL nuclear labeling, we demonstrated that a combined imaging approach (RCM and FCM) improved diagnostic performance, especially sensitivity, when compared with RCM alone. Surprisingly, we found minimal improvements in specificity in the blinded study. False-positives were more prevalent in cases with smudged PARPi-FL staining, possibly attributable to the variability in tissue quality. Furthermore, ex vivo tissues do not image as well as skin in vivo (*31–33*), probably because of tissue dehydration and alterations in refractive index and optical properties. Differences in the training of the 2 readers may have impacted improvements in sensitivity and specificity. We do not anticipate these tissue-related issues during in vivo imaging in patients (our ultimate goal). Thus, we expect better results, in terms of both higher sensitivity and higher specificity, with use of RCM-and-FCM imaging, when performed in patients through a clinical trial.

The next critical issue that makes a contrast agent suitable for topical application is permeability through intact skin. We successfully demonstrated that PARPi-FL can passively diffuse through the stratum corneum after topical application in ex vivo human tissues and in vivo pig skin. Skin is characterized by a tightly and coordinately regulated molecular transport system, which allows molecules with low molecular weight (<500 Da) and lipophilicity (logP, 1–3) to permeate the stratum corneum. Thus, the borderline molecular weight and lipophilicity of PARPi-FL (620 Da; logP, 2.9) makes it suitable for topical application and transepidermal delivery. We found that PARPi-FL at a 10 μM concentration and 30 min yielded consistent labeling in nucleated cells throughout the epidermis into the dermis in human and pig tissues. To deliver the dye, we attached reservoirs to the skin; however, this delivery approach would not be feasible in patients. Thus, to demonstrate clinical feasibility, we also tested PARPi-FL permeability and detectability using a saturated gauze (mimicking a nicotine patch) applied to the skin under occlusion, which yielded similar results (Supplemental Fig. 5), laying the foundation for developing a cream- or gel-based formulation for topical application in clinics. Furthermore, PARPi-FL application to the skin did not influence the subsequent H&E staining of tissue (Supplemental Fig. 6).

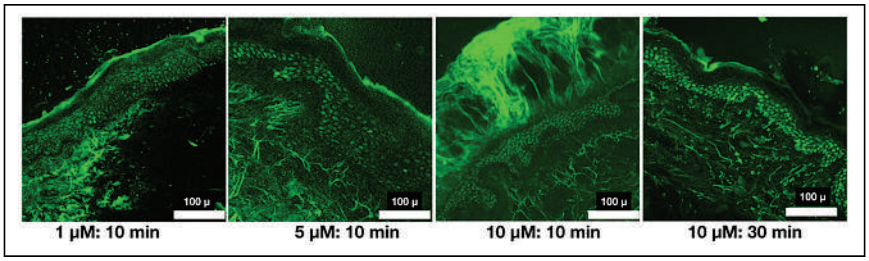

FIGURE 5. PARPi-FL successfully permeates through intact skin in ex vivo human tissue. Increased nuclear labeling is found for longer periods; maximum labeling and intensity are found for 10 μM and 30 min.

CONCLUSION

Higher PARP1 expression was found in BCCs than in normal skin structures, allowing specific PARPi-FL labeling in BCCs. Enhanced contrast provided by PARPi-FL–labeled nuclei leads to higher sensitivity and specificity for BCC diagnosis with RCM-and-FCM imaging than for RCM imaging alone. PARPi-FL can be delivered

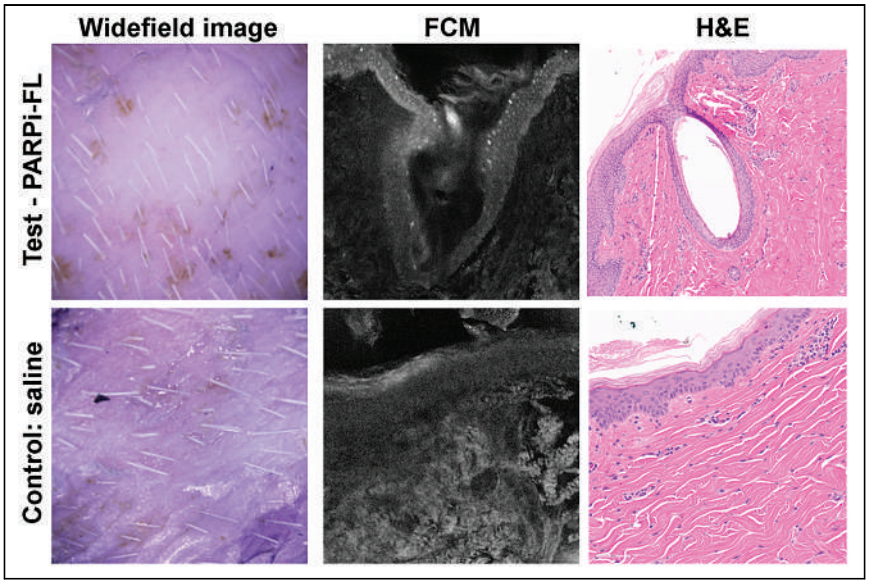

FIGURE 6. Successful PARPi-FL staining confirmed in vivo after topical application in live pig model. Representative wide-field, FCM, and H&E images demonstrate positive nuclear staining in basal layer of epidermis in test image (PARPi-FL), with absence of nuclear labeling in control image.

KEY POINTS

QUESTION: Can PARPi-FL combined with reflectance contrast improve detection of BCCs?

PERTINENT FINDINGS: Higher PARP1 expression and PARPi-FL staining were confirmed in nuclei of tumor cells than in normal skin structures. In a blinded study by 2 readers, diagnostic accuracy for BCCs was higher for combined PARPi-FL and reflectance contrast than for reflectance contrast alone. The permeability of PARPi-FL through passive diffusion was also confirmed in human skin and in vivo in pigs.

IMPLICATIONS FOR PATIENT CARE: Improving noninvasive diagnosis will directly impact clinical care and management of BCCs by reducing benign biopsies and enabling nonsurgical management of less aggressive BCC subtypes.

into the dermis (1–10 μM, 10–30 min) after passive topical application, suggesting promising potential for clinical use in patients. However, staining was found to be heterogeneous in 8% of thick specimens, suggesting that a combination of FCM with RCM may be necessary for improving clinical diagnosis of BCCs in vivo in patients.

DISCLOSURE

This work was supported by National Institutes of Health grants P30 CA008748, R01 EB020029 (Milind Rajadhyaksha), and R01 CA204441 (Thomas Reiner); the MSK Imaging and Radiation Sciences Program; and the MSK Society Grant (Manu Jain). Thomas Reiner, Susanne Kossatz, and Christian Brand are shareholders of Summit Biomedical Imaging, LLC. Thomas Reiner and Susanne Kossatz are coinventors on a filed U.S. patent (WO2016164771) held by MSK that covers methods for PARPi-FL. Thomas Reiner is a coinventor on a U.S. patent (WO2012074840), held by the General Hospital Corporation, that covers PARPi-FL composition. Thomas Reiner is a paid consultant for Theragnostics, Inc. Christian Brand serves as the chief scientific officer at Summit Biomedical Imaging, LLC. Christi Alessi-Fox is a former employee of, holds equity in, and is currently a consultant with Caliber Imaging and Diagnostics. Milind Rajadhyaksha is a former employee of and owns equity in Caliber Imaging and Diagnostics; the VivaScope is the commercial version of an original laboratory prototype that he developed at Massachusetts General Hospital, Harvard Medical School. No other potential conflict of interest relevant to this article was reported.

ACKNOWLEDGMENTS

We acknowledge Dr. Evan Matros and the PPBC team, Brandon Possum and the Mohs Lab, Eric Chan and the MCCF Core, the MSK–Animal Imaging Core Facility, the Radiochemistry and Molecular Imaging Probes Core, the Nuclear Magnetic Analytical Core, and the MSK Center for Molecular Imaging and Nanotechnology.

REFERENCES

1. Rogers HW, Weinstock MA, Feldman SR, Coldiron BM. Incidence estimate of nonmelanoma skin cancer (keratinocyte carcinomas) in the U.S. population, 2012. *JAMA Dermatol.* 2015;151:1081–1086.
2. Work Group; Invited Reviewers, Kim JYS, Kozlow JH, Mittal B, Moyer J, Olencki T, Rodgers P. Guidelines of care for the management of basal cell carcinoma. *J Am Acad Dermatol.* 2018;78:540–559.
3. Wozniak-Rito A, Zalaudek I, Rudnicka L. Dermoscopy of basal cell carcinoma. *Clin Exp Dermatol.* 2018;43:241–247.
4. Reiter O, Mimouni I, Gdalevich M, et al. The diagnostic accuracy of dermoscopy for basal cell carcinoma: a systematic review and meta-analysis. *J Am Acad Dermatol.* 2019;80:1380–1388.
5. Altamura D, Menzies SW, Argenziano G, et al. Dermatoscopy of basal cell carcinoma: morphologic variability of global and local features and accuracy of diagnosis. *J Am Acad Dermatol.* 2010;62:67–75.
6. Dinnes J, Deeks JJ, Chuchu N, et al. Visual inspection and dermoscopy, alone or in combination, for diagnosing keratinocyte skin cancers in adults. *Cochrane Database Syst Rev.* 2018;12:CD011901.
7. Rajadhyaksha M, Grossman M, Esterowitz D, Webb RH, Anderson RR. In vivo confocal scanning laser microscopy of human skin: melanin provides strong contrast. *J Invest Dermatol.* 1995;104:946–952.
8. Rajadhyaksha M, González S, Zavislan JM, Anderson RR, Webb RH. In vivo confocal scanning laser microscopy of human skin II: advances in instrumentation and comparison with histology. *J Invest Dermatol.* 1999;113:293–303.
9. Rajadhyaksha M, Anderson RR, Webb RH. Video-rate confocal scanning laser microscope for imaging human tissues in vivo. *Appl Opt.* 1999;38:2105–2115.
10. Guitera P, Menzies S, Argenziano G, et al. Dermoscopy and in vivo confocal microscopy are complementary techniques for diagnosis of difficult amelanotic and light-coloured skin lesions. *Br J Dermatol.* 2016;175:1311–1319.
11. Ruini C, Hartmann D, Saral S, Krammer S, Ruzicka T, von Braunmühl T. The invisible basal cell carcinoma: how reflectance confocal microscopy improves the diagnostic accuracy of clinically unclear facial macules and papules. *Lasers Med Sci.* 2016;31:1727–1732.
12. Nelson SA, Scope A, Rishpon A, et al. Accuracy and confidence in the clinical diagnosis of basal cell cancer using dermoscopy and reflex confocal microscopy. *Int J Dermatol.* 2016;55:1351–1356.
13. Liopyris K, Navarrete-Dechent C, Yélamos O, Marchetti M, Rabinovitz H, Marghoob A. Clinical, dermoscopic and reflectance confocal microscopy characterization of facial basal cell carcinomas presenting as small white lesions on sun-damaged skin. *Br J Dermatol.* 2019;180:229–230.
14. Dinnes J, Deeks JJ, Saleh D, et al. Reflectance confocal microscopy for diagnosing cutaneous melanoma in adults. *Cochrane Database Syst Rev.* 2018;12:CD013190.

15. Lupu M, Popa IM, Voiculescu VM, et al. A retrospective study of the diagnostic accuracy of in vivo reflectance confocal microscopy for basal cell carcinoma diagnosis and subtyping. *J Clin Med.* 2019;8:449.
16. Jain M, Pulijal SV, Rajadhyaksha M, Halpern AC, Gonzalez S. Evaluation of bedside diagnostic accuracy, learning curve, and challenges for a novice reflectance confocal microscopy reader for skin cancer detection in vivo. *JAMA Dermatol.* 2018;154:962–965.
17. Witkowski AM, Łudzik J, DeCarvalho N, et al. Non-invasive diagnosis of pink basal cell carcinoma: how much can we rely on dermoscopy and reflectance confocal microscopy? *Skin Res Technol.* 2016;22:230–237.
18. Xiong Y-Q, Ma S-J, Mo Y, Huo S-T, Wen Y-Q, Chen Q. Comparison of dermoscopy and reflectance confocal microscopy for the diagnosis of malignant skin tumours: a meta-analysis. *J Cancer Res Clin Oncol.* 2017;143:1627–1635.
19. Witkowski AM, Łudzik J, Arginelli F, et al. Improving diagnostic sensitivity of combined dermoscopy and reflectance confocal microscopy imaging through double reader concordance evaluation in telemedicine settings: a retrospective study of 1000 equivocal cases. *PLoS One.* 2017;12:e0187748.
20. Rajadhyaksha M, Gonzalez S, Zavislan JM. Detectability of contrast agents for confocal reflectance imaging of skin and microcirculation. *J Biomed Opt.* 2004;9:323–331.
21. Reiner T, Lacy J, Keliher EJ, et al. Imaging therapeutic PARP inhibition in vivo through bioorthogonally developed companion imaging agents. *Neoplasia.* 2012;14:169–177.
22. Carney B, Kossatz S, Lok BH, et al. Target engagement imaging of PARP inhibitors in small-cell lung cancer. *Nat Commun.* 2018;9:176.
23. Kossatz S, Brand C, Gutiontov S, et al. Detection and delineation of oral cancer with a PARP1 targeted optical imaging agent. *Sci Rep.* 2016;6:21371.
24. Irwin CP, Portorreal Y, Brand C, et al. PARPi-FL-a fluorescent PARP1 inhibitor for glioblastoma imaging. *Neoplasia.* 2014;16:432–440.
25. Kossatz S, Pirovano G, França PDDS, et al. Validation of the use of a fluorescent PARP1 inhibitor for the detection of oral, oropharyngeal and oesophageal epithelial cancers. *Nat Biomed Eng.* 2020;4:272–285.
26. de Souza França PD, Kossatz S, Brand C, et al. A phase I study of a PARP1-targeted topical fluorophore for the detection of oral cancer. medRxiv website. https://www.medrxiv.org/content/10.1101/2020.11.09.20228536v1.full. Published November 12, 2020. Accessed January 31, 2022.
27. Thurber GM, Yang KS, Reiner T, et al. Single-cell and subcellular pharmacokinetic imaging allows insight into drug action in vivo. *Nat Commun.* 2013;4:1504.
28. Olson AH. *Image Analysis Using the Aperio ScanScope.* Aperio Technologies Inc.; 2006.
29. LoMartire R, LoMartire MR. Package rel: reliability coefficients. R Package Documentation website. https://rdrr.io/cran/rel/. Accessed February 23, 2022.
30. Wickham H, Chang W, Wickham MH. Package 'ggplot2'. Create elegant data visualisations using the grammar of graphics. Version 2(1). 2016. The Comprehensive R Archive Network (CRAN) website. https://cran.r-project.org/web/packages/ggplot2/ggplot2.pdf. Accessed February 23, 2022.
31. Rajadhyaksha M, Menaker G, Flotte T, Dwyer PJ, González S. Confocal examination of nonmelanoma cancers in thick skin excisions to potentially guide Mohs micrographic surgery without frozen histopathology. *J Invest Dermatol.* 2001;117:1137–1143.
32. Patel YG, Nehal KS, Aranda I, Li Y, Halpern AC, Rajadhyaksha M. Confocal reflectance mosaicing of basal cell carcinomas in Mohs surgical skin excisions. *J Biomed Opt.* 2007;12:034027.
33. Gareau DS, Patel Y, Li Y, et al. Confocal mosaicing microscopy in skin excisions: a demonstration of rapid surgical pathology. *J Microsc.* 2009;233:149–159.

Effects of Tracer Uptake Time in Non–Small Cell Lung Cancer ^{18}F-FDG PET Radiomics

Guilherme D. Kolinger[1], David Vállez García[1,2], Gerbrand Maria Kramer[2], Virginie Frings[2], Gerben J.C. Zwezerijnen[2], Egbert F. Smit[3,4], Adrianus Johannes de Langen[4], Irène Buvat[5], and Ronald Boellaard[1,2]

[1]Medical Imaging Center, University Medical Center Groningen, University of Groningen, Groningen, The Netherlands; [2]Department of Radiology and Nuclear Medicine, Amsterdam University Medical Center, VU Medical Center, Amsterdam, The Netherlands; [3]Department of Pulmonology, Amsterdam University Medical Center, VU Medical Center, Amsterdam, The Netherlands; [4]Department of Thoracic Oncology, Antoni van Leeuwenhoek Hospital, Amsterdam, The Netherlands; and [5]Laboratoire d'Imagerie Translationnelle en Oncologie, INSERM, Institut Curie, Université Paris-Saclay, Orsay, France

PET radiomics applied to oncology allow the measurement of intratumoral heterogeneity. This quantification can be affected by image protocols; hence, there is an increased interest in understanding how radiomic expression on PET images is affected by different imaging conditions. To address that interest, this study explored how radiomic features are affected by changes in ^{18}F-FDG uptake time, image reconstruction, lesion delineation, and radiomic binning settings. **Methods:** Ten non–small cell lung cancer patients underwent ^{18}F-FDG PET on 2 consecutive days. On each day, scans were obtained at 60 and 90 min after injection and reconstructed following EARL version 1 and with point-spread-function resolution modeling (PSF-EARL2). Lesions were delineated with an SUV threshold of 4.0, with 40% of SUV_{max}, and with a contrast-based isocontour. PET image intensity was discretized with both a fixed bin width (FBW) and a fixed bin number before the calculation of the radiomic features. Repeatability of features was measured with the intraclass correlation coefficient, and the change in feature value over time was calculated as a function of its repeatability. Features were then classified into use-case scenarios based on their repeatability and susceptibility to tracer uptake time. **Results:** With PSF-EARL2 reconstruction, 40% of SUV_{max} lesion delineation, and FBW intensity discretization, most features (94%) were repeatable at both uptake times (intraclass correlation coefficient $>$ 0.9), 35% being classified for dual-time-point use cases as being sensitive to changes in uptake time, 39% were classified for cross-sectional studies with an unclear dependency on time, 20% were classified for cross-sectional use while being robust to uptake time changes, and 6% were discarded for poor repeatability. EARL version 1 images had 1 fewer repeatable feature (neighborhood gray-level different matrix coarseness) than PSF-EARL2; the contrast-based delineation had the poorest repeatability of the delineation methods, with 45% of features being discarded; and fixed bin number resulted in lower repeatability than FBW (45% and 6% of features were discarded, respectively). **Conclusion:** Repeatability was maximized with PSF-EARL2 reconstruction, lesion delineation at 40% of SUV_{max}, and FBW intensity discretization. On the basis of their susceptibility to uptake time, radiomic features were classified into specific non–small cell lung cancer PET radiomics use cases.

Key Words: PET; radiomics; texture analysis; repeatability; dual-time-point

J Nucl Med 2022; 63:919–924
DOI: 10.2967/jnumed.121.262660

For staging and treatment response evaluation of patients with non–small cell lung cancer (NSCLC), ^{18}F-FDG PET/CT is an important technique. This evaluation can be achieved either visually or using SUVs and total lesion glycolysis measurements (*1–5*). However, these semiquantitative approaches ignore possible tracer uptake heterogeneity within the tumor (*6*), overlooking potentially useful information. To address this issue, the field of Radiomics has been developed to perform measurements of textural information available in medical images, resulting in a more complete phenotyping of the tumor (*7–9*).

PET radiomics in oncology allow the extraction of several features characterizing tumor uptake, shape, and intratumoral heterogeneity (*10–13*). This approach showed promising results, including lesion histological sub-type identification, aided automated tumor delineation and disease-free survival prediction (*14–18*). Despite this success, radiomic features are sensitive to image noise, lesion segmentation method, signal intensity discretization, and several image settings, including PET acquisition and reconstruction settings (*11,19–26*). This sensitivity leads to difficulties in multicenter studies, possibly explaining why the results have poor reproducibility, leading to skepticism about the usefulness of radiomics (*9,19,27–31*). Furthermore, these issues are amplified by the lack of negative publications on the field (*32*). Strategies have been developed to mitigate this variability and thus improve the postreconstruction harmonization of textural features (*33–35*).

One aspect of ^{18}F-FDG PET radiomics that has not been extensively explored is its uptake time dependence. The time between tracer injection and image acquisition alters the uptake in metabolically active regions where ^{18}F-FDG gradually accumulates, affecting SUV-related metrics and their repeatability (*36–38*). ^{18}F-FDG PET/CT textural analysis from dual-time-point static scans has been used to differentiate benign from malignant pulmonary lesions despite features presenting a wide range of accuracy (*39,40*). Time-related PET radiomics have been also explored as dynamic features (*41*). However, neither of these studies assessed how uptake time could influence textural feature repeatability.

Received May 28, 2021; revision accepted Sep. 21, 2021.
For correspondence or reprints, contact Guilherme D. Kolinger (g.domingues.kolinger@umcg.nl).
Published online Dec. 21, 2021.

Our hypothesis was that different features have different levels of dependence on uptake time and that this dependence may be influenced by image settings. Therefore, we evaluated how radiomic features (SUV-based and textural) are affected by uptake time and whether its effects are smaller or larger than the effects of feature repeatability. On the basis of each feature's repeatability and dependence on uptake time, features are classified into cross-sectional or single-injection dual-time-point use cases. Several image settings are considered, including PET/CT image reconstruction algorithms, lesion delineation methods, and intensity discretization strategies.

MATERIALS AND METHODS

Dataset

Ten patients with confirmed stage IIIB or IV NSCLC underwent double baseline ^{18}F-FDG PET/CT on a Gemini TF scanner (Philips Healthcare), as previously described (*5,20*). Patients fasted for 6 h or more, and then a low-dose CT scan was acquired for attenuation correction followed by a whole-body ^{18}F-FDG PET scan 60 min after tracer injection. Thirty minutes later, a second whole-body PET scan and low-dose CT scan were obtained. This procedure was repeated within 3 d of the first scan for test–retest measurements. All PET data were normalized and corrected for scatter and random events, dead time, attenuation, and decay. Two reconstruction protocols were used, one following the EARL version 1 guidelines (EARL1) and another with point-spread-function resolution modeling (PSF-EARL2) (*42–44*). The PET images had a final resolution of 144 × 144 × 254 voxels with a voxel size of 4 × 4 × 4 mm^3. The average injected activity was 248 MBq (range, 194–377 MBq) on the first day and 238 MBq (range, 192–392 MBq) on the second day. The average postinjection start times were 61 min (range, 59–67 min) and 92 min (range, 90–97 min) on the first day and 60 min (range, 60–63 min) and 90 min (range, 90–95 min) on the second day. All patients gave written informed consent before enrollment, and the study was approved by the Medical Ethics Review Committee of the Vrije Universiteit Medical Center (Dutch trial register NTR3508; https://www.trialregister.nl/).

Radiomic Feature Extraction

Lesions were delineated and radiomic features extracted using LIFEx (version 6.30) (*45*). All lesions were included for the analysis, namely the primary and metastatic lesions (intra- and extrathoracic), yielding 1–10 lesions as a function of the patient. Lesions were delineated on the PSF-EARL2 PET images using an isocontour at 40% of each lesion's SUV_{max}, and then radiomic features were extracted with intensity discretization using a fixed bin width (FBW) of 0.25 g/mL, ranging from 0–60 g/mL for each lesion (the 60 g/mL upper bound was higher than the SUV_{max} of all lesions). This combination of image and processing settings was considered the reference settings for radiomic analysis, as they were previously shown to optimize test–retest variability (*19,36,46*). Other image settings were explored, including lesion delineation and feature extraction from EARL1 images, lesion delineation with a fixed isocontour at an SUV threshold of 4.0 (SUV4) and a contrast-based isocontour at 0.5 × SUV_{peak} + background SUV (contrast; background SUV was the mean uptake in a shell 2 cm away from the volume defined at 70% of SUV_{max}, excluding voxels with SUV > 4), and intensity discretization with a fixed bin number (FBN) of 64 bins in a variable range of SUV_{min}–SUV_{max}.

In total, 49 radiomic features from 7 classes were extracted (the full list is given in Supplemental Table 1; supplemental materials are available at http://jnm.snmjournals.org): 6 conventional PET metrics, 5 shape-based features, 6 histogram-based features, 7 gray-level cooccurrence matrix (GLCM) features, 11 gray-level run-length matrix (GLRLM) features, 11 gray-level zone-length matrix (GLZLM) features, and 3 neighborhood gray-level difference matrix (NGLDM) features. Features were obtained only for lesions that included at least 64 voxels. LIFEx's feature definition is in compliance with the Image Biomarker Standardisation Initiative (*47,48*).

Data Analysis

Features calculated from images obtained at different time points on the first day of scans were statistically compared using pairwise Wilcoxon signed-rank tests. *P* values below 0.05 were considered statistically significant after Benjamini–Hochberg false-discovery-rate correction. A change in feature value was measured as a function of uptake time by using its test–retest variability at 60 min after injection as a baseline (analogous to a *z* score):

$$z = \frac{(RF_{90} - RF_{60}) - \text{mean } TRT_{60}}{TRT_{60}\ SD}.$$

RF_{60} and RF_{90} represent the radiomic feature values at 60 and 90 min after injection, respectively. TRT_{60} is the test–retest difference between the feature values at the second- and first-day scans (at 60 min after injection). Therefore, the effects of uptake time on radiomic features were contextualized with respect to repeatability: *z* scores lower than 1 indicate changes with an uptake time less than test–retest variability, and *z* scores higher than 1 show a change larger than repeatability.

A feature was considered repeatable if the intraclass correlation coefficient (agreement type, 2-way mixed-effects model, single rating) between test and retest scans (same reconstruction, delineation method, and discretization) was higher than 0.9 at both time points. A feature was defined as robust against change in uptake time if it was not significantly affected by uptake time after false-discovery-rate correction and if its change from 60 to 90 min was less than from one day to another (i.e., mean *z* score < 1). Finally, features were assigned to a use case on the basis of their

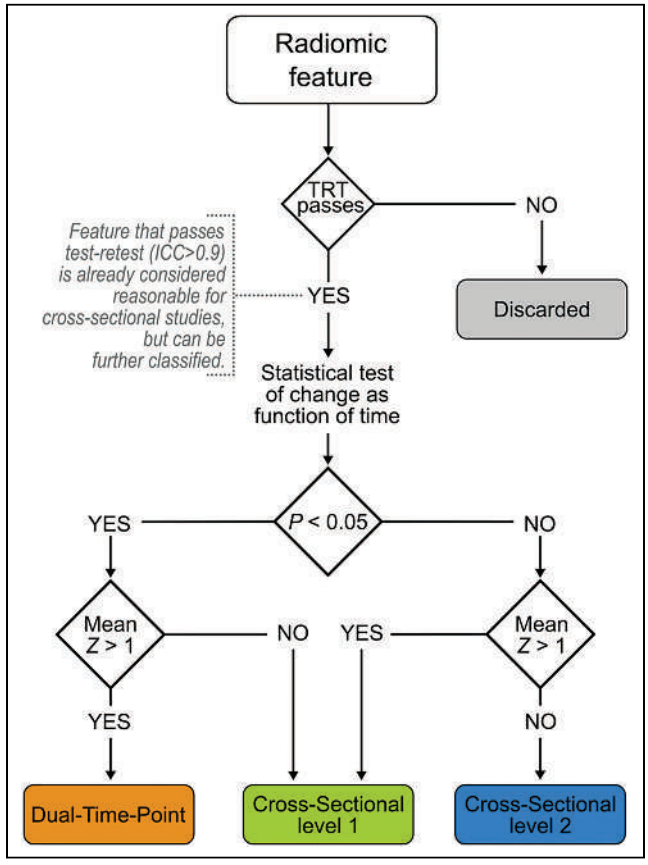

FIGURE 1. Flowchart for use-case classification of radiomic features. TRT = test–retest; ICC = intraclass correlation coefficient.

repeatability and susceptibility to uptake time (Fig. 1): features that were repeatable and susceptible to uptake time were classified for dual-time-point studies, repeatable features with an uncertain response to uptake time were classified as cross-sectional level 1 (CS1), repeatable features that were robust to uptake time were classified as cross-sectional level 2 (CS2), and features with poor repeatability at any time point were discarded. Statistical analysis was done using R, version 4.0.4.

RESULTS

Feature Dependence on Uptake Time

All conventional features were significantly affected by uptake interval and increased in value with increased uptake time (Fig. 2, positive mean *z* score). Shape features did not significantly differ between the 2 uptake times. Half the histogram features were affected by uptake time (histogram entropy log10 and histogram entropy log2 are equivalent after rescaling with *z* scores). Four of 7 GLCM features significantly increased over time, and only 1 decreased. One GLRLM, 2 GLZLM, and 2 NGLDM features were not statistically significantly dependent on uptake time (Fig. 2). The features of each class with the highest *z* score and a statistically significant ($P < 0.05$) dependence on uptake time were conventional SUV_{mean}, histogram entropy, GLCM dissimilarity, GLRLM long-run high-gray-level emphasis, GLZLM short-zone low-gray-level emphasis, and NGLDM contrast (average *z* score ± SD: 1.36 ± 0.98, 1.04 ± 0.73, 1.35 ± 1.29, 1.38 ± 1.69, −1.24 ± 1.86, and 1.28 ± 2.10, respectively).

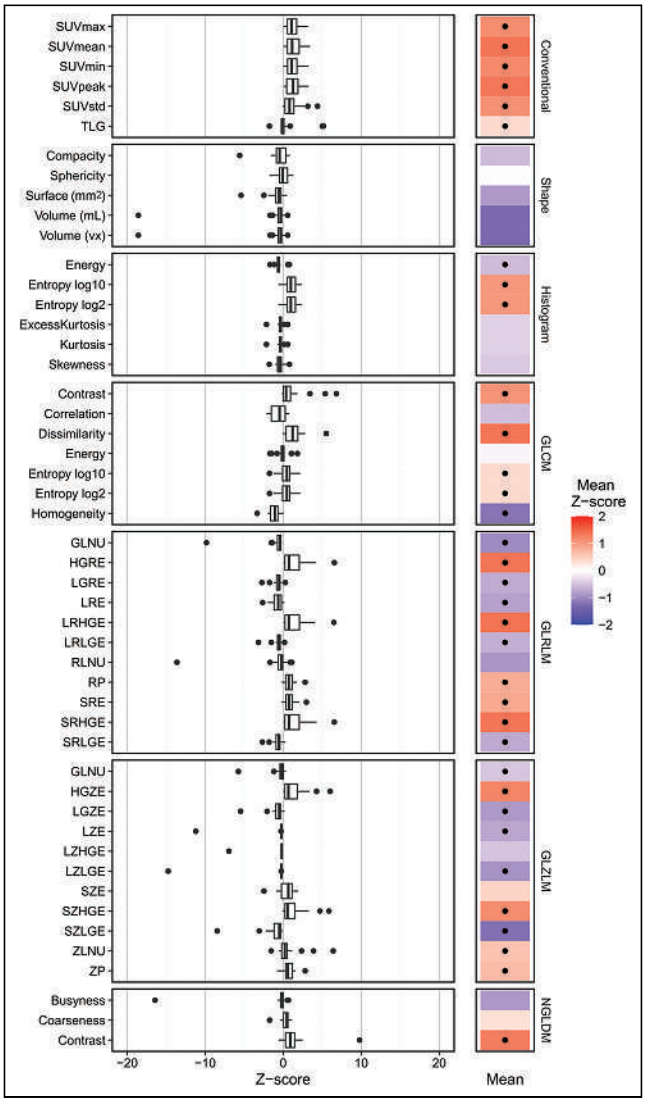

FIGURE 2. Effect of uptake time on radiomic features. (Left) Distribution of *z* scores for each feature. *z* scores were calculated using test–retest variability on scan at 60 min after injection as baseline. (Right) Mean *z* score of each feature (dot indicates statistical significance). Analysis was of images with reference settings. Abbreviations are defined in Supplemental Table 1.

Radiomic Feature Use-Case Classification

Ninety-four percent (46/49) of the features had reliable repeatability (intraclass correlation coefficient > 0.9, Supplemental Fig. 1). In total, 35% (17/49) of features were classified as dual-time-point, 39% (19/49) as CS1, and 20% (10/49) as CS2; 6% (3/49) were discarded (Supplemental Fig. 1). No conventional feature was classified for CS2 use cases, no shape feature was classified for dual-time-point use cases, and no NGLDM feature was classified for CS1 use cases. The remaining feature classes had a mixed use-case classification (Fig. 3).

Influence of Image Settings on Repeatability and Use-Case Classification

The reference settings (PSF-EARL2 reconstruction, 40% of SUV_{max} delineation, and FBW discretization) had fewer discarded features than did other image settings (Fig. 4). Images had 1 fewer repeatable feature (NGLDM coarseness) with EARL1 (and recommended delineation and discretization) than with PSF-EARL2 (Fig. 4). With PSF-EARL2 and FBW discretization, the contrast-based lesion delineation method had poorer repeatability than the other methods, and SUV4 had fewer repeatable features than 40% of SUV_{max} (22, 6, and 3 features discarded, respectively). Lastly, repeatability was considerably lower for FBN than for FBW (22 and 3 discarded features with recommended reconstruction and delineation, respectively; Supplemental Fig. 2).

Using the reference delineation and discretization, EARL1 had no conventional feature classified for dual-time-point use cases (Fig. 4; Supplemental Fig. 3). Histogram features were classified only for CS1 use cases (or were discarded), whereas all shape features were classified for CS2. In total, 8% (4/49) of features had a dual-time-point classification, 67% (33/49) had CS1, 16% (8/49) had CS2, and 8% (4/49) were discarded with EARL1 reconstruction when using the reference delineation and discretization.

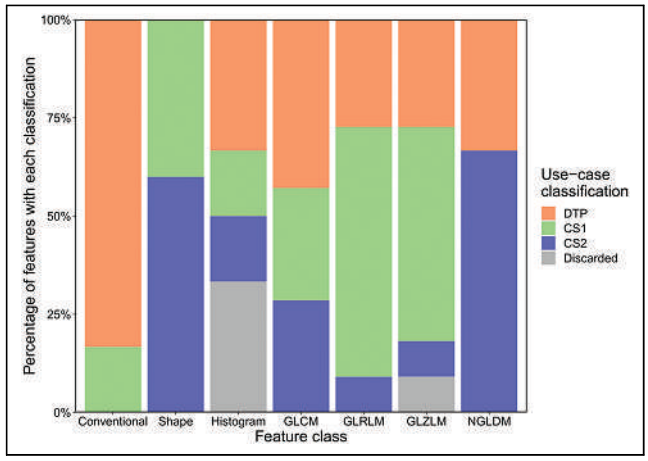

FIGURE 3. Percentage of radiomic features with each use-case classification for each feature class. Analysis was of images with reference settings. DTP = dual time point.

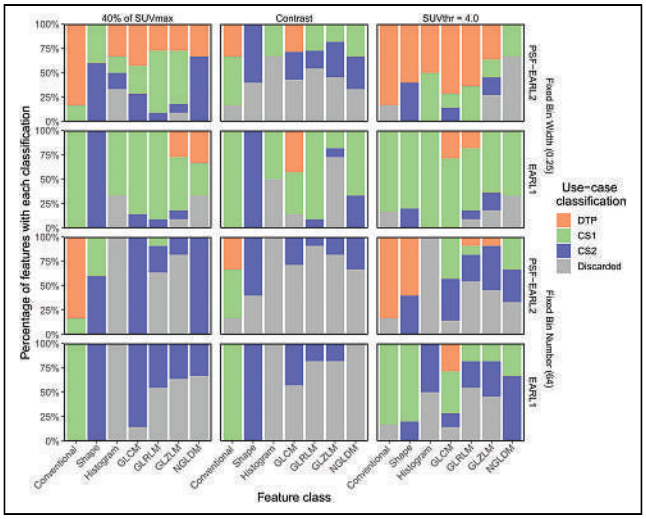

FIGURE 4. Percentage of radiomic features with each use-case classification for each feature class in all image setting configurations. Columns of panels show different lesion delineation methods, and rows show different image reconstructions and intensity discretization strategies. Analysis was of images with reference settings. DTP = dual time point; SUVthr = SUV threshold.

Despite using the reference reconstruction and discretization, the contrast-based delineation approach resulted in 45% (22/49) of features being discarded (Fig. 4; Supplemental Fig. 3). With SUV4, 12% (6/49) of features were discarded, and all repeatable conventional features had a dual-time-point classification; other feature classes had mixed use-case classifications.

Using FBN for discretization resulted in use-case classifications different from those of FBW, even when both used the reference reconstruction and delineation methods (Fig. 4). The exceptions were the conventional and shape features, since those are not dependent on the image intensity discretization (Supplemental Fig. 3). With PSF-EARL2, 40% of SUV_{max}, and FBN, only 1 gray-level–based feature was classified for CS1: GLRLM run length nonuniformity. Furthermore, all GLCM and NGLDM features were robust to uptake time with FBN discretization (CS2 use cases), and all histogram features were discarded (Fig. 4).

DISCUSSION

This study demonstrated that for PET images reconstructed with PSF-EARL2, lesion delineation with 40% of SUV_{max}, and intensity discretization using FBW, most (94%) traditional and gray-level–based features were repeatable on scans at both 60 and 90 min after injection. From the radiomic features assessed, 35% were repeatable and able to detect a change as a function of uptake time (dual-time-point), 39% were repeatable but had an unclear dependency on uptake time (CS1), 20% were repeatable and robust against uptake time changes (CS2), and 6% were not repeatable (discarded). Additionally, analyses performed on PET images reconstructed using EARL1, lesion delineation using a contrast-based approach or a fixed threshold method, and intensity discretization using a fixed number of bins decreased repeatability and led to different use-case classifications of radiomic features.

Overall, more features significantly increased (22/49) with time than decreased (12/49), as found previously (*49*). Conventional features increased over time, as expected (*50,51*), and shape features slightly decreased in the delayed PET scan. This decrease in volume due to a higher threshold for lesion delineation (at 40% of SUV_{max}) agrees with the lower metabolic tumor volume of breast cancer for delayed PET scans (*52*). The statistically significant histogram features affected by uptake time were energy (decreased) and entropy (increased). The first is related to the uniformity of the distribution and the second to its randomness, therefore reflecting an increase in tumor heterogeneity on delayed ^{18}F-FDG PET scans (*52*). Yet, these features were not significantly affected by uptake time on peripheral nerve sheath tumors with a relatively low ^{18}F-FDG uptake (*49*), emphasizing that translation of radiomic results between different tumor types must be performed with caution even with first-order features.

The increase in GLRLM run percentage, GLZLM zone percentage, and NGLDM contrast over time reflects an increased heterogeneity, as run percentage and zone percentage are low for highly uniform volumes of interest (*47*) and contrast is related to the intensity difference between neighboring regions. However, there was a decrease in GLRLM and GLZLM nonuniformity, suggesting a reduction in heterogeneity over time. These nonuniformity features have previously been reported as being dependent on time (*49,52*), but with a small effect size and a direction of change that was not uniform across studies. Therefore, more features suggest an increase in tumor heterogeneity over time than a decrease, agreeing with previous findings for advanced breast cancer (*52*) but disagreeing with peripheral nerve sheath tumor results (*49*). This incompatibility may come from the uptake levels in the tumors. The present study and Garcia-Vicente et al. (*52*) assessed tumors with relatively high ^{18}F-FDG uptake and found increasing heterogeneity over time, whereas Lovat et al. (*49*) studied low-uptake lesions.

Radiomic features classified for CS1 use cases were repeatable at both uptake times but did not have any clear relationship with uptake time—that is, were neither robust nor sensitive. These features may be suitable for cross-sectional studies if all images are acquired with similar postinjection times. The dependence of the CS1 features on time could explain some of their variability and range previously found on lung cancer assessment (*15,25,46*). Other repeatable features were robust against changes in uptake time (CS2) and are recommended for studies with an inconsistent postinjection scanning time. In contrast, repeatable features statistically significantly and substantially affected by uptake time were classified for dual-time-point use cases. Like CS1 features, dual-time-point features may be used on images acquired with a similar uptake time (e.g., SUV_{mean}) but can also measure the effect of time on feature values. Previous studies have reported a possible added benefit of a dual-time-point scanning protocol for differentiation between benign and malignant pulmonary lesions with textural features (*39,40*) and for breast cancer intratumoral heterogeneity assessment (*52*). Unfortunately, given the different nature of the lesions and analysis settings in those previous studies, it is not possible to directly compare the radiomic features found useful by those authors with the ones we identified as appropriate for dual-time-point studies.

As shown previously (*19*), EARL1 reconstructions resulted in worse repeatability than PSF-EARL2. Additionally, PSF-EARL2 reconstructions also displayed higher heterogeneity (*20*) and are recommended for textural analysis. Concerning the lesion delineation method, a fixed isocontour lesion delineation (SUV4) yielded poorer repeatability than an adaptive threshold based on 40% of SUV_{max}, as expected from the literature (*36*). The contrast-based delineation had the poorest repeatability of all methods and is thus not recommended for radiomics. Furthermore, previous findings that the repeatability of FBW intensity discretization is superior to that of FBN for PET radiomics were reproduced (*19,46,47*). In historical cohorts for which only EARL1 reconstruction is available, few

features are viable for dual-time-point studies (Fig. 4). With lesion delineation at 40% of SUV_{max} and discretization with FBW, the EARL1 protocol still provides several repeatable radiomic features.

The analysis of data from a single scanner vendor and the inclusion of a single tumor type (NSCLC, including intra- and extrathoracic lesions), especially given that features have different levels of expression for different cancer types, are some limitations of our study, and multicenter studies are needed to verify our findings. Furthermore, voxel size affects radiomic feature values and lesion delineation. However, the impact of voxel size on feature use-case classification still needs to be explored. Data from static scans 30 min apart were evaluated. Nevertheless, it is possible that additional radiomic information could be obtained from scans acquired farther apart in uptake time. Finally, several features were analyzed under different image conditions on only 10 subjects. This study may thus be subject to type 1 errors although a false-discovery-rate correction was applied to the statistical analysis.

In summary, EARL1 reconstruction led to classification of fewer features for dual-time-point use cases than did PSF-EARL2. Textural features were not robust against changes in uptake interval when SUV4 was used for lesion delineation, showing that for NSCLC radiomics, this method should be applied only to PET images acquired with a similar uptake time. Furthermore, most features were discarded when the contrast-based delineation method or the FBN intensity discretization was used, and their use is not recommended for NSCLC ^{18}F-FDG PET radiomic studies.

CONCLUSION

This study demonstrated that PET radiomics can be repeatable, summarized the features' susceptibility to postinjection PET scanning time, and classified the features into reliable use cases for NSCLC radiomics: dual-time-point and cross-sectional studies. Repeatability and the use case of radiomic features depended on PET image reconstruction, lesion delineation, and intensity discretization, and recommendations were provided accordingly.

DISCLOSURE

This project received funding from the European Union's Horizon 2020 research and innovation program under the Marie Skłodowska-Curie Innovative Training Network (grant agreement 764458). Irène Buvat is involved in the development of LIFEx. No other potential conflict of interest relevant to this article was reported.

KEY POINTS

QUESTION: Is the change in radiomic features with ^{18}F-FDG uptake time larger than their repeatability, and can that change be used for temporal textural analysis?

PERTINENT FINDINGS: PET image reconstruction with point-spread-function modeling, lesion delineation at 40% of SUV_{max}, and intensity discretization with FBW resulted in repeatable radiomic features on scans at 60 and 90 min after injection and provided reliable information for cross-sectional and dual-time-point studies.

IMPLICATIONS FOR PATIENT CARE: Radiomic features were identified and classified for potential use cases in cross-sectional and dual-time-point protocols, providing reliable information about tumor heterogeneity for NSCLC assessment.

REFERENCES

1. Graham MM, Peterson LM, Hayward RM. Comparison of simplified quantitative analyses of FDG uptake. *Nucl Med Biol.* 2000;27:647–655.
2. Hoekstra CJ, Paglianiti I, Hoekstra OS, et al. Monitoring response to therapy in cancer using [^{18}F]-2-fluoro-2-deoxy-d-glucose and positron emission tomography: an overview of different analytical methods. *Eur J Nucl Med.* 2000;27:731–743.
3. Fletcher JW, Djulbegovic B, Soares HP, et al. Recommendations on the use of ^{18}F-FDG PET in oncology. *J Nucl Med.* 2008;49:480–508.
4. Toma-Dasu I, Uhrdin J, Lazzeroni M, et al. Evaluating tumor response of non-small cell lung cancer patients with ^{18}F-fludeoxyglucose positron emission tomography: potential for treatment individualization. *Int J Radiat Oncol Biol Phys.* 2015;91:376–384.
5. Kramer GM, Frings V, Hoetjes N, et al. Repeatability of quantitative whole-body ^{18}F-FDG PET/CT uptake measures as function of uptake interval and lesion selection in non-small cell lung cancer patients. *J Nucl Med.* 2016;57:1343–1349.
6. O'Connor JPB, Rose CJ, Waterton JC, Carano RAD, Parker GJM, Jackson A. Imaging intratumor heterogeneity: role in therapy response, resistance, and clinical outcome. *Clin Cancer Res.* 2015;21:249–257.
7. Gillies RJ, Kinahan PE, Hricak H. Radiomics: images are more than pictures, they are data. *Radiology.* 2016;278:563–577.
8. Zwanenburg A. Radiomics in nuclear medicine: robustness, reproducibility, standardization, and how to avoid data analysis traps and replication crisis. *Eur J Nucl Med Mol Imaging.* 2019;46:2638–2655.
9. Liu Z, Wang S, Dong D, et al. The applications of radiomics in precision diagnosis and treatment of oncology: opportunities and challenges. *Theranostics.* 2019;9:1303–1322.
10. Buvat I, Orlhac F, Soussan M. Tumor texture analysis in PET: where do we stand? *J Nucl Med.* 2015;56:1642–1644.
11. Ha S, Choi H, Paeng JC, Cheon GJ. Radiomics in oncological PET/CT: a methodological overview. *Nucl Med Mol Imaging.* 2019;53:14–29.
12. Lambin P, Rios-Velazquez E, Leijenaar R, et al. Radiomics: extracting more information from medical images using advanced feature analysis. *Eur J Cancer.* 2012;48:441–446.
13. Orlhac F, Soussan M, Maisonobe J-A, Garcia CA, Vanderlinden B, Buvat I. Tumor texture analysis in ^{18}F-FDG PET: relationships between texture parameters, histogram indices, standardized uptake values, metabolic volumes, and total lesion glycolysis. *J Nucl Med.* 2014;55:414–422.
14. Pfaehler E, Mesotten L, Kramer G, et al. Textural feature based segmentation: a repeatable and accurate segmentation approach for tumors in PET Images. In: Papież BW, Namburete AIL, Yaqub M, Noble JA, eds. *Medical Image Understanding and Analysis.* Springer; 2020:3–14.
15. Mattonen SA, Davidzon GA, Benson J, et al. Bone marrow and tumor radiomics at ^{18}F-FDG PET/CT: impact on outcome prediction in non–small cell lung cancer. *Radiology.* 2019;293:451–459.
16. Lee JW, Lee SM. Radiomics in oncological PET/CT: clinical applications. *Nucl Med Mol Imaging.* 2018;52:170–189.
17. Kirienko M, Cozzi L, Rossi A, et al. Ability of FDG PET and CT radiomics features to differentiate between primary and metastatic lung lesions. *Eur J Nucl Med Mol Imaging.* 2018;45:1649–1660.
18. Kirienko M, Cozzi L, Antunovic L, et al. Prediction of disease-free survival by the PET/CT radiomic signature in non-small cell lung cancer patients undergoing surgery. *Eur J Nucl Med Mol Imaging.* 2018;45:207–217.
19. Pfaehler E, Beukinga RJ, de Jong JR, et al. Repeatability of ^{18}F-FDG PET radiomic features: a phantom study to explore sensitivity to image reconstruction settings, noise, and delineation method. *Med Phys.* 2019;46:665–678.
20. van Velden FHP, Kramer GM, Frings V, et al. Repeatability of radiomic features in non-small-cell lung cancer [^{18}F]FDG-PET/CT studies: impact of reconstruction and delineation. *Mol Imaging Biol.* 2016;18:788–795.
21. Shiri I, Rahmim A, Ghaffarian P, Geramifar P, Abdollahi H, Bitarafan-Rajabi A. The impact of image reconstruction settings on ^{18}F-FDG PET radiomic features: multi-scanner phantom and patient studies. *Eur Radiol.* 2017;27:4498–4509.
22. Reynés-Llompart G, Sabaté-Llobera A, Llinares-Tello E, Martí-Climent JM, Gámez-Cenzano C. Image quality evaluation in a modern PET system: impact of new reconstructions methods and a radiomics approach. *Sci Rep.* 2019;9:10640.
23. Ketabi A, Ghafarian P, Mosleh-Shirazi MA, Mahdavi SR, Rahmim A, Ay MR. Impact of image reconstruction methods on quantitative accuracy and variability of FDG-PET volumetric and textural measures in solid tumors. *Eur Radiol.* 2019;29:2146–2156.
24. Yan J, Chu-Shern JL, Loi HY, et al. Impact of image reconstruction settings on texture features in ^{18}F-FDG PET. *J Nucl Med.* 2015;56:1667–1673.
25. Bashir U, Azad G, Siddique MM, et al. The effects of segmentation algorithms on the measurement of ^{18}F-FDG PET texture parameters in non-small cell lung cancer. *EJNMMI Res.* 2017;7:60.

26. Leijenaar RTH, Nalbantov G, Carvalho S, et al. The effect of SUV discretization in quantitative FDG-PET radiomics: the need for standardized methodology in tumor texture analysis. *Sci Rep.* 2015;5:11075.
27. Pfaehler E, van Sluis J, Merema BBJ, et al. Experimental multicenter and multivendor evaluation of PET radiomic features performance using 3D printed phantom inserts. *J Nucl Med.* 2020;61:469–476.
28. Hatt M, Lucia F, Schick U, Visvikis D. Multicentric validation of radiomics findings: challenges and opportunities. *EBioMedicine.* 2019;47:20–21.
29. Traverso A, Wee L, Dekker A, Gillies R. Repeatability and reproducibility of radiomic features: a systematic review. *Int J Radiat Oncol Biol Phys.* 2018;102: 1143–1158.
30. Desseroit M-C, Tixier F, Weber WA, et al. Reliability of PET/CT shape and heterogeneity features in functional and morphologic components of non-small cell lung cancer tumors: a repeatability analysis in a prospective multicenter cohort. *J Nucl Med.* 2017;58:406–411.
31. Konert T, Everitt S, Fontaine MDL, et al. Robust, independent and relevant prognostic ^{18}F-fluorodeoxyglucose positron emission tomography radiomics features in non-small cell lung cancer: are there any? *PLoS One.* 2020;15:e0228793.
32. Buvat I, Orlhac F. The dark side of radiomics: on the paramount importance of publishing negative results. *J Nucl Med.* 2019;60:1543–1544.
33. Da-Ano R, Visvikis D, Hatt M. Harmonization strategies for multicenter radiomics investigations. *Phys Med Biol.* 2020;65:24TR02.
34. Da-Ano R, Masson I, Lucia F, et al. Performance comparison of modified ComBat for harmonization of radiomic features for multicenter studies. *Sci Rep.* 2020;10: 10248.
35. Orlhac F, Boughdad S, Philippe C, et al. A postreconstruction harmonization method for multicenter radiomic studies in PET. *J Nucl Med.* 2018;59:1321–1328.
36. Kolinger GD, Vállez García D, Kramer GM, et al. Repeatability of [^{18}F]FDG PET/CT total metabolic active tumour volume and total tumour burden in NSCLC patients. *EJNMMI Res.* 2019;9:14.
37. Kaalep A, Burggraaff CN, Pieplenbosch S, et al. Quantitative implications of the updated EARL 2019 PET-CT performance standards. *EJNMMI Phys.* 2019;6:28.
38. Lasnon C, Salomon T, Desmonts C, et al. Generating harmonized SUV within the EANM EARL accreditation program: software approach versus EARL-compliant reconstruction. *Ann Nucl Med.* 2017;31:125–134.
39. Nakajo M, Jinguji M, Aoki M, Tani A, Sato M, Yoshiura T. The clinical value of texture analysis of dual-time-point ^{18}F-FDG-PET/CT imaging to differentiate between ^{18}F-FDG-avid benign and malignant pulmonary lesions. *Eur Radiol.* 2020;30:1759–1769.
40. Chen S, Harmon S, Perk T, et al. Diagnostic classification of solitary pulmonary nodules using dual time ^{18}F-FDG PET/CT image texture features in granuloma-endemic regions. *Sci Rep.* 2017;7:9370.
41. Noortman WA, Vriens D, Slump CH, et al. Adding the temporal domain to PET radiomic features. *PLoS One.* 2020;15:e0239438.
42. Panin VY, Kehren F, Michel C, Casey M. Fully 3-D PET reconstruction with system matrix derived from point source measurements. *IEEE Trans Med Imaging.* 2006;25:907–921.
43. Armstrong IS, Kelly MD, Williams HA, Matthews JC. Impact of point spread function modelling and time of flight on FDG uptake measurements in lung lesions using alternative filtering strategies. *EJNMMI Phys.* 2014;1:99.
44. Boellaard R, Delgado-Bolton R, Oyen WJG, et al. FDG PET/CT: EANM procedure guidelines for tumour imaging—version 2.0. *Eur J Nucl Med Mol Imaging.* 2015;42:328–354.
45. Nioche C, Orlhac F, Boughdad S, et al. LIFEx: a freeware for radiomic feature calculation in multimodality imaging to accelerate advances in the characterization of tumor heterogeneity. *Cancer Res.* 2018;78:4786–4789.
46. Orlhac F, Soussan M, Chouahnia K, Martinod E, Buvat I. ^{18}F-FDG PET-derived textural indices reflect tissue-specific uptake pattern in non-small cell lung cancer. *PLoS One.* 2015;10:e0145063.
47. Zwanenburg A, Vallières M, Abdalah MA, et al. The image biomarker standardization initiative: standardized quantitative radiomics for high-throughput image-based phenotyping. *Radiology.* 2020;295:328–338.
48. Product. LIFEx website. https://www.lifexsoft.org/index.php/product. Accessed March 22, 2022.
49. Lovat E, Siddique M, Goh V, Ferner RE, Cook GJR, Warbey VS. The effect of post-injection ^{18}F-FDG PET scanning time on texture analysis of peripheral nerve sheath tumours in neurofibromatosis-1. *EJNMMI Res.* 2017;7:35.
50. Lowe VJ, DeLong DM, Hoffman JM, Coleman RE. Optimum scanning protocol for FDG-PET evaluation of pulmonary malignancy. *Lung Cancer.* 1995;36:883–887.
51. Boellaard R. Standards for PET image acquisition and quantitative data analysis. *J Nucl Med.* 2009;50(suppl 1):11S–20S.
52. Garcia-Vicente AM, Molina D, Pérez-Beteta J, et al. Textural features and SUV-based variables assessed by dual time point ^{18}F-FDG PET/CT in locally advanced breast cancer. *Ann Nucl Med.* 2017;31:726–735.

Predicting the Outcome of Epilepsy Surgery by Covariance Pattern Analysis of Ictal Perfusion SPECT

Jila Taherpour[1], Mariam Jaber[1], Berthold Voges[2], Ivayla Apostolova[1], Thomas Sauvigny[3], Patrick M. House[2], Michael Lanz[2], Matthias Lindenau[4], Susanne Klutmann[1], Tobias Martens[5], Stefan Stodieck[2], and Ralph Buchert[1]

[1]Department of Diagnostic and Interventional Radiology and Nuclear Medicine, University Medical Center Hamburg-Eppendorf, Hamburg, Germany; [2]Department of Neurology and Epileptology, Protestant Hospital Alsterdorf, Hamburg, Germany; [3]Department of Neurosurgery, University Medical Center Hamburg-Eppendorf, Hamburg, Germany; [4]Medical Practice Bredow & Partner, Neurology, Hamburg, Germany; and [5]Department of Neurosurgery, Medical Center Asklepios St. Georg, Hamburg, Germany

Previous studies on the utility of specific perfusion patterns in ictal brain perfusion SPECT for predicting the outcome of temporal lobe epilepsy surgery used qualitative visual pattern classification, semiquantitative region-of-interest analysis, or conventional univariate voxel-based testing, which are limited by intra- and interrater variability or low sensitivity to capture functional interactions among brain regions. The present study performed covariance pattern analysis of ictal perfusion SPECT using the scaled subprofile model for unbiased identification of predictive covariance patterns. **Methods:** The study retrospectively included 18 responders to temporal lobe epilepsy surgery (Engel I-A at 12 mo follow-up) and 18 nonresponders (≥Engel I-B). Ictal SPECT images were analyzed with the scaled subprofile model masked to group membership for unbiased identification of the 16 covariance patterns explaining the highest proportion of variance in the whole dataset. Individual expression scores of the covariance patterns were evaluated for predicting seizure freedom after temporal lobe surgery by receiver-operating-characteristic analysis. Kaplan–Meier analysis including all available follow-up data (up to 60 mo after surgery) was also performed. **Results:** Among the 16 covariance patterns only 1 showed a different expression between responders and nonresponders ($P = 0.03$). This favorable ictal perfusion pattern resembled the typical ictal perfusion pattern in temporomesial epilepsy. The expression score of the pattern provided an area of 0.744 (95% CI, 0.577–0.911, $P = 0.004$) under the receiver-operating-characteristic curve. Kaplan–Meier analysis revealed a statistical trend toward longer seizure freedom in patients with positive expression score ($P = 0.06$). The median estimated seizure-free time was 48 mo in patients with positive expression score versus 6 mo in patients with negative expression score. **Conclusion:** The expression of the favorable ictal perfusion pattern identified by covariance analysis of ictal brain perfusion SPECT provides independent (from demographic and clinical variables) information for the prediction of seizure freedom after temporal lobe epilepsy surgery. The expression of this pattern is easily computed for new ictal SPECT images and, therefore, might be used to support the decision for or against temporal lobe surgery in clinical patient care.

Key Words: epilepsy; surgery; SPECT; ictal; covariance analysis

J Nucl Med 2022; 63:925–930
DOI: 10.2967/jnumed.121.262702

Temporal lobe epilepsy (TLE) surgery fails to provide a major reduction in seizure frequency in a nonnegligible fraction of patients with pharmacotherapy-refractory TLE (*1*). Furthermore, postoperative morbidity including psychiatric disorders, visual field defects, and cognitive impairment is observed in about 20% of the patients (*2*). Thus, there is a clinical need for additional preoperative predictors of surgical outcome to support the decision for or against TLE surgery in individual patients.

Ictal brain SPECT with ^{99m}Tc-labeled hexamethyl-propyleneamine oxime (^{99m}Tc-HMPAO) or ethyl cysteinate dimer (^{99m}Tc-ECD) is widely used to identify the seizure onset zone (SOZ) by regional hyperperfusion during the seizure. In patients with mesial TLE, ictal hyperperfusion typically involves the anteromesial temporal region as well as the anterolateral and inferior temporal neocortex (*3,4*). Other patterns with posterior extension of the ipsilateral temporal hyperperfusion, bitemporal hyperperfusion, more limited hyperperfusion in the ipsilateral temporal lobe or atypical patterns with hyperperfusion predominantly in other than anterotemporal brain regions have also been described in mesial TLE (*3,4*).

Previous studies on the utility of specific perfusion patterns in ictal brain perfusion SPECT for predicting the outcome of epilepsy surgery used qualitative visual classification of the ictal perfusion pattern (*4*), semiquantitative region-of-interest analysis (*4*), or conventional voxel-based testing based on applying the same univariate statistical test and the same significance threshold at each single voxel of the SPECT image (*5–7*). Visual classification of ictal perfusion patterns is limited by intra- and interrater variability (*8*). The same is true for conventional voxel-based testing, because the interpretation of the resulting statistical maps is usually left to the physician. Furthermore, relevant information in the ictal SPECT image might be missed by region-of-interest–based and conventional voxel-based analysis when it does not reach the predefined significance threshold.

Against this background, the present study used scaled subprofile model principal component analysis (SSM-PCA) (*9–14*) for unbiased identification of covariance patterns for prediction of TLE surgery outcome from ictal perfusion SPECT.

MATERIALS AND METHODS

Patients for Covariance Pattern Analysis

We searched our database according to the following inclusion (I) criteria: (I1) ictal SPECT with ^{99m}Tc-ECD or ^{99m}Tc-HMPAO for presurgical evaluation, (I2) age at ictal SPECT ≥ 16 y, (I3) ictal tracer injection during a partial seizure, (I4) selective amygdalo-hippocampectomy or

Received Jun. 7, 2021; revision accepted Sep. 9, 2021.
For correspondence or reprints, contact Ralph Buchert (r.buchert@uke.de).
Published online Sep. 30, 2021.

anteromedial temporal resection after ictal SPECT, and (I5) follow-up ≥ 12 mo after surgery. These criteria were fulfilled by 65 patients. From these, patients were excluded if they met one or more of the following exclusion (E) criteria: (E1) brain surgery before ictal SPECT or any other regional defect (n = 8), (E2) no clear correlate of the seizure at ictal tracer injection in electroencephalography (EEG) (n = 3), (E3) tracer injection during a secondarily generalized partial seizure (n = 10), (E4) latency of the tracer injection after electrical seizure onset > 60 s (n = 5), (E5) electrical seizure duration after tracer injection < 20 s (n = 8), and (E6) strong head motion during SPECT (n = 1). This resulted in the exclusion of 29 patients. The remaining 36 patients were included in the covariance pattern analysis (44% women; median age at ictal SPECT, 41.8 y; interquartile range, 24.9–47.7 y). Ictal SPECT was performed with ^{99m}Tc-ECD in 27 (75%) of these patients. ^{99m}Tc-HMPAO was used in the remaining 9 patients (25%).

The need for written informed consent was waived by the ethics review board of the general medical council of the state of Hamburg, Germany.

Perfusion SPECT

Tracer was injected during video-EEG monitoring at all ictal injections. SPECT imaging of 40-min duration was performed with a double-head camera (Symbia T2 or E.CAM; Siemens) equipped with fanbeam or low-energy high-resolution collimators and angular steps of 2.8° or 3.0°. Projection data were retrieved from the archive for consistent retrospective image reconstruction: filtered backprojection with Butterworth filter of order 5 and cutoff 1.5 cycles/cm into transaxial SPECT slices with 3.9-mm cubic voxels, Chang attenuation correction (μ = 0.12/cm), no scatter correction, and postfiltering with an isotropic gaussian kernel with 8 mm full width at half maximum.

Surgery

Twenty-six patients (14 responders, 12 nonresponders) underwent selective amygdalo-hippocampectomy, and the remaining 10 patients (4 responders, 6 nonresponders) were submitted to anteromedial temporal resection. Surgery was performed in the right hemisphere in 24 (67%) patients and in the left hemisphere in 12 (33%) patients.

Selective amygdalo-hippocampectomy was performed using a frontobasolateral transsylvian approach (*15*). After getting access to the M1 complex of the middle cerebral artery and the temporal branches, the mesial temporal structures were identified and subpial resection of the uncal region and amygdala was performed. The hippocampal formation was removed en bloc to the level of the midbrain tectum and submitted to neuropathologic examination.

The anteromedial temporal resection was conducted via temporal craniotomy. The posterior limit of the neocortical resection was defined at about 5 cm from the temporal pole on the nondominant hemisphere and 4 cm on the dominant hemisphere. The temporal pole was removed en block. Subsequently, the temporomesial structures (amygdala, hippocampus and parahippocampal gyrus) were removed to the level of the midbrain tectum. Temporal pole and hippocampal formation were submitted to neuropathologic examination.

Follow-up

Postsurgical follow-up included at least 1 outpatient visit 3–6 mo after surgery and at least 1 inpatient visit 12 mo after surgery. The 12-mo inpatient visit comprised detailed medical history, brain MRI, neuropsychologic examination, and 3- to 4-d video-EEG monitoring. On the basis of the complete data collected at these visits, the outcome at 12 mo after surgery was categorized retrospectively according to the Engel Epilepsy Surgery Outcome Scale (*16*). The results are summarized in Figure 1. For the covariance pattern analysis, the outcome at 12 mo was dichotomized: patients with Engel I-A were considered responders (n = 18); all patients with Engel I-B or worse were considered nonresponders (n = 18).

Clinical follow-up at 24, 36, 48, and 60 mo was available in 14, 11, 11, and 10 responders, respectively (proportion of patients with Engel I-A: 86%, 82%, 73%, and 70%). Clinical follow-up at 24, 36, 48, and 60 mo was available in 15, 11, 9, and 6 nonresponders (all Engel I-B or worse at all time points).

Image Preprocessing

Tracer-specific normal databases and templates in the Montreal Neurologic Institute (MNI) space were generated as described in the supplemental materials (available at http://jnm.snmjournals.org).

Then, all individual SPECT images, including the 36 ictal SPECT and the 48 normal SPECT from the normal databases, were stereotactically normalized (affine) to MNI space using the statistical parametric mapping software package (SPM12; The Wellcome Centre for Human Neuroimaging, UCL Queen Square Institute of Neurology) and the corresponding custom-made SPECT template. Stereotactically normalized SPECT images were filtered with an isotropic gaussian kernel with 15 mm full width at half maximum and then scaled to the individual mean tracer uptake of the filtered image in a cerebrum parenchyma mask predefined in MNI space.

Voxelwise mean, SD, and coefficient of variance were computed from the stereotactically normalized, filtered, and scaled SPECT images, separately for the ^{99m}Tc-ECD and for the ^{99m}Tc-HMPAO normal database.

Individual stereotactically normalized, filtered, and scaled ictal SPECT images were transformed voxelwise to z scores using the following formula: z score = (individual tracer uptake – M)/SD, where M and SD are the mean value and the SD of normal ^{99m}Tc-ECD or normal ^{99m}Tc-HMPAO uptake (depending on the tracer used in this subject) in the considered voxel.

Finally, ictal z score images of the subjects in whom TLE surgery was performed in the left hemisphere were left–right flipped at the midsagittal plane so that the right side was the site of surgery in all ictal z score images.

Visual SPECT Interpretation

Visual interpretation of the ictal SPECT images was performed independently by 2 readers masked to all other data. The readers first lateralized the SOZ on the basis of regional hyperperfusion (left, right, both hemispheres, no hyperperfusion) and then localized the SOZ (temporal, frontal, parietal, occipital). In the case of temporal hyperperfusion,

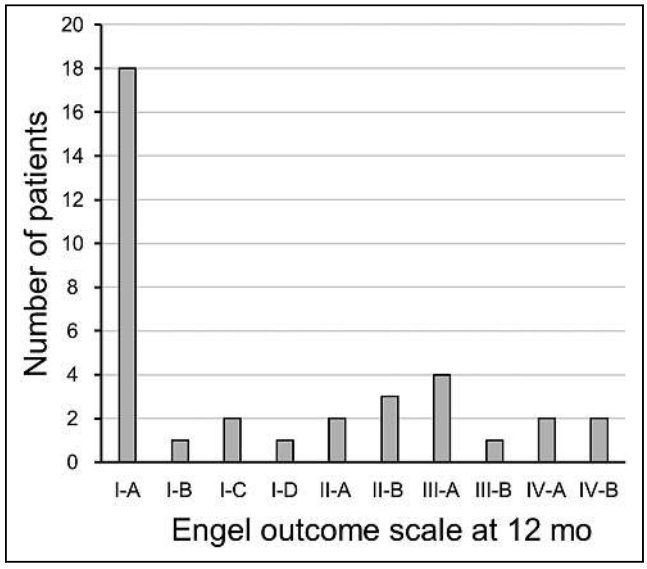

FIGURE 1. Engel Epilepsy Surgery Outcome Scale at 12 mo after TLE surgery. Patients with Engel I-A at 12 mo were considered responders; all other patients were considered nonresponders.

additional hyperperfusion in ipsilateral insular cortex, basal ganglia, and thalamus was considered to be a propagation effect that supports ipsilateral temporal seizure onset (*17*). Each reader interpreted all images twice. Images with discrepant interpretation with respect to lateralization or localization in the 2 reading sessions were assessed a third time to obtain an intrareader consensus. Finally, images with discrepant intrareader consensus with respect to lateralization or localization between the 2 readers were assessed in a common reading session of the 2 readers to obtain an interreader consensus.

Conventional Univariate Voxel-Based Analysis

z score maps of ictal SPECT were compared voxelwise between responders and nonresponders using the unpaired *t* test model implemented in SPM12. The latency of the tracer injection after electrical seizure onset in EEG was considered as a covariate. The significance level was set at uncorrected $P = 0.005$. Minimum cluster size was 1 mL.

Identification of a Prognostic Covariance Pattern Analysis

Spatial covariance analysis of the ictal *z* score images was performed with SSM-PCA implemented in the freely available Scan Analysis and Visualization Processor software package (version ScAnVP7.0w) (*10*). The covariance analysis was restricted to the same cerebrum parenchyma mask that was used for intensity scaling in order to avoid truncation artifacts. The ictal *z* score maps were not log-transformed for SSM-PCA in order to avoid truncation of negative *z* scores. Negative *z* scores indicate regional reduction of tracer uptake, which represents a relevant component of ictal perfusion patterns.

SSM-PCA with log-transformation was used to assess differences in normal cerebral uptake between ^{99m}Tc-ECD and ^{99m}Tc-HMPAO in the corresponding normal databases.

Statistical Analysis

Proportions are given as percentage and were compared between 2 groups using the Fisher exact test. Nominal variables with more than 2 possible values are given as percentages and were compared between groups using Pearson χ^2 test. Continuous variables are given as median and interquartile range and were compared using the nonparametric Mann–Whitney *U* test. All tests were 2-sided. A *P* value of less than 0.05 was considered significant.

The individual expression scores of the 16 covariance patterns identified by SSM-PCA in the ictal *z* score images were compared between responders and nonresponders using the unpaired *t* test.

The prognostic power of the expression score of a given covariance pattern in ictal *z* score images was assessed by receiver-operating-characteristic (ROC) analysis. In addition, the expression score was dichotomized (≤ 0 vs. >0) and then tested as a factor in Kaplan–Meier analysis of seizure freedom (Engel I-A), taking into account the total individual follow-up period. The log-rank test was used to compare the difference in seizure-free time for statistical significance.

Data Availability

All covariance patterns identified in this study are available on request. Custom-made ^{99m}Tc-ECD and ^{99m}Tc-HMPAO templates as well as voxelwise mean and SD images of the ^{99m}Tc-ECD and ^{99m}Tc-HMPAO normal databases are also available on request.

RESULTS

Demographic, clinical, ictal SPECT, and surgery data of the 36 patients included in the SSM-PCA are summarized in Table 1. Responders and nonresponders did not differ with respect to sex, age at ictal SPECT, age at first seizure, duration of disease, seizure frequency, and proportion of patients with impairment of awareness in most seizures. Responders and nonresponders also did not differ with respect to lateralization (relative to TLE surgery) of seizure semiology, interictal EEG, ictal EEG, and MRI before ictal SPECT (Table 1). They also did not differ with respect to delay of surgery after ictal SPECT, side of resection, and neuropathology of the surgical specimen (Table 1). The proportion of patients in whom ictal SPECT was performed with ^{99m}Tc-ECD was higher among the responders (94% vs. 56%, $P = 0.02$). The latency of tracer injection relative to the electrical seizure start was shorter in the responders (median, 30 vs. 40 s, $P = 0.02$). Tracer dose for ictal SPECT and electrical duration of the seizure after tracer injection did not differ between responders and nonresponders.

^{99m}Tc-ECD and ^{99m}Tc-HMPAO SPECT templates generated from the normal databases are shown in Supplemental Figure 1A. The voxelwise coefficient of variance of the tracer uptake in the 2 normal databases is shown in Supplemental Figure 1B. The first covariance pattern obtained by SSM-PCA of the 48 SPECT of the normal databases (Supplemental Fig. 2) explained 28.2% of the total variance and was the only pattern with significantly different expression between the 2 tracer-specific normal databases ($P < 0.001$; all other patterns: $P \geq 0.15$).

Visual interpretation of the ictal SPECT identified the ipsilateral temporal lobe as SOZ in 12 (67%) responders and in 14 (78%) nonresponders. Visual interpretation localized the SOZ in the contralateral temporal lobe in 2 responders (11%). Bilateral hyperperfusion was described in 1 responder (6%). None of the nonresponders showed more pronounced contralateral or bilateral temporal hyperperfusion. The SOZ was localized to the temporal lobe in all patients with ictal hyperperfusion. No regional hyperperfusion was detected in 3 (17%) responders and in 4 (22%) nonresponders. The differences in the visual lateralization of ictal SPECT between responders and nonresponders were not significant ($P = 0.35$).

The mean *z* score maps of ictal SPECT are shown in Figure 2. The statistical parametric maps obtained by voxel-based statistical comparison of the *z* score maps between responders and nonresponders revealed higher *z* scores (more pronounced hyperperfusion) in responders in the contralateral (relative to resection) temporal and occipital lobe (Fig. 3A). There was a small cluster of lower *z* scores (more pronounced hypoperfusion) in responders in the mesial frontal lobe (mainly ipsilateral, Fig. 3A).

Among the 16 covariance patterns determined by SSM-PCA in the 36 ictal SPECT only 1, the favorable ictal perfusion pattern (FIPP), showed different expression between responders and nonresponders ($P = 0.03$, Fig. 3B; all other patterns: $P \geq 0.10$). The individual expression score of the FIPP provided an area of 0.744 (95% CI, 0.577–0.911; $P = 0.004$) under the ROC curve for the differentiation of responders from nonresponders (Fig. 4A). Kaplan–Meier analysis revealed a statistical trend toward longer seizure freedom in patients with positive FIPP expression score than patients with negative FIPP expression score ($P = 0.06$, Fig. 4B). The median estimated seizure-free time was 48 mo (positive expression score) versus 6 mo (negative expression score).

DISCUSSION

This study used SSM-PCA to identify a covariance pattern (FIPP) in ictal brain perfusion SPECT whose expression is predictive of seizure freedom after TLE surgery. The FIPP expression score is easily computed for new ictal SPECT images to support their interpretation with respect to the chance of the patient to become seizure-free by TLE surgery. The computation is fully automatic and, therefore, does not require special expertise, in contrast to visual interpretation of ictal SPECT images.

TABLE 1
Demographic, Clinical, SPECT, and Surgical Data

Data	Responder*	Nonresponder*	$P^{\dagger}$
Number of patients	18	18	
Sex (% females)	44	44	1.00
Age at ictal SPECT (y)	43 [28–49]	34 [24–48]	0.24
Age at first seizure (y)	14 [6–23]	12 [4–23]	0.61
Duration of disease at SPECT (y)	22 [15–34]	21 [11–33]	0.56
Mean seizure frequency in last 12 mo before ictal SPECT (seizures/mo)	5 [3–21] (n = 15)	14 [5–23] (n = 16)	0.36
With impairment of awareness in most seizures during the last 12 mo (%)	77 (n = 13)	79 (n = 14)	1.00
Lateralization of seizure semiology: ipsilateral to resection/contralateral/both/no (%)	93/7/0/0 (n = 14)	90/0/0/10 (n = 10)	0.35
Lateralization of MRI: ipsilateral to resection/contralateral/both/no (%)	94/0/0/6 (n = 18)	82/0/6/12 (n = 17)	0.45
Lateralization of ictal EEG before ictal SPECT: ipsilateral to resection/contralateral/both/no (%)	88/6/6/0 (n = 16)	88/0/0/12 (n = 17)	0.26
Lateralization of interictal EEG before ictal SPECT: ipsilateral to resection/contralateral/both/no (%)	83/6/11/0	67/0/22/11	0.26
Tracer of ictal SPECT (% ^{99m}Tc-ECD)	94	56	0.02
Tracer activity administered for ictal SPECT (MBq)	524 [479–639]	578 [501–632]	0.34
Latency of tracer injection to seizure start in EEG (s)	30 [25–35]	40 [30–49]	0.02
Seizure duration after injection according to EEG (s)	74 [43–147]	57 [31–106]	0.28
Delay of surgery after ictal SPECT (mo)	10 [4–27]	6 [2–24]	0.70
Side of TLE surgery (% right)	67	67	1.00
Neuropathology of surgical specimen: normal/sclerosis/mass lesion/focal cortical dysplasia	13/75/6/6 (n = 16)	17/67/17/0 (n = 12)	0.66

*Continuous variables are given as median, with interquartile range in brackets. If a variable was not available in all patients, the number of patients for that variable is given in parentheses.
$^{\dagger}P$ values are not corrected for multiple testing.

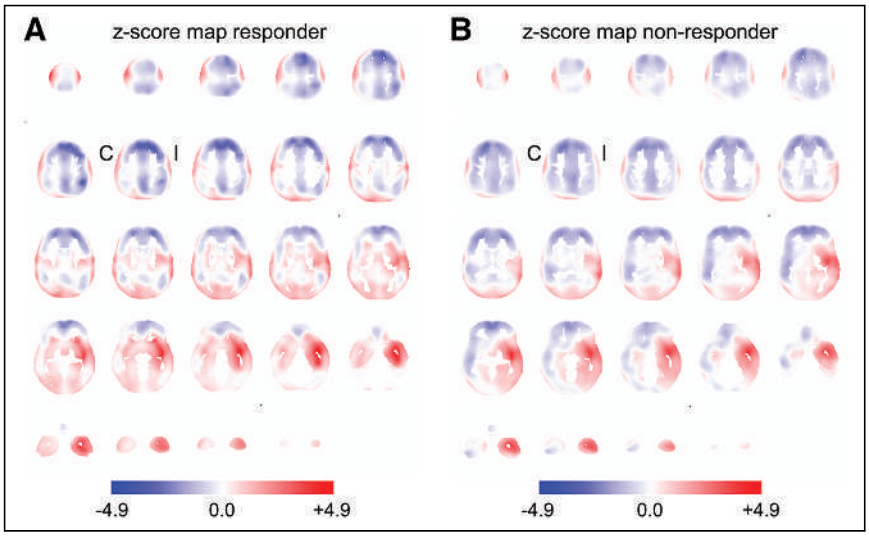

FIGURE 2. Mean z score maps of ictal SPECT in the 18 responders (A) and 18 nonresponders (B) in MNI space. Positive z scores (red) indicate increased perfusion (relative to custom-made normal databases); negative z scores (blue) indicate reduced perfusion. C = contralateral to TLE surgery; I = ipsilateral to TLE surgery.

SSM-PCA is stable with respect to variable image characteristics associated with different scanners for image acquisition or different software for image preprocessing (*18*), simplifying widespread clinical use. We hypothesize that the FIPP identified in this monosite study is useful also for other sites.

The FIPP comprises more pronounced ictal hyperperfusion in the anterior part of the ipsilateral (to resection) temporal lobe, less pronounced posterior extension of the ictal hyperperfusion in the ipsilateral temporal lobe, hyperperfusion in the contralateral temporal lobe (less pronounced than ipsilateral), hypoperfusion in the precuneus/posterior cingulate cortex area and in the ipsilateral parietotemporal region, and more pronounced hypoperfusion in the anterior frontal lobe (Fig. 3B). The FIPP resembles the typical perfusion pattern during complex partial seizures in patients with

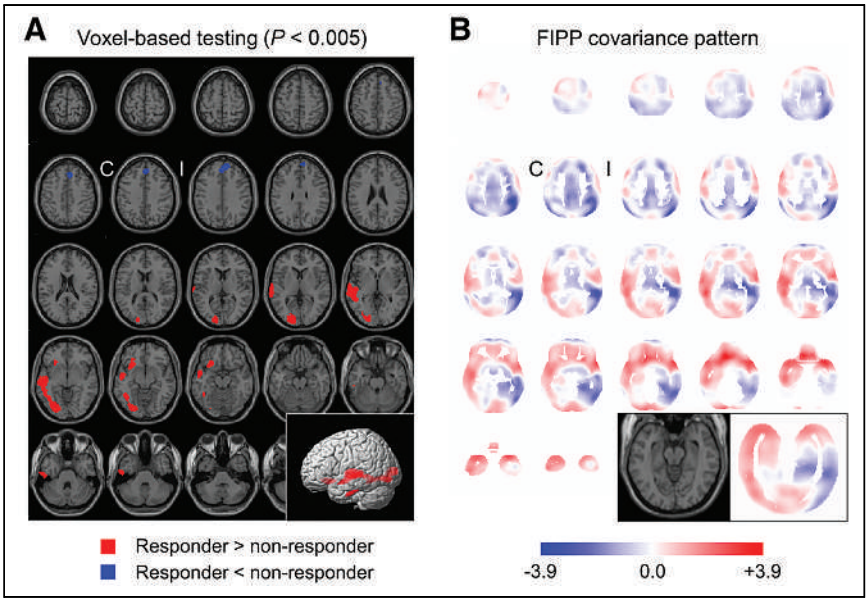

FIGURE 3. Statistical maps of hyperperfusion (red) and hypoperfusion (blue) obtained by conventional univariate voxel-based 1-sided *t* tests corrected for injection latency, thresholded at $P = 0.005$, and overlaid to the statistical parametric mapping (SPM) single-subject template (A). (B) FIPP. C = contralateral to TLE surgery; I = ipsilateral to TLE surgery.

mesial TLE (*4,17,19–21*). Pronounced ictal hyperperfusion in the anterior ipsilateral temporal lobe is the most consistent finding in ictal perfusion SPECT in mesial temporal epilepsy (*3,22*). The lack of this pointer is a known risk factor of worse TLE surgery outcome (*4*). Hyperperfusion beyond the ipsilateral mesial temporal lobe might be explained by seizure propagation (*23,24*) or intrinsic epileptogenicity of the hyperperfused areas beyond the mesial temporal lobe. The FIPP suggests that hyperperfusion in the contralateral temporal lobe is predictive of good outcome of TLE surgery and, therefore, most likely is due to seizure propagation via interhemispheric connections. A SPECT mirror image defined as ictal hyperperfusion contralateral to the seizure onset that is rather symmetric to the ipsilateral ictal hyperperfusion is observed in ≥50% of epilepsy patients (*25*). The SSM-PCA was masked not only to group membership (responders vs. nonresponders) but also to the results of visual interpretation and univariate voxel-based analysis. Thus, all images were handled equally by the SSM-PCA. In particular, no difference was made between ictal SPECT with or without mirror image. The aim of SSM-PCA is fully unbiased identification of the covariance patterns explaining the highest proportion of variance in the whole dataset reflecting between- and within-group differences with the same accuracy (*9*).

Ictal hyperperfusion was stronger in the contralateral than in the ipsilateral temporal lobe in 2 (11%) responders so that visual interpretation suggested the contralateral temporal lobe as SOZ (Supplemental Fig. 3). Both subjects were seizure-free for ≥36 mo after surgery. The FIPP expression score was borderline in both. Incorrect lateralization by visual interpretation of ictal perfusion SPECT in 5%–8% of patients with mesial-temporal epilepsy has been described previously (*4,25–27*).

None of the tested demographic, clinical, and surgical variables showed a statistically significant difference between the responders and the nonresponders in this study (Table 1). This suggests that the FIPP expression score provides independent prognostic information beyond these variables.

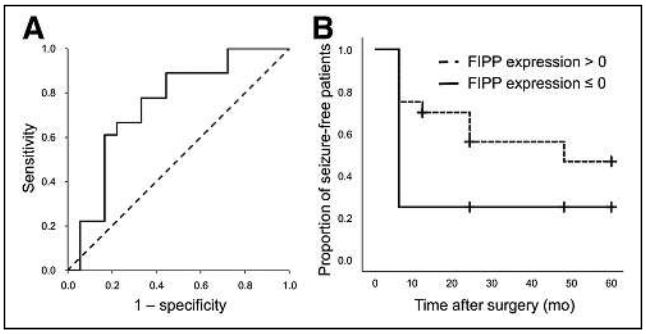

FIGURE 4. ROC analysis of FIPP expression score for identification of responders (A), and Kaplan–Meier analysis of patients with positive FIPP expression score versus patients with negative FIPP expression score (B).

In clinical routine, visual evaluation and univariate voxel-based analysis of ictal perfusion SPECT are usually restricted to the localization of the SOZ. Classification of ictal perfusion patterns (beyond SOZ localization) for predicting surgery outcome is not common in clinical routine. On the other hand, the FIPP expression score alone is not useful for SOZ localization. Thus, visual analysis supported by univariate voxel-based analysis and SSM-PCA are complementary methods.

The following limitations of this study should be noted. First, the latency of tracer injection relative to the electrical seizure start differed between responders and nonresponders. Ictal perfusion patterns are dynamic and, therefore, depend on the injection time (*17*). To account for this, the latency of the tracer injection was considered as covariate in the conventional univariate voxel-based analysis, although the difference was rather small (median latency 10 s shorter in responders than nonresponders). The fact that the resulting statistical map (Fig. 3A) is compatible with the FIPP (Fig. 3B) suggests that a potential effect of the injection latency on the FIPP is small. Furthermore, variability of the *z* score maps associated with between-subject variability of the injection latency might have been captured by one (or more) covariance patterns without affecting the FIPP. Second, the FIPP was derived from *z* score images and therefore might not be applicable to SPECT uptake images. The transformation to *z* scores was used to allow pooling of ^{99m}Tc-ECD and ^{99m}Tc-HMPAO SPECT. SSM-PCA of the uptake images in the ^{99m}Tc-ECD subsample confirmed the major findings of SSM-PCA of the *z* score images in the whole sample (section "Identification of a prognostic covariance pattern in the ^{99m}Tc-ECD subsample" including Supplemental Table 1 and Supplemental Figs. 4 and 5). It also outperformed region-of-interest–based analyses (section "Region-of-interest based prediction in the ^{99m}Tc-ECD subsample" and Supplemental Fig. 6). SSM-PCA might also be applied directly to pooled uptake images, which probably would result in one (or more) covariance patterns covering the regional differences in tracer uptake between

^{99m}Tc-ECD and ^{99m}Tc-HMPAO. Third, rather restrictive eligibility criteria were used in this study. The use of the FIPP expression score should be restricted to ictal perfusion SPECT that fulfil the same criteria. For example, patients with brain surgery before ictal perfusion SPECT or any other major defect in tracer uptake (e.g., due to a stroke) should be excluded, because the defect might have a relevant impact on the FIPP expression score. Further studies should evaluate the FIPP expression score in independent patient samples and compare it with visual classification by experienced readers.

CONCLUSION

This study identified a covariance pattern in ictal perfusion SPECT whose expression provided independent information for the prediction of complete seizure freedom after TLE surgery. This favorable ictal perfusion pattern (FIPP) resembled the typical ictal perfusion pattern in mesial temporal epilepsy. The expression of the FIPP is easily computed for new ictal SPECT images and, therefore, might be used to support the decision for or against TLE surgery in clinical patient care.

DISCLOSURE

No potential conflict of interest relevant to this article was reported.

KEY POINTS

QUESTION: This study used the scaled subprofile model for unbiased identification of a covariance pattern in ictal brain perfusion SPECT for predicting the outcome of TLE surgery.

PERTINENT FINDINGS: The identified favorable ictal perfusion pattern resembled the typical ictal perfusion pattern in temporomesial epilepsy. The expression score of the pattern provided an area of 0.744 (95% CI, 0.577–0.911; $P = 0.004$) under the ROC curve for predicting seizure freedom 12 mo after surgery.

IMPLICATIONS FOR PATIENT CARE: The expression score of the favorable ictal perfusion pattern is easily computed automatically for new ictal SPECT images and, therefore, might be used to support the decision for or against TLE surgery in clinical patient care.

REFERENCES

1. West S, Nevitt SJ, Cotton J, et al. Surgery for epilepsy. *Cochrane Database Syst Rev.* 2019;6:CD010541.
2. Brotis AG, Giannis T, Kapsalaki E, Dardiotis E, Fountas KN. Complications after anterior temporal lobectomy for medically intractable epilepsy: a systematic review and meta-analysis. *Stereotact Funct Neurosurg.* 2019;97:69–82.
3. Ho SS, Berkovic SF, McKay WJ, Kalnins RM, Bladin PF. Temporal lobe epilepsy subtypes: differential patterns of cerebral perfusion on ictal SPECT. *Epilepsia.* 1996;37:788–795.
4. Ho SS, Newton MR, McIntosh AM, et al. Perfusion patterns during temporal lobe seizures: relationship to surgical outcome. *Brain.* 1997;120:1921–1928.
5. Apostolova I, Tast C, Wilke F, Lindenau M, Buchert R. Ictal perfusion SPECT in presurgical epilepsy diagnosis: prognostic value of perfusion pattern for outcome of amygdalohippocampectomy [abstract]. *J Nucl Med.* 2010;51 (suppl 2):1798.
6. Tast C. Ictal perfusion SPECT in presurgical evaluation of epilepsy: Exploratory analysis of perfusion patterns with regard to prognostic relevance [in German] [MD thesis]. Hamburg: Department of Nuclear Medicine, University Medical Center Hamburg-Eppendorf, University Hamburg; 2012.
7. Kazemi NJ, Worrell GA, Stead SM, et al. Ictal SPECT statistical parametric mapping in temporal lobe epilepsy surgery. *Neurology.* 2010;74:70–76.
8. Lee HW, Hong SB, Tae WS. Opposite ictal perfusion patterns of subtracted SPECT. Hyperperfusion and hypoperfusion. *Brain.* 2000;123:2150–2159.
9. Alexander GE, Moeller JR. Application of the scaled subprofile model to functional imaging in neuropsychiatric disorders: a principal component approach to modeling brain function in disease. *Hum Brain Mapp.* 1994;2:1–16.
10. Eidelberg D. Metabolic brain networks in neurodegenerative disorders: a functional imaging approach. *Trends Neurosci.* 2009;32:548–557.
11. Moeller JR, Strother SC, Sidtis JJ, Rottenberg DA. Scaled subprofile model: a statistical approach to the analysis of functional patterns in positron emission tomographic data. *J Cereb Blood Flow Metab.* 1987;7:649–658.
12. Spetsieris P, Ma Y, Peng S, et al. Identification of disease-related spatial covariance patterns using neuroimaging data. *J Vis Exp.* 2013;76:e50319.
13. Spetsieris PG, Eidelberg D. Scaled subprofile modeling of resting state imaging data in Parkinson's disease: methodological issues. *Neuroimage.* 2011;54: 2899–2914.
14. Moeller JR, Strother SC. A regional covariance approach to the analysis of functional patterns in positron emission tomographic data. *J Cereb Blood Flow Metab.* 1991;11:A121–A135.
15. Yaşargil MG, Teddy PJ, Roth P. Selective amygdalo-hippocampectomy: operative anatomy and surgical technique. *Adv Tech Stand Neurosurg.* 1985;12:93–123.
16. Engel J. Outcome with respect to epileptic seizures. In: Engel J, ed. Surgical Treatment of the Epilepsies. New York: Raven Press; 1987:553–571.
17. Dupont P, Zaknun JJ, Maes A, et al. Dynamic perfusion patterns in temporal lobe epilepsy. *Eur J Nucl Med Mol Imaging.* 2009;36:823–830.
18. Peng S, Ma Y, Spetsieris PG, et al. Characterization of disease-related covariance topographies with SSMPCA toolbox: effects of spatial normalization and PET scanners. *Hum Brain Mapp.* 2014;35:1801–1814.
19. Blumenfeld H, McNally KA, Vanderhill SD, et al. Positive and negative network correlations in temporal lobe epilepsy. *Cereb Cortex.* 2004;14:892–902.
20. Tae WS, Joo EY, Kim JH, et al. Cerebral perfusion changes in mesial temporal lobe epilepsy: SPM analysis of ictal and interictal SPECT. *Neuroimage.* 2005;24: 101–110.
21. Van Paesschen W, Dupont P, Van Driel G, Van Billoen H, Maes A. SPECT perfusion changes during complex partial seizures in patients with hippocampal sclerosis. *Brain.* 2003;126:1103–1111.
22. Kim BJ, Hong SB, Seo DW. Differences in ictal hyperperfusion of limbic-related structures between mesial temporal and neocortical epilepsy. *Epilepsy Res.* 2008; 81:167–175.
23. Connors BW, Pinto DJ, Telfeian AE. Local pathways of seizure propagation in neocortex. *Int Rev Neurobiol.* 2001;45:527–546.
24. Jenssen S, Roberts CM, Gracely EJ, Dlugos DJ, Sperling MR. Focal seizure propagation in the intracranial EEG. *Epilepsy Res.* 2011;93:25–32.
25. Huberfeld G, Habert MO, Clemenceau S, Maksud P, Baulac M, Adam C. Ictal brain hyperperfusion contralateral to seizure onset: the SPECT mirror image. *Epilepsia.* 2006;47:123–133.
26. Lee SK, Lee SH, Kim SK, Lee DS, Kim H. The clinical usefulness of ictal SPECT in temporal lobe epilepsy: the lateralization of seizure focus and correlation with EEG. *Epilepsia.* 2000;41:955–962.
27. Wichert-Ana L, Velasco TR, Terra-Bustamante VC, et al. Typical and atypical perfusion patterns in periictal SPECT of patients with unilateral temporal lobe epilepsy. *Epilepsia.* 2001;42:660–666.

Relationship Between ^{18}F-Flortaucipir Uptake and Histologic Lesion Types in 4-Repeat Tauopathies

Keith A. Josephs[1], Nirubol Tosakulwong[2], Stephen D. Weigand[2], Marina Buciuc[1], Val J. Lowe[3], Dennis W. Dickson[4], and Jennifer L. Whitwell[3]

[1]*Department of Neurology, Mayo Clinic, Rochester, Minnesota;* [2]*Department of Health Sciences Research, Mayo Clinic, Rochester, Minnesota;* [3]*Department of Radiology, Mayo Clinic, Rochester, Minnesota; and* [4]*Department of Neuroscience, Mayo Clinic, Rochester, Minnesota*

Progressive supranuclear palsy (PSP) and corticobasal degeneration (CBD) are 4-repeat (4R) tauopathies with overlapping, but also morphologically distinct, tau immunoreactive lesions that vary in count by brain region. ^{18}F-flortaucipir PET uptake has been reported to correlate with overall tau burden, and—in 1 CBD case—to have greater affinity to threads than tangles. We determined whether ^{18}F-flortaucipir uptake is associated with histologic lesion type in 4R tauopathies. **Methods:** We performed semiquantitative regional lesion counts on pretangles/neurofibrillary tangles, threads, oligodendroglial coiled bodies, tufted astrocytes, and astrocytic plaques in 29 cases of autopsied 4R tauopathy (PSP, 16; CBD, 13). Regression models were used for statistical analyses. **Results:** ^{18}F-flortaucipir uptake marginally correlated with threads in the precentral cortex ($P = 0.04$) and with astrocytic lesions in the red nucleus ($P = 0.05$). **Conclusion:** The findings do not support ^{18}F-flortaucipir's having differential affinity to any 4R tau lesion type.

Key Words: progressive supranuclear palsy; corticobasal degeneration; PET; pathology; AV-1451

J Nucl Med 2022; 63:931–935
DOI: 10.2967/jnumed.121.262685

Progressive supranuclear palsy (PSP) and corticobasal degeneration (CBD) are 4-repeat (4R) tauopathies that are pathologically characterized by overlapping lesion distributions and morphologies, as well as distinct tau immunoreactive lesions that vary in count (amount), depending on which brain region is assessed (*1,2*). Both PSP and CBD are characterized by the presence of pretangles/neurofibrillary tangles (neuronal), oligodendroglial coiled bodies (glial), and threads (neuronal > glial), whereas PSP has only tufted astrocytes (glial) and CBD has only astrocytic plaques (glial) (*1,2*). CBD has a predominantly corticostriatal distribution of lesion burden with less involvement of brain stem regions, whereas PSP has a predominantly brain stem distribution of lesion burden.

^{18}F-flortaucipir (also known as ^{18}F-Av-1451 and ^{18}F-T807) is a small indole ligand that is made with a radioactive fluorine isotope that robustly binds to paired helical filament (3R + 4R) tau that occurs in Alzheimer disease brains (*3,4*). Therefore, ^{18}F-flortaucipir is considered an antemortem biomarker for visualizing underlying paired helical filament tau in Alzheimer disease. Regional ^{18}F-flortaucipir PET uptake has been described in clinical syndromes suspected to have underlying 4R tau (*5*) and in a few autopsied cases of 4R tauopathies where uptake was reported to correlate with histopathologic tau lesion burden (*6,7*). In these individual cases, a correlation was identified by assessing the relationship between ^{18}F-flortaucipir uptake across multiple brain regions and histopathologic tau lesion count, whereby count was treated as a single variable combining all lesion types. ^{18}F-flortaucipir uptake has been shown to have greater affinity for threads than for tangles, again across multiple brain regions, in a single CBD case (*7*). More recently, in an autopsied case series we found correlations between ^{18}F-flortaucipir and histologic tau to be selective and limited to only a few brain regions, particularly the red nucleus of the midbrain (*8*). We did not assess lesion type, however.

Given these findings, we aimed to investigate in a relatively large autopsy-confirmed cohort of PSP and CBD cases with antemortem ^{18}F-flortaucipir whether ligand uptake does indeed show evidence of differential affinity for threads and, if so, whether such a relationship would be region-specific or whether different regions would show different lesion affinities. We hypothesize that ^{18}F-flortaucipir uptake would correlate to overall tau burden in the red nucleus but not to any single specific lesion since all lesion types are represented in the red nucleus in CBD or PSP.

MATERIALS AND METHODS

Participant Cohort

All participants were prospectively recruited by the Neurodegenerative Research Group at Mayo Clinic, Minnesota, as part of a National Institutes of Health–funded grant and met 2 inclusion criteria: completion of antemortem volumetric head MRI, ^{18}F-flortaucipir PET, and Pittsburgh compound B PET; and a brain autopsy with a pathologic diagnosis of PSP or CBD between April 7, 2016, and April 6, 2021.

The study was approved by the Mayo Clinic Institutional Review Board, and all patients gave written informed consent to participate in the study.

Neuropathologic Evaluation and Diagnosis

All patients had a standardized neuropathologic evaluation in accordance with accepted published methodologies (*9*), including immunohistochemistry to detect 4R tau immunoreactive lesions using an antibody to phospho-tau (CP13; 1:1,000; IgG1 to phospho-serine 202, gift from the late Peter Davies, Feinstein Institute). PSP and CBD pathologic diagnoses were rendered according to published criteria

Received Jul. 12, 2021; revision accepted Sep. 21, 2021.
For correspondence or reprints, contact Keith A. Josephs (josephs.keith@mayo.edu).
Published online Sep. 23, 2021.

(*1,2*). PSP was diagnosed if there were globose neurofibrillary tangles, tufted astrocytes, and oligodendroglial coiled bodies in cardinal nuclei (*2*), whereas CBD was diagnosed if there were balloon neurons, as well as tau-specific lesions of pretangles, astrocytic plaques, and threads in cardinal nuclei (*1*). Additional pathologic findings were documented as previously described (*8*).

Semiquantitative 4R Tau Lesion Count

We assessed the burden (lesion count) of tau-specific lesions with anti-CP13 antibodies and immunohistochemistry. Lesions were counted by a single neuropathologist in the cerebellar dentate, midbrain tegmentum, substantia nigra, red nucleus, subthalamic nucleus, ventral thalamus, globus pallidus, striatum, superior frontal cortex, and precentral (motor) cortex. For each of these 10 regions, we determined lesion count for pretangles/neurofibrillary tangles, coiled bodies, tufted astrocytes (PSP only), and astrocytic plaques (CBD only) (Fig. 1) scored using a semiquantitative 4-point scale as follows: 0, absent lesions; 1+, few lesions (1–3 per ×200 field); 2+, moderate number of lesions (4–6 per ×200 field); and 3+, frequent number of lesions (7 or more per ×200 field). The density of neuropil threads was also graded on the same 0–3 scale (Fig. 1). This semiquantitative scale was published in 2006, in an article that displays specific exemplars or representative images for each score, for 3 of the lesions analyzed in this study (*10*).

PET Analysis

All participants underwent a standardized MRI protocol at 3 T that included a magnetization-prepared rapid gradient-echo (MPRAGE) sequence. ^{18}F-flortaucipir and Pittsburgh compound B PET scans were acquired using a PET/CT scanner (Discovery MR750; GE Healthcare) (*11*). All MPRAGE scans were normalized to the Mayo Clinic Adult Lifespan Template and segmented via unified segmentation with Mayo Clinic Adult Lifespan Template priors or settings. ^{18}F-flortaucipir images were coregistered to the MPRAGE using 6°-of-freedom registration in SPM12. Region-level data were calculated for the MPRAGE-space ^{18}F-flortaucipir PET to allow for correlations with histopathology. Our analysis was performed on the hemisphere to match the hemisphere sampled at autopsy. To assess for correlations between ^{18}F-flortaucipir uptake and histology lesion counts, we selected regions of interest that matched the regions assessed at autopsy. The Mayo Clinic Adult Lifespan Template atlas was used to assess uptake in the superior frontal, motor cortex, thalamus, globus pallidus, and striatum; the Deep Brain Stimulation Intrinsic Template (*12*) atlas for uptake in the substantia nigra, subthalamic nucleus, and red nucleus; and an in-house–developed atlas for the midbrain and cerebellar dentate, as previously described (*5*). All regional uptake values were divided by median uptake in the cerebellar crus gray matter to calculate SUV ratio (SUVR). A 2-compartment partial-volume correction was performed (*13*). The analyses were also repeated using PET data without partial-volume correction. Regional volumes were also calculated from the MPRAGE for the same 10 regions to allow for the assessment of potential confounding effects due to atrophy. Global Pittsburgh compound B SUVRs were calculated as previously described (*14*) and converted to centiloid units as follows: centiloid = $100 \times [(-0.1620 + 0.9467 \times \text{global Pittsburgh compound B SUVR}) - 1.009]/1.067$ (*15*).

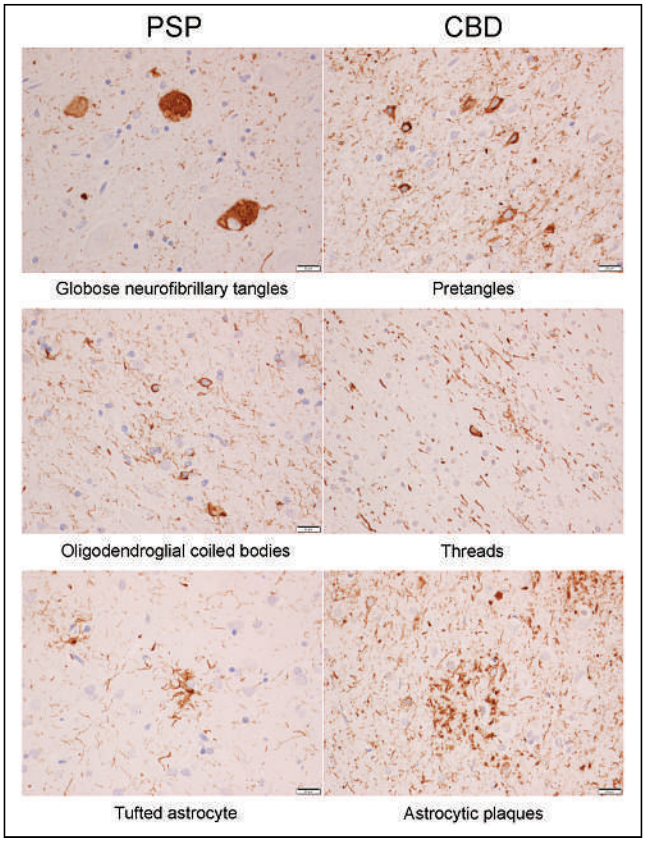

FIGURE 1. Different types of 4R tau lesions in PSP and CBD. Bar at lower right of each image indicates magnification level.

Statistical Analysis

For each region, we fit a linear regression model with log-transformed tau PET SUVR as the response and semiquantitative tau lesion burden scores as the predictors of interest. We incorporated the lesion count scores in several ways to have a more complete understanding of their effects. In our first approach, we included the scores for the 4 lesion types as 4 separate predictors in the model. In the second approach, we included the sum of the scores of the preneurofibrillary or neurofibrillary tangles plus tau threads as a first predictor and the sum of the scores of coiled bodies and astrocytic lesions as a second predictor. In the last approach, we summed all 4 semiquantitative scores to form a single numeric composite. We used the natural logarithm as the response in these models to reduce skew, maintain the regression assumption of constant variance, and allow an interpretation of the effect of tau burden in terms of percentage difference in PET uptake. All models included time from PET scan to death, age at death, and total intracranial volume as covariates.

RESULTS

We identified 29 cases that met our inclusion criteria of having had an antemortem ^{18}F-floratаucipir PET scan, died with autopsy, and had a pathologic diagnosis of PSP ($n = 16$) or CBD ($n = 13$). Table 1 shows the demographic characteristics of all 29, as well as differences between those with PSP and those with CBD. Those with CBD were younger by an average of 3 y at the time of the scan and were more likely to have aging-related tau astrogliopathy and argyrophilic grains disease at death as secondary pathologies.

The distribution of pathology across regions is shown in Figure 2. The only associations between tau pathology and ^{18}F-flortaucipir uptake that reached marginal significance were between ^{18}F-flortaucipir uptake and total lesion burden in the red nucleus ($P = 0.05$) and the precentral gyrus ($P = 0.04$) (Fig. 3). The association in the red nucleus was driven mainly by glial lesions, that is, astrocytic lesions, whereas the association in the precentral gyrus was driven by neuronal lesions, that is, threads. We also observed a trend for the subthalamic nucleus to show relationships like those of the red nucleus. The results remained the same using PET data without partial-volume

TABLE 1
Participant Characteristics

Characteristic	All (n = 29)	CBD (n = 13)	PSP (n = 16)	P
Female	12 (41%)	6 (46%)	6 (38%)	0.72
Education (y)	16 (12, 16)	14 (12, 16)	16 (14, 16)	0.29
Age at death (y)	74 (68, 78)	68 (60, 74)	78 (69, 80)	0.009
Age at tau PET (y)	70 (67, 77)	67 (58, 73)	76 (68, 78)	0.02
Tau PET to death (y)	1.3 (0.93, 2.43)	1.2 (0.93, 1.50)	1.4 (1.0, 2.5)	0.71
APOE carrier	3 (12%)	1 (9%)	2 (14%)	>0.99
22	0 (0%)	0 (0%)	0 (0%)	
23	5 (20%)	2 (18%)	3 (21%)	
33	17 (68%)	8 (73%)	9 (64%)	
34	2 (8%)	0 (0%)	2 (14%)	
44	1 (4%)	1 (9%)	0 (0%)	
NFT-positive	27 (93%)	12 (92%)	15 (94%)	>0.99
Braak NFT stage				0.18
1	4 (15%)	0 (0%)	4 (29%)	
2	5 (19%)	4 (33%)	1 (7%)	
3	9 (35%)	5 (42%)	4 (29%)	
4	8 (31%)	3 (25%)	5 (36%)	
5	0 (0%)	0 (0%)	0 (0%)	
6	0 (0%)	0 (0%)	0 (0%)	
ARTAG-positive	18 (64%)	11 (85%)	7 (47%)	0.05
Grain disease–positive	13 (46%)	7 (54%)	6 (40%)	0.71
MoCA	18 (10, 22)	12 (7, 20)	18 (16, 23)	0.18
UPDRS III	56 (44, 72)	53 (44, 72)	59 (47, 72)	0.61
PiB PET SUVRs	1.43 (1.37, 1.75)	1.41 (1.37, 1.44)	1.73 (1.37, 1.93)	0.30
aβ centiloid	17 (12, 46)	16 (12, 18)	44 (12, 61)	0.30

APOE = apolipoprotein E; NFT = neurofibrillary tangle; ARTAG = aging-related tau astrogliopathy; MoCA = Montreal Cognitive Assessment; UPDRS III = Movement Disorders Society sponsored revision of Unified Parkinson Disease Rating Scale; PiB = Pittsburgh compound B; Aβ = β-amyloid.

Data are median and interquartile range or number and percentage. P values are from Fisher exact test or Wilcoxon rank sum test when appropriate.

correction (Supplemental Fig. 1; supplemental materials are available at http://jnm.snmjournals.org). There was no evidence that volumes differed by ^{18}F-flortaucipir uptake or that volumes were smaller in those with low uptake (Fig. 4).

DISCUSSION

In this study of 29 cases of autopsied PSP and CBD (4R tauopathies) with antemortem ^{18}F-flortaucipir imaging, we found marginal associations between ligand uptake and histopathologic lesion count when combining all lesion types in 2 regions only, the red nucleus and the precentral gyrus. The association in the precentral gyrus appeared to be more related to threads, whereas in the red nucleus it appeared to be related to astrocytic lesions.

It is well known that ^{18}F-flortaucipir binds strongly to tau in Alzheimer disease but not to tau in PSP and CBD. Two hypotheses for this differential affinity include binding affinity's being related to the tau isoform or to the structure of the tau filaments. That is, differential binding of ^{18}F-flortaucipir is related to the ligand's having stronger affinity for tau enriched with mixed 3R + 4R tau isoforms than for tau enriched with predominantly 4R tau isoforms (*3*) or to ^{18}F-flortaucipir's binding better to paired helical filamentous tau that characterizes the tau filaments in Alzheimer disease (*3*). It is also possible, however, that differential binding is related to ultrastructural differences between the tau in Alzheimer disease and the tau in 4R tauopathies. A recent cryoelectron microscopic study and another study showed that 4R tauopathies have unique tau aggregated ultrastructural confirmations that differ from that of Alzheimer disease (*16,17*).

Neither threads nor astrocytic lesions in PSP and CBD are enriched with mixed 3R + 4R tau or are characterized by paired helical filaments. The marginal correlations identified in the 2 regions in this study confirm our previous findings (*8*). However, they do not support ^{18}F-flortaucipir's having differential affinity for any one lesion type. We are not able to biologically elucidate why there were correlations of significance between ligand uptake and those 2 specific lesion types in red nucleus and precentral gyrus. One explanation could be that there is some Alzheimer (3R + 4R paired helical filament) tau that is codeposited with 4R tau in these 2 regions. An argument against this

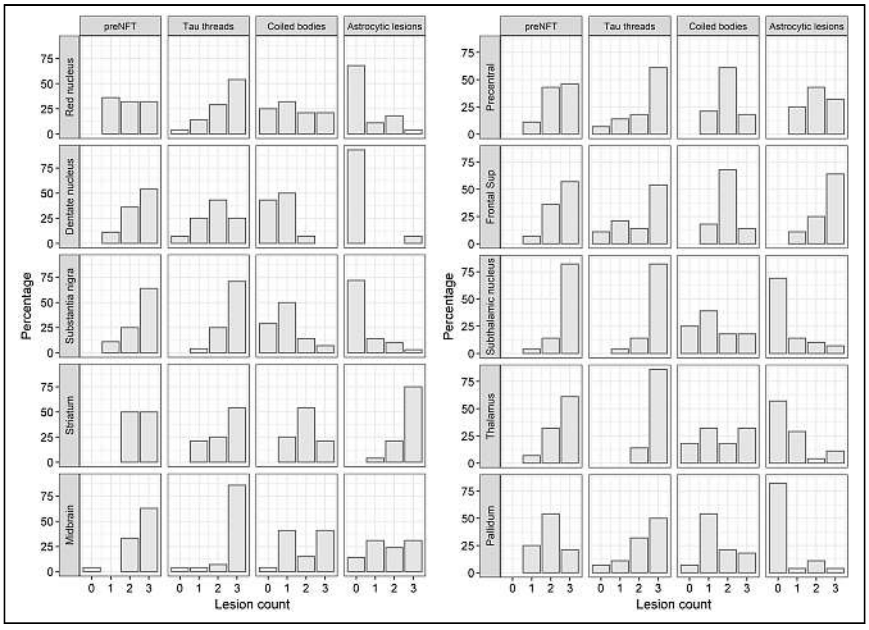

FIGURE 2. Histograms showing distribution of lesion count scores across cases for each region and each tau lesion type.

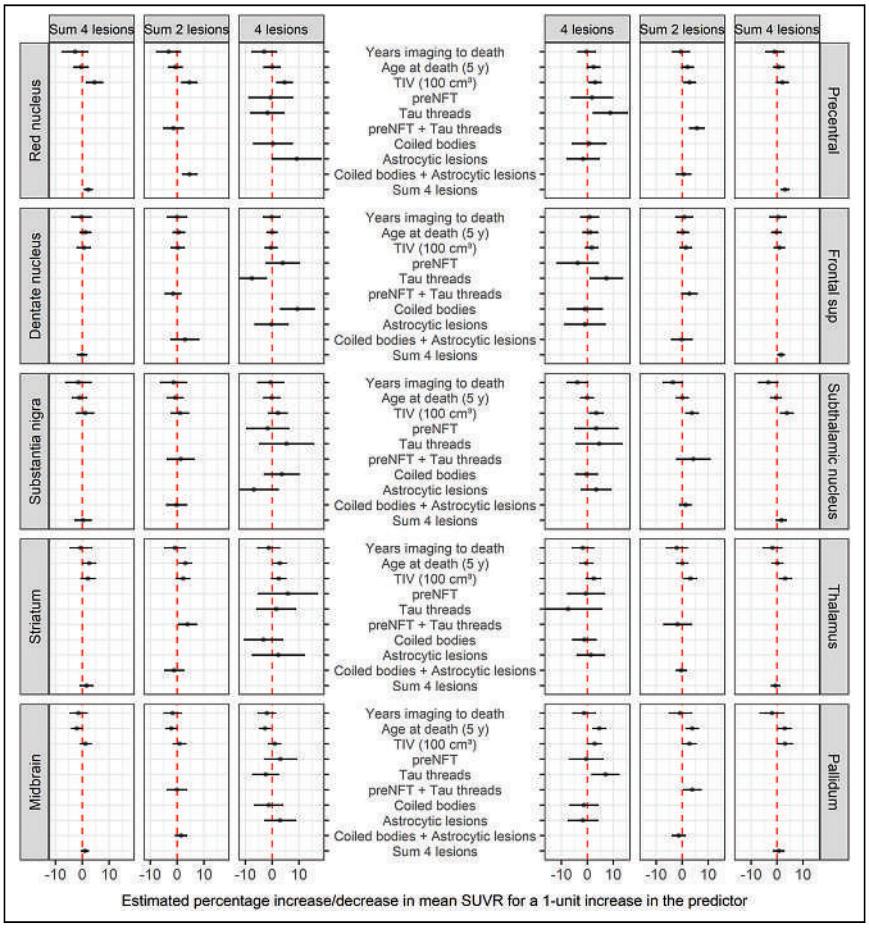

FIGURE 3. Relationships between ^{18}F-flortaucipir uptake (SUVR) and lesion type, adjusting for time from imaging to death, age at death, and total intracranial volume. NFT = neurofibrillary tangle; TIV = total intracranial volume.

explanation is that the highest Braak neurofibrillary tangle stage in any of the 29 patients in this study was IV (most were Braak neurofibrillary tangle stages 0–III), and hence there was no Alzheimer-type tau in any of the 10 regions analyzed in this study. Furthermore, we have previously shown that ^{18}F-flortaucipir PET is not sensitive to low levels of tau pathology (*8*). Another is that we are observing correlations that are influenced by regional off-target binding. This latter explanation is supported by previous studies that have found evidence that ^{18}F-flortaucipir binds to neuromelanin and melanin-containing cells (*3,18*), iron (*19*), monoamine oxidase B inhibitors (*20*), and vascular structures (*21*), to name a few. It is also a possibility that binding could be related to a yet-to-be-identified pathologic lesion or process that may or may not vary in burden by regions in PSP and CBD.

The comprehensive analyses, including modeling the relationships with and without partial-volume correction, excluded the likelihood that our results were influenced by volume loss. Other strengths to our study include the large number of autopsy-confirmed cases with a 4R tauopathy that had antemortem ^{18}F-flortaucipir and that all underwent semiquantitative scoring by a single neuropathologist with over 30 y of experience with PSP and CBD pathology. Limitations include the fact that a quantitative histologic measure was not used, although semiquantitative scales were also used in the recent international study of the distribution patterns of tau pathology in PSP, which was performed with the intent to inform tau-neuroimaging distribution patterns (*22*). Other limitations are that the distribution of lesion severity within regions of interest—and the fact that the histologic region of interest represents a small sampled area within the larger ^{18}F-flortaucipir region of interest—could have impacted the ability to detect correlations. Furthermore, PET SUVRs can be influenced by different biologic and technical factors (*23*).

CONCLUSION

The results of this study do not support differential affinity of ^{18}F-flortaucipir for any histologic lesion, including threads, in 4R tauopathies.

DISCLOSURE

This study was funded by NIH grants RF1-NS112153, R01-DC12519, R01-NS89757, and R01-DC14942. Val Lowe serves on the scientific advisory board of AVID Radiopharmaceuticals. No other potential conflict of interest relevant to this article was reported.

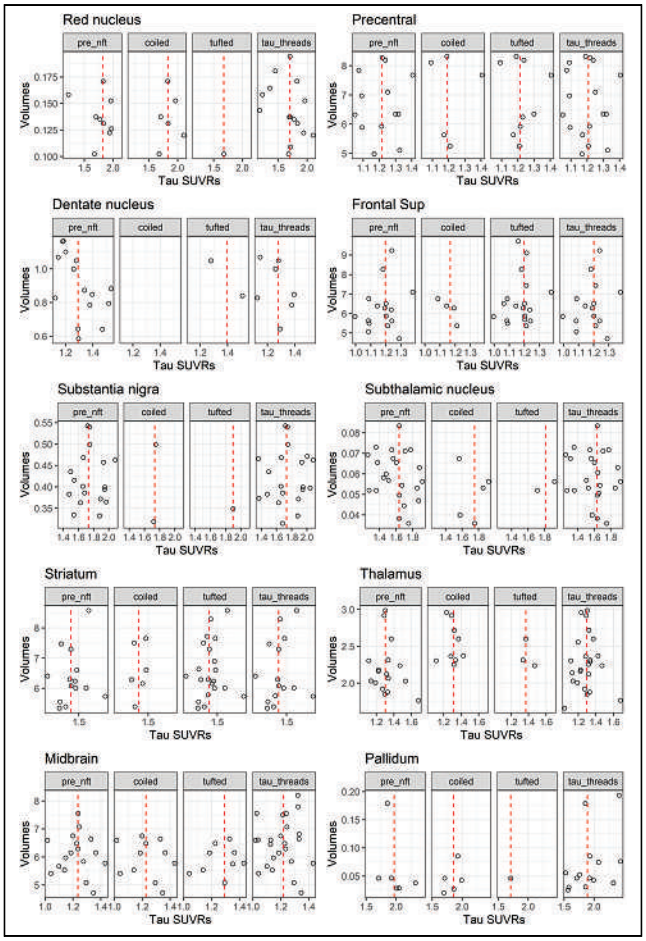

FIGURE 4. Scatterplots showing relationship between tau SUVR and volume across regions in cases that had frequent lesion counts (score = 3). Red dashed line represents median tau SUVR. nft = neurofibrillary tangles.

ACKNOWLEDGMENT

We acknowledge the Mayo ADIR Laboratory for PET processing pipelines.

KEY POINTS

QUESTION: Is ^{18}F-flortaucipir uptake in 4R tauopathies related to histologic lesion type?

PERTINENT FINDINGS: In this PET pathologic study of 29 autopsied patients who underwent ^{18}F-flortaucipir PET while alive and later died with autopsy-confirmed PSP or CBD, we semiquantified histologic lesion types in multiple brain regions and looked for associations between ligand uptake and lesion type using linear regression. We found only 2 weak associations.

IMPLICATIONS FOR PATIENT CARE. There is little evidence linking ^{18}F-flortaucipir uptake to any one lesion type in 4R tauopathies. Hence, other factors must be considered when designing second and third generations of 4R tau PET ligands.

REFERENCES

1. Dickson DW, Bergeron C, Chin SS, et al. Office of Rare Diseases neuropathologic criteria for corticobasal degeneration. *J Neuropathol Exp Neurol.* 2002;61:935–946.
2. Hauw JJ, Daniel SE, Dickson D, et al. Preliminary NINDS neuropathologic criteria for Steele-Richardson-Olszewski syndrome (progressive supranuclear palsy). *Neurology.* 1994;44:2015–2019.
3. Lowe VJ, Curran G, Fang P, et al. An autoradiographic evaluation of AV-1451 tau PET in dementia. *Acta Neuropathol Commun.* 2016;4:58.
4. Xia CF, Arteaga J, Chen G, et al. [^{18}F]T807, a novel tau positron emission tomography imaging agent for Alzheimer's disease. *Alzheimers Dement.* 2013;9:666–676.
5. Whitwell JL, Lowe VJ, Tosakulwong N, et al. [^{18}F]AV-1451 tau positron emission tomography in progressive supranuclear palsy. *Mov Disord.* 2017;32:124–133.
6. Josephs KA, Whitwell JL, Tacik P, et al. [^{18}F]AV-1451 tau-PET uptake does correlate with quantitatively measured 4R-tau burden in autopsy-confirmed corticobasal degeneration. *Acta Neuropathol (Berl).* 2016;132:931–933.
7. McMillan CT, Irwin DJ, Nasrallah I, et al. Multimodal evaluation demonstrates in vivo ^{18}F-AV-1451 uptake in autopsy-confirmed corticobasal degeneration. *Acta Neuropathol (Berl).* 2016;132:935–937.
8. Ghirelli A, Tosakulwong N, Weigand SD, et al. Sensitivity-specificity of tau and amyloid beta positron emission tomography in frontotemporal lobar degeneration. *Ann Neurol.* 2020;88:1009–1022.
9. Montine TJ, Phelps CH, Beach TG, et al. National Institute on Aging-Alzheimer's Association guidelines for the neuropathologic assessment of Alzheimer's disease: a practical approach. *Acta Neuropathol (Berl).* 2012;123:1–11.
10. Josephs KA, Mandrekar JN, Dickson DW. The relationship between histopathological features of progressive supranuclear palsy and disease duration. *Parkinsonism Relat Disord.* 2006;12:109–112.
11. Whitwell JL, Ahlskog JE, Tosakulwong N, et al. Pittsburgh compound B and AV-1451 positron emission tomography assessment of molecular pathologies of Alzheimer's disease in progressive supranuclear palsy. *Parkinsonism Relat Disord.* 2018;48:3–9.
12. Ewert S, Plettig P, Li N, et al. Toward defining deep brain stimulation targets in MNI space: a subcortical atlas based on multimodal MRI, histology and structural connectivity. *Neuroimage.* 2018;170:271–282.
13. Schwarz CG, Therneau TM, Weigand SD, et al. Selecting software pipelines for change in flortaucipir SUVR: balancing repeatability and group separation. *Neuroimage.* 2021;238:118259.
14. Jack CR Jr, Wiste HJ, Weigand SD, et al. Defining imaging biomarker cut points for brain aging and Alzheimer's disease. *Alzheimers Dement.* 2017;13:205–216.
15. Schwarz CG, Tosakulwong N, Senjem ML, et al. Considerations for performing level-2 centiloid transformations for amyloid PET SUVR values. *Sci Rep.* 2018;8:7421.
16. Zhang W, Tarutani A, Newell KL, et al. Novel tau filament fold in corticobasal degeneration. *Nature.* 2020;580:283–287.
17. Tarutani A, Miyata H, Nonaka T, et al. Human tauopathy-derived tau strains determine the substrates recruited for templated amplification. *Brain.* 2021;144:2333–2348.
18. Marquié M, Normandin MD, Vanderburg CR, et al. Validating novel tau positron emission tomography tracer [F-18]-AV-1451 (T807) on postmortem brain tissue. *Ann Neurol.* 2015;78:787–800.
19. Choi JY, Cho H, Ahn SJ, et al. Off-target ^{18}F-AV-1451 binding in the basal ganglia correlates with age-related iron accumulation. *J Nucl Med.* 2018;59:117–120.
20. Vermeiren C, Motte P, Viot D, et al. The tau positron-emission tomography tracer AV-1451 binds with similar affinities to tau fibrils and monoamine oxidases. *Mov Disord.* 2018;33:273–281.
21. Saint-Aubert L, Lemoine L, Chiotis K, Leuzy A, Rodriguez-Vieitez E, Nordberg A. Tau PET imaging: present and future directions. *Mol Neurodegener.* 2017;12:19.
22. Kovacs GG, Lukic MJ, Irwin DJ, et al. Distribution patterns of tau pathology in progressive supranuclear palsy. *Acta Neuropathol (Berl).* 2020;140:99–119.
23. Adams MC, Turkington TG, Wilson JM, Wong TZ. A systematic review of the factors affecting accuracy of SUV measurements. *AJR.* 2010;195:310–320.

First-in-Humans Brain PET Imaging of the GluN2B-Containing *N*-methyl-D-aspartate Receptor with (*R*)-^{11}C-Me-NB1

Lucas Rischka*[1], Chrysoula Vraka*[2], Verena Pichler[2,3], Sazan Rasul[2], Lukas Nics[2], Gregor Gryglewski[1], Patricia Handschuh[1], Matej Murgaš[1], Godber M. Godbersen[1], Leo R. Silberbauer[1], Jakob Unterholzner[1], Christoph Wotawa[1], Ahmed Haider[4], Hazem Ahmed[4], Roger Schibli[4], Thomas Mindt[2,5,6], Markus Mitterhauser[2,5], Wolfgang Wadsak[2,7], Andreas Hahn[1], Rupert Lanzenberger[1], Marcus Hacker[2], and Simon M. Ametamey[4]

[1]*Department of Psychiatry and Psychotherapy, Medical University of Vienna, Vienna, Austria;* [2]*Division of Nuclear Medicine, Department of Biomedical Imaging and Image-guided Therapy, Medical University of Vienna, Vienna, Austria;* [3]*Department of Pharmaceutical Chemistry, University of Vienna, Vienna, Austria;* [4]*Centre for Radiopharmaceutical Sciences ETH-PSI-USZ, Institute of Pharmaceutical Sciences ETH, Zurich, Switzerland;* [5]*Ludwig Boltzmann Institute Applied Diagnostics, Vienna, Austria;* [6]*Institute of Inorganic Chemistry, University of Vienna, Vienna, Austria; and* [7]*Center for Biomarker Research in Medicine (CBmed), Graz, Austria*

The *N*-methyl-D-aspartate receptor (NMDAR) plays a crucial role in neurodegenerative diseases such as Alzheimer disease and in the treatment of major depression by fast-acting antidepressants such as ketamine. Given their broad implications, GluN2B-containing NMDARs have been of interest as diagnostic and therapeutic targets. Recently, (*R*)-^{11}C-Me-NB1 was investigated preclinically and shown to be a promising radioligand for imaging GluN2B subunits. Here, we report on the performance characteristics of this radioligand in a first-in-humans PET study. **Methods:** Six healthy male subjects were scanned twice on a fully integrated PET/MR scanner with (*R*)-^{11}C-Me-NB1 for 120 min. Brain uptake and tracer distribution over time were investigated by SUVs. Test–retest reliability was assessed with the absolute percentage difference and the coefficient of variation. Exploratory total volumes of distribution (V_T) were computed using an arterial input function and the Logan plot as well as a constrained 2-tissue-compartment model with the ratio of rate constants between plasma and tissue compartments (K_1/k_2) coupled (2TCM). SUV was correlated with V_T to investigate its potential as a surrogate marker of GluN2B expression. **Results:** High and heterogeneous radioligand uptake was observed across the entire gray matter with reversible kinetics within the scan time. SUV absolute percentage difference ranged from 6.9% to 8.5% and coefficient of variation from 4.9% to 6.0%, indicating a high test–retest reliability. A moderate correlation was found between SUV averaged from 70 to 90 min and V_T using Logan plot (Spearman $\rho = 0.44$). Correlation between V_T Logan and 2TCM was $r = 0.76$. **Conclusion:** The radioligand (*R*)-^{11}C-Me-NB1 was highly effective in mapping GluN2B-enriched NMDARs in the human brain. With a heterogeneous uptake and a high test–retest reliability, this radioligand offers promise to deepen our understanding of the GluN2B-containing NMDAR in the pathophysiology and treatment of neuropsychiatric disease such as Alzheimer disease and major depression. Additionally, it could help in the selection of appropriate doses of GluN2B-targeting drugs.

Key Words: glutamate; *N*-methyl-d-aspartate (NMDA); GluN2B subunits; neurodegenerative disease; PET

Received Apr. 12, 2021; revision accepted Aug. 26, 2021.

For correspondence or reprints, contact Simon M. Ametamey (simon.ametamey@pharma.ethz.ch), Marcus Hacker (marcus.hacker@meduniwien.ac.at), or Rupert Lanzenberger (rupert.lanzenberger@meduniwien.ac.at).

*Contributed equally to this work.

Published online Oct. 7, 2021.

J Nucl Med 2022; 63:936–941
DOI: 10.2967/jnumed.121.262427

The *N*-methyl-D-aspartate receptor (NMDAR) constitutes a heterotetrameric glutamate-gated ion channel that mediates key physiologic functions such as synaptic transmission, plasticity, and higher cognitive functions in the mammalian central nervous system (*1,2*). Despite their homeostatic relevance, NMDARs trigger pathophysiologic processes on excessive activation, thereby prompting apoptotic cascades that ultimately result in neurodegeneration (*3*). Moreover, NMDAR dysfunctions have been implicated in a multitude of neuropsychiatric disorders including Alzheimer disease, vascular dementia, Parkinson disease, stroke, traumatic brain injury, depression, and schizophrenia (*4,5*). Recent studies demonstrated that activation of extrasynaptic NMDARs, which are typically enriched with the GluN2B subunit, resulted in excitotoxicity, whereas activation of synaptic NMDARs had protective effects (*4*). As such, subtype-selective modulation of GluN2B-containing NMDARs has been suggested as a promising drug development strategy that would provide therapeutic efficacy, while concurrently sparing physiologic NMDAR functions (*6,7*). Despite strenuous research and development efforts, GluN2B-selective antagonists showed only limited clinical efficacy so far (*8*). Although underlying causes may have been of multifactorial origin, it has been suggested that the availability of an appropriate GluN2B-targeted probe would facilitate drug development (*9*). Indeed, a radioligand to visualize GluN2B-containing NMDARs in the living human brain is currently lacking. Thus, it is of paramount value to develop such tools to further elucidate the versatile roles of GluN2B-containing NMDARs in neurodegenerative and other neuropsychiatric diseases, as well as to guide future drug development efforts via target engagement studies.

Despite the plethora of attempts to develop a suitable NMDAR PET radioligand, most reported probes suffered from major drawbacks such as low brain uptake, radiometabolites entering the brain, prominent off-target binding particularly to σ1 receptors, and brain uptake inconsistent with the known expression profile (*10,11*). To date, the most promising structural class of GluN2B-targeted PET radioligands are the *2,3,4,5*-tetrahydro-1H-benzazepine derivatives (*12–15*). A recent publication by Haider et al. reported on the

benzazepine derivative (*R*)-^{11}C-Me-NB1 (Fig. 1) as a potential PET radioligand for imaging the GluN2B-containing NMDARs. Biodistribution and PET imaging studies in rodents showed an uptake pattern in brain regions known to express the GluN2B subunits of the NMDAR, with the lowest uptake in the cerebellum, a brain region known to have low to negligible GluN2B subunits in rodents. Specificity of (*R*)-^{11}C-Me-NB1 binding was substantiated in blocking studies in a dose-dependent manner, and selectivity over σ1 receptors was confirmed using σ1 receptor knockout mice (*15*).

Considering the promising characteristics of this radioligand in rodents, the current work aims to translate the utility of (*R*)-^{11}C-Me-NB1 for imaging the GluN2B subunits of the NMDAR to humans. To the best of our knowledge, this work signifies the first assessment of a GluN2B PET imaging probe in the living human brain.

MATERIALS AND METHODS

Participants and Study Design

Six healthy male subjects (mean age ± SD, 23.3 ± 2.9) were recruited for the study. All participants were free from internal, neurologic, or psychiatric disorders assessed via a thorough medical history, physical examination, electrocardiogram, and routine laboratory parameters. Exclusion criteria were neurologic diseases or psychiatric disorders; illness 2 wk before recruitment; history of drug or atopic allergy; myocardial infarction; history of cancer or liver or renal disease; family history of prolonged QT interval; MRI or PET contraindications; consumption of tobacco products 3 mo before recruitment; history of drug or alcohol abuse; and significant prior radiation exposure in the past 10 y. After detailed explanation of the study design, all subjects gave written informed consent. The study was registered in the EudraCT database (2018-002933-39) and approved by the Ethics Committee of the Medical University of Vienna (ethics no. 1980/2018). Procedures were performed in accordance with the Declaration of Helsinki. Subjects were reimbursed for participation.

Tracer Preparation

(*R*)-^{11}C-Me-NB1 was produced on a fully automated Tracerlab FX2 C synthesis module (GE Healthcare) by applying ^{11}C-CO_2 from a PETtrace 860 (GE Healthcare). ^{11}C-CH_3I was reacted with the enantiomerically pure des-methyl good manufacturing practice–grade precursor (*R*)-NB1 in dimethylformamide and in the presence of Cs_2CO_3 following previously published procedures (*15*). Minor synthetic adaptations included the use of a SupelcosilTM LC-ABZ+ column (5 μm, 250 × 10 mm; Bellonte) and a mobile phase of 60% acetonitrile/40% aqueous Na_2HPO_4 (0.02 mol/L) for the final product purification. After high-performance liquid chromatography (HPLC) purification, the product was trapped on a Sep-Pak Plus, C18 Cartridge (Waters), washed with 10 mL of H_2O for injection, eluted with 1.5 mL of ethanol, and formulated for human application using 10 mL of NaCl (0.9%) and 6 mL of phosphate-buffered saline. Product quality was assessed according to the guidance of radiopharmaceutical preparations of the European Pharmacopoeia (*16*). Molar activities were calculated through assessment of radioactivity at the end of synthesis and determination of nonradioactive (*R*)-Me-NB1 via HPLC. Values were decay-corrected to the time of tracer administration.

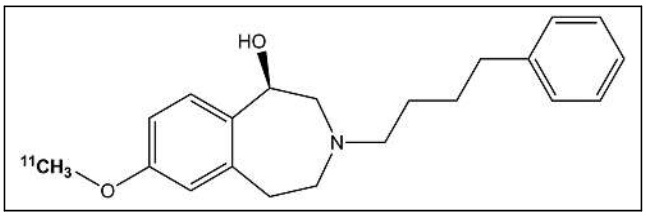

FIGURE 1. Chemical structure of (*R*)-^{11}C-Me-NB1.

PET Imaging

All participants underwent 2 measurements on a fully integrated PET/MR scanner (mMR Biograph; Siemens) lasting for 120 min. The mean interval between the scans was 18.2 ± 8.8 d (range, 6–28 d), and measurements started between 4:30 and 6:00 PM (central European time; mean difference between the measurement start times, 21 ± 24 min; range, 0–60 min). PET data were acquired in 3-dimensional list-mode. The radioligand (*R*)-^{11}C-Me-NB1 was administered as a bolus through a cubital vein (mean injected dose, 448 ± 34 MBq; 5.98 ± 0.85 MBq/kg of body weight; 0.15 ± 0.11 nmol/kg of body weight; 1 value was excluded because of technical HPLC issues). There were no adverse events or clinically detectable pharmacologic effects in any of the subjects. No changes in vital signs, laboratory results, or electrocardiograms were observed. During the scan, subjects were instructed not to fall asleep, to observe a black crosshair on a gray background presented on a screen at the end of the gantry, to let their thoughts wander, and to not move any body part. Additionally, head movement was minimized with stabilizing cushions within the head coil.

Arterial Blood Sampling, Metabolite Analyses, and Arterial Input Function

Before each measurement, arterial and venous cannulas were inserted in the radial artery and a cubital vein of the opposite arm for arterial blood sampling and administration of the radioligand. Arterial blood was drawn automatically for the first 6 min (Twilite II system; Swisstrace). Manual blood samples were taken at 3, 4, 5, 10, 20, 30, 40, 60, 80, 100, and 120 min and were immediately measured in a γ-counter (Wizard^2, 3″; Perkin Elmer), for whole blood activity and, after centrifugation, for plasma activity. The γ-counter was cross-calibrated to the PET/MR scanner. Radiometabolites were determined for the time points 5, 10, 20, 30, 40, and 60 min by HPLC using an Agilent 1260 Infinity system (pumps, degasser and ultraviolet detector) connected to a motorized valve (BESTA; Motorventil) and a radiodetector (RamonaStar; Elysia-Raytest). A column switching method (*17*) was used to concentrate a lipophilic radiometabolite and the parent compound, while a more hydrophilic radiometabolite eluted from the column. Up to 5 mL of plasma were directly injected into the HLB OASIS column (OASIS resin; Waters) with the mobile phase consisting of 1% acetonitrile and water. In an initial pilot study, a recovery rate of 99.6% was observed for the parent compound. After pump switching, the HLB OASIS column was backflushed with a mobile phase consisting of 60% acetonitrile and 40% 50 mM ammonium acetate, pH 9. The second radiometabolite was separated from the parent compound using a XSelect column (HSS T3, 3.5 μm, 100 × 4.6 mm; Waters) equipped with the corresponding precolumn. The areas under the curves were decay-corrected. The parent compound was identified by the retention time of the reference standard.

MRI

Simultaneously with the PET acquisition, a structural T1-weighted image was acquired with a magnetization prepared rapid gradient echo sequence (echo time/repetition time = 4.21/2,200 ms, inversion time = 900 ms, flip angle = 9°, 160 sagittal slices, voxel size = 1 × 1 × 1.1 mm) for attenuation correction of the PET data and spatial normalization and to rule out structural abnormalities.

PET Processing

PET data were reconstructed with an ordinary Poisson ordered-subset expectation maximization algorithm (3 iterations, 21 subsets) and binned into 12 × 5, 6 × 10, 3 × 20, 6 × 30, 9 × 60, 15 × 300, and 3 × 600 s frames. In addition to standard corrections, data were

corrected for attenuation and scatter with a pseudo-CT approach (*18*) based on the structural MRI of the first measurement.

Preprocessing was performed with SPM12 (Wellcome Trust Centre for Neuroimaging), as previously described (*19*). Briefly, PET data were corrected for head motion (quality setting = 1) and coregistered to the structural MRI. The structural MRI was spatially normalized to MNI space, and the transformation matrix was applied to the coregistered PET images.

Regions of Interest (ROIs)

Time–activity curves were extracted for the following ROIs from the Harvard-Oxford atlas and the probabilistic cerebellar atlas (https://fsl.fmrib.ox.ac.uk/fsl/fslwiki/Atlases): frontal, temporal, parietal, occipital, cingulate, and somatosensory cortex as well as the subcortical regions thalamus, striatum, amygdala, and hippocampus and the cerebellar gray matter, excluding the vermis. Additionally, the white matter structures centrum semiovale (extracted from the SPM12 tissue probability map), corpus callosum (from the Hammers N30R83 atlas (*20*)), and the cerebellar white matter (*21*) were investigated (Fig. 2, top row). The left and corresponding right side of each ROI were averaged.

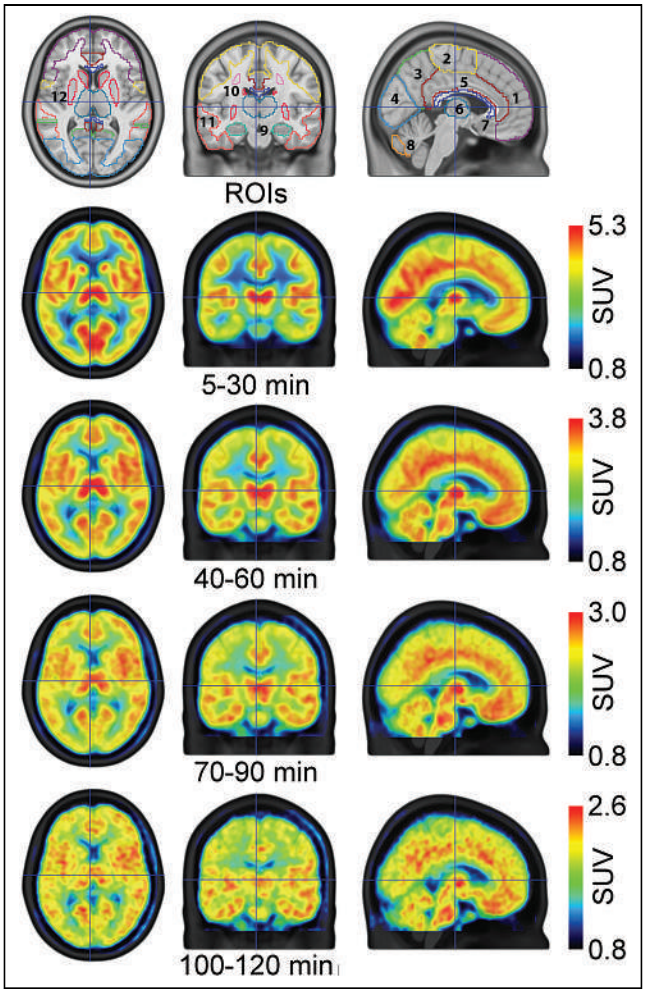

FIGURE 2. ROIs and SUV_{mean} maps. First row depicts investigated ROIs covering cortical, subcortical, and white matter structures: 1, frontal cortex; 2, somatosensory cortex; 3, parietal cortex; 4, occipital cortex; 5, cingulate cortex; 6, thalamus; 7, corpus callosum; 8, cerebellar gray matter; 9, hippocampus; 10, centrum semiovale; 11, temporal cortex; 12, striatum. Amygdala and cerebellar white matter are not visible in the presented slices (MNI space, x = −4, y = 16, z = 7 mm). Remaining rows depict radioligand distribution in terms of SUV for various time points (averaged across subjects).

Brain Uptake

To investigate brain uptake and tracer distribution over time, SUVs were computed as activity concentration in tissue divided by administered dose per kilogram of body weight. For further analyses and demonstration purposes, SUV time–activity curves and SUV voxelwise maps were averaged for the time points 5–30, 40–60, 70–90, and 100–120 min.

In an exploratory approach, NMDAR binding (total volume of distribution, V_T) was quantified with the Logan plot using PMOD 4.2 (PMOD Technologies Ltd.; www.pmod.com). For potential clinical applicability with high patient comfort, only the first 90 min of the data were used for the estimation of V_T. The start time of the fit of the Logan plot (t*) could not be determined automatically for the centrum semiovale because of high noise levels. Hence, the t* of the corpus callosum was used due to similar kinetics (Fig. 3). A time–stability analysis was performed from 40 to 120 min for 4 regions with varying uptake (temporal and parietal cortex, striatum, and hippocampus) to verify that measuring for 90 min is suitable.

A second exploratory analysis was conducted, quantifying V_T with a constrained 2-tissue-compartment model with the ratio of rate constants between plasma and tissue compartments (K_1/k_2) coupled (2TCM) for a measurement duration of 90 min. K_1/k_2 was estimated across all gray matter regions because of different kinetics in the white matter regions.

Statistics

To assess the test–retest reliability, absolute percentage difference (APD), as well as the coefficient of variation (COV), were calculated between the 2 measurements for each ROI. Since there is no ground truth, the APD was determined as $APD[\%] = |m1 - m2|/((m1 + m2)/2) \times 100$. $COV[\%]$ was calculated as $(SD/mean) \times 100$. The intraclass correlation coefficient for absolute agreement was computed for each region of the averaged SUV time points. SUV averaged from 70 to 90 min was correlated with V_T Logan plot estimated for 90 min across all ROIs. Finally, V_T Logan plot for 90 min was correlated with V_T 2TCM.

RESULTS

Radiochemistry

After sterile filtration at the end of synthesis, 4.16 ± 1.31 GBq of (*R*)-^{11}C-Me-NB1 was obtained with a radiochemical purity of 97.5% ± 1.6%. Molar activity ranged from 35 to 1,115 GBq/μmol (1 value was excluded because of technical HPLC issues). All preparations were within the limits set by the European Pharmacopoeia.

Blood Data Analysis

(*R*)-^{11}C-Me-NB1 was metabolized with 29.6% ± 5.5% of the parent fraction left after 20 min and 15.7% ± 3.3% after 40 min (Supplemental Fig. 1A; supplemental materials are available at http://jnm.snmjournals.org). Two radioactive metabolites were identified, which were more polar than the parent radioligand and showed baseline separation on the HPLC chromatograms (Supplemental Figs. 1B and 1C).

Brain Uptake

The radioligand exhibited reversible pharmacokinetics (see the rate constant from compartment representing specific binding to compartment representing nondisplaceable binding in tissue [k_4] obtained from 2TCM below) within the measurement time, and an area-specific brain uptake pattern was observed (Figs. 2, 3, and 4). At peak (~15–20 min after injection), SUV was highest in the striatum (4.5) and lowest in the white matter regions centrum semiovale and corpus callosum (both 1.8), followed by cerebellar white matter (2.6). Cortical regions showed similar kinetics, particularly after 60 min. In contrast, the kinetics of centrum semiovale and corpus callosum varied markedly from the other regions (Fig. 3). SUV_{mean} time–activity curves and SD of representative regions are depicted in Supplemental Figure 2.

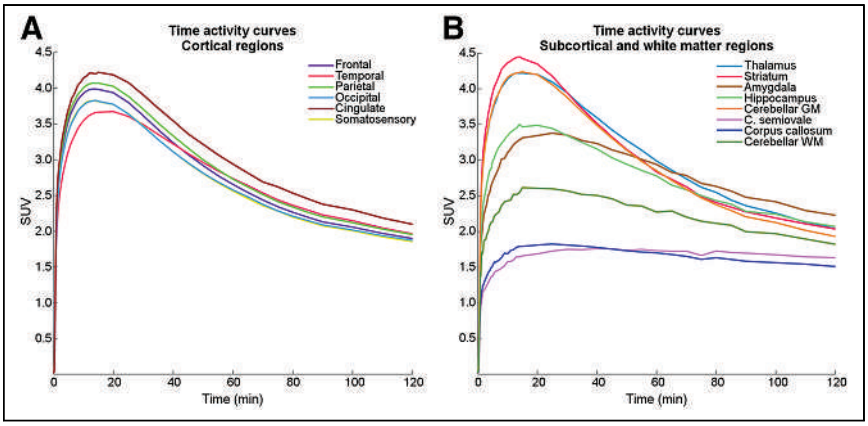

FIGURE 3. Kinetics of (*R*)-^{11}C-Me-NB1. Reversible kinetics were obtained within measurement time. (A) Time–activity curves demonstrate homogeneous kinetics in cortical regions. (B) Subcortical regions showed variable kinetics, with highest uptake observed in striatum. Lowest SUV and markedly different kinetics were observed in centrum semiovale and corpus callosum.

The time–stability analysis of the exploratory Logan plot revealed that measuring for 90 min is feasible with an underestimation of approximately 10% (Supplemental Fig. 3, solid line). In addition, t* was evaluated as a function of measurement time (dashed line). Logan plots of 1 representative subject are depicted in Supplemental Figure 4 to show linearity. The V_T of the Logan plot varied between 12.8 in the corpus callosum and 19.0 mL/cm^{-3} in the amygdala (Fig. 4B). The average V_T across all regions was comparable between the first and second measurement (15.2 vs. 15.9 mL/cm^{-3}).

For the 2TCM, the model did not converge for white matter regions (i.e., centrum semiovale, corpus callosum, and cerebellar white matter). One subject did not show reasonable V_T in 1 measurement and was therefore excluded from further analyses. The 2TCM confirmed the reversible binding with k_4 between 0.02 (somatosensory cortex) and 0.04 (cerebellar gray matter). V_T 2TCM was slightly higher than with the Logan plot (Supplemental Fig. 5).

A moderate correlation was achieved between Logan plot 90 min and SUV 70–90 min (Spearman $\rho = 0.44$). Spearman rank correlation was used because of the presence of an outlier in V_T in the test–retest analysis (Fig. 5C). The correlation between V_T Logan and 2TCM was good ($r = 0.76$) with the caveat of 1 excluded subject and only gray matter regions (Supplemental Fig. 5).

Test–Retest Reliability

High test–retest reliability was obtained for SUVs with slightly increasing values over time. Average APD across all ROIs was 6.9% versus 8.5% for SUV 5–30 min versus 100–120 min and COV was 4.9% versus 6.0% (Fig. 5A). The intraclass correlation coefficient decreased from excellent (0.85 SUV 5–30 min) to moderate (0.58 SUV 100–120 min)

For V_T Logan plot, the variability was slightly higher (mean APD 10.5%, mean COV 7.4%), which is caused by the same subject that did not show reasonable V_T in the 2TCM (Fig. 5B). In comparison, for V_T 2TCM, mean APD was 8.2% and mean COV 5.8%, slightly lower than with Logan plot (1 subject excluded, only gray matter regions). Investigation of the medians in Figure 5A and 5B exhibits similar APD between SUV and V_T except for the centrum semiovale and the corpus callosum.

Complete lists of the SUVs for the various time points, V_T for Logan plot, and 2TCM for the test and retest measurement, alongside the values for APD and COV, are shown in Supplemental Tables 1–4.

DISCUSSION

In this study, the potential of (*R*)-^{11}C-Me-NB1, a selective and specific radioligand for imaging the GluN2B subunits of the NMDAR in rodents, was examined for its performance characteristics in humans and utility in a clinical setting.

(*R*)-^{11}C-Me-NB1 has several advantages over previously published GluN2B PET radioligands (*10*). These include high specificity to the target receptor and topologic distribution that matches the known expression pattern (*22,23*). Furthermore, the radioligand is easily and efficiently synthesized in good radiochemical yields using a 1-step synthetic approach.

The results of the metabolite analysis showed the presence of 2 hydrophilic radiolabeled compounds, which were more polar than parent (*R*)-^{11}C-Me-NB1 and likely unable to cross the blood–brain barrier. This reasoning is based on previous studies in rodents that showed that more than 95% of radioactivity in rodent brain was intact (*R*)-^{11}C-Me-NB1 (*14*). In a recent study using mice liver microsomes, glucuronidation of the benzylic hydroxyl group and hydroxylation of the aromatic moiety in Me-NB1 were reported. Although we did not identify the radiometabolites, the HPLC profile suggests that the 2 hydrophilic radiometabolites may correspond to a hydroxylated species and the glucuronide of (*R*)-^{11}C-Me-NB1, respectively (*24*).

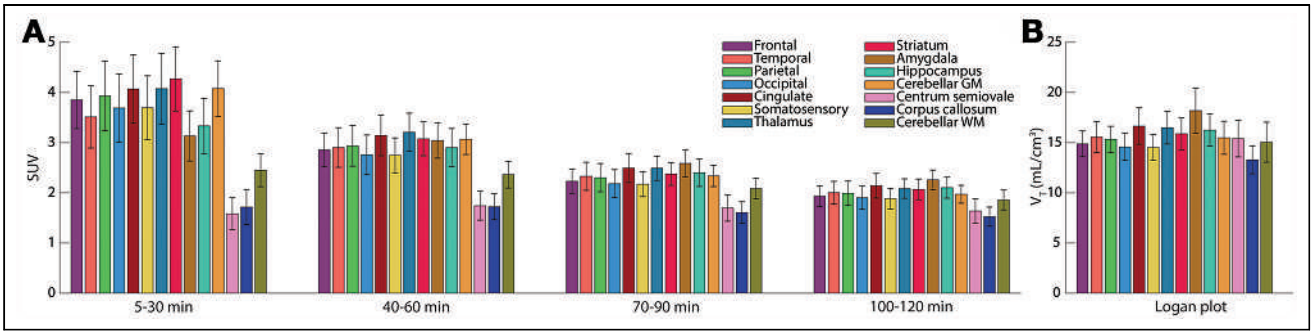

FIGURE 4. SUV and V_T using Logan plot. (A) SUV of each ROI for several time points. (B) Exploratory V_T computed with Logan plot.

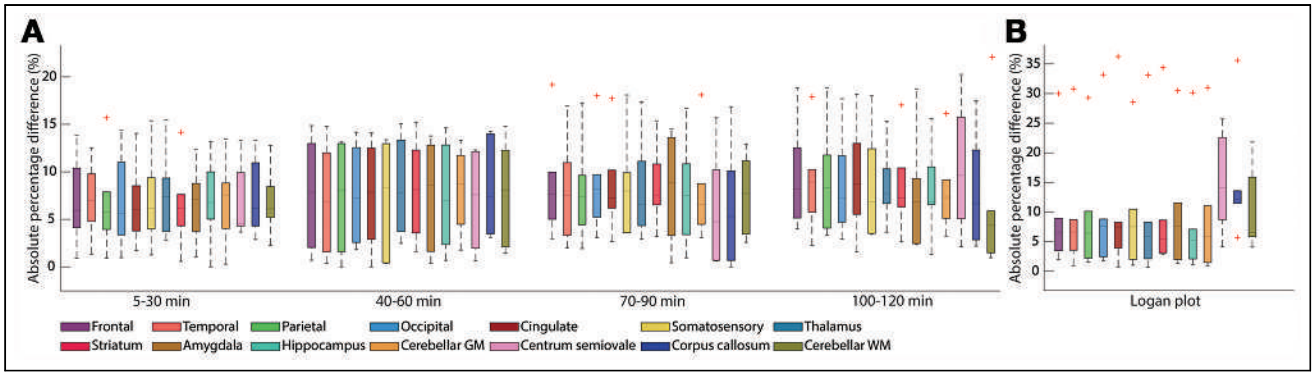

FIGURE 5. Absolute percentage difference (APD) of SUV and Logan plot. (A) APD of SUV is comparable over time in most regions with slightly larger interquartile ranges for 40–60 min. (B) APD of Logan plot visualizes similar median differences as for SUV but with 1 outlier.

Brain uptake and distribution of (*R*)-^{11}C-Me-NB1 in humans were similar to those in rodent studies in most brain regions, including the cortex, striatum, and thalamus. However, although the cerebellum exhibited generally low radioligand uptake in rodents (*14*), cerebellar uptake in humans was region-dependent. Indeed, whereas the cerebellar white matter was among regions with limited tracer uptake, the cerebellar gray matter exhibited high (*R*)-^{11}C-Me-NB1 uptake in the present study. Whether the cerebellar uptake of (*R*)-^{11}C-Me-NB1 in humans reflects specific binding would need to be confirmed in blocking studies with GluN2B antagonists such as CP-101,606.

An important feature of a useful radioligand is the pharmacokinetic profile for absolute quantification. In this regard, (*R*)-^{11}C-Me-NB1 exhibited reversible binding to the GluN2B-enriched NMDAR, which was quantifiable with the Logan plot and 2TCM. The moderate correlation between V_T and SUV 70–90 min might indicate a substitution of the absolute quantification although this requires further validation, including a comprehensive assessment of different modeling strategies.

Another benefit is the high test–retest reliability of around 8% (APD) for SUV and V_T 2TCM and 11% for V_T Logan plot, for a desirable measurement time of 90 min. The reliability is similar to that of other successfully translated radioligands (*25*), making it a promising tool for clinical applications.

We acknowledge the small sample size of 6 subjects but suggest that this is acceptable for a first proof-of-concept study in humans. A limitation is that only young men were included. Hence, further work is required to assess potential sex differences and alterations with age.

The possibility to map GluN2B-enriched NMDAR in humans now enables receptor occupancy studies for drug development to treat neurodegenerative and other neuropsychiatric diseases. The notion is to modulate GluN2B-containing NMDAR with selective antagonists. However, substances such as EVT-101 or CERC-301 did show in vitro but not in vivo displacement of (*R*)-^{11}C-Me-NB1 in rodents (*14*) and limited efficacy in humans for CERC-301 (*8*). In contrast, CP-101,606 competed with (*R*)-^{11}C-Me-NB1 in rodents (*14*) and demonstrated antidepressant effects similar to ketamine in a clinical trial (*26*). However, the further development of the GluN2B antagonist was discontinued because of side effects (*27*). Hence, GluN2B-specific radioligands could aid the clinical investigations of the mechanism of action behind these drugs and the correlation between efficacy and receptor occupancy.

CONCLUSION

For the first time (to our knowledge), a GluN2B subunit NMDAR-specific radioligand showing valuable characteristics in terms of pharmacokinetics and brain uptake was successfully translated into humans. A heterogeneous brain uptake with a robust test–retest variability (<10%) was demonstrated. In an exploratory analysis, we showed that absolute quantification of the total volume of distribution with the Logan plot is feasible. The results suggest that (*R*)-^{11}C-Me-NB1 is a promising radioligand for visualizing the GluN2B-containing NMDARs in humans and potentially could be used in drug development programs to select appropriate doses of GluN2B-targeting drugs.

DISCLOSURE

This project was supported in part by the Swiss National Science Foundation grant numbers 310030E-160403/1 and 310030E-182872/1 to Prof. Simon M. Ametamey. Matej Murgaš is funded by the Austrian Science Fund FWF DOC 33-B27. Leo R. Silberbauer is a recipient of a DOC fellowship of the Austrian Academy of Sciences. Simon M. Ametamey and Ahmed Haider are coinventors of the filed patent number US2017/0224852A1. Rupert Lanzenberger received travel grants or conference speaker honoraria within the last 3 y from Bruker BioSpin MR and support from Siemens Healthcare regarding clinical research using PET/MR. He is a shareholder of the start-up company BM Health GmbH since 2019. Without relevance to this work, Wolfgang Wadsak received within the last 3 y research grants from ITM Medical Isotopes GmbH and Scintomics. He is a part-time employee of CBmed GmbH and a cofounder of MINUTE medical GmbH. Without relevance to this work, Markus Mitterhauser is scientific advisor for ROTOP Pharma GmbH. No other potential conflict of interest relevant to this article was reported.

KEY POINTS

QUESTION: Is (*R*)-^{11}C-Me-NB1 a suitable radioligand to map the GluN2B- NMDAR in the human brain?

PERTINENT FINDINGS: The radioligand demonstrated an area-specific brain uptake pattern with reversible pharmacokinetics and a high test–retest reliability.

IMPLICATIONS FOR PATIENT CARE: The possibility to map the GluN2B subunits of NMDAR provides new opportunities for the treatment of neuropsychiatric disorders such as Alzheimer disease and major depression in terms of drug development.

ACKNOWLEDGMENTS

The authors are particularly grateful to Dietmar Winkler, Pia Baldinger-Melich, and Paul Michenthaler for clinical support. We thank Murray B. Reed, Vera Ritter, Daniel Pacher, Sebastian Klug, Marcel Koseler, Harald Ibeschitz, Natalie Schindler, Karsten Bamminger, Tim Wollenweber, and Marius Ozenil for technical support. Furthermore, we also thank Yves Auberson and Nicholas Seneca from Novartis for their technical support.

REFERENCES

1. Dingledine R, Borges K, Bowie D, Traynelis SF. The glutamate receptor ion channels. *Pharmacol Rev.* 1999;51:7–61.
2. Bliss TVP, Collingridge GL. A synaptic model of memory: long-term potentiation in the hippocampus. *Nature.* 1993;361:31–39.
3. Sattler R, Tymianski M. Molecular mechanisms of calcium-dependent excitotoxicity. *J Mol Med.* 2000;78:3–13.
4. Hardingham GE, Bading H. Synaptic versus extrasynaptic NMDA receptor signalling: implications for neurodegenerative disorders. *Nat Rev Neurosci.* 2010;11:682–696.
5. Ikonomidou C, Turski L. Why did NMDA receptor antagonists fail clinical trials for stroke and traumatic brain injury? *Lancet Neurol.* 2002;1:383–386.
6. Mony L, Kew JNC, Gunthorpe MJ, Paoletti P. Allosteric modulators of NR2B-containing NMDA receptors: molecular mechanisms and therapeutic potential. *Br J Pharmacol.* 2009;157:1301–1317.
7. Ahmed H, Haider A, Ametamey SM. N-methyl-D-Aspartate (NMDA) receptor modulators: a patent review (2015-present). *Expert Opin Ther Pat.* 2020;30:743–767.
8. Ibrahim L, Diaz Granados N, Jolkovsky L, et al. A randomized, placebo-controlled, crossover pilot trial of the oral selective NR2B antagonist MK-0657 in patients with treatment-resistant major depressive disorder. *J Clin Psychopharmacol.* 2012;32:551–557.
9. Gruber S, Ametamey SM. Imaging the glutamate receptor subtypes: much achieved, and still much to do. *Drug Discov Today Technol.* 2017;25:27–36.
10. Fuchigami T, Nakayama M, Yoshida S. Development of PET and SPECT probes for glutamate receptors. *ScientificWorldJournal.* 2015;2015:716514.
11. Fu H, Tang W, Chen Z, et al. Synthesis and preliminary evaluations of a triazole-cored antagonist as a PET imaging probe ([^{18}F]N2B-0518) for GluN2B subunit in the brain. *ACS Chem Neurosci.* 2019;10:2263–2275.
12. Ahmed H, Haider A, Varisco J, et al. Structure–affinity relationships of 2,3,4,5-Tetrahydro-1 H -3-benzazepine and 6,7,8,9-Tetrahydro-5 H -benzo[7]annulen-7-amine analogues and the discovery of a radiofluorinated 2,3,4,5-Tetrahydro-1 H -3-benzazepine congener for imaging GluN2B subunit-containing N-Methyl-d-Aspartate receptors. *J Med Chem.* 2019;62:9450–9470.
13. Ahmed H, Wallimann R, Haider A, et al. Preclinical development of ^{18}F-OF-NB1 for imaging GluN2B-containing *N*-Methyl-D-Aspartate receptors and its utility as a biomarker for amyotrophic lateral sclerosis. *J Nucl Med.* 2021;62:259–265.
14. Haider A, Herde AM, Krämer SD, et al. Preclinical evaluation of benzazepine-based PET radioligands (*R*)- and (*S*)-^{11}C-Me-NB1 reveals distinct enantiomeric binding patterns and a tightrope walk between GluN2B- and σ1-receptor-targeted PET imaging. *J Nucl Med.* 2019;60:1167–1173.
15. Krämer SD, Betzel T, Mu L, et al. Evaluation of 11 C-Me-NB1 as a potential PET radioligand for measuring GluN2B-containing NMDA receptors, drug occupancy, and receptor cross talk. *J Nucl Med.* 2018;59:698–703.
16. *Radiopharmaceutical Preparations (Radiopharmaceutica, 8.0/1483). European Pharmacopoeia (Europäisches Arzneibuch).* 8th ed. Vienna, Austria: Official Austrian Version, Verlag Oesterreich GmbH; 2008; 1167–1173 (8. Ausgabe Grundwerk).
17. Vasdev N, Collier T. Design and prototype of an automated column-switching HPLC system for radiometabolite analysis. *Pharmaceuticals (Basel).* 2016;9:51.
18. Burgos N, Cardoso MJ, Thielemans K, et al. Attenuation correction synthesis for hybrid PET-MR scanners: application to brain studies. *IEEE Trans Med Imaging.* 2014;33:2332–2341.
19. Rischka L, Gryglewski G, Pfaff S, et al. Reduced task durations in functional PET imaging with [^{18}F]FDG approaching that of functional MRI. *Neuroimage.* 2018;181:323–330.
20. Gousias IS, Rueckert D, Heckemann RA, et al. Automatic segmentation of brain MRIs of 2-year-olds into 83 regions of interest. *Neuroimage.* 2008;40:672–684.
21. van Baarsen KM, Kleinnijenhuis M, Jbabdi S, Sotiropoulos SN, Grotenhuis JA, van Cappellen van Walsum AM. A probabilistic atlas of the cerebellar white matter. *Neuroimage.* 2016;124:724–732.
22. Rigby M, Le Bourdellès B, Heavens RP, et al. The messenger RNAs for the N-methyl-D-aspartate receptor subunits show region-specific expression of different subunit composition in the human brain. *Neuroscience.* 1996;73:429–447.
23. Enoch MA, Rosser AA, Zhou Z, Mash DC, Yuan Q, Goldman D. Expression of glutamatergic genes in healthy humans across 16 brain regions; Altered expression in the hippocampus after chronic exposure to alcohol or cocaine. *Genes Brain Behav.* 2014;13:758–768.
24. Börgel F, Galla F, Lehmkuhl K, Schepmann D, Ametamey SM, Wünsch B. Pharmacokinetic properties of enantiomerically pure GluN2B selective NMDA receptor antagonists with 3-benzazepine scaffold. *J Pharm Biomed Anal.* 2019;172:214–222.
25. Nord M, Finnema SJ, Schain M, Halldin C, Farde L. Test-retest reliability of [^{11}C]AZ10419369 binding to 5-HT(1B) receptors in human brain. *Eur J Nucl Med Mol Imaging.* 2014;41:301–307.
26. Preskorn SH, Baker B, Kolluri S, Menniti FS, Krams M, Landen JW. An innovative design to establish proof of concept of the antidepressant effects of the NR2B subunit selective N-Methyl-D-Aspartate antagonist, CP-101,606, in patients with treatment-refractory major depressive disorder. *J Clin Psychopharmacol.* 2008;28:631–637.
27. Machado-Vieira R, Henter ID, Zarate CA. New targets for rapid antidepressant action. *Prog Neurobiol.* 2017;152:21–37.

Synaptic Vesicle Glycoprotein 2A Is Affected in the Central Nervous System of Mice with Huntington Disease and in the Brain of a Human with Huntington Disease Postmortem

Daniele Bertoglio[1], Jeroen Verhaeghe[1], Leonie Wyffels[1,2], Alan Miranda[1], Sigrid Stroobants[1,2], Ladislav Mrzljak[3], Celia Dominguez[3], Mette Skinbjerg[3], Jonathan Bard[3], Longbin Liu[3], Ignacio Munoz-Sanjuan[3], and Steven Staelens[1]

[1]*Molecular Imaging Center Antwerp (MICA), University of Antwerp, Wilrijk, Belgium;* [2]*Department of Nuclear Medicine, Antwerp University Hospital, Edegem, Belgium; and* [3]*CHDI Management/CHDI Foundation, Los Angeles, California*

Synaptic dysfunction is a primary mechanism underlying Huntington disease (HD) progression. This study investigated changes in synaptic vesicle glycoprotein 2A (SV2A) density by means of ^{11}C-UCB-J small-animal PET imaging in the central nervous system of mice with HD. **Methods:** Dynamic ^{11}C-UCB-J small-animal PET imaging was performed at clinically relevant disease stages (at 3, 7, 10, and 16 mo) in the heterozygous knock-in Q175DN mouse model of HD and wild-type littermates (16–18 mice per genotype and time point). Cerebral ^{11}C-UCB-J analyses were performed to assess genotypic differences during presymptomatic (3 mo) and symptomatic (7–16 mo) disease stages. ^{11}C-UCB-J binding in the spinal cord was quantified at 16 mo. ^{3}H-UCB-J autoradiography and SV2A immunofluorescence were performed postmortem in mouse and human brain tissues. **Results:** ^{11}C-UCB-J binding was lower in symptomatic heterozygous mice than in wild-type littermates in parallel with disease progression (7 and 10 mo: $P < 0.01$; 16 mo: $P < 0.0001$). Specific ^{11}C-UCB-J binding was detectable in the spinal cord, with symptomatic heterozygous mice displaying a significant reduction ($P < 0.0001$). ^{3}H-UCB-J autoradiography and SV2A immunofluorescence corroborated the in vivo measurements demonstrating lower SV2A in heterozygous mice ($P < 0.05$). Finally, preliminary analysis of SV2A in the human brain postmortem suggested lower SV2A in HD gene carriers than in controls without dementia. **Conclusion:** ^{11}C-UCB-J PET detected SV2A deficits during symptomatic disease in heterozygous mice in both the brain and the spinal cord and therefore may be suitable as a novel marker of synaptic integrity widely distributed in the central nervous system. On clinical application, ^{11}C-UCB-J PET imaging may have promise for SV2A measurement in patients with HD during disease progression and after disease-modifying therapeutic strategies.

Key Words: SV2A; ^{11}C-UCB-J; spinal cord; Huntington disease; animal model

J Nucl Med 2022; 63:942–947
DOI: 10.2967/jnumed.121.262709

Huntington disease (HD) is an autosomal dominant neurodegenerative disorder caused by an expanded polyglutamine repeat in exon 1 of the gene encoding the huntingtin protein (*1*), leading to the expression of mutated huntingtin (mHTT). Pathologic features of HD include widespread progressive accumulation of mHTT, selective neurodegeneration, and forebrain atrophy (*2,3*).

A growing body of evidence suggests that mHTT induces synaptic transmission dysfunction (*4*), so synaptic dysfunction represents one of the main mechanisms underlying the progression of HD (*5*). Alterations in presynaptic proteins, including regulators of endocytosis and exocytosis of synaptic vesicles such as synaptosome-associated protein 25 and rabphilin 3A, have been reported in both clinical (*6,7*) and preclinical (*8–10*) postmortem studies. Previous work demonstrated that mHTT abnormally associates with synaptic vesicles, resulting in impaired synaptic function (*11*), and changes in synaptic proteins correlate with behavioral deficits (*10*), Thus, alterations in synaptic proteins may be suitable as candidate markers for monitoring HD progression (*12–14*). Given the current lack of effective treatment for preventing the disease or halting its progression, synaptic markers may play an important role in the development and evaluation of novel disease-modifying therapies throughout the entire central nervous system (CNS) (*15*).

Among presynaptic proteins, synaptic vesicle glycoprotein 2A (SV2A) is an essential vesicle membrane protein involved in neurotransmitter release and is expressed ubiquitously in synapses of the brain (*16,17*). Recent studies reported that SV2A can be imaged noninvasively in nonhuman primates, humans, and rodents by use of PET with the selective and high-affinity radioligand ^{11}C-UCB-J (*18–20*). ^{11}C-UCB-J PET may be suitable as a proxy for assessing synaptic density in vivo given its optimal clinical and preclinical pharmacokinetics and quantification properties (*20,21*). Thus, it provides a quantitative measure of synaptic changes during HD progression.

Here, we investigated ^{11}C-UCB-J PET imaging for quantifying cerebral SV2A levels at clinically relevant disease stages in the knock-in Q175DN mouse model of HD (*22–24*). Additionally, given the evidence of mHTT pathology in the spinal cord (*25*), we evaluated the use of ^{11}C-UCB-J PET imaging for detecting SV2A density changes in the rodent cervical spinal cord. Finally, postmortem measurements of SV2A were obtained in the mouse brain as well as in the human brain in a preliminary exploratory evaluation.

MATERIALS AND METHODS

Animals

Male wild-type (WT) mice ($n = 35$) and age-matched heterozygous knock-in Q175DN littermates ($n = 35$) (C57BL/6J background; CHDI-81003019) were obtained from Jackson Laboratories. The animals were

Received Jun. 8, 2021; revision accepted Aug. 26, 2021.
For correspondence or reprints, contact Steven Staelens (steven.staelens@uantwerpen.be) or Daniele Bertoglio (daniele.bertoglio@uantwerpen.be).
Published online Sep. 16, 2021.

housed singly in individually ventilated cages under a 12-h light/dark cycle in a temperature- and humidity-controlled environment with food and water ad libitum and at least 1 wk to acclimatize. All experiments were approved by the Ethical Committee for Animal Testing (ECD 2017–27) at the University of Antwerp (Antwerp, Belgium) and followed European Committee Guidelines (decree 2010/63/CEE).

The Q175DN model displays moderately slow disease progression with the hallmark of mHTT accumulation increasing from 3 to 12 mo (*26*). This animal model features motor deficits appearing around 6 mo and cognitive decline around 10 mo (*22,27*). Thus, ^{11}C-UCB-J PET imaging was performed at clinically relevant disease stages: cross-sectional at 3 mo (presymptomatic stage; 16 mice per genotype); longitudinal at 7, 10, and 16 mo (appearance, progression, and advanced symptomatic stages, respectively; 19 mice per genotype).

Tracer Radiosynthesis

^{11}C-UCB-J synthesis was performed on an automated synthesis module (Carbosynthon I; Comecer) by adapting the previously described procedure (*18*) to our system (*20*). Average radiochemical purity was greater than 99%, and molar activity (mean ± SD) was 96.5 ± 13.3 GBq/μmol.

^{11}C-UCB-J Dynamic Small-Animal PET Scan

Small-animal PET/CT imaging was performed on 2 Siemens Inveon PET/CT scanners (Siemens Preclinical Solutions). Animal preparation was performed as previously described (*20*). At the start of the dynamic small-animal PET scan, animals were injected via the tail vein with a bolus of ^{11}C-UCB-J (5.4 ± 1.3 MBq) over a 12-s interval (1 mL/min) by use of an automated pump (Pump 11 Elite; Harvard Apparatus). The activity was injected in a trace dose, keeping the cold mass within 2.0 μg/kg across time points for consistency. Data were acquired in list-mode format. After the small-animal PET scan, a 10-min CT scan (80 kV; 500 μA) was performed for coregistration and attenuation correction. Detailed information on the scan parameters is reported in Supplemental Table 1 (supplemental materials are available at http://jnm.snmjournals.org). Published work from our group (*20*) was reanalyzed for blocking validation of ^{11}C-UCB-J binding in the spinal cord. Blocking was achieved by pretreatment with levetiracetam injected intraperitoneally at either 50 (n = 4) or 200 (n = 4) mg/kg 30 min before radioligand delivery. Representative SUV images were generated on the basis of the interval from 10 to 90 min.

Image Processing and Analysis

Acquired PET data were reconstructed into 33 frames of increasing length (12 × 10 s, 3 × 20 s, 3 × 30 s, 3 × 60 s, 3 × 150 s, and 9 × 300 s). For quantitative analysis, all images were reconstructed using a list-mode iterative reconstruction with spatially variant resolution modeling, 8 iterations, and 16 subsets of the 3-dimensional ordered-subset expectation maximization algorithm (*28*). Normalization, dead time, and CT-based attenuation corrections were applied. PET image frames were reconstructed on a 128 × 128 × 159 grid with 0.776 × 0.776 × 0.796 mm^3 voxels. PET images were processed and analyzed using PMOD 3.6 software (PMOD Technologies).

Spatial normalization of the PET images was done through brain normalization of the PET images to an ^{11}C-UCB-J PET template as previously described (*20*). Using the volume-of-interest template based on the Waxholm atlas (*29*), time–activity curves of different regions (striatum, motor cortex, hippocampus, and thalamus) were extracted from the images. The cervical spinal cord volume of interest was manually delineated on the individual CT images (by a researcher blind to condition), and time–activity curves were extracted. Kinetic modeling was performed to fit the time–activity curves to a standard 1-tissue compartmental model to determine the total volume of distribution (V_T) by use of a noninvasive image-derived input function (IDIF); the V_T determined by use of the IDIF [$V_{T\ (IDIF)}$] was used as a surrogate of the V_T estimate, as we recently validated (*20*). No genotypic difference in the plasma-to-whole blood ratio or plasma radiometabolites was present between genotypes; therefore, no correction was applied (*20*).

Parametric $V_{T\ (IDIF)}$ and K_1 maps were generated in PMOD through voxelwise analysis (1-tissue compartmental model) (*20*). Brain parametric maps were represented as averages for each genotype overlaid on a 3-dimensional mouse brain MRI template for anatomic reference, whereas maps focusing on the spinal cord were represented as data for an individual animal overlaid on CT.

Mouse Brain Tissue

On termination of the longitudinal study, 16-mo-old animals (WT, n = 16; heterozygous, n = 13) were euthanized by decapitation while anesthetized, and brains were snap-frozen in 2-metylbuthane at −35°C for 2 min and preserved at −80°C until use. Serial sagittal sections (20 μm thick) were collected starting at 1.80 mm in the lateral bregma (*30*) in triplicate on Superfrost Plus slides (Thermo Fisher Scientific) using a cryostat (Leica).

Postmortem Human Brain Tissue

Freshly frozen postmortem superior frontal gyrus tissue was obtained from The Netherlands Brain Bank, Netherlands Institute for Neuroscience (open access: www.brainbank.nl). All material was collected from donors for or from whom written informed consent for a brain autopsy and the use of the material and clinical information for research purposes had been obtained by The Netherlands Brain Bank. Ethics permission for the study was obtained from the Committee for Medical Ethics of the University of Antwerp/Antwerp University Hospital (20/13/155).

Tissue was obtained from female donors (age range, 50–67 y) with a postmortem interval of less than 8 h for all cases. Because SV2A has been reported to be decreased in patients with Alzheimer disease (*31*), tissue was assessed for evidence of neurologic morbidities (β-amyloid and tauopathy) through immunostaining. After the exclusion of controls who did not have dementia but were positive for β-amyloid aggregates or tau tangles and the exclusion of symptomatic HD gene carriers who were positive for β-amyloid aggregates or tau tangles, only 1 control without dementia (ID 2017–005; 60-y-old female; postmortem interval = 5.5 h) and 1 symptomatic HD gene carrier (ID 2017–060; 57-y-old female; postmortem interval = 6.7 h) were included in the investigation. Although the CAG repeat length for individuals with HD was not available in The Netherlands Brain Bank database, the presence of mHTT aggregates was confirmed histologically. Serial sections (10 μm thick) were collected on Superfrost Plus slides using a cryostat.

Autoradiography

^{3}H-UCB-J autoradiography was performed on mice at 16 mo as well as on postmortem human tissue as previously described (*32*) after the validation of SV2A selectivity using a blocking solution (1 nM ^{3}H-UCB-J plus 1 mM levetiracetam in binding buffer) to validate ^{3}H-UCB-J specificity for SV2A (Supplemental Fig. 1). ^{3}H-UCB-J was synthesized at Pharmaron and had a molar radioactivity of 1,295 MBq/μmol and a radiochemical purity of greater than 99%.

Regional quantification was performed without knowledge of genotype using Fiji software (National Institutes of Health). ^{3}H-UCB-J binding was measured in triplicate on 3 manually drawn slices. Region-specific binding of ^{3}H-UCB-J was measured by converting the mean gray matter values into radioactivity density (Bq/mg) using commercial tritium standards (American Radiolabeled Chemicals). Next, using ^{3}H-UCB-J molar activity on the day of the experiment, radioactivity density was converted into binding density (fmol/mg) for each region.

Immunofluorescence

SV2A immunofluorescence was determined in mice at 16 mo as well as in postmortem human tissue. Sections were air dried for 5 min

and incubated with 4% paraformaldehyde for 15 min for tissue postfixation. Next, slices were rinsed using phosphate-buffered saline (PBS), and nonspecific binding sites were blocked using 20% normal donkey serum in PBS for 1 h. Then, sections were incubated with an anti-SV2A primary antibody (rabbit antimouse; 1:400; 66724 [Cell Signaling Technologies]) in antibody diluent containing 5% normal donkey serum in PBS overnight at room temperature. On the next day, sections were washed with PBS before being incubated for 1 h with a secondary donkey anti-rabbit antibody (1:100; Alexa Fluor 488 [Jackson ImmunoResearch]) in antibody diluent containing 5% normal donkey serum in PBS. After washes with PBS, sections were mounted with 4′,6-diamidino-2-phenylindole (Vector Laboratories), and coverslips were added. Images at magnifications of ×20 and ×100 were acquired for quantification with a high-throughput fluorescence microscope (Nikon) with NIS-Elements Software (Nikon).

Quantification was performed without knowledge of genotype using Fiji software. Because the white matter was devoid of a specific signal, after conversion into an 8-bit gray scale, an intensity threshold was set to remove the background signal in the white matter (threshold, 27 of 255) and convert images into binary data. Regions of interest (striatum, motor cortex, hippocampus, and thalamus for mouse tissue; cortical gray matter for human tissue) were manually drawn on each image, and the percentage of surface area after thresholding was measured as the positive area. Quantification was done in triplicate (3 slices) for each region, and the average was used for statistical analysis.

Statistical Analysis

All data were normally distributed, as assessed using the Shapiro–Wilk test. Longitudinal PET data were analyzed with a linear mixed model by fitting each region separately using ^{11}C-UCB-J $V_{T\ (IDIF)}$ or K_1 determined by use of the IDIF as the dependent variable; genotype (WT and heterozygous), time (7, 10, and 16 mo), and the interaction between genotype and time (genotype × time) as fixed effects; and subjects as a random effect. The comparison was performed to evaluate regional temporal and genotypic differences. A 2-way ANOVA (with genotype and region as variables) was applied to investigate the 3-mo data and postmortem analyses. A 1-way ANOVA was used for blocking analysis in the spinal cord, whereas an unpaired t test was used to compare the genotypic differences in spinal cord SV2A PET. A Pearson correlation test was used to determine the relationship between variables. Normality and 2-way ANOVA were performed with GraphPad Prism (v 9.0) statistical software (GraphPad Software), analysis of the linear mixed model was performed with JMP Pro 13 (SAS Institute Inc.), and calculation of the effect size d was performed with G*Power software (http://www.gpower.hhu.de/). P values were corrected for multiple comparisons using the Tukey test. Data are represented as mean ± SD. All tests were 2-tailed, and statistical significance was set at $P < 0.05$.

RESULTS

SV2A Density Decreased with HD Progression

Longitudinal mean $V_{T\ (IDIF)}$ parametric maps of ^{11}C-UCB-J at 7, 10, and 16 mo displayed a broad cerebral reduction of ^{11}C-UCB-J binding in symptomatic heterozygous mice compared with WT littermates (Fig. 1A). Accordingly, ^{11}C-UCB-J $V_{T\ (IDIF)}$ values were significantly lower in heterozygous mice than in WT animals at all stages of disease investigated (i.e., 7, 10, and 16 mo) in parallel with HD progression (e.g., −13.4% ± 3.4% [$P < 0.01$], −10.8% ± 4.0% [$P < 0.01$], and −20.3% ± 4.0% [$P < 0.0001$] at 7, 10, and 16 mo, respectively, in the striatum) (Fig. 1B and Supplemental Table 2). Notably, the reduced ^{11}C-UCB-J uptake was not related to altered K_1 values (delivery rate of the tracer) (Supplemental Fig. 2), suggesting that the reduced binding did not reflect a mere decrease in cerebral perfusion.

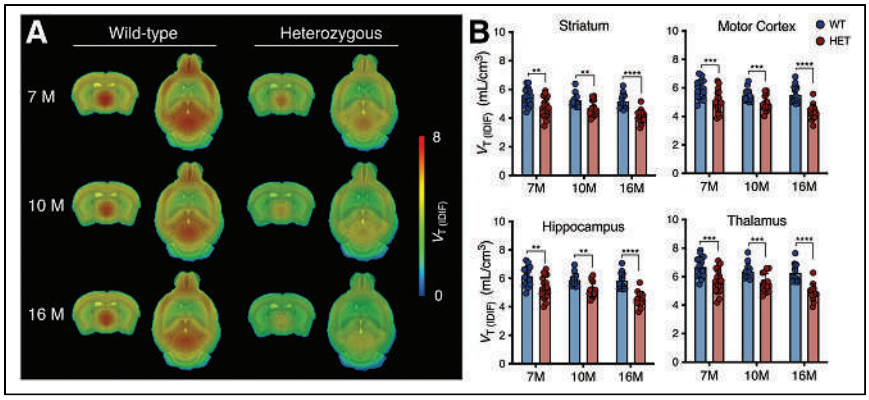

FIGURE 1. ^{11}C-UCB-J binding is reduced in symptomatic heterozygous (HET) mice. (A) Mean parametric ^{11}C-UCB-J $V_{T\ (IDIF)}$ maps of 7-, 10-, and 16-mo-old mice overlaid on MRI template for anatomic localization. (B) Cerebral $V_{T\ (IDIF)}$ quantification denoting significant reduction in HET mice compared with WT littermates. $^{**}P < 0.01$. $^{***}P < 0.001$. $^{****}P < 0.0001$.

No difference in ^{11}C-UCB-J $V_{T\ (IDIF)}$ values between WT and presymptomatic heterozygous mice (3 mo) was observed ($F_{1,116} = 2.847$ [$P = 0.092$]; e.g., −3.1% ± 4.1% for the striatum) (Fig. 2). $V_{T\ (IDIF)}$ values at different ages are reported in Supplemental Table 3.

SV2A Levels Were Reduced in Spinal Cord of Symptomatic Heterozygous Mice

We explored the potential application of ^{11}C-UCB-J PET for the detection of SV2A in the mouse spinal cord. ^{11}C-UCB-J binding was quantifiable and specific, as validated after pretreatment with levetiracetam ($F_{2,10} = 78.96$ [$P < 0.0001$]) (Fig. 3).

Next, on the basis of clinical evidence indicating the presence of mHTT pathology in the spinal cord, we quantified ^{11}C-UCB-J PET in the cervical spinal cord of symptomatic heterozygous mice (16 mo). ^{11}C-UCB-J binding was significantly lower in the cervical

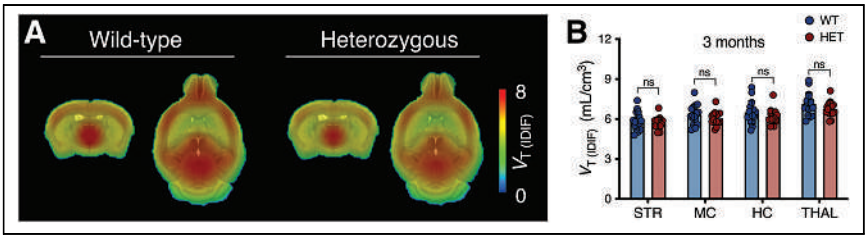

FIGURE 2. ^{11}C-UCB-J binding is not altered in presymptomatic heterozygous (HET) mice. (A) Mean parametric ^{11}C-UCB-J $V_{T\ (IDIF)}$ maps of 3-mo-old mice overlaid on MRI template for anatomic localization. (B) Cerebral $V_{T\ (IDIF)}$ quantification at 3 mo does not differ between genotypes. HC = hippocampus; MC = motor cortex; ns = not significant; STR = striatum; THAL = thalamus.

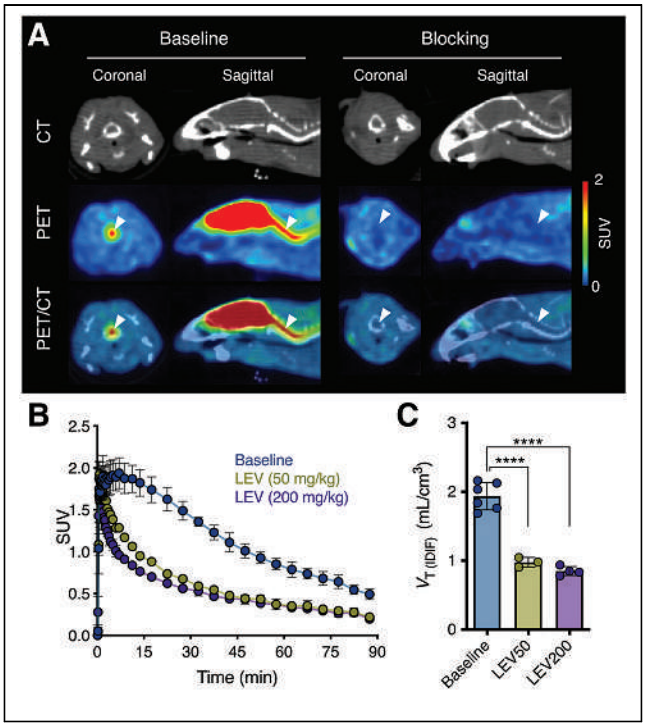

FIGURE 3. ^{11}C-UCB-J binding is specific and quantifiable in mouse spinal cord. (A) Representative ^{11}C-UCB-J SUV PET/CT images of WT mouse at baseline and after pretreatment with levetiracetam (LEV, 200 mg/kg, intraperitoneal). Arrowheads indicate cervical spinal cord. (B) Cervical spinal cord SUV time–activity curves showing dose-dependent blocking effect. (C) Quantification of ^{11}C-UCB-J $V_{T\ (IDIF)}$ in cervical spinal cord. LEV50 = LEV at 50 mg/kg; LEV200 = LEV at 200 mg/kg. ****$P < 0.0001$.

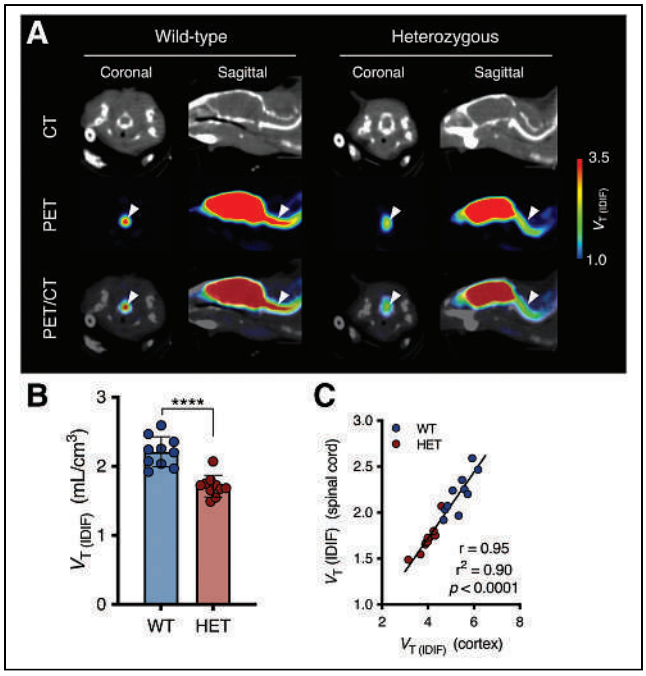

FIGURE 4. ^{11}C-UCB-J binding is decreased in spinal cord of symptomatic heterozygous (HET) mice. (A) Representative maps of 16-mo-old mice overlaid on CT. Arrowheads indicate cervical spinal cord. (B) Spinal $V_{T\ (IDIF)}$ is significantly lower in 16-mo-old HET mice than in WT mice. ****$P <$ 0.0001. (C) Correlation between spinal and cortical ^{11}C-UCB-J binding.

spinal cord of heterozygous mice than in that of WT littermates (−22.5% ± 3.8% [$P < 0.0001$]) (Fig. 4B), and there was a strong association with cortical quantification ($r^2 = 0.90$ [$P < 0.0001$]) (Fig. 4C).

Postmortem Rodent and Human Studies Corroborated SV2A Reduction in HD

^{3}H-UCB-J–specific binding was significantly lower in heterozygous mice than in WT littermates ($F_{1,104} = 35.77$ [$P < 0.0001$]; e.g., −22.1% ± 8.3% for the striatum), in agreement with the in vivo measurement and as corroborated by SV2A immunostaining ($F_{1,104} = 51.42$ [$P < 0.0001$]; e.g., −12.0% ± 4.5% for the striatum) (Fig. 5A).

We performed a preliminary assessment of ^{3}H-UCB-J binding in postmortem human cortex tissues from a control and an HD gene carrier (Fig. 5B). Both ^{3}H-UCB-J–specific binding and SV2A immunostaining indicated a lower SV2A signal in the HD gene carrier (Fig. 5C).

DISCUSSION

This work assessed synaptic integrity using the PET radioligand ^{11}C-UCB-J in heterozygous mice at clinically relevant presymptomatic and symptomatic stages of the disease. To our knowledge, this work represents the first evidence of in vivo changes in SV2A density. In particular, changes in synaptic density were detectable at all symptomatic stages of HD with mHTT accumulation broadly affecting SV2A levels in the entire CNS.

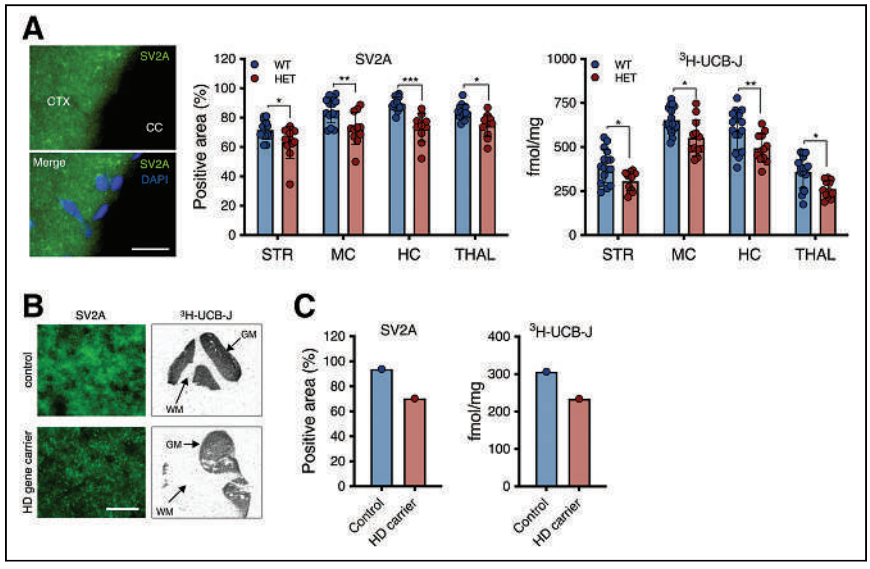

FIGURE 5. Postmortem quantification displayed SV2A reduction in HD. (A) SV2A immunostaining and ^{3}H-UCB-J–specific binding in murine brain. (B) Representative SV2A immunostaining and ^{3}H-UCB-J total binding autoradiograms of human control and HD gene carrier. (C) ^{3}H-UCB-J–specific binding and SV2A immunostaining tissue suggest reduction in cortical SV2A in human tissue. *$P < 0.05$. **$P < 0.01$. ***$P < 0.001$. CC = corpus callosum; CTX = cortex; DAPI = 4′,6-diamidino-2-phenylindole; GM = gray matter; HC = hippocampus; HET = heterozygous; MC = motor cortex; ns = not significant; STR = striatum; THAL = thalamus; WM = white matter. Scale bar = 20 μm.

Despite mounting evidence indicating that mHTT induces presynaptic transmission dysfunction during the progression of HD (*4,5*), to date no clinical or preclinical studies have assessed alterations in presynaptic proteins in vivo. Nonetheless, cross-sectional findings in animal models of HD suggested a reduction in different synaptic proteins in different animal models at symptomatic but not presymptomatic stages of the disease (*8–10*), in agreement with our observations in vivo in heterozygous mice as well as in vitro in the tissues of mice with HD and postmortem human tissue.

Since the development of SV2A radioligands for in vivo imaging of SV2A (*18,19*), preclinical and clinical investigations have been restricted to the brain despite the fact that SV2A is distributed in all gray matter, including the spinal cord (*33*). Thus, on the basis of our previous levetiracetam blocking study (*20*), we evaluated the specificity of the ^{11}C-UCB-J signal in the cortical spinal cord; we demonstrated the capability of SV2A PET imaging in the spinal cord of a living animal. Interestingly, Lambeng et al. reported a 2- to 3-fold difference in SV2A expression in the spinal cord compared with the cerebral cortex in the rat (*33*). In the present work, we measured a 2.5-fold difference in ^{11}C-UCB-J binding between the spinal cord and the motor cortex, in agreement with the previous report for the rat (*33*). Next, on the basis of the clinical evidence of mHTT pathology in the spinal cord (*25*), we explored ^{11}C-UCB-J binding in the cervical spinal cord of symptomatic heterozygous mice and observed a decline in SV2A density of a magnitude similar to that in the brain. Altogether, these observations support the exploration of SV2A PET imaging as a synaptic integrity marker in spinal cord–related disorders, such as amyotrophic lateral sclerosis, as well as spinal cord injury. On the basis of recent evidence that levetiracetam treatment leads to functional recovery in spinal cord injury models (*34*), the latter is currently being investigated by our group.

In recent years, the use of PET imaging in the identification of different striatal markers for monitoring HD progression has significantly progressed (*35–41*). However, since the whole CNS is affected in HD, noninvasive markers with a ubiquitous brain distribution, such as ^{11}C-UCB-J PET imaging, may provide unique insights for elucidating global pathophysiologic changes during HD. Intriguingly, the clinical feasibility of detecting SV2A decline has been reported in other neurodegenerative disorders, including Alzheimer disease and Parkinson disease (*31,42*).

CONCLUSION

Collectively, these findings demonstrate significant SV2A deficits in the brain and spinal cord of symptomatic heterozygous mice. ^{11}C-UCB-J PET imaging may be a promising marker for the assessment of synaptic integrity in patients with HD during disease progression and after disease-modifying therapeutic strategies.

DISCLOSURE

This work was funded by CHDI Foundation, Inc., a nonprofit biomedical research organization exclusively dedicated to developing therapeutics that will substantially improve the lives of HD-affected individuals. D. Bertoglio is supported by the Research Foundation Flanders (FWO; 1229721N) and the University of Antwerp (BOF KP; FFB210050). The University of Antwerp also funded the work through partial assistant professor positions for J. Verhaeghe and L. Wyffels and full professor positions for S. Stroobants and S. Staelens. L. Wyffels and S. Stroobants are also supported by Antwerp University Hospital through departmental positions. No other potential conflict of interest relevant to this article was reported.

ACKNOWLEDGMENTS

We thank Philippe Joye, Caroline Berghmans, Eleni Van der Hallen, and Annemie Van Eetveldt of MICA for their valuable technical assistance.

KEY POINTS

QUESTION: Is SV2A density affected during the progression of HD?

PERTINENT FINDINGS: In this ^{11}C-UCB-J PET study, we demonstrated brain and spinal cord SV2A deficits during symptomatic HD in mice, highlighting the potential of SV2A PET as a marker in the entire CNS.

IMPLICATIONS FOR PATIENT CARE: ^{11}C-UCB-J PET imaging may be a unique CNS functional marker for HD and may have promise as an application for SV2A measurement in patients with HD during disease progression and following therapeutic interventions.

REFERENCES

1. The Huntington's Disease Collaborative Research Group. A novel gene containing a trinucleotide repeat that is expanded and unstable on Huntington's disease chromosomes. *Cell.* 1993;72:971–983.
2. Rüb U, Vonsattel JP, Heinsen H, Korf HW. The neuropathology of Huntingtons disease: classical findings, recent developments and correlation to functional neuroanatomy. *Adv Anat Embryol Cell Biol.* 2015;217:1–146.
3. Waldvogel HJ, Kim EH, Tippett LJ, Vonsattel JP, Faull RL. The neuropathology of Huntington's disease. *Curr Top Behav Neurosci.* 2015;22:33–80.
4. Rozas JL, Gomez-Sanchez L, Tomas-Zapico C, Lucas JJ, Fernandez-Chacon R. Presynaptic dysfunction in Huntington's disease. *Biochem Soc Trans.* 2010;38:488–492.
5. Sepers MD, Raymond LA. Mechanisms of synaptic dysfunction and excitotoxicity in Huntington's disease. *Drug Discov Today.* 2014;19:990–996.
6. Smith R, Klein P, Koc-Schmitz Y, et al. Loss of SNAP-25 and rabphilin 3a in sensory-motor cortex in Huntington's disease. *J Neurochem.* 2007;103:115–123.
7. Fourie C, Kim E, Waldvogel H, et al. Differential changes in postsynaptic density proteins in postmortem Huntington's disease and Parkinson's disease human brains. *J Neurodegener Dis.* 2014;2014:938530.
8. Smith R, Petersen A, Bates GP, Brundin P, Li JY. Depletion of rabphilin 3A in a transgenic mouse model (R6/1) of Huntington's disease, a possible culprit in synaptic dysfunction. *Neurobiol Dis.* 2005;20:673–684.
9. Shirendeb UP, Calkins MJ, Manczak M, et al. Mutant Huntington's interaction with mitochondrial protein Drp1 impairs mitochondrial biogenesis and causes defective axonal transport and synaptic degeneration in Huntington's disease. *Hum Mol Genet.* 2012;21:406–420.
10. Smith GA, Rocha EM, McLean JR, et al. Progressive axonal transport and synaptic protein changes correlate with behavioral and neuropathological abnormalities in the heterozygous Q175 KI mouse model of Huntington's disease. *Hum Mol Genet.* 2014;23:4510–4527.
11. Li H, Wyman T, Yu ZX, Li SH, Li XJ. Abnormal association of mutant Huntington with synaptic vesicles inhibits glutamate release. *Hum Mol Genet.* 2003;12:2021–2030.
12. Milnerwood AJ, Gladding CM, Pouladi MA, et al. Early increase in extrasynaptic NMDA receptor signaling and expression contributes to phenotype onset in Huntington's disease mice. *Neuron.* 2010;65:178–190.
13. DiProspero NA, Chen EY, Charles V, Plomann M, Kordower JH, Tagle DA. Early changes in Huntington's disease patient brains involve alterations in cytoskeletal and synaptic elements. *J Neurocytol.* 2004;33:517–533.
14. Milnerwood AJ, Raymond LA. Early synaptic pathophysiology in neurodegeneration: insights from Huntington's disease. *Trends Neurosci.* 2010;33:513–523.
15. Tabrizi SJ, Ghosh R, Leavitt BR. Huntington lowering strategies for disease modification in Huntington's disease. *Neuron.* 2019;101:801–819.

16. Bajjalieh SM, Frantz GD, Weimann JM, McConnell SK, Scheller RH. Differential expression of synaptic vesicle protein 2 (SV2) isoforms. *J Neurosci.* 1994;14: 5223–5235.
17. Janz R, Sudhof TC. SV2C is a synaptic vesicle protein with an unusually restricted localization: anatomy of a synaptic vesicle protein family. *Neuroscience.* 1999;94: 1279–1290.
18. Nabulsi NB, Mercier J, Holden D, et al. Synthesis and preclinical evaluation of ^{11}C-UCB-J as a PET tracer for imaging the synaptic vesicle glycoprotein 2A in the brain. *J Nucl Med.* 2016;57:777–784.
19. Finnema SJ, Nabulsi NB, Eid T, et al. Imaging synaptic density in the living human brain. *Sci Transl Med.* 2016;8:348ra96.
20. Bertoglio D, Verhaeghe J, Miranda A, et al. Validation and noninvasive kinetic modeling of [^{11}C]UCB-J PET imaging in mice. *J Cereb Blood Flow Metab.* 2020; 40:1351–1362.
21. Finnema SJ, Nabulsi NB, Mercier J, et al. Kinetic evaluation and test-retest reproducibility of [^{11}C]UCB-J, a novel radioligand for positron emission tomography imaging of synaptic vesicle glycoprotein 2A in humans. *J Cereb Blood Flow Metab.* 2018;38:2041–2052.
22. Menalled LB, Kudwa AE, Miller S, et al. Comprehensive behavioral and molecular characterization of a new knock-in mouse model of Huntington's disease: zQ175. *PLoS One.* 2012;7:e49838.
23. Heikkinen T, Lehtimaki K, Vartiainen N, et al. Characterization of neurophysiological and behavioral changes, MRI brain volumetry and ^{1}H MRS in zQ175 knock-in mouse model of Huntington's disease. *PLoS One.* 2012;7:e50717.
24. Peng Q, Wu B, Jiang M, et al. Characterization of behavioral, neuropathological, brain metabolic and key molecular changes in zQ175 knock-in mouse model of Huntington's disease. *PLoS One.* 2016;11:e0148839.
25. Sciacca G, Cicchetti F. Mutant huntingtin protein expression and blood-spinal cord barrier dysfunction in Huntington disease. *Ann Neurol.* 2017;82:981–994.
26. Carty N, Berson N, Tillack K, et al. Characterization of HTT inclusion size, location, and timing in the zQ175 mouse model of Huntington's disease: an in vivo high-content imaging study. *PLoS One.* 2015;10:e0123527.
27. Heikkinen T, Bragge T, Bhattarai N, et al. Rapid and robust patterns of spontaneous locomotor deficits in mouse models of Huntington's disease. *PLoS One.* 2020; 15:e0243052.
28. Miranda A, Bertoglio D, Glorie D, Stroobants S, Staelens S, Verhaeghe J. Validation of a spatially variant resolution model for small animal brain PET studies. *Biomed Phys Eng Expr.* 2020;6:045001.
29. Johnson GA, Badea A, Brandenburg J, et al. Waxholm space: an image-based reference for coordinating mouse brain research. *Neuroimage.* 2010;53:365–372.
30. Paxinos G, Franklin K. *The Mouse Brain in Stereotaxic Coordinates.* 2nd ed. Cambridge, MA: Academic Press; 2003.
31. Chen MK, Mecca AP, Naganawa M, et al. Assessing synaptic density in Alzheimer disease with synaptic vesicle glycoprotein 2A positron emission tomographic imaging. *JAMA Neurol.* 2018;75:1215–1224.
32. Glorie D, Verhaeghe J, Miranda A, De Lombaerde S, Stroobants S, Staelens S. Sapap3 deletion causes dynamic synaptic density abnormalities: a longitudinal [^{11}C]UCB-J PET study in a model of obsessive-compulsive disorder-like behaviour. *EJNMMI Res.* 2020;10:140.
33. Lambeng N, Gillard M, Vertongen P, Fuks B, Chatelain P. Characterization of [^{3}H]ucb 30889 binding to synaptic vesicle protein 2A in the rat spinal cord. *Eur J Pharmacol.* 2005;520:70–76.
34. Lima R, Gomes ED, Cibrao JR, et al. Levetiracetam treatment leads to functional recovery after thoracic or cervical injuries of the spinal cord. *NPJ Regen Med.* 2021;6:11.
35. Häggkvist J, Toth M, Tari L, et al. Longitudinal small-animal PET imaging of the zQ175 mouse model of Huntington disease shows in vivo changes of molecular targets in the striatum and the cerebral cortex. *J Nucl Med.* 2017;58: 617–622.
36. Bertoglio D, Kosten L, Verhaeghe J, et al. Longitudinal characterization of mGluR5 using ^{11}C-ABP688 PET imaging in the Q175 mouse model of Huntington disease. *J Nucl Med.* 2018; 59:1722–1727.
37. Bertoglio D, Verhaeghe J, Kosten L, et al. MR-based spatial normalization improves [^{18}F]MNI-659 PET regional quantification and detectability of disease effect in the Q175 mouse model of Huntington's disease. *PLoS One.* 2018;13: e0206613.
38. Russell DS, Barret O, Jennings DL, et al. The phosphodiesterase 10 positron emission tomography tracer, [^{18}F]MNI-659, as a novel biomarker for early Huntington disease. *JAMA Neurol.* 2014;71:1520–1528.
39. Pavese N, Andrews TC, Brooks DJ, et al. Progressive striatal and cortical dopamine receptor dysfunction in Huntington's disease: a PET study. *Brain.* 2003;126: 1127–1135.
40. Russell DS, Jennings DL, Barret O, et al. Change in PDE10 across early Huntington disease assessed by [^{18}F]MNI-659 and PET imaging. *Neurology.* 2016;86: 748–754.
41. Bertoglio D, Kosten L, Verhaeghe J, et al. Longitudinal characterization of mGluR5 using ^{11}C-ABP688 PET imaging in the Q175 mouse model of Huntington disease. *J Nucl Med.* 2018;59:1722–1727.
42. Matuskey D, Tinaz S, Wilcox KC, et al. Synaptic changes in Parkinson disease assessed with in vivo imaging. *Ann Neurol.* 2020;87:329–338.

Feasibility of In Vivo Imaging of Fibroblast Activation Protein in Human Arterial Walls

Meiqi Wu[1], Jing Ning[2], Jingle Li[2], Zhichao Lai[3], Ximin Shi[1], Haiqun Xing[1], Marcus Hacker[2], Bao Liu[3], Li Huo[1], and Xiang Li[2]

[1]*Department of Nuclear Medicine, State Key Laboratory of Complex Severe and Rare Diseases, Center for Rare Diseases Research, Beijing Key Laboratory of Molecular Targeted Diagnosis and Therapy in Nuclear Medicine, Peking Union Medical College Hospital, Chinese Academy of Medical Science and Peking Union Medical College, Beijing, China;* [2]*Division of Nuclear Medicine, Department of Biomedical Imaging and Image-Guided Therapy, Medical University of Vienna, Vienna, Austria; and* [3]*Department of Vascular Surgery, Peking Union Medical College Hospital, Chinese Academy of Medical Sciences and Peking Union Medical College, Beijing, China*

Increased expression of fibroblast-activating protein (FAP) in fibrous caps may contribute to progression of atherosclerotic plaques. **Methods:** Forty-one patients who underwent ^{68}Ga-conjugated quinoline-based FAP inhibitor (^{68}Ga-FAPI-04) PET/CT for noncardiovascular indications were retrospectively analyzed. Correlations were assessed between the uptake of ^{68}Ga-FAPI-04 in large arterial walls (SUV_{max} and target-to-background ratio, TBR) and degree of calcification and cardiovascular risk factors. **Results:** Focal arterial uptake of ^{68}Ga-FAPI-04 or calcification was detected in 1,177 arterial segments in all 41 patients. TBR was negatively correlated with the degree of calcification (Hounsfield units) ($r = -0.27$, $P < 0.01$). Mean TBR in higher-risk patients was greater than in lower-risk patients (2.2 ± 0.3 vs. 1.8 ± 0.3, $P < 0.01$). Immunohistochemical labeling of carotid plaques exhibited prominent FAP expression in a thin fibrous cap and moderate FAP expression in a thick cap. **Conclusion:** ^{68}Ga-FAPI-04 PET/CT might have potential for imaging fibroblastic activation in the arterial wall.

Key Words: ^{68}Ga-FAPI-04; fibroblast-activating protein; PET/CT; active arterial wall

J Nucl Med 2022; 63:948–951
DOI: 10.2967/jnumed.121.262863

Atherosclerosis is the primary cause of cardiovascular disease, defined by the chronic, progressive accumulation of lipids and fibrous elements in large arterial walls. The major contributors to plaque vulnerability include a large necrotic core, a thin fibrous cap, expansive remodeling, neovascularization, plaque hemorrhage, and adventitial inflammation (*1*). The identification of specific biomarkers of plaque vulnerability remains highly important, yet difficult (*2*). Destabilization of fibrous caps is mediated by collagen degeneration and the activity of extracellular proteases (*1*). Fibroblast-activating protein (FAP) is a type II membrane-bound serine protease (*3*). Preliminary ex vivo analysis detected higher FAP expression in human atherosclerotic aortic plaques than in plaque-free arterial walls; particularly, FAP expression increased in thin-capped compared with thick-capped atheromas (*4,5*). Recently, the development of PET imaging using several ^{68}Ga-labeled FAP inhibitors (FAPIs) introduced the possibility of noninvasive, in vivo visualization of human FAP expression (*6*). In this study, we aimed to quantify the arterial fibroblast activation via ^{68}Ga-conjugated quinoline-based FAP inhibitor (^{68}Ga-FAPI-04) PET/CT imaging in correlation with cardiovascular risk factors.

MATERIALS AND METHODS

Patients

Forty-one patients (10 women and 31 men; mean age ± SD, 59 ± 11 y) with suggestive hepatic lesions ($n = 27$) or IgG4-related disease ($n = 14$) underwent ^{68}Ga-FAPI-04 PET/CT imaging between January 2019 and January 2020. The baseline characteristics and cardiovascular risk factors were documented (Table 1). The exclusion criteria included periaortitis, vasculitis, and chemotherapy within 4 wk. The study protocol complied with the tenets of the Declaration of Helsinki and its later amendments. The study protocol was approved by the institutional review board of Peking Union Medical College Hospital, and all subjects signed an informed consent form before undergoing imaging.

Radiopharmacy and PET/CT Scans

Radiolabeling with ^{68}Ga-FAPI-04 was performed as previously described (*7,8*). All subjects underwent scans on a dedicated PET/CT scanner (Polestar m660; SinoUnion) after an uptake time of 42–70 min after intravenous injection of ^{68}Ga-FAPI-04 (92.5–260 MBq). After an unenhanced low-dose CT scan (120 keV, 30–50 mA), PET images were obtained from the tip of the skull to the mid thigh in 3-dimensional mode with a scan time of 2 min per bed position.

Image Analysis

We performed an active-segment analysis (target-to-background ratio [TBR] ≥ 1.6) in the 5 major arteries, including the aortic arch, ascending aorta, thoracic aorta, abdominal aorta, and iliac arteries (*9*). The regions of interest were manually drawn around each active segment (10-mm diameter), and SUV_{max} was determined from transaxial PET/CT images. The TBR of each active segment was derived as the segment's SUV_{max} divided by the SUV of the blood pool (average SUV_{mean} of 3 regions of interest within the vena cava). We calculated the mean TBR of all active arterial segments to assess the overall burden for each patient (*9*). The radioactivity in calcified arterial segments with a minimum density of 130 Hounsfield units (HU) on unenhanced CT images was also assessed (*10*). Two experienced nuclear medicine physicians assessed the PET/CT images. Discrepancies were reassessed by the 2 readers working in

Received Jul. 8, 2021; revision accepted Sep. 9, 2021.
For correspondence or reprints, contact Li Huo (huoli@pumch.cn).
Published online Sep. 16, 2021.

TABLE 1
Baseline Patient Characteristics (n = 41)

Characteristic	Data
Age (y)	59 ± 11
Sex ratio (female-to-male)	1:3.1
Hepatic lesion suggestive of malignancy	27 (66%)
IgG4-related disease	14 (34%)
Body mass index (kg/m^2)	23 ± 3
Risk factors	
Hypertension	12 (30%)
Diabetes mellitus	10 (24%)
Dyslipidemia	7 (17%)
Smoking	21 (51%)
History of cardiovascular event	4 (10%)

Qualitative data are number and percentage; continuous data are mean and SD.

consensus. All analyses were conducted using Hybrid 3D (Hermes Medical Solutions).

Immunohistochemistry to Assess FAP Expression in Carotid Arterial Plaques

Cryosections of tissue samples containing carotid plaques were obtained from patients who underwent endarterectomy secondary to carotid artery stenosis. Fibrous caps were identified as collagen-rich tissues visualized with elastin Masson trichrome stain separating the lumen from the necrotic core. Immunohistochemistry assessed the FAP expression with anti-FAP antibody (1:300, SP325; Abcam).

Statistics

Parametric variables are expressed as mean ± SD or as median along with first and third quartiles. Arterial segments were categorized on the basis of calcification (noncalcified [<130 HU], mildly calcified [130–399 HU], or severely calcified [≥400 HU]). Patients were divided into high-risk (prevalence of ≥4 cardiovascular risk factors) and low-risk (<4 cardiovascular risk factors) groups. FAPI uptake was compared among the 3 calcification groups by 1-way ANOVAs. The variation in mean TBR for each patient in different cardiovascular risk factor groups and high-risk or low-risk groups was assessed by unpaired t tests. Interobserver reliability was tested in all patients with intraclass correlation coefficients using a 2-way random model applying absolute agreement. All statistical analyses were performed using SPSS Statistics (version 25, IBM Corp.). P values of less than 0.05 denoted statistical significance.

RESULTS

^{68}Ga-FAPI-04 Uptake of Active Arterial Segments and Relationship to Calcification

In total, 1,177 arterial segments of focal uptake of ^{68}Ga-FAPI-04 or calcification were identified in all 41 patients. The mean SUV_{max} and mean TBR for ^{68}Ga-FAPI-04 were 1.6 ± 0.5 and 2.0 ± 0.7, respectively. Among all assessed arterial segments, the abdominal aorta exhibited the highest number of segments (n = 379), followed by the thoracic aorta (n = 272) and the ascending aorta (n = 203). Analysis of all 1,177 segments showed a significant correlation between the extent of calcification (HU) and the intensity of ^{68}Ga-FAPI-04 uptake (TBR) (r = −0.27, P < 0.01; Fig. 1A). Noncalcified segments had significantly higher uptake (TBR, 2.2 ± 0.6; n = 603) than mildly calcified segments (TBR, 1.9 ± 0.8; n = 220) (P < 0.01). Severely calcified segments exhibited the lowest uptake of ^{68}Ga-FAPI-04 (TBR, 1.7 ± 0.6; n = 354) (P < 0.01) (Fig. 1B). The correlation coefficient was 0.89 (95% CI, 0.80–0.95) for interobserver agreement on TBR.

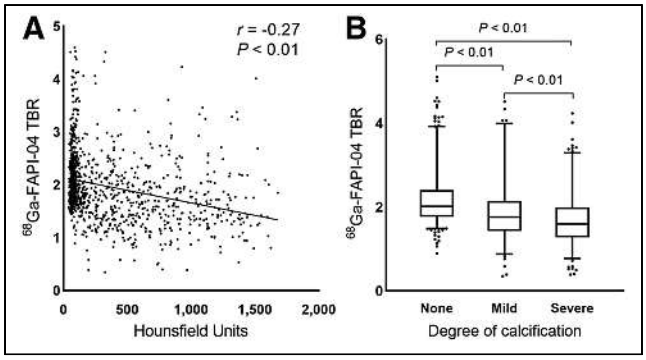

FIGURE 1. ^{68}Ga-FAPI-04 uptake correlates with degree of calcification in per-segment analysis (n = 1,177).

Relationship Between Arterial ^{68}Ga-FAPI-04 Uptake and Cardiovascular Risk Factors

The mean number of active arterial segments per patient was 29 ± 13 (range, 8–78). In the per-patient analysis, the mean TBR for ^{68}Ga-FAPI-04 was 1.9 ± 0.4. The mean individual TBR was significantly higher in overweight or obese patients (body mass index ≥ 24.0, 2.2 ± 0.4; n = 10) than in those with normal weight (1.8 ± 0.3; n = 21). There was no significant difference in ^{68}Ga-FAPI-04 uptake in other cardiovascular risk factor groups (Fig. 2), including male sex, older age, hypertension, diabetes mellitus, dyslipidemia, smoking habits, and past cardiovascular events. The mean TBR and the number of identified arterial segments in the high-risk patients with 4 or more cardiovascular risk factors (TBR_{mean}, 2.2 ± 0.3; segment number, 36 ± 17; n = 15) was significantly higher than that in the low-risk patients (TBR_{mean}, 1.8 ± 0.3; segment number, 24 ± 9; n = 26) (both P < 0.01). Figure 3 shows examples of radiotracer uptake patterns of ^{68}Ga-FAPI-04 in the arterial wall. All patients in the figure were over 60 y old with more than 4 cardiovascular risk factors.

FAP Expression in Human Carotid Atherosclerotic Plaques

Collagen tissue was assessed by Masson trichrome staining (Fig. 4, in blue) of human carotid arterial plaques. On the basis of the fibrous cap thickness, the specimens were characterized as thin-capped (<65 μm) or thick-capped (≥65 μm) plaques. Immunohistochemical labeling with an anti-FAP antibody in sections demonstrated a prominent FAP expression in the thin fibrous cap, versus a relatively lower expression in the thick fibrous cap (Fig. 4). Specific FAPI expression localized in denatured collagen fibers (Fig. 4).

DISCUSSION

To our knowledge, this was the first noninvasive study to describe the expression of FAP in human arterial walls via ^{68}Ga-FAPI-04 PET/CT imaging. In this retrospective study of a noncardiovascular cohort, we observed significantly elevated uptake in noncalcified active arterial segments compared with advanced chronic lesions presenting extensive calcification, and we observed elevated ^{68}Ga-FAPI-04 uptake in patients with increased cardiovascular risk factors. We also found higher arterial uptake in

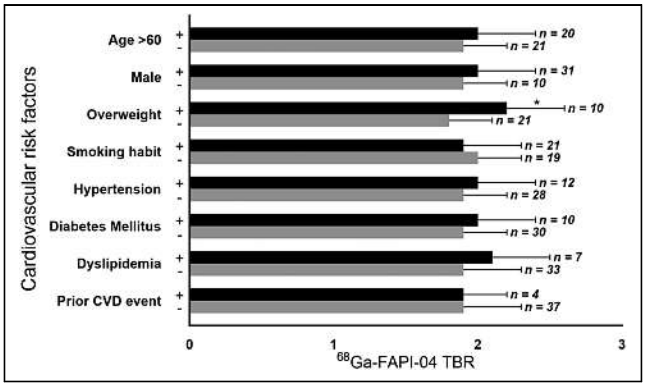

FIGURE 2. Comparison of overall arterial ^{68}Ga-FAPI-04 burden with respect to cardiovascular risk factors. CVD = cardiovascular disease. *Statistically significant difference ($P < 0.05$) in ^{68}Ga-FAPI-04 TBRs between patients who were overweight/obese or normal weight based on their body mass index.

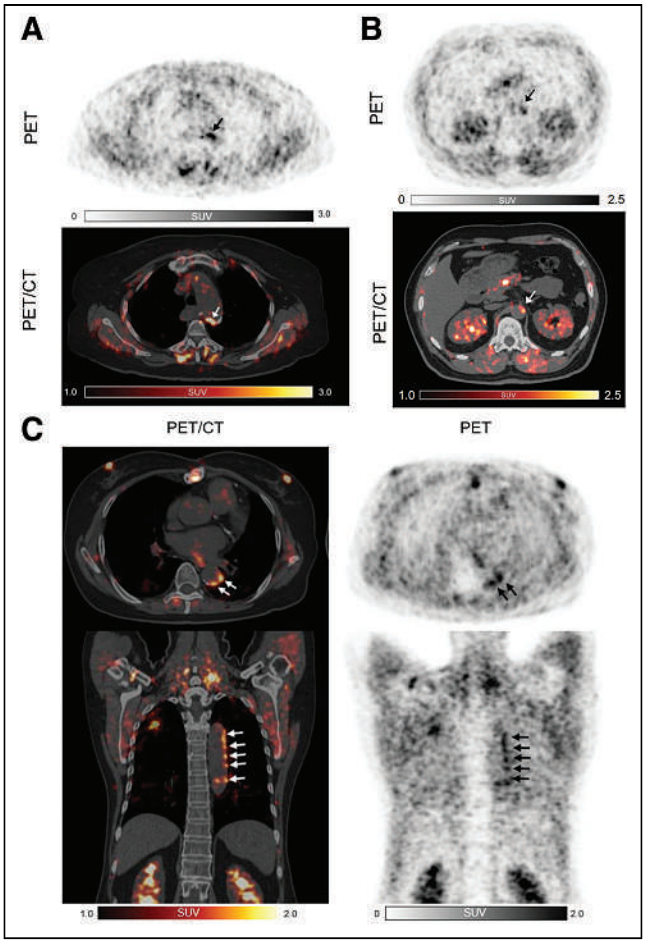

FIGURE 3. Three examples of ^{68}Ga-FAPI-04 uptake by active arterial segments. All 3 patients were over 60 y old with history of hypertension and dyslipidemia. Patients A and C also had diabetes mellitus and experienced myocardial infarction and percutaneous coronary intervention. Patient A was obese (body mass index, 30.0), and patient B had history of heavy smoking.

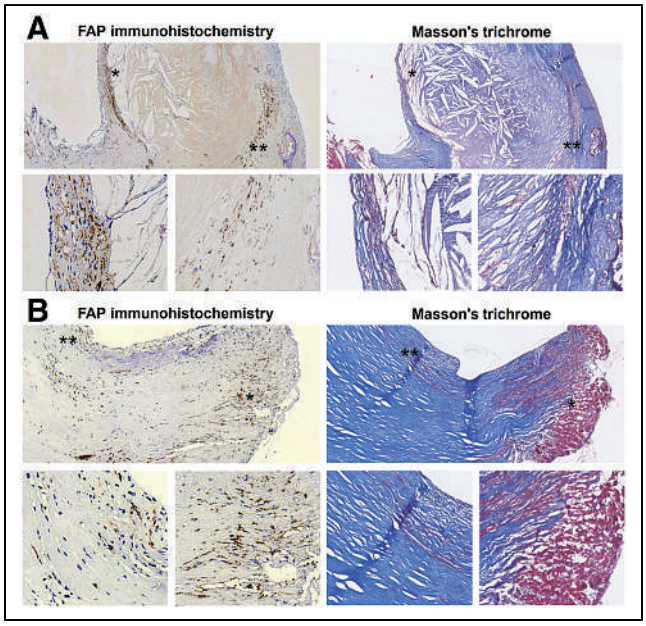

FIGURE 4. FAP expression in thin-capped (A) and thick-capped (B) human carotid atherosclerotic plaque lesions. Masson staining shows collagen-rich thin and thick fibrous caps. Plaque A had thin fibrous cap with major FAP expression (*). Fibrosis-rich region in intima also showed moderate FAP expression (**). Plaque B had thick fibrous cap with sparse FAP expression overall and FAP expression only in denatured collagen fibers (* and **).

high-risk patients than in low-risk patients. Obesity presented a relatively more prominent impact on arterial uptake, in comparison to other cardiovascular risk factors. This observation might be related to increased image noise in obese patients.

The role of FAP in atherosclerosis is complex. Evrard et al. detected a significant number of endothelial-lineage–derived cells expressing FAP in rupture-prone, thin-capped plaques—more so than in stable plaques in atherosclerosis-prone mice and ex vivo human aortic plaques (*11*). Nonetheless, Monslow et al. demonstrated colocalization of FAP and vascular cell adhesion molecule 1, which marked vascular smooth muscle cells with a proliferative and matrix-producing tendency in atherosclerotic mice (*12*). In accordance with pioneering results from studies by Evrard and Monslow, elevated FAP expression in both thin fibrous caps and fibrosis (collagen-rich tissues in the intima) was detected in our immunohistologic findings. The role of FAP in both remodeling and stabilizing the extracellular matrix in atherosclerosis is under further investigation. Interpretation of the ^{68}Ga-FAPI-04 signal in arterial walls is challenging. We found increased FAPI uptake in noncalcified and low-level calcified lesions, compared with higher-level calcified lesions, as might indicate that aggravated fibroblast activation is irrelevant to arterial calcification burden. Nonetheless, there is a need for further evidence of arterial fibrosis quantification and calcification activation.

The retrospective and noncardiovascular nature of this study led to several inevitable limitations. The first is that the discriminatory value of FAPI uptake needs to be further validated in a cardiovascular cohort. The second is that none of the patients had concurrent histologic evidence, autoradiography, or other in vivo enhanced imaging approaches that may further facilitate identification of atherosclerotic plaques (*13*). The third is that scans were performed using a routine protocol that was not optimal for vessel imaging (*14*). The fourth is that coronary arterial lesions were not assessed because the PET scans were not cardiac-gated, with increased motion effects and partial-volume effects. Finally,

a fifth limitation is that because of the inherent limitation of unenhanced CT, noncalcified segments could be underestimated. Although we did not use the novel whole arterial segmentation method, such a method may allow a more global impression of tracer activity across vessel beds (*15*). Overall, our preliminary study provides a potentially feasible method to image atherosclerosis in vivo by ^{68}Ga-FAPI-04 PET/CT. Prospective studies using ^{68}Ga-FAPI-04 PET imaging in symptomatic atherosclerotic cohorts are warranted.

CONCLUSION

^{68}Ga-FAPI-04 PET/CT might have potential for imaging fibroblast activation in the arterial wall, which could provide new insights into the pathologic mechanisms. Further studies to investigate the performance of FAP imaging in symptomatic atherosclerosis cohorts are highly warranted.

DISCLOSURE

This work was sponsored in part by the National Natural Science Foundation of China (grant 82071967), CAMS Initiative for Innovative Medicine (grant CAMS-2018-I2 M-3-001), Tsinghua University-Peking Union Medical College Hospital Initiative Scientific Research Program (grant 52300300519), National Key Research and Development Program of China (grant 2016YFC0901500), and Fundamental Research Funds for the Central Universities (grant 3332020009). No other potential conflict of interest relevant to this article was reported.

KEY POINTS

QUESTION: How well does ^{68}Ga-FAPI-04 PET/CT perform for imaging of arterial walls in humans?

PERTINENT FINDINGS: In this retrospective analysis of 41 patients, we observed elevated ^{68}Ga-FAPI-04 uptake in patients with increased cardiovascular risk factors.

IMPLICATIONS FOR PATIENT CARE: ^{68}Ga-FAPI-04 PET/CT has potential as a feasible method of imaging fibroblastic activation in the arterial wall and may provide new insights into the pathologic mechanisms driving its progression.

REFERENCES

1. Finn AV, Nakano M, Narula J, Kolodgie FD, Virmani R. Concept of vulnerable/unstable plaque. *Arterioscler Thromb Vasc Biol.* 2010;30:1282–1292.
2. MacAskill MG, Newby DE, Tavares AAS. Frontiers in positron emission tomography imaging of the vulnerable atherosclerotic plaque. *Cardiovasc Res.* 2019;115:1952–1962.
3. Šimková A, Bušek P, Šedo A, Konvalinka J. Molecular recognition of fibroblast activation protein for diagnostic and therapeutic applications. *Biochim Biophys Acta Proteins Proteom.* 2020;1868:140409.
4. Brokopp CE, Schoenauer R, Richards P, et al. Fibroblast activation protein is induced by inflammation and degrades type I collagen in thin-cap fibroatheromata. *Eur Heart J.* 2011;32:2713–2722.
5. Stein S, Weber J, Nusser-Stein S, et al. Deletion of fibroblast activation protein provides atheroprotection. *Cardiovasc Res.* 2021;117:1060–1069.
6. Loktev A, Lindner T, Mier W, et al. A tumor-imaging method targeting cancer-associated fibroblasts. *J Nucl Med.* 2018;59:1423–1429.
7. Luo Y, Pan Q, Yang H, Peng L, Zhang W, Li F. Fibroblast activation protein targeted PET/CT with (68)Ga-FAPI for imaging IgG4-related disease: comparison to (18)F-FDG PET/CT. *J Nucl Med.* 2021;62:266–271.
8. Shi X, Xing H, Yang X, et al. Fibroblast imaging of hepatic carcinoma with (68)Ga-FAPI-04 PET/CT: a pilot study in patients with suspected hepatic nodules. *Eur J Nucl Med Mol Imaging.* 2021;48:196–203.
9. Bucerius J, Hyafil F, Verberne H, et al. Position paper of the Cardiovascular Committee of the European Association of Nuclear Medicine (EANM) on PET imaging of atherosclerosis. *Eur J Nucl Med Mol Imaging.* 2016;43:780–792.
10. Weiberg D, Thackeray JT, Daum G, et al. Clinical molecular imaging of chemokine receptor CXCR4 expression in atherosclerotic plaque using (68)Ga-Pentixafor PET: correlation with cardiovascular risk factors and calcified plaque burden. *J Nucl Med.* 2018;59:266–272.
11. Evrard SM, Lecce L, Michelis KC, et al. Endothelial to mesenchymal transition is common in atherosclerotic lesions and is associated with plaque instability. *Nat Commun.* 2016;7:11853.
12. Monslow J, Todd L, Chojnowski JE, Govindaraju PK, Assoian RK, Pure E. Fibroblast activation protein regulates lesion burden and the fibroinflammatory response in apoe-deficient mice in a sexually dimorphic manner. *Am J Pathol.* 2020;190:1118–1136.
13. Grosse GM, Bascunana P, Schulz-Schaeffer WJ, et al. Targeting chemokine receptor CXCR4 and translocator protein for characterization of high-risk plaque in carotid stenosis ex vivo. *Stroke.* 2018;49:1988–1991.
14. Hu Y, Hu P, Hu B, Chen W, Cheng D, Shi H. Dynamic monitoring of active calcification in atherosclerosis by (18)F-NaF PET imaging. *Int J Cardiovasc Imaging.* 2021;37:731–739.
15. Kwiecinski J, Tzolos E, Adamson PD, et al. Coronary (18)F-Sodium Fluoride uptake predicts outcomes in patients with coronary artery disease. *J Am Coll Cardiol.* 2020;75:3061–3074.

Albumin Binder–Conjugated Fibroblast Activation Protein Inhibitor Radiopharmaceuticals for Cancer Therapy

Mengxin Xu*[1], Pu Zhang*[1], Jie Ding[2], Junyi Chen[1], Li Huo[2], and Zhibo Liu[1,3]

[1]*Radiochemistry and Radiation Chemistry Key Laboratory of Fundamental Science, Beijing National Laboratory for Molecular Sciences, College of Chemistry and Molecular Engineering, Peking University, Beijing, China;* [2]*Department of Nuclear Medicine, Peking Union Medical College Hospital, Chinese Academy of Medical Science and Peking Union Medical College, Beijing, China; and* [3]*Peking University–Tsinghua University Center for Life Sciences, Beijing, China*

Fibroblast activation protein (FAP) has become an attractive target for diagnosis and therapy, and a series of FAP inhibitor (FAPI)–based radiotracers has been developed and had excellent performance for diagnosis outcomes in clinical applications. Yet, their fast clearance and insufficient tumor retention have hampered their further clinical application in cancer treatment. In this study, we developed 2 albumin binder–conjugated FAPI radiotracers, TEFAPI-06 and TEFAPI-07. They were derived from FAPI-04 and were optimized by conjugating 2 types of well-studied albumin binders, 4-(*p*-iodophenyl) butyric acid moiety (TEFAPI-06) and truncated Evans blue moiety (TEFAPI-07), to try to overcome the above limitations at the expense of prolonging the blood circulation. **Methods:** TEFAPI-06 and TEFAPI-07 were synthesized and labeled with ^{68}Ga, ^{86}Y, and ^{177}Lu successfully. A series of cell assays was performed to identify the binding affinity and FAP specificity in vitro. PET imaging, SPECT imaging, and biodistribution studies were performed to evaluate the pharmacokinetics in pancreatic cancer patient–derived xenograft (PDX) animal models. The cancer treatment efficacy of ^{177}Lu-TEFAPI-06 and ^{177}Lu-TEFAPI-07 were evaluated in pancreatic cancer PDX–bearing mice. **Results:** The binding affinities (dissociation constants) to FAP of ^{68}Ga-TEFAPI-06 and ^{68}Ga-TEFAPI-07 were 10.16 ± 2.56 nM and 7.81 ± 2.28 nM, respectively, which were comparable with that of ^{68}Ga-FAPI-04. Comparative PET imaging of HT-1080-FAP and HT-1080 tumor–bearing mice and a blocking study showed the FAP-targeting ability in vivo of these 2 tracers. Compared with ^{177}Lu-FAPI-04, PET imaging, SPECT imaging, and biodistribution studies of TEFAPI-06 and TEFAPI-07 demonstrated their remarkably enhanced tumor accumulation and retention, respectively. Notable tumor growth inhibition by ^{177}Lu-TEFAPI-06 and ^{177}Lu-TEFAPI-07 were observed, whereas the control group and the group treated by ^{177}Lu-FAPI-04 showed a slight therapeutic effect. **Conclusion:** Two albumin binder–conjugated FAPI radiopharmaceuticals have been developed and evaluated in vitro and in vivo. Significantly improved tumor uptake and retention were observed, compared with the original FAPI tracer. Both ^{177}Lu-TEFAPI-06 and ^{177}Lu-TEFAPI-07 showed remarkable growth inhibition of PDX tumors, whereas the side effects were almost negligible, demonstrating that these radiopharmaceuticals are promising for further clinical translational studies.

Key Words: albumin binder; FAP inhibitor; radionuclide therapy

J Nucl Med 2022; 63:952–958
DOI: 10.2967/jnumed.121.262533

Fibroblast activation protein (FAP) is overexpressed in cancer-associated fibroblasts, which are one of the main tumor stroma components and constitute a major proportion of cells within the tumor (*1,2*). Though stromal cells are not malignant, the growth factor and chemokine produced by stromal cells, especially cancer-associated fibroblasts, can lead to the direct stimulation of tumor cell growth, migration, and progression (*3*). Considering the vital role in tumor survival and cancer growth, cancer-associated fibroblast–targeted diagnosis and therapy via the biomarker FAP have become an attractive strategy for tumor treatment (*4,5*). FAP-targeted radiopharmaceutical therapy might deliver therapeutic radioisotopes to cancer-associated fibroblasts. It damages the stromal cells and the neighboring tumor cells through the crossfire effect of the β- or α-emitting radionuclides, potentially augmenting the therapeutic efficacy (*6*).

Recently, a variety of quinolone-based FAP inhibitor (FAPI) radiopharmaceuticals has been developed and demonstrated excellent uptake in different FAP-positive tumors of cancer patients (*7–9*). For FAP-targeted radiotherapy, an emerging strategy is to directly modify the inhibitor structure to enhance tumor uptake and retention while keeping the accumulation in nontarget tissues unchanged or decreasing it (*10–12*). A series of FAPI probes, including FAPI-04, FAPI-21, and FAPI-46, has been successfully developed; their improved pharmacokinetic properties make them promising candidates for therapeutic outcome improvement (*13–16*). Though this is one of the optimal ways to develop therapeutic radiopharmaceuticals, the relatively rapid washout from the tumor is still a considerable limitation. Besides, it may be challenging to achieve notable enhancement of pharmacokinetic properties by subtle structure modification.

Several studies have shown that prolonging the blood circulation of drug molecules using albumin-binder moieties could remarkably improve the therapeutic dose (*17*). 4-(*p*-iodophenyl) butyric acid and truncated Evans blue moieties are the most widely used albumin binders. The previous studies suggest that they can enhance the tumor uptake and retention of radiopharmaceuticals, resulting in improved therapeutic efficacy (*18–23*). Further clinical translation studies also validate the promise of this strategy to be a platform technology for radiopharmaceutical development (*24–26*). Therefore, we were curious whether attaching an albumin-binder moiety to the FAPI

Received May 11, 2021; revision accepted Sep. 25, 2021.
For correspondence or reprints, contact Zhibo Liu (zbliu@pku.edu.cn).
*Contributed equally to this work.
Published online Sep. 30, 2021.

molecules would improve the FAP-targeted radiotherapy efficacy at the expense of increased retention in blood.

In this study, 2 albumin binder–FAPI conjugates, TEFAPI-06 and TEFAPI-07, were developed by logistic fabrication of 3 functional components: a quinoline-based FAPI originating from FAPI-04, a chelator (i.e., DOTA group) that allows radionuclide labeling for imaging (^{68}Ga or ^{86}Y) or therapy (^{177}Lu), and an albumin binder: 4-(*p*-iodophenyl) butyric acid moiety (TEFAPI-06) or truncated Evans blue moiety (TEFAPI-07). The purpose of the study was to evaluate whether the modification improves tumor retention in vivo and which albumin binder better matches FAPI molecules. A series of detailed experiments and comparisons, including cell binding assays, a PET imaging study, a biodistribution study, and a radiotherapy study, was performed. The results demonstrated these 2 albumin binder–conjugated FAPI radiotracers to have high FAP binding affinity and specificity, enhanced tumor retention, and improved radiotherapy efficacy.

MATERIALS AND METHODS

Ligands and Radionuclides

The synthesis route and chemical characterization of TEFAPI-06 and TEFAPI-07 are described in Supplemental Figures 1–20 (supplemental materials are available at http://jnm.snmjournals.org). ^{68}Ga-Cl_3 was eluted with a solution of 0.6 M hydrochloride from a ^{68}Ge–^{68}Ga generator (iThemba LABS). ^{86}Y-Cl_3 was produced with a 14.6-MeV cyclotron; the target design follows our previous report (*27*), and the purification procedure follows the previous protocol (*28*). ^{177}Lu-Cl_3 in a solution of 0.1 M hydrochloride was purchased from ITG.

Radiolabeling and Stability In Vitro

The radiolabeling of ^{68}Ga, ^{86}Y, and ^{177}Lu was performed by incubation with 50 nmol of precursor at pH 4.5–5.0 at 90°C for 10 min. The product was purified by C18 column extraction, and the radiochemical purity was determined by high-performance liquid chromatography equipped with a radioactivity detector. The stability of ^{177}Lu-TEFAPI-06 and ^{177}Lu-TEFAPI-07 in saline and human serum was monitored from 2 to 168 h using radio–high-performance liquid chromatography (*13*). More details about the radiochemistry, the quality control testing, and the stability assay can be found in the supplemental materials (section 3).

Cell Culture and Assay

The human fibrosarcoma cell line (HT-1080), and the HT-1080 cell line transfected with human FAP gene (HT-1080-FAP, from WuXi AppTec), were cultivated in Eagle minimum essential medium containing 10% fetal bovine serum, 1% antibiotic–antimycotic, and a 4 μg/mL concentration of blasticidin S at 37°C under conditions of 5% carbon dioxide. For competition assays, HT-1080-FAP cells were seeded in 6-well plates and cultivated until they reached about 1.2×10^6 cells per well. The cells were incubated simultaneously with unlabeled FAPI-04, TEFAPI-06, or TEFAPI-07 (10^{-5}–10^{-9} M) with ^{68}Ga-FAPI-04 in 1 mL of fresh medium without fetal bovine serum for 1 h. The medium was removed, and the cells were washed twice with phosphate-buffered saline (PBS). Subsequently, the cells were lysed with 0.5 mL of 1 M NaOH and washed with 0.5 mL of PBS twice, and the NaOH (0.5 mL) and PBS (0.5 mL × 2) were collected to determine the uptake counts. For saturation binding assays, HT-1080-FAP and HT-1080 cells were seeded in 24-well plates and cultivated until they reached about 2×10^5 cells per well. ^{68}Ga-FAPI-04, ^{68}Ga-TEFAPI-06, or ^{68}Ga-TEFAPI-07 was diluted to a concentration 0.01–200 nM in fresh medium without fetal bovine serum. The cells were incubated in the above solution for 1 h and then washed twice with PBS. The lysed cells and the PBS for washing were collected to determine the counts.

Tumor-Bearing Animal Models

All animal care and experimental procedures were performed by following the animal protocols (CCME-LiuZB-2) approved by the ethics committee of Peking University. The mice were from the Beijing Vital River Laboratory Animal Technology Co., Ltd. For cell-line–derived xenograft models, 5×10^6 HT-1080-FAP or HT-1080 cells were subcutaneously inoculated into the right shoulder of 6-wk-old female nu/nu-mice. To establish the patient-derived xenograft (PDX) model, tumor specimens were obtained from patients who underwent presurgical ^{68}Ga-FAPI-04 PET/CT imaging to confirm that the tumor was FAP-positive. After surgical resection, the tumor specimens were immediately placed in ready-to-use fresh tissue preservation solution (TM2701-100) and transported under refrigerated conditions within 2 h. The research protocol was approved by the Institutional Ethics Committee of Peking Union Medical College Hospital (JS-2628). Six-week-old female nonobese diabetic/severe combined immunodeficiency (NOD/SCID) mice were used to establish the PDX models. After being removed from the preservation solution, the tumor specimens were immediately immersed in sterile PBS solution and minced with scissors, and the fragments were then implanted subcutaneously into the left and right shoulders of the mice, which were anesthetized with isoflurane in advance. Engraftment efficiency was determined by ^{68}Ga-FAPI-04 PET/CT imaging (Supplemental Fig. 21A). Immunohistochemical staining (Supplemental Fig. 21B) demonstrated that the pancreatic cancer PDX model used in this study was indeed FAP-overexpressed.

Small-Animal PET Imaging

All PET scans were performed on a Mediso nanoScan PET 122S small-animal PET/CT imaging system. For the 60-min dynamic PET

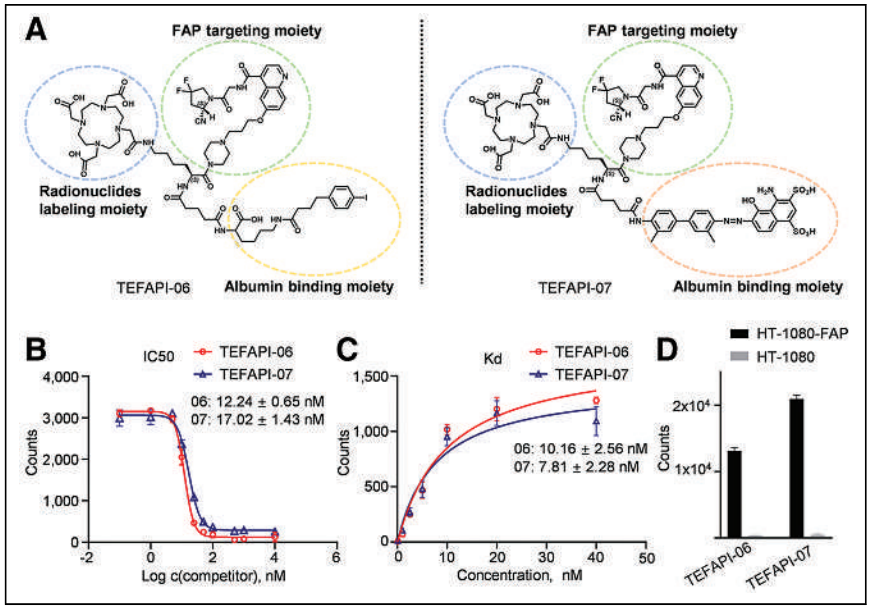

FIGURE 1. (A) Chemical structures of TEFAPI-06 and TEFAPI-07. (B) Competition assays of TEFAPI-06 and TEFAPI-07. (C) Saturation binding assays of radiolabeled TEFAPI-06 and TEFAPI-07. (D) Cellular uptake assays of ^{68}Ga-TEFAPI-06 and ^{68}Ga-TEFAPI-07 in HT-1080-FAP and HT-1080 cells. IC_{50} = half-maximal inhibitory concentration.

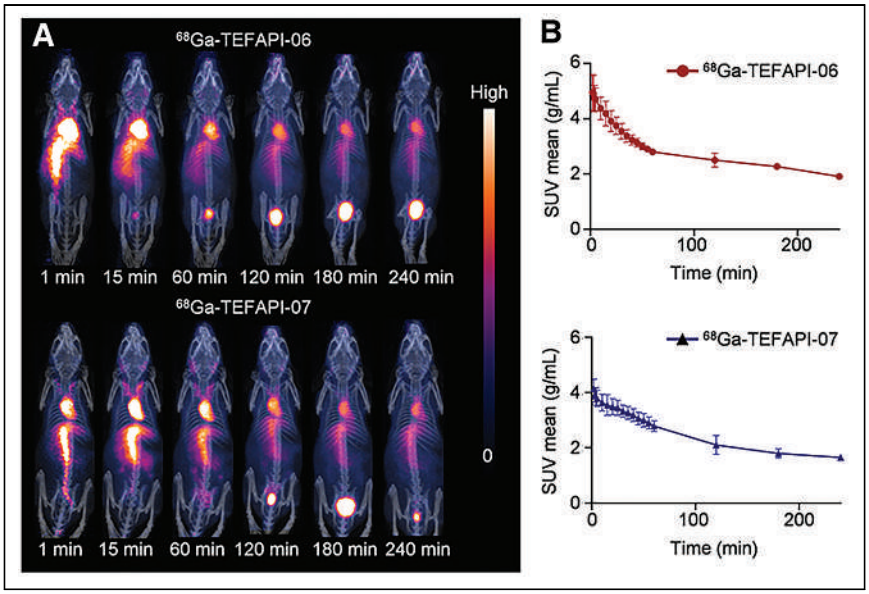

FIGURE 2. (A) Dynamic PET imaging of ^{68}Ga-TEFAPI-06 and ^{68}Ga-TEFAPI-07 in healthy NOD/SCID mice. (B) Corresponding blood time–activity curves of ^{68}Ga-TEFAPI-06 and ^{68}Ga-TEFAPI-07.

scan, 29.6–37.0 MBq of ^{68}Ga-TEFAPI-06 or ^{68}Ga-TEFAPI-07 were given to healthy NOD/SCID mice through tail-vein injection. The static PET imaging was performed on mice bearing pancreatic PDX tumors, HT-1080-FAP tumors, and HT-1080 tumors at the indicated time points after intravenous injection of 7.4–11.1 MBq of ^{86}Y-FAPI-04,^{86}Y-TEFAPI-06, or ^{86}Y-TEFAPI-07.

Small-Animal SPECT Imaging

SPECT scans were performed on a Mediso nanoSPECT/CT imaging system. ^{177}Lu-TEFAPI-06 or ^{177}Lu-TEFAPI-07 SPECT imaging was performed on pancreatic cancer PDX–bearing mice at the indicated time points after intravenous injection of 37 MBq of ^{177}Lu-TEFAPI-06 or ^{177}Lu-TEFAPI-07, respectively.

Biodistribution Study

PDX-bearing mice were injected with 925.0 kBq of ^{177}Lu-TEFAPI-06 or ^{177}Lu-TEFAPI-07 for an ex vivo biodistribution study. The mice were killed at 24 h and 96 h after injection, the counts of the different organs were measured with a γ-counter, and the data were normalized to percentage injected dose (%ID)/g using 1% of total counts.

Radiotherapy Study

^{68}Ga-FAPI-04 PET imaging was performed to evaluate the tumor volume, and the mice were treated when their average tumor volume reached 35 mm^3. The PDX-bearing mice (6 groups, 7–9 mice per group) were treated by saline, 3.7 MBq of ^{177}Lu-FAPI-04, 1.85 MBq of ^{177}Lu-TEFAPI-06, 3.7 MBq of ^{177}Lu-TEFAPI-06, 1.85 MBq of ^{177}Lu-TEFAPI-07, or 1.85 MBq of ^{177}Lu-TEFAPI-07. Tumor volume and body weight were monitored every 2 or 3 d, and the animals were euthanized when the tumor volume exceeded 1,000 mm^3. Histopathologic staining was performed with an antihuman FAP monoclonal antibody (ab207178; Abcam), and hematoxylin and eosin staining was performed as previously described (*29*).

RESULTS

Radiochemistry and Stability In Vitro

The radiolabeling yield of TEFAPI-06 and TEFAPI-07 (Fig. 1A) was over 90%, and the radiochemical purity was over 99% ($n > 20$). The specific activity of ^{68}Ga-FAPI-04, ^{68}Ga-TEFAPI-06, and ^{68}Ga-TEFAPI-07 was 5.2–6.7 GBq/μmol. The specific activity of ^{86}Y-TEFAPI-06 and ^{86}Y-TEFAPI-07 was 2.2–3.4 GBq/μmol. The specific activity of ^{177}Lu-FAPI-04, ^{177}Lu-TEFAPI-06, and ^{177}Lu-TEFAPI-07 was 2.9–4.4 GBq/μmol. Stability of ^{177}Lu-TEFAPI-06 and ^{177}Lu-TEFAPI-07 in saline and human serum was analyzed using radio–high-performance liquid chromatography, as shown in Supplemental Figure 22. The radiochemistry purity of both ^{177}Lu-TEFAPI-06 and ^{177}Lu-TEFAPI-07 was still over 90% after incubation in saline and human serum for 7 d.

Binding Assay

As shown in Figure 1B and Supplemental Figure 23A, cellular uptake of ^{68}Ga-FAPI-04 can be significantly inhibited by treatment with cold TEFAPI-06 and TEFAPI-07. The ligand concentrations required for 50% inhibition (half-maximal inhibitory concentration) of TEFAPI-06 and TEFAPI-07 are 12.24 ± 0.65 nM and 17.02 ± 1.43 nM, respectively. The dissociation constants of ^{68}Ga-TEFAPI-06 and ^{68}Ga-TEFAPI-07 were 10.16 ±

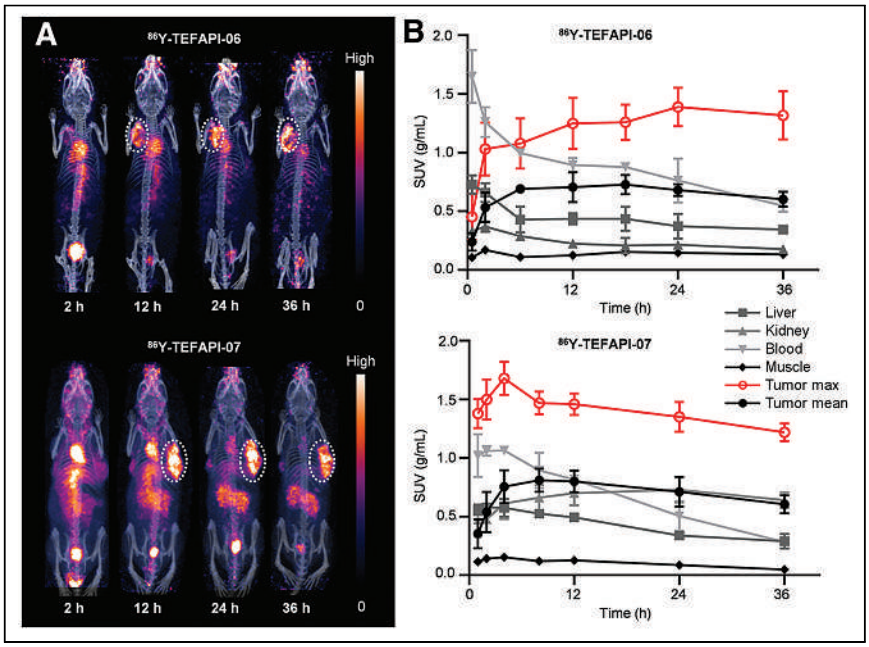

FIGURE 3. (A) PET imaging of ^{86}Y-TEFAPI-06 and ^{86}Y-TEFAPI-07 in PDX-bearing mice. (B) Time–activity curves for tumor and major organs of ^{86}Y-TEFAPI-06 and ^{86}Y-TEFAPI-07.

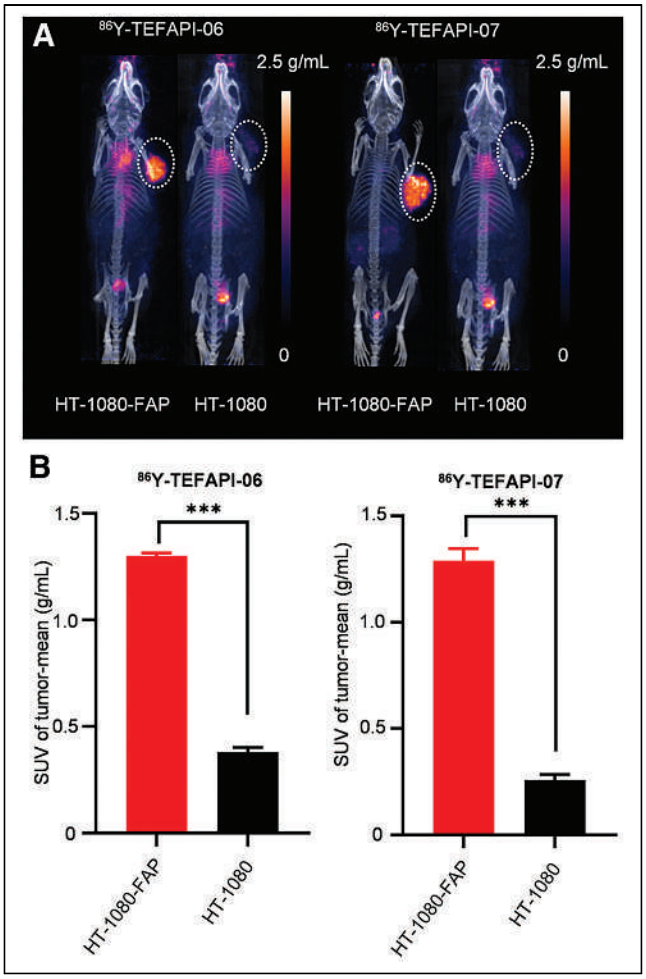

FIGURE 4. (A) PET imaging of ^{86}Y-TEFAPI-06 and ^{86}Y-TEFAPI-07 in HT-1080-FAP and HT-1080 tumor–bearing mice at 24 h after injection. (B) Uptake of ^{86}Y-TEFAPI-06 and ^{86}Y-TEFAPI-07 in HT-1080-FAP and HT-1080 tumors at 24 h after injection. ***$P < 0.001$.

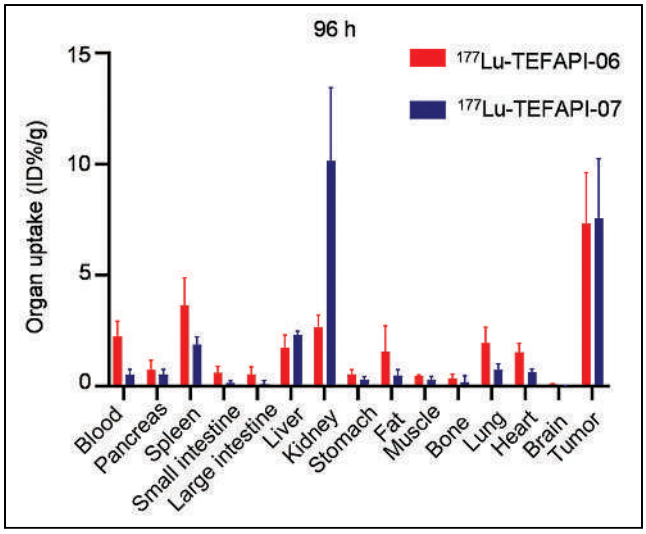

FIGURE 5. Biodistribution study of ^{177}Lu-TEFAPI-06 and ^{177}Lu-TEFAPI-07 in pancreatic cancer PDX–bearing mice at 96 h after injection ($n = 5$).

2.56 nM and 7.81 ± 2.28 nM (Fig. 1C), respectively, which are comparable to that of ^{68}Ga-FAPI-04 (1.91 ± 0.62 nM, Supplemental Fig. 23B). As shown in Figure 1D, both ^{68}Ga-TEFAPI-06 and ^{68}Ga-TEFAPI-07 exhibited almost negligible uptake in HT-1080 cells but had significant uptake in HT-1080-FAP cells. We also performed the binding assays in 0.05% human serum albumin (*20*), with the following results. The half-maximal inhibitory concentrations of TEFAPI-06 and TEFAPI-07 were 11.39 ± 1.15 nM and 27.68 ± 5.00 nM, respectively, in the presence of albumin. The dissociation constants of TEFAPI-06 and TEFAPI-07 were 4.37 ± 0.81 nM and 19.12 ± 5.54, respectively, in the absence of albumin. The half-maximal inhibitory concentration and dissociation constant of TEFAPI-07 were slightly impacted by the presence of albumin, which may be the reason why blood clearance was faster than for TEFAPI-06.

Small-Animal PET Imaging

To evaluate the in vivo pharmacokinetics of these 2 radiotracers, dynamic PET imaging of ^{68}Ga-TEFAPI-06 and ^{68}Ga-TEFAPI-07 was performed on healthy NOD-SCID mice. The signal in heart peaked rapidly at about 2 min after injection and then declined gradually. For ^{68}Ga-TEFAPI-06, the signal decreased by 35.70% ± 4.74% from 10 to 60 min after injection, a decrease that was greater than that of ^{68}Ga-TEFAPI-07 (23.15% ± 2.16%), whereas from 60 to 240 min after injection, the signal decreased by 31.80% ± 1.15% and 40.56% ± 5.25% for ^{68}Ga-TEFAPI-06 and ^{68}Ga-TEFAPI-07, respectively, resulting in a similar proportion in the decrease of these 2 radiotracers from 10 to 240 min, at 56.18% ± 2.50% and 54.28% ± 4.98% for ^{68}Ga-TEFAPI-06 and ^{68}Ga-TEFAPI-07, respectively. As shown in Figure 2, for both ^{68}Ga-TEFAPI-06 and ^{68}Ga-TEFAPI-07, most of the radioactivity was retained in the blood circulation during the monitoring period, and the uptake in other organs, such as the liver, spleen, and kidney, was lower than in the heart or main blood vessels.

To identify the tumor-targeting ability and monitor the in vivo pharmacokinetics quantitatively over a longer period, TEFAPI-06, TEFAPI-07, and FAPI-04 were labeled with the radionuclide ^{86}Y, which has a half-life of 14.7 h, and the PET imaging was performed using pancreatic cancer PDX–bearing mice. As shown in Figure 3 and Supplemental Figure 24, for both ^{86}Y-TEFAPI-06 and ^{86}Y-TEFAPI-07, tumor was completely visible at 2 h after injection. The tumor SUV_{mean} of ^{86}Y-TEFAPI-06 peaked at 0.73 at 18 h after injection, and that of ^{86}Y-TEFAPI-07 peaked at 0.81 at 8 h after injection. Then, the tumor SUV_{mean} decreased slowly but still remained high until 36 h after injection, with a value of 0.602 and 0.606 for ^{86}Y-TEFAPI-06 and ^{86}Y-TEFAPI-07, respectively. However, the tumor SUV_{mean} of ^{86}Y-FAPI-04 peaked at 0.35 at 0.2 h after injection and then decreased rapidly, and the areas under the curve for TEFAPI-07 and TEFAPI-06 were 35.5-fold and 37.9-fold that for FAPI-04.

To further confirm the FAP specificity in vivo of these 2 radiotracers, PET imaging of HT-1080-FAP and HT-1080 tumor–bearing mice was performed. As shown in Figure 4, Supplemental Figure 25, and Supplemental Figure 26, the uptake of ^{86}Y-TEFAPI-06 and ^{86}Y -TEFAPI-07 in HT-1080-FAP tumors was consistently 2- to 6-fold higher than that in HT-1080 tumors. A blocking study was also performed, as shown in Supplemental Figure 27; tumor uptake decreased at 12 h and 24 h after treatment with cold TEFAPI-06 and TEFAPI-07.

Small-Animal SPECT Imaging

To further characterize these 2 molecules, SPECT imaging was conducted on PDX tumor models for a longer time. As shown in Supplemental Figure 28, high tumor–to–nontargeted-tissue signal ratios were

TABLE 1
Biodistribution Results for ^{177}Lu-TEFAPI-06 and ^{177}Lu-TEFAPI-07

	^{177}Lu-TEFAPI-06				^{177}Lu-TEFAPI-07			
	24 h		96 h		24 h		96 h	
Organ	Mean	SD	Mean	SD	Mean	SD	Mean	SD
Blood	12.32	1.33	2.25	0.68	5.64	1.49	0.51	0.24
Pancreas	2.01	0.26	0.75	0.42	2.16	0.69	0.53	0.22
Spleen	3.00	0.66	3.66	1.22	2.69	0.87	1.88	0.34
Small intestine	2.55	0.64	0.61	0.28	1.19	0.26	0.16	0.09
Large intestine	1.66	0.27	0.53	0.35	1.15	0.33	0.10	0.15
Liver	2.98	0.64	1.74	0.57	3.21	0.81	2.31	0.17
Kidney	3.20	0.84	2.66	0.54	8.67	2.30	10.16	3.28
Stomach	1.75	0.17	0.54	0.21	1.20	0.45	0.29	0.14
Fat	1.86	0.90	1.55	1.17	1.82	1.18	0.48	0.25
Muscle	1.09	0.18	0.45	0.05	1.00	0.37	0.28	0.16
Bone	1.32	0.30	0.35	0.20	1.71	0.63	0.18	0.28
Lung	4.33	1.44	1.95	0.70	2.58	0.75	0.73	0.28
Heart	3.70	1.59	1.51	0.42	2.53	1.19	0.62	0.17
Brain	0.37	0.08	0.09	0.03	0.23	0.09	−0.01	0.04
Tumor	8.68	0.73	7.33	2.28	7.87	2.08	7.57	2.68

Data are %ID/g.

observed for both ^{177}Lu-TEFAPI-06 and ^{177}Lu-TEFAPI-07 until 144 h after injection. The blood circulation properties of these 2 molecules were similar to those found in the previous PET study.

Biodistribution Study

To further evaluate the metabolic properties in vivo, biodistribution studies using the pancreatic cancer PDX–bearing mice were performed. As shown in Figure 5 and Table 1, the tumor uptake of ^{177}Lu-TEFAPI-06 and ^{177}Lu-TEFAPI-07 were, respectively, 8.68 ± 0.73 %ID/g and 7.87 ± 2.08 %ID/g at 24 h after injection, and the tumor-to-liver ratios were 2.91 and 2.45, respectively. The tumor uptake remained high until 96 h after injection, at 7.33 ± 2.28 %ID/g and 7.57 ± 2.68 %ID/g for ^{177}Lu-TEFAPI-06 and ^{177}Lu-TEFAPI-07, respectively, and the tumor-to-liver ratios increased to 4.21 and 3.28, respectively. As is consistent with the results of PET and SPECT imaging, the kidney uptake of ^{177}Lu-TEFAPI-07 remained high at both 24 and 96 h after injection, at 8.67 ± 2.30 and 10.16 ± 3.28 %ID/g, respectively, whereas the kidney uptake of ^{177}Lu-TEFAPI-06 was much lower, at 2.66 ± 0.54 %ID/g, at 96 h after injection. By comparison, the blood clearance of ^{177}Lu-TEFAPI-06 (24 h, 13.32 ± 1.33 %ID/g; 96 h, 2.25 ± 0.68 %ID/g) was slower than that of ^{177}Lu-TEFAPI-07 (24 h, 5.64 ± 1.50 %ID/g; 96 h, 0.51 ± 0.24 %ID/g).

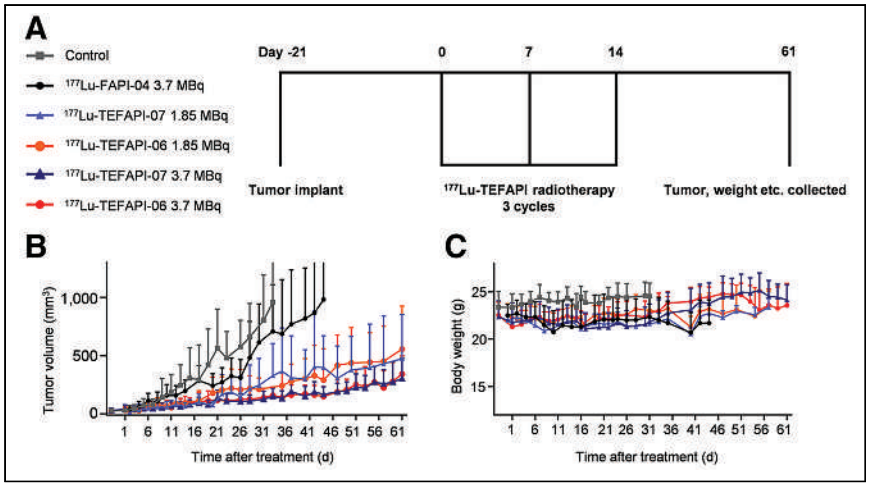

FIGURE 6. Treatment assay of ^{177}Lu-TEFAPI-06 and ^{177}Lu-TEFAPI-07 in pancreatic cancer PDX-bearing mice. (A) Design of therapy protocols and treatment scheme. (B) Tumor growth curve after treatment (n = 7–9 mice for each group). (C) Body weight change after treatment.

Radiotherapy Study

To make the assessment of therapeutic efficacy more relevant to the clinical setting, pancreatic cancer PDX–bearing mice were used for the indicated radiotherapy study (Fig. 6A). In a comparison to the group treated by saline or 3.7 MBq of ^{177}Lu-FAPI-04, the groups treated with 1.85 MBq or 3.7 MBq of ^{177}Lu-TEFAPI-06 and ^{177}Lu-TEFAPI-07, respectively, showed remarkable suppression of tumor growth (Fig. 6B). No statistical difference in treatment efficacy was observed between ^{177}Lu-TEFAPI-06 and ^{177}Lu-TEFAPI-07. This result corroborates the PET imaging and biodistribution studies, as they showed equally high uptake in the tumors. Except for the control group

treated with only saline, transient weight loss was observed for all treatment groups, including ^{177}Lu-FAPI-04, but then returned to the healthy level 7 d after the initial treatment. Hematoxylin and eosin staining of the main organs revealed that side effects from ^{177}Lu-TEFAPI-06 and ^{177}Lu-TEFAPI-07 treatment were almost negligible (Supplemental Fig. 29).

DISCUSSION

The purpose of this study was to develop FAPI-based radiopharmaceuticals that are more effective than the existing candidates for FAP-targeted radiotherapy. Two different albumin binders, 4-(*p*-iodophenyl) butyric acid and truncated Evans blue moieties, were chosen to be attached with FAPI-04. The resulting TEFAPI-06 and TEFAPI-07 were synthesized and radiolabeled with ^{68}Ga, ^{86}Y, and ^{177}Lu. The radiolabeled TEFAPIs exhibited good stability in saline and human serum and high FAP binding affinity in vitro. In addition, SPECT imaging and biodistribution studies of ^{177}Lu-TEFAPI-06 and ^{177}Lu-TEFAPI-07 showed that tumor uptake was still notable even at 6 d after the injection. Meanwhile, almost no radioactive signal could be detected for ^{177}Lu-FAPI-04 at 24 h after injection. We also wondered whether further modifications of the structure may lengthen the blood circulation and, thus, increase the tumor accumulation. However, it can be challenging to balance treatment efficacy against potential side effects from blood circulation.

With regard to the clearance pathway, there was no significant difference in uptake between ^{177}Lu-TEFAPI-06 and ^{177}Lu-TEFAPI-07 in tumor and main organs, except for the kidney. For TEFAPI-07, both the PET and the SPECT imaging results showed significantly higher kidney uptake than that of TEFAPI-06. Of note, imaging indicated that there was no obvious clearance of TEFAPI-07 from the kidneys over time, a finding that was consistent with the results of the biodistribution study. Besides, because both TEFAPI-06 and ^{177}Lu-TEFAPI-07 have relatively longer blood circulation than the classic radiopharmaceuticals, the side effects may not be negligible. Therefore, a comprehensive hematoxylin- and eosin-staining study of major organs was performed, and no tissue damage was observed (Supplemental Fig. 29).

As reported in previous studies, the radiolabeled albumin binder may target the tumor because of enhanced permeability and retention of albumin (*30,31*). Thus, we were curious about whether the enhanced tumor uptake and retention of ^{177}Lu-TEFAPI-06 and ^{177}Lu-TEFAPI-07 are FAP-dependent. The PET imaging results of FAP-positive (HT-1080-FAP) and FAP-negative (HT-1080) tumor–bearing mice showed much higher uptake by FAP-positive tumors than by FAP-negative tumors, demonstrating that the higher tumor uptake was dependent on the FAP-targeting ability in vivo. For the blocking study, the tumor uptake of ^{68}Ga-FAPI-04 decreased significantly when the mice were treated with cold TEFAPI-06 and TEFAPI-07 until 24 h after injection—a finding that supported the possibility that the prolonged tumor retention of these 2 radiotracers was also dependent mainly on their excellent FAP-targeting ability in vivo.

CONCLUSION

In this study, 2 albumin binder–conjugated FAPIs, denoted as TEFAPI-06 and TEFAPI-07, were developed to optimize the pharmacokinetics of current FAPI radiopharmaceuticals for cancer radiotherapy. Compared with ^{177}Lu-FAPI-04, both ^{177}Lu-TEFAPI-06 and ^{177}Lu-TEFAPI-07 showed enhanced uptake and retention in tumors. The tumor accumulations were highly FAP-selective and resulted in remarkable inhibition of PDX tumor growth, with negligible side effects. Their promising pharmacokinetics warrant further investigations toward clinical translation for the treatment of FAP-positive cancers.

DISCLOSURE

This work was funded by the Beijing Municipal Natural Science Foundation (grant Z200018), the Special Foundation of the Beijing Municipal Education Commission (grant 3500-12020123), the National Natural Science Foundation of China (grants U1867209 and 21778003), the Ministry of Science and Technology of the People's Republic of China (grant 2017YFA0506300), and the Li Ge-Zhao Ning Life Science Youth Research Foundation (grant LGZNQN202004). Mengxin Xu, Pu Zhang, Junyi Chen, and Zhibo Liu are consultants for Borui Biotech. No other potential conflict of interest relevant to this article was reported.

ACKNOWLEDGMENT

The NMR measurements were performed at the Analytical Instrumentation Center of Peking University.

KEY POINTS

QUESTION: Do albumin binder–conjugated FAPI radiopharmaceuticals have high FAP specificity and provide enhanced tumor retention and improved radiotherapy efficiency?

PERTINENT FINDINGS: Albumin binder–conjugated FAPI radiopharmaceuticals exhibited notably improved tumor uptake and retention compared with the original FAPI tracers and showed remarkable inhibition of PDX tumor growth, with negligible side effects.

IMPLICATIONS FOR PATIENT CARE: Albumin binder conjugation is a promising strategy in the development of FAP-targeted radiopharmaceuticals for treating cancers.

REFERENCES

1. Hamson EJ, Keane FM, Tholen S, Schilling O, Gorrell MD. Understanding fibroblast activation protein (FAP): substrates, activities, expression and targeting for cancer therapy. *Proteomics Clin Appl.* 2014;8:454–463.
2. Park JE, Lenter MC, Zimmermann RN, Garin-Chesa P, Old LJ, Rettig WJ. Fibroblast activation protein, a dual specificity serine protease expressed in reactive human tumor stromal fibroblasts. *J Biol Chem.* 1999;274:36505–36512.
3. Li H, Fan X, Houghton J. Tumor microenvironment: the role of the tumor stroma in cancer. *J Cell Biochem.* 2007;101:805–815.
4. Calais J. FAP: the next billion dollar nuclear theranostics target? *J Nucl Med.* 2020;61:163–165.
5. Lo A, Wang L-CS, Scholler J, et al. Tumor-promoting desmoplasia is disrupted by depleting FAP-expressing stromal cells. *Cancer Res.* 2015;75:2800–2810.
6. Fischer E, Chaitanya K, Wüest T, et al. Radioimmunotherapy of fibroblast activation protein positive tumors by rapidly internalizing antibodies. *Clin Cancer Res.* 2012;18:6208–6218.
7. Jansen K, Heirbaut L, Verkerk R, et al. Extended structure–activity relationship and pharmacokinetic investigation of (4-quinolinoyl)glycyl-2-cyanopyrrolidine inhibitors of fibroblast activation protein (FAP). *J Med Chem.* 2014;57:3053–3074.
8. Loktev A, Lindner T, Mier W, et al. A tumor-imaging method targeting cancer-associated fibroblasts. *J Nucl Med.* 2018;59:1423–1429.
9. Lindner T, Altmann A, Krämer S, et al. Design and development of ^{99m}Tc-labeled FAPI tracers for SPECT imaging and ^{188}Re therapy. *J Nucl Med.* 2020;61:1507–1513.
10. Giesel FL, Adeberg S, Syed M, et al. FAPI-74 PET/CT using either ^{18}F-AlF or cold-kit ^{68}Ga labeling: biodistribution, radiation dosimetry, and tumor delineation in lung cancer patients. *J Nucl Med.* 2021;62:201–207.

11. Kratochwil C, Flechsig P, Lindner T, et al. ^{68}Ga-FAPI PET/CT: tracer uptake in 28 different kinds of cancer. *J Nucl Med.* 2019;60:801–805.
12. Windisch P, Zwahlen DR, Koerber SA, et al. Clinical results of fibroblast activation protein (FAP) specific PET and implications for radiotherapy planning: systematic review. *Cancers (Basel).* 2020;12:2629.
13. Lindner T, Loktev A, Altmann A, et al. Development of quinoline-based theranostic ligands for the targeting of fibroblast activation protein. *J Nucl Med.* 2018;59:1415–1422.
14. Loktev A, Lindner T, Burger E-M, et al. Development of fibroblast activation protein–targeted radiotracers with improved tumor retention. *J Nucl Med.* 2019;60:1421–1429.
15. Watabe T, Liu Y, Kaneda-Nakashima K, et al. Theranostics targeting fibroblast activation protein in the tumor stroma: ^{64}Cu- and ^{225}Ac-labeled FAPI-04 in pancreatic cancer xenograft mouse models. *J Nucl Med.* 2020;61:563–569.
16. Ballal S, Yadav MP, Kramer V, et al. A theranostic approach of [^{68}Ga]Ga-DOTA.SA.FAPi PET/CT-guided [^{177}Lu]Lu-DOTA.SA.FAPi radionuclide therapy in an end-stage breast cancer patient: new frontier in targeted radionuclide therapy. *Eur J Nucl Med Mol Imaging.* 2021;48:942–944.
17. Liu Z, Chen X. Simple bioconjugate chemistry serves great clinical advances: albumin as a versatile platform for diagnosis and precision therapy. *Chem Soc Rev.* 2016;45:1432–1456.
18. Müller C, Farkas R, Borgna F, Schmid RM, Benešová M, Schibli R. Synthesis, radiolabeling, and characterization of plasma protein-binding ligands: potential tools for modulation of the pharmacokinetic properties of (radio)pharmaceuticals. *Bioconjug Chem.* 2017;28:2372–2383.
19. Benešová M, Umbricht CA, Schibli R, Müller C. Albumin-binding PSMA ligands: optimization of the tissue distribution profile. *Mol Pharm.* 2018;15:934–946.
20. Kelly JM, Jeitner TM, Ponnala S, et al. A trifunctional theranostic ligand targeting fibroblast activation protein-α (FAPα). *Mol Imaging Biol.* 2021;23:686–696.
21. Kelly JM, Amor-Coarasa A, Nikolopoulou A, et al. Dual-target binding ligands with modulated pharmacokinetics for endoradiotherapy of prostate cancer. *J Nucl Med.* 2017;58:1442–1449.
22. Lau J, Jacobson O, Niu G, Lin KS, Bénard F, Chen X. Bench to bedside: albumin binders for improved cancer radioligand therapies. *Bioconjug Chem.* 2019;30:487–502.
23. Kuo HT, Lin KS, Zhang Z, et al. Novel ^{177}Lu-labeled albumin-binder-conjugated PSMA-targeting agents with extremely high tumor uptake and enhanced tumor-to-kidney absorbed dose ratio. *J Nucl Med.* 2021;62:521–527.
24. Kramer V, Fernández R, Lehnert W, et al. Biodistribution and dosimetry of a single dose of albumin-binding ligand [^{177}Lu]Lu-PSMA-ALB-56 in patients with mCRPC. *Eur J Nucl Med Mol Imaging.* 2021;48:893–903.
25. Zhang J, Hao W, Weiss OJ, Cheng Y, Chen X. Safety, pharmacokinetics and dosimetry of a long-acting radiolabeled somatostatin analogue ^{177}Lu-DOTA-EB-TATE in patients with advanced metastatic neuroendocrine tumors. *J Nucl Med.* 2018;59:1699–1705.
26. Wang H, Cheng Y, Zhang J, Jie Z, Chen X. Response to single low-dose ^{177}Lu-DOTA-EB-TATE treatment in patients with advanced neuroendocrine neoplasm: a prospective pilot study. *Theranostics.* 2018;8:3308–3316.
27. Wang Q, Wang Y, Ding J, et al. A bioorthogonal system reveals antitumour immune function of pyroptosis. *Nature.* 2020;579:421–426.
28. Avila-Rodriguez MA, Nye JA, Nickles RJ. Production and separation of non-carrier-added ^{86}Y from enriched ^{86}Sr targets. *Appl Radiat Isot.* 2008;66:9–13.
29. Ren J, Xu M, Chen J, et al. PET imaging facilitates antibody screening for synergistic radioimmunotherapy with a ^{177}Lu-labeled αPD-L1 antibody. *Theranostics.* 2021;11:304–315.
30. Kelly J, Amor-Coarasa A, Ponnala S, et al. Trifunctional PSMA-targeting constructs for prostate cancer with unprecedented localization to LNCaP tumors. *Eur J Nucl Med Mol Imaging.* 2018;45:1841–1851.
31. Kelly JM, Amor-Coarasa A, Ponnala S, et al. Albumin-binding PSMA ligands: implications for expanding the therapeutic window. *J Nucl Med.* 2019;60:656–663.

Feasibility of Acquisitions Using Total-Body PET/CT with an Ultra-Low ^{18}F-FDG Activity

Yan Hu[1–3], Guobing Liu[1–3], Haojun Yu[1–3], Ying Wang[4], Chenwei Li[4], Hui Tan[1–3], Shuguang Chen[1–3], Jianying Gu[5], and Hongcheng Shi[1–3]

[1]*Department of Nuclear Medicine, Zhongshan Hospital, Fudan University, Shanghai, China;* [2]*Nuclear Medicine Institute of Fudan University, Shanghai, China;* [3]*Shanghai Institute of Medical Imaging, Shanghai, China;* [4]*United Imaging Healthcare Co., Ltd., Shanghai, China; and* [5]*Department of Plastic Surgery, Zhongshan Hospital, Fudan University, Shanghai, China*

The present study aimed to evaluate the feasibility of ultra-low ^{18}F-FDG activity in total-body PET/CT oncologic studies. **Methods:** Thirty patients with cancer were enrolled prospectively and underwent a total-body PET/CT scan 60 min after injection of an ultra-low ^{18}F-FDG activity (0.37 MBq/kg). Of the 30 enrolled patients, 11 were diagnosed with colorectal cancer (CRC). PET raw data were acquired within 15 min and reconstructed using data from the first 1, 2, 4, 8, and 10 min and the entire 15 min (G1, G2, G4, G8, G10, and G15, respectively). Image quality was qualitatively assessed twice by 2 readers using a 5-point Likert scale. The Cohen κ-test was used to investigate the intra- and interreader agreement. The SUV_{max} of lesions; the SUV_{max}, SUV_{mean}, and SD of the livers; the tumor-to-background ratio; and the signal-to-noise ratio were measured and compared. The acquisition time for a clinically acceptable image quality using an ultra-low-activity injection was determined. In a matched-pair study, 11 patients with CRC who received a full ^{18}F-FDG activity (3.7 MBq/kg) with an acquisition time of 2 min were selected retrospectively by matching sex, height, weight, body mass index, glucose level, uptake time, and pathologic types with the 11 CRC subjects in the prospective study. Qualitative and quantitative analyses were performed and compared between the 11 patients with CRC in the ultra-low-activity group and their matched full-activity controls. **Results:** Qualitative analysis of image quality showed good intra- and interreader agreements (all $\kappa > 0.7$). All the images acquired for 8 min or longer scored over 3 (indicating clinical acceptability). There was no significant difference in tumor-to-background ratio and liver signal-to-noise ratio among all the images acquired for 8 min or longer. In the matched study, no significant difference was found in the image quality score and quantitative parameters between the ultra-low-activity group with an 8-min acquisition and the full-activity group with a 2-min acquisition. **Conclusion:** An ultra-low ^{18}F-FDG activity with an 8-min acquisition in a total-body PET/CT study can achieve acceptable image quality equivalent to that in the full-activity group after a 2-min acquisition.

Key Words: ultra-low activity; image quality; total-body PET/CT

J Nucl Med 2022; 63:959–965
DOI: 10.2967/jnumed.121.262038

PET is an important tool for in vivo quantification of physiologic, biochemical, or pharmacologic processes. ^{18}F-FDG PET is a sensitive imaging method for staging, restaging, and therapy response monitoring of malignancies (*1–4*). However, radiation exposure is a concern for adults, and even more so for pediatric patients, because of the summed doses from both the PET and the CT scans. According to the current procedure guideline of the European Association of Nuclear Medicine for ^{18}F-FDG–based PET/CT oncologic imaging, the minimum time–mass activity product, defined as the product of injected activity and the acquisition duration per bed position, is 14 or 7 MBq·min/kg for a PET system that applies a PET bed overlap of less than or equal to 30% or more than 30%, respectively (*5*). This time–mass activity product is based on the performance of a current conventional PET scanner with an axial field of view of 15–25 cm. With the advent of the total-body PET/CT scanner with ultra-high sensitivity, the time–mass activity product of ^{18}F-FDG could be significantly reduced. Previously, our group investigated the effects of a short acquisition duration on image quality and lesion detectability using the latest PET/CT scanner model, which demonstrated the feasibility of a significantly shorter acquisition time while maintaining image quality and diagnostic performance (*6,7*). By contrast, several studies have proposed a reduction in the injected ^{18}F-FDG activity with total-body PET/CT (*8–10*). A recent study investigated the kinetics of ^{18}F-FDG in healthy volunteers using a 10-times reduction of the injected activity (0.37 MBq/kg) in a total-body PET/CT scanner, which showed an image quality equivalent to that of full-activity imaging (*11*). However, to the best of our knowledge, no studies have investigated the effects of a 10-times reduction of the injected activity on ^{18}F-FDG PET image quality in patients with various types of cancers. In the study on ^{18}F-FDG kinetics, "full activity" had different definitions, 3.7 or 4.4 MBq/kg, according to the adjusted routine practice in our department. Therefore, in the present study, the lower value of 3.7 MBq/kg was used as the full activity definition. The purpose of the study was to investigate the feasibility of a 10-times reduction of the injected activity for ^{18}F-FDG PET imaging in a total-body PET/CT scan for oncologic application.

MATERIALS AND METHODS

Patients

Thirty patients with various cancers and all referred for a total-body ^{18}F-FDG PET/CT study from June to September 2020 were enrolled prospectively in the first part of this study. All patients had pathologically diagnosed malignant tumors. The exclusion criteria included lesions less than 10 mm in diameter, no uptake of ^{18}F-FDG in primary lesions, disease

Received Feb. 3, 2021; revision accepted Sep. 9, 2021.
For correspondence or reprints, contact Hongcheng Shi (shi.hongcheng@zs-hospital.sh.cn) or Jianying Gu (zhongshanhospital@163.com).
Published online Sep. 30, 2021.

in the liver precluding measurement of quantitative metrics in the normal liver, body mass index of at least 30 kg/m^2, blood glucose level of more than 7.0 mmol/L, and an ^{18}F-FDG uptake time of more than 70 min. On the basis of our previous work, an ultra-low ^{18}F-FDG activity (0.37 MBq/kg) was administered (*11*). During the uptake phase, patients were instructed to remain quiet in a warm room for about 60 min and drink 0.5–1 L of water. In the subsequent matched study, 11 patients with colorectal cancer (CRC) who underwent full-^{18}F-FDG-activity (3.7 MBq/kg) total-body PET/CT imaging were selected retrospectively from our database and matched with the same demographic and pathologic results of the 11 patients with CRC in the ultra-low-activity group; the sex, height, weight, body mass index, blood glucose level, and uptake time were well matched. The uptake procedure in the matched study was the same as that in the ultra-low-activity group. The study was approved by the Institutional Review Board of Zhongshan Hospital, Fudan University, and written informed consent was obtained from all the subjects in the prospective study. The need for written informed consent was waived for the 11 patients in the matched study given its retrospective design with anonymous retrieval of imaging data.

Data Acquisition and Reconstruction

All patients fasted for at least 6 h before the ^{18}F-FDG injection, and their level of fasting blood glucose was no more than 7.0 mmol/L. All PET/CT scans were performed in a total-body PET/CT scanner (uEXPLORER; United Imaging Healthcare) with an axial field of view of 194 cm. The PET images of the ultra-low-activity group were acquired after 15 min and then reconstructed using the first 1, 2, 4, 8, and 10 min of data by temporally down-sampling from the acquired 15-min raw data to simulate faster acquisitions, hereafter referred to as G1, G2, G4, G8, G10, and G15, respectively. The PET images of the full-activity group were reconstructed using an acquisition time of 2 min, hereafter referred to as g2. PET reconstructions were performed using the ordered-subset expectation maximization algorithm with the following parameters: time of flight and point-spread-function modeling, 3 iterations, 20 subsets, matrix of 192 × 192, slice thickness of 1.443 mm, and gaussian filter of 3 mm in full width at half maximum.

Image Quality Assessment

The PET image quality was assessed independently by 2 readers (both nuclear medicine physicians and both with 5 y or more of experience in interpreting PET/CT images). The qualitative analysis of image quality was scored on a Likert scale of 1–5 (1, unacceptable image quality: extremely poor contrast with significant noise; 2, poor image quality: low contrast with noise; 3, acceptable image quality: moderate contrast with noise; 4, good image quality: good contrast with less noise; 5, excellent image quality: perfect contrast with minimal noise). A score of 3 indicated the minimum acceptable image quality for clinical reporting. For each patient, all the PET images were loaded into the viewer using software (uWS-MI, R001; United Imaging Healthcare). The order of the PET images was randomized by an independent operator. The readers were unaware of the patient's demographic information, medical history, and acquisition duration. In addition, each reader reassessed the image quality 1 wk later to eliminate the memory effect, using a different order of patients and PET images. The image quality values of each reader were averaged and compared between the ultra-low- and full-activity groups.

In a separate session performed 1 wk after the second qualitative assessment, the quantitative analysis of image quality was first performed by 1 of the 2 readers by manually drawing a 2-dimensional circular region of interest (ROI) with a diameter of 2 cm on the homogeneous area of the right lobe of the liver. ROIs were placed automatically at exactly the same location and slice for the entire loaded PET series. The ROI was carefully drawn to avoid lesions and was at least 1 cm away from the edge of the liver. The SUV_{max}, the SUV_{mean}, and the SD were recorded. The SUV_{max} of the primary lesion was delineated at the corresponding PET transverse slice with the maximum diameter in the CT images for comparison of image datasets. The size of the ROIs was adapted to the lesion size. The liver signal-to-noise ratio (SNR) was calculated by dividing the SUV_{mean} by its SD, and the tumor-to-background ratio (TBR) was calculated by dividing the lesion SUV_{max} by the liver SUV_{max}.

Statistical Analysis

Statistical analysis was conducted using SPSS 20.0 (IBM Corp.) and Prism 6.0 (GraphPad Software Inc.). Numeric parameters are presented as the mean ± SD, and categoric variables are described as frequencies. A P value of less than 0.05 indicated statistical significance. The intra- and interreader agreement for the qualitative scores was analyzed using the Cohen κ-test (0.00–0.20 = low; 0.21–0.40 = medium; 0.41–0.60 = moderate; 0.61–0.80 = good; 0.81–1.00 = excellent). The Kolmogorov–Smirnov test was performed to test the normality of the objective image quality, and the Wilcoxon rank-sum test was used to compare these parameters in G1–G10 with those in G15. The Fisher exact test and an independent-sample t test were used to compare the categoric and numeric variables between the ultra-low- and full-activity groups, respectively.

RESULTS

Patient Demographics in Ultra-Low-Activity Group

The patient demographics in the ultra-low-activity group are summarized in Table 1. Thirty patients were enrolled in the

TABLE 1
Demographics of Patients in Ultra-Low-Activity Group

Variable	Dataset
Sex*	
Men	20
Women	10
Age (y)†	66.1 ± 8.44 (48.00–77.00)
Height (cm)†	165.5 ± 7.25 (157.00–186.20)
Weight (kg)†	62.28 ± 10.2 (44.80–88.00)
BMI (kg/m^2)†	22.73 ± 3.28 (15.76–29.75)
Blood glucose (mmol/L)†	5.75 ± 0.66 (4.80–7.00)
Uptake time (min)†	60.97 ± 5.96 (51.00–70.00)
Injected dose (MBq)†	25.53 ± 4.07 (17.76–33.67)
Primary tumor type*	
HCC and ICC	4
CRC	11
Lung cancer	1
Pancreatic cancer	3
Esophageal cancer	2
Mediastinal sarcoma	1
Bladder cancer	4
Ovarian cancer	2
Lymphoma	1
Laryngeal cancer	1

*Number of patients.
†Data are presented as mean ± SD followed by range in parentheses.
BMI = body mass index; HCC = hepatocellular carcinoma; ICC = intrahepatic cholangiocarcinoma.

TABLE 2
Subjective Image Quality Score in Ultra-Low-Activity Group

	Image quality score			
	Likert scale score		Cohen κ-test result	
Acquisition duration (min)	Reader 1*	Reader 2*	Intrareader agreement	Interreader agreement
1	1.10 ± 0.31	1.14 ± 0.35	0.898 (0.694–1.000)	0.849 (0.530–1.000)
2	2.07 ± 0.37	2.10 ± 0.41	0.902 (0.711–1.000)	0.885 (0.674–1.000)
4	3.00 ± 0.38	2.90 ± 0.49	0.895 (0.688–1.000)	0.750 (0.492–1.000)
8	4.07 ± 0.53	3.97 ± 0.63	0.900 (0.701–1.000)	0.852 (0.638–1.000)
10	4.38 ± 0.49	4.38 ± 0.49	0.921 (0.738–1.000)	0.854 (0.648–1.000)
15	4.62 ± 0.49	4.59 ± 0.50	0.945 (0.812–1.000)	0.930 (0.790–1.000)

*Mean value and SD were calculated on basis of subjective scores for each patient.
Data in parentheses are 95% CIs.

prospective part of the study (20 men and 10 women; mean age of 66.10 ± 8.44 y). The average fasting blood glucose level was 5.75 ± 0.66 mmol/L, and the mean uptake time after injection was 60.97 ± 5.96 min. Diagnoses of the malignancies were confirmed using pathologic examinations.

Image Quality in Ultra-Low-Activity Group

The subjective image quality scores of the ultra-low-activity group are summarized in Table 2. The intra- and interreader agreements were good for the subjective image quality score (all $\kappa > 0.7$). In groups with an acquisition duration of 8 min or longer, the agreement was excellent (all $\kappa > 0.85$). There was a significant difference in image quality regarding the Likert scale between G15 and the other groups (G1–G10) ($P < 0.001$). All images with an 8-min acquisition time or longer had a score over 3 and were judged acceptable for clinical reporting.

As shown in Table 3 and Figures 1 and 2, the lesion SUV_{max} increased with the duration of acquisition; however, the difference was significant for an acquisition time of only 1 min compared with that for G15 (all $P > 0.05$). The liver SUV_{max} decreased with longer acquisition times, and the TBR increased; however, the difference was significant for both parameters only for acquisition times shorter than 4 min ($P < 0.05$). The liver SUV_{mean}, SD, and SNR are summarized in Table 4. There was no difference in the liver SUV_{mean} among all the groups ($P > 0.05$). The liver SD decreased rapidly from G1 to G15, whereas the SNR increased progressively. However, there were no statistical differences between G8, G10, and G15 ($P > 0.05$). Therefore, images from G8 had an image quality equivalent to that from G15 and were suitable for clinical reporting.

Patient Demographics of Matched Patients in Ultra-Low-Activity and Full-Activity Groups

Eleven patients (7 men and 4 women in each group) with CRC (10 well-to-moderately differentiated adenocarcinoma and 1 high-grade intraepithelial neoplasia) were enrolled in the matched study. The demographics of the patients with CRC in G8 and g2 are provided in Table 5. As expected, a significant difference in the injected dose was found between G8 and g2 ($P < 0.001$), although other variables, including sex, body mass index, blood glucose, uptake time, and pathologic classification, were well matched, without significant differences (all $P > 0.05$).

Comparison of Image Quality Between G8 and g2

The results from the subjective and objective analyses of image quality in G8 and g2 are shown in Table 6. The visual image quality score in G8 was 3.91 ± 0.30, which was equivalent to that in g2 (3.82 ± 0.60). The lesion SUV_{max} and TBR in G8 (23.43 ± 8.64 and 7.07 ± 2.74) were slightly lower than those in g2 (24.22 ± 12.15 and 7.56 ± 3.51) but without statistical significance (all $P > 0.05$). The liver SUV_{mean} and liver SD were similar in G8

TABLE 3
Quantitative Image Quality in Ultra-Low-Activity Group

Acquisition duration (min)	Lesion SUV_{max}	Liver SUV_{max}	TBR
1	12.44 ± 5.00*	4.56 ± 0.86*	2.84 ± 1.36*
2	14.58 ± 6.86	3.80 ± 0.60*	3.89 ± 1.80*
4	16.95 ± 7.78	3.53 ± 0.52	4.83 ± 2.18
8	18.09 ± 8.26	3.31 ± 0.50	5.53 ± 2.50
10	18.37 ± 8.06	3.21 ± 0.46	5.78 ± 2.50
15	18.96 ± 7.93	3.08 ± 0.42	6.18 ± 2.52

*Significant difference compared with that in G15 ($P < 0.05$).
Data are presented as mean ± SD, based on measurement in ROIs.

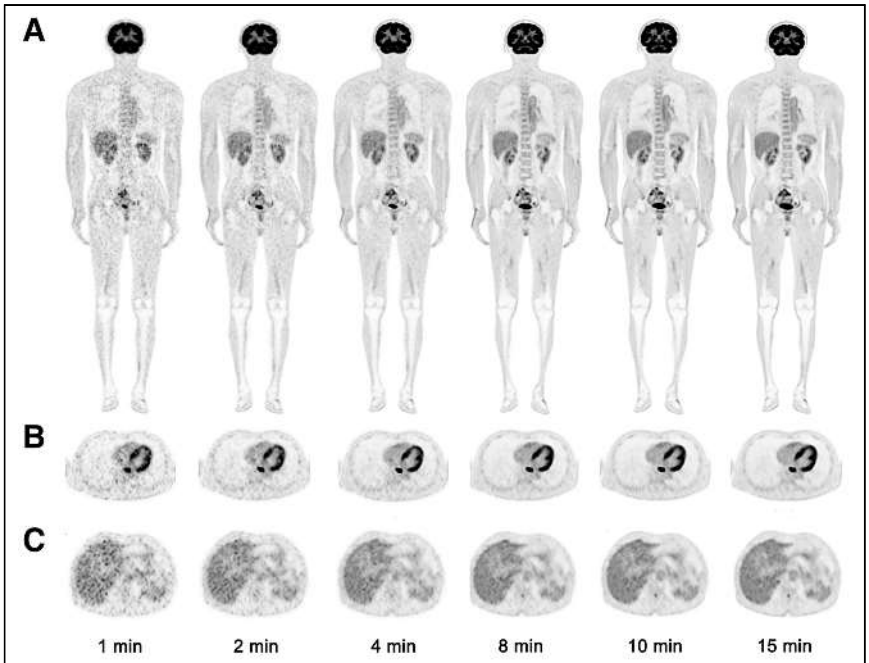

	Acquisition duration (min)					
	1	2	4	8	10	15
Visual score	1.12 ± 0.32	2.09 ± 0.38	2.97 ± 0.41	4.03 ± 0.56	4.38 ± 0.49	4.60 ± 0.49
Lesion SUVmax	12.44 ± 5.00	14.58 ± 6.86	16.95 ± 7.78	18.09 ± 8.26	18.37 ± 8.06	18.96 ± 7.93
Liver SUVmax	4.56 ± 0.86	3.80 ± 0.60	3.53 ± 0.52	3.31 ± 0.50	3.21 ± 0.46	3.08 ± 0.42
Liver SUVmean	2.80 ± 0.48	2.78 ± 0.44	2.77 ± 0.43	2.73 ± 0.38	2.72 ± 0.39	2.70 ± 0.38

FIGURE 1. PET images of 63-y-old man with esophagus cancer. Coronal slice of whole body (A), transverse view of intense uptake of lesions in esophagus (B), and transverse view of liver (C) are shown in G1, G2, G4, G8, G10, and G15 reconstructions. More superior image quality of liver was observed in G8 than in G1 and G2 on visual assessment.

and g2 (liver SUV_{mean} [mean ± SD], 2.78 ± 0.33 vs. 2.84 ± 0.47, and liver SD [noise in liver], 0.21 ± 0.05 vs. 0.23 ± 0.08, respectively). The SNRs in G8 and g2 were 13.77 ± 2.14 and 13.40 ± 2.90, respectively, without a significant difference (P = 0.716). None of the quantitative parameters showed significant differences between the groups (all $P >$ 0.05), indicating an equivalent performance between the 2 groups (Figs. 3 and 4).

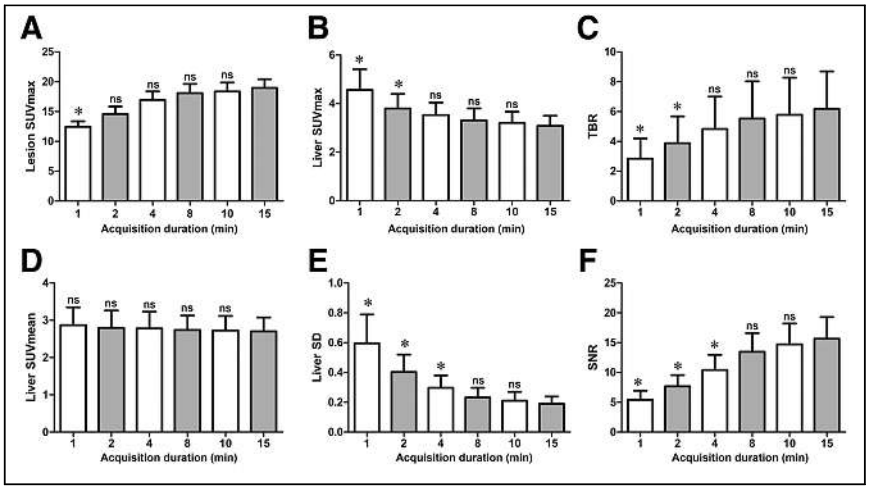

FIGURE 2. Box plot of lesion SUV_{max} (A), liver SUV_{max} (B), TBR (C), liver SUV_{mean} (D), liver SD (E), and SNR (F). Lesion SUV_{max}, TBR, and SNR increased with extension of acquisition time, whereas liver SUV_{max}, liver SUV_{mean}, and SD decreased. Compared with G15, no significant differences for these parameters were found in G8 and G10. *$P < 0.05$. ns = not significant.

DISCUSSION

The 194-cm-long total-body PET/CT system has a spatial resolution of approximately 3.0 mm and a system sensitivity of up to 174 kcps/MBq with NEMA NU-2-2018 (*12*). The system enables excellent image quality and provides new opportunities to assess clinical imaging protocol modifications such as shorter scan durations, low-activity tracer injection, delayed imaging, or repeated scans. The current study assessed the feasibility of using a low-activity ^{18}F-FDG injection. The dominant physical characteristic of the total-body PET scanner is its high sensitivity, being 40-fold higher than that of current systems (*13*). The SNR in PET images, representing the image quality, is proportional to the square root of the product of system sensitivity, injected activity, and acquisition time (*14*). For the total-body PET/CT scanner, the data quality is as important as the data quantity (i.e., total true counts). Data quality is often measured as noise-equivalent counts, which are calculated as $T^2/(T + R)$, where T and R are the trues and randoms, respectively. The random rate is considered to be proportional to the square of the injected activity, whereas the true rate is proportional to the injected activity, so the random rate is approximately 100 times higher in the full-activity situation than in the ultra-low-activity (one tenth of a full-activity dose) situation. As a result, if the ultra-low-activity data and the full-activity data have equivalent total true counts, the ultra-low-activity data would have a higher noise-equivalent count, that is, better data quality. Therefore, it is possible to achieve comparable image quality with a shorter acquisition time than that estimated from the rule of constant product of the acquisition time and the activity. Our previous studies demonstrated the capability of the total-body PET/CT scanner to achieve good image quality with a reduced injected activity of up to one half and one seventh the recommended standard in the clinic (3.7 MBq/kg) (*9,15*). However, these studies were on only a small number of cases and did not evaluate both the qualitative and the quantitative aspects. Therefore, the current study aimed to provide qualitative and quantitative assessments of image quality after injection of an ultra-low ^{18}F-FDG activity in oncologic patients using the total-body PET/CT scanner.

Our results demonstrated that images taken 8 min after injection of an ultra-low

TABLE 4
SUV_{mean}, SD, and SNR of Liver

Parameter	Acquisition duration (min)					
	1	2	4	8	10	15
Liver SUV_{mean}*	2.80 ± 0.48	2.78 ± 0.44	2.77 ± 0.43	2.73 ± 0.38	2.72 ± 0.39	2.70 ± 0.38
Liver SD*	0.56 ± 0.19†	0.38 ± 0.11†	0.28 ± 0.08†	0.21 ± 0.06	0.19 ± 0.06	0.18 ± 0.05
SNR*	5.41 ± 1.53†	7.67 ± 1.88†	10.41 ± 2.54†	13.46 ± 3.13	14.72 ± 3.46	15.65 ± 3.64

*Data are presented as mean ± SD, based on measurement in ROIs.
†Significant difference compared with that in G15 ($P < 0.05$).

TABLE 5
Demographics of Patients in G8 and g2

Variable	G8	g2	*P*
Sex*			0.201
Men	7	7	
Women	4	4	
Height (cm)†	166.05 ± 6.48	167.82 ± 10.01	0.627
Weight (kg)†	62.96 ± 11.87	71.52 ± 18.22	0.208
BMI (kg/m^2)†	22.75 ± 3.46	25.00 ± 3.92	0.168
Blood glucose (mmol/L)†	5.81 ± 0.61	5.31 ± 0.53	0.054
Uptake time (min)†	62.91 ± 5.50	58.00 ± 5.57	0.051
Injected dose (MBq)†	24.79 ± 4.44	271.21 ± 61.42	<0.001‡
Pathologic*			1.000
WMDA	10	10	
HGIN	1	1	

*Number of patients.
†Data are presented as mean ± SD, based on data from each subject.
‡Significant difference between G8 and g2 ($P < 0.001$).
BMI = body mass index; WMDA = well-to-moderately differentiated adenocarcinoma; HGIN = high-grade intraepithelial neoplasia.

TABLE 6
Qualitative Image Quality Score and Quantitative Parameters in the Ultra-Low-Activity Group and Full-Activity Group

Parameter	G8	g2	*P*
Image quality score	3.91 ± 0.30	3.82 ± 0.60	0.311
Lesion SUV_{max}	23.43 ± 8.64	24.22 ± 12.15	0.863
Liver SUV_{max}	3.39 ± 0.54	3.17 ± 0.55	0.354
Liver SUV_{mean}	2.78 ± 0.33	2.84 ± 0.47	0.747
Liver SD	0.21 ± 0.05	0.23 ± 0.08	0.544
TBR	7.07 ± 2.74	7.56 ± 3.51	0.738
SNR	13.77 ± 2.14	13.40 ± 2.90	0.716

Data are presented as mean ± SD. Mean value and SD were calculated on basis of Likert score for each patient. Mean value and SD of other quantitative parameters were calculated on basis of measurement in ROIs.

^{18}F-FDG activity provided acceptable image quality for clinical reporting. The liver SUV_{mean} showed good consistency for all PET series, without significant differences between groups among G1–G15. However, the liver SNR showed a lack of significant differences between groups only among G8–G15. Lesion SUV_{max} and TBR in G8 and G10 did not significantly differ from those in G15. On the basis of the above results, an 8-min PET acquisition time with an ultra-low-activity injection protocol could yield diagnostic-level image quality for clinical oncologic applications.

In this study, we found that lesion SUV_{max} increased along with the acquisition time, a finding that was inconsistent with a previous study (*6*). We hypothesized that the additional uptake time (with a maximum of 15 min) will be more noticeable when the acquired counts are reduced. The effect on the increased accumulation of ^{18}F-FDG in the malignant lesions will be more significant and thus increase the lesion SUV, as observed in the time–activity curves in previous studies (*16,17*). Additionally, a discrepancy between qualitative and quantitative analysis was found. In the quantitative analysis, the TBR and SNR were higher for G10–G15 than for G8, but without statistical differences. The liver SD

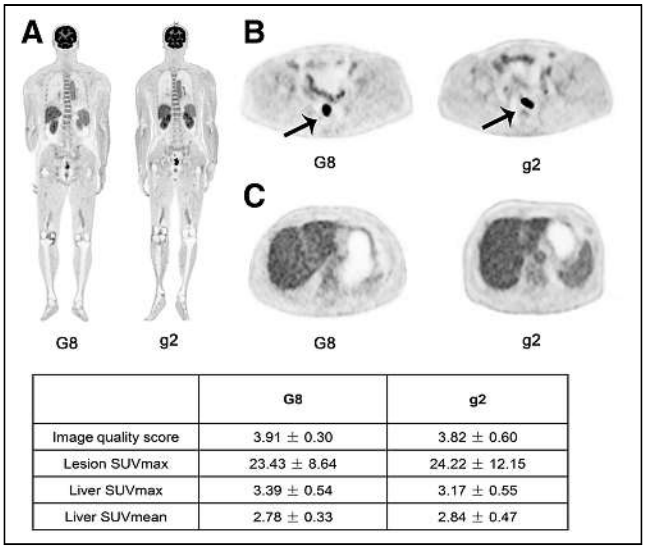

	G8	g2
Image quality score	3.91 ± 0.30	3.82 ± 0.60
Lesion SUVmax	23.43 ± 8.64	24.22 ± 12.15
Liver SUVmax	3.39 ± 0.54	3.17 ± 0.55
Liver SUVmean	2.78 ± 0.33	2.84 ± 0.47

FIGURE 3. PET images of 63-y-old man with CRC reconstructed in G8 and another 63-y-old man with CRC reconstructed in g2 (A, coronal slice of the whole body; B, transverse view of CRC lesion [arrow]; C, transverse image of liver). Image quality in G8 was comparable to that in g2, which meets standard for clinical diagnosis.

decreased as the acquisition time increased, but no significant difference was observed between G8 and G15. In this study, we used lesion TBR, liver SNR, and SD as the indices of quantitative image quality. However, the qualitative analysis process was far more complex as it could be influenced by the reader's experience, preference, and training before the analysis.

In conventional whole-body PET/CT imaging, PET acquisition is performed in a step-and-shoot mode with 6–7 bed positions. The total-body PET/CT imaging uses a 1-step acquisition mode because the 194-cm axial field of view can cover the patient's entire body in 1 bed position. Our previous study reported that a total-body PET scan with a 2-min acquisition time and an injected activity of 4.4 MBq/kg could yield images superior to the average image quality (*6*). The liver SUV_{max} and SD in the 2 studies showed a similar tendency with the acquisition time, but with different values. This is mainly caused by the difference in the uptake time of the enrolled patients between the 2 studies. Although a 60-s acquisition can maintain the diagnostic performance at a sufficient level, as reported in the previous study (*6*), the injected activity was 18% higher than the full activity in this study. Thus, in the matched-pair part of this study, a 2-min acquisition was selected as the control to evaluate the image quality and feasibility of ultra-low ^{18}F-FDG activity in total-body PET/CT imaging. Compared with full activity using 2 min of acquisition, the image quality of ultra-low ^{18}F-FDG activity using 8 min of acquisition revealed an equivalent result. The concept of an ultra-low-activity ^{18}F-FDG PET scan has several benefits. One is the significant reduction of radiation from the PET radiotracers, which is approximately 7 mSv in a conventional PET whole-body examination (*18*). If activity can be reduced to one tenth, it allows for increased use of PET scans in radiation-sensitive populations (infants, children, and adolescents). For pediatric imaging, there are risks associated with the acquisition duration and injected dose. An increased injected activity is associated with an increased risk of radiation-induced cancer in the pediatric population (*19*). According to recently published guidelines, images of diagnostic image quality using the lowest possible dose are desired in pediatric ^{18}F-FDG PET/CT for oncology (*5*). The ultra-low ^{18}F-FDG activity, with reduced radiation exposure, will provide a more feasible solution for pediatric imaging. In addition, the ultra-low ^{18}F-FDG activity is an attractive option for repeated scans for monitoring treatment response. It may become an effective strategy for patient management without concerns about the cumulative absorbed radiation dose.

Our study has several limitations. First, 30 patients with 10 types of cancer were enrolled prospectively in the study. The highest body weight in the enrolled cases was 88 kg. Image quality can be influenced by patient size (weight and body mass index), and image quality might be degraded because of excessive attenuation in heavier patients (*5*). Additionally, only patients with CRC were validated in the matched study. Although they were well matched on the basis of the demographic and pathologic features, some marginal differences remained. The relatively small number of patients enrolled in the matched study meant that there was a potential selection bias. Second, although ^{18}F-FDG is the most widely used radiotracer in oncologic studies, it is not applicable to all types of cancer, because not all tumors are ^{18}F-FDG–avid. Furthermore, the extent of ^{18}F-FDG uptake is easily affected by certain factors. Respiratory motion might blur the lesions on which the impact of the SUV measurement may differ with different acquisition times (*20*). We selected lesions at least 10 mm in diameter (measured on CT images), for which the error induced by the respiratory motion could be minimized. Finally, the 2-dimensional ROI did not necessarily capture the true SUV_{max} of the whole tumor volume, as limited by the current measurement software. The reconstruction parameters used in this study were the same as those with the standard activity used in our department without specific modification. However, these parameters were based on the high counts and the clinical requirements for diagnosis. To improve lesion detection, we applied point-spread-function modeling in the PET reconstruction, the same as in routine practice, which may cause a bias in the

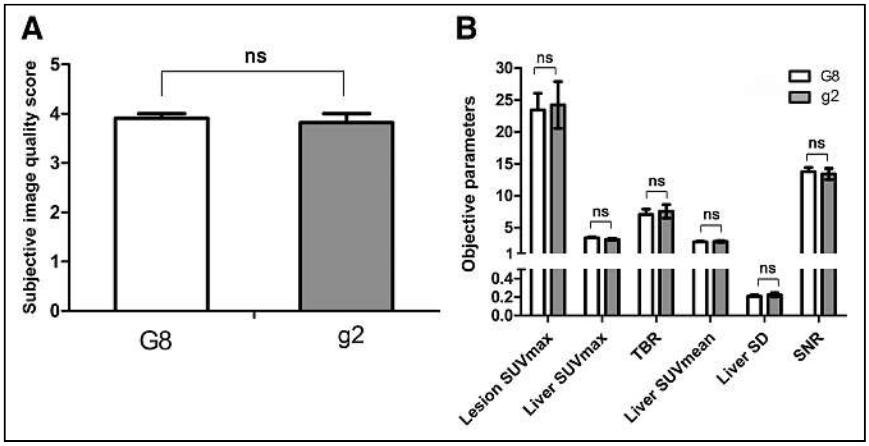

FIGURE 4. Bar graph of values of subjective image quality score (A) and objective parameters (B) between G8 and g2. Comparable result of qualitative and quantitative analysis was shown between the 2 groups. ns = not significant.

quantitative estimate. Future studies should compare the point-spread-function reconstruction with the non–point-spread-function reconstruction, as well as investigate the optimal reconstruction parameters for the ultra-low ^{18}F-FDG activity.

CONCLUSION

The study demonstrated that use of an ultra-low ^{18}F-FDG activity (0.37 MBq/kg) in total-body PET/CT was feasible for oncologic studies, with a clinical diagnostic-level image quality achieved. Further investigation will be performed to explore the optimal reconstruction parameters for an ultra-low ^{18}F-FDG activity in the clinic.

DISCLOSURE

This study was supported by the National Science Foundation for Scholars of China (grant 81871407 to Hongcheng Shi), the Shanghai Municipal Key Clinical Specialty (grant shslczdzk03401), the Three-Year Action Plan of Clinical Skills and Innovation of the Shanghai Hospital Development Center (grant SHDC2020CR3079B to Hongcheng Shi), and the Shanghai Science and Technology Committee (grant 20DZ2201800). No other potential conflict of interest relevant to this article was reported.

KEY POINTS

QUESTION: Does an ultra-low ^{18}F-FDG activity (0.37 MBq/kg) in total-body PET/CT compromise image quality?

PERTINENT FINDINGS: This study demonstrated that the image quality seen using an ultra-low ^{18}F-FDG activity in total-body PET/CT meets clinical requirements.

IMPLICATIONS FOR PATIENT CARE: Total-body PET/CT imaging with an ultra-low ^{18}F-FDG activity can be used in radiation-sensitive populations such as infants, children, and adolescents, as well as in patients who need repeated scans to monitor treatment response.

REFERENCES

1. Martin O, Schaarschmidt BM, Kirchner J, et al. PET/MRI versus PET/CT for whole-body staging: results from a single-center observational study on 1,003 sequential examinations. *J Nucl Med.* 2020;61:1131–1136.
2. Findlay JM, Antonowicz S, Segaran A, et al. Routinely staging gastric cancer with ^{18}F-FDG PET-CT detects additional metastases and predicts early recurrence and death after surgery. *Eur Radiol.* 2019;29:2490–2498.
3. Noda Y, Goshima S, Kanematsu M, et al. ^{18}F-FDG uptake on positron emission tomography as a predictor for lymphovascular invasion in patients with lung adenocarcinoma. *Ann Nucl Med.* 2016;30:11–17.
4. Husby JA, Reitan BC, Biermann M, et al. Metabolic tumor volume on ^{18}F-FDG PET/CT improves preoperative identification of high-risk endometrial carcinoma patients. *J Nucl Med.* 2015;56:1191–1198.
5. Boellaard R, Delgado-Bolton R, Oyen WJG, et al. FDG PET/CT: EANM procedure guidelines for tumour imaging: version 2.0. *Eur J Nucl Med Mol Imaging.* 2015;42:328–354.
6. Zhang YQ, Hu PC, Wu RZ, et al. The image quality, lesion detectability, and acquisition time of ^{18}F-FDG total-body PET/CT in oncological patients. *Eur J Nucl Med Mol Imaging.* 2020;47:2507–2515.
7. Zhang X, Cherry SR, Xie Z, Shi H, Badawi RD, Qi J. Subsecond total-body imaging using ultrasensitive positron emission tomography. *Proc Natl Acad Sci USA.* 2020;117:2265–2267.
8. Cherry SR, Jones T, Karp JS, Qi J, Moses WW, Badawi RD. Total-body PET: maximizing sensitivity to create new opportunities for clinical research and patient care. *J Nucl Med.* 2018;59:3–12.
9. Badawi RD, Shi H, Hu P, et al. First human imaging studies with the EXPLORER total-body PET scanner. *J Nucl Med.* 2019;60:299–303.
10. Zhang X, Zhou J, Cherry SR, Badawi RD, Qi J. Quantitative image reconstruction for total-body PET imaging using the 2-meter long EXPLORER scanner. *Phys Med Biol.* 2017;62:2465–2485.
11. Liu G, Hu P, Yu H, et al. Ultra-low-activity total-body dynamic PET imaging allows equal performance to full-activity PET imaging for investigating kinetic metrics of ^{18}F-FDG in healthy volunteers. *Eur J Nucl Med Mol Imaging.* 2021;48:2373–2383.
12. Spencer BA, Berg E, Schmall JP, et al. Performance evaluation of the uEXPLORER total-body PET/CT scanner based on NEMA NU 2-2018 with additional tests to characterize PET scanners with a long axial field of view. *J Nucl Med.* 2021;62:861–870.
13. Poon JK, Dahlbom ML, Moses WW, et al. Optimal whole-body PET scanner configurations for different volumes of LSO scintillator: a simulation study. *Phys Med Biol.* 2012;57:4077–4094.
14. Yan J, Schaefferkoette J, Conti M, Townsend D. A method to assess image quality for low-dose PET: analysis of SNR, CNR, bias and image noise. *Cancer Imaging.* 2016;16:26.
15. Tan H, Sui X, Yin H, et al. Total-body PET/CT using half-dose FDG and compared with conventional PET/CT using full-dose FDG in lung cancer. *Eur J Nucl Med Mol Imaging.* 2021;48:1966–1975.
16. Yang M, Lin Z, Xu Z, et al. Influx rate constant of ^{18}F-FDG increases in metastatic lymph nodes of non-small cell lung cancer patients. *Eur J Nucl Med Mol Imaging.* 2020;47:1198–1208.
17. Tan H, Gu Y, Yu H, et al. Total-body PET/CT: current applications and future perspectives. *AJR.* 2020;215:325–337.
18. Huang B, Law MWM, Khong PL. Whole-body PET/CT scanning: estimation of radiation dose and cancer risk. *Radiology.* 2009;251:166–174.
19. Fahey FH. Dosimetry of pediatric PET/CT. *J Nucl Med.* 2009;50:1483–1491.
20. Liu C, Pierce LA II, Alessio AM, Kinahan PE. The impact of respiratory motion on tumor quantification and delineation in static PET/CT imaging. *Phys Med Biol.* 2009;54:7345–7362.

The Will Rogers Phenomenon and PSMA PET/CT

TO THE EDITOR: Soon after initiating ^{18}F-PSMA imaging, our team realized that we were able to detect and stage prostate cancer with far greater sensitivity than former imaging technologies allowed. One of our early cases involved identification of disease we had difficulty characterizing because the low-dose CT scan and standard PET reconstructions were unable to fully resolve the abnormalities. We therefore increased the CT scanner tube potential to 120 reference mAs (CareDose 4D; Siemens) and applied the higher-resolution option (HiRez; Siemens) on the PET scanner to a 400 × 400 matrix with increased imaging time in the abdomen and pelvis. Now, clear identification of positive 3-mm lymph nodes is a routine event.

We recently saw a clearly positive PSMA PET scan within pelvic lymph nodes smaller than 3 mm in a patient after radical prostatectomy with a prostate-specific antigen rise from 0.02 to 0.09 ng/mL. This use has truly unleashed the capabilities of high-resolution PET/CT and the promise of this technology.

How is patient care impacted? For the first time, I have heard my colleagues refer to this as the "classic Will Rogers phenomenon," a term often used to describe stage migration. Will Rogers, a renowned vaudeville cowboy whose career peaked in the 1930s, is purported to have said, "When the Okies left Oklahoma and moved to California, they raised the average intelligence level in both states." Stage migration occurs when disease is reclassified either by changes in technology or by changes in staging algorithms. In the end, survival in the healthier patient group improves, as the least healthy patients have been eliminated from the group by upstaging of their disease. The less healthy group also has better survival, as the patients can enter the group at an earlier time in their disease process.

Stage migration is not unfamiliar to the nuclear medicine community, who witnessed the changes in delivery of care for thyroid cancer. Although the death rate from thyroid cancer is stable, there was a marked increase in disease detection. As a consequence, treatment algorithms were modified.

However, the similarity to thyroid cancer is only superficial at best. Prostate cancer has far greater complexity in treatment options, and guidelines are based on large-scale prospective clinical trials. It will take years to incorporate the effects of stage migration through modification of treatment options. I hope that these issues are addressed for all men in their 60s and 70s, as we may find the baby boomer generation reclassified as the chemically castrate generation.

Nicholas C. Friedman*
Edward Hines, Jr.
**VA Hospital*
Hines, Illinois
E-mail: nicholas.friedman@va.gov

Published online Dec. 9, 2021.
DOI: 10.2967/jnumed.121.263556

Nuclear Medicine Textbook: Methodology and Clinical Applications

D. Volterrani, P.A. Erba, I. Carrió, H.W. Strauss, and G. Mariani, eds.

Springer, 2019, 1,331 pages, $179.99

Nuclear medicine is a small specialty, but it has been and continues to be one of the most innovative and exciting branches of medicine. Nuclear medicine combines biology, chemistry, physics, and mathematics with the art and science of clinical medicine. Tracer-principle–based radiopharmaceutical therapy and diagnosis, which may be targeted and integrated systematically in the form of theranostics, may be applied to all major organ systems and disease processes. Theranostics was born about 80 years ago with radioiodine in the imaging and treatment of thyroid diseases. Therefore, whereas the concept is not new, it has undergone a renaissance with the development of novel agents for imaging and targeted radionuclide therapy of cancer (e.g., neuroendocrine tumors, prostate cancer, and pheochromocytoma/paraganglioma). Other agents are anticipated relatively soon that are targeted to chemokine receptors and fibroblast activation protein, with the list expanding as further biologic insights and biomarker developments emerge. Nuclear medicine and theranostics are also anticipated to cultivate a rational link between precision health and precision medicine.

There have been many comprehensive textbooks published on the science and clinical practice of nuclear medicine. However, nuclear medicine is a fast-advancing field that demands new textbooks or relatively frequent updates to the ones previously published. Here, I review a book published by Springer in 2019. The book is entitled *Nuclear Medicine Textbook: Methodology and Clinical Applications* and is edited by five renowned academic experts in nuclear medicine: three from the University of Pisa, one from the Autonomous University of Barcelona (past editor of the *European Journal of Nuclear Medicine and Molecular Imaging*), and one from Cornell University Weill (past editor of *The Journal of Nuclear Medicine* and past president of the Society of Nuclear Medicine and Molecular Imaging). The editors also contributed as coauthors to several chapters, along with a remarkable 122 invited international contributors, most from Italy but also contributors from Austria, Germany, Japan, Jordan, Spain, Sweden, The Netherlands, and the United States.

This comprehensive book is structured into 51 chapters organized as 3 parts and encompasses 1,331 pages, with numerous tables, graphs, diagrams, and high-quality images, many in color. Part I, on basic science, includes 16 chapters covering a brief history of radiation and radioactivity; radiation physics and radiation protection; radiopharmaceuticals (categorized conveniently under single-photon–emitting, positron-emitting, and therapy); instrumentation, including camera systems; image data acquisition; processing and quantification techniques; and principles and interpretation of CT and MRI as an introduction to hybrid imaging. Part I culminates with an expedient summary of radioguided biopsy and surgery in the relevant clinical scenarios. Part II, on clinical applications, has 22 chapters covering all major organ system diseases in both adults and children, with an emphasis on hybrid imaging, including a chapter on the expanding utility of PET/CT in dose painting and radiation treatment planning in several malignancies. Part III, on practice and procedures, contains 13 chapters and provides useful ancillary information on the radiochemistry of single-photon–emitting and positron-emitting radiopharmaceuticals, their quality assurance procedures, their regulatory processes in both Europe and the United States, quality control of instrumentation and camera systems, practice guidelines for major nuclear medicine procedures, and dual-energy x-ray absorptiometry for assessment of bone mineral density. Part III closes with 36 nononcologic and 42 oncologic illustrative teaching cases (mostly ^{18}F-FDG PET, with a few cases of ^{18}F-FDOPA and ^{18}F-fluorocholine PET) and techniques for optimal image interpretation, along with concise and informative reporting of results, including sample reports for 56 different clinical scenarios and nuclear medicine procedures. Each chapter includes learning objectives and key learning points, with cited references or additional suggested readings. The book ends with a convenient glossary of abbreviated terms and a detailed index.

This practical book is particularly useful for trainees but is also of considerable value to seasoned physicians in nuclear medicine or radiology and to practitioners in other branches of medicine and surgery interested in the applicability of nuclear medicine procedures to their disciplines. Other professionals, including technologists, medical physicists, and radiation safety officers, can also benefit from this textbook. This book will be a great resource in the library of any clinical department or medical school.

In the end, I paraphrase a frequently repeated quotation from the Californian public television personality Huell Howser (1945–2013), who, in his "California's Gold" program, explored the natural, cultural, and historical features of California. He always ended this program by saying, " … and this is truly a fine example of California's gold." In that same spirit, I must say that *Nuclear Medicine Textbook: Methodology and Clinical Applications* is a fine example of nuclear medicine's gold.

Hossein Jadvar
USC Keck School of Medicine
University of Southern California
Los Angeles, California
E-mail: jadvar@med.usc.edu

Published online Dec. 9, 2021
DOI: 10.2967/jnumed.121.263612

Explore SNMMI's Online Career Center!

Explore the benefits of the SNMMI Career Center by logging in or creating a new account today.

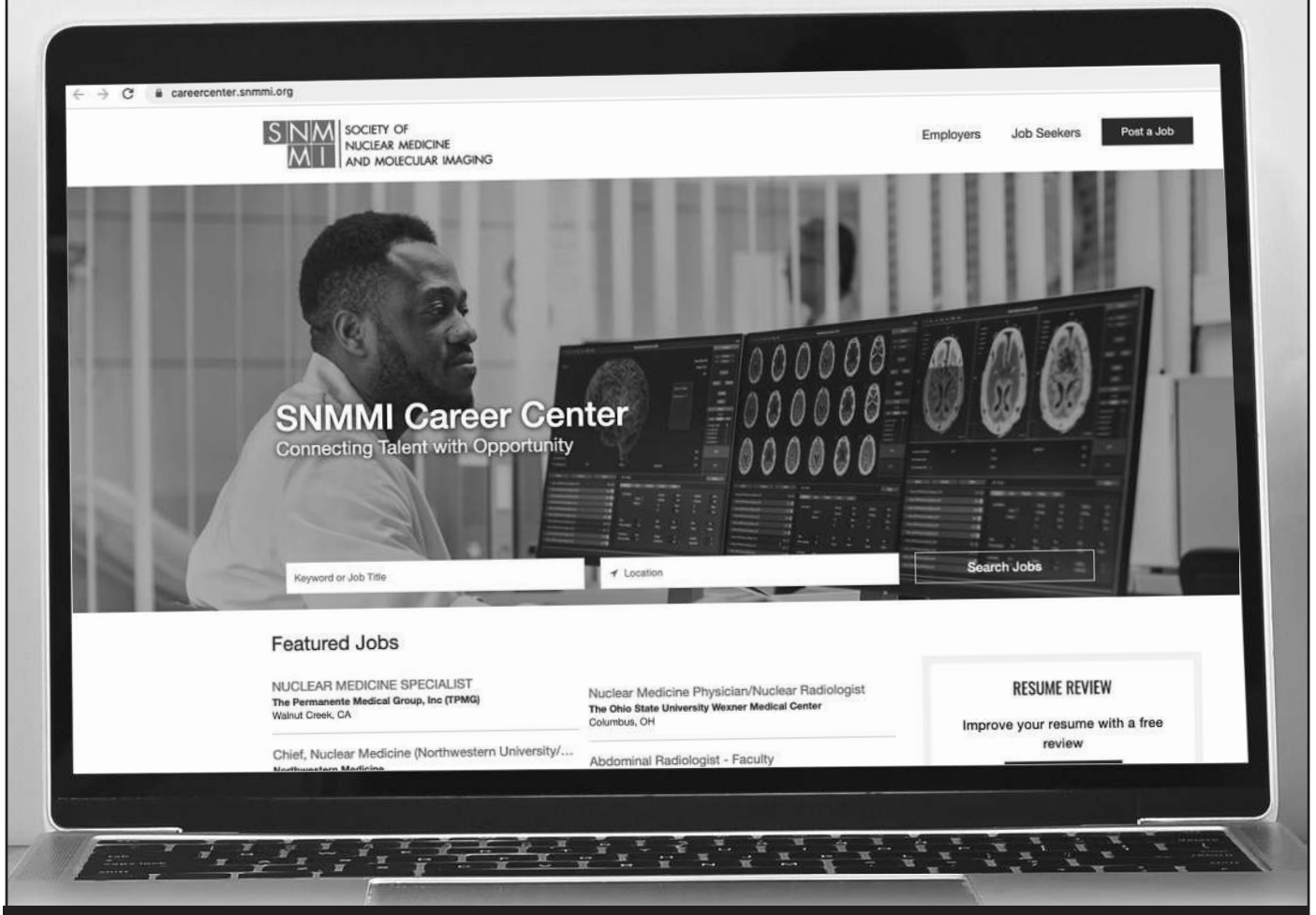

careercenter.snmmi.org

**Note: Single sign-on has been enabled for this platform and you can use your member login credentials to access the Career Center. If you are unsure of your password, to go to the SNMMI password reset link to create a new password.*

SNMMI Value Initiative

SOCIETY OF NUCLEAR MEDICINE & MOLECULAR IMAGING

NOW AVAILABLE

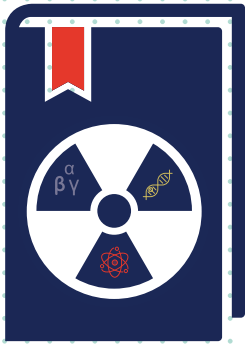

80 Hour Radionuclide Authorized User TRAINING COURSE

The Society of Nuclear Medicine and Molecular Imaging (SNMMI) and American Society of Nuclear Cardiology (ASNC) are excited to announce the launch of a new online course designed to provide nuclear medicine physicians with the knowledge needed to establish a culture of safety and quality in their practice.

The **ASNC/SNMMI 80 Hour Radionuclide Authorized User Training Course** features lectures on radiation protection and safe radioisotope handling, physics and instrumentation, radiochemistry and radiopharmaceuticals, radiation biology, and nuclear medicine mathematics and statistics, and will fulfill the 80 hours of classroom training that the U.S. Nuclear Regulatory Commission (NRC) and Agreement States require for physicians to become authorized users of radioisotopes for imaging and localization studies.

LEARN MORE: www.snmmi.org/80HourCourse

SNMMI Value Initiative
SOCIETY OF NUCLEAR MEDICINE & MOLECULAR IMAGING

American Society of Nuclear Cardiology

REACH EVEN GREATER HEIGHTS WITH CARDIAC PET IMAGING

RUBY™ partners with you to help establish and grow your cardiac PET program today – and well into the future. Our RUBY-FILL® (Rubidium Rb 82 Generator) and RUBY Rubidium Elution System™ are supported by our comprehensive line of offerings, including financial modeling, reimbursement consultancy, education, and marketing expertise – as well as 24-hour customer assistance to ensure your growing PET practice runs smoothly and efficiently. **Isn't it time to discover how far you can soar?**

Visit booth #1226 to learn more

INDICATION FOR USE:

RUBY-FILL is a closed system used to produce rubidium Rb 82 chloride injection for intravenous use. Rubidium Rb 82 chloride injection is a radioactive diagnostic agent indicated for Positron Emission Tomography (PET) imaging of the myocardium under rest or pharmacologic stress conditions to evaluate regional myocardial perfusion in adult patients with suspected or existing coronary artery disease. (1)

WARNING: HIGH LEVEL RADIATION EXPOSURE WITH USE OF INCORRECT ELUENT AND FAILURE TO FOLLOW QUALITY CONTROL TESTING PROCEDURE

Please see full prescribing information for complete boxed warning

High Level Radiation Exposure with Use of Incorrect Eluent

Using the incorrect eluent can cause high Strontium (Sr 82) and (Sr 85) breakthrough levels (5.1)

- **Use only additive-free 0.9% Sodium Chloride Injection USP to elute the generator (2.5)**
- **Immediately stop the patient infusion and discontinue the use of the affected RUBY-FILL generator if the incorrect solution is used to elute the generator (4)**
- **Evaluate the patient's radiation absorbed dose and monitor for the effects of radiation to critical organs such as bone marrow (2.9)**

Excess Radiation Exposure with Failure to Follow the Quality Control Testing Procedure

Excess radiation exposure occurs when the levels of Sr 82 or Sr 85 in the Rubidium Rb 82 Chloride injection exceed specified limits. (5.2)

- **Strictly adhere to the generator quality control testing procedure (2.6)**
- **Stop using the generator if it reaches any of its Expiration Limit. (2.7)**

The risk information provided here is not comprehensive. Please visit RUBY-FILL.com for full Prescribing Information including BOXED WARNING. You are encouraged to report negative side effects of prescription drugs to the FDA. Visit www.fda.gov/Safety/MedWatch or call 1-800-FDA-1088.

Jubilant DraxImage Inc. dba Jubilant Radiopharma™
16751 Trans-Canada Highway, Kirkland, Quebec, Canada H9H 4J4
Phone: 1.888.633.5343 / 514.630.7080
www.jubilantradiopharma.com

RUBY-FILL® RUBIDIUM Rb82 GENERATOR | JUBILANT RADIOPHARMA

6
22

The Journal of Nuclear Medicine

June 2022 ■ Vol. 63 ■ Pages 805–967